Oscillating grid turbulence and its influence on gas liquid mass transfer and mixing in non-Newtonian media

Tom Lacassagne

N°d'ordre NNT : 2018LYSEI103

THESE de DOCTORAT DE L'UNIVERSITE DE LYON
opérée au sein de
L'Institut National des Sciences Appliquées de Lyon

Ecole Doctorale N° 162
MEGA – Mécanique Energétique Génie Civil et Acoustique

Spécialité : Mécanique des fluides

Soutenue publiquement le 30/11/2018, par :
Tom Lacassagne

Oscillating grid turbulence and its influence on gas liquid mass transfer and mixing in non-Newtonian media

---

Devant le jury composé de :

CHAMPAGNE, Jean-Yves	Professeur, INSA Lyon	Président du Jury
HEBRARD, Gilles	Professeur, INSA Toulouse	Rapporteur
POLIDORI, Guillaume	Professeur, URCA, Reims	Rapporteur
HERLINA, Herlina	Dr. Ing., KIT, Karlsruhe	Examinatrice
EL HAJEM, Mahmoud	Maitre de Conférences, INSA Lyon	Directeur de thèse
SIMOENS, Serge	Directeur de Recherche, CNRS	Co-directeur de thèse

Remerciements

Contrairement à une idée répandue, le travail d'un doctorant n'est pas totalement dépourvu d'interractions sociales.

Je profite donc de ces quelques lignes pour remercier les gens qui m'ont accompagné un bout du chemin, plus ou moins long, au cours de ces trois dernières années et quelques mois.

Merci tout d'abord aux professeurs Gilles Hébrard et Guillaume Polidori d'avoir accepté d'en être les rapporteurs, et au Dr. Herlina pour sa participation au jury.Je remercie l'INSA de Lyon d'avoir financé cette thèse. J'y aurais finalement passé plus de 8 ans (affection, opportunités ou syndrome de Stockholm, libre à chacun de se demander pourquoi!), accumulé énormément de souvenirs et surtout beaucoup appris.

Je tiens également à remericer les nombreuses personnes rencontrées au fil des expériences, des conférence ou des (du!) CST pour leur aide matérielle, leurs conseils, ou tout simplement leur oeil extérieur qui ont grandement contribué à cette thèse: Frédéric Augier (IFPEN), Mahmed Boutaous (CETHIL), Régis Philippe (LGPC), Jean-Marie Bluet (INL), Laetitia Martinie (LamCos), Claude Inserra (LabTau).

Un grand merci également au LMFA de Philippe Blanc-Benon pour son acceuil, et à tous ses membres qui m'ont aidé un moment ou l'autre. Merci en particulier à Nathalie Grosjean pour ses conseils précieux en matière de PIV, à Valéry Botton, Emmanuel Mignot ou encore Cyril Mauger pour les dépanages de matériel en tout genre, et à Trong-Dai NGuyen et ses imprimantes 3D Raion sans qui ni étanchéité ni stéréo PIV n'auraient pu fonctionner.

Merci ensuite à mes collègues et amis doctorants ou ex-doctorants Trong-Dai Nguyen, chef Bongo Djimako, Hassan Barkai Allatchi, Sara Cleve, Armando Femat-Ortiz, Clément Perrot-Minot Sebastien Pouchoulin, Nouhayla El-Gahani, Hossein Ghaffarian, Virgile Tavernier, Gaby Launay. Tous toujours disponibles pour "porter des trucs", éponger des fuites, parler géopolitique ou manger des gateaux!

Merci à Jean-Yves Champagne d'avoir joué par le sauveur administratif au début, et d'être sorti de sa retraite à la fin, pour faire partie du jury. Merci à Serge Simoëns et Mahmoud EL Hajem pour la confiance et la liberté qu'il m'ont accordé, et le juste dosage entre autonomie et conseils qu'ils ont su trouver. Je joint à ce remerciement Cyril, qui sans faire partie de l'encadrement de cette thèse, est le premier à m'y avoir donné gout, et m'a de nombreuses fois conseillé et encouragé.

Un immense merci à ma famille et mes amis de s'être interressé à ce que je faisais. Merci à eux de m'avoir posé des questions, d'avoir compris les réponses (pour les scientifiques de la bande), d'avoir essayé de me faire croire qu'ils comprenaient, ou d'avoir eu l'honneteté de me dire que non.

Mon dernier et plus grand remerciement est pour Soline. Elle était la bien avant le début, m'a soutenu pendant, et sera là bien après la fin. Deux thèse pour le prix d'une, c'était une grande aventure, mais ni la première ni la dernière qu'on vivra ensemble.

Abstracts

Short abstract (EN - 300 words)

The study of turbulence induced mass transfer at the interface between a gas and a liquid is of great interest in many environmental phenomena and industrial processes. Even though this issue has already been studied for several decades, its understanding is still not good enough to create realistic models (RANS or sub-grid LES), especially when considering a liquid phase with a complex rheology. This experimental work aims at studying fundamental aspects of turbulent mass transfer at a flat interface between carbon dioxide and a Newtonian or non-Newtonian liquid, stirred by homogeneous and quasi isotropic turbulence.

Non-Newtonian fluids studied are aqueous solutions of a model polymer, Xanthan gum (XG), at various concentrations, showing viscoelastic and shear-thinning properties. Optical techniques for the acquisition of the liquid phase velocity field (Stereoscopic Particle Image Velocimetry, SPIV) and dissolved gas concentration field (Inhibited Planar Laser Induced Fluorescence, I-PLIF) are for the first time coupled, keeping a high spatial resolution, to access velocity and concentration statistics in the first few millimetres under the interface. A new version of I-PLIF is developed. It is designed to be more efficient for near surface measurements, but its use can be generalized to other single or multiphase mass transfer situations. Bottom shear turbulence in the liquid phase is generated by an oscillating grid apparatus. The mechanisms of turbulence production and the characteristics of oscillating grid turbulence (OGT) are studied. The importance of the oscillatory component of turbulence is discussed. A mean flow enhancement effect upon polymer addition is evidenced. The mechanisms of turbulent mass transfer at a flat interface are finally observed in water and low concentration polymer solutions. A conditional analysis of turbulent mass fluxes allows to distinguish the type of events contributing to mass transfer and discuss their respective impact in water and polymer solutions.

Key words: Non-Newtonian media, Oscillating grid turbulence, Gas-liquid Mass transfer, Mixing, PIV, PLIF

Résumé court (FR - 300 mots)

L'étude du transfert de masse turbulent aux interfaces gaz-liquide est d'un grand intérêt dans de nombreuses applications environnementales et industrielles. Bien que ce problème soit étudié depuis de nombreuses années, sa compréhension n'est pas encore suffisante pour la création de modèles de transfert de masse réalistes (de type RANS ou LES sous maille), en particulier en présence d'une phase liquide à rhéologie complexe. Ce travail expérimental a pour but l'étude des aspects fondamentaux du transfert de masse turbulent à une interface plane horizontale entre du dioxyde de carbone gazeux et une phase liquide newtonienne ou non, agitée par une turbulence homogène quasi isotrope.

Les milieux liquides non newtoniens étudiés sont des solutions aqueuses d'un polymère dilué à des concentrations variables et aux propriétés viscoélastiques et rhéofluidifiantes. Deux méthodes de mesure optiques permettant l'obtention du champ de vitesse de la phase liquide (SPIV) et de concentration du gaz dissout (I-PLIF) sont couplées tout en maintenant une haute résolution spatiale, afin de déduire les statistiques de vitesse et de concentration couplées dans les premiers millimètres sous la surface. Une nouvelle version de I-PLIF est développée pour les mesures en proche surface. Elle peut également s'appliquer dans différentes études de transfert de masse. La turbulence de fond est générée par un dispositif de grille oscillante. Les mécanismes de production et les caractéristiques de la turbulence sont étudiés. L'importance de la composante oscillante de la turbulence est discutée, et un phénomène d'amplification de l'écoulement moyen est mis en évidence.Les mécanismes du transfert de masse turbulent à l'interface sont finalement observés pour l'eau et une solution de polymère dilué à faible concentration. L'analyse conditionnelle des flux de masse turbulent permet de mettre en évidence les évènements contribuant au transfert de masse et de discuter de leur impact relatif sur le transfert total.

Mots-clef : Milieux non newtoniens, Turbulence de grille oscillante, Transfer de masse gaz-liquide, Mélange, PIV, PLIF

Résumé long (FR - 1500 mots)

L'étude du transfert de masse turbulent aux interfaces gaz-liquide est d'un grand intérêt dans de nombreuses applications environnementales et industrielles. La turbulence joue par exemple un rôle majeur dans l'accélération de la dissolution des gaz atmosphériques, comme le dioxyde de carbone, dans les océans, lacs et rivières. Les mêmes mécanismes d'accélération interviennent dans de nombreux dispositifs ou procédés industriels, comme les photobioréacteurs pour la culture de microalgues ou les réacteurs polyphasiques dans l'industrie chimique et pharmaceutique. Dans de nombreuses applications, les phénomènes physiques mis en jeu dépendent des propriétés plus ou moins complexes de la phase liquide, comme par exemple sa rhéologie.

Bien que ce problème du transfert de masse diphasique turbulent soit étudié depuis de nombreuses années, sa compréhension n'est pas encore suffisante pour la création de modèles de transfert de masse réalistes (de type RANS ou LES sous maille), en particulier en présence d'une phase liquide à rhéologie complexe. Pour des fluides Newtoniens comme l'eau, les mécanismes locaux de transfert de masse dans de très fines sous-couche proche de l'interface sont encore mal compris. D'un point de vue global, des corrélations empiriques sont établies, pour des fluides Newtoniens, afin de déterminer la vitesse de dissolution d'un gaz dans une phase liquide à partir de la géométrie d'un système donné et des propriétés de la turbulence. Ces corrélations ne permettent pas de prédire efficacement cette vitesse dans le cas de fluides non-Newtoniens. La encore, il manque des informations sur les phénomènes locaux de transfert.

Ce travail expérimental a pour but l'étude des aspects fondamentaux du transfert de masse turbulent à une interface plane horizontale entre du dioxyde de carbone gazeux et une phase liquide, newtonienne ou non, agitée par une turbulence de fond, homogène quasi isotrope, et associée à un faible écoulement moyen.

Le dioxyde de carbone est un gaz dont la diffusivité, comme les autres gaz atmosphériques, est bien plus lente en phase liquide qu'en phase gazeuse. Il est choisi pour sa compatibilité avec les techniques de mesures utilisées au cours de cette thèse, mais aussi pour les nombreuses applications environnementales et industrielles où on le retrouve. Les milieux liquides non newtoniens étudiés sont des solutions aqueuses d'un polymère dilué, la gomme de xanthane, à des concentrations variables et aux propriétés viscoélastiques et rhéofluidifiantes. Ce polymère est choisi pour sa forte résistance aux variations de pH, permettant de l'utiliser en présence de dioxyde de carbone dissout ou d'autres substances acides. Une importante étude préliminaire de caractérisation des interraction entre dioxyde de carbone et la gomme de xanthane a été réalisée. On démontre que les modifications en termes de rhéologie ou d'équilibres chimique sont mineures lorsque les deux espèces sont mises en présence.

Le cas d'une surface libre plane horizontale est choisi de manière à visualiser le comportement de la turbulence et du transfert de masse proche d'une interface de forme simple. Deux méthodes de mesure optiques permettant l'obtention du champ de vitesse de la phase liquide (SPIV) et de concentration du gaz dissout (I-PLIF) sont couplées tout en maintenant une haute résolution spatiale, afin de déduire les statistiques de vitesse, de concentration, et les flux de mase turbulents dans les premiers millimètres sous la surface. La méthode SPIV permet de mesurer les trois composantes du champ de vitesse dans un plan vertical, ce qui n'avait jamais été fait auparavant. La technique de mesure de concentration de gaz dissout est basée sur l'acquisition du signal de fluorescence d'un marqueur initialement mélangé à la phase liquide. L'intensité et la couleur de rayonnement de ce marqueur dépendent localement du pH, et donc par équilibre chimique, de la concentration de gaz dissout. Déjà utilisée

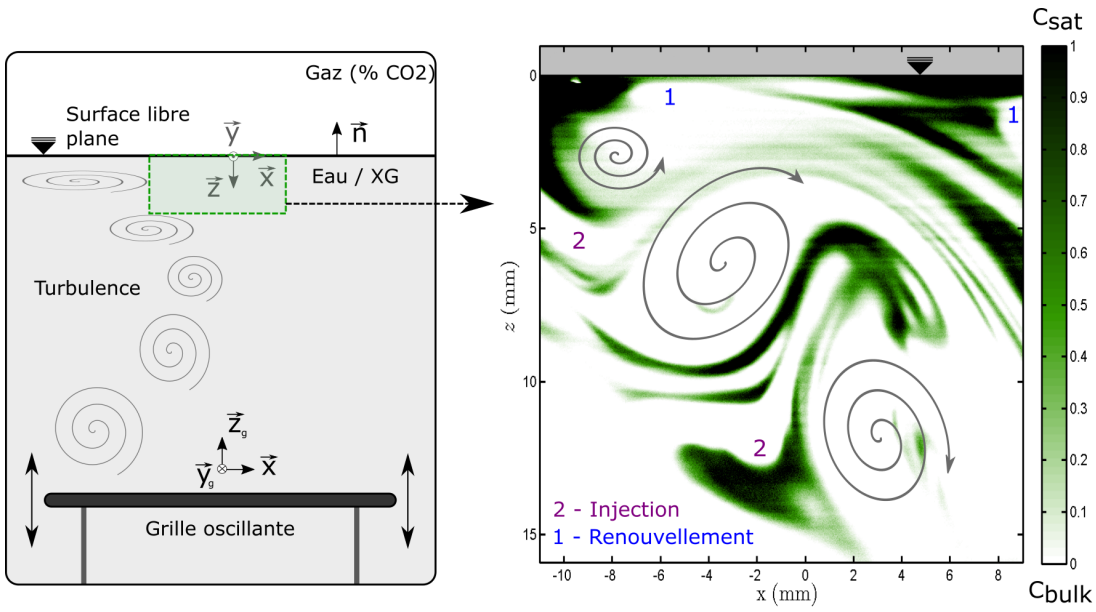

FIGURE 1 – Principes du transfert de masse gaz-liquide en présence d'une turbulence de fond générée par grille oscillante

pour mesurer des champs de concentration de dioxyde de carbone dans diverses configurations diphasiques ou turbulentes, la méthode a été améliorée dans le cadre de cette thèse afin de faciliter son utilisation dans le cas de systèmes optiques non fins, avec des interfaces diphasiques, ou présentant de fortes instationarités d'éclairement. Il a également été vérifié qu'elle était applicable en solution de polymère dilué. En plus de l'utilisation de la SPIV, le couplage spatial et temporel de ces deux méthodes optiques, la résolution spatiale supérieure aux mesures existantes, et leur application à des solutions de polymère dilué constituent la nouveauté de ce travail.

La turbulence de fond est quant à elle générée par un dispositif de grille oscillante, étudié depuis de nombreuses années dans l'eau (1, gauche) , et permettant d'y générer une turbulence contrôlée, isotrope et homogène dans les plans horizontaux, avec un faible écoulement moyen. Cet outil permet donc d'étudier les effets de la turbulence seule sur le transfert de masse à l'interface, en s'affranchissant des effets liés aux gradients moyens de vitesse. Cependant, si les caractéristiques de cette turbulence sont bien connues pour l'eau, elles n'ont jamais été décrites dans des solutions non-Newtoniennes de polymère dilué.

Au cours de cette thèse, les caractéristiques de la turbulence de grille oscillante dans l'eau et dans des solutions de gomme de xanthane sont étudiées. On s'intéresse en particulier aux mécanismes de génération de cette turbulence par la grille et à son évolution dans l'ensemble de la cuve. L'importance de la composante oscillante de la turbulence, corrélée au déplacement de la grille, est discutée. Il apparait que cette composante disparait en dehors de la zone de balayage de la grille. Un phénomène d'amplification de l'écoulement moyen lors de l'ajout de polymère est également mis en évidence. Les différentes phases d'évolution de l'écoulement moyen permettent de dégager deux concentrations critiques de polymère. Enfin, les lois d'évolution de la turbulence avec la distance à la grille, connues pour l'eau, sont établies pour des solutions de polymère dilué à différentes concentrations. On observe en particulier une augmentation du taux de décroissance de la turbulence et une augmentation du taux de croissance des échelles intégrales pour de très faibles concentrations de polymère ($C_{XG} < 50$ ppm).

Les mécanismes du transfert de masse turbulent (figure 1, droite) à l'interface sont fi-

nalement observés pour l'eau et une solution de polymère dilué à faible concentration (C_{XG} < 100 ppm). En revanche notre dispositif de mesure permet de visualiser avec une bonne précision les phénomènes hydrodynamiques et de transfert de masse ayant lieu dans et autour de la zone définie comme la sous-couche visqueuse. Les principaux concepts de l'hydrodynamique proche de la surface libre, établis dans l'eau, son également vérifiés pour les fluides non newtoniens étudiés : le transfert d'énergie de la composante verticale vers les composantes horizontales est ainsi mis en évidence. Un mécanisme de dissipation des fluctuations horizontales, propre au polymère mais semblable à celui introduit par la pollution de surface, semble également apparaitre. L'étude des flux de quantité de mouvement permet de décrire la complexité de l'hydrodynamique sous la surface. Les statistiques de concentration de gaz dissout sont ensuite obtenues via une analyse fine des mesures PLIF. A partir des statistiques de concentration et de vitesse couplées, les flux de masse turbulents sont obtenus. Leur analyse conditionnelle permet de mettre en évidence les évènements contribuant au transfert de masse et de discuter de leur impact relatif sur le transfert total. Une différence de comportement ente eau et fluide non Newtonien en termes de transfert de masse est d'ores et déjà observée pour une très faible concentration de polymère dilué (C_{XG} = 10 ppm). Cette différence se matérialise par une modification apparente de la vitesse de transfert de masse global.

Ces mesures ouvrent de nombreuses pistes dans l'étude du transfert de masse depuis un gaz vers une liquide non-newtonien en présence de turbulence. Les mesures stéréo PIV permettraient en particulier d'étudier les relations entre les évènements verticaux de transfert de masse et les modèles à divergence de surface permettant de prédire la vitesse de transfert. La résolution spatiale de ces mesures permet également d'investiguer des phénomènes très proches de la surface, dans l'eau comme dans les fluides complexes. Une analyse spectrale des flux de masse turbulents permettrait à terme d'identifier, dans les deux types de milieux, les tailles de structures à l'origine des différents évènements de transfert de masse, et ainsi discuter leur importance relative dans la vitesse du processus.

Contents

List of Figures

List of Tables

Nomenclature

Abbreviations

DIC Dissolved Inorganic Carbon dioxide

I – PLIF Inhibited Planar Laser Induced Fluorescence

I^r_{pH} – PLIF Ratiometric, pH sensitive Inhibited Planar Laser Induced Fluorescence

I^r_T – PLIF Ratiometric, temperature sensitive Inhibited Planar Laser Induced Fluorescence

I_{O_2} – PLIF Inhibited Planar Laser Induced Fluorescence for dissolved oxygen concentration measurement

I_{pH} – PLIF pH sensitive Inhibited Planar Laser Induced Fluorescence

I_T – PLIF Temperature sensitive Inhibited Planar Laser Induced Fluorescence

2D2C Two dimensions, two components

2D3C Two dimensions, three components

BJ Related to Brumley and Jirka (1987)

CG Close Grid region

CWL Continuous Wave Laser

CY Carreau-Yasuda (fitting, law...)

DNS Direct Numerical Simulation

DPS Dilute polymer solution

DR Drag Reduction

FT Full Tank

GN Grid neighborhood region

HIT Homogeneous Isotropic Turbulence

HT Related to Hopfinger and Toly (1976)

HXi Hexadecan i

LES Large Eddy Simulation

LIF Laser Induced Fluorescence

MCFD Multiphase Computational Fluid Dynamics

Nd:YAG Neodymium-doped Yttrium Aluminium Garnet (laser)

OGT Oscillating Grid Turbulence

PDF Probability Density Function

PEO Poly-Ethylene Oxide

PIV Particle Image Velocimetry

PLIF Planar Laser Induced Fluorescence

POD Proper Orthogonal Decomposition

PTV Particle Tracking Velocimetry

Qi Quadrant i

RANS Reynolds Averaged Navier Stokes Equations

RASJA Random Array of Synthetic Jets Actuators (Variano and Cowen, 2013)

SPIV Stereoscopic Particle Image Velocimetry

SZ (Grid) Sweep Zone region

TKE Turbulent Kinetic Energy

TT Related to Thompson and Turner (1975)

XG Xanthan gum

Chemistry

[.] Molar concentration

F*l* Fluorescein sodium (all forms included)

Fl^+ Cationic forms of fluorescein sodium

Fl^- Mono-anionic forms of fluorescein sodium

Fl^n Neutral forms of fluorescein sodium

Fl^{2-} Dianionic forms of fluorescein sodium

H_2CO_3 Carbonic acid

$H_2CO_3^*$ Apparent carbonic acid (carbonic acid plus aqueous carbon dioxide

$NaOH$ Sodium hydroxide

CO_2 Carbon dioxide

CO_3^{2-} Carbonate ion

HCO_3^- Hydrogen carbonate ion

O_2 Di-oxygen

Dimensionless numbers

Ca Capillary number

De Deborah number

Fr Froude number

Ha Hatta number

Re Reynolds number

Re_g Grid Reynolds number

Re_T Turbulent Reynolds number

Re_λ Reynolds number based on the Taylor microscale

Sc Schmidt number

St PIV particles Stokes number

Wi Weissenberg number

Statistics and operations

$\langle a \rangle_{\phi,rms}$ Phase rms of a

$\langle a \rangle_\phi$ Phase average of a

$\langle a \rangle_{rms}$ Root mean square (rms) value of a

$[a]_X$ Average of field a along dimension X

$[a]_{rms,X}$ RMS of field a along dimension X

$\mathbf{a} \cdot \mathbf{b}$ Dot product of a and b

∇ Gradient (nabla) operator

$\otimes$ Tensor product

$\overline{a}$ Statistical average of a

a' Turbulent fluctuation of a

a^* Oscillatory/periodic fluctuation of a

P(a,b) Joint probability of variables a and b

Symbols

α Scheimpflung angle

β Instantaneous surface divergence

$\dot{\boldsymbol{\gamma}}$ Shear rate tensor

$\boldsymbol{\nu_T}$ Eddy viscosity tensor

$\boldsymbol{\sigma}$ Cauchy stress tensor

$\boldsymbol{\tau}$ Shear stress tensor

δI_1 Intensity collected from spectral band 1

δI_2 Intensity collected from spectral band 2

ΔS Grid stroke sampling definition

Δt PIV time interval

δ_B Batchelor sub-layer

δ_D Apparent diffusive film thickness

$\delta_D^{(app)}$ (Apparent) diffusive sub-layer

δ_O Outer diffusive sub-layer

δ_ν Viscous sub-layer

δ_η Kolmogorov sub-layer

ϵ Fluorescein molar extinction coefficient (I-PLIF)

ϵ Turbulent dissipation rate

η Kolmogorov length scale

η_B Batchelor scale

Γ Mean to turbulence ratio

κ Wave number

λ_e Laser excitation wavelength

λ_f (fluorescence) Wavelength

λ_{ij}^k Taylor micro scale for components i and j in dimension k

$\mathbf{g}$ Gravity

$\mathbf{I}$ Identity matrix

$\mathbf{U}$ Liquid phase instantaneous velocity

$\mathcal{T}_{mo}$ Mean flow to oscillatory motion energy transfer term

$\mathcal{T}_{mt}$	Mean flow to turbulence energy transfer term
$\mathcal{T}_{ot}$	Oscillatory motion to turbulence energy transfer term
μ	Dynamic viscosity
μ_0	Zero shear rate viscosity
μ_∞	Infinite shear rate viscosity
μ_{app}	Apparent (approximated) viscosity
ν	Kinematic viscosity
Ω	Out-of-plane vorticity
ϕ	Fluorescence quantum yield (I-PLIF)
ρ	Density
ρ_p	PIV particles density
σ	Surface tension
θ	Stereoscopic PIV angle
Ξ	Grid solidity parameter
A	Optical constant
a	Newtonian to non-Newtonian transition parameter
C	Fluorescent dye concentration
C_i^k	Concentration of species i in phase k
$C_{b,i}^k$	Bulk concentration of species i in phase k
$C_{sat,i}^k$	Saturation concentration of species i in phase k
C_b	ROI bulk concentration
C_s	Measured surface concentration
$C_{1_{HT}}$	Hopfinger and Toly's constant for u'_x
$C_{2_{HT}}$	Hopfinger and Toly's constant for u'_z
C_{bt}	Bottom tank dissolved gas concentration
C_{sat}	Saturation concentration defined by Henry's law
C_{TT}	Thompson and Turner's constant
C_{XG}	Xanthan gum concentration
d	Grid bar size
D_i	Molecular diffusion coefficient of species i in water
D_i^k	Molecular diffusion coefficient of species i in phase k
dI_a	Local absorbed intensity
dI_f	Local fluoresced light intensity
dt	Camera's exposure time
e_L	Laser sheet thickness
f	Grid oscillations frequency
f	Lens focal length
f_{acq}	Acquisition frequency
G	Elastic modulus
G'	Storage/elastic modulus
G''	Dissipation/loss modulus
H_j^i	Homogeneity index of component j along dimension i
H_G	Average grid - bottom distance
H_S	Average grid - surface distance
$H_{c,i}$	Henry constant of species i
H_{tot}	Total fluid height in the tank
I_0	Laser output intensity
I_f	Fluoresced intensity
I_i	Incident intensity
I_r	Received fluoresced light intensity
I_s^{ij}	Isotropy indicator in dimensions i,j
k	Turbulent kinetic energy
K_a	Reaction constant of hydrogen carbonate production
K_b	Reaction constant of carbonate production
k_g	Gas side gas-liquid mass transfer coefficient
K_h	Reaction constant of carbonic acid production
k_L	Liquid side gas-liquid mass transfer coefficient
L_s	Length of fluid sample crossed by the incident beam
L_∞	Bulk integral length scale of turbulence
$L_{ij,\alpha}^k$	α percent integral length scale for components i and j in dimension k

L_{ij}^{k}	Integral length scale for components i and j in dimension k
L_{obs}	Distance between a point in the fluid and the sensor
M	Grid mesh parameter
m_i^k	Mass of species i in phase k
n_x	Exponent of the Hopfinger and Toly's decay law for u'_{rms}
N_p	Number of slices for the grid stroke sampling
p	liquid phase pressure
p_i^*	Partial pressure of species i
R	Spectral bands ratio
R^*	Wavelengths ratio
R_n	Normalized intensity ratio
R_r	Ratio submitted to re-absorption
R_{ij}^{k}	Correlation coefficient of components i and j in dimension k
S	Grid oscillations amplitude/stroke
S_ϕ	Spectral quantum yield
s_{px}	Surface of the laser sheet corresponding to one camera pixel
T	Characteristic deformation time
T^c	Integral concentration time scale
t_c	Characteristic relaxation time of a material/solution
t_D	Typical time scale of diffusion
T_g	Gas phase temperature
V_k	Volume of phase k
Z_h	Horizontal homogeneity limit for oscillating grid turbulence
K_L	Total gas-liquid mass transfer coefficient
t_{CY}	Characteristic polymer time scale extracted from CY fitting

Introduction

> All life is an experiment. The more experiments you make the better.
>
> Ralph Waldo Emerson

The study of mass transfer at the interface between a gas and a liquid is of great interest in many environmental phenomena and industrial processes. In the industry, the physics of mass transfer defines the efficiency of diphasic mixing and degassing in stirred tanks, bubble columns, or even more complex mixing tank geometries. As an example, in photobioreactors for micro-algae production, gaseous carbon dioxide CO_2 has to be dissolved into the culture waters to be then consumed through photosynthesis. Optimizing micro-alga production requires a better understanding and modelling of this CO_2 dissolution so that the mass transfer rate from gaseous to aqueous phase can be predicted and maximized (Valiorgue et al., 2014). From an environmental point of view, the same mechanisms also control the dissolution of atmospheric gases into the oceans, rivers and lakes, and have therefore a huge impact on climate and biodiversity. Even though this issue has already been studied for several decades, its understanding is still not good enough to create realistic models suitable for implementation in Multiphase Computational Fluid Dynamics (MCFD) codes. The difficulty in depicting such phenomena lies in the fact that they depend on numerous factors, among which, the diffusivity of transported species, the shape and dynamics of the interface, the characteristics of turbulence in each phase, the presence of chemical reactions, microorganisms, photocatalysis, and the possibly complex rheology of the liquid side.

Due to its strong ability in passive scalar mixing, turbulence is one of the main contributors to the efficiency of mass transfer. Its action is nevertheless quite complex, and it can have multiple effects in the full process. For example turbulence may both accelerate the growth of micro-organism by enhancing carbon dioxide dissolution into the culture medium, or reduce it by destroying cell clusters (San et al., 2017). In fermentation broths, the development of bacteria is powered by gas dissolution and turbulence. Yet this development causes the transition of the liquid phase from a Newtonian low viscosity to a high viscosity shear-thinning behavior, which itself tends to reduce mass transfer efficiency (Gabelle et al., 2011).

The part played by turbulence in gas-liquid mass transfer has been the subject of a huge amount of work for almost a century (Lewis and Whitman (1924) to Wissink et al. (2017)), but the exact mechanisms of mass transfer turbulent enhancement still remain unclear. Several investigations have been made using numerical simulations, channel flows, or stirred tank experiments (Herlina and Wissink, 2014; Turney and Banerjee, 2013; Variano and Cowen, 2013). Because of their environmental applications, most of these studies focused on dissolution of atmospheric gas into water, considered to be slow diffusion species. All studies

involving atmospheric gases and large Reynolds numbers on the liquid-side with respect to the one on the gas side agree on the fact that the influence of the interface on liquid-side turbulence is significant at very small depth of the order of 1 cm. The main challenge of current works is to achieve sufficient spatial resolution of simulations or experimental observations in order to describe the mass transfer phenomenon inside those small interfacial layers. Such a spatial resolution is nowadays achievable numerically thanks to the improvement of computational power allowing the use of direct numerical simulation (DNS) at small scales (Herlina and Wissink, 2014; Wissink et al., 2017). Experimentally, a wide range of optical techniques, boosted by growing data processing capacity, can be used to access instantaneous, multi-point and information of many properties of the flow: velocity, pressure, scalar field concentration (as in figure 2)...

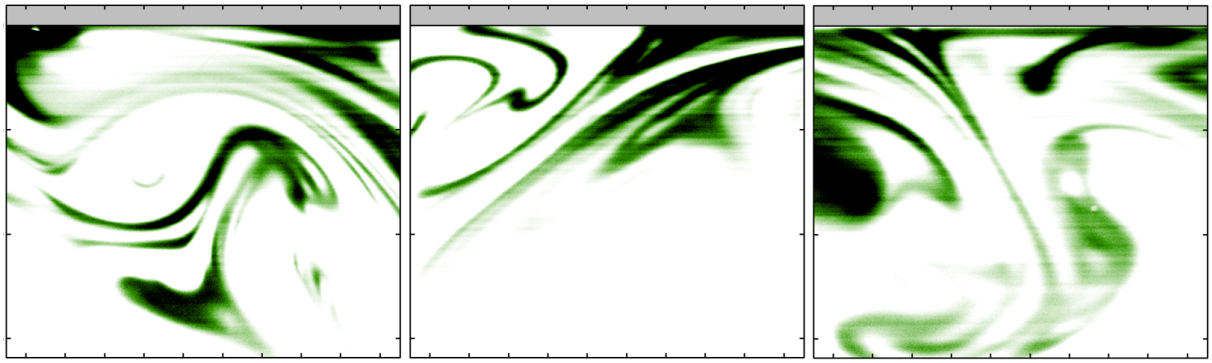

Figure 2 – Example of three instantaneous dissolved gas fields obtained by fluorescence imaging. White color represent the null dissolved gas concentration, green intermediate concentrations and black high concentrations (in arbitrary unit). Each picture is 19 mm wide along the horizontal dimension, and 16 mm along the vertical (depth). The gray rectangle denotes the gaseous phase saturated with CO_2.

While the understanding of turbulent gas-liquid mass transfer in water and more generally Newtonian fluids has improved in the last decades, the influence of the fluid's complex aspect and non-Newtonian behavior on fundamental principles of turbulent gas-liquid mass transfer remain unknown. The behavior of such fluids being very different from that of Newtonian liquids, specific features due to shear thinning or viscoelastic behaviors appear industrial processes (Gabelle et al., 2011; Xiao et al., 2014). Efficient models for Newtonian fluids fail at predicting mass transfer in non-Newtonian fluids. Despite the apparent interest for many industrial applications, the literature still lacks fundamental experiments and simulations to describe non-Newtonian turbulent mass transfer. Such studies have the same spatial resolution issues than experimentation in water with additional complexity brought by the coupling between polymer chains and turbulence.

One of the most popular experimental setups to study turbulence alone without any strong mean flow and its effects on mass transfer at a free surface is the oscillating grid system. Oscillating grid turbulence (OGT) has been used from more than 40 years and is still used nowadays (Hopfinger and Toly, 1976; Thompson and Turner, 1975) to study fundamental aspects of turbulence near solid boundaries (McCorquodale and Munro, 2018), in stratified media (Verso et al., 2017), and at gas-liquid interfaces (Brumley and Jirka, 1987; Chiapponi et al., 2012), or its action on dispersed phases of cells or fibers (Cuthbertson et al., 2018; Mahamod et al., 2017; Nagami and Saito, 2013; Rastello et al., 2017; San et al., 2017). Yet OGT has been used with non-Newtonian media only in a few studies (Liberzon et al., 2009; Wang et al., 2016), and never in a two phase configuration.

The present work is one of the first experimental focus on fundamental aspects of turbulent gas-liquid mass transfer in complex fluids. It organizes around three main guideline questions:

- How can non intrusive optical techniques be improved in order to get useful data at the small scales of turbulent mass transfer ?
- How does oscillating grid turbulence (OGT), long time studied in water, behave in complex polymer solutions; and how can we use the OGT tool to generate controlled turbulence in such fluids?
- What are the effects of complex rheological properties, in particular those of dilute polymer solutions, on near surface hydrodynamics, turbulent mixing, and mass transfer mechanisms at gas-liquid interfaces ?

With the aim of bringing part of the answers to those key questions, this work is focused on the case study of a well known gas: carbon dioxide. Optical metrology is developed and implemented in order to document its dissolution and turbulent mass transfer. Complex fluids are here modeled by shear thinning viscoelastic solutions of Xanthan Gum (XG). An oscillating grid system is designed for the study of turbulent gas-liquid mass transfer, and its behavior tested in non-Newtonian solutions. Turbulent gas-liquid mass transfer is finally addressed in simplified and fundamental conditions: at a flat interface with only liquid side bottom shear turbulence generated by an oscillating grid.

In this context, the manuscript is structured as follows. The first chapter is an introduction to the main concepts and phenomena studied in this thesis, namely gas-liquid mass transfer, turbulence and its mixing efficiency, and non-Newtonian fluids. The second chapter presents the two main experimental techniques employed throughout this thesis. A significant part of the chapter is dedicated to the development and improvement of the fluorescence based method used for dissolved gas concentration measurement. In the third chapter, results of an experimental study of OGT in water and dilute polymer solution are detailed. This chapter is also used to introduce and characterize XG. The last chapter details the experimental observations of carbon dioxide dissolution into water and aqueous XG solutions at a flat interface and under the action of OGT. As a conclusion, the main results exposed in the previous chapters are summarized, and perspectives and guidelines of future works are discussed.

Chapter 1

Definitions

It is better to know some of the
questions than all of the answers

James Thurber

Contents

Abstract (En)

This chapter provides an introduction to the main concepts and phenomena studied in this thesis. It starts with a definition of gas-liquid mass transfer and a presnetation of its main applications. Mass transfer from a gaseous phase towards a liquid one finds is ruled by Henry's law, which determines the equilibrium concentration ultimately reached by each phase. The speed at which transfer occurs depends on many parameters, among which the nature and shape of the interface, the aerodynamics of the gaseous phase, or in our focus, the hydrodynamics of the liquid phase. More specifically, liquid side turbulence enhances mass transfer in many environmental an industrial applications. Turbulence should then be defined, and this is done in the second part of the chapter. To do so, the governing equations of hydrodynamics and mass transport are expressed, and their stochastic version used for turbulent flow description are detailed. Characteristic quantities of turbulence and turbulent mixing are also defined. The last part of this chapter consists in a description and a definition of non-Newtonian fluids. The behavior of turbulence within those fluids is even more complex than the Newtonian case. Constitutive equations, modified governing equations, and specific quantities are introduced to try and describe it.

Résumé (Fr)

Ce chapitre sert d'introduction aux principaux concepts et phénomènes étudiés au cours de cette thèse. Il débute par une définition du transfert de masse gaz-liquide et une présentation de ses applications. Le transfert de masse d'une phase gazeuse vers une phase liquide trouve son origine dans la loi de Henry qui détermine la concentration d'équilibre entre les deux phases. La vitesse à laquelle se produit le transfert dépend de nombreux paramètres, parmi lesquels, la nature et la forme de l'interface l'aérodynamique de la phase gazeuse, ou encore celui qui nous intéresse dans cette thèse : l'hydrodynamique de la phase liquide. En particulier, la turbulence en phase liquide accélère le transfert de masse dans le cadre de nombreuses applications environnementales ou industrielles. Il convient donc de définir la turbulence, ce qui est fait dans une seconde partie. Pour ce faire les équations fondamentales de l'hydrodynamique et du transport de matière dans les fluides sont introduites, et leur version stochastique permettant de décrire les écoulements turbulents est présentée. Les grandeurs caractéristiques de la turbulence et du mélange en phase liquide sont finalement introduites. Enfin, la dernière partie de ce chapitre propose une description et une définition de ce que sont les fluides non Newtoniens. Présents dans de nombreuses applications, le comportement de la turbulence au sein de ces fluides est grandement complexifié par rapport au cas newtonien. Divers modèles de comportement, équations modifiées, et grandeurs spécifiques sont proposées pour tenter de décrire au mieux ces comportements.

This chapter provides introduction to the main concepts that will be used in the rest of the manuscript. Gas-liquid mass transfer, turbulence, and non-Newtonian fluids are introduced. The term of mass transfer is first defined, and physical phenomena governing mass transfer between a gaseous and a liquid phase are explained. Some common examples of gas-liquid mass transfer situations are also described. The second section starts with a brief introduction to turbulent flows and their governing equations and scaling. The effect of turbulence on passive scalar mixing in fluid flows is then discussed. In the last section, the non-Newtonian nature of a fluid is defined, and a brief review of existing non-Newtonian behaviors and their industrial, environmental, biological or every-day life applications is presented. Finally, relevant dimensionless numbers and governing equations for the description of non-Newtonian flows are defined.

In particular, non-Newtonian and turbulence-related definitions are later used in chapter 3 for the study of turbulence in shear thinning and viscoelastic dilute polymer solutions (DPS). Mass transfer physics is then added in chapter 4 to discuss gas dissolution at a flat gas-liquid interface in Newtonian or non-Newtonian media.

1.1 Gas-liquid mass transfer

In this section, the main principles of mass transfer are defined, and in particular those of mass transfer between a gaseous and a liquid phase. The concepts explained in the first paragraph are used to define a global approach to mass transfer measurements in a second paragraph, and illustrated by concrete industrial and environmental examples in the last paragraph.

1.1.1 Main principles

Mass transfer of a given species between two phases ϕ_1 and ϕ_2 is defined as the exchange of part or all the mass of this species from one phase to the other. This exchange is based on a thermodynamic transformation, chemical reaction, or both, allowing part of the species to change phase. One may distinguish between changes of state, which are purely thermodynamical processes involving one single species (e.g water boiling or condensation), and mass transfer between phases, which can be a combination of thermodynamical and chemical reactions and often involve two or more species (e.g. dissolution of salt into water). Depending on the two phases involved and the physics of the mass transfer, different names may be used (see figure 1.1).

In real life situations, many phases may be present at the same time, each of which containing several chemical species. Rivers and water ways and their interfaces with both atmospheric gases and bottom solid sediments, or industrial bubble columns reactors with solid catalyst particles are two good examples of how complex multiphase mass transfer situations can be.

All mass transfer problems are ruled by the mass conservation principle, which states that the total mass of a given element over all phases remains constant between the initial and the final states. Dealing with chemical reactions, one as to keep in mind that the conserved mass is not necessarily that of the chemical species, but the mass of chemical elements. A general mass conservation equation for species i in phase k of a system of N phases could be written as

$$\frac{dm_i^k}{dt} = \mathscr{P}_i^k - \mathscr{C}_i^k + \sum_{p=1}^{\mathrm{N}} \mathscr{J}_i^{p\longrightarrow k} \tag{1.1}$$

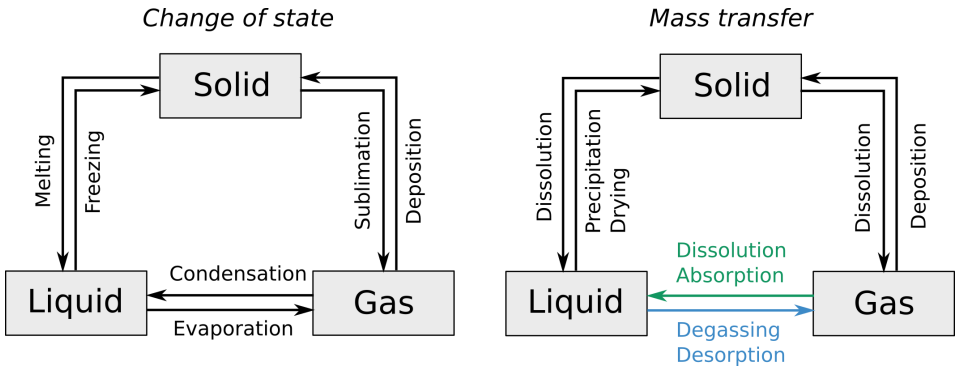

Figure 1.1 – Names of two phases mass transfer involving a single (change of state) or several species (mass transfer)

.

Where $\mathscr{P}_i^k$ and $\mathscr{C}_i^k$ are respectively the rates of production and consumption of species i in phase k, due for example to chemical reactions occurring in this phase; and $\mathscr{J}_i^{p\longrightarrow k}$ is the mass flux of species i from phase p to k. For a system with only two phases exchanging a single species i, and no production or consumption terms, this equation simplifies to:

$$\frac{dm_i^1}{dt} = \mathscr{J}_i^{2\longrightarrow 1} = -\mathscr{J}_i^{1\longrightarrow 2} = -\frac{dm_i^2}{dt} \tag{1.2}$$

Similar equations can be derived for the concentration C_i^k of species i in phase k. C_i^k is the intensive quantity corresponding to mass, which is extensive [1]

$$\frac{d\mathrm{C}_i^1}{dt} + \nabla j_i^{2\longrightarrow 1} = 0 \tag{1.3}$$

where ∇ is the gradient operator. This equation is the general governing equation for passive scalar transport. As defined above, the mass flux $j_i^{2\longrightarrow 1}$ is the net quantity of the considered species transferred from phase 2 to 1 in a time increment dt, per surface unit. This local mass flux is a function of the local gradient of concentration: if a concentration gradient exists, diffusion occurs in order to balance that gradient.

Diffusion is the displacement of species in a fluid induced by molecular dynamics. It is characterized by the molecular diffusion coefficient of species i in phase 1 D_i^1 in m^2/s. The greater the diffusion coefficient, the faster a species "moves" across a fluid at rest. According to Stokes-Einstein relationship, the diffusion coefficient of a species i in a solvent k scales as

$$\mathrm{D}_i^k \sim \frac{\theta}{r\mu} \tag{1.4}$$

where θ is the temperature, μ the dynamic viscosity and r the apparent radius of the molecule being diffused. For a given species, the diffusion coefficient thus increases with increasing temperature or decreasing viscosity. The previous relationship is valid for large molecules moving through Newtonian solvents under Brownian motion.

Fick's second law of diffusion assumes the local mass flux to be proportional to the local concentration gradient such that $j_i^{2\longrightarrow 1} = \mathrm{D}_i^1 \nabla \mathrm{C}_i^1$ (Fick, 1855). Other mechanisms can also be responsible of component motion in the fluid (electrical, magnetical, hydodynamic...). The

[1] **Intensive** quantities are quantities for which the magnitude does not depend on the size of the system, for example temperature or pressure. **Extensive** quantities are quantities for which are directly proportional to the amount of matter present in the system, for example the number of moles, volume, flow rate. Homogeneous systems are defined as systems where intensive quantities have the same value at all points.

most common one is of course the motion of the fluid itself. Transport of species by fluid motion is called convection or advection[2]. One of the hardest challenges in mass transfer studies is to account for the effect of advection in complex situations and complex fluids. Most of the time, the interactions between fluid motion and diffusion process at the interface are not well understood, mainly because the regions in which mass transfer occurs is beyond the spatial resolution capacity of many experimental methods and numerical simulations.

In the following sections, emphasis is given to gas-liquid mass transfer situations. However, most of the concept discussed remain valid for many other two phase mass transfer situations. We consider hereinafter the case a source gaseous phase ϕ_2 transferring mass to a liquid phase ϕ_1.

1.1.2 Global mass flux and mass transfer coefficient

Most of the mass transfer studies do not focus on local aspects but rather on estimating a global evolution of C_i^1 in the receptive fluid phase. The key parameter to estimate is then the global mass flux at the interface, which is generally written as :

$$j_i^{2\longrightarrow 1} = \frac{K_L}{L}\nabla C_i^1 \tag{1.5}$$

Where L is a typical length of transfer. The global mass balance equation for the ϕ_1 to ϕ_2 mass transfer is then:

$$\frac{\partial C_i^1}{\partial t} = K_L \frac{a}{V_1}\nabla^2 C_i^1 \tag{1.6}$$

with $L = V_1 / a$. The speed of a mass transfer process is thus conditioned by three main factors:

- **the surface of exchanges** a, and more specifically the ratio between this surface area and the volume of the receptive phase V_1.[3]
- the **gradient** of species ∇C_i^1. It can be related to **the tension** at the interface $\Delta C_i^1 = C_{i,sat}^1 - C_{i,b}^1$, which is the difference between the "bulk" (far from the interface) concentration $C_{b,i}^1$ of i in phase ϕ_1 at a given time, and the concentration $C_{sat,i}^1$ for which the two phases would be at equilibrium.
- **the mass transfer coefficient/velocity** of species i from 1 to 2, which depends itself on the physical and chemical mechanisms involved in mass transfer

1.1.2.a Surface of exchanges and interface gradient

For a constant V_1, the larger the surface, the faster the global transfer. Mass transfer is all the more efficient when the interfacial area is maximized with respect to the volume of the receptive phase. This one of the reasons for which mass transfer around bubbles at a given rise velocity is more efficient for a large number of small bubble than for fewer larger

[2] Here the term advection is preferably used in order to avoid confusion with heat transfer

[3] Note that a does not appear in equation (1.3) since it is a local mass transfer equation, but that the total mass flux in a global configuration is an integration of the mass flux per unit surface over the total surface of exchanges.

bubbles [4] .

When a gaseous and a liquid phase are in contact at an interface, the saturation value $C_{sat,i}$ in the liquid phase is fixed by the partial pressure of the same species in the gaseous phase p_i^* according to Henry's law [5] (Henry, 1803):

$$p_i^* = H_{c,i} C_{sat,i} \tag{1.7}$$

Where $H_{c,i}$ is a constant fixed by the gas-liquid couple used and by temperature. $\Delta C = C^1_{sat,i} - C^1_i$ powers mass transfer until the saturation value $C_{sat,i}$ is reached at every point of the volume of fluid.

1.1.2.b Mass transfer coefficient

The mass transfer coefficient K_L is the major parameter used to estimate the efficiency of mass transfer, which depends on many factors. The main ones are diffusion properties of the dissolved gas, chemical reactions involving transferred species, and hydrodynamics of the liquid phase.

For a gas-liquid interface where only diffusion occurs, Lewis and Whitman (1924) showed that the mass transfer coefficient may be decomposed as a series association of two mass transfer velocities, one on the liquid side k_L and one on the gas side k_g:

$$\frac{1}{K_L} = \frac{1}{k_L} + \frac{RT_g Hc}{k_g} \tag{1.8}$$

With R = 8.314 J.K^{-1}.mol^{-1} the ideal gas constant, and T_g the gas temperature. The inverse of mass transfer velocities evaluate resistance to mass transfer: $1/K_L$ is the equivalent resistance to mass transfer of two resistances in series, the liquid side one and the gas side one. For poorly soluble gases such as oxygen, nitrogen, or carbon dioxide, Henry's law constant H_c is about $H_c \sim 10^{-4}$ mol.m^{-3}.Pa^{-1} and $k_g >> k_L$. This implies that $\frac{RT_g H_c}{k_g}$, the gas side resistance, is weak, and that $K_L \sim k_L$.

With that picture, the mass flux going from the gaseous to the liquid phase is equal to the mass flux crossing the diffusive film. In other words, the concentration profile is linear in the diffusive layer (see figure 1.2) and the mass transfer coefficient is (Lewis and Whitman, 1924):

$$K_L = \frac{D_i}{\delta_D} \tag{1.9}$$

where $\delta_D = \frac{\Delta C^1_i}{\nabla_{int} C^1_i}$ is the diffusive film thickness, deduced from the concentration gradient at the interface $\nabla_{int} C^1_i$. The thinner the diffusive film, the larger the mass transfer velocity. Effects of advection on mass transfer can now quite easily be understood: by removing saturated fluid from the interface or by mixing efficiently the receptive phase, the thickness of the liquid film can be reduced and strong concentration gradients can be maintained at

[4] In reality, the question of mass transfer around bubbles is more complex since it also involves advection at the interface, which depends on the bubble rise velocity. This bubble rise velocity increases with buoyancy effects, and so with the bubble size

[5] This writing of Henry's law assumes that the thermodynamical activity coefficient of the dissolved gas γ_i and its fugacity coefficient ϕ_i are both equal to unity These assumptions are valid in thermodynamically ideal solutions, for which concentrations of salt and dissolved species are small, which is assumed to be the case here.

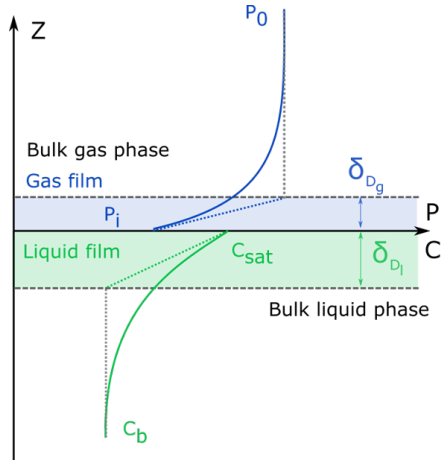

Figure 1.2 – Concept of the diffusion film in gas-liquid mass transfer

the interface, thus improving the diffusion efficiency. For example, the rising of bubbles in water due to buoyancy effects allows for the replacement of saturated fluid in the vicinity of the interface and to efficient mass transfer (Valiorgue et al., 2013; Vega-Martínez et al., 2017). As for bulk mixing, one of the most efficient process in that matter is without doubt turbulence. The reasons for this efficiency are explained in section 1.2.2. Fluid motion impact on the estimation of mass transfer coefficient is complex, and therefore many different models and empirical correlations exist depending on the type of flow and on the type of interface. It is worth noting that advection in the gaseous phase has the same effect on k_g, and thus on K_L for more soluble gases or in situations where gas-phase motions are much stronger that liquid phase motions (Zappa et al., 2007).

By consumption of the dissolved gas, chemical reactions can have an enhancing effect on mass transfer since it tends to lower concentration C_i^1 and sustain the concentration gradient ΔC. The efficiency of this enhancement depends on reaction kinetics versus diffusion: the quicker the reaction, the better its chances to happen entirely in the diffusive film. On the other hand, the faster the diffusion the better chances for the reaction to happen in the bulk. If reactions occur in the diffusive film, their impact on the interface gradient is much more significant. Moreover, if the reaction is not total, the nature of the limiting reactant and the extent of reaction strongly impact molecular diffusion.

The mass transfer velocity K_L, can be expressed as

$$K_L = f(\text{Fluid properties}, \text{Diffusion}, \text{Advection}, \text{Reaction}, \text{Interface shape and contamination}, ...) \tag{1.10}$$

With

- Fluid properties: temperature, density, shear dependent or constant viscosity, elasticity, presence of surfactant ...
- Diffusion: diffusion coefficient
- Advection: mean flows, turbulence, chaotic advection, mixing ...
- Reaction: consumption/production, kinetics ...
- Interface shape: Surface tension, interface deformation, bubbles sizes and shapes, bubbles breakup or coalescence...

All these characteristics are usually expressed in terms of representative non-dimensional numbers (Reynolds, Schmidt, Hatta, Bond...) providing correlation relationships. For example, mass transfer models at flat gas-liquid interfaces are usually function of the Reynolds and the Schmidt number accounting respectively for hydrodynamics of the liquid phase and diffusion effects (Theofanous, 1984; Turney and Banerjee, 2013). In bubbly flows, the effect of bubbles shapes and surface tension is included by the addition of Bond and Froude numbers to the correlation relationships (Kawase et al., 1987). Non-Newtonian properties can also be considered by introducing the Deborah or Weissenberg number (Nakanoh and Yoshida, 1980; Yagi and Yoshida, 1975).

The use of such global correlation relationships for the estimation of mass transfer coefficient is useful if one wants to estimate a global mass transfer velocity based on easily accessible process parameters. It is then possible to predict the evolution of concentration in the receptive phase quite easily, which is very interesting in terms of process or environmental engineering. However, these correlations have to be considered with caution: they are very specific to their situation and should be only used in the range of parameter values for which they have been built. The development of new correlation relationships requires both extensive parametric studies (Barrut et al., 2012; Theofanous, 1984; Turney and Banerjee, 2013) and the understanding of the local physics of mass transfer phenomena (Valiorgue et al., 2013; Variano and Cowen, 2013).

1.1.3 Examples

With those preliminary remarks, the key aspects of efficient gas-liquid mass transfer systems emerge. Chemical reactions using the transferred species as a reactant, maximization of interfacial areas, introduction of advection, efficient mixing of the liquid or gas phase, lengthening of the time of contact between the two phases are factors that contribute to make such processes more efficient. Example of common mass transfer devices or situations are exposed in what follows and in figure 1.3 as an illustration of the concepts discussed above.

- **Stratified flows**: Free surface flows are commonly found in both industrial (open channels, sewers, two phase flows in pipes...) and environmental situations (rivers,

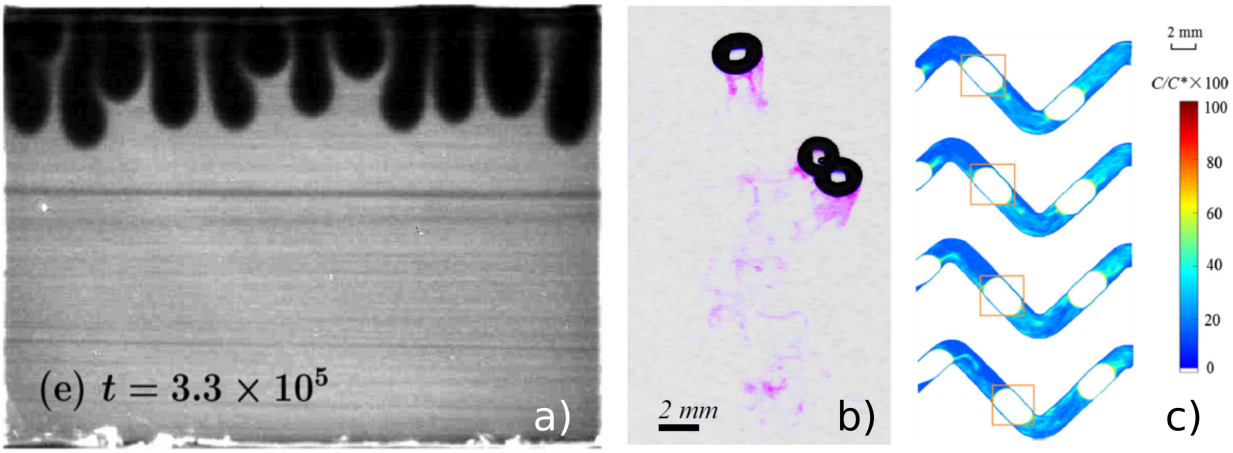

Figure 1.3 – Examples of gas-liquid mass transfer situations - fundamental aspect. (a) Convective instability triggered by CO_2 dissolution at a flat free surface measured by Vreme et al. (2016) fig. 2. (b) Visualisation of oxygen dissolution around a swarm of rising bubble by a colorimetric technique extracted from Dietrich and Hebrard (2018) figure 7. (c) Oxygen dissolution around Taylor bubbles in a meandering millichannel, extracted from Yang et al. (2017), fig.8a

oceans...). In such conditions, mass transfer occurs at the free surface and is enhanced by advection that may be due to the strong mean flow, re-circulations, and turbulence generated by bottom friction, wind shear or buoyancy (Magnaudet and Calmet, 2006; Sanjou et al., 2017; Turney and Banerjee, 2013). For example, rivers and oceans absorb an important part of greenhouse gases because of fluid side motion and turbulence (Banerjee, 2007; Gharahjeh et al., 2017; Zappa et al., 2007). Wastewater treatement plants on the other side release gases into the atmosphere under liquid motion and wind action (Prata et al., 2018). In the industry, stratified flows are used for example for mass transfer in photobioreactors (Valiorgue, 2012; Valiorgue et al., 2014).

- **Bubbly flows**: One of the best ways to maximize the gaz-liquid interfacial area is to create gas bubble into the liquid. Bubbles rise under buoyancy effect, which also causes advection of the dissolved gas at low energetic cost. Bubble swarms even produce turbulence in the liquid phase, thus further accelerating advection (Alméras et al., 2015, 2016; Ansari et al., 2018; Bouche et al., 2013). The applications of bubbly flows to mass transfer situations are numerous. One may cite the use of Taylor bubbles in micro or millifluidic setups (Kuhn and Jensen, 2012; Yang et al., 2017) or in tubular reactors (Butler et al., 2016; Nogueira et al., 2003), bubble columns (Chaumat et al., 2005; Chu et al., 2017; Fleischer et al., 1996; Kawase et al., 1987; Kováts et al., 2017; Manjrekar et al., 2017; Sellin et al., 2017) , or airlifts (Barrut et al., 2012; Han et al., 2017).

- **Agitated vessels**: Agitated vessels are commonly used in the food, pharmaceutical and chemical industries for their strong mixing ability (Escudié and Liné, 2003; Guillard et al., 2000; Hu et al., 2010). Intense liquid side turbulence in such devices is known to increase mass transfer at the free surface as in channel flows (de Lamotte et al., 2017) and to enhance bubble swarm dissolution by strongly increasing advection, bubbles time of travel and breakup in the fluid (Abdullah and Adesina, 2017; Gabelle et al., 2011; Lauwaert et al., 2017; Pashaei et al., 2017; Petříček et al., 2017).

Of course, many other cases of efficient gas-liquid mass transfer exist (falling film, plunging jets...). Moreover, in several devices, gas-liquid mass transfer is part of a complex multiphysical process. In structured pack columns for example (Solomenko, 2016), the complexity of solid wall geometries is such that mass transfer strongly depends on the triple contact line dynamics between gas-liquid and solid phases. In algae culture or other bioprocesses (Barrut et al., 2013; Chaumat et al., 2005; San et al., 2017), the growth and life of organic suspension has a strong action on both hydrodynamic and chemical aspects of mass transfer (action on viscosity or density, dissolved gas consumption, gas production...). In this thesis, focus is made on the effect of liquid side turbulence on mass transfer. To that extent, let us define turbulence, its properties and its effects in a liquid phase.

1.2 Turbulence

In this second section, an introduction to turbulence and its main properties is first proposed. Several quantities commonly used to quantify and measure turbulence properties are defined. In a second step, the effect of turbulence on the mixing of a passive scalar transported by the fluid are discussed.

1.2.1 General definitions

This section is based on the course "Cours de turbulence" (Turbulence courses) by F. Laadhari and J-N. Gence, Université Claude Bernard Lyon 1, University of Lyon (2015).

1.2.1.a What is turbulence?

It is very hard to give a precise definition of turbulence, even if most of the flows found in natural or industrial processes can be considered turbulent. River flows, oceanic currents, atmospheric dynamics, are some example of turbulent flows one may find in the environment. In the industry, most of the flows in pipes, tanks or channels are turbulent. As mentioned earlier (1.1.3), bubble swarms also generate turbulence.

Turbulent flows are seemingly unsteady and unpredictable, and observed to be composed of a wide size-range of whirling structures, called eddies. It implies that in turbulent flows, some fluid particles may move along directions that are not parallel to stream lines, whereas in laminar flows, all particles follow the "main" flow direction (that can be unidirectional, for example in pipe flows, or very complex as in laminar stirred tanks and chaotic flows). The existence of turbulent eddies is a tremendous asset for mixing. It indeed promotes scalar advection in all directions of the fluid. Turbulence is thus highly wanted in industrial mixers or reactors, and the best tool of anyone who mixes sugar in his coffee. On the other hand, the randomness of fluid velocity structures makes it almost impossible to predict with confidence the future motion of individual fluid particles. This makes for example the job of meteorologists all the more difficult. Sudden and violent changes in velocity directions, locally in the flow, due to turbulent eddies also generates high fluctuations of local shear stress, which might break suspended matter such as fibers, or limit the growth of cells or bio-organisms. For those reasons and from an industrial point of view, turbulence may be a wanted or unwanted feature of the flow. From an environmental point of view, turbulence is the reason behind many observed phenomena, even if its action is not always well known (greenhouse gas capture in the oceans, suspended matter clustering...).

1.2.1.b Fluid motion equations

Governing equations do exist to predict fluid motion even in turbulent situations: these are the Navier Sotkes (NS) equations. Applying Newton's second law to fluid particles moving in an Eulerian frame, one can derive the following Navier Stokes momentum equation.

$$\frac{\partial \rho \mathbf{U}}{\partial t} + \nabla \cdot \left(\rho \mathbf{U} \otimes \mathbf{U}\right) = -\nabla \cdot p\mathbf{I} + \nabla \cdot \boldsymbol{\sigma} + \rho \mathbf{g} \tag{1.11}$$

Where ρ is the density, U the velocity field, p the pressure field, $\boldsymbol{\sigma}$ the Cauchy stress tensor, and $\mathbf{g}$ the gravity acceleration. The dot product and tensor product are respectively noted $\cdot$ and $\otimes$. Bolds symbols represent tensor or vector quantities.
Mass conservation equation for a fluid volume translates into the continuity equation:

$$\frac{\partial \rho}{\partial t} + \nabla . \left(\rho \mathbf{u}\right) = 0 \tag{1.12}$$

In any fluid, the Cauchy stress tensor $\boldsymbol{\sigma}$ can be decomposed into a hydrostatic or normal stress component $\zeta (\nabla \cdot \mathbf{U}) \mathbf{I}$, where ζ defines the "bulk" viscosity and $\mathbf{I}$ the identity matrix; and a deviatoric part corresponding to shear stress $\boldsymbol{\tau}$ such that:

$$\boldsymbol{\sigma} = \zeta (\nabla \cdot \mathbf{U}) \mathbf{I} + \boldsymbol{\tau} \tag{1.13}$$

In incompressible fluids, the mass conservation condition stated by equation (1.12) imposes that the normal stress is null. Shear stress can be expressed as a function of the velocity field and other parameters such as the kinematic or dynamic viscosity ν or μ, with $\nu = \mu/\rho$. This expression is called the constitutive equation of the fluid. For a Newtonian isotropic and incompressible fluid, $\boldsymbol{\tau}$ is said to be proportional to the shear rate tensor $\dot{\boldsymbol{\gamma}} = \nabla\mathbf{U} + \nabla^{\mathrm{T}}\mathbf{U}$, which translates in term of constitutive equation into:

$$\boldsymbol{\tau} = \mu\left(\nabla\mathbf{U} + \nabla^{\mathrm{T}}\mathbf{U}\right) = \mu\dot{\boldsymbol{\gamma}} \tag{1.14}$$

Using this constitutive equation, the fact that for an incompressible fluid $\partial\rho/\partial t = 0$, and including gravity effects $\rho\mathbf{g}$ into the pressure term, equations (1.11) and (1.12) in index based notation become:

$$\frac{\partial \mathrm{U}_i}{\partial t} + \mathrm{U}_j\frac{\partial \mathrm{U}_i}{\partial x_j} = -\frac{1}{\rho}\frac{\partial \mathrm{P}}{\partial x_i} + \nu\frac{\partial^2 \mathrm{U}_i}{\partial x_j \partial x_j} \tag{1.15}$$

$$\frac{\partial \mathrm{U}_i}{\partial x_i} = 0 \tag{1.16}$$

Where U_i (resp. U_j) is the velocity component in dimension i (resp. j). All index-based equation use Einstein's summation convention. In equation (1.15), the first term is the rate of variation of the velocity component U_i, the second term represents advection of velocity by itself, or inertia. It is from this terms that comes the non linearity of the system that complexifies its resolution. The third term is related to pressure gradients in the fluid, and the last term embodies viscous dissipation of the motion.

Equations (1.15) and (1.16) fully describe the dynamics of incompressible Newtonian fluids, including turbulence. Yet, no generalised analyticall solution has been found so far, and the exact reasons for transition from laminar to turbulent flows are not fully understood even today. The origin of turbulence can be related to the competition between inertial and viscous effects. If the advection term of equation (1.15) becomes large with respect to the dissipation one, the flow regime is observed to change from laminar to turbulent. The relevant dimensionless quantity to describe the ratio of inertia over viscosity is the Reynolds number defined as

$$\mathrm{Re} = \frac{\mathrm{U}_0\mathrm{L}}{\nu} \tag{1.17}$$

Where U_0 is a characteristic velocity scale of the flow and L a reference length scale, for example a pipe diameter, stirrer blade size, or the typical size of the largest eddies. As a consequence, turbulence is a high-Reynolds number phenomenon. Considering that the advection term is non linear, the motion of the fluid particles when inertia dominates is highly dependent on small variations of the initial and boundary conditions, and since most of the time such conditions are not exactly known, the flow appears unpredictable.

1.2.1.c Reynolds decomposition

Due to these features, deterministic descriptions are often impossible, and one has to use stochastic methods to characterize scalar or vector fields in the fluid. One of the most common way of doing is called the Reynolds average decomposition and consist in splitting any field of interest f in an average component $\overline{f}$ and a fluctuating component f' representative of turbulence, such that $f = \overline{f} + f'$. This lays for example for the velocity field:

$$\mathrm{U}(\mathrm{M}, t) = \overline{\mathrm{U}}(\mathrm{M}, t) + u'(\mathrm{M}, t) \tag{1.18}$$

With such a decomposition, equation (1.15) breaks into

$$\frac{\partial \overline{\mathrm{U}}_i}{\partial t} + \overline{\mathrm{U}}_j \frac{\partial \overline{\mathrm{U}}_i}{\partial x_j} = -\frac{1}{\rho}\frac{\partial \overline{\mathrm{P}}}{\partial x_i} + \nu \frac{\partial^2 \overline{\mathrm{U}}_i}{\partial x_j \partial x_j} - \frac{\partial \overline{u'_i u'_j}}{\partial x_j} \tag{1.19}$$

$$\frac{\partial \overline{u'}_i}{\partial t} + \overline{\mathrm{U}}_j \frac{\partial u'_i}{\partial x_j} + u'_j \frac{\partial \overline{\mathrm{U}}_i}{\partial x_j} + u'_j \frac{\partial u'_i}{\partial x_j} - \frac{\partial \overline{u'_i u'_j}}{\partial x_j} = -\frac{1}{\rho}\frac{\partial p'}{\partial x_i} + \nu \frac{\partial^2 \overline{u'}_i}{\partial x_j \partial x_j} \tag{1.20}$$

The incompressibility equation (1.16) also becomes:

$$\frac{\partial \overline{\mathrm{U}}_i}{\partial x_i} = 0; \tag{1.21}$$

$$\frac{\partial u'_i}{\partial x_i} = 0 \tag{1.22}$$

A governing equation for the turbulent kinetic energy, defined as $k = \frac{1}{2}\overline{u'_i u'_i}$ can be derived from equation (1.20):

$$\underbrace{\frac{\partial k}{\partial t}}_{(1)} + \underbrace{\overline{\mathrm{U}}_r \frac{\partial k}{\partial x_r}}_{(2)} = \underbrace{-\overline{u'_i u'_r}\frac{\partial \overline{\mathrm{U}}_i}{\partial x_r}}_{(3)} \underbrace{-\frac{\partial \overline{u'_r u'_i u'_j}}{\partial x_r}}_{(4)} \underbrace{-\frac{1}{\rho}\frac{\partial \overline{p' u_i}}{\partial x_i}}_{(5)} \underbrace{+\nu\left(\frac{\partial^2 k}{\partial x_r \partial x_r} + \frac{\partial^2 \overline{u'_i u'_r}}{\partial x_i \partial x_r}\right)}_{(6)} \underbrace{-\frac{\nu}{2}\overline{\left(\frac{\partial u'_i}{\partial x_r} + \frac{\partial u'_r}{\partial x_i}\right)^2}}_{(7)} \tag{1.23}$$

Where the term (1) is the kinetic energy rate of variation, term (2) represents advection by mean flows, term (3) production by mean gradients, term (4) energy flux ruled by fluctuating motion (triple correlation), term (5) pressure velocity correlation, term (6) molecular diffusion, and term (7) dissipation.

1.2.1.d Closure relations

Fluctuating and average velocity fields are strongly coupled. In particular, compared to equation (1.15), a new term appears in the average velocity field equation ((1.19)): the spatial gradient of what is called the Reynolds stress tensor $\overline{u'_i u'_j}$. The Reynolds stress tensor represents the flux density of momentum associated with fluctuating motion. In other words, it quantifies the intensity of random (*i.e.* turbulent) eddies. Because the expression of the Reynolds stress is not known, the equations are not closed. A closure relation linking Reynolds stress to velocities or velocity fluctuations is needed if one wants to solve numerically the Reynolds averaged NS equations. A common closure strategy is to define an "eddy" or turbulent viscosity by writing

$$\overline{u'_i u'_j} = \nu_{\mathrm{T},ij} \frac{\partial \overline{\mathrm{U}}_i}{\partial x_j} \tag{1.24}$$

where $\nu_{\mathrm{T},ij}$ is the eddy viscosity 9 components tensor, so that equation (1.19) becomes

$$\frac{\partial \overline{\mathrm{U}}_i}{\partial t} + \overline{\mathrm{U}}_j \frac{\partial \overline{\mathrm{U}}_i}{\partial x_j} = -\frac{1}{\rho}\frac{\partial \overline{\mathrm{P}}}{\partial x_j} + (\nu + \nu_{\mathrm{T},ij}) \frac{\partial^2 \overline{\mathrm{U}}_i}{\partial x_j \partial x_j} \tag{1.25}$$

The next step is then to estimate this turbulent viscosity $\nu_{T,ij}$. To do so, one of the most basic ideas is to assume that turbulence is statistically homogeneous and isotropic. Equation (1.23) can thus be simplified and becomes:

$$\frac{\partial k}{\partial t} = -\frac{\nu}{2}\overline{\left(\frac{\partial u_i'}{\partial x_j} + \frac{\partial u_j'}{\partial x_i}\right)} = -\bar{\epsilon} \tag{1.26}$$

where $\bar{\epsilon}$ is the mean turbulence dissipation rate, hereinafter denoted ϵ for simplification. A governing equation for ϵ can be derived from the Reynolds averaged NS equations. It is of the form

$$\frac{\partial \epsilon}{\partial t} = \Delta(k, \epsilon) \tag{1.27}$$

By dimensional analysis, one may show that $\Delta = C_{\epsilon_2}\frac{k}{\epsilon}$, with the empirical constant $C_{\epsilon_2} \simeq 1.92$. The turbulent viscosity is then $\forall(i,j), \nu_{T,ij} = \nu_T = C_\mu \frac{k^2}{\epsilon}$, with $C_\mu \simeq 0.09$. The system composed of equations (1.26) and (1.27) can then be solved to describe the behavior of turbulence. This closure system is called the $k-\epsilon$ model. Of course it is limited by the very strong starting hypothesis of homogeneous and isotropic turbulence. More advanced models, eddy viscosity based or not, have been developed to solve the closure problem throughout the years (Durbin, 2018; Rodi, 2017). A good understanding of turbulence properties and its behavior in the specific situation of interest is necessary for the choice or determination of an appropriate closure relationship. When no existing closure model fits to the situation, fundamental turbulence studies and experimental observations are needed in order to develop a convenient one.

1.2.1.e Root mean square values

The ensemble root mean square operator is defined as $\langle f \rangle_{rms} = \sqrt{\frac{1}{N}\sum f^2}$ for the field f over a N sized discrete set of data. Applying it to velocity fluctuations, $\langle u' \rangle_{rms}$ is commonly used to quantify the intensity of turbulence. It can be computed at any point of a given field and thus yield a field of root mean squared turbulent fluctuations. Later in the manuscript (chapters 3 and 4) we will also use this definition to compute the ensemble root mean square of the correlation of two fluctuations, such as $\langle u_i' u_j' \rangle_{rms}$ or $\langle u_i' c' \rangle_{rms}$. This less conventional use of the rms somehow corresponds to an intensity of correlations independent of their ensemble averaged value. Finally, for phase resolved measurement, we can define the phase rms value of a field f at point k of the phase ϕ as the root mean square value of f over the ensemble of data N_k corresponding to position k in the phase. It is denoted $\langle f \rangle^k_{\phi,rms}$ (see chapter 3).

1.2.1.f Two point correlation and scales

Turbulence is said to be composed of a wide range of eddies of different sizes, or turbulent structures. The identification of a turbulent structure and the definition of its size is however delicate. Visually, one may define an eddy as a region of correlated swirling motion: the motion of each particle is essentially a rotation around a given point representing the center of the structure, and highly correlated to its neighbor's motion. It naturally endorses the use of the correlation coefficient for the identification of flow structures. The two point correlation coefficient R_{ij} between fluctuating components u_i' and u_j' is defined as:

$$R_{ij}(\mathbf{r}, t) = \frac{\overline{u_i' u_j'}(\mathbf{r}, t)}{\sqrt{\overline{u_i'^2}(t)\,\overline{u_j'^2}(t)}} \tag{1.28}$$

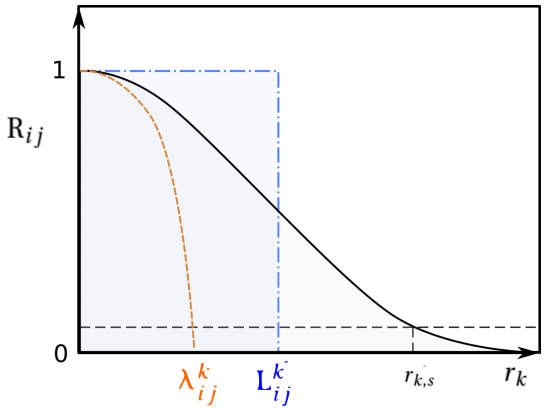

Figure 1.4 – Possible shapes of the correlation curves and definition of the integral and Taylor length scale

where $\mathbf{r}$ is the vector between two points in the fluid at which are measured u_i' and u_j' at instant t. By definition, $R_{ij}(\mathbf{o},t) = 1$ and $R_{ij}(-\mathbf{r},t) = R_{ij}(\mathbf{r},t)$. If $R_{ij} = 1$, u_i' measured at the first point and u_j' measured at the second are perfectly correlated. When $R_{i,j} \to 0$, they are uncorrelated. The correlation level decreases with $\mathbf{r}$. The apparent size of a structure can be estimated by statistically averaging curves for R_{ij}, and defining a threshold correlation level for which points are said to belong to the turbulent structure centered at $\mathbf{r} = 0$. The threshold is reached for a given separation value $\mathbf{r}_S$, which is an estimation of the size of the structure (see figure 1.4).

Another, less arbitrary definition is to define the size of the structure along a given dimension of $\mathbf{r}$ as:

$$L_{ij}^k = \int_0^\infty R_{ij}((r_k,0,0),t)dr_k \tag{1.29}$$

L_{ij}^k is called the integral length scale of u_i', u_j' fluctuations in dimension $k = 1..3$. In a three dimensional space, 9 integral length scales exist. They provide information on the typical size of the largest structures of the flow. Another interesting feature of the correlation coefficient curve is the rate at which the correlation coefficient decreases, which in some way depends on the size of the smallest structures of the flow. This is directly linked to the curvature of the R_{ij} curve at $r_k = 0$. For given components u_i' and u_j' and along a given dimension k, it is possible to define the Taylor microscale λ_{ij}^k as value of r_k as the intersection between the $R_{ij}^k = 0$ axis and the tangent parabola at $r_k = 0$ (see figure 1.4). This Taylor microscale can be used to evaluate the order of magnitude of velocity fluctuations gradients, which are representative of the small structures of turbulence. It is also often used to construct a small scale-based Reynolds number Re_λ which quantifies the intensity of turbulence regardless of the large scale forcing:

$$Re_\lambda = \frac{\langle u' \rangle_{rms} \lambda}{\nu} \tag{1.30}$$

With $\langle u' \rangle_{rms}$ the root mean square of velocity fluctuations and λ a representative Taylor micro scale of the flow. By analogy to the ensemble average $\overline{U}$, $\langle u' \rangle_{rms}$ is the root mean square value of u' over the set of data used to compute $\overline{U}$.

1.2.1.g Turbulence spectrum

The usefulness of correlation coefficient is limited to the definition of the two typical length scale of the flow, namely the integral length scale and Taylor microscale. In order to get

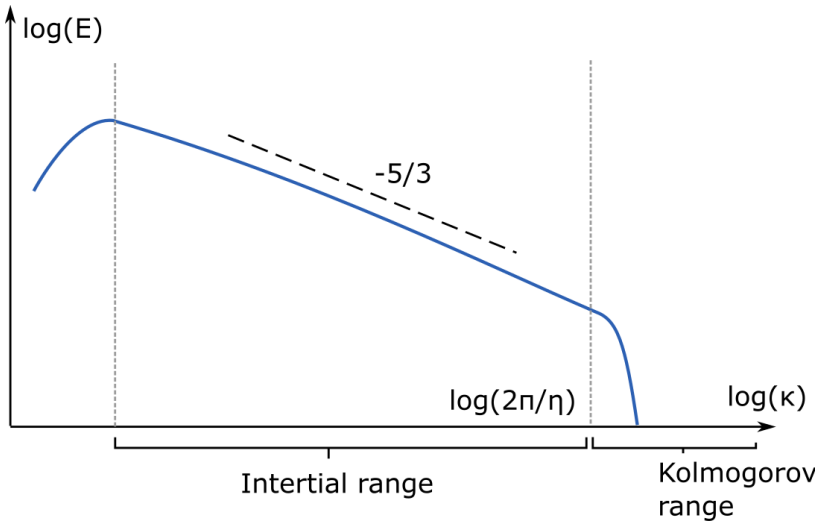

Figure 1.5 – Typical shape of the kinetic energy spectrum defined by Kolmogorov 1941 scaling. Energy is transferred from low to high wavenumbers (large to small structures) in a cascade process, and dissipated in the Kolmogorov range.

information on the role of different structure sizes, the three dimensional Fourier transform of the Reynolds stress tensor Φ is used. It is defined as the following volume integral

$$\Phi(\kappa, t) = \frac{1}{(2\pi)^3} \int_{\mathbb{R}^3} \overline{u_i' u_j'}(\mathbf{r}, t) e^{-i\kappa.\mathbf{r}} dV_r \tag{1.31}$$

Here κ is the wave number. It is representative of structure of typical size l such that $\kappa = 2\pi/l$. The unidimensionnal turbulence spectrum in direction k is then defined as:

$$\overline{u_i' u_j'}(t) = \int_{-\infty}^{+\infty} \mathrm{E}_{ij}^k(\kappa_k, t) d\kappa_k \tag{1.32}$$

One or three dimensional spectra somehow quantify the amount of kinetic energy carried by structures, size by size. Φ can be related to the turbulent kinetic energy by the following relation:

$$k = \frac{1}{2} \int_{\mathbb{R}^3} \Phi_{ii}(\kappa, t) dV_r \tag{1.33}$$

The basics of turbulence's spectral scaling were stated by Kolmogorov (Kolmogorov, 1941a,b,c, 1962), and are nowadays referred to as Kolmogorov 41 or K41 theory. The bigger structures are the ones that carry most of the kinetic energy. This energy is transferred to smaller scales in a cascade process, which is characterized by a $-5/3$ slope in the spectrum's inertial sub-range, as sketched on figure 1.5. Energy is then dissipated by viscous effects at small scales. The typical length scale under which viscous dissipation prevails is called the Kolmogorov microscale scale:

$$\eta = \left(\frac{\nu^3}{\epsilon} \right)^{\frac{1}{4}} \tag{1.34}$$

with ϵ the turbulent dissipation rate defined previously. It is assumed that this small scale dissipation is universal and exists in every turbulent flows. The inertial sub-range should also be visible in any turbulent flow with a high enough Reynolds number, *i.e.* a broad enough range of scales between the large scales at which the energy is injected and the small scales at which it is ultimately dissipated. This reference framework will be used as a basis of turbulence-passive scalar interactions developped in section 1.2.2.

1.2.1.h Triple decomposition

In some cases, the flow may display a periodic behavior due to external forcing or waves. Blade motion in stirred tanks (Escudié and Liné, 2003), periodic vortex shedding at rigid boundaries in free surface flows (Mignot et al., 2016), or pulsating flow in blood vessels induced by periodic heartbeats (Holdsworth et al., 1999) are good examples of flows in which an oscillatory/organised/periodic effect is present. Oscillating grid turbulence used in this work is another one. In such flows, the time average of the oscillatory component of the flow is null. Hence when using Reynolds decomposition to describe them, periodic fluctuations are included in u' while they are not strictly speaking turbulent fluctuations.

To be able to distinguish turbulence from organised motion, Hussain and Reynolds (1970) proposed a triple decomposition of the velocity field, that will be called triple decomposition hereinafter. The total instantaneous velocity field is this time written as the sum of the average velocity $\overline{\mathrm{U}}$, the periodic fluctuation u^* and the turbulent fluctuation u'.

$$\mathrm{U}(\mathrm{M},t) = \overline{\mathrm{U}}(\mathrm{M},t) + u^*(\mathrm{M},t) + u'(\mathrm{M},t) \tag{1.35}$$

The averaged NS equation (1.19) then becomes (Escudié and Liné, 2003):

$$\frac{\partial \overline{\mathrm{U}}_i}{\partial t} + \overline{\mathrm{U}}_j \frac{\partial \overline{\mathrm{U}}_i}{\partial x_j} = -\frac{1}{\rho}\frac{\partial \overline{\mathrm{P}}}{\partial x_i} + \nu \frac{\partial^2 \overline{\mathrm{U}}_i}{\partial x_j \partial x_j} - \frac{\partial \overline{u'_i u'_j}}{\partial x_j} - \frac{\partial \overline{u^*_i u^*_j}}{\partial x_j} \tag{1.36}$$

given that pressure decomposes the same way, and with $\overline{u^*} = 0, \overline{u'} = 0, \overline{p^*} = 0, \overline{p'} = 0$, $\overline{u^* u'} = 0$ and $\overline{p^* p'} = 0$.

Mean, oscillatory and turbulent velocity fields are also coupled. Compared to the classical equation (1.19), the additional $\frac{\partial \overline{u^*_i u^*_j}}{\partial x_j}$ term appears. It involves stresses $\overline{u^*_i u^*_j}$ induced by the oscillatory motion. The turbulent kinetic energy has been introduced in section 1.2.1.c. Mean and oscillatory kinetic energy can be defined in a similar fashion, respectively as $\mathrm{K} = \frac{1}{2}\overline{\mathrm{U}}_i \overline{\mathrm{U}}_i$ and $k^* = \frac{1}{2}\overline{u^*_i u^*_i}$.

Hussain and Reynolds (1970) derived governing equations for k, k^* and K:

$$\begin{aligned}
&\underbrace{\frac{\partial k'}{\partial t}}_{(1)} + \underbrace{\overline{\mathrm{U}}_j \frac{\partial k'}{\partial x_j}}_{(2)} = \underbrace{-\frac{1}{\rho}\frac{\partial}{\partial x_j}\left[\overline{u'_j\left(p' + \frac{1}{2}\rho u'_i u'_i\right)}\right]}_{(3)} + \underbrace{\left(-\overline{u'_i u'_j}\right)\frac{\partial \overline{\mathrm{U}}_i}{\partial x_j}}_{(4)} + \underbrace{\overline{\left(-\left\langle u'_i u'_j\right\rangle_\phi \frac{\partial u^*_i}{\partial x_j}\right)}}_{(5)} \\
&\underbrace{+\overline{u^*_j \frac{\partial}{\partial x_j}\left\langle \frac{1}{2} u'_i u'_j \right\rangle_\phi}}_{(6)} + \underbrace{\nu \frac{\partial}{\partial x_j}\left[\overline{u^*_i\left(\frac{\partial u'_i}{\partial x_j} + \frac{\partial u'_j}{\partial x_i}\right)}\right]}_{(7)} - \underbrace{\frac{\nu}{2}\overline{\left(\frac{\partial u'_i}{\partial x_j} + \frac{\partial u'_j}{\partial x_i}\right)^2}}_{(8)}
\end{aligned} \tag{1.37}$$

Where (1) is the accumulation term, (2) is advection by the mean flow,(3) (6) and (7) are diffusion terms, term (8) dissipation, and terms (4) and (5) are exchanges with mean and turbulent components. $\langle a \rangle_\phi$ is the phase averaged quantity of a.

$$\underbrace{\frac{\partial k^*}{\partial t}}_{(1)} + \underbrace{\overline{\mathrm{U}}_j \frac{\partial k^*}{\partial x_j}}_{(2)} = \underbrace{-\frac{1}{\rho}\frac{\partial}{\partial x_j}\left[u_j^*\left(p^* + \frac{1}{2}\rho k^*\right)\right]}_{(3)} + \underbrace{\left(-\overline{u_i^* u_j^*}\right)\frac{\partial \overline{\mathrm{U}}_i}{\partial x_j}}_{(4)} - \underbrace{\overline{\left(-\left\langle u_i' u_j' \right\rangle_\phi \frac{\partial u_i^*}{\partial x_j}\right)}}_{(5)}$$
$$\underbrace{+\nu\frac{\partial}{\partial x_j}\left[\overline{u_i^*\left(\frac{\partial u_i^*}{\partial x_j} + \frac{\partial u_j^*}{\partial x_i}\right)}\right]}_{(6)} \underbrace{-\frac{\nu}{2}\left(\frac{\partial u_i^*}{\partial x_j} + \frac{\partial u_j^*}{\partial x_i}\right)^2}_{(7)} \tag{1.38}$$

Where term (1) is the accumulation term, term (2) is advection by the mean flow, terms (3) and (6) are diffusion, term (7) is dissipation, and terms (4) and (5) are exchanges with mean and turbulent components.

$$\underbrace{\frac{\partial \mathrm{K}}{\partial t}}_{(1)} + \underbrace{\overline{\mathrm{U}}_j \frac{\partial \mathrm{K}}{\partial x_j}}_{(2)} = \underbrace{-\frac{1}{\rho}\frac{\partial \overline{\mathrm{U}}_i \overline{\mathrm{P}}}{\partial x_i}}_{(3)} \underbrace{-\left(-\overline{u_i' u_j'} - \overline{u_i^* u_j^*}\right)\frac{\partial \overline{\mathrm{U}}_i}{\partial x_j}}_{(4)} \underbrace{-\frac{\partial}{\partial x_j}\left[\overline{\mathrm{U}}_i\left(-\overline{u_i' u_j'} - \overline{u_i^* u_j^*}\right)\right]}_{(5)}$$
$$\underbrace{+\nu\frac{\partial}{\partial x_j}\left[\overline{\mathrm{U}}_i\left(\frac{\partial \overline{\mathrm{U}}_i}{\partial x_j} + \frac{\partial \overline{\mathrm{U}}_j}{\partial x_i}\right)\right]}_{(6)} \underbrace{-\frac{\nu}{2}\left(\frac{\partial \overline{\mathrm{U}}_i}{\partial x_j} + \frac{\partial \overline{\mathrm{U}}_j}{\partial x_i}\right)^2}_{(7)} \tag{1.39}$$

Where term (1) is the accumulation term, term (2) is advection by the mean flow, term (3) is the pressure velocity correlation, terms (5) and (6) are diffusion terms, term (7) is dissipation, and term (4) is the transfer to other components' kinetic energy. From equations (1.37), (1.38) and (1.39), it is possible to extract the exchange terms (respectively numbered (5), (4) and (5), and (4)) and identify the expression of the kinetic energy transfer between each components of the velocity field (Escudié and Liné, 2003):
Mean to turbulent component:

$$\mathscr{T}_{mt} = -\overline{u_i' u_j'}\frac{\partial \overline{\mathrm{U}}_i}{\partial x_j} \tag{1.40}$$

Mean to oscillatory component:

$$\mathscr{T}_{mo} = -\overline{u_i^* u_j^*}\frac{\partial \overline{\mathrm{U}}_i}{\partial x_j} \tag{1.41}$$

Oscillatory to turbulent component:

$$\mathscr{T}_{ot} = \overline{\left(-\left\langle u_i' u_j' \right\rangle_\phi \frac{\partial u_i^*}{\partial x_j}\right)} \tag{1.42}$$

Each of these transfer terms is a product of a gradient of mean or turbulent motion and a stress term of organized and turbulent motion. The direct transfer from mean flow to turbulent motion $\mathscr{T}_{mt}$ is equivalent to the turbulence production by mean flow in Reynolds classical decomposition. However in the present case, the mean flow also transfers part of its energy to the periodic one ($\mathscr{T}_{mo}$) and part of the turbulent kinetic energy production comes from the organized motion ($\mathscr{T}_{ot}$). In order to fully understand turbulence in oscillatory flows, the knowledge of these transfer terms is required.

The main features and properties of turbulence being established, the next section explains the efficiency of turbulence in mixing and mass transfer enhancement.

1.2.2 Turbulence and mixing

This section is based on the course "Mélange turbulent" (Turbulent Mixing) by J-N. Gence and W. Bos at Ecole Centrale de Lyon, University of Lyon (2015).

1.2.2.a Definition of mixing

The mixed state of a scalar quantity in a fluid can be defined quite instinctively as the state at which the value of this scalar is homogeneous in the whole fluid domain. The vagueness of this definition lies in what can be called "homogeneous". Several levels of homogeneity can be specified, corresponding to different levels of mixing. Let us start with a fluid domain initially separated in two regions, one half scalar saturated and the other one scalar free (figure 1.6). Macro mixing is the process of dispatching scalar concentration everywhere in the fluid without necessarily reaching local homogeneity of the concentration at the smallest scales (figure 1.6 b). It is defined at the scale of the experimental setup spatial resolution or the computational domain grid size. Conversely, micro mixing is the action of reaching local homogeneity at small scale (*i.e.* at the molecular level) regardless of the macro-mixing state (figure 1.6 d). Intermediate steps are defined as meso-mixing (figure 1.6 c). Perfect mixing is said to be achieved when homogeneity is reached at all spatial scales, *i.e.* when all levels of mixing are completed (figure 1.6 e).

1.2.2.b Velocity scales versus scalar scales

When no fluid motion exists, only diffusion acts on mixing. A dimensional analysis of the diffusion equation (1.46) shows that the typical time scale of diffusion is $t_D \sim L^2/D$ with L a typical length scale over which diffusion occurs and D the diffusion coefficient. Obviously, reaching a macro mixed state using only diffusion takes a long time if the mixing region is large or the diffusivity low. For example, if dissoved CO_2 is the passive scalar, the typical mixing time to diffuse through a 5 cm fluid layer is $t_D \sim 10^6$ s. The key effect of fluid motion on mixing is that it is able to stretch and deform scalar patches whatever their size is. In doing so, it moves scalar "almost everywhere" in the fluid, increases the exchanges area between saturated and non saturated fluid, and sharpens the concentration gradients. Diffusion is always the final mechanism of mixing in a sense that it ultimately achieves mixing at the smaller scales, but thanks to the multiplication of diffusion spots an enhancement of local scalar gradients, the overall mixing time is greatly reduced. In laminar flows, stretching of scalar structures can be performed by chaotic advection (Burghelea et al., 2004). For the sake of brevity, this will not be developed here. Turbulence is a good mixing tool, since it

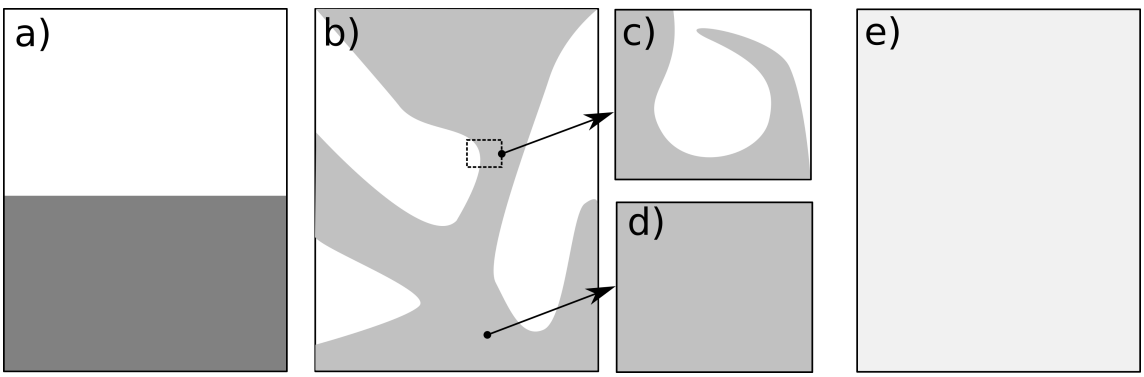

Figure 1.6 – Different states of mixing: a) No mixing, b) Macro mixed state, c) Meso mixed scale, d) Micro mixed scale, e) Fully mixed state.

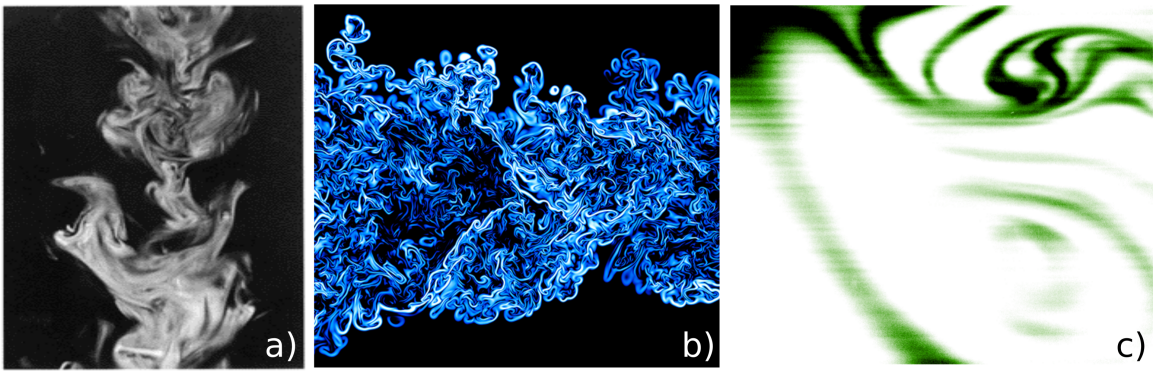

Figure 1.7 – Examples of turbulent mixing. a) Visualization of turbulent passive scalar mixing in grid turbulence at high Schmidt number by Simoens and Ayrault (1994). b) Scalar dissipation field obtained by direct numerical simulation with variable viscosity, revealing the small scales of turbulent mixing, source: http://www.gauss-centre.eu, copyright: CNRS UMR 6614 CORIA and JSC. c) Turbulent stretching of dissolved gas patches under a free surface, experimental observations, present study (chapter 4).

stirs the fluid with velocity structures at various sizes. It is thus able to act on both macro and meso mixing by stretching a wide range of scales. Typical scalar structures that appear in turbulent mixing situations are illustrated in figure 1.7. In order to explain this mutliscale effect, let us consider the case of a passive scalar patch interacting with different sizes of turbulent eddies.
The action of velocity structures on patches of scalar in the fluid depend on the size of the scalar patch and of the velocity structure. If the patch is much smaller than the turbulent eddy, it is mostly advected . If the eddy is much smaller than the scalar patch, it is not able to stretch the structure. But if the sizes are comparable, then stretching and deformation occurs (see figure 1.8), as inevitably, scalar patches will overlap two velocity structures of different vorticity level. Successive stretching and deformation of scalar patches tends to reduce the typical patch size, create smaller and smaller scalar structures and sharper and sharper gradients, letting smaller and smaller velocity structures play their role in the mixing process. The question is then to know down to which scale are the effects of turbulence efficient.

An important quantity in mixing studies is the Schmidt number. It is defined as the ratio between the diffusion coefficient of momentum, that is to say the viscosity ν, and the diffusion coefficient of the passive scalar D.

$$Sc = \frac{\nu}{D} \tag{1.43}$$

The Schmidt number quantifies the relative effects of advection and diffusion. Depending on its value, the smallest existing scales may belong either to the scalar or to the velocity field. If $Sc << 1$, scalar diffusion is fast with respect to momentum diffusion by viscosity, which means that small scalar scales are efficiently smoothed out by diffusion before smaller velocity scales can deform them. Hence velocity scales smaller than the smallest turbulent patch exist. If $Sc >> 1$, diffusion is slow and does not manage to efficiently smooth the scalar structures created by even the smaller velocity scales of turbulence. Hence scalar scales smaller than the smallest velocity scale exist. The Batchelor scale is defined as the smallest scale of scalar structure that can exist before being smoothed out by diffusion. It is expressed as

$$\eta_B = \frac{\eta}{Sc^{1/2}} = \left(\frac{\nu D^2}{\epsilon}\right)^{\frac{1}{4}} \tag{1.44}$$

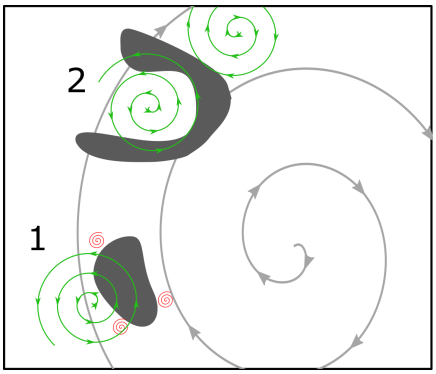

Figure 1.8 – Mixing at different scales. A scalar patch (in grey) is advected by larger scales (gray), not modified by smaller scales (red) and deformed by equivalent size structures (green).

Sc<< 1 thus corresponds to situations where $\eta_B > \eta$ (in that case the Batchelor scale is also called the Corsin scale), and Sc >> 1 to $\eta_B < \eta$. Let L_k be the length scale of the largest turbulent structures carrying most of the kinetic energy k, the range of turbulent scales that may act on scalar structures is $\eta^+ < l < L_k$, with $\eta^+ = \max(\eta_B, \eta)$. For the case of Sc >> 1, which is considered in this thesis, $\eta_B < \eta$ and so $\eta^+ = \eta$, all the turbulent scales down to the Kolmogorov one may act on scalar structures.

Scale effect considerations are of interest in the further application of turbulent mixing principles in presence of boundary layers, and especially at gas-liquid interfaces which is the scope of this work. The Kolmogorov and Batchelor scales are used to define characteristic sub-layers and define which type of structure may *a priori* interact with the scalar diffusive boundary layer that develops under the interface (see section 4.1).

1.2.2.c Turbulent advection diffusion equation

Considering the passive scalar transport equation (1.3), it can be simplified as follows dropping the 1 and $1 \rightarrow 2$ superscripts and the i index of part 1, for thesake of simplicity.

$$\frac{dC}{dt} + \nabla \cdot \mathbf{j} = 0 \tag{1.45}$$

If only molecular diffusion plays a role in phase 1, it becomes

$$\frac{dC}{dt} + \nabla \cdot (D\nabla C) = \frac{dC}{dt} + D\nabla^2 C = 0 \tag{1.46}$$

with ∇^2 the Laplacian operator. Note that the effect of chemical reaction can be introduced using a source term $\mathscr{R}$ positive if species i is produced or negative if it is consumed.

$$\frac{dC}{dt} = -\nabla \cdot (D\nabla C) + \mathscr{R} \tag{1.47}$$

Most of the time, $\mathscr{R}$ depends on the concentration value or on its gradient, and can be included in the expression of the net flux $\mathbf{j}$. When fluid motion exists in the receptive phase, advection takes place and equation (1.46) becomes:

$$\frac{\partial C}{\partial t} + \mathbf{U} \cdot \nabla C = -D\nabla^2 C = -\nabla \cdot \mathbf{j} \tag{1.48}$$

Using Reynolds decomposition on the scalar field as it has been done on the velocity field (see section 1.2.1.c), one gets the equation for the mean concentration field $\overline{\mathrm{C}}$:

$$\frac{\partial \overline{\mathrm{C}}}{\partial t} + \overline{\mathrm{U}}_i \frac{\partial \overline{\mathrm{C}}}{\partial x_i} = -\frac{\partial j_i}{\partial x_i} = -\frac{\partial}{\partial x_i}\left(\overline{u_i' c'} - \mathrm{D}\frac{\partial \overline{\mathrm{C}}}{\partial x_i}\right) \tag{1.49}$$

Where $\mathrm{C} = \overline{\mathrm{C}} + c'$ is the Reynolds decomposition of overall total concentration C into mean and fluctuating components $\overline{\mathrm{C}}$ and c'. This last equation shows that the total concentration flux can be separated into two parts $\mathbf{j} = \mathbf{j^T} + \mathbf{j^D}$: a diffusion flux $\mathbf{j^D}$ with $j_i^{\mathrm{D}} = -\mathrm{D}\frac{\partial \overline{\mathrm{C}}}{\partial x_i}$ and an advection flux or turbulent flux $\mathbf{j^T}$ with $j_i^{\mathrm{T}} = -\overline{u_i' c'}$.

The estimation of this scalar flux is the main problem of any mass transfer study, since it requires the knowledge of both the diffusion and turbulent advection parts, the most complicated one to obtain being the turbulent one. The situation is the same that for closure relations for Reynolds stresses needed to solve the Reynolds averaged NS equations. The understanding of the physics behind turbulent mass transfer is required to build accurate closure models for $\overline{u_i' c'}$. The most common closure strategy is to define an "eddy" diffusivity, using the same principle as for the definition of eddy viscosity. This consists in writing the turbulent mass flux $\overline{u_i' c'}$ as

$$\overline{u_i' c'} = \mathrm{D}_{\mathrm{T},i}\frac{\partial \overline{\mathrm{C}}}{\partial x_i} \tag{1.50}$$

where $\mathrm{D_T}$ is the apparent diffusion coefficient associated to turbulence in dimension i. Equation (1.49) then becomes:

$$\frac{\partial \overline{\mathrm{C}}}{\partial t} + \overline{\mathrm{U}}_i . \frac{\partial \overline{\mathrm{C}}}{\partial x_i} = -(\mathrm{D} + \mathrm{D}_{\mathrm{T},i})\frac{\partial^2 \overline{\mathrm{C}}}{\partial x_i^2} \tag{1.51}$$

In regions of high turbulence intensity, one usually gets $\mathrm{D}_{\mathrm{T},j} >> \mathrm{D}$ and so $\mathrm{D} + \mathrm{D}_{\mathrm{T},j} \approx \mathrm{D}_{\mathrm{T},j}$. Eddy diffusivity values can be predicted by more or less complex models based on the nature of turbulence and its properties Nguyen (2013), and are often reduced to a single constant value using homogeneity and isotropy hypothesis, or are dependent on local turbulent properties.

1.2.2.d Turbulence and mass transfer

In many mass transfer situations, most of the mass flux is oriented in a principal transfer direction, here arbitrarily chosen to be z. Equation (1.49) along z (corresponding to $k = 3$) is:

$$\frac{\partial \overline{\mathrm{C}}}{\partial t} + \overline{\mathrm{U}_z} . \frac{\partial \overline{\mathrm{C}}}{\partial z} = -\frac{\partial j_z}{\partial z} = -\frac{\partial}{\partial z}\left(\mathrm{D}\frac{\partial \overline{\mathrm{C}}}{\partial z} - \overline{c' u_z'}\right) \tag{1.52}$$

Here again, the expression of the turbulent mass flux $\overline{u_z' c'}$ is not known *a priori*. The closure relation consists in expressing the mass flux $j_z = -\mathrm{D}\frac{\partial \overline{\mathrm{C}}}{\partial z} + \overline{c' u_z'}$ by an expression of type

$$j_z = \mathrm{K_L} \times \Delta \mathrm{C} \tag{1.53}$$

if all the resistance to mass transfer can be assumed to happen on the liquid side, as explained in section 1.1.2.b. $\Delta \mathrm{C} = \mathrm{C}_{sat} - \mathrm{C}$ is the gradient of scalar concentration, that is to say the difference between its saturated value (value for which the equilibrium is reached) and its current one, and $\mathrm{K_L}$ is the local mass transfer coefficient (or velocity) expressed in m/s.

As a conclusion, the random and multiscale behavior of turbulence makes it both arduous to describe and very efficient in mixing passive scalar in the liquid phase. Both these aspects are the reason why study of turbulence-enhanced gas-liquid mass transfer is still a very active field of research. A higher degree of complexity is introduced when dealing with non-Newtonian fluid. By making viscosity dependent on liquid phase velocities, one introduces many complex behaviors, explained in the first part of the next section. Most of the concepts and equations defined in the previous section also become ambiguous, or change when viscosity is no longer constant. New relevant quantities and governing equations for non-Newtonian fluids are defined in the second part of the next section.

1.3 Non-Newtonian fluids

The following section starts with a definition of what is called a non-Newtonian fluid, and a quick presentation of the most common non-Newtonian behaviors. The implications of such behaviors for the flow governing equations and the definition of usual fluid mechanics related quantities is then explained.

A fluid is said to be Newtonian when the viscous stress tensor depends linearly on the strain rate. This is expressed by the constitutive equation (1.14) for Newtonian liquids. Dynamic viscosity μ is then equal to the proportionality constant between shear stress τ and shear rate $\dot{\gamma}$:

$$\tau_{ij} = \mu \dot{\gamma}_{i,j} \tag{1.54}$$

Thus defined, Newtonian fluids are supposed to answer to any shear imposed without any response time, and follow the Navier-Stokes equations (1.19) and(1.20) defined in section 1.2.1. Viscosity of Newtonian fluids may depend on pressure and temperature conditions, but never on time, shear rate, or shear stress. Fluids that exhibit such dependencies are called non-Newtonian. In non-Newtonian fluids, the relationship between shear rate and shear stress is non linear. The shear stress tensor can be written as the product between the $\dot{\boldsymbol{\gamma}}$ tensor and, viscosity which is itself a function of the invariants of $\dot{\boldsymbol{\gamma}}$:

$$\tau_{ij} = \mu(\mathrm{I}_{\dot{\boldsymbol{\gamma}}}, \mathrm{II}_{\dot{\boldsymbol{\gamma}}}, \mathrm{III}_{\dot{\boldsymbol{\gamma}}})\dot{\gamma}_{ij} \tag{1.55}$$

In incompressible fluids, $\mathrm{I}_{\dot{\boldsymbol{\gamma}}} = \dot{\gamma}_{i,i} = 0$. In most of the situations, equation (1.55) can be simplified to

$$\tau_{ij} = \mu(\mathrm{II}_{\dot{\boldsymbol{\gamma}}})\dot{\gamma}_{ij} \tag{1.56}$$

Where $\mathrm{II}_{\dot{\boldsymbol{\gamma}}} = \dot{\gamma}_{ij}\dot{\gamma}_{ji}$ will be hereinafter denoted as $\dot{\gamma}$ and referred to as the shear rate value [6]. The key is then to define the $\mu = \mu(\dot{\gamma})$ law. Many types of non-Newtonian behavior exist, due to many different physical phenomena, and leading to various expressions for this law. A brief overview is proposed in this section.

1.3.1 Non-Newtonian behaviors

In many industrial and natural situations, liquid phases may contain small sized particles, droplets, bubbles, cells, large molecules, fibers, or any other micro scale objects giving those fluids specific macroscopic properties. One speaks in that case of complex fluids. Because of the various response of suspended components to applied stress (mechanical, physico-chemical, aggregation...), complex fluids are most of the time non-Newtonian and

[6] Different from the shear rate tensor $\dot{\boldsymbol{\gamma}}$ in bold.

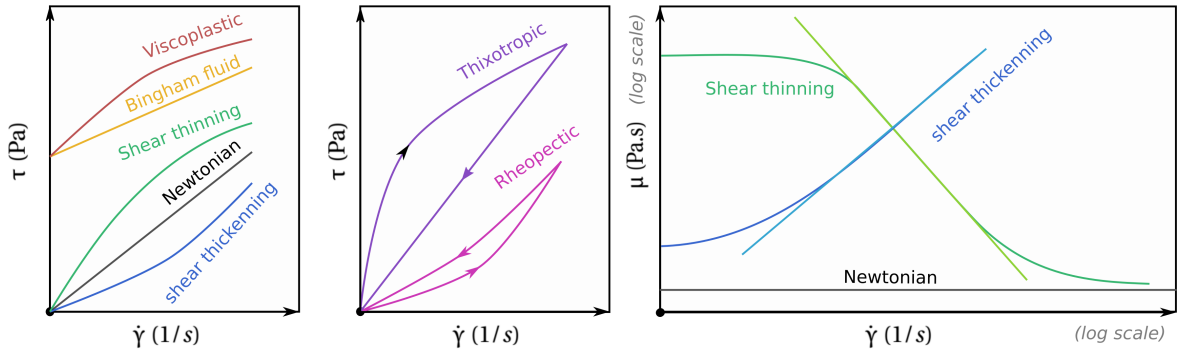

Figure 1.9 – Sketch of non-Newtonian behaviors

.

may exhibit rather elaborate relationships between shear stress and shear rate (figure 1.9). One may distinguish several categories of non-Newtonian complex fluids, that are briefly introduced in what follows. Of course, some fluids may combine several of these behaviors making the understanding of their dynamic even more complex.

1.3.1.a Shear thickening and shear thinning

Shear thickening or shear thinning fluids (sometimes called respectively dilatant and pseudo-plastic), are fluids for which the viscosity increases (first case) or decreases with the shear rate (second case, 1.9). Famous examples of shear thickening and thinning fluids are respectively cornstarch and ketchup or toothpaste. Shear dependency of the viscosity is a feature frequently found in complex fluids and is due to the presence of additives and their nature. When additive concentration is high enough, the overall zero shear rate viscosity of the liquid increases compared to the one of the solvent alone. Applying a shear rate, the viscosity evolution then depends on the suspended additive's behavior. Shear thickening often arises for concentrated colloids or fibers suspensions. Under certain conditions, colloids interaction forces may increase with shear and make the fluid transition to a solid-like behavior through a major increase in viscosity (Melrose et al., 1996). Shear thickening also happens when high shear rates cause rigid colloidal particles collision and the formation of local solid like hydroclusters of particles. This property is used to build body armors or military bullet proof equipment for example (Wagner and Wetzel, 2009), and can also be found in honey or pizza dough.

On the other hand shear thinning in complex fluids comes from the ability of some molecules to deform and adapt to the shearing flow. Long chain polymers diluted in Newtonian solvents are good example of molecules that can be deformed by a flow. At low shear rate, they increase the liquid viscosity like any suspension. At high shear rates, the flexibility of their carbon backbone allows them to stretch and align with the main shear direction as sketched on figure 1.10, thus leading to a decrease in the solution's viscosity. Polymer chains are not the only elements giving shear thinning properties to a liquid. For example, blood's non-Newtonian behavior is caused by red blood cells gathering in lines and which eventually split up and deform when passing through narrow vessels (Baskurt and Meiselman, 2003; Brust et al., 2013). The shear thinning property are of interest when one wants to efficiently spread a liquid film on a solid surface without having it flowing when the spreading shear stress is no longer applied. Paint on a wall is an example of such an application, but a less known similar behavior is found in human tears for example (Tiffany, 1994). Pseudo plasticity is widely used in the food industry to enhance sensory quality (flavor release, mouth feel)

in food products and guarantee a high degree of pourability (Katzbauer, 1998). Shear thinning behavior are frequently encountered in industrial stirred tanks and fermentation broths (Cabaret et al., 2008; Gabelle et al., 2011; Kawase et al., 1987, 1992; Pedersen et al., 1994): during fermentation process, the viscosity of the culture medium evolves from low viscosity Newtonian to highly viscous and shear thinning. They can also be found in geophysical fluids (mud) or in concrete because of the presence of long organic macro-molecules with a behavior analog to the one of polymer chains in solutions.

For shear thinning or thickening fluids, the viscosity is written as a function of the norm of the local shear rate $\dot{\gamma}$.

$$\mu = f(\dot{\gamma}) \tag{1.57}$$

A common model to explicit equation 1.57 is the power law model for which one writes:

$$\mu = K_\mu . \dot{\gamma}^{n-1} \tag{1.58}$$

Where K_μ is the power law constant and n the power law exponent. If $n = 1$, $\mu = K_\mu$ and the fluid is Newtonian. $n > 1$ values lead to an increase in viscosity with increasing shear rates, which corresponds to shear-thickening fluids. $n < 1$ corresponds to the shear thinning case (figure 1.9, right part). For many complex fluids, viscosity may appear constant in very low or very high shear rate ranges. In that case one may define two viscosity plateau values μ_0 and μ_∞, such that μ tends to μ_0 when the shear rate tends to zero, and to μ_∞ when it tends to infinity. The Carreau-Yasuda model allow to account for these Newtonian ranges:

$$\frac{\mu - \mu_\infty}{\mu_0 - \mu_\infty} = \left(1 + \left(t_{CY}\dot{\gamma}\right)^a\right)^{\frac{n-1}{a}} \tag{1.59}$$

Where t_{CY} is a characteristic time scale of the solution, n the power law decay constant, and a the parameter representing the sharpness of the transition between power law and Newtonian behavior at high or low shear rate (figure 1.9, right part, dark green curve).

1.3.1.b Viscoelasticity

Viscoelastic fluids are fluids that can present elastic properties as well as viscous ones. In fact, viscoelasticity can be found in solids as well as in liquids: elasticity comes from the solid-like behaviors, and viscous property are representative of a fluid like nature. This in between behaviors characterizing what is called "soft" matter can be found in elastomers, rubbers, gels... Highly concentrated polymer solutions are good examples of viscoelastic fluids (Poryles and Vidal, 2017). Entangled polymer chains tend to form a quite elastic network that has a quasi solid-like behavior at low deformation or low shear rate. But elasticity can also be found in dilute polymer solutions, because of the mechanical behavior of polymer molecules. Depending on the polymer chains conformation, their stretching can be more or

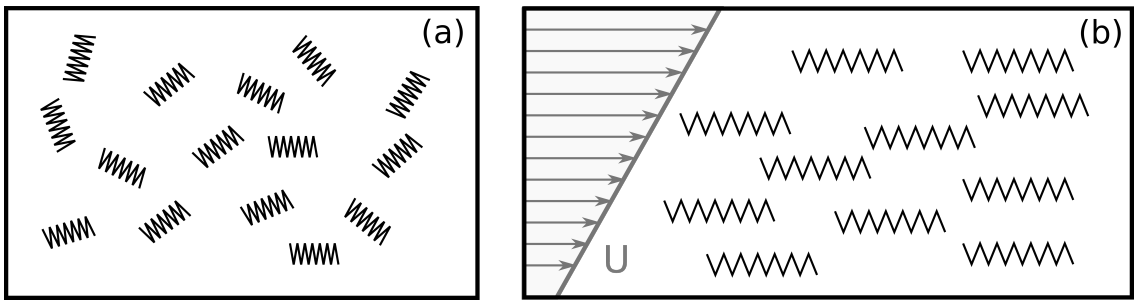

Figure 1.10 – Schematic representation of an unsheared (a) and sheared (b) dilute polymer solution

less elastic and reversible. Energy taken from the fluid during this coil-stretch transition and stored in the deformed polymer chains can be restored to the fluid under different shear conditions. These fluid-polymer interactions give birth to a whole new turbulent behavior for dilute polymer solutions, which is addressed in section 3. Viscoelasticity is of course also not limited to polymer solutions and also appears in other fluids, for example in blood (Thurston and Henderson, 2006).

A basic model to describe viscoelastic properties is the Maxwell model in which the fluid response to stress is modeled by a spring damper in series system:

$$\dot{\gamma} = \frac{\dot{\tau}}{G} + \frac{\tau}{\mu} \tag{1.60}$$

Where G is the elastic modulus, τ the stress, and the relaxation time of the material is $t_c = \frac{\mu}{E}$. Maxwell model is well adapted to describe the behavior of viscoelastic fluids. When the material is closer to a solid, spring and damper are placed in parrallel configuration: this is the Kelvin-Voigt model in which $\tau = G\gamma + \mu\dot{\gamma}$. More complex models can be built using springs and damper blocks in different configuration (e.g. the Jeffrey model, see Nguyen (2013)). All of these rely on the assumption that the response of the fluid component at the root of the non-Newtonian behavior of the fluid remains within the linear elasticity domain (e.g. that the polymer are only weakly elongated by the shear stress). In most of the numerical models used in fluid mechanics, the Maxwell model is replaced by more complex constitutive models such as Oldroyd-B (based on the Jeffrey model) or FENE-P (Finitely Extensible Non linear Elastic with a Peterlin closure), accounting for non linear polymer fluid interactions (Nguyen et al., 2016).

1.3.1.c Yield stress fluids

Sometimes, pseudoplatic and/or viscoelastic behavior can be associated with a yield stress under which no flow occurs and the fluid behaves like a solid body. This type of fluid is called viscoplastic. A yield stress fluid that behaves like a newtonian fluid once the minimum yield stress is applied is called a Bingham fluid. As an illustration, in entangled polymer solutions, the shear stress needed to break the entanglement network can be seen as the yield stress above which the polymer solution flows. However, the notion of yield stress and flow/no flow distinction is only valid under given observation conditions (Barnes, 1999). In fact, viscoelasticity and yield stress are properties that can be found in all liquid and solid materials: everything flows if one waits long enough, everything can behave like a solid if one looks at it for a time short enough. This idea, first stated by Heraclitus of Ephesus around 500 BC was translated into the dimensionless Deborah number by Reiner (1964).

$$De = \frac{t_c}{T} \tag{1.61}$$

Where t_c is a characteristic relaxation time of the solid or fluid material, and T is the characteristic time scale of the observed deformation. For a rigid solid, T is infinite and for a non viscoelastic liquid T tends to zero. Hence large Deborah numbers correspond to liquid like behaviors, and low Deborah numbers to solid like ones.

1.3.1.d Thixotropy and rehopecty

Finally, thixotropic and antithixotropic (or rheopectic) fluids are fluids for which the viscosity decreases or increases as the stress is applied, and comes back to its rest value as soon

as the stress is released. Such fluids are prone to hysteresis phenomena. Whipped cream, protein solutions are for example antithixotropic. Synovial fluid contained in human body's joints, or cement paste are thixotropic (Chhabra, 2010). It corresponds to fluids for which shear rate or shear stress variations trigger chemical or physical modification of the fluid at a time scale longer than the time scale of shear variations. For example, polymer solutions may be such that the time scale of chain deformation is long with respect to the time scale of the mean flow, leading to a time dependent shear thinning. Pressure variations due to shear stress may also give rise to slow modification of the physico-chemical properties of the polymer (such as sol-gel transition) and thus a slow viscosity decreases or increases as long as the shear stress is maintained. Thixotropic behavior are of great interest in pharmaceutical applications such as drug delivery (Lee et al., 2009).

1.3.2 Flow equations and characteristic numbers in non-Newtonian liquids

1.3.2.a Definition of classical parameters

The definition of the most common non-dimensional parameters based on viscosity mechanics becomes ambiguous in non-Newtonian, shear thinning or thickening fluids. The Reynolds number defined by equation 1.17, and the Schmidt number defined by equation 1.43 requires a constant scale viscosity. It can be chosen in different ways. For an *a priori* definition based on available rheological data, one may chose the zero shear rate viscosity or the average viscosity based on the flow curve. Using experimental similarities, one may also define an equivalent Newtonian viscosity as the viscosity of a Newtonian fluid that would lead to similar variations of a set of control variables. This method is frequently used in stirred tanks where the apparent viscosity is set as the viscosity of the Newtonian fluid that leads to the same power consumption at the stirring shaft (see Metzner and Otto (1957) and section 3.1.2.c).

If the average or local shear rate is available through measurement, one may evaluate the scale viscosity by converting the average shear rate through the visocity-shear rate relationship (Gabelle et al., 2011). It is also possible to deduce a mapping of local viscosity from the measured shear rate field. More than the definition of a scale viscosity and a global Reynolds or Schmidt number, this last option also allows to estimate local values of these numbers. This approach in local studies aiming at a better understanding of small scale phenomena (Nguyen, 2013).

1.3.2.b Relevant dimensionless numbers

In order to compare liquid versus solid like response to solicitation, the Deborah number as been defined previously (see eq. 1.61) as the ratio between characteristic time scales of the fluid t_c and of the experiment/solicitation T. In viscoelastic flows, the Weissenberg number is defined as the ratio of elastic forces over viscous ones, which can be written as follow using the Maxwell model:

$$\mathrm{Wi} = t_c \dot{\gamma} \tag{1.62}$$

The Weissenberg number is in some sens similar to the Deborah number and the two are often confused. Their physical meaning is yet slightly different. Wi somehow quantifies the degree of anisotropy/alignment of the polymer chains or suspended matter induced by the deformation. It is thus appropriate to describe flows with a constant shear history such, for example flows with a constant mean shear(figure 1.10). The definition of De is based on the

response time of the fluid. It is thus more convenient to describe instationnary flows (Poole, 2012).

A last parameter of interest when studying non-Newtonian effects caused by dilute polymers is the solution concentration. It has to be noted that concentration directly affects solution time scales (see section 3.2), so the Deborah and Weissenberg numbers both depend on concentration.

1.3.2.c Governing equations with shear variable viscosity

As mentioned earlier, non-Newtonian behaviors are characterized by various constitutive equations for the stress tensor. Equation (1.15) has to be written as:

$$\frac{\partial U_i}{\partial t} + U_j \frac{\partial U_i}{\partial x_j} = -\frac{1}{\rho}\frac{\partial P}{\partial x_i} + \frac{1}{\rho}\frac{\partial \tau_{ij}}{\partial x_j} \tag{1.63}$$

and τ_{ij} is modeled by the constitutive equation. The mass conservation equation remains unchanged. In fluids for which viscosity is a function of the shear rate, such as shear thinning fluids, local variations of the rate of deformation induce spatial variations of the viscosity value, and additional stress due to these viscosity variations appear (Gavrilov and Rudyak, 2016). In turbulent flows, viscosity may be decomposed, as other fields, into an average and a fluctuating component $\overline{\mu}$ and μ' (or $\overline{\nu}$ and ν') such that $\mu = \overline{\mu} + \mu'$ (or $\nu = \overline{\nu} + \nu'$). The shear stress can then be written as (Gori and Boghi, 2011)

$$\tau_{ij} = \overline{\tau}_{ij} + \tau'_{ij} = (\overline{\mu} + \mu')\left(\overline{\dot{\gamma}}_{ij} + \dot{\gamma}'_{ij}\right) \tag{1.64}$$

with

$$\overline{\tau}_{ij} = \overline{\overline{\mu}\overline{\dot{\gamma}}_{ij} + \overline{\mu}\dot{\gamma}'_{ij} + \mu'\overline{\dot{\gamma}}_{ij} + \mu'\dot{\gamma}'_{ij}} = \overline{\mu}\overline{\dot{\gamma}}_{ij} + \overline{\mu'\dot{\gamma}'_{ij}} \tag{1.65}$$

and

$$\tau'_{ij} = \mu'\overline{\dot{\gamma}}_{ij} + \overline{\mu}\dot{\gamma}'_{ij} + \mu'\dot{\gamma}'_{ij} - \overline{\mu'\dot{\gamma}'_{ij}} \tag{1.66}$$

These conditions are valid for what is called a Generalized Newtonian Fluid (GNF): a fluid for which viscosity is a function of the instantaneous shear rate but not of the history of deformation (Pinho, 2003). In a GNF, the Reynolds averaged momentum equation becomes:

$$\rho\frac{\partial \overline{U}_i}{\partial t} + \rho\overline{U}_j\frac{\partial \overline{U}_i}{\partial x_j} = -\frac{\partial \overline{P}}{\partial x_i} + \frac{\partial \overline{\mu}\overline{\dot{\gamma}}_{ij}}{\partial x_j} - \rho\frac{\partial \overline{u'_i u'_j}}{\partial x_j} + \frac{\partial \overline{\mu'\dot{\gamma}'_{ij}}}{\partial x_j} \tag{1.67}$$

This equation is very similar to (1.19) where viscosity would be replaced by its average value, except that:

- statistically averaged viscosity $\overline{\mu}$ is still locally variable and can not be taken out of the gradient operator in the second term of the left hand side of the equation
- an additional stress term appears due to local viscosity fluctuations. This last term is the gradient of what is called the polymeric stress tensor $\overline{\mu\dot{\gamma}_{ij}}$ (Gori and Boghi, 2011) or non-Newtonian stress tensor (Gavrilov and Rudyak, 2016), which quantifies the effect of turbulent viscosity fluctuations.

The governing equation for turbulent kinetic energy with shear dependent viscosity can also be derived:

$$\underbrace{\frac{\partial k}{\partial t}}_{(1)} + \underbrace{\overline{\mathrm{U}}_r \frac{\partial k}{\partial x_r}}_{(2)} = \underbrace{-\frac{1}{\rho}\frac{\partial \overline{p' u_r}}{\partial x_r}}_{(3)} \underbrace{-\frac{\partial \overline{u_r' u_i' u_j'}}{\partial x_r}}_{(4)} + \underbrace{\frac{\partial}{\partial x_r}\left(\overline{\nu}\frac{\partial k}{\partial x_r} - \overline{\nu}\overline{\frac{\partial u_i' u_r'}{\partial x_i}} + \overline{\nu'\frac{\partial u_i' u_r'}{\partial x_i}} + \overline{\nu'\frac{\partial k}{\partial x_r}} + \overline{u_i'\nu'\dot{\gamma}_{ir}}\right)}_{(5)}$$
$$\underbrace{-\overline{u_i' u_r'}\overline{\dot{\gamma}}_{ir}}_{(6)} \underbrace{-\overline{\nu'\dot{\gamma}_{ir}'}\overline{\dot{\gamma}}_{ir}}_{(7)} \underbrace{-\left(\overline{\nu}\overline{\dot{\gamma}_{ir}'\dot{\gamma}_{ri}'} + \overline{\nu'\dot{\gamma}_{ir}'\dot{\gamma}_{ri}'}\right)}_{(8)} \tag{1.68}$$

The physical meaning of each term is explained below:

- (1): Accumulation term
- (2): Advection of kinetic energy by the mean flow
- (3): Pressure velocity correlation
- (4): Triple correlation representing advection of kinetic energy by velocity fluctuations
- (5): Transport of turbulent kinetic energy by viscosity. The first two terms of this group are also present in Newtonian fluids, for which $\overline{\nu} = \nu$ is constant over the whole domain and can be taken out of the gradient. The last three terms represent transport and diffusion due to viscosity fluctuations and can thus only be found in non-Newtonian media.
- (6): Production by the Reynolds stress
- (7): Production by the polymeric stress tensor
- (8): Dissipation terms.

This equation can only be solved together with incompressibility condition and the constitutive equation defining the average viscosity $\overline{\mu}$ at any point in the fluid using the local shear rate $\dot{\gamma}$. Classical closure relationship based on eddy viscosity may still be used for Reynolds stress computation. However, additional cross correlation terms involving fluctuating viscosity also require closure expressions (Gavrilov and Rudyak, 2016). Such expressions are based on simplification hypothesis specific to flow conditions, that can only be validated through experimental measurements.

A triple decomposition approach can be adopted as well. Based on the previous decomposition, we introduce here the triple decomposition of viscosity into a mean, an oscillatory, and a turbulent part so that $\mu = \overline{\mu} + \mu^* + \mu'$ or $\nu = \overline{\nu} + \nu^* + \nu'$. The mean shear stress is then

$$\overline{\tau}_{ij} = \overline{\mu}\overline{\dot{\gamma}}_{ij} + \overline{\mu^*\dot{\gamma}_{ij}^*} + \overline{\mu'\dot{\gamma}_{ij}^*} + \overline{\mu^*\dot{\gamma}_{ij}'} + \overline{\mu'\dot{\gamma}_{ij}'} \tag{1.69}$$

and the averaged momentum equation is

$$\underbrace{\rho\frac{\partial \overline{\mathrm{U}}_i}{\partial t}}_{(1)} + \underbrace{\rho\overline{\mathrm{U}}_j\frac{\partial \overline{\mathrm{U}}_i}{\partial x_j}}_{(2)} = \underbrace{-\frac{\partial \overline{\mathrm{P}}}{\partial x_j}}_{(3)} \underbrace{-\rho\frac{\partial \overline{u_i' u_j'}}{\partial x_j}}_{(4)} \underbrace{-\rho\frac{\partial \overline{u_i^* u_j^*}}{\partial x_j}}_{(5)} + \underbrace{\frac{\partial \overline{\tau}_{ij}}{\partial x_j}}_{(6)} \tag{1.70}$$

(1), (2) and (3) are the usual accumulation, advection, and pressure terms. (4) and (5) are Reynolds stress associated to fluctuating and oscillatory components (see 1.2.1.h). (6) is the production of momentum by shear stress, that can be decomposed into

$$\underbrace{\frac{\partial \overline{\tau}_{ij}}{\partial x_j}}_{(6)} = \frac{\partial}{\partial x_j}\left(\underbrace{\overline{\mu}\overline{\dot{\gamma}}_{ij}}_{(6.1)} + \underbrace{\overline{\mu^* \dot{\gamma}^*_{ij}}}_{(6.2)} + \underbrace{\overline{\mu^* \dot{\gamma}'_{ij}}}_{(6.3)} + \underbrace{\overline{\mu' \dot{\gamma}^*_{ij}}}_{(6.4)} + \underbrace{\overline{\mu' \dot{\gamma}'_{ij}}}_{(6.5)} \right) \tag{1.71}$$

The (6.1) term embodies "Newtonian" viscous effects and corresponds to the second order partial derivative term in equation (1.36). The non-Newtonian tensor expressed in equation (1.67) is found in term (6.5). The terms (6.2) to (6.4) appear because of oscillatory viscosity fluctuations, and represent the stress induced by interactions between oscillatory and turbulent velocity fluctuations and viscosity fluctuations.

1.3.2.d The case of viscoelastic fluids

When dealing with viscoelastic fluids, the most common approach is to solve NS equations together with a governing equation for the properties of extensible materials present in the solution, such as polymer chains conformation (eg. in the FENE-P model). An additional stress term is then added to the momentum equation in order to account for elastic properties and momentum exchanged between the solvent and the suspended components (Nguyen et al., 2016). The governing equation for polymer chains conformation consists in a model relating chain extension to external stress applied by the flow on each polymer molecule. Assuming that molecules are much smaller than the size of a fluid particle, energy storage and retribution from the polymer in each fluid particles is accessed through the statistical properties of one of its characteristic quantity. When stress is applied, the polymer chain deforms under the action of the flow. Deformed molecules that reach regions of the flow in which the stress decreases deform back elastically to their initial state, thus giving energy back to the fluid.

If the deformation of polymer chains can be assumed small, their elastic response is considered linear. Linear viscoelasticity models are analog to spring-damper systems, where the spring represents suspended matter elasticity and damper the viscous drag exerted by the fluid. Such models are associated with a linear differential equation for the total stress (e.g. equation (1.60) for the Maxwell model, alos equivalent to Olroyd B conformation equation). On the other hand if deformations can not be assumed small enough to stay in the linear regime, more elaborate non-linear models are needed. In the most recent FENE-P model, the conformation tensor is defined as the statistical average of the correlation orientation vector of each polymer chain. A non-linear differential equation is then constructed to describe the bounded deformation of polymer chains, and this equation is solved together with the Navier stokes modified equations including an additional source term due to energy exchanges between the fluid and the polymer (Nguyen et al., 2016).

In situations where viscoelasticity is coupled with a strong dependency of viscosity on the shear rate, the GNF model can also be extended to account for elastic behaviors by introducing the effects of elongational viscosity into the constitutive equation. This is done by making μ dependent not only on the shear rate but also on the strain rate which is, as $\dot{\gamma}$, related to the invariants of $\dot{\boldsymbol{\gamma}}$ (Pinho, 2003).

In this chapter, the general concepts of gas-liquid mass transfer, turbulence, scalar transport and non-Newtonian property of a fluid have been introduced. The non-Newtonian nature of a fluid obviously deeply modifies the properties of turbulence in it, and a precise description of turbulence properties themselves is a key to understand gas-liquid mass at gas-liquid interfaces in turbulent flows. The next chapter presents a set of experimental technique that can be applied to visualize and measure small scales of turbulence and mass transfer of CO_2 in the vicinity of gas-liquid interfaces.

Chapter 2

Optical measurements

L'observation est l'investigation d'un phénomène naturel, et l'expérience est l'investigation d'un phénomène modifié par l'investigateur.

Claude Bernard

Contents

Abstract (En)

In this second chapter, optical measurements techniques applied to the studied phenomena are presented. The first one is Particle Image Veocimetry (PIV), in its classical or stereoscopic version (SPIV). It allow the measurement on two (PIV) or three (SPIV) components of the velocity field of a gaseous or in our case liquid phase within a planar section of the flow. Throughout this thesis, PIV is taken from the user point of view. The section of this chapter dedicated to it thus essentially explains the main principles of the method, and the conditions necessary to achieve quality PIV measurements in the conditions of the present study. The second technique introduced enables local measurement of dissolved gas concentration (in particular CO_2) in the liquid phase. It is based on the ability of the dissolved gas to inhibit the laser induced fluorescence of a dye previously homogeneously mixed into the liquid. This type of method is called Inhibited Planar Laser Induced Fluorescence (I-PLIF). It is here addressed from a developer standpoint. Indeed, a new version based on the use of the ratio of two fluorescence wavelengths (colors) is implemented. This new approach allows to free oneself of many uncertainties introduced by light sheet perturbation or phenomena occurring outside of the field of view.

Résumé (Fr)

Dans ce second chapitre, les techniques de diagnostic optique appliquées utilisées sont présentées. La première technique présentée dans ce chapitre est la Vélocimétrie par Imagerie de Particules (VIP ou PIV pour Particle Image Velocimetry), dans sa version classique ou stéréoscopique (SPIV). Elle permet la mesure dans un plan de deux (PIV) ou trois (SPIV) composantes du champ de vitesse de l'écoulement en phase gazeuse ou dans notre cas liquide. Au cours de cette thèse, la PIV est abordée d'un point de vue "utilisateur", et la partie de ce chapitre qui y est consacrée présente donc essentiellement les grands principes de la méthode, et les conditions nécessaires à l'obtention de mesures PIV ou SPIV de qualité (épaisseur du plan laser, concentration en particule, optiques...). La seconde technique présentée permet la mesure de concentration de gaz dissout dans la phase liquide. Elle repose sur la capacité du scalaire à mesurer à éteindre la fluorescence (excitée par laser) d'un marqueur préalablement introduit dans le milieu en concentration homogène. Cette famille de méthode porte le nom de PLIF (pour Planar Laser Induced Fluorescence) Inhibée. Elle est ici abordée d'un point de vue autant "développeur" qu'"utilisateur". En effet, une nouvelle version de cette technique basée sur l'utilisation de deux longueurs d'ondes de fluorescence au lieu d'une seule est proposée. Cette nouvelle version, permet de s'affranchir de nombreuses sources d'erreur liées aux perturbations de l'éclairement laser ou aux phénomènes intervenant hors du champ d'observation.

Publication
Lacassagne T., Simoëns S., Hajem M. E. and Champagne J.-Y. Ratiometric, single-dye, pH-sensitive inhibited laser-induced fluorescence for the characterization of mixing and mass transfer. *Experiments in Fluids*, 59(1):21, Jan. 2018. doi: 10.1007/s00348-017-2475-y.

This chapter aims at introducing the two main categories of techniques used in this thesis' experimental procedures. In the first section, the one used for liquid phase velocity measurement, namely Particle Image Velocimetry (PIV) in mono and Steroscopic (SPIV) configurations is briefly explained. The particularities specific to PIV and SPIV applications to turbulent liquid flows are mentioned, and the error causes and uncertainty evaluations are discussed.

In the second section, the fluorescence based metrology used for pH or dissolved gas concentration measurement in aqueous media is presented. This part also displays some innovations and improvements of the existing methodology. In particular the development of a new ratiometric pH sensitive Planar Laser Induced Fluorescence technique ($I^r_{pH}-$PLIF) and its applications to two different test experiments are detailed. The chemistry of CO_2 dissolution into water is first recalled, as a first necessary step to understand the relevance of pH based inhibited fluorescence measurements for this study. A non exhaustive state of the art of PLIF and Inhibited PLIF is then proposed, and the fluorescent dye used throughout this thesis is introduced. The novel $I^r_{pH}-$PLIF method is developed in the following sections, and applied to a monophasic test case. Finally, its usefulness for pH measurement in dilute polymer solutions is discussed, and a diphasic test case is briefly introduced. Measurement coupling of SPIV with PLIF and compatibility considerations are addressed later in chapter 4 of the manuscript.

2.1 Liquid phase velocity measurement: Particle Image Velocimetry

2.1.1 Principle

2.1.1.a Particle Image Velocimetry (PIV)

Particle image Velocimetry is the most commonly used particle based imaging method for fluid flows velocity measurement in laboratory experiments and in the industry. It is an optical technique enabling the determination of local instantaneous flow velocity in a two dimensional plane of measurement. It is considered as non intrusive since no probe is introduced in the flow apart from seeding particles. PIV has been developed from the 80's and quickly improved with the use of image processing techniques and the appearance of adapted pulsed lasers. It is nowadays used in many industrial and academic situations involving single liquid or gas single phase or multiphase flows with more or less complex geometries.

A tremendous amount of PIV applications to liquid phase flows exist, from fundamental turbulence measurements (Herlina and Jirka, 2008; Liberzon, 2011) to industrial reactors study (de Lamotte et al., 2017; Gabelle, 2012), free surface and open flows phenomena (Launay, 2016; Turney and Banerjee, 2013), bubby flows (Kováts et al., 2017) and countless others.

Many detailed descriptions of the theory of PIV are available in the literature, for example in Adrian (2005); Keane and Adrian (1990); Raffel et al. (2013). A brief description of its functioning is proposed in what follows.

The basic principle is to measure the displacement of small particles introduced into the fluid prior to the experiment, by illuminating those particles and taking snapshots of their position at successive instants. Assuming particles follow the flow, the fluid velocity can be deduced directly from the particle displacement divided by the time interval between snapshots.

Unlike Particle Tracking Velocimetry (PTV) for which each particle's displacement is determined by Lagrangian tracking, PIV estimates the motion of groups of particles by cross correlation of two consecutive snapshots. Several particles are isolated from a first image, and their new position on the following image is found (figure 2.1) by image correlation.

Practically, the images are separated into interrogation windows. The window extracted from frame 2 is virtually shifted over interrogation window extracted from frame 1, and the cross correlation coefficient X_{Corr} for each shift (dx, dy) is computed as:

$$X_{Corr}(dx, dy) = \sum_{x,y} I_1(x, y) I_2(x + dx, y + dy) \tag{2.1}$$

Where I_1 and I_2 are the pixel intensities of frames 1 and 2 respectively. The pixel shift (dx_p, dy_p) for which the correlation between interrogation window from frames 1 and 2 is maximum (see figure 2.1) thus defines the measured particle displacement. It can be seen as the most probable displacement for the selected group of particles. Displacement values in non-integer number of pixels can be deduced using sub-pixel interpolation techniques. The value of the main peak of correlation coefficient divided by the value of its second highest peak is called peak ratio. It somehow quantifies the unicity of the displacement found by correlation and thus the quality of PIV measurement. The larger the peak ratio, the higher the probability that initial particles are those that have been identified on the second image.

This image-correlation based approach has many advantages. Image correlation is easily performed by modern computers which makes data treatment quite quick. It also intrinsically produces a Cartesian meshed set of vectors without non measured zones (which is not the case for PTV for example). Finally, it is possible to use the velocity field computed from a first coarse processing (a first pass) as an indicator to where to search for groups of particles on the second image, and refine the velocity field by successive processing (passes) with decreasing interrogation window size.

Recent softwares (DaVis 8 for example) make it possible to use non square interrogation windows (rectangle, circles, ellipsoids...), which is useful when flows exhibit a preferential displacement direction. Confusion between look-alike particle groups can also be reduced by using Gaussian-weighted interrogation windows.

The quality and accuracy of PIV measurements depend on many factors, some of which are listed hereinafter.

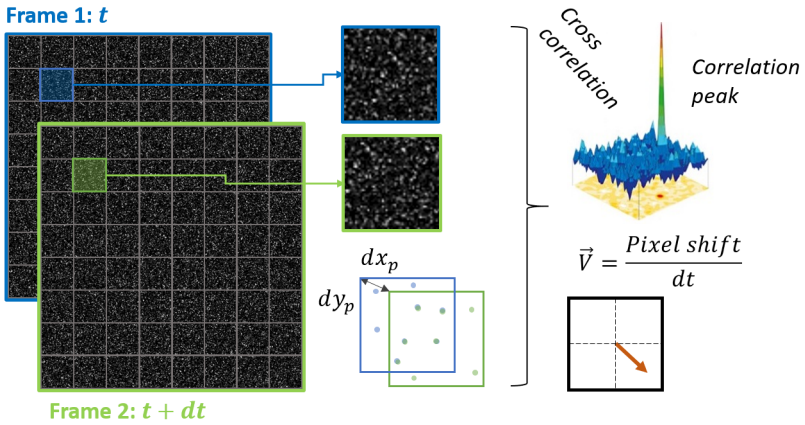

Figure 2.1 – Principle of PIV measurements

Spatial and temporal resolution: Since one single displacement vector is calculated for each group of particles, it is the size of the interrogation window that sets the spatial resolution of the technique, more precisely the size of the interrogation window of the last pass. Typically, treatments may start by 64 × 64 px interrogation window and be refined down to 12 × 12 px. Spatial resolution in metric units then depends on optical magnification of the setup, on the physical pixel size of the sensor, and on particle sizes.

The maximum temporal resolution depends on the time interval between two sub-images or frames. For slow flows, a single acquisition frequency can be used, and velocity fields are computed between frames at instants t_1 and t_2, t_2 and t_3 and so on, with $t_2 = t_1 + 1/f_{acq}$. This option is called single frame PIV. For fast phenomena such as turbulent flows, one may not be able to detect small, short-lived structures using single frame PIV, since frequencies of common pulsed lasers are limited to a few tens of Hertz (a few kHz for fast PIV lasers). Using single frame PIV for high velocity flow results in under estimation of the velocity field, as particles seeding the faster structures present on the first image will be absent from the second one.

To be able to measure instantaneous velocity fields without fast PIV devices, double frame PIV lasers and cameras are used: two laser sources are timed so that the first one emits a pulse at time t_1 and the second one at $t_1 + dt$. Double frame cameras record a frame for each pulse, and the image correlation process between frames at t_1 and $t_1 + dt$ yields an instantaneous velocity field for time t_1. The following instantaneous field is computed for t_2 between t_2 and $t_2 + dt$ with $t_2 = t_1 + 1/f_{acq}$ and so on. Doing so, one may not be able to follow turbulent structures in time, but snapshot field measured are good estimates of instantaneous velocity fields, which can then be used for ensemble averaging and statistical study of turbulence from an Eulerian point of view. First limited in terms of acquisition frequencies, the development of powerful laser and LED light sources and the improvement of imaging and recording devices makes it now possible to use PIV with high frame rate (up to several kHz for what is called fast PIV), and thus time-resolve fast phenomena, such as turbulence. Nevertheless, these high rates are still not able to time resolve the highest Reynolds flows [1].

The main prerequisite to achieve PIV measurements is to check seeding particles behavior against flow, and laser enlightenment.

Particle Stokes number: The stokes number allows to check that particles do follow the flow. It is defined as the ratio of the particle characteristic time over a characteristic time of the flow.

$$\mathrm{St} = \frac{1}{18}\frac{\rho_p d_p^2 \mathrm{V}}{\rho \nu \mathrm{L}} \tag{2.2}$$

Where ρ_p and ρ are the densities of the particle material and of the fluid respectively, d_p is the particle diameter, ν the fluid kinematic viscosity and V and L velocity and length scales of the flow. If the Stokes number is below 1, it means that the response time of particles to flow solicitation is small, hence that the particles are good tracers of the fluid dynamics. Obviously, low stokes numbers are easily achieved for particles with densities close to that of the fluid. For turbulent flows with equivalent densities, particle one decade smaller than the typical Kolmogorov scale should follow even the smallest structures of the flow. If the particle density is much higher than the fluid density, then the particle diameter need to be

[1] The maximum acquisition frequencies are around f_{acq} = 10 kHz for fast PIV setups, versus flow frequencies higher than 100 kHz for high Reynolds number flows

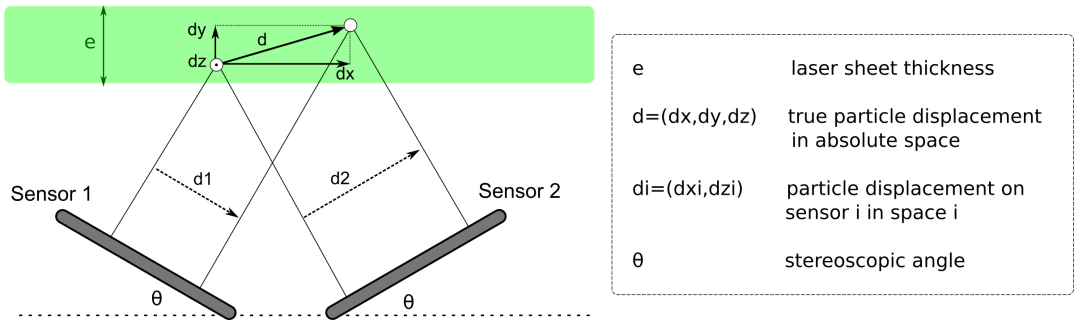

Figure 2.2 – Principle of stereoscopic PIV measurements using 2 cameras sketched for a single particle

considerably smaller. Limits of such hypothesis have been studied in details by Keane and Adrian (1990); Raffel et al. (2013); Simoëns (1992).

Particle size and density: Since velocity measurement is based on correlation of images of particles, the quality of particle imaging has to bee good enough. Particle images on camera sensors have to be encoded on at least two or three pixels, otherwise one will only be able to see the displacement of particles in terms of an integer number of pixels. This problem is known as peak locking, and corresponds to unusable sub-pixel determination.

Unlike Particle Tracking Velocimetry for which Lagrangian tracking is limited to a small number of particles, PIV requires a large number of seeding particles. Image correlation is more accurate if the number of particles in each interrogation window is important. Typically, one must have at least 10 particles per interrogation window. Yet, increasing particle density too much may cause light scattering effects of either incident illumination light or reflected light in non optically thin systems and decrease the signal over noise ratio of images, so particle density has to be considered carefully.

Particle displacement: Particle displacement is one of the main issue in optimizing PIV setups. Indeed it inherently depends on the measured flow, which may present regions with large velocities and regions with low velocities. It is commonly said that the particle displacement should be about one third or fourth of the interrogation window. It should be small enough to make sure that most of the particles used to determine the maximum of correlation stay in the interrogation window between two frames. It should yet be large enough for a displacement to be accurately measured, thus larger than the inter-pixel distance. Particle displacement requirements can be fulfilled either by adapting the size of interrogation windows, or by tuning the time interval between frames. It is thus necessary to have an *a priori* knowledge of the maximum displacement to be expected. Another point of concern is the three dimensional effects: displacements are measured in a plane, but particles may be subject to out-of-plane motion. If the time interval between two frames is too large, particle groups may move out of the laser sheet and correlation process won't be able to retrieve them on the second frame as well. Classical two-dimensional PIV should theoretically be limited to 2D flows for which no out of plan motion exists. If used for three dimensional flow, one must make sure that out-of-plane displacement is negligible in the time interval between frames.

Light sheet, depth of focus and exposure time: PIV methodology can be applied wherever particle illumination is possible no matter the light source. The quantity of particles detected

and the quality of their images is yet crucial and depends on light source and collection optic characteristics. For most of fluid mechanics applications however, powerful light sources are required to be able to measure flow characteristics at good spatial and temporal resolution. Indeed, when using small particles and high frame rate (i.e small time available for light collection) to achieve high spatial and temporal resolution, strong enlightenment intensity is needed so that usable particle images can be recorded. The best option is to use pulsed lasers or LEDS since they focus high intensity light on a small shot duration (of the order of 10 ns). Moreover, their beams can easily be shaped into sheets using converging and diverging lenses.

Particles should stay inside the focus zone of the camera during illumination. This depth of focus should be greater than the LASER sheet thickness, otherwise some illuminated particles out of the focus range may appear as blurry light spot on images. Exposure time is the time during which particle-reflected photons are collected by the camera's sensor (It corresponds to the laser pulse duration when using pulsed laser sources). The longer the exposure time the brighter the particle images and the better the signal over noise ratio. However for PIV applications using continuous illumination, long exposure times may lead to stick-shaped particle images and poor correlation precision.

2.1.1.b Stereoscopic Particle Image Velocimetry

Stereoscopic Particle Image Velocimetry (SPIV) is a variation of PIV providing measurement of the out-of-plane velocity component. It is therefore a 2D3C (2 dimensions 3 Components) method where classical PIV is only a 2D2C one. The displacement of particles are recorded by two (or more) cameras. The real 3 component displacement is reconstructed from the measured displacement on each camera's sensor (Hu, 2013).

Developped in the late 1980's (Jacquot and Rastogi, 1981), SPIV is nowadays used in various studies for both gaseous and liquid flow velocity measurements (Hori and Sakakibara, 2004; Sakakibara et al., 2004; Vernet, 2010).

Two main configuration exists: translation and rotational systems. In translation systems, the optical axis of each cameras are parallel to each other and all orthogonal to the light sheet. The main advantage of this system is the fact that all image fields show a uniform magnification, since object plane, lens plane and image plane are parallel to each other (Prasad, 2000). Thus, the tuning of lenses and cameras is approximately the same as it would have been for a classical PIV application except that one additional camera is added with a similar tuning. However in doing so, there is only a small area of the region of interest common to all camera sensors. In other words, part of what an individual camera sees can not be seen by the others and is therefore useless for the SPIV measurement. Moreover, if the distance between different cameras axes is too large, lenses are used beyond their limits of specification and important deformations may occur on the images. This is prejudicial since a good accuracy on the out-of-plane component measurement precisely requires a large distance between optical axes.

To overcome those major issues, one may use rotation systems for which the cameras axis are no longer parallel to each other but are rotated so that they intersect in the object/LASER plane. Cameras may be positioned on the same or opposite sides of the LASER sheet (Hu, 2013). The displacement seen by each sensor is a projection of the real particle displacement as sketched on figure 2.2.

The angle between cameras axis and the normal to the LASER sheet should be increased in order to increase the accuracy of the out-of-plane component measurement (Prasad and Jensen, 1995). The maximum precision angle for measurement is gaseous flows was found

by Prasad (2000) to be $\theta = 45°$. One major feature of rotation systems is that the magnification is no longer uniform on the field of view (Prasad, 2000). Moreover, depending on camera and lens' adjustments, the depth of focus of each camera may not be sufficient to see distinctly the whole observation field from the SPIV slanted point of view. A solution to that problem is to shift the lens' axis from the camera's axis introducing a so called "Scheimpflung angle" α. This misalignment distorts the depth of focus and adapts it to the measurement zone as illustrated on figure 2.3 (orange areas) so that the full field becomes clear. The optimal Scheimpflung angle is found when the observation plane, the lens' plane and the camera's plane are colinear. This is the Scheimpflung condition detailed in Prasad (2000) state of art on SPIV techniques .

Image distortion and heterogeneity of magnification being large in such systems, the spatial calibration procedure is all the more important. All deformed images have to be stretched back to a common Cartesian grid before velocity computation. To do so, an image of a Cartesian reference test pattern is recorded by each camera and used to correct image deformation.

That can be achieved by a general distortion compensation procedure as proposed by Soloff et al. (1997). Another approach is to use a pinhole model coupled to particle based self calibration technique developed by Wieneke (2004, 2005), which works as follows:

- First, spatial distortions of each camera is calibrated using a pinhole model (Sturm, 2014; Willert, 2006). This corresponds to a first 3D fitting (figure 2.4 a).
- Then, images of the same set of particles are recorded by the different cameras at the same instant, and a cross correlation is performed between those images to deduce a disparity mapping (Wieneke, 2005) (figure 2.4 b)).
- Finally, this disparity mapping is used to quantify the residual calibration errors and correct the pinhole model fit parameters (Wieneke, 2005). Images of particles coming from each cameras should indeed be strictly identical once cleared from distortion by the pinhole fitting model. With a perfect spatial calibration, their cross correlation should not yield any residual field. From the disparity mapping it is thus possible to correct potential misalignments between the test pattern and the light sheet during the recording of calibration image.
- Improved spatial calibration can then be re-computed using the new fit parameters.

Iterating the previous operation, one can reach an optimal distortion correction and mapping, thus minimizing further velocity field computation errors. The residual displacement error achievable is typically of the order of one pixel. This last option is the one currently used in the DaVis software (LaVision, 2011a) and has been used to calibrate the SPIV results presented in this manuscript.

2.1.2 Application to turbulent liquid flows

Two main locks have to be lifted for PIV and SPIV application to turbulent liquid flows.

First, the fast behavior of turbulence has to be accounted for. With a fast enough PIV setup, either single or double frame, one may be able to reach acquisition period $1/f_{acq}$ below the Kolmogorov time scale. If so, it is possible to resolve in time all turbulent structures and get information on spectral behavior of turbulence. On the other hand, if the PIV acquisition rate is too slow for temporal resolution of structures, one may use double frame

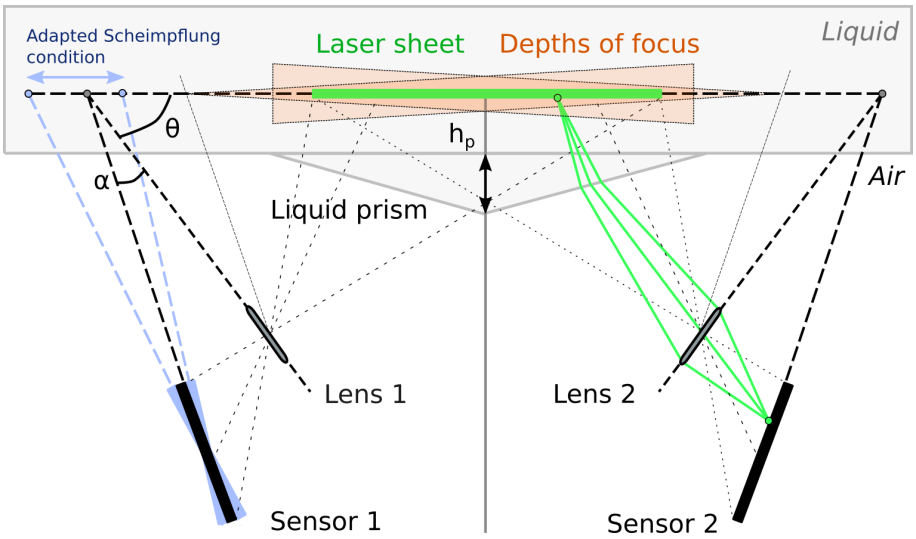

Figure 2.3 – Sketch of a rotation system using a liquid prism and Scheimpflung condition, adapted from Hu (2013) and Prasad and Jensen (1995).The Scheimpflung angle is α and θ is the stereoscopic angle. Orange triangles represent the focus zone of each camera. h_p is the height of the liquid prism. Angle α may be adapted due to the air liquid interface as sketched on the left part of the figure.

PIV at slow frame rate to extract sets of uncorrelated velocity fields and ultimately access statistical properties of the velocity fields and turbulence. In both cases an estimation of the characteristic time scales is needed prior to any experiments.

Second is the fact that when applied to liquid flows, an air-liquid interface necessarily exists between the cameras and the region of interest. Optical tuning of cameras and calibrations thus have to account for the optical path crossed by the particle re-emitted light in the liquid, and acknowledge if it suffers from deformations (figure 2.3, green beams).

Spatial calibration using test patterns easily account for deformation due to refraction when PIV is applied to wall bounded flows, since the optical path crossed by reflected light remains constant throughout the experiment. The inclination between camera's axis and the normal to the tank's walls increases refraction phenomena at the wall and blurs the visualization. This is even more the case using rotational SPIV system enforcing Scheimpflung condition. To avoid or at least limit refraction effects, the camera or lens' axis have to be aligned with the normal to the wall of the tank containing the liquid flow. That is achieved either by designing specific tank geometries (Hori and Sakakibara, 2004) or by adding a liquid prism between the wall and cameras, as explained in Prasad and Jensen Prasad and Jensen (1995) (Sakakibara et al., 2004; Vernet, 2010). In doing so, one limits deformations and chromatic aberrations due to refraction but also invalidates the Scheimpflung condition. The Scheimpflung angle α between camera and lens's axis has to be adapted so that the depth of focus of the system fits the region of interest (Prasad and Jensen, 1995) (see figure 2.3, left part).

2.1.3 Post-processing and Uncertainties

2.1.3.a Post-processing

Several post-processings can be used to improve the quality of computed vector fields. A criterion on peak ratio value can be used to remove spurious vectors. For example one can choose to delete vectors for which the peak ratio of correlation is below 1.2, chosen empirically. Empty spaces can be filled out by interpolation. Median filtering can be applied to

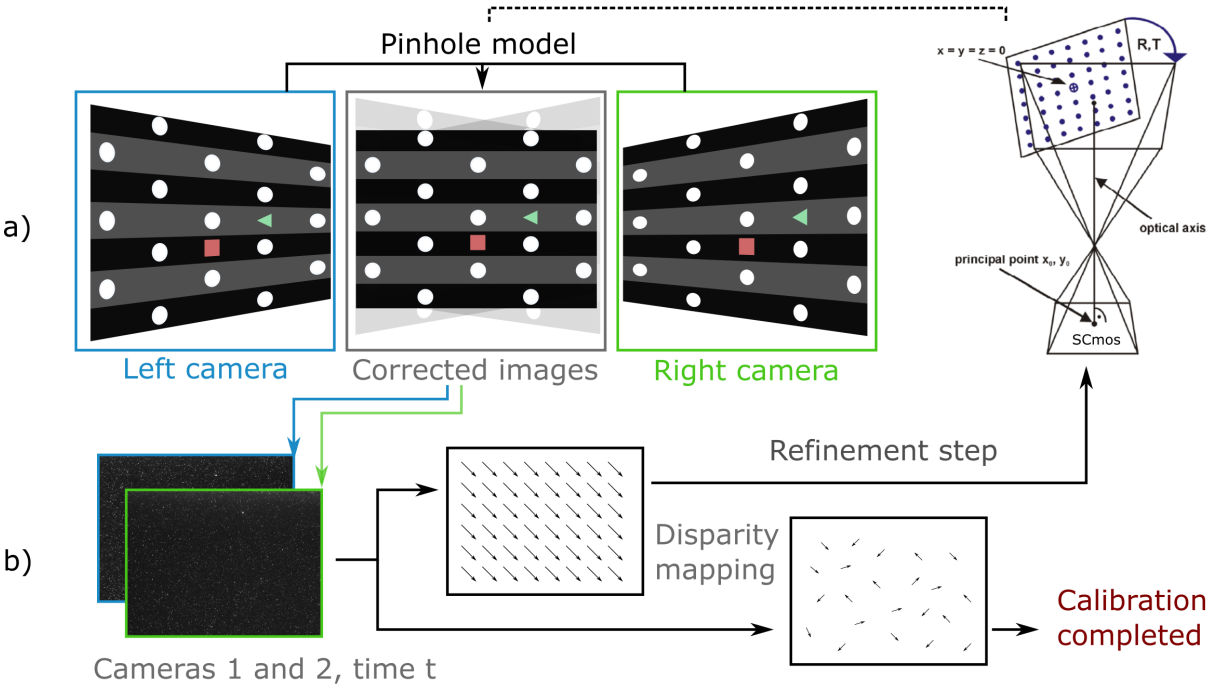

Figure 2.4 – SPIV calibration steps.a) Correction of image distortion using a reference pattern (schematic view with artificially enhanced deformation). The right part is a skecth of the pinhole-model extracted from Wieneke (2004) figure 2. b) Self calibration on particles: ensemble average of correlation maps between images taken at the same instant t and coming from the two cameras. The disparity mapping is strong and organized if alignment error between the cameras, laser sheet ant reference pattern exist, or low and random if the calibration is satisfactory.

get rid of spurious vectors not deleted by the previous step. This has to be applied only if the previous step leaves only a small percentage of empty space in the ROI (less than 1). Finally, spatial smoothing can be used (as done in this work). In the following chapters, post-processing steps applied to data sets will be specified

2.1.3.b Error estimation

Error and uncertainty estimation for PIV measurements is still an ongoing issue. Uncertainty of velocity measurements by PIV may be due to several factors among which:

- Image quality
- Seeding concentration and quality
- Flow properties (velocities, gradients, out-of-plane motion...)
- Particle superposition
- Optical distortions
- Timing errors (e.g. lags between LASER pulses and camera shutters)
- Laser sheet stability
- Spatial reconstruction errors for SPIV only

Several methods have been proposed to try and quantify uncertainties linked to different sources for PIV and SPIV. Uncertainty surface method has been advanced by Timmins et al. (2012). They performed a parametric study of PIV error varying several factors such as particle image size, particle density, displacement and shear values, and constructed a database of error sources and their impact on uncertainty. The peak ratio method developed by Charonko and Vlachos (2013) gives a direct empirical relationship between displacement uncertainty and the peak ratio value. The image matching or Particle disparity method by Sciacchitano et al. (2015) consists in using the measured displacement field to dewrap the second frame particle image end compare it to the first frame. The difference between frame 1 and dewrapped frame 2 is used as an error estimation. Lately, Wieneke (2015) expanded the image matching method of Sciacchitano et al. (2015) by taking into account the contribution of each pixel to the correlation peak. The basic principle is still to dewrap the second frame and compare it to the first on, but instead of estimating the error using the correlation between frame 1 and dewrapped frame 2, the influence of each pixel is accounted for by fitting the residual field correlation factors with a Gaussian function and measuring for each pixel the difference between this Gaussian function and the computed correlation. This method efficiently estimates uncertainty due to poor image quality or seeding and strong flow gradients. The limits stated by Wieneke (2015) are that it is neither able to detect spurious velocity vectors nor strong peak locking effects.

Stereoscopic reconstruction error can also be accounted for by in the following way (LaVision, 2011b):

- Images of each cameras are re-scaled to a common Cartesian space using the spatial calibration
- Frames 1 of each cameras taken at the same instant are inter-correlated using the same size and number of passes as the velocity field computation process, thus yielding a reconstruction error field
- This reconstruction error field can then be used as a threshold for vector reconstruction, forbidding the three-component vector building from measured displacement if the reconstruction error is above a given value.
- When reconstruction error is below the threshold, vectors are computed and the error value is included into the peak displacement uncertainty that is then used in Wieneke (2015) uncertainty estimation method. It is therefore propagated to all further computed quantities and a full part of the final error estimation.

Statisticall error estimation method by Wieneke (2015) coupled to stereoscopic reconstruction error computation is one of the most up to date method for uncertainty quantification of SPIV data. It is applied to the results presented in chapter 4.

2.2 pH and dissolved gas concentration measurement: Inhibited Planar Laser Induced Fluorescence

The method for measurement of the two or three velocity components in a planar region of interest has been detailed. Now let us introduce the one used for the measurement of passive scalar field, namely Planar Laser Induced Fluorescence (PLIF). Since the use of this technique is motivated by a need to measure dissolved carbon dioxide (CO_2) fields in aqueous media, the next section starts with a brief introduction to CO_2 and the chemistry of its dissolution into water and aqueous solutions. A brief history of the development of PLIF and Inhibited PLIF (I-PLIF) techniques is then proposed and the main principles common to all variations of the PLIF and I-PLIF techniques are explained. The section goes on with a detailed presentation of a new pH sensitive I-PLIF method developed during this thesis. In this context, the fluorescent dye is characterized, and a the theoretical bases of the method is established and verified by a spectrofluorimetric study. A first test case of the application of the method to a turbulent liquid flow is presented. The applicability of the technique to dilute polymer solutions is discussed in anticipation to chapter 4, and the basis for a second test case, this time diphasic, are set. Finally, the uncertainties and errors associated to this new technique, and the possible improvements that can be made are debated.

2.2.1 Carbon dioxide and its dissolution into aqueous media

During this thesis, we aim at studying the turbulent dissolution of a high Schmidt number gas at a gas-liquid interface with Newtonian or non-Newtonian liquids. Based on several reasons listed in the following paragraph the choice was made to use CO_2. The two next paragraphs are focused on the complex chemistry of this gas' dissolution into water and aqueous solutions, and to the kinetics of this chemistry.

2.2.1.a The interest of studying carbon dioxide

The dissolution of gaseous carbon dioxide $CO_{2(g)}$ into aqueous media is part of many environmental and industrial processes. For example, the production of micro-algae in photobireactors mostly depends on their ability to efficiently feed the microorganisms with dissolved carbon dioxide $CO_{2(aq)}$. It is known that dissolution is quicker when turbulence is induced in the water flow, for example by strong bubbling or water phase circulation. Yet, a critical turbulent intensity can also damage the micro-algae (San et al., 2017) and reduce production. Knowing the key parameters for an efficient turbulent mass transfer with relatively low Reynolds number is of interest for such processes (Valiorgue et al., 2014; Vasumathi et al., 2017).

A similar problem can be found in the oceans where the balance between mass transfer and turbulent intensity conditions the growth and size of phytoplankton blooms (Variano and Cowen, 2013). By increasing the sea water pH near the interface, plankton induces chemical pumping of CO_2 into water and contribute significantly to the atmospheric greenhouse gas balance.

This leads us to maybe the most obvious reason of studying CO_2 dissolution: the development of efficient CO_2 sequestration devices for the limitation of greenhouse gas emissions and the regulation of climate change. Storage or bio-remediations processes are numerous and most of the time require as a first step the dissolution of gaseous CO_2 into a liquid phase: photocatalytic conversion (Chu et al., 2017), algae production (Valiorgue et al., 2014), dissolution in aquifers (Al Mansoori et al., 2010), porous reservoirs storage and geo-

logical sequestration (Huppert and Neufeld, 2014; Someya et al., 2005). Development of CO_2 bio-remediation methods have gained interest in the last decades, but the physics of CO_2 dissolution and mass transfer from gaseous phase to turbulent liquid flow has to be better understood to improve these processes.

The last motivation for the use of CO_2 in this thesis is more of a fluid mechanics one: CO_2 and other atmospheric gases are considered as high Schmidt number scalars (see definition of the Schmidt number in chapter 1). The molecular diffusion coefficient of the dissolved form of the gas D_{CO_2} is low as compared to the kinematic viscosity of water ν, which means that diffusion is prone to be much slower than convection once in the liquid phase. Typical values of diffusion coefficient and Schmidt number of CO_2 and oxygen are $D_{CO_2} \approx 1.9 \times 10^{-9}$ m^2.s^{-1}, $Sc_{CO_2} \approx 527$ and $D_{O_2} \approx 2 \times 10^{-9}$ m^2.s^{-1}, $Sc_{O_2} \approx 500$ [2]. Once fully dissolved in water, the behavior of CO_2 is analog to any passive scalar and so studying dissolved CO_2 mixing can be a way of studying high Schmidt number passive scalar mixing in a more general way.

However, where oxygen or nitrogen dissolution into water are non reactive and only depend on a partial pressure equilibrium, CO_2 dissolution involves several successive chemical reaction detailed in the following paragraph. CO_2 is therefore a reactive scalar that can still be seen as a passive scalar if one assumes that these reactions are total and instantaneous after dissolution. If so, they don't play any role in mixing and are not "seen" by the flow. On the other hand, if one assumes that they are slow compared to the typical flow time scale, the reaction kinetics play a role in mass transfer and mixing. This point is also discussed in the following paragraph.

These chemical reactions are acid base equilibria, thus CO_2 concentration acts on the pH of the liquid phase. CO_2 has therefore been chosen over oxygen and other gases in order to use and develop a specific metrology for pH measurement. The interest of such method is that it can be used not only in CO_2 concentration measurement but also in any passive or reactive, macro or micro mixing study leading to pH variations of the liquid phase. The technique, called I_{pH} – PLIF, and its variations are presented in details hereinafter.

2.2.1.b Dissolution reactions and kinetics

As mentioned above, when dissolved in aqueous media under the effect of its gas partial pressure, CO_2 interacts with water to form carbonic acid H_2CO_3 through the following reaction:

$$CO_{2(aq)} + H_2O = H_2CO_3 \tag{2.3}$$

With a reaction constant at 25°C of (Stumm and Morgan, 1996)[3]:

$$K_h = \frac{[H_2CO_3]}{[CO_2]_{aq}} = 1.7 * 10^{-3} \tag{2.4}$$

Since this reaction consumes aqueous CO_2, more gas has to dissolve into the fluid to fulfill Henry's law equilibrium. One can see that in the case of reactive gases dissolution, the final amount of gas dissolved into the fluid is greater than that of a non reactive gas with a similar Henry's law constant.

[2] If not specified otherwise, D_i is the diffusion coefficient of species i in pure water in what follows

[3] All reaction constants and pK values are given for a temperature of 25°C

Carbonic acid formed then dissociates into hydrogen carbonate HCO_3^-, and hydrogen carbonate into carbonate CO_3^{2-} through the successive acid-base equilibria:

$$H_2CO_3 + H_2O = HCO_3^- + H_3O^+ \tag{2.5}$$

$$HCO_3^- + H_2O = CO_3^{2-} + H_3O^+ \tag{2.6}$$

With respective reactions constants (Stumm and Morgan, 1996):

$$K_a = \frac{[H_3O^+][HCO_3^-]}{H_2CO_3]} = 2.52 * 10^{-4} \tag{2.7}$$

$$K_b = \frac{[H_3O^+][CO_3^{2-}]}{[HCO_3^-]} = 4.68 * 10^{-11} \tag{2.8}$$

Introducing $pK_i = -log(K_i)$ this gives the following pK for reactions 2.3, 2.5 and 2.6:

$$\begin{cases} pK_h = 2.77 \\ pK_a = 3.60 \\ pK_b = 10.33 \end{cases} \tag{2.9}$$

These values indicate that aqueous CO_2, carbonic acid and hydrogen carbonate ions are present at acidic and neutral pHs, whereas carbonate ions are mostly found in basic media.

Carbonic acid is called a polytropic acid, since it dissociates several successive times. With this reactive behavior, it is no longer relevant to consider only the aqueous form $CO_{2(aq)}$ to fully describe the presence of gas in the fluid, as it would be for a non reactive gas. A common way to describe the dissolution of CO_2 into water is the Dissolved Inorganic Carbon dioxyde (DIC) concentration, defined as the sum of all carbonate species' concentrations:

$$DIC = [CO_2]_{aq} + H_2CO_3 + [HCO_3^-] + [CO_3^{2-}] \tag{2.10}$$

Reactions 2.3, 2.5 and 2.6 clearly show how carbon dioxide absorption by water is responsible of its acidification. After a given time, a volume of water submitted to a constant partial pressure of gaseous CO_2 will eventually reach an equilibrium point DIC - pH or $[CO_{2(aq)}]$-pH. This equilibrium depends on several factors, among which:

- The constant partial pressure of CO_2 imposed, which sets the saturated equilibrium concentration $[CO_2]_{aq}$ through Henry's law
- The temperature conditions, which will have an influence on the reaction constants of all the equilibria involved
- Other chemical species or solid impurities present inside the water at the initial state and that may either react directly with dissolved CO_2, reaction products, or affect reactions equilibria indirectly (catalysts). Three main properties may be defined to quantify the presence of such species into water and describe their influence:
  - **Water Hardness** is a measurement of the propotion of minerals into water, or water mineralisation, mostly due to Magnesium Mg and Calcium Ca composed species. These minerals are able to react directly with aqueous CO_2, like $CaCO_3$ (Calcite) $CaCO_3(s) + CO_2 = Ca^{2+} + 2HCO_3^-$ for example. By consuming aqueous CO_2, these reactions have a "pumping" effect, increasing the amount of carbon dioxyde dissolved into the water at equivalent pH (Stumm and Morgan, 1996).

- **Alkalinity** is generally defined as the total amount of bases that can react with a strong acid. In carbonate systems, alkalinity strongly depends on the completion of the two acid-base reactions 2.5 and 2.6 since they produce successive bases of the polytropic system. The presence of other bases at the initial state determines the CO_2-pH equilibrium of water and therefore the equilibrium pH for a given amount of gas dissolved.
- **Salinity** is the amount of salt present in the liquid (Salts being defined as ionic compounds resulting from the neutralization of an acid and a base). Its value has an influence on water conductivity and ionic strength, and might therefore alter the values of any other reaction constants leading to a shift in their equilibria. It also affects the fugacity equilibrium which plays a role in Henry's law.

This last conclusion gives an insight on why carbonates equilibrium differs between sea water, mineral water or distilled water. In order to fully describe the chemical state of such systems, every reaction involved has to be taken into account simultaneously. For obvious environmental reasons, the behavior of carbonate systems in sea water and/or the influence of salinity has been widely studied for several decades by chemists and oceanographs (Fox, 1909; Portier and Rochelle, 2005; Weiss, 1974). As for this study, the focus is kept on dissolution reactions into distilled water. Initial salinity, hardness and alkalinity and their influence on the dissolution may be considered negligible. Special care is taken with water filtration in order to achieve adequate conditions.

Under those assumptions and at constant temperature, the pH of water is set only by CO_2 dissolution, itself set by the partial pressure of CO_2 in the gas above water. Knowing the reaction constants K_h,K_a, and K_b, it is possible to deduce all carbonate species proportions with respect to the DIC as a function of the pH value. In order to do that, equations (2.4),(2.7) and (2.8) have to be associated with the equation for electric charge conservation

$$[HCO_3^-] + 2[CO_3^{2-}] + [HO^-] - [H_3O^+] = 0 \tag{2.11}$$

Using water self equilibrium equation

$$K_w = [H_3O^+][HO^-] \tag{2.12}$$

and the definition of pH: $[H_3O^+] = 10^- pH$, one gets a 4 by 4 linear system, with $[CO_2]_{aq}$, $[H_2CO_3]$, $[HCO_3^-]$ and $[CO_3^{2-}]$ to be computed for a given pH input.

$$\begin{bmatrix} K_h & -1 & 0 & 0 \\ 0 & K_a & -10^{-pH} & 0 \\ 0 & 0 & K_b & -10^{-pH} \\ 0 & 0 & -1 & -2 \end{bmatrix} \times \begin{bmatrix} [CO_2]_{aq} \\ [H_2CO_3] \\ [HCO_3^-] \\ [CO_3^{2-}] \end{bmatrix} = \begin{bmatrix} 0 \\ 0 \\ 0 \\ -10^{-pH} + 10^{pH-pK_w} \end{bmatrix} \tag{2.13}$$

Inverting and solving numerically this system with Matlab, one can get the evolution of each species concentration as a function of pH. Dividing them by the DIC obtained simply using equation (2.10). It is then possible to plot the Bjerrum plots of the polytropic of carbonate species, that is to say the ratio of each species concentration over total concentration (DIC) on the pH range of interest (figure 2.5).

Several conclusions may be extracted from that graph:

- Carbonic acid H_2CO_3 is always present is small proportion with respect to the other species. That is why in the litterateur, it is generally artificially associated with $[CO_2]_{aq}$

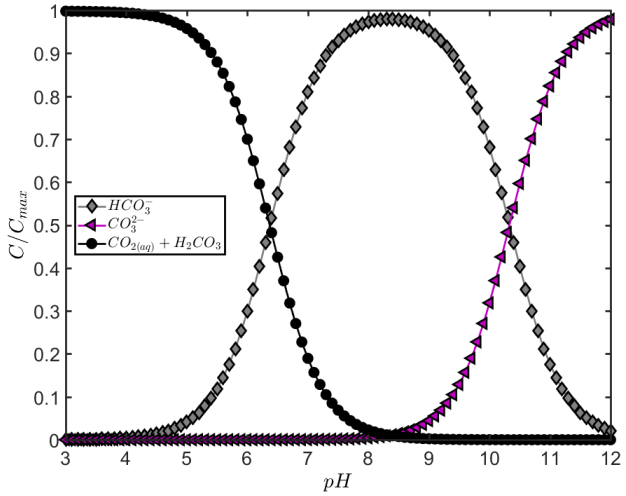

Figure 2.5 – Bjerrum plot of carbonate species into water

and denoted $[H_2CO_3]^*$ such that $[H_2CO_3]^* = [H_2CO_3] + [CO_2]_{aq}$. Equation 2.5 and the constant K_a (2.7) have to be modified as follows

$$H_2CO_3^* + H_2O = HCO_3^- + H_3O^+ \tag{2.14}$$

with

$$\begin{cases} K_{ap} = \frac{[H_3O^+][HCO_3^-]}{[H_2CO_3]^*} \\ pK_{ap} = 6.38 \end{cases} \tag{2.15}$$

This way of doing is equivalent to what has been presented above and rather frequent in the literature (Soli and Byrne, 2002; Stumm and Morgan, 1996). It is shown here for information but won't be used after.

- At pH under 8.5, $[CO_3^{2-}]$ is rather small and negligible compare to other species' concentration.

Influence of starting pH on acidification of water by dissolved carbon dioxide: In a will of optimisation of experimental procedures involving fluorescence (Kuhn and Jensen, 2012) or present study in section 2.2, it is usefull to quantify the effect of an initially high pH on the behavior of carbon dioxyde dissolution into water. In that section as in the rest of this study, water is assumed perfectly distilled and the initial pH is set by addition of a given quantity of sodium hydroxide NaOH to the water. This is equivalent to fixing a non zero alkalinity for the water, using only one component. That modification of the initial condition is accounted for in the electroneutrality equation (2.11) by adding a constant $[Na^+]$ concentration corresponding to the concentration needed to set the water pH at a give value. This initial concentration is computed from the wanted initial pH, using the fact that sodium hydroxide is a strong base, with

$$pH_0 = 14 + log([NaOH]_0). \tag{2.16}$$

It gives for the electroneutrality:

$$[HCO_3^-] + 2[CO_3^{2-}] + [HO^-] - [H_3O^+] - [Na^+] = 0 \tag{2.17}$$

The previous approach is used again with equation (2.17) replacing equation (2.11), using different values for the initial pH. The evolution of aqueous carbon dioxide and DIC concentration as a function of pH can then be plotted on a semilog graph as below for different initial pHs (figure 2.12). Experimental data points have been obtained using a pH sensor and a dissolved CO_2 probe, as explained in appendix D. When the starting pH reaches very basic values, typically above 10, a shortcut reaction to the hydration of carbon dioxide may appear and aqueous CO_2 directly hydrate into HCO_3^- through the following reaction (Stumm and Morgan, 1996):

$$CO_{2(aq)} + HO^- = HCO_3^- \tag{2.18}$$

This reaction, negligible at pH under 8 and dominant at pH above 10 tends to accelerates the consumption of aqueous carbon dioxide and the production of HCO_3^-. In that sense, the shortcut reaction 2.18 acts as a catalyst to reactions 2.3+2.5 since it accelerates the conversion of CO_2 into HCO_3^- without modifying the final equilibrium state (Stumm and Morgan, 1996) [4].

To summarize, the addition of sodium hydroxide to distilled water has two effects on carbon dioxide equilibria. The first one is an overall increase in pH: more carbon dioxide is needed to come down to a given pH when a base is present, conversely for a given amount of carbon dioxide, the pH will logically be higher. The second one is a catalyst effect induced by the shortcut reaction leading to an increase in the overall hydration rate.

2.2.1.c Kinetics and use of pH for gas concentration measurements

As mentioned previously, the difference between reactive and passive mass transfer in presence of liquid phase turbulence lies in the compared time scales of reaction and advection. If the chemical reactions are fast enough so that one can assume that they happen before any advection takes place, the mixed scalar can be considered passive since in any advected fluid particles the chemical reactions have reached equilibrium. On the other hand, if the reaction time scale is comparable or longer than the advection time scale, fluid particles with different chemical reaction advancement and different compositions can be advected.

Let us consider a simple mass transfer configuration. A gas-liquid interface is set at a saturated carbon dioxide concentration, and a diffusive film of thickness δ develops on the liquid side, the size of delta being fixed by the flow conditions in the liquid phase. This configuration corresponds to a Lewis and Whitman (1924) model for mass transfer that will be addressed in chapter 4. If reaction is faster than diffusion, chemical equilibrium is reached before reactants can be advected outside of the δ layer. If it is slow however, the reactants can diffuse further than δ before the reaction is complete, and the equilibrium will be achieved in the bulk (out of the diffusion layer). The Hatta number is used to quantify the relative influence of reaction versus diffusion. It is defined as

$$Ha^2 = \delta \frac{k[R_A]^{n-1}}{D_A} \tag{2.19}$$

where k is the reaction rate at which reactant R_A is consumed, D_A is the diffusion coefficient of this reactant in the liquid and n the order of reaction.

- **Ha**< 0.3 means that reaction process is slower than diffusion, and therefore occur essentially in the bulk, far from the interface

[4] Since the final equilibrium state is not modified, the addition of this shortcut reaction to the Matlab equation system is not needed.

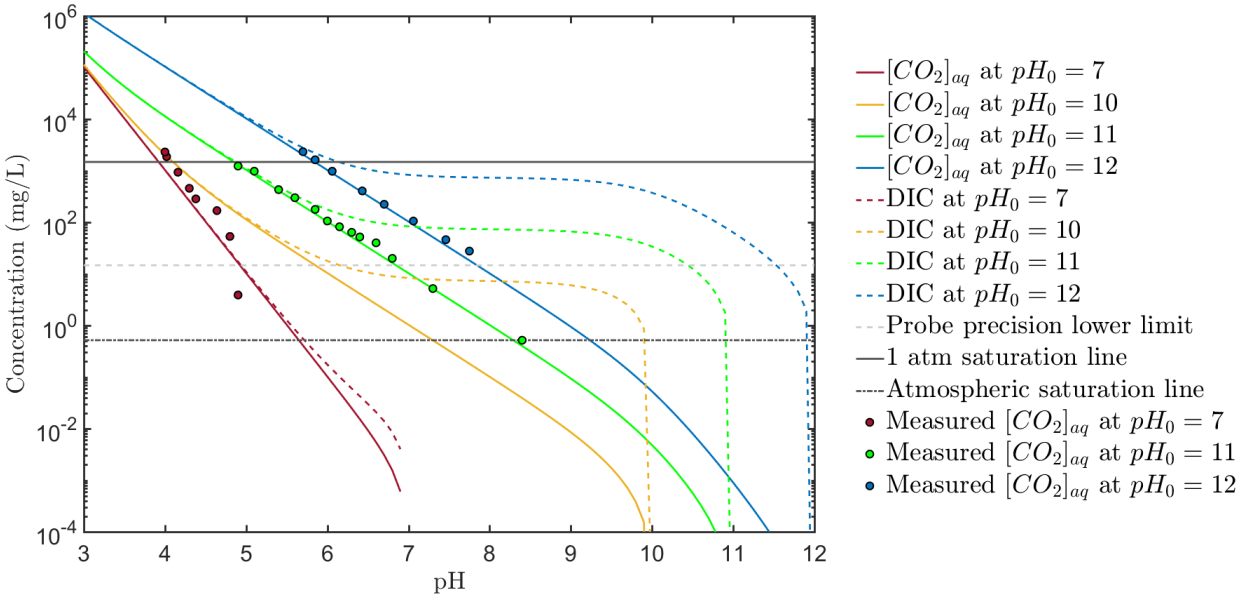

Figure 2.6 – Relationship between pH and dissolved carbon dioxide concentration in distilled water or sodium hydroxide solutions. Full and dashed lines are $[CO_2]$ and DIC computed using the Matlab system. Markers are experimental data (see appendix D)

- 0.3 <**Ha**< 3 means that the time scales for reaction and diffusion phenomena are close, hence the reactions start in the diffusion film and complete in the bulk
- **Ha**> 3 means that the reaction reaches equilibrium in the diffusive film and the species mixed in the bulk are that of the final state of reactions (products and remaining reactants)

The quicker the reaction, the better its chances to happen entirely in the diffusive film. The higher D_A the faster the diffusion and hence the better chances for the reaction to happen in the bulk. As for the effect of turbulence on the liquid side, it will be shown later (chapter 4) that it tends to thin down the diffusion layer δ (thus increasing the concentration gradient and the mass transfer).

If one wants to use pH as a tracer of dissolved CO_2 bulk mixing, one should check that the reaction is complete in the diffusive sub-layer. In carbon dioxide hydration kinetics, the slowest reaction is equation 2.3. The two others are acid base equilibrium that one can consider almost instantaneous (Stumm and Morgan, 1996). Hydration kinetics of carbon dioxide are solved using Matlab. A typical 99 % reaction completion time of 0.24 s is found. Computing the Hatta number using the inverse of this reaction time for k and an order of magnitude of 100 μm for δ (Batchelor sub-layer as defined by Herlina (2005)) one gets Ha $\approx$ 5, hence the reaction is confirmed to happen entirely in the diffusive layer.

Note that if the experimental setup is good enough to be able to measure concentrations within the chosen δ, the relevant quantity to compute the Hatta number and check for pH tracking validity is no longer δ but rather the minimum depth under the saturated interface at which one is able to perform measurement. This is however not the case for the experiments of chapter 4.

To be able to track temporal carbon dioxide concentration variations, it should also be checked that the pH-CO_2 equilibrium can be reached between two successive frames. The acquisition period should be greater than a typical reaction time scale (Asher and Litchendorf, 2008; Valiorgue et al., 2013). In a configuration similar to the experiments presented in

chapter 4, Asher and Litchendorf (2008) found that there is a measurable pH change at time scales as short as 0.2 s, close to the 0.24 s found here.

2.2.2 PLIF and I-PLIF

2.2.2.a Introduction to LIF and PLIF techniques

Laser Induced fluorescence (LIF) consists in triggering the fluorescent of a dye mixed in the fluid by the means of a continuous or pulsed laser source. The measurement of the dye's fluoresced light intensity leads to the quantitative determination of its concentration C in the triggered region thanks to a linear relationship between C and the fluoresced light intensity. This relationship remains linear only if the laser excitation intensity remains in the weak excitation regime (Chaze et al., 2016). The first LIF measurements were punctual, achieved by focusing the laser beam on a point in the flow (Komori et al., 1993; Papanicolaou and List, 1988), or 1D along a laser beam crossing the flow (Koochesfahani and Dimotakis, 1986). It is also possible to illuminate a whole volume, for example a droplet of liquid, the measurement being in that case an integration of the wanted parameter over the whole volume thickness (Chaze et al., 2017).

An interesting variation of LIF is its Planar version, called PLIF. In PLIF, the laser beam is shaped into a thin plane using a cylindrical diverging lens. Using a multi-pixel light sensitive sensors (CMOS or CCD), one can record the fluorescence signal coming from this plane and thus compute the corresponding instantaneous concentration field with an excellent spatial resolution. By scanning the laser sheet through a volume of measurement, one may even reconstruct a 3D volume of measured scalar (Dahm et al., 1991; Prasad and Sreenivasan, 1990). For further details on general PLIF technique and its uses, the reader is advised the review by Crimaldi (2008).

The extension of PLIF method that will be considered here relies on the fact that for some fluorescent dyes, the emission intensity may also depend on the local value of a scalar quantity of the flow. This makes it possible to deduce directly the value of this scalar from fluoresced light intensity measurement when the dye is homogeneously mixed in the fluid at fixed concentration. Such techniques will hereinafter be referred to as $I_i - PLIF$ as they are versions of PLIF where fluorescence inhibition by species or scalar i occurs. For example, Rhodamine's thermal sensitivity can be used for temperature measurements ($I_T - PLIF$) in different types of flows (Coolen et al., 1999; Crimaldi, 2008; Sakakibara et al., 1997). The dissolved concentration of oxygen into water also tends to decrease the fluorescence of Ruthenium with a Stern-Volmer type quenching law, as used by Jimenez (2013), Xu et al. (2017) or Roudet et al. (2017). This variation could be called $I_{O_2} - PLIF$.

2.2.2.b $I_{pH} - PLIF$

In 1987, Walker (1987) proposed a technique equivalent to $I_T - PLIF$ to measure punctually the pH value in acid/base reactive flows. His method is based on the pH dependency of the fluorescence of a family of dyes called fluoresceins, characterized by Lindqvist (1960) and Martin and Lindqvist (1975) (see part 2.2.3).

His work was used as a base for further development of pH sensitive Inhibited Planar Laser Induced Fluorescence ($I_{pH} - PLIF$) and its application to the measurement of the dissolution of carbon dioxide around bubbles (Kuhn and Jensen, 2012; Valiorgue et al., 2013) or at flat surfaces (Asher and Litchendorf, 2008; Variano and Cowen, 2013). Indeed, it is well known that the dissolution of gaseous carbon dioxide into water results in the decomposition of the dissolved gas into carbonic acid. Carbonic acid reacts with water through two

successive acid/base reactions to form sodium carbonate, bicarbonate, and protons, hence decreasing the pH (Stumm and Morgan, 1996). Providing that these reactions' kinetics are fast enough (Asher and Litchendorf, 2008; Valiorgue et al., 2013), it is possible to access an instantaneous 2 dimensional dissolved gas concentration field thanks to $I_{pH}-$PLIF. The accuracy of this method is nevertheless limited by three main factors:

Interfaces: In presence of a moving interface such as a bubble or a free surface, laser reflections on this interface may result in heterogeneous and time-variable excitation intensity distribution in the laser sheet. If this distribution varies during the measurement, it becomes impossible to account for its heterogeneity simply using a reference image.

Variations of excitation intensity field: When confronted to non optically thin geometries, the absorption of the laser intensity on its path to the region of interest across the fluid becomes non negligible. If the area submitted to pH variation is small, this attenuation can easily be accounted for by using a reference image at a constant pH to correct Beer-Lambert absorption (keeping in mind the limitations denoted above). This is the case of figure 2.7 a.

pH dependency of molar extinction coefficient: The main issue is that fluorescein's molar extinction coefficient ϵ depends on the pH. So if the area submitted to pH variations is large, the overall variations of molar extinction coefficient due to the pH may become important. The intensity of excitation light reaching any point of the region of interest becomes function of the molar extinction coefficients encountered by the laser beam on its path, hence of the pH field, as in figure 2.7 b and c. It is assumed that the molar extinction coefficient is equivalent to a molar absorption coefficient, namely that all light attenuation comes from absorption by dye molecules. No other attenuation source exists (presence of particles ...). Valiorgue et al. (2013) developed a correction procedure to overcome this effect, later completed by Souzy (2014). The principle introduced by Valiorgue is to record a series of images at different homogeneous pH before the measurement, and to build a specific calibration relation between intensity and pH for each pixel of the recorded image. The variations of excitation intensity due to the global pH variation with time are therefore taken into account. To tackle the issue of local pH heterogeneity, Souzy (2014) proposes to compute the value of the molar extinction coefficient of pixel columns n from the pH value at column of pixel $n-1$ for all images acquired during the measurements (figure 2.7). Scanning images from the column of pixel closer to the laser n_0 to the furthest, and using the "pixel-by-pixel" calibration of Valiorgue, the pH and ϵ field accounting for extinction coefficient variations on the laser path are simultaneously obtained.

This last procedure still presents some flaws. First the region of interest (ROI) has to be larger or equal to the region of the flow submitted to pH variation (ROV), otherwise the first column of pixel can't even be used as a reference since its pH is not known. Second, the step-by-step computation of pH and ϵ introduces a cumulative error that could become important for the last columns of pixel treated. A last problem is the necessity to know the complete beam's path through the flow, which can only be achieved to the cost of spatial resolution.

This pixel-by-pixel calibration is also very long when treating several acquired images of fluorescence fields, since each pixel has to be calibrated and treated individually. To the authors' knowledge, very few people apart from Valiorgue have preferred the accuracy of the calibration over the time needed for treatment (Kuhn and Jensen, 2012). Most of the time a compromise between spatial resolution and processing time is made by averaging the intensity values over groups of pixels before calibration and treatment.

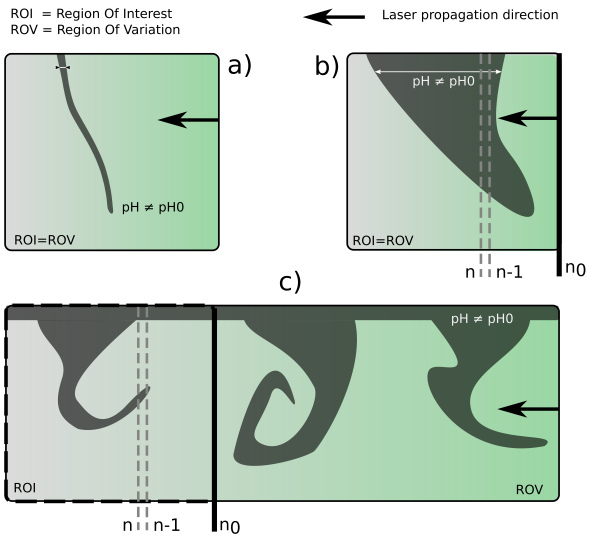

Figure 2.7 – Configurations of high laser attenuation a) easily correctable b) Correctable using a pixel-by-pixel method (Souzy, 2014), c) Non correctable with a single color technique

2.2.2.c Ratiometric developments and I_T^r – PLIF

To overcome the limitations stated above for non optically thin systems, an improvement of I – PLIF has been developed by Coppeta and Rogers (1998). The principle of this so-called "two-color" or ratiometric inhibited PLIF (later denoted as I_i^r – PLIF for inhibition by species i) is to collect the fluorescent light emitted at two different wavelengths by a single dye or a pair of fluorescent dyes excited by the same laser. One wavelength is chosen such that its fluoresced light intensity strongly depends on the scalar quantity to measure, and the other one so that it does not. Dividing the first wavelength intensity field by the second one, the effects of heterogeneous or scalar-dependent excitation intensity mapping are corrected, since the excitation intensity is common to both fluoresced wavelengths. The two wavelengths may come from two different dyes, in which case the I_T^r – PLIF may be defined as "two colors - two dyes" (2c/2d) (Chaze et al., 2016, 2017; Fenner and Stephan, 2017; Natrajan and Christensen, 2009; Sakakibara and Adrian, 1999), or from the spectrum of a single one, in which case one speaks of "two colors - one dye" method (2c/1d) (Bruchhausen et al., 2005; Coolen et al., 1999).

Since all fluorescence wavelengths collected come from the same excitation intensity, this last quantity does not impact the ratio of measured intensities, and only the dye concentrations and the targeted scalar characteristic do. The ratiometric procedure can consequently easily account for any temporal power drift of pulsed or Continuous Wave Lasers (CWL) during measurements, or for heterogeneous and time variable distribution of excitation intensity in the laser sheet and the region of interest.

In two dyes systems, it is possible to measure relatively high fluoresced light intensity signals for both scalar sensitive and insensitive wavelengths. The major difficulty is to find a pair of dyes excitable by the same laser wavelength, and with a minimal spectral overlap between them to avoid spectral conflicts, as explained later. The measured ratio of fluorescence intensities also depends on the ratio of the two dyes concentrations, that needs to be exactly known and remain constant everywhere in the fluid during the experiment. For example, when confronted to turbulent flows, it must be assumed that the two dyes diffuse similarly (Lavieille et al., 2004). On the other hand, single dye methods may be easier to implement since they only require to know the absorption and fluorescence spectra and the concentration of a single fluorescent compound. They are also less chemically intrusive

since they only require the addition of one chemical component instead of two inside the fluid. But as for two dyes systems, the dye has to be wisely chosen to avoid spectral conflicts.

Spectral conflicts are due to overlaps between absorption and/or fluorescence spectra of one or several dyes. They have been classified in three main categories (Chaze et al., 2016; Coppeta and Rogers, 1998), sketched in figure 2.8:

- **Type I** conflicts are specific to two dyes systems and arise when the two fluorescence spectra of the two selected dyes partially overlap, so that some of the fluorescence of one dye can be wrongly interpreted as coming from the other dye. Sakakibara and Adrian (1999) addressed this situation in the context of temperature sensitive measurements and showed that this strongly reduces the accuracy of measurements.

- **Type II** conflicts are due to an interference between the absorption spectrum of one dye and the fluorescence of the same or the other dye. They are therefore not limited to two dyes systems, but extend to single dye systems where the Stokes shift is small (wavelength lag between the absorption and the emission peaks of a fluorescent molecule as sketched one figure 2.8). In that case, part of the fluoresced light intensity emitted is reabsorbed, and the fluoresced light intensity measured by the sensor becomes dependent on the length of fluid crossed by the fluorescence signal to reach it. Such effect can be neglected if this path is short enough (see section 2.2.4.a). If this is not the case, it can be corrected using a reference fluorescence ratio image to normalize the measured intensities, inasmuch as the spectral overlapping does not depend on the scalar quantity to be measured. A three-color method can also be used to corrects the adverse effect that reabsorption does not affect to the same extent all the wavelengths within a detection band (Lavieille et al., 2004).

- If the spectral overlapping area depends on the measured scalar, type II conflicts becomes a **type III** one (figure 2.8b). The intensity collected by the sensor is not only dependent on the path length of the fluorescence signal between the laser sheet and the light collection device, but also on the scalar values encountered by the fluoresced light emission signal on its way to the sensor. If this path length or the dye concentration are too important for fluorescence re-absorption phenomena to be neglected (see section 2.2.6.b), this conflict can not be corrected by ratiometric methods (2c/2d or 2c/1d).

Since the proof of concept of the ratiometric methodology made by Coppeta and Rogers (1998) for both temperature and pH measurements, the temperature sensitive version has been regularly used and improved (Bruchhausen et al., 2005; Chaze et al., 2016; Coolen et al., 1999; Fenner and Stephan, 2017; Lavieille et al., 2004; Natrajan and Christensen, 2009; Rochlitz and Scholz, 2018; Sakakibara and Adrian, 1999). Recent studies show that it is possible to measure efficiently temperature distribution inside droplets impinging on hot solid surfaces with good spatial and temporal resolution (Chaze et al., 2017) or the evaporation of ehtanol meniscus (Fenner and Stephan, 2017; Fenner, 2017).

The pH sensitive ratiometric PLIF (hereinafter referred to as $I^r_{pH}-$PLIF) has been mainly used in its two dyes version (2c/2d) for pH measurement in macromixing and micromixing studies and two-phase flows mass transfer (Kováts et al., 2017; Lehwald et al., 2010; Passaggia et al., 2017). Someya et al. (2005) used quinine and sulforhodamine to visualise the dissolution of carbon dioxide droplets in high pressures vessels. Passaggia et al. (2017) used Rho-

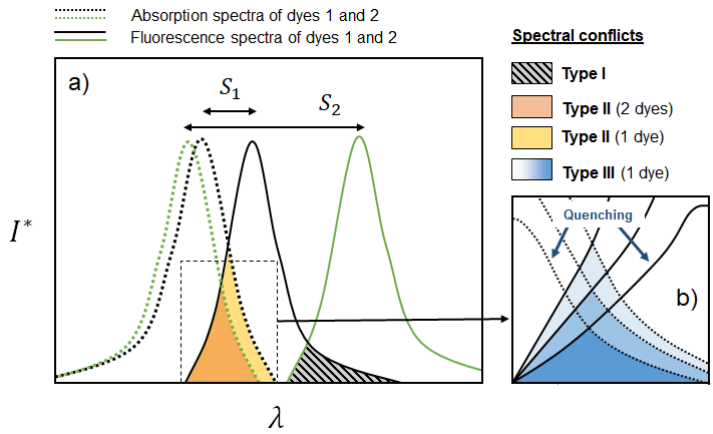

Figure 2.8 – Illustration of the different types of spectral conflicts. Type I and type II for one and two dyes configurations (a), and example of type III for one dye configuration (b). S_1 and S_2 are the Stokes shifts of dye 1 and 2 respectively

damine and fluorescein respectively as reference and pH sensitive dyes to study the turbulent horizontal convection driven by buoyancy gradient in water. Regarding two phase flows, Kräuter et al. (2014) measured liquid side boundary layers of dissolved amonia concentration by ratiometric fluorescence of pyranine triggered by strong LED excitation. Kováts et al. (2017) show that bubble shadows and laser sheet heterogeneity can be reduced drastically by using a two-color technique for pH measurement. The only use of single dye I^r_{pH} – PLIF other than the ones presented hereinafter has been very recently published by Kong et al. (2018). They use the pH dependency of the C-SNARF fluorescence spectrum to measure pH fields and deduce dissolved carbon dioxide concentration fields around rising bubbles. Their method is very similar to the one presented here and has been developed at the same time without exchanges between the two research teams. However, the strong type III spectral conflicts associated to C-SNARF excitation and fluorescence spectra could make it difficult to adapt to non optically thin systems. Other uses of ratiometric fluorescence pH measurement can be found in the field of health science, e.g. in cellular biology as a mean of visualizing and understanding cellular processes (Bassnett et al., 1990; Buckler and Vaughan-Jones, 1990; Morris, 1990), or in ophthalmology (Doughty, 2014). It should be mentioned that two-color variants also exist for classical (i.e non-inhibited) PLIF and present the same advantages (Bouche et al., 2013). Without coming back on issues linked to fluorescence reabsorption and spectral conflicts, another issue of such methods is that the two dyes also have to behave in a similar fashion when injected in the receiving fluid. For example, they should have identical diffusion coefficients, otherwise one a constant dye concentrations ratio is not guaranteed, and this may introduce bias in the fluoresced intensities ratio.
The following paragraphs present a "two colors - one dye" (2c/1d) methodology developed for pH measurement inside aqueous turbulent flows. A single dye system is chosen over a two dyes one in order to keep the method as simple to implement and as weakly chemically intrusive as possible. The method will hereinafter be called "two-color" or ratiometric, without specifying that it is a "single dye" version.

2.2.3 Fluorescein sodium

2.2.3.a Introduction to fluoresceins

Fluoresceins are fluorescent molecules used in many scientific domains thanks to their high water solubility, high fluorescence quantum yield, and high sensitivity to several physico-chemical parameters like temperature or pH. They can be found for example in medical applications (*in-vivo* drug tracking, tumor targeting...) and are among the most common fluorescent dyes used in PLIF application. A wide variety of fluoresceins exists. The one used here is fluorescein dissodium salt, also called fluorescein sodium, and has been purchased at Alfa Aesar.

Stable at solid state in the form of a red-orange powder, it has the ability to emit fluorescence radiation. Its spectrum is centered around the wavelength λ_f = 515 nm when excited by a λ_e = 488 nm incident wavelength. Experimental spectra are presented in section 2.2.5 figure 2.15.

2.2.3.b Physico-Chemical properties

Once dissolved into water, fluorescein decomposes into several forms through a rather complex set of polytropic equilibria. These have been studied by Martin and Lindqvist (1975) who showed that 9 forms of fluorescein exist and can be classified into 4 categories: cations Fl^+, neutral forms Fl^n, anions Fl^- and dianions Fl^{2-}. For the needs of this study, the acid/base equilibria of fluorescein sodium dissolved in water have been numerically solved using Matlab, and the Bjerrum plot (concentration of each form divided by total product concentration) of the four categories' concentrations as a function of pH are plotted in figure 2.9. The system of equations including carbon dioxide and fluorescein sodium equilibria is detailed in appendix D.

Each of these forms plays its own role in the absorption and emission processes, having its own molecular extinction coefficient ϵ and its own quantum yield ϕ (Guilbault, 1990). It has also been shown that among all the possible forms, only the anionic ones Fl^- and Fl^{2-} have the ability to fluoresce.

Experimental curves of fluoresced light intensity or molar extinction coefficients as a function of pH have been plotted by Martin and Lindqvist (1975) and Walker (1987). They showed that relative fluoresced light intensity or relative extinction coefficient reaches its

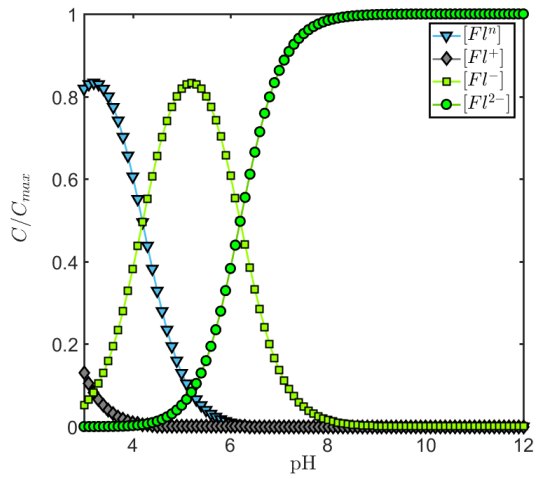

Figure 2.9 – Bjerrum plots of fluorescein sodium system

plateau value around pH=8, and that the maximum pH sensitivity lays between pH=5 and pH=8. It corresponds well to the variations of acidity that could be caused by CO_2 dissolution and therefore makes it an efficient tracer for its absorption into water for example.

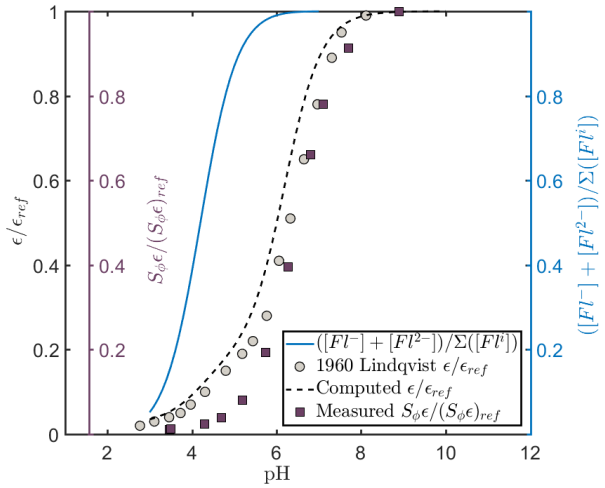

Figure 2.10 – Evolution of the normalized molar extinction coefficient at $\lambda_e = 491$ nm computed from the values of table 2.1 using matlab (dashed line), and measured by Lindqvist (1960) (circles). The full line is the concentration of fluorescent species normalized by total fluorescein concentration. Square markers show the normalized excitation spectrum intensity values $\frac{S_\phi(\lambda_f,pH)\epsilon(\lambda_e,pH)}{S_\phi(\lambda_f,pH_{ref})\epsilon(\lambda_e,pH_{ref})}$ measured for $\lambda_f = 513\ nm$ at $\lambda_e = 491$ nm (see section 2.2.5 for measurements and 2.2.4.b for a definition of S_ϕ)

This behavior can be understood using a simple approach based on the proportion of fluorescent forms of fluorescein. The computation of $[Fl^-] + [Fl^{2-}]$ with Matlab (details in appendix D) gives us the trend drawn in figure 2.10 for the sum of the fluorescent species' concentration as a function of pH. A theoretical computation of ϵ for $\lambda_e = 491$ nm can be made using the corresponding values of all extinction coefficients determined by Klonis and Sawyer (1996) reported in table 2.1 and a simple mixing law to estimate a total extinction coefficient.

$$\epsilon(\lambda_e, pH) = \sum_{i=1}^{N} \epsilon^i(\lambda_e).[Fl^i](pH) \tag{2.20}$$

Fluorescein form	ϵ ($M^{-1}.cm^{-1}$)
Fl^+	30
Fl^n	2700
Fl^-	16000
Fl^{2-}	88000

Table 2.1 – Extinction coefficient values at $\lambda = 491$ nm from Klonis and Sawyer (1996)

The same reasoning can be made for fluorescence quantum yield:

$$\phi(pH) = \sum_{i=1}^{N} \phi_i.[Fl_i](pH) \tag{2.21}$$

With N = 4.

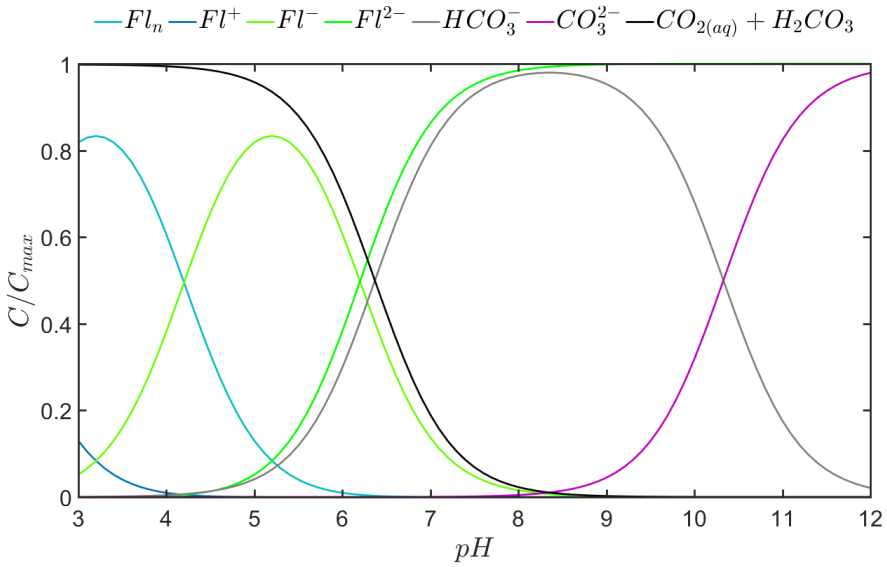

Figure 2.11 – Bjerrum plot of the full fluorescein - carbon dioxide system. For fluorescein species, C_{max} = [Fl_n] + [Fl^+] + [Fl^-] + [Fl^{2-}], for carbonate species, C_{max} = DIC.

2.2.3.c Carbon dioxide - Fluorescein interactions

As mentioned before, the fluorescent dye used in this study is composed of several chemical species involved in acid-base equilibria. Since we use this specific property to investigate the mass transfer of another acidic species, which is CO_2, it has to be verified that the quantities of dye used do not modify the carbonate chemical equilibria. If these are modified by the presence of fuorescein, the previously established pH-CO2 relationships become invalid and this could lead to systematic error on concentration measurements.

In order to check for that intrusiveness beforehand, the polytropic equilibria of fluorescein sodium are solved together with the hydration reactions of carbon dioxide hydration by extending the existing Matlab procedure. This theoretical solving can be completed by experimental measurements of pH-CO_2 equilibria in aqueous fluorescein sodium solutions at different concentrations. Both the theoretical and experimental approach are detailed in appendix D.

Figure 2.11 shows the bjerrum plot of the full fluorescein carbonate system obtained by the matlab simulation for a total fluorescein concentration of 5.10^{-7} M. Figure 2.12 shows the pH-CO_2 behavior of distilled water, fluorescein and sodium hydroxide solutions at different concentrations. From both graphs it seems clear that even if pKa's are close to each other, the effect of low concentration fluorescein is negligible on most of the pH range. High fluorescein concentrations however may lead to important shifts of pHs of zero CO_2 concentrations solutions simply because fluorescein is itself a set of weak acids that may decrease the initial pH when concentrated enough. This effect is suppressed when the initial pH is set to higher values by the addition of sodium hydroxide. DIC index are always higher in presence of sodium hydroxide since the high pH enhances hydration reaction kinetics. The precision range of the experiments is not wide enough to be able to check the effects of fluorescein at low carbon dioxide concentration. Available experimental data are presented in appendix D. The exponential slopes found experimentally correspond well to the simulated cases.

As a last remark, high fluorescein concentration solutions also show a surprising foaming tendency when bubbled with carbon dioxide. We assume that this effect is due to a probable

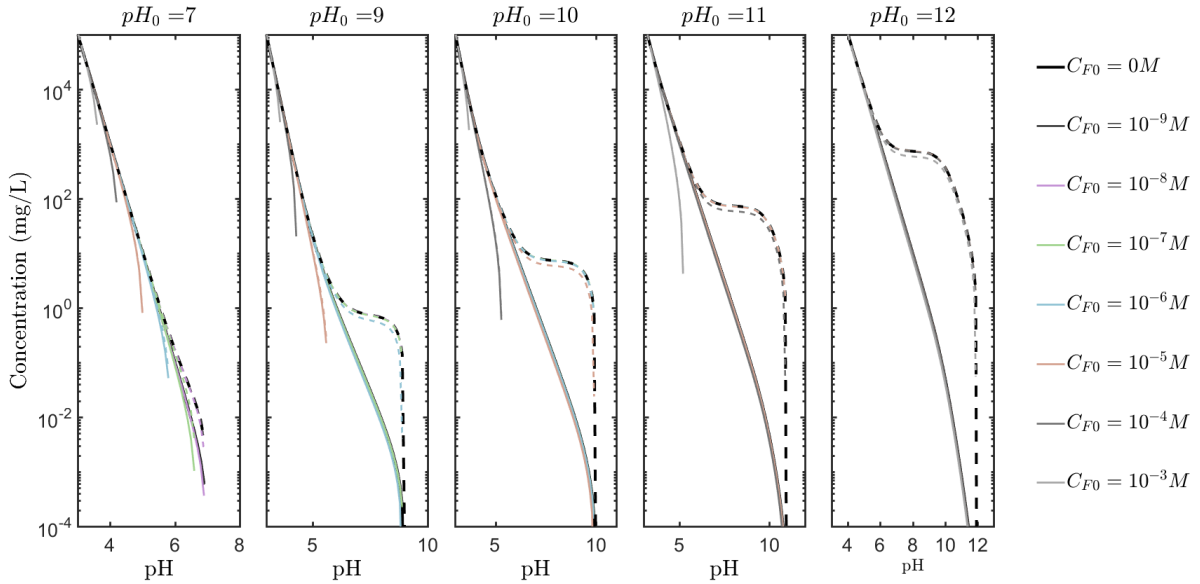

Figure 2.12 – Numerical resolution of pH-[CO_2] equilibria with different fluorescein and sodium hydroxide concentrations. Fluorescein concentration C_{F0} is varied between 0 and 10^{-3} M, and [NaOH] tuned so that the acidity at [CO_2] = 0 mg/L is between $pH_0 = 7$ and $pH_0 = 12$.

surfactant production by chemical reaction between carbon dioxide and fluorescein. This point is addressed in appendix D. Since the onset of foaming is observed for much higher concentrations than the fluorescein concentration range used in PLIF applications, this possible surfactant production is assumed negligible in the rest of the manuscript.

2.2.4 Theory of $I^r_{pH} - PLIF$

2.2.4.a Equations for a single emission wavelength

For a given excitation wavelength λ_e, the incident intensity at point M of the fluid may be written according to Beer-Lambert absorption law as

$$I_i(M) = I_0 A . e^{-\int_0^{L_s(M)} C(r)\epsilon(\lambda_e, pH(r))dr} \tag{2.22}$$

where I_0 is the output laser intensity, A is a constant which depends on the optical setup used to format the laser sheet, $L_s(M)$ is the length crossed by a laser beam before reaching point M, $C(r)$ is the concentration of fluorescent dye in the fluid at any point and ϵ the extinction coefficient of the dye. This last quantity varies inside the fluid since it depends on the local pH values.

During measurements, pH spatial variations make every pH dependent quantities spatially variable. In what follows, we will express these quantities as a function of the position M. To simplify the equations, $\epsilon(pH(M))$ for example will be written as $\epsilon(M)$. As for C however, if the dye is perfectly mixed with the fluid prior to the experiments, it is itself independent of the location.
The absorbed incident intensity $dI_a(M)$ at point M can then be expressed as

$$dI_a(M) = I_i(M) C \epsilon(\lambda_e, M) dV \tag{2.23}$$

and from equation (2.22)

$$dI_a(M) = I_0 A C \epsilon(\lambda_e, M) . e^{-C\int_0^{L_s(M)} \epsilon(\lambda_e, r)dr} dV \tag{2.24}$$

and the fluoresced light intensity $dI_f(M)$ emitted by this volume is

$$dI_f(M) = \phi(M).dI_a(M) \tag{2.25}$$

or, from equation ((2.24))

$$dI_f(M) = I_0 AC\phi(M)\epsilon(\lambda_e, M).e^{-C\int_0^{L_s(M)}\epsilon(\lambda_e,r)dr}dV \tag{2.26}$$

Equation ((2.26)) can be integrated over a small volume V_s centered around M, assuming that ϵ at λ_e and ϕ in V_s are constant within this volume.

$$I_f(M) = \int_{V_s} dI_f \tag{2.27}$$

and from equation (2.26) it comes that

$$I_f(M) = I_0 AC\phi(M)\epsilon(\lambda_e, M)V_s.e^{-C\int_0^{L_s(M)}\epsilon(\lambda_e,r)dr} \tag{2.28}$$

Typically, $V_s = s_{px}.e_L$ where e_L is the laser sheet thickness and s_{px} the surface of the area recorded on a single pixel of the sensor (see figure 2.13).

The fluoresced intensity $I_r(M)$ reaching the sensor coming from point M is then

$$I_r(M) = I_f(M).e^{-C\int_0^{L_{obs}(M)}\epsilon(\lambda_f,r).dr} \tag{2.29}$$

where $L_{obs}(M)$ is the distance traveled in the fluid by fluoresced light of wavelength λ_f emitted from point M before reaching the sensor.

The term $e^{-C\int_0^{L_{obs}(M)}\epsilon(\lambda_f,r).dr}$, represents the re-absorption of fluoresced light by the fluid, that can lead to type II or III spectral conflicts (see section 2.2.2.c). It can be neglected if $C\epsilon L_{obs} << 1$ for all M of the observed region. This is a part of the "optically thin system" assumptions of Walker (1987). Typically for fluorescein sodium, the fluorescence extinction coefficient for $\lambda = \lambda_f = 515$ nm is $\epsilon \sim 10^4$ $M^{-1}.cm^{-1}$ at $pH > 12$ where it reaches its maximum (Klonis and Sawyer, 1996; Martin and Lindqvist, 1975). For the fluorescein sodium concentration used in the present study $C = 5.10^{-7}$ M, $L_{obs} << \frac{1}{\epsilon C} = 200$ cm is required to fulfill this condition.

If this is verified for the chosen λ_f, $I_r(M) \approx I_f(M)$ and so

$$I_r(M) \approx I_0 ACV_s\phi(M).\epsilon(\lambda_e, M).e^{-C\int_0^{L_s(M)}\epsilon(\lambda_e,r)dr} \tag{2.30}$$

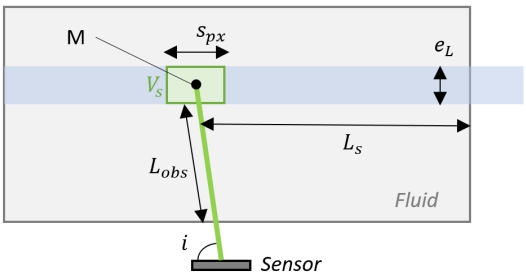

Figure 2.13 – Distances and parameters of the beams' paths

2.2.4.b Equations for the ratio of two wavelengths or spectral bands

Considering now a polychromatic fluoresced light and not only a single emitted wavelength, equation ((2.30)) becomes

$$I_r(\lambda_f, M) \approx I_0 A C V_s \epsilon(\lambda_e, M) S_\phi(\lambda_f, M).e^{-C\int_0^{L_s(M)} \epsilon(\lambda_e, r)dr} \tag{2.31}$$

S_ϕ may be seen as the "spectral" quantum yield of fluorescence, that is to say the amount of absorbed energy turned into fluorescence light at wavelength λ_f, with $\phi(M) = \int_0^\infty S_\phi(\lambda_f, M)d\lambda_f$.

Since only S_ϕ depends on λ_f, the ratio R^* of the received intensity at two different fluoresced wavelengths λ_1 and λ_2 (see figure 2.14a) from the same given point M can simply be expressed from equation ((2.31)) as

$$R^*(\lambda_1, \lambda_2, M) = \frac{I_r(\lambda_1, M)}{I_r(\lambda_2, M)} = \frac{S_\phi(\lambda_1, M)}{S_\phi(\lambda_2, M)} \tag{2.32}$$

In the same way, the ratio R for fluoresced intensity integrated over two spectral bands (see figure 2.14b) is

$$R(\lambda_1^{inf}, \lambda_1^{sup}, \lambda_2^{inf}, \lambda_2^{sup}, M) = \frac{\int_{\lambda_1^{inf}}^{\lambda_1^{sup}} S_\phi(\Lambda, M)d\Lambda}{\int_{\lambda_2^{inf}}^{\lambda_2^{sup}} S_\phi(\Lambda, M)d\Lambda} \tag{2.33}$$

In both cases, one can see that for known fluorescence wavelengths, the ratio depends only on M, that is to say on the local value of the pH, which is precisely what is needed.

For the technique to be suitable for pH measurement, it has to be checked that this ratio is monotonous for the chosen spectral bands or wavelengths, and that its dynamic of variation is large enough to ensure a good sensitivity of measurement. This validation is the object of the spectrofluorimetric study presented in part 2.2.5.

2.2.5 Spectral study

2.2.5.a Measurements and data treatement

Fluorescence excitation and emission spectra have been plotted using an FLS90 Edinburgh Instruments spectrofluorimeter. A monochromatic excitation light is passed through a sample solution of fluorescent dye that may contain additional precised. The fluorescence signal emitted by the sample solution is then recorded by a detector, allowing to plot the full spectrum of fluoresced light wavelengths. Excitation spectra are obtained by measuring the fluoresced light intensity at a given wavelength λ_f for a range of excitation wavelengths λ_e.

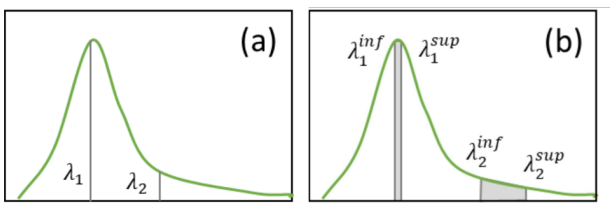

Figure 2.14 – Selection of fluorescence wavelengths (a) and spectral bands (b)

Fluorescence emission spectra are obtained measuring the fluoresced light intensity of different wavelengths λ for a given excitation wavelength λ_e. The wavelengths chosen for the present study are given in table 2.2.

The opening and exposure time of the spectrofluorimeter have been set so that its output signal at the intensity peak of the most basic sample at the best excitation wavelength is close to its maximum voltage without being saturated. By that means, the best dynamical range is obtained and the error reduced, even for highly acidic samples yielding weak fluorescence signals.

The samples consist in fluorescein sodium solutions at C = 5.10^{-7} M, the pH of which is set by two types of buffer solutions, sodium carbonate / sodium bicarbonate and citric acid / sodium phosphate, allowing for a pH variation between 3.5 and 10.3.

2.2.5.b Results

From figure 2.15 a, the pH dependency of fluorescein sodium behavior can clearly be seen. The fluoresced light intensity peak strongly decreases with acidity especially in the range between pH = 8 and pH = 5 but its position remains at λ_f = 515 nm (see figure 2.15 a and c). The dependency of the excitation spectrum on the pH can also be seen on the figure, but what differs from the fluorescence one is that the peak excitation wavelength varies when the pH becomes lower than 5.5 (2.15 a and b). The excitation peak at λ_e = 488 nm tends to decrease and an other excitation peak at λ_e = 437 nm appears.

This second peak corresponds to the absorption maximum wavelength for the neutral Fl^n, cationic Fl^+ and monoanionic Fl^- forms of fluorescein, whereas 488 nm is the maximum absorption wavelength of the di-anionic form (Klonis and Sawyer, 1996; Martin and Lindqvist, 1975). Under monochromatic excitation of λ_e = 488 nm, the decrease in fluoresced light intensity can therefore be explained by two factors: the fact that the extinction coefficient is decreased with acidity, and the fact that 488 nm is no longer the preferred absorption wavelength when reaching acidic pHs. Let's take the example of absorption and fluorescence at pH 4: even if one of the two fluorescent forms, Fl^-, is still present (see Bjerrum plots in figure 2.9) and the total concentration of fluorescent species is still relatively high (see figure 2.10), the excitation of the single fluorescent form left is not optimal.

This feature will not be further addressed in the present work, but it could be of great interest if one wants to extend the sensitivity of fluorescein-based I – PLIF techniques to acidic pHs. Using simultaneously λ_e = 488 nm and λ_e = 437 nm excitation, provided for example by two different laser sources, it would be possible to trigger both fluorescent forms of fluorescein at their optimal excitation intensity. As compared to the case of a single excitation wavelength, this could increase the level of fluoresced light intensity especially in the pH range between 4 and 5 where Fl^- dominates (see figure 2.9), and extend the measurable intensity range, hence the sensitivity, to the low pH regions.

Finally, it can be seen in figure 2.15 that the two spectra overlap in the 490 – 510 nm region. The overlapping area increases with the pH, thus leading to a type III spectral conflict. When applying the method to cases where fluorescence re-absorption is not

Type of spectrum	λ_e **(nm)**	λ_f **(nm)**
Excitation	400 - 510	513
Fluorescence	470	475 - 650
Fluorescence	488	492 - 650

Table 2.2 – Wavelengths used for the present spectral study

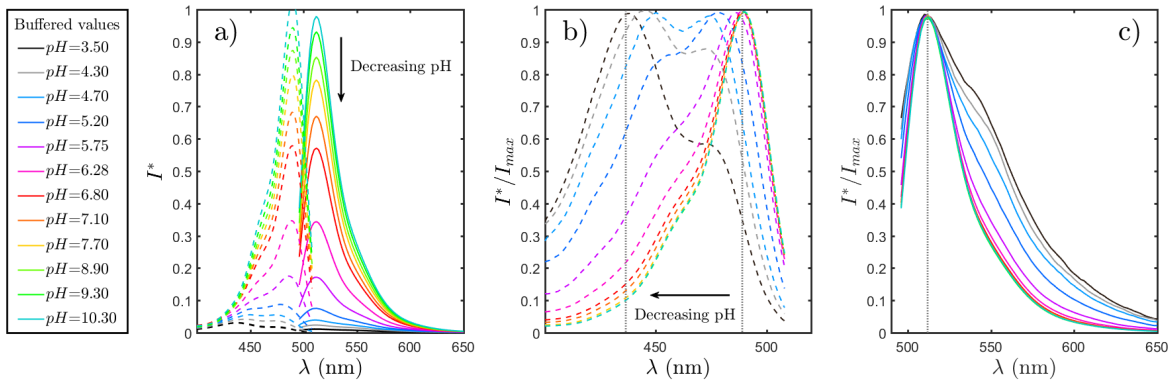

Figure 2.15 – Excitation (dashed lines) and fluorescence spectra (full lines) of C = 5.10^{-7} M fluorescein sodium solution as a function of pH (a) Raw spectra (arbitrary units) (b) Excitation spectra normalized by their maximum intensity (c) Fluorescence spectra normalized by their maximum intensity. Dotted lines mark the position of absorption and emission peaks.

negligible, this could cause important errors. This point is addressed later on in section 2.2.6.

A possible improvement of the method would be to use a dye that exhibits a shift in emission frequency with a minimum decrease in fluoresced light intensity when decreasing the pH. This would allow for a good signal over noise ratio regardless of the pH measurement range while ensuring a strong variation of spectral band intensities ratio. Fluoresceien sodium does not exhibit such feature, but it seems to be the case for C-SNARF excited at λ_e = 532 nm (Kong et al., 2018). However, this dye presents a strong type III spectral conflict: the absorption peak and emission peak at high pHs are located at almost the same wavelength. This increases the risk of fluorescence reabsorption especially for the first spectral band chosen by Kong et al. (2018), and thus limits the use of C-SNARF to optically thin configurations.

2.2.5.c Proposition of two spectral bands

Based on the previous spectra it is clear that the best pH dependency dynamics for the fluorescence signal is found around the peak wavelength, and that the tail of the spectrum (wavelengths above 560 nm) is far less sensitive to pH variations. The ratio R* defined in equation ((2.32)) for λ_1 = 515 nm and λ_2 > 560 nm should therefore be suitable to study pH variations (see figure 2.16).

Nevertheless, this ratio R* of wavelengths is technically difficult to measure. Indeed, when using an optical setup to collect the fluoresced light and not a specifically designed spectrofluorimeter, the intensity level of wavelength λ_2 has to be sufficiently above the measurement noise, which means that λ_2 has to be close enough to the fluorescence peak. Moreover, separation of colors with such optical setups is done by optical filters placed in front of the recording cameras. Those filters select ranges of wavelengths and not discrete ones. It is therefore more convenient to use the expression of the ratio R for spectral bands expressed in equation ((2.33)), and one has to check that the amount of light collected from spectral band 2 is high enough (figure 2.17).

The best compromise between dynamics of the R ratio, available optical filters, and intensity level collected from band 2 was found to be with λ_1^{inf} = 510 nm, λ_1^{sup} = 520 nm, λ_2^{inf} = 560 nm and $\lambda_2^{sup} \rightarrow +\infty$. This couple of spectral bands also presents the advantage of

leaving the 532 nm neighborhood open (see figure 2.16). This is useful if one wants to couple the concentration measurements with PIV techniques using Nd:YAG pulsed laser emitting at 532 nm wavelengths, as needed in the present study.

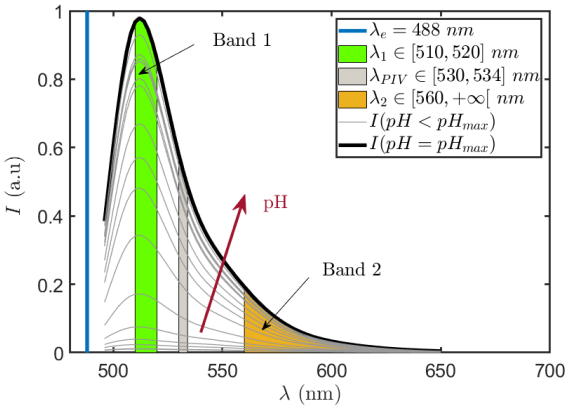

Figure 2.16 – Location of chosen spectral bands: band 1 in green and band 2 in orange. The gray stripe represents the spectral band admitted by optical filters generally used for PIV measurements. Excitation wavelength is represented by the blue vertical line. Black solid line is the fluorescence spectrum measured at the maximum fluoresced light intensity, dashed lines are spectra measured at lower pHs, pH increases with the red arrow.

The behavior of fluorescence emission at chosen spectral bands can be derived by numerically integrating the measured excitation spectra at different pHs. It is then easy to compute the ratio curve $R = f(pH)$ (see figure 2.17).

For the two selected spectral bands indicated in figure 2.16, pH dependency of the integrated intensities δI_1 and δI_2 and of the ratio R are plotted in figure 2.17. Both intensities have the same S-shaped curve, reaching their maximum at pH around 9. As expected, the intensity variations of δI_2 are lower than that of δI_1 (figure2.16). The ratio R is strictly increasing over the whole pH range, and exhibits a good dynamics between pH 4 and 8, and a quasi-linear trend between pH 5 and 7. At acidic pH, integrated intensity over band 2 is larger than over band 1 since it is wider, hence the ratio is below 1. On the contrary, for basic pH, band 1 integrated intensity is much higher since it captures the fluorescence peak, which is no longer inhibited, hence the ratio is above 1. The whole curve can be fitted by an hyperbolic tangent function, which is a reflection of the exponential behavior of chemical equilibria of the several forms of fluorescein responsible for quantum yield variations. Ratio points measured for a lower fluorescein sodium concentration (not presented here) also fit well to the same curve, hence fluorescein sodium concentration in the $[10^{-8} - 10^{-7}]$ M domain has no influence on the shape of the fluorescence spectrum.

These results therefore confirm the possible application of single dye I^r_{pH} – PLIF using fluorescein sodium, at least from the spectral point of view. For the proof of concept to be completed, a test case of turbulent monophasic pH mixing is proposed in the following section.

2.2.6 Monophasic test case: acidic jet in water

A monophasic turbulent round jet was used as a benchmark to test the I^r_{pH} – PLIF method. This type of flow has been widely studied in the literature (Papanicolaou and List, 1988; Papantoniou and List, 1989) and has been used as a test flow for the development of PLIF techniques by Walker (1987), Bruchhausen et al. (2005) or Chaze et al. (2016) for example. In this

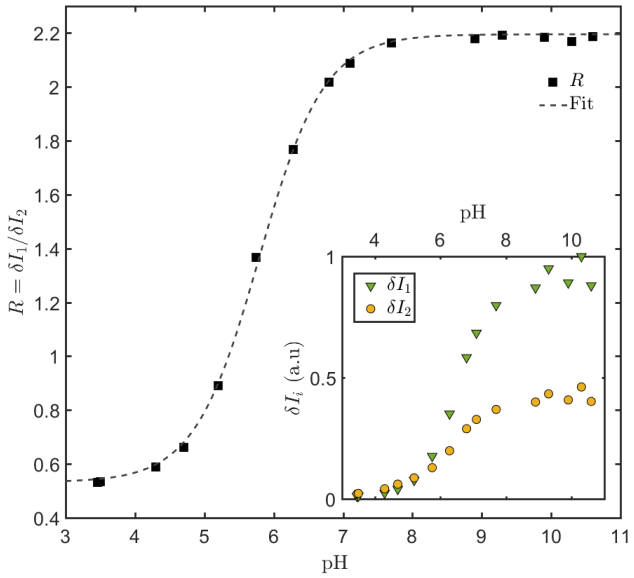

Figure 2.17 – Spectral band intensities and ratio as a function of pH measured by spectrofluorimetry. Main figure: Computed ratio and hyperbolic fitting, Insert: Spectral band intensities

section, the calibration procedure is first addressed, and the case of an acidic jet immersed in a neutral solution is then studied. The pH fields given by the proposed method are compared to the ones obtained using single color I_{pH} – PLIF with different calibration procedures.

2.2.6.a Experimental setup

The turbulent jet is created by a D = 1 mm nozzle placed inside a 277 × 277 × 500 mm^3 Plexiglas tank. About 100 L of fluorescein sodium solution at a given concentration C in water are prepared. V_0 = 40 L of it are placed inside the measurement tank and V_1 = 20 L are placed in a secondary tank. Chlorhydric acid HCl (typically 200 µL at 1 M) is then added to the secondary tank to decrease its pH down to about 4.6. The acidic solution thus formed is injected in the main tank to generate the turbulent jet (figure 2.18). This first step allows the fluorescein concentrations of the jet and the receiving fluid to be rigorously identical, so that the fluoresced light intensity variations observed during the measurements can only be explained by pH variations. The remaining volume V_2 = 60 L of fluorescein solution is stored in a reservoir and can be used to replace the acidified fluid of the main tank between two experiments. The pH inside tanks 1 and 2 are checked prior to the experiment using a Hanna Checker pH meter. Since HCl is a strong acid, the relationship between pH and concentration of transported scalar is $pH = -log(C_A)$ and the injection concentration is $C_{A,inj} \simeq 2.10^{-5}$ M. Temperatures in both tanks are checked to be equal and remain constant during the whole experiment. The chosen type of fluoresceine is moreover weakly dependent on temperature, so that the possible low temperature variations does not influence the measurements. Finally, it is assumed that no chemical reaction occurs between HCl and fluorescein(like what is done for CO_2).

A pump connected to tank 2 generates an injection flow rate of about Q ≃ 0.15 $L.min^{-1}$ which yields a velocity of about U ≃ 3 $m.s^{-1}$ and a jet Reynolds number $Re_J = \frac{UD}{\nu} \simeq 3000$ at room temperature (T = 20°C, fixed throughout the experiments). At this flow rate, the volume of acidic fluid injected during the time of measurement (typically 2 minutes) is less than 0.3 % of the initial volume of neutral fluid, which leads to a bulk concentration increase

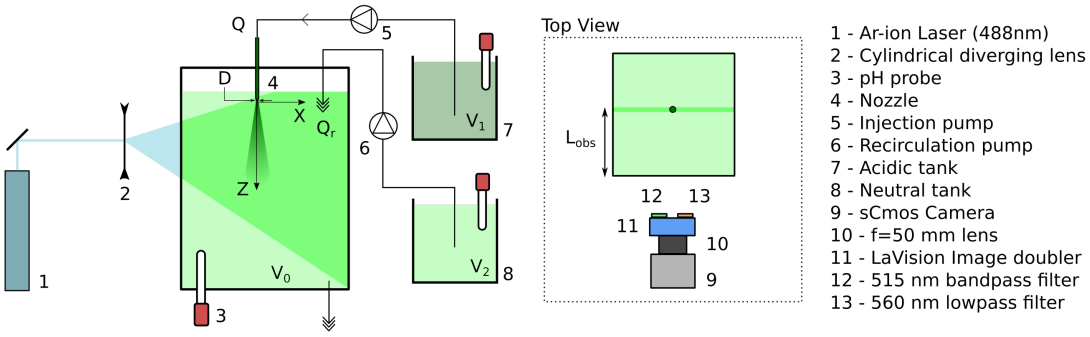

Figure 2.18 – Sketch of the setup designed for the turbulent jet experiment

of 10^{-7} M. It can therefore be assumed that the bulk concentration $C_{A,\infty}$ in the tank remains constant and equal to zero during the time of experiment.

The jet region is illuminated by a $\lambda_e = 488$ nm laser sheet of thickness $e_L \simeq 1$ mm using a Stabilite 2017 Argon-Ion Continuous Wave Laser. The fluorescence spectral bands are separated using two optical filters, one band-pass of central wavelength 515 nm and bandwidth 10 nm, and one long-pass of cutoff wavelength 560 nm. Both filters are placed on the two "eyes" of a LaVision image doubler. Thanks to an optical prism, this device duplicates the image on two halves of the sensor, allowing the two fluorescence signal to be recorded on the same sensor, using the same lens and magnification. Here a Lavision SCmos camera is equipped with a $f = 50$ mm lens.

The pixel size/spatial size correspondence is $dx = dy = 0.1$ mm/pixel. The sampling volume V_s defined in section 2.2.4.a is therefore $V_s = dx \times dy \times e_L = 0.01$ mm^3. This quantifies the spatial resolution achievable by this setup. Intensities on measurement images reach up to 22000 gray levels for band 1 and 7000 gray levels for band 2. At the lowest measured pH, intensities are always above 1400 gray levels, much higher than the noise level (of about 400 gray levels).

Each image is split into two sub-images corresponding to the two halves of the sensor recording each wavelength. A reference image of a test pattern is taken prior to the experiment to enable the separation of the two parts of the recorded image and their spatial correlation. The camera exposure time is set at $dt = 20$ ms as a best compromise between the amount of fluorescence light collected on both parts of the sensor and the temporal resolution. The region of interest is cropped out, and the spatial correlation for each sub-image is found using the two sub-images extracted from the recorded test-pattern. Sub-image 2 of the test pattern is shifted and rotated over sub-image 2 in order to maximize the cross correlation between sub-images 1 and 2. The same translation/rotation is then applied to every recorded image.

2.2.6.b Calibration

The calibration procedure is performed by taking images of several solutions at homogeneous pH under constant laser excitation. The sub-images for each spectral band exhibit heterogeneous distribution of fluoresced light intensity due to Beer-Lambert's absorption and pH dependency of extinction coefficient, as shown in figure 2.19 a. Even if the ratiometric technique intrinsically corrects all inhomogeneities linked to excitation intensity, variations, introduced by the optical setup used to collect fluorescence, remain. As shown in

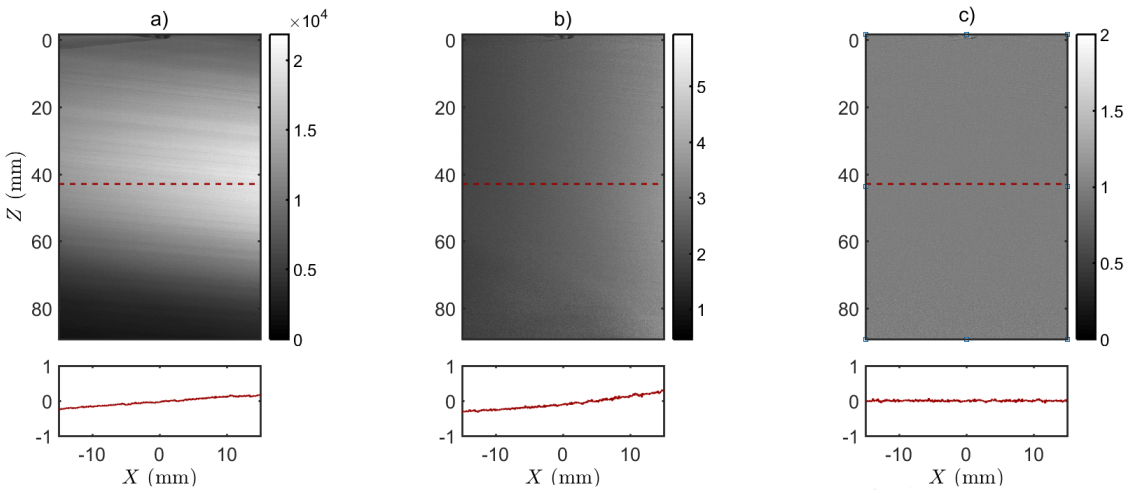

Figure 2.19 – Calibration images at homogeneous pH = 7, (a) is the raw intensity fluorescence for band 1 in arbitrary units, (b) is the raw ratio, and (c) is the normalized ratio. Horizontal variation profiles at Z = 43 mm (dotted line) defined for each quantity i as $(i - i_m)/i_m$ are plotted under each field, i_m being the average of i over the horizontal profile.

figure 2.19 b, a spatial gradient of ratio, mostly horizontal, is introduced by these optical distortion and still has to be accounted for.

For that purpose, each calibration ratio field recorded is normalized by a reference ratio field taken at any pH.

$$\mathrm{R}_n(\mathrm{M}, p\mathrm{H}) = \frac{\mathrm{R}(\mathrm{M}, p\mathrm{H})}{\mathrm{R}_{ref}(\mathrm{M}, p\mathrm{H}_{ref})} \tag{2.34}$$

Where R_n is the normalized ratio which should not depend on M, and R_{ref} is the raw ratio field measured at reference $p\mathrm{H}_{ref}$.

Applying such correction, the normalized ratio images become homogeneous (figure 2.19 c). The same normalization step is then applied to measurement images. In what follows, the normalized ratio R_n is called R for simplicity.

The experimental ratio as a function of pH is plotted in figure 2.20. The hyperbolic trend predicted by the spectral study is found, which confirms that $\mathrm{R} = f(p\mathrm{H})$ calibration

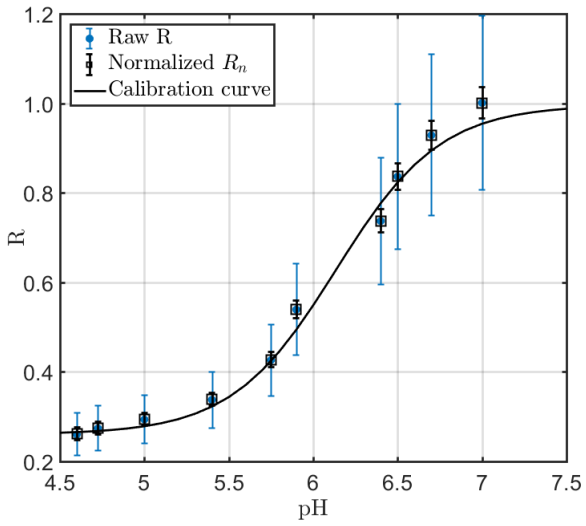

Figure 2.20 – Measured ratio as a function of pH

curve can be used for pH measurements. The error on the ratio, computed as the root mean square of the ratio values on the whole field, is of about 20 % (blue vertical bars) for raw fields due to the spatial heterogeneity, and falls to below 5 % (black vertical bars) for normalized ratio fields, as shown by the error bars of figure 2.20. This error is no longer due to an heterogeneous distribution but rather to a random noise of pixel intensity values.

It is checked that the laser power output as no influence on the value of the measured ratio. Recorded fluoresced light intensities for each spectral band and the associated ratio are plotted versus laser power on figure 2.21 for pH 4.5 and 6.3. Above a critical power output, the ratio does not depend on excitation intensity. Under that value, the signal over noise ratio and laser stability is not good enough for reliable measurements and ratio values change. The influence of laser power output variations during the course of a measurement is adresed later in section 2.2.6.c.

Finally, the impact of fluorescence re-absorption on fluorescence ratio can be illustrated by performing a calibration in similar optical setup but using a much higher fluorescein concentration, for example $C = 3.1.10^{-5}$ M. The path length of fluorescence towards the sensor is $L_{obs} = 13.5$ cm which gives $C\epsilon L_{obs} \simeq 0.07$ for $C = 5.10^{-7}$ M at pH = 7 and $C\epsilon L_{obs} \simeq 4.22$ for the higher concentration, same pH. This last case should therefore be ascribed to re-absorption phenomena and the type III spectral conflict may become important.

In figure 2.22, it appears that R_r does not follow the same monotonic increasing trend when fluorescence re-absorption occurs. On the contrary the ratio tends to decrease with increasing pH (squares). A first approach explanation of this phenomenon can be proposed: since spectral band 1 is closer to the absorption domain than band 2, it is the one of the two bands that is the most sensitive to re-absorption (down-pointing triangles). As extinction coefficient ϵ increases with the pH for all wavelengths, the proportion of band 1 fluorescence being reabsorbed also does. On the other hand, band 2's overlapping region with the absorption spectrum is much smaller than that of band 1, and so it is less prone to fluorescence re-absorption (up-pointing triangles). The pH increase still leads to increasing fluoresced intensity. Combining the two band's behaviors, the ratio decreases with increasing pH.

It seems clear that for cases where re-absorption and spectral conflict can not be avoided, *i.e.* when either the re-absorption path or dye concentration are large enough, the technique can not be used as it is presented here, and the use of a further correction procedure is required.

2.2.6.c Results and interpretations

Comparison of I_{pH} − PLIF and I^r_{pH} − PLIF

In this paragraph, the results obtained by I^r_{pH} − PLIF are compared to those calculated by I_{pH} − PLIF using spectral band 1 only. Two calibration procedures are used for the single color approach. The one proposed by Souzy (2014), that is to say a pixel-by-pixel treatment accounting for extinction coefficient variations and where the curve for intensity as a function of pH is fitted by a 5^{th} degree polynomial, and the common reference image normalization .

Before going any further, it has to be noted that the time needed to read, calibrate, and process a single image is at least 10 times longer for the pixel-by pixel single color technique (typically 40 min with a common desktop computer) than for the simple normalization one color technique or the two-color one (4 min for calibration, less that 0.5 s for one image processing). This comes from the fact that each pixel has to be individually calibrated and treated for the first case, whereas a single fitting step is required in other cases. This time difference increases with the image resolution and the degree used for polynomial fitting of

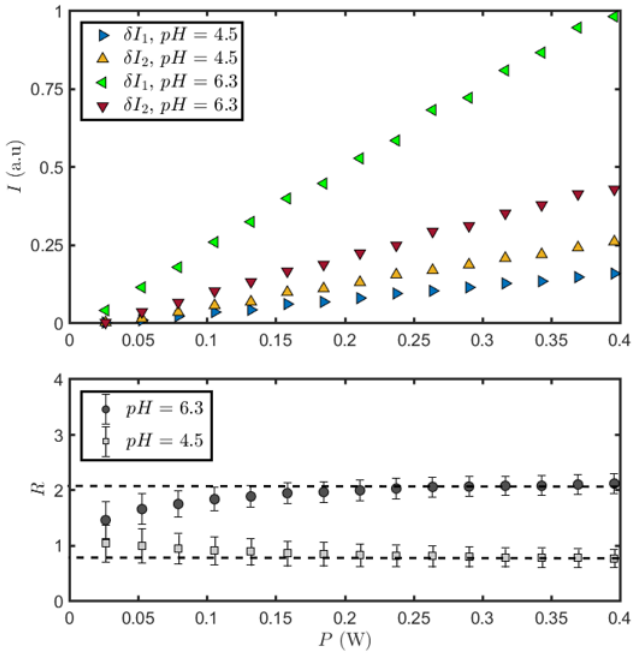

Figure 2.21 – Evolution of the two spectral bands' fluoresced light intensity and of the ratio with laser power output for two pH

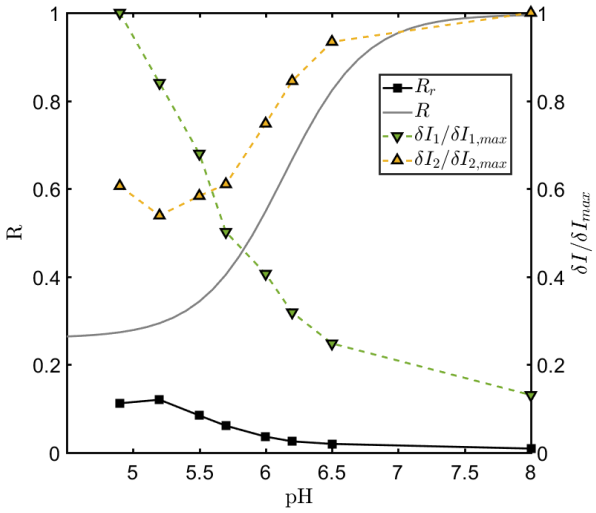

Figure 2.22 – Effect of fluorescence re-absorption on spectral band intensities and Ratio. Full line: Experimental curve for ratio without re-absorption R (figure 2.20), triangles: normalized intensity collected from band 1 (down-pointing) and 2 (up-pointing), squares: R_r ratio with re-absorption

intensity curves.

Needless to say that it becomes a real issue when one wants to process sets of several hundreds of images. Regarding the use of single color techniques, it has to be noted that in this case, the region submitted to pH variations is small with respect to the whole laser path inside the fluid, hence the standard normalization procedure is sufficient and the pixel-by-pixel calibration is not required (as explained in section 2.2.2.b).

Three instantaneous concentration fields are compared in figure 2.23. The scalar field

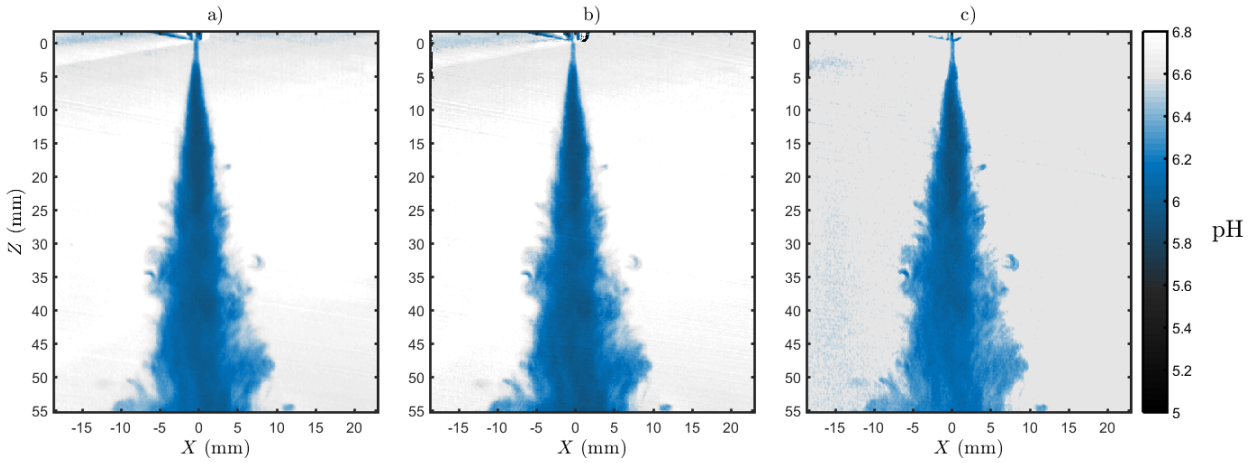

Figure 2.23 – Comparison of instantaneous pH field obtained by I_{pH} – PLIF using standard normalization (a) and pixel-by-pixel calibration (b), or by I^r_{pH} – PLIF (c)

obtained using the ratiometric technique appears to be less noisy than both single color version. Most of the "excitation noise" is corrected. For example, darker stripes due to the tank's wall scratches visible in figure 2.23 a and b, at the bottom right corner, almost completely disappear in figure 2.23 c. This tends to show that the two-color version is as expected more efficient when one has to deal with noisy excitation signal and reflections.

This feature is even better illustrated at the top of the figure, near the source of the jet. Here, unsteady reflections have been artificially introduced by making the free surface close to the jet oscillate. Such time dependent perturbations are still visible in figure2.23 b and disappear on c.

One last interesting feature to be illustrated is the effect of unsteady laser output power (or intensity) hereinafter called power drift. For the two-color method indeed, the laser power has no influence on the ratio, and so the power drift should be intrinsically corrected, providing that the power level remains sufficient for the two band's intensities to be measured with reasonable uncertainty.

In figure 2.24 are plotted time series of δI_1 and R along with the corresponding pHs obtained by a one or two-color procedure, respectively denoted pH_1 and pH_2. All quantities are measured at two points, one reference point in the bulk above the jet nozzle (figure 2.24 a) and one point inside the jet (figure 2.24 b). A random evolution of laser power input is imposed and leads directly to strong variations of δI_1. As expected, this induces an important error on the one color computed pH. For example, when δI_1 is decreased by 50 %, pH_1 is underestimated by about 7 % at point a and b. The ratio however remains almost constant with time in the bulk, and also inside the jet where most of its variations are not correlated to the variations of δI_1 and correspond to turbulent pH fluctuations. pH_2 consequently remains unchanged by the power drift.

Only at times between $t = 30$ s and $t = 35$ s appears an important ratio and pH_2 variation at both points, reaching a plateau value between $t = 31$ s and $t = 32$ s. This corresponds to a case where the laser power output is such that the fluorescence signal is too low to be measured, especially at acidic pH where it falls of 100 %, i.e no more fluorescence coming from band 1 is measured either inside (b) or outside the jet (a). Ratio and pH computation from such low fluorescence signal is highly uncertain and can lead to large errors on pH_2. It still requires the power drift to be really strong for the ratiometric method to be laser power dependent.

Jet characteristics

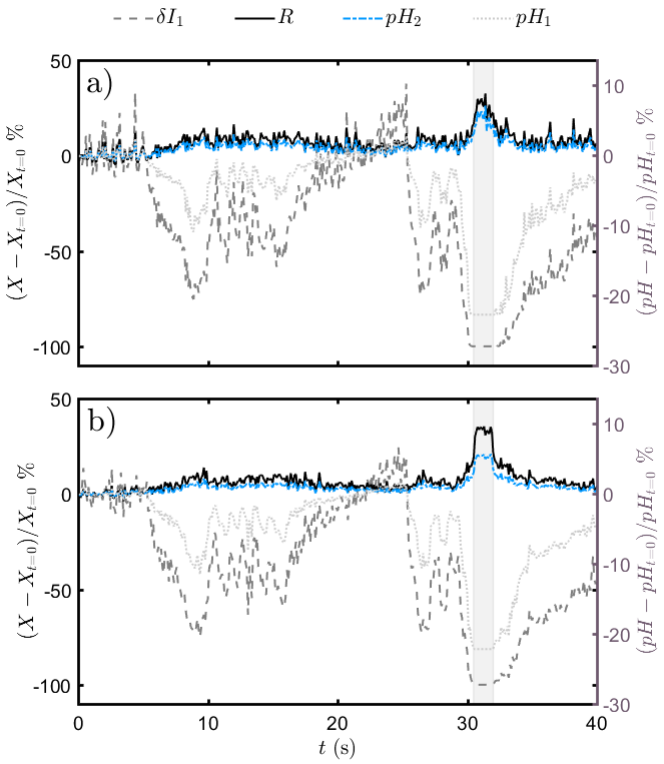

Figure 2.24 – Relative variations of band 1 intensity ratio and pH computed using single or two-color technique, in the bulk (a) and inside the jet (b) when applying a random laser power drift. Relative variations of δI_1 (dashed gray line) and R (full black line) are indicated on the left vertical axis and relative variations of pH_1 (doted light gray curve) and pH_2 (blue curve) on the right vertical axis.

I^r_{pH}−PLIF measurements are finally used to describe the jet characteristics. The pH fields are converted into concentration using the equation $pH = -log(C_A)$. Images at a $f_{acq} = 10$ Hz recording rate are collected and used to obtain average and rms concentration. For the jet Reynolds number considered, the integral time scale of turbulence is about $\tau_L = 320$ µs, much smaller than the time between two frames, hence successive recorded images are not statistically correlated. It is checked that 500 images are enough to reach statistical convergence of average and rms fields.

However, an important limitation of the method arises here: acquisition of fluorescence images with sufficient gray level require a rather long exposure time of 20 ms. This is much longer than the integral turbulent time scale of the jet. Consequently, turbulent concentration fluctuations are spatially smoothed, and so the rms profiles should be interpreted carefully.

Figure 2.25 shows the scaled acid mean concentration evolution along the jet centerline. The usual hyperbolic decaying law for passive scalar concentration is found for the range between 20 and 60 nozzle diameters (Chaze et al., 2016; Papanicolaou and List, 1988; Papantoniou and List, 1989; Zarruk and Cowen, 2008).

Transverse concentration profiles are shown in figure 2.26. The mean (a) and rms (b) concentration profiles at Z/D = 30 are scaled by their values at the centerline of the jet, and the jet width is normalized by the profile's distance to the nozzle.

The scaled mean concentration profile in figure 2.26 a corresponds to the results found by Dahm and Dimotakis (1987) (DD87). As for rms profiles in figure 2.26 b, it presents the expected shape with a peak value around X/Z = 0.1. Nevertheless, considering that it is taken

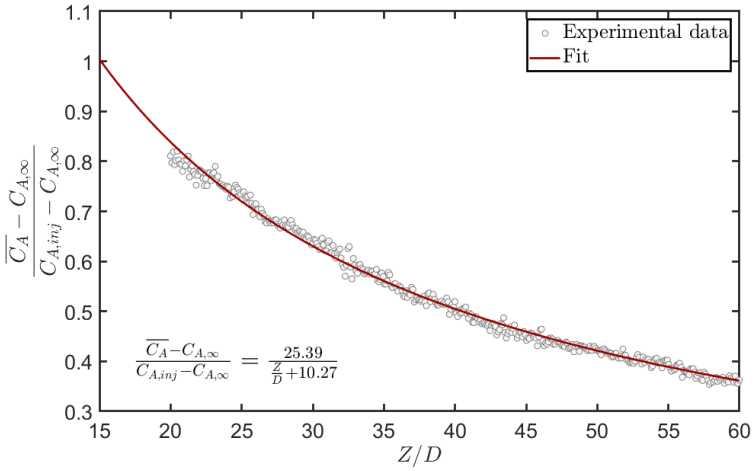

Figure 2.25 – Evolution of acid concentration along the jet centerline

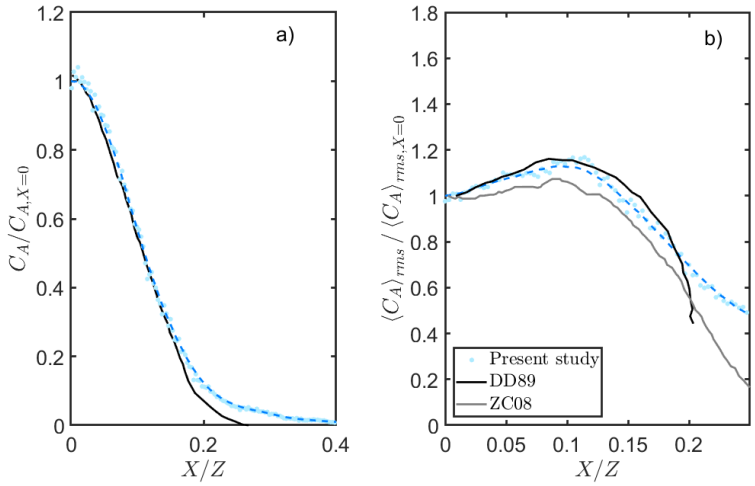

Figure 2.26 – Transverse profiles of averaged (a) and rms (b) concentration for Z/D = 30, normalized by their respective values at X = 0. Present study is compared to the results of Dahm and Dimotakis (1987) (DD87) and Zarruk and Cowen (2008) (ZC08). DD87: Z/D = 300, Re = 5000; ZC08: 63 < Z/D < 77, Re = 4000

closer to the nozzle (Z/D = 30 versus Z/D > 60) and for a lower Reynolds than for Dahm and Dimotakis (1987) or Zarruk and Cowen (2008) (ZC08), it should stay under both DD87 and ZC08 curves.

With the presented experimental design, accuracy of the result is not guaranteed for large Z/D, mainly due to an insufficient illumination leading to a poor signal to noise ratio in the far jet region. The current setup was meant to perform a proof of concept of I^r_{pH} – PLIF. An in depth jet study would require to adapt it and enlarge the region of interest to Z/D values where an effective measurement of rms concentration profiles could be done.

2.2.7 Effect of polymer additive on PLIF measurements

The aim of this paragraph is to briefly check that the presence of dilute polymer in the liquid does not significantly affect fluorescence. For reasons exposed in the next chapters, Xanthan gum (XG) has been chosen as a model polymer for this study. The adverse effects of fluorescein and carbon dioxide on XG rheology, and of XG on pH versus dissolved carbon dioxide

equilibria are studied with more detail in section 4.2.3. In order to check that pH metrology is not altered by the presence of polymer, the excitation and fluorescence spectra of different aqueous solutions of fluorescein sodium and XG are measured using in the same conditions than the spectrofluorimetric study of section 2.2.5 and plotted in figure 2.27.

Both the excitation and emission spectra show no dependency on the XG concentration. Moreover, the present solutions being in the dilute range and remaining optically clear, no scattering or global attenuation is observed and the fluorescence signal intensity is in no way affected by the presence of polymer in this range of concentrations. R = $f(pH)$ calibration curves measured with the experimental setup, presented later in chapter 4(section 4.2.4.b) for water and XG are also found to be similar (figure 2.28). This confirms that I^r_{pH} – PLIF can easily be applied to pH measurements in dilute XG solutions.

2.2.8 Diphasic test case: fixed bubble dissolution in dilute polymer solution

The jet test case sowed that I^r_{pH} – PLIF can be used to efficiently account for laser sheet heterogeneity and extinction variation while reducing the time required for image processing. A second test case is now proposed to show that the method can also be used in multiphase configurations and complex fluids. Here the dissolution of carbon dioxide bubbles trapped under a rigid surface into water and shear thinning dilute polymer solutions is studied. The optical setup is similar to the one presented in section 2.2.6. The jet injection system is replaced by an immersed Plexiglas substrate under which a bubble is positioned, like in the study by Duplat et al. (2017). Fluoresced light intensity fields are highly heterogeneous due to Beer Lambert absorption, imperfections on tank's wall, and laser sheet reflection and shades caused by the bubble (figure 2.29 b). As expected, heterogeneity is efficiently removed from the pH field by using the ratiometric technique. We have thus demonstrated the usefulness of the radiometric technique for our study. It is now necessary to quantify the error levels.

2.2.9 Error estimation

Precision of I^r_{pH} – PLIF is limited by several factors. An attempt to quantify the uncertainty linked to some of them is presented in the following paragraph.

2.2.9.a Error propagation for the single color method

As previously explained, single color inhibited PLIF is subject to several error sources, among which the heterogeneity of excitation light sheet. This may arise in presence of absorbing or reflecting interfaces in the fluid, but also because of tank's walls roughness and scratches, resulting in darker stripes on fluorescence images (see figure 2.30 a). Those gray level variations may change with time because of laser output fluctuations, and can thus not be corrected even by a pixel by pixel calibration. Because of the non linear relationship between fluoresced light intensity and pH (except for the central pH range), and between pH and dissolved gas concentration, even barely visible intensity variations may lead to large error on carbon dioxide concentration values, as sketched in figure 2.30. The test image shown on the figure comes from measurement of CO_2 dissolving in water at a flat interface, chapter 4 (a darker patch corresponding to plunging dissolved carbon dioxide is visible on the top right corner). Intensity variations caused by the darker stripes on sub-figure a lead to intensity fluctuations (oscillations around the smoothed profile). When computing pH or dissolved CO_2 fields using the raw intensity profiles, these oscillations ultimately lead to significant

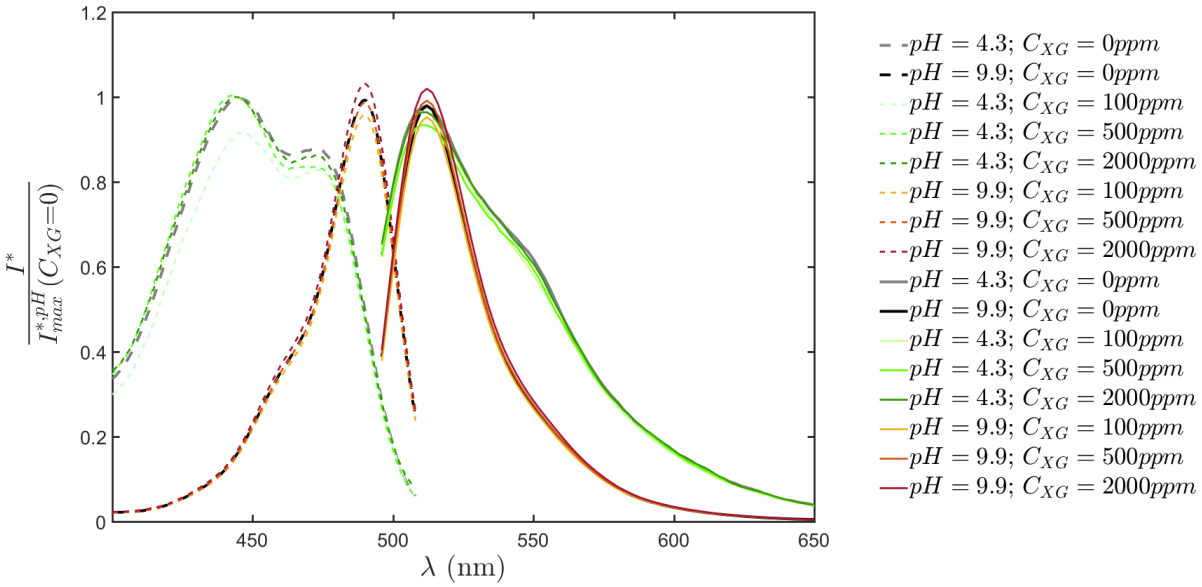

Figure 2.27 – Influence of XG concentration on excitation (dashed lines) and fluorescence (full lines) spectra of fluorescein at 5.10^{-7} M. Spectras are normalized by the maximum value of their corresponding spectrum at same pH and C_{XG} = 0 ppm.

error on measured concentration profiles (up to 10% variations from the smoothed values). Ratiometric improvements eliminates such source of error.

2.2.9.b Laser sheet thickness

Laser sheet thickness is not strictly speaking a source of error but rather a limit to the spatial resolution. When the depth of focus of the optical setup is larger than this laser sheet thickness, the "planar" fluorescence information is in fact averaged on the whole laser sheet thickness. This is most of the time the case for macroscopic PLIF applications. One can therefore not distinguish scalar structures smaller than this thickness which consequently becomes the maximum spatial resolution of the method. Nevertheless, $I_{pH}-$PLIF is intrinsically able to measure micromixing, which is not the case for classical PLIF.

Argon Ion lasers such as the one used in this thesis can be shaped into laser sheet of down to several hundreds of micrometers. Here the sheet thickness is approximately 250 µm .

2.2.9.c Optical distortion

Optical distortion arise when the optical equipment are not used in Gaussian conditions, that is to say when light rays only make small angles with optical axis, and cross each device close to its center. Unfortunately when dealing with large experiments and regions of interest, these conditions may not be fulfilled. This gives rise to geometric and chromatic aberration. The efficiency of optical filters can also be affected, in particular it is known that the filtering yield of band-pass or long-pass filters depends on the angle of incidence and light polarization. This explains the need of a ratio normalization step during calibration (section 2.2.6.b).

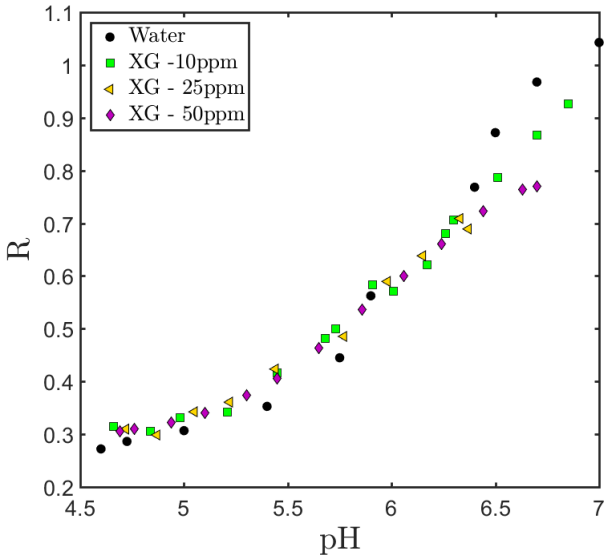

Figure 2.28 – R = $f(p\mathrm{H})$ calibration curves for water and dilute XG solutions. Ratios for water have been measured using the optical setup presented in section 2.2.6.a (curve from figure 2.20), ratios for XG solutions have been measured using the setup presented in section 4.2.4.b.

2.2.9.d Noise level

In the ratiometric method, relative uncertainty over R depends on intensity uncertainties over the two bands δI_1 and δI_2. One can write

$$\frac{\Delta R}{R} = \frac{\Delta \delta I_1}{\delta I_1} + \frac{\Delta \delta I_2}{\delta I_2} \tag{2.35}$$

The higher the measured intensity on both bands and the lower the noise level ΔI, the lower the relative uncertainty on R. The values of gray level intensity on the two spectral bands depends on many factors: camera settings (exposure time, $\#f$ number, dynamics), geometric configuration (Beer-Lambert absorption, fluorescence re absorption, scattering), and of course fluorescence intensity. The noise level depends only on camera settings. A sufficient signal over noise ratio can thus be ensured by increasing each band's signal with higher fluorescent dye concentration, higher laser power or longer exposure time; each of these mod-

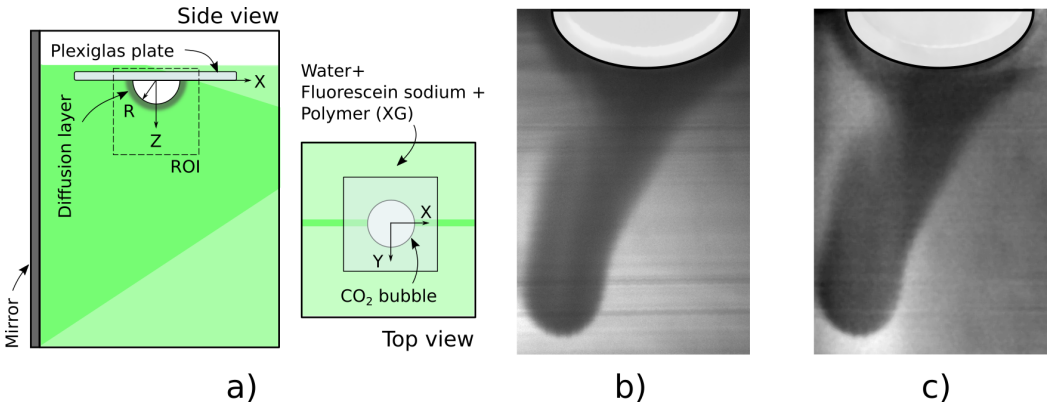

Figure 2.29 – Diphasic test case for I^r_{pH} – PLIF, a): Sketch of the bubble dissolution condition. b) and c): Fluoresced light intensity (band 1) and intensity ratio around the CO_2 bubble dissolving XG solution

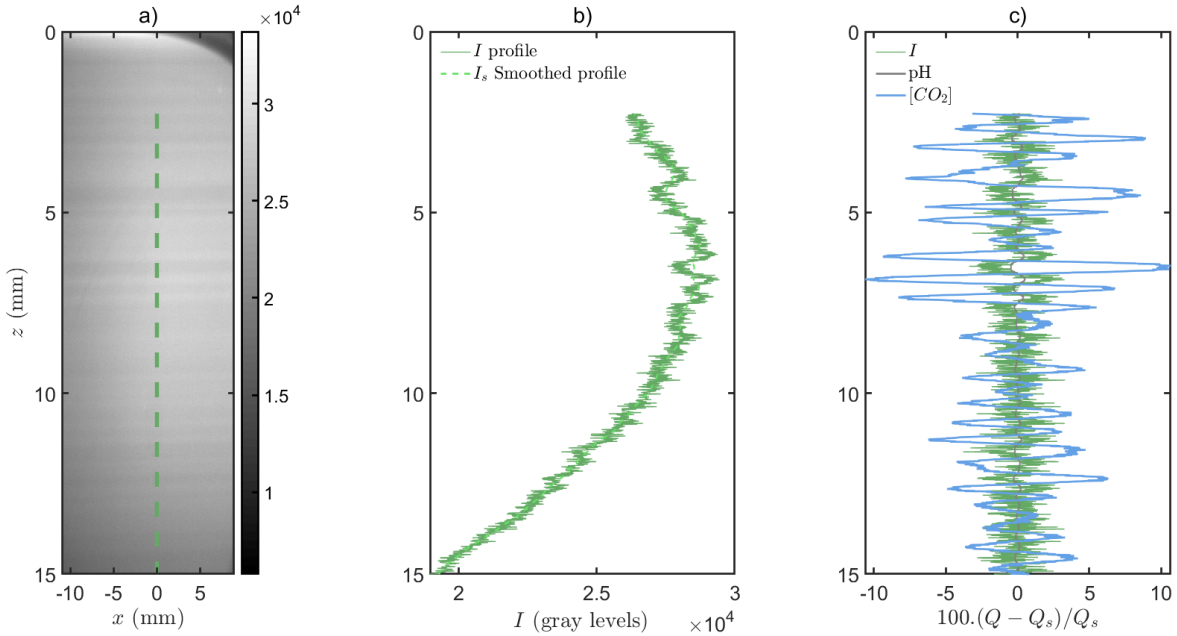

Figure 2.30 – I_{pH} – PLIF noise related errors. The test image shown here comes from measurements of CO_2 dissolving at a flat interface with water. a) Example of raw fluoresced intensity image with darker stripes due to wall scratches. b) Intensity profile extracted along the green dashed vertical line of sub-figure a), the dark green line is the raw intensity (with noise), and the light green dashed line the smoothed signal. c) Relative difference between smoothed and raw values $100.(Q-Q_s)/Q_s$. Q can denote intensity, pH or [CO_2]. Green line: relative intensity variations with respect to the smoothed profile. Gray and blue lines: resulting relative pH (respectively CO_2) variations. For those last two curves, Q is the profile deduced from raw intensity values, and Q_s is computed from the smoothed intensity values.

ifications acting to the detriment of other factors such as time resolution or fluorescence re-absorption. One can also use highly sensitive camera to achieve a noise level as low as possible.

Estimating the ratio uncertainty in I^r_{pH} – PLIF is quite complex since it depends on both the optical setup and the pH values to be measured. In the following figure 2.31), $\Delta\delta R/R$ is calculated with equation (2.35) as a function of measured intensities δI_1 and δI_2 for three different noise levels $\Delta\delta I = \Delta\delta I_1 = \Delta\delta I_2$ with $\Delta\delta I = [1, 10, 100]$ gray levels. This figure can be used as a tool to quickly estimate a relative ratio uncertainty, simply knowing the noise level of the camera and the range of variations of gray level intensities on each spectral bands during the measurements.

At high signal over noise ratio (*i.e.* high δI_1 and δI_2 and low ΔI), the relative uncertainty on the measured ratio is quite good, below 1 % for at least 1000 gray levels of signal and 10 gray levels of noise for example. This corresponds to the blue region on the figure 2.31. For low signal over noise ratio however, the error on the ratio becomes important (yellow region on the figure). Note that since concentration is ultimately an exponential function of the ratio, such imprecision could lead to tremendous error of concentration measurement.

High pH values correspond to high intensities on both spectral bands, and so to good signal over noise ratio for both these bands. On the other hand, low pH values yield weak fluorescence signal for the two colors, and so the signal over noise ratio is decreased. Consequently, according to equation (2.35) and the corresponding figure 2.31, relative uncertainty on the ratio increases with decreasing pH, especially in the very acidic domain (pH<5). This is illustrated by the $\frac{\Delta R}{R} = f(pH)$ curve drawn on the left hand side of figure 2.32. One typi-

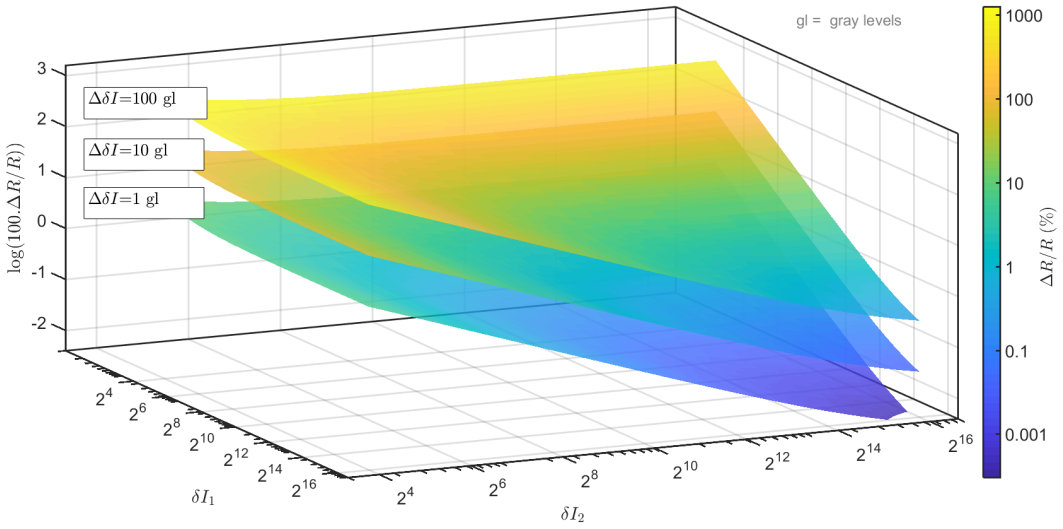

Figure 2.31 – Relative uncertainty mapping of ratio as a function of measured spectral band intensities δI_1 and δI_2.

cally gets $\delta I_1 \simeq 1400$ gray levels and $\delta I_2 \simeq 2000$ gray levels for pH = 4.6. Considering a global uncertainty of $\Delta\delta I_1 = \Delta\delta I_2 = 1$ gray level, the relative uncertainty on the ratio is $\Delta R/R \sim 0.1\%$ for pH = 4.6 and falls to 0.05% for pH = 7.

2.2.9.e Low dynamics range

The relative ratio uncertainty can be estimated as previously explained. However its impact on pH and dissolved carbon dioxide concentration uncertainties is yet to be expressed. With given experimental conditions (associated to specific intensity and ratio values), it is possible to compute the maximum error on pH and concentration ensuing from the uncertainty on ratio measurement. This is done by taking the ratio value R and introducing the absolute uncertainty $\pm\Delta R = R \times \frac{\Delta R}{R}$ derived from the previous estimation in the equation for pH calculation. In what follows, errors on pH and carbon dioxide concentrations are computed using the optical conditions of the jet experiment (even if pH variations where not caused by carbon dioxide injection in that case). For a given ratio value, one can thus compute two different pH, pH(R + ΔR) and pH(R − ΔR). The absolute pH error caused by ratio uncertainty is then

$$\Delta p\mathrm{H} = p\mathrm{H}(\mathrm{R} + \Delta\mathrm{R}) - p\mathrm{H}(\mathrm{R} - \Delta\mathrm{R}) \tag{2.36}$$

The same method is then used to estimate the absolute error on carbon dioxide concentration:

$$\Delta[\mathrm{CO_2}] = [\mathrm{CO_2}](p\mathrm{H}(\mathrm{R} + \Delta\mathrm{R})) - [\mathrm{CO_2}](p\mathrm{H}(\mathrm{R} - \Delta\mathrm{R})) \tag{2.37}$$

As previously mentioned, lower pH yield lower fluorescence intensities and lower signal over noise ratios, hence higher ratio relative uncertainties. They should thus correspond to the highest pH and concentration errors. However, an additional effect is introduced by the shape of the $R = f(p\mathrm{H})$ calibration curve. Indeed for pH below 5 or about 8, ratio tends to plateau values where the technique is not able to tell the difference between two close pH values, and where even very small ratio variations lead to large pH shifts. In these regions, the

$\pm\Delta$R is thus bound to cause large ΔpH, and so pH and concentration measurement error drastically increases in both the high and low pH domain.

The error on pH and concentrations as a function of the relative uncertainty on ratio are plotted in figure 2.32, right hand side. The abscissa axis ΔR/R increases with decreasing pH. Decreasing ΔR/R, uncertainty is very good (below 0.05%) until the upper plateau value of the ratio is reached. The left peak of both purple and green curves then correspond to the high pH, high ratio, part of the calibration curve, (and so low uncertainty ratio). Going the other way around and increasing ΔR/R corresponds to decreasing R and the pH. Since the fluoresced light intensity globally decreases along with pH, the signal over noise ratio decreases and the uncertainty increases. When the low-pH plateau value for ratio is reached, not only is the signal over noise ratio relatively poor, but the error associated to a small ratio variation is also very large. Both effects lead to a strong increase in pH error and concentration error.

As a conclusion, for a given optical setup, pH and concentration measurement errors associated to $I^r_{pH}-$PLIF can be quite low, providing that the signal over noise ratio is high enough and that the pH stays within the measurable range. Lower signal over noise ratio tend to globally increase the uncertainties, and measuring pH values belonging to the plateau ranges of the $R = f(pH)$ calibration curve leads to very large errors.

2.2.10 Conclusion on $I^r_{pH}-$PLIF

In this work, the interest of the original $I^r_{pH}-$PLIF technique has been demonstrated. The ratio of intensities from two well chosen spectral bands of fluorescein's fluorescence spectrum increases with the pH, with a good dynamics in the range between pH 5 and 7. This behavior comes from the wavelength-variable pH dependency of fluorescein's quantum yield. It can be used to translate two recorded fluorescence fields into a quantitative pH field thanks to an initial calibration procedure, in a similar way to what is currently done for temperature measurements. The use of a single dye lowers the potential chemical intrusiveness of the technique, and makes it more suitable for the study of turbulent flows than two dyes versions.

Two limitations are still to be mentioned. First of all, the overlapping between fluorescein's absorption and emission spectra leads to an unsolvable form of spectral conflict. This conflict can cause fluorescence re-absorption if the path crossed by fluoresced light is long, or if the dye concentration level is too important. It can therefore introduce large errors on the measured ratio, hence on the computed pH fields.

Second is the fact that fluorescence recording on SCmos sensors requires a rather long exposure time, typically of 20 ms in the present study. This is especially due to the fact that since a single dye is used, at least one of the two-color emits a relatively low fluorescence signal. Thus, a longer exposure time is needed for a significant signal from this color to be recorded. It implies that the faster scales of turbulence can not be captured. To decrease this exposure time, more powerful continuous light sources or pulsed lasers can be used to increase the excitation intensity. This limitation is thus not associated to the technique itslef but rather to the setup used. Fluctuations of emitted intensity output known to occur for pulsed lasers are automatically corrected by the use of ratiometric technique in a way similar to power drift corrections presented in section 2.2.6.c (Bruchhausen et al., 2005). However, increasing the laser output intensity may generate excitation intensities above the linear domain limit (Chaze et al., 2016), or introduce photo-bleaching effects. Furthermore, pulsed laser are difficult to find for the present excitation wavelength, and generation of pulses from continuous laser at this wavelength adds supplementary difficulties.

To conclude, $I^r_{pH}-$PLIF presents two main assets:

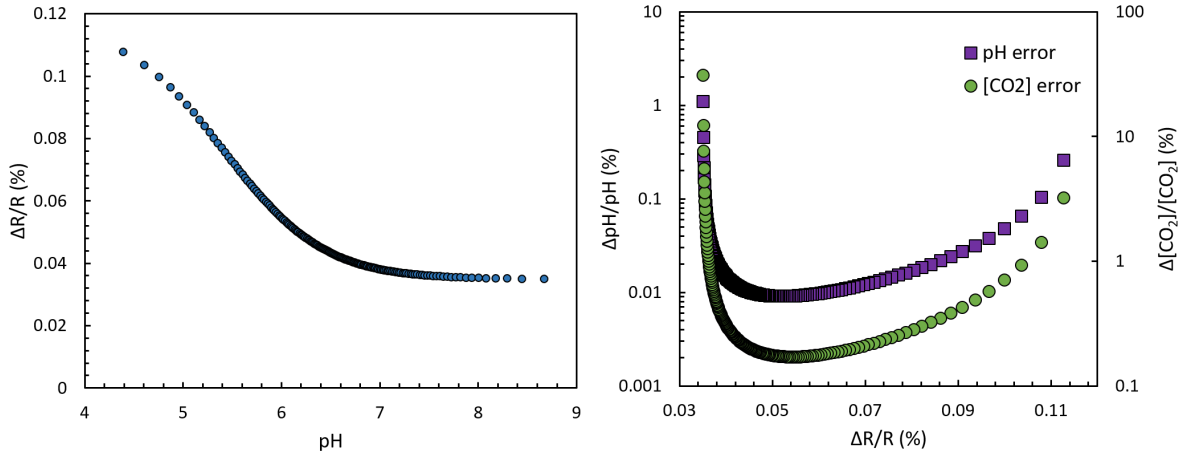

Figure 2.32 – Effect of pH on ratio uncertainty (a) and of ratio uncertainty on pH and concentration measurement (b) in the jet experiment case (different axis for pH and concentration errors)

- It can be applied anywhere in the flow, even on small regions, regardless of the incident light absorption conditions outside the region of interest. Indeed, the knowledge of the laser path across the fluid and the pH variation it may encounter on its way to the ROI is not required. This makes the technique interesting for studying small scale or local phenomena, or for accessing specific regions of complex flows.

- It intrinsically corrects several errors that can't be accounted for by single color techniques, such as time variations of excitation intensity or reflections at moving interfaces. Recent temperature and pH measurement in multiphase configurations (Chaze et al., 2017; Fenner and Stephan, 2017; Kong et al., 2018; Kováts et al., 2017) offer interesting perspectives for further I^r_{pH} – PLIF applications.

In chapter 4 , both one-color and ratiometric versions of the PLIF are used for the study of carbon dioxide dissolution under flat surfaces. The most suitable version of the technique would have been the ratiometric one, for reasons detailed later. However, most of the experiments were performed before the development of our I^r_{pH} – PLIF method and are therefore only available in single color version. In so, results may exhibit heterogeneity due to laser excitation variations, and additional error on the measured dissolved gas concentration values may appear because of the unknown laser path between the wall of the tank and the ROI. These are discussed in due time in chapter 4, and in appendix G.

Chapter 3

Oscillating grid turbulence in Newtonian and non-Newtonian fluids

> When I meet God, I am going to ask him two questions, why relativity? and why turbulence? I really believe he will have an answer for the first.
>
> Werner Heisenberg

Contents

Abstract (En)

This chapter aims at studying the effects of shear-thinning dilute polymer on oscillating grid turbulence. It starts by a general literature review on turbulence in DPS, in industrial or fundamental conditions. In the second section of the chapter, the model polymer used for this study, namely Xanthan Gum (XG) is introduced, and its behavior is characterized extensively. In the third section, the oscillating grid device used throughout this thesis is described. The last section presents the results of the PIV study of OGT in water and dilute XG solutions. In water, turbulence behavior in our OGT setup corresponds to what was expected from the literature review. The ability of OGT to turn periodic flow into non-periodic turbulence is evidence by performing phase resolved velocity measurement in the vicinity of the grid and showing that oscillatory motion is negligible versus turbulence outside of the grid sweep region. Several effects of low concentration polymer addition on OGT are observed. The first one is an enhancement of mean flows and persistent recirculations in the tank. The modification of energy distribution and transfers between mean, oscillatory, and turbulent velocity components close to the grid is also depicted. Finally the decay of turbulence in the grid stirred tank is characterized for various polymer concentrations in the dilute and semi dilute regime. Critical concentrations for OGT hydrodynamics are evidenced and compared to the ones predicted by the polymer's rehological behavior.

Résumé (Fr)

Ce chapitre a pour objectif l'étude de la turbulence de grille oscillante dans une solution de polymère dilué aux propriétés rhéofluidifiantes. Il débute par une étude bibliographique de la turbulence en solution de polymère dilué dans différentes configurations industrielles ou fondamentales. Dans un second temps, le polymère modèle choisi pour notre étude, à savoir la gomme de xanthane (XG) est présenté, décrit et caractérisé. Une troisième sous partie permet de décrire le dispositif de grille oscillante conçu et utilisé durant cette thèse. Les résultats de l'étude PIV de la turbulence de grille oscillante en eau et solution de XG sont présentés dans la dernière partie. Pour l'eau, le comportement de la turbulence correspond aux prédictions de la littérature. En particulier, au moyen de mesures résolues en phase autour de la zone de battement de la grille, on met en avant la capacité du dispositif à transformer un écoulement périodique en une turbulence apériodique. Différents effets propres à l'ajout de polymère dilué au milieu sont observés. Le premier est une intensification et structuration de l'écoulement moyen dans la cuve. La répartition et les échanges d'énergie entre les composantes moyenne, oscillante et turbulente de l'écoulement proche de la grille sont également modifiés. Enfin, la décroissance de la turbulence dans la cuve est caractérisée pour une large gamme de concentration de polymères dans le régime dilué ou semi dilué. Les concentrations critiques observées via ces études hydrodynamiques sont comparées à celles issues de l'étude rhéologique du polymère.

Even though turbulence is present in most of the flows encountered in the environment or in the industry, generating controlled turbulence at the laboratory scale to investigate in depths its behavior and interactions with other phenomena is not an easy task. Laboratory experiments or numerical simulations of turbulent flows are most of the time scaled down versus real life situations. It is often difficult to achieve high Reynolds number necessary to visualize a fully developed turbulence with the range of homogeneous and isotropic scales associated to it. When aiming at studying turbulence on its own, or the interactions of turbulence with another phenomenon in absence of mean flow, additional hardships arise. Numerical simulations can create turbulence without mean flow, but are still limited in terms of achievable Reynolds number. Experimentally, the difficulty is to get rid of the mean flows. High Reynolds number and quasi isotropic and homogeneous turbulence are indeed achievable with setups such as fixed grid turbulence, but associated to a strong mean motion. It was for that original purpose of generating homogeneous isotropic turbulence in absence of mean shear that oscillating grid turbulence (OGT) was initially designed in the 1970's. Previous studies showed that mean flow always exist inside oscillating grid stirred tanks, but OGT remains one of the simplest ways of generating laboratory flow with a low mean flow to turbulence intensity ratio and good homogeneity and isotropy.

In this chapter, the effect of non-Newtonian properties on oscillating grid turbulence are investigated. The underlying objective is to achieve a better understanding of OGT in dilute polymer solution (DPS), and ultimately facilitate our interpretation of the turbulent mass transfer measurements at the free surface that will be presented in chapter 4. The chapter is structured in the following way. First the literature background about oscillating grid turbulence in Newtonian fluids, turbulence in dilute polymer solutions, and grid turbulence (fixed or oscillating) in dilute polymer solutions is depicted. The polymer chosen for this study is then introduced and characterized, as well as the oscillating grid setup used. Finally, an experimental study of OGT in water and DPS is presented.

3.1 Background

3.1.1 Oscillating grid turbulence in Newtonian liquids

Grid turbulence is an experimental mean of generating turbulence in liquid or gas flows with the objective of making this turbulence as homogeneous and as isotropic as possible. To that end, a rigid grid of square mesh is placed in a channel perpendicular to a main flow of uniform velocity. Downstream of the grid, turbulence is created by the interactions between the wakes of the grid bars. The central part of the flow being almost not affected by the wall perturbations, turbulence proves to be experimentally homogeneous and isotropic (Comte-Bellot and Corrsin, 1966). Best results for homogeneity and isotropy are achieved for a given solidity fixed accordingly to the shape of the grid bars and reached far from the grid (at least 20 meshes away).

A longer list of requirements on how to try and achieve homogeneous isotropic turbulence with fixed grid experiments (HIT) can be found in Hearst (2015). Even when they are fulfilled, the produced turbulence does not fully correspond to HIT because its spectrum does not always exhibit the famous $-5/3$ slope characteristic of inertial sub-range in HIT. This is often attributed to an insufficient Taylor based Reynolds number Re_λ, *ie* a too weak turbulence. To increase the intensity of turbulence, active and fractal grids have been developed. Active grids use injectors or mobile solid parts fixed on the grid mesh (Hideharu, 1991; Isaza et al., 2009; Mydlarski and Warhaft, 1996) and allow to reach experimentally the inertial range of HIT. Fractal grids (Hearst, 2015; Seoud and Vassilicos, 2007) are rectangular

mesh grids presenting fractal patterns. Because of their specific shape, they can input turbulent energy at a wider range of scales and thus generate a highly homogeneous and fast decaying turbulence.
All of these setups can be used for fundamental turbulence studies (Isaza et al., 2009; Thormann and Meneveau, 2014), or to investigate the relationships between turbulence and other physical phenomena such as mixing (Simoens and Ayrault, 1994; Suzuki et al., 2010), boundary layers at rigid walls (Sharp et al., 2009) and so on.

Nevertheless, they all share the same drawback of having a poor turbulence over mean flow intensity ratio. The dynamical range of velocities is dominated by the mean flow and precision of fluctuation measurement is not guaranteed. This is a major lock to the study of turbulence interactions with other phenomena. The mere presence of a strong mean flow also makes the application of the optical measurement techniques presented in the previous section more complicated: particles or tagged fluorescent molecules quickly move out of the field of view of the cameras, and several cameras in parallel are necessary to track turbulence properties on large distances at a high spatial resolution. To lift off the mean flow lock and achieve turbulence production close to HIT at low mean flow intensity, another type of grid turbulence experiments has been developed and is presented in what follows.

3.1.1.a Introduction to oscillating grid turbulence

The principle of Oscillating Grid Turbulence (OGT) is to produce turbulence in a fluid initially at rest by making a grid oscillate at a frequency f and with an amplitude or stroke S. It is commonly said that the jets and wakes behind the grid's holes and bars interact to generate turbulence (Herlina, 2005; Hopfinger and Toly, 1976; Thompson and Turner, 1975; Voropayev and Fernando, 1996), which then diffuses away from the grid. In other words, turbulence comes from the shearing of the fluid by the grid. It is of great interest for turbulence study since it theoretically creates almost no mean flow and therefore allows to study the effects of turbulence alone, which is not the case for fixed grid systems. This point is discussed in section 3.1.1.c. OGT is also supposed to yields a quasi-homogeneous and isotropic turbulence in horizontal planes when measured far enough from the grid's top position. Finally, as seen from a gas-liquid interface located far enough from the grid, OGT resembles bottom shear turbulence that is generated by friction at the bottom of channels or river, but without the strong mean current associated to such situations.

The first oscillating grid apparatus was designed by Rouse and Dodu (1955) to study turbulent diffusivity across a density interface located above the grid and consisted in a square mesh grid in a cylindrical tank. Later, Bouvard and Dumas (1967) performed hot-fiber measurements of grid generated turbulence in water, using a perforated plate as an oscillating grid. A full characterization of OGT in prismatic tanks came with the pioneer works of Thompson and Turner (1975) and Hopfinger and Toly (1976). Thompson and Turner (1975) studied several types of grids with different mesh size M and different bar shapes, and showed that the best homogeneity and intensity of turbulence was achieved with square section bars and a solidity parameter $\Xi = \frac{d}{\mathrm{M}}\left(2 - \frac{d}{\mathrm{M}}\right)$ lower than 0.4. Hopfinger and Toly (1976) added that the walls of the tank should be planes of symmetry for the grid, in order to minimize the recirculation effects in the tank. For the same reason, the grid's average position should be at least $2.5 \times \mathrm{M}$ above the bottom of the tank (Xuequan and Hopfinger, 1986). Horizontal homogeneity of turbulence is reached when the distance from the grid's mean position is greater than a empirically determined value Z_h expressed in numbers of mesh parameter, with $2\mathrm{M} < \mathrm{Z}_h < 4\mathrm{M}$ depending on the study.

These principles have been applied in nearly every oscillating grid experiments ever since (Asher and Pankow, 1986; Brumley and Jirka, 1987; Chiapponi et al., 2012; Herlina, 2005; Matsunaga et al., 1999; Mcdougall, 1979; McKenna, 2000; Nokes, 1988; Xuequan and Hopfinger, 1986).

OGT has been used for many purposes in research, among which the study of interactions between turbulence and solid impermeable boundaries (McCorquodale and Munro, 2017, 2018), of turbulence and gas-liquid mass transfer at a free surface (Brumley and Jirka, 1987; Chiapponi et al., 2012; Herlina, 2005; McKenna and McGillis, 2004a), in stratified media (Hopfinger and Toly, 1976; Thompson and Turner, 1975; Verso et al., 2017; Xuequan and Hopfinger, 1986), or to study the behavior of bubbles, cells, fibers, and flocculation aggregates in suspended in a turbulent liquid phase (Cuthbertson et al., 2018; Mahamod et al., 2017; Nagami and Saito, 2013; Rastello et al., 2017; San et al., 2017).

In order to achieve a full spatial homogeneity of turbulence in the three dimension of space, a few authors tried to use two simultaneous oscillating grids operated either in phase opposition or synchronization (Schulz et al., 2006; Shy et al., 1997). They showed that within a small region of interest located between the two vibrating grids, turbulence could be considered roughly homogeneous in three dimensions. Obviously, this setup can not be used when studying the interaction of turbulence with an interface or a density stratification and was not considered for the present study.

Apart from fundamental turbulence effects studies, oscillating grids are also used as flotation cells (Cuthbertson et al., 2018; Massey et al., 2012; Safari et al., 2017) in tanks with various shapes (tubular, prismatic...) and with various number of grids. Finally, it is worth noting that OGT has been almost never simulated numerically. Only the recent work by Zhang et al. (2017) presents a Lattice Boltzmann simulation of OGT and numerically visualizes the interactions between jets and wakes behind the grid bars and holes leading to turbulence generation.

3.1.1.b Turbulence intensity and decay law

Based on the grid oscillation parameters, a grid Reynolds number Re_g can be defined (Janzen et al., 2010; Matsunaga et al., 1999):

$$\mathrm{Re}_g = \frac{f \mathrm{S}^2}{\nu} \tag{3.1}$$

Expressions for the root mean square (rms) of velocity fluctuations and for the integral length scale of turbulence as a function of the distance from the grid have been derived respectively by Hopfinger and Toly (1976) and Thompson and Turner (1975):

$$\begin{aligned} \langle u'_x \rangle_{rms} &= \mathrm{C}_{1_{\mathrm{HT}}}.f.\mathrm{S}^{1.5}.\mathrm{M}^{0.5}.\mathrm{Z}^{-n_x} \\ \langle u'_z \rangle_{rms} &= \mathrm{C}_{2_{\mathrm{HT}}}.\langle u'_x \rangle_{rms} \end{aligned} \tag{3.2}$$

$$\mathrm{L}_\infty = \mathrm{C}_{\mathrm{TT}}.\mathrm{Z}_g \tag{3.3}$$

Where, $\mathrm{L}_\infty = \mathrm{L}^x_{xx}$ is the integral length scale of horizontal turbulent fluctuations along the horizontal direction, $\mathrm{C}_{\mathrm{TT}} \simeq 0.1$,$\mathrm{C}_{1_{\mathrm{HT}}} \simeq 0.25$, $\mathrm{C}_{2_{\mathrm{HT}}} \simeq 1.2$, and $n_x = 1$ in the original works.

It is then possible to define a turbulent Reynolds number as

$$\mathrm{Re}_\mathrm{T} = \frac{2 \langle u'_x \rangle_{rms} \mathrm{L}_\infty}{\nu} \tag{3.4}$$

Using equations (3.2) and (3.3), it comes that

$$Re_T \propto \frac{f S^{1.5} M^{0.5}}{\nu} \propto Re_g \left(\frac{M}{S}\right)^{0.5} \tag{3.5}$$

and so the turbulence based Reynolds number should be constant with Z for given oscillation parameters.

These relationships have been verified by a number of studies using grid stirred tanks (Brumley and Jirka, 1987; Chu and Jirka, 1992; Herlina, 2005; Matsunaga et al., 1999; Mcdougall, 1979; Nokes, 1988; Silva and Fernando, 1992; Verso et al., 2017; Xuequan and Hopfinger, 1986) up to the values of the different constants which vary among the works ($C_{TT} \in [0.1..0.4]$, $C_{1_{HT}} \in [0.2..0.3]$, $C_{2_{HT}} \in [1.1..1.3]$). The proportionality coefficient between the integral length scale and the distance to the grid C_{TT} was also found to depend on the S/M ratio (Hopfinger and Toly, 1976; Wan Mohtar, 2016).

Some studies suggest that equation (3.2) may only be valid for specific ranges of frequency and strokes. For strokes values lower than M for example, Nokes (1988) and more recently Wan Mohtar (2016) found that the exponent n_x of the decay law for $\langle u'_x \rangle_{rms}$ may be different from unity, and that $\langle u'_z \rangle_{rms}$ decay law has a different exponent n_z than n_x. Equations (3.2) should then be written $\langle u'_x \rangle_{rms} \sim Z^{-n_x}$ and $\langle u'_z \rangle_{rms} \sim Z^{-n_z}$, with stroke dependent n_z and n_x.

As for the frequency range, Mcdougall (1979) and Shy et al. (1997) mention the existence of a cutoff grid frequency at $f \simeq 7$ Hz above which the dependency of $\langle u'_x \rangle_{rms}$ and $\langle u'_z \rangle_{rms}$ on f is no longer linear.

We can mention that a generalization of the works of Hopfinger and Toly (1976) and Thompson and Turner (1975) was proposed by Matsunaga et al. (1999). The strategy was to describe turbulence generated by the oscillating grid using a $k-\epsilon$ type modeling. We will yet not discuss it here for the sake of brevity.

3.1.1.c Mean flows

At first, the concept of OGT generating no mean flow but only isotropic and homogeneous turbulence was rather well believed. The development of PIV techniques allowing further investigations of the flow inside OGT tanks, it became clear that mean flow exist even when matching the requirements detailed in section 3.1.1.a). McKenna and McGillis (2004a) studied the mean flows in an oscillating grid tank using PIV and showed that persistent mean flow cells always existed, with relative high kinetic energy level as compared to the turbulent kinetic energy. Moreover, these mean flow seem to be poorly repeatable and strongly dependent on initial conditions (Herlina, 2005). It is therefore really hard to predict the mean flow that could occur in the oscillating tank during a specific measurement, and this is one of the main limitations of OGT systems. McCorquodale and Munro (2018) recently suggested a method for reducing mean flows in OGT using an inner box placed inside the stirred tank to separate the wall-induced vortices from the rest of the flow.

Some studies suggest that lower mean flows an better turbulence over mean flow ratios could be obtained using Randomly Actuated Jets Array (RASJA) instead of oscillating grid to generate turbulence. Variano et al. (2004) developed such a device, and showed that the mean flow velocity magnitude was always less than 10 % of the turbulent velocity scale, whereas in oscillating grid tanks it can reach 50 % or even 100 %. Their RASJA device was also able to produce turbulence intensities hard to reach with OGT systems. Oscillating grid turbulence has yet been chosen for this study because it has been far more studied in the

litterature than RASJA, and already applied once to the study of turbulence in dilute polymer solutions (Liberzon et al., 2009).

All the previous conclusions are only valid when considering OGT in water (or other Newtonian fluids). The goal is here to study OGT in non-Newtonian solutions. So let us first of all review the characteristics of turbulence in DPS.

3.1.2 Turbulence in dilute polymer solutions

Understanding the flow dynamics of non-Newtonian fluids is a current question for many industrial and environmental applications. In particular, turbulence in non-Newtonian liquids occurs in several industrial applications ifor the food process or pharmaceutical industries (Chhabra and Richardson, 1999; Kukura et al., 2002). The level of its understanding has not reached that of turbulence in Newtonian fluid yet. This is mostly because the interactions between suspended matter giving the fluid its non-Newtonian properties are multiple and complex, and strongly depend on the nature and properties of this suspended matter. The following paragraph will focus on the known effect of dilute polymer on turbulence. Polymers are widely studied as flow additives because they are at the origin of the non-Newtonian properties of the fluid in many applications (Chhabra, 2010), and also because the wide range of existing polymers allows to use them to build model fluids reproducing the behaviors of other non-Newtonian media. For example, the specific rheology of blood, which is due to red blood cells, is often modeled using a mixture of glycerol and XG (Najjari et al., 2016). The following literature overview starts with the first historically observed effect of polymer on a turbulence-related property of the flow: drag reduction. The action of viscoelasticity is then briefly explained. Finally, the influence of polymer concentration and shear thinning are considered.

3.1.2.a Drag reduction

In the late 1940's, Toms (1948) discovered that a very small concentration of polymer diluted in a solvent could drastically reduce drag. The phenomenon is called Tom's effect or drag reduction. Drag reduction may decrease the pressure drop in a pipe by up to 80 % (Doorn et al., 1999), and it is therefore of paramount interest in many applications such as hydraulics systems or oil and gas industry. This is why a huge number of studies have addressed this topic since the 1950's. The review by Nadolink and Haigh (1995) already listed more than 2500 entries.

The main concepts of drag reduction briefly summarized here have been treated extensively by Lumley (1969) and more recently by Sreenivasan and White (2000). The basic principle is that the small polymer molecules introduced in the solvent act as molecular springs, undergoing coil-stretch transformations thus storing part of the kinetic energy of the flow. This is especially efficient in high shear regions close to the walls and leads to an apparent increase in the buffer layer thickness of the boundary layer and a drastic reduction of the friction. For a given concentration of polymer, the friction coefficient variations as a function of the Reynolds number departs from the classical Prandtl-Karman law when reaching an onset Reynolds number. This is called the onset of drag reduction (Sreenivasan and White, 2000). The higher the polymer concentration, the lower the Reynolds number at the onset. When further increasing Re after the onset, the friction factor decreases extremely rapidly until it reaches an asymptotic trend. Depending on the nature of the polymer, two types of drag reduction leading to two asymptotic slopes are possible. In type A drag reduction, the friction coefficient tends to what is called the maximum drag reduction asymptote empirically determined by Virk (1975a) (see Sreenivasan and White (2000), figure 1). In type B drag

reduction, it ultimately follows a Prandtl-Karman slope shifted towards lower friction coefficients (Virk and Wagger, 1990). The drag reduction level of this last curve is fixed by the polymer concentration. Type A is characteristic of flexible random coiled and highly deformable polymer chains (eg. PolyEthylene Oxide PEO), and type B of relatively rigid, elongated and undeformable molecules (e.g Xanthan gum)(Virk, 1975b). This last observation stresses the importance of polymer conformation and rigidity in its interactions with the flow.

Putting aside boundary layer effects, bulk turbulence can be modified by two main properties of the dilute polymer solutions considered here: viscoelasticity and shear-thinning (or more generally shear-dependent viscosity). Governing equations for shear thinning and viscoelastic fluid flows based on the classical Navier Stokes equations and relevant constitutive equations have been presented in section 1.3.2.c. These sets of equations can either be solved by direct numerical simulations (DNS) at a high computational cost, or by using Reynolds averaged equations and physical models, the construction of which, used as closure relations for the equation systems, requires a deep understanding of the physics behind these interactions. Such an understanding ensues from DNS and experimental studies. In the two next paragraphs, both experimental and numerical studies are presented in order to try and represent the current state of understanding of polymer effects on bulk turbulence through both variable viscosity and viscoelastic effects.

3.1.2.b Viscoelasticity in bulk turbulence

The physical mechanisms of drag reduction relies on the interactions between polymer chains and the flow and the scales at which polymers can take or give energy to the fluid. Such interactions should also impact turbulence in the homogeneous isotropic case, without high shear and boundary layers effects. However, fewer study address the effect of dilute polymer on bulk turbulence. The major difficulty is that the polymer characteristic length scale is molecular, way smaller that both the Kolmogorov and the integral length scales of turbulence (Lumley, 1969). Studying the polymer-flow interactions therefore requires the resolution of both large and small (even molecular) scales of the flow which is numerically costly and experimentally challenging.

A polymer may have several effects on the flow depending on its nature, its conformation, and its concentration, characterized by Weissenberg number We or Deborah number De (see below). For most of drag reduction and polymer-turbulence interaction studies, the typical concentrations used are so small that the effects of polymer on the overall fluid viscosity is often neglected. Even at small concentration, the viscoelastic property of dilute polymer has a great impact.

The idea generally accepted is that viscoelasticity mainly acts on the small scales of the flow. The first observations of such property were made by Gadd (1965) and Barnard and Sellin (1969) by injecting colored dilute polymer solution into a similar but transparent solution either at rest (Gadd, 1965, 1966) or passed through a fixed grid. They found that the small scales of mixing were substantially reduced in dilute polymer solution as compared to water. Theses observations were then confirmed by the measurement of turbulent velocity fluctuations behind a fixed grid by Fabula (1966) and Greated (1969).

It can be explained by the fact that the polymer chains structure gives them the ability to deform elastically and store energy at small scales, which tends to truncate or modify the flow energy cascade before reaching the Kolmogorov scale (Nguyen et al., 2016; Tabor and de Gennes, 1986; Warholic et al., 1999, 2001; Xi et al., 2013). Lumley (1973) conceptually defined this limit as the scale for which the characteristic time scale of turbulence and the relaxation time of the polymer are equal. Polymer chains are deformed by scales smaller

than the Lumley one l_l and advected by the larger ones. This large scales thus supposedly do not store any energy into the polymer chains and the cascade of energy remains unchanged in their domain. The Weissenberg number Wi may be defined as the ratio of the polymer relaxation time over the turbulence komogorov time scale. By definition, Wi= 1 at the Lumley scale. Tabor and de Gennes (1986) later set the bases of the elastic theory by defining a scale l_e as the scale at which the energy stored inside the polymer chains is equal to the kinetic energy of the flow. Polymer molecules are expected to deform for scales $l < l_l$ but are considered to be little deformed for $l > l_e$. All flow scales under l_l may deform the polymer chains, but only flow scales smaller than l_e are themselves affected by the polymer response. In the so called elastic range between l_l and l_e, the slope of the fluid's energy spectrum should be -3 (figure 3.1). However this theory assues that there exists flow scales $l_l < l < l_e$ for which polymer chains are deformed whithout the flow being affected. To complete that gap in the theory, Xi et al. (2013) recently introduced a new elastic length scale l_c defined as the scale at which the energy transfer rates from polymers to the flow and from the flow to polymer chains are equal. This last length scale defines the modifications of the flow spectrum in the inertial sub-range under the effect of elasticity.

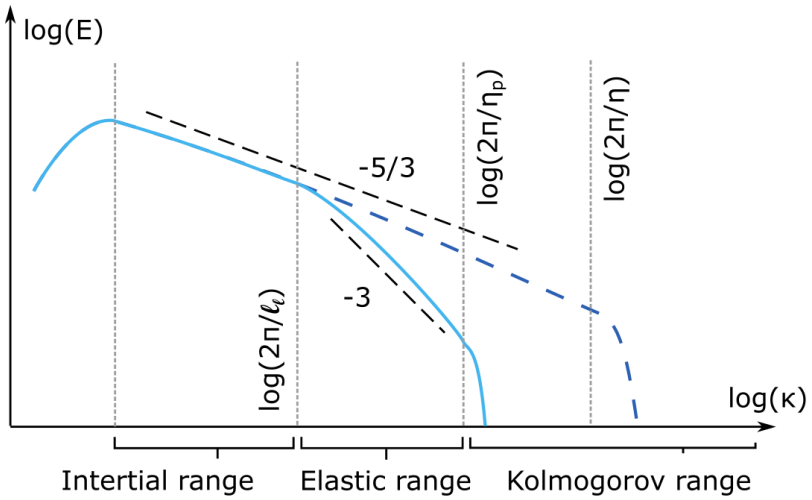

Figure 3.1 – Schematic representation of the fluid energy spectrum for viscoelastic turbulence, adapted from Vonlanthen (2010)

Numerically speaking, the effect of polymers on turbulence is generally addressed using the Navier Stokes equations coupled to a constitutive equation for the polymer. This last equation is based on the statistical properties of the conformation tensor, which is the second order correlation of the orientation vectors of each chain. Because individual polymer chains are much smaller than the achievable spatial resolution, the conformation tensor is averaged into each unit of the solved mesh.One formulation for the conformation equation compatible with shear thinning polymer is the Finite Extension Nonlinear Elastic model with a Peterlin closure (FENE-P) assuming a bounded deformation for the polymer chains (Cocconi et al., 2017; De Angelis et al., 2005; Nguyen et al., 2016).

Experimentally speaking, it is still impossible to access the state of deformation and orientation of the polymer chains with current experimental methods, but advanced optical techniques such as PIV or PTV allow for accurate measurements of the flow velocity and turbulence properties. Common setup used are *Washing machine* configurations in which turbulence is forced by baffled or unbaffled rotating disks placed all around a small volume of fluid (Crawford et al., 2008; Liberzon et al., 2005, 2006; Ouellette et al., 2009). Liberzon (2011) performed measurement in a cavity flow as a benchmark for further numerical stud-

ies. Other configurations have been considered as means to study the propagation of the turbulent/non-turbulent interface such as oscillating grid turbulence (Liberzon et al., 2009), see section 3.1.3.b) or spherical rotating grids (Cocconi et al., 2017).

It has been shown from DNS (Cocconi et al., 2017; De Angelis et al., 2005) and experiments (Liberzon, 2011; Liberzon et al., 2005, 2006; Warholic et al., 2001) that the eulerian quantities of the flow (strain, enstrophy, Reynolds stress, velocity gradients fields) are strongly reduced at small scales in viscoelastic solutions. The same conclusions can also be drawn using an experimental lagrangian approach. Crawford et al. (2008) for example performed time resolved measurement of lagrangian acceleration of tracer particles in a *wahsing-machine* turbulence and found that the rms and isotropy of particle accelerations were substantially decreased in DPS as compared to water.

Viscous dissipation is reduced as the dissipation by the polymer chain increases: polymer chains store energy at small scales and so the small scales of turbulence are damped, leading to the observed small scale suppression effect. This is consistent with the concept of a cutoff scale for polymer action, as scales larger than the cutoff value remain undamped. But the effect of polymer also propagates to larger scales. This can translate for example into an increase of integral length scales and of large scale fluctuations of velocity (De Angelis et al., 2005; Liberzon, 2011; Liberzon et al., 2006). Nguyen et al. (2016) recently studied the flow-polymer interactions in the dissipative range and showed that the polymer pumps energy at small scale when it is deformed by the flow structures, and can give back a part of this energy to the flow at larger scales thus explaining the up-scales propagation observed experimentally. For weak viscoelasticity, this behavior gives birth to a new spectral range of slope -6 between the viscoelastic and the dissipative range.

Another interesting feature observed in flows with strong means shears such as channel flows (Cai et al., 2009; Gupta et al., 2005) is an increase of turbulence anisotropy. It comes from the tendency of polymer chains to align with the main shear direction. This often leads to an increase in tangential velocity fluctuations and a decrease in the normal ones. This effect was lately observed to happen during the propagation of a turbulent/non-turbulent interface as well, where polymer chains tend to align with the turbulent front (Cocconi et al., 2017).

When forcing turbulence by energy injection at scales larger than the cutoff scale, polymers do not play a role at the turbulence production step, and non-Newtonian effect are found to appear for concentrations larger than typical drag reduction concentrations (Liberzon et al., 2006). In channels or pipes, most of the strain field to be reduced can be found near the walls, and the forcing is done at small scales (roughness of the wall), hence the polymer effects are felt at lower concentrations. For example, Cai et al. (2009) observed that viscoelasticity strongly decreased both the frequency and the intensity of burst events generated at the bottom of a channel flow by inhibiting the small scale coherent structures in the sheared sub-layer.

This last remark leads us to a less studied aspect in DPS bulk turbulence, that is the influence of polymer concentrations. Liberzon et al. (2009) compared only two different polymer concentrations in an oscillating grid device, both supposedly in the dilute regime for the polymer solution. They found significant differences but were unable to define a concentration related behavior due to the lack of data points. Ouellette et al. (2009) studied the modification of velocity structure functions measured in a *washing machine* device. Even in the dilute condition where polymer chains are supposed to be disentangled, different regimes of concentration influence were observed: at low concentrations, its value seems to have little effect on the structure function. When higher than an experimental

critical concentration however, the characteristic scale for which structure function start to differ from the water case tends to increase. In any cases, the small scale suppression effect is observed to increase with the concentration.

For high concentrations, polymer solutions depart from the dilute regime to enter the semi-dilute or even concentrated/entangled regime where interactions between molecules are no longer negligible. Depending on the polymer, the transition between dilute and entangled may comprise several intermediate steps, each of which having its own scaling law for the viscosity or relaxation time scale as a function of polymer concentration (Wyatt and Liberatore, 2009). However, increasing polymer concentration always leads to an overall increase of the solutions viscosity, even within the dilute regime, and the viscoelastic behavior of dilute polymer solutions becomes most of the time associated with shear thinning or shear thickening effects (1.3). In several experimental investigations on bulk turbulence, the amount of polymer added is assumed so small that the viscosity of the solution can be considered constant and close to that of the solvent (Cai et al., 2009; Crawford et al., 2008; Liberzon et al., 2006, 2009; Ouellette et al., 2009). In the numerical approach, the additional viscosity due to the polymer chains ν_p is considered small as compared to the solvent viscosity ν (De Angelis et al., 2005). Some experimental studies report measurements with polymer concentrations leading to high zero shear rate viscosities (Cai et al., 2009; Vonlanthen and Monkewitz, 2013), but no real investigation is made on the influence of viscosity variations on viscoelastic effects.

3.1.2.c Shear thinning effects in stirred tanks

As mentioned earlier in chapter 1, high viscosity and shear thinning properties are commonly found in bio-reactors, fermentation systems and industrial stirred tank in which the flow regimes range from laminar to highly turbulent. Many works in those fields therefore studied the effects of shear-dependent viscosity and viscoelasticity on the aspects relevant to stirred cells design: power consumption, mixing efficiency, and gas-liquid mass transfer enhancement (addressed later in chapter 4).

One of the first studies of agitation in shear thinnning fluid was made by Metzner and Otto (1957). Under laminar flow assumption and modeling the fluid rheology by a power law, they defined the apparent viscosity of the stirred fluid as the viscosity of the Newtonian fluid which would, in similar stirring conditions, consume the same mechanical power. With the objective of building correlations between non-Newtonian effects and parameters of interest such as power consumption, mixing time or mass transfer coefficients, many researchers used this apparent viscosity as an indicator of the non-Newtonian property of the fluid, with more or less success (Cabaret et al., 2008; Gabelle et al., 2011; Garcia-Ochoa and Gomez, 1998; Nishikawa et al., 1981). This approach is interesting since it allows to define classical fluid mechanics numbers based on viscous effects such as the Reynolds or the Schmidt number (see section 1.3.2). It is yet limited for two main reasons.

- By defining a single apparent viscosity for the whole tank while considering a power law fluid, one automatically assumes that either the shear rate is homogeneous in the whole tank, or it is not but the fluid acts as a Newtonian fluid of similar viscosity. Thus one can not distinguish any local effects of viscosity on turbulence, mass transfer and so on. In order to include local effects, one has to measure the local variations of shear rates, which is most of the time a difficult task.

- The concept of apparent viscosity can not capture any viscoelastic effect of the fluid. To account for viscoelasticity, one need to include the fluid characteristic time scale into the correlation. Yagi and Yoshida (1975) for example showed that the Deborah number could be used to such an extent.

Regardless of the way shear thinning and viscoelasticity effects are modeled in correlations, the following conclusions may be drawn from to all studies of viscous non-Newtonian solutions in stirred tanks. The first one is that a highly shear thinning causes "caverns" to develop around impellers(see figure 3.2). Around the blades, the shear rate is high because of the forcing of the blades, and consequently the viscosity is low, the fluid flows easily and can show turbulent features. Moving away from the impeller, viscous dissipation of motion strongly diminishes the shear rate, which leads to an increase of viscosity and an even stronger dissipation. The consequence is that the fluid far away from the blades is practically motionless (Adams and Barigou, 2007; Arratia et al., 2006; Patel et al., 2014; Xiao et al., 2014). Hence, mixing of a scalar is efficient within the cavern, but it is very hard for the scalar to diffuse out-of the cavern and so full mixing in the tank is hard to achieve. If a gas is bubbled through the liquid while stirring, this cavern effect will lead to the formation of a large gas patch around the impeller by bubble coalescence, also reducing the mass transfer (Gabelle et al., 2011; Yagi and Yoshida, 1975). Cavern effect may be avoided by shifting the impeller axis of rotation with respect to the axis of symmetry of the tank, or using multiple impellers with off centered shafts (Cabaret et al., 2008).

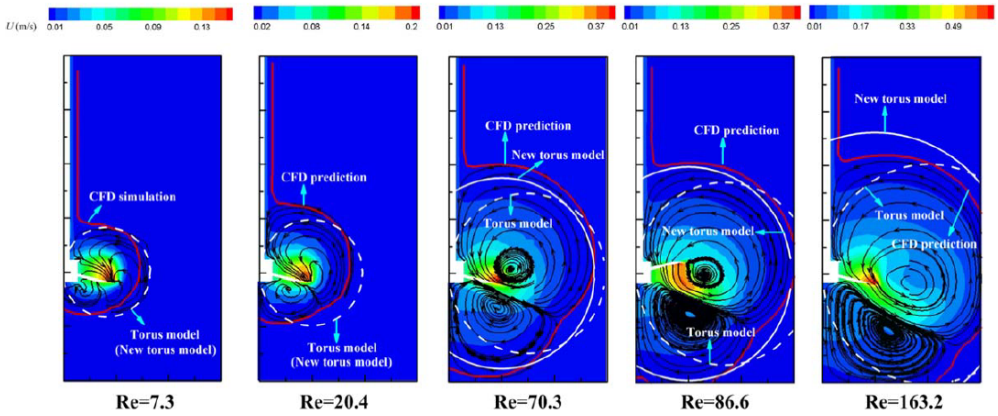

Figure 9. Streamlines and velocity contour at various *Re* obtained by CFD simulation.

Figure 3.2 – Illustration of a flow cavern in a stirred tanks obtained by CFD simulations and analytical modelling by Xiao et al. (2014)

The second effect observed, maybe more intuitive, is that the stirring of polymer solutions of given zero shear rate and infinite shear rate viscosities μ_0 and μ_∞ consumes less power than the stirring of a Newtonian fluid of viscosity $\mu = (\mu_0 + \mu_\infty)/2$. This comes from the fact that power consumption depends on the viscosity around blade which is decreased by blade motions in case of a shear thinning fluid (Metzner and Otto, 1957). Power consumption is further decreased when gas is injected into the fluid while stirring (Gabelle et al., 2011).

The last conclusions, of greater interest for the present study, is that shear thinning seems to lead to a rearrangement of mean flows, turbulence, or oscillatory motions. Increasing viscosity of the liquid while remaining in the turbulent regime only tends to decrease kinetic energy and turbulence intensity. Increasing polymer concentration and so shear thinning effect leads not only to increasing viscosity and decreasing turbulence intensity but also to a

modification of the flow structure (Sossa-Echeverria and Taghipour, 2012; Wang et al., 2014). Modifications of the flow associated to modifications of the shear thinning property (represented for example by a different slope of its power law) are not similar to modifications that would be due to a simple decrease in Reynolds number (Venneker et al., 2010; Wang et al., 2014). A difference in energy transfer between average, organized and turbulent energy is also observed (Gabelle et al., 2013, 2017). Yet, the relative influence of viscosity, shear thinning and viscoelasticity remains poorly understood since most of the time, the influence of dilute polymer is considered only through an increase in effective viscosity. Viscosity and shear thinning effects are hard to tell appart Venneker et al. (2010).

The influence of polymer on turbulence is thus addressed in different ways in the literature. Two separate branches exist, one focused on explaining drag reduction effects, mostly considering the viscoelastic property without any viscosity variations, and the other one aiming at understanding shear thinning effects on hydrodynamics and mixing in industrial configurations. We will use here information coming from both sides of the literature to better understand turbulence in shear thinning, viscoelastic DPS. Let us continue with a literature review on how the previously presented behaviors apply to grid turbulence.

3.1.3 Grid turbulence in dilute polymer solutions

3.1.3.a Fixed grid turbulence

The influence of non-Newtonian behavior on grid turbulence has been mainly studied for classical (passive) fixed grid configuration. Fabula (1966), Barnard and Sellin (1969), Greated (1969), Friehe and Schwarz (1970) and McComb et al. (1977) were the first to study the effect of drag reducing polymer (PEO, or Poly Ethylene Oxide) on the pressure drop and the turbulence decay law in a grid setup, and showed that polymer additives tend to decrease both turbulent energy and dissipation rate. Doorn et al. (1999) later used PIV to study fixed grid turbulence in dilute polymer and surfactant solutions and showed that grid turbulence for such fluids was much more anisotropic and decayed more slowly. Vonlanthen and Monkewitz (2013) used similar PIV measurements to look at turbulent spectra and Lumley scales in grid turbulence of dilute polymer solutions. They confirm that above this scale, the velocity spectra is the same as in the Newtonian case. Below, the energy spectrum slope is -3 instead of $-5/3$, which corresponds to an elastic turbulence range. In their experiments, they find that both the shape of the energy spectrum and the lumley scale evolved with time. This likely comes from the destruction of polymer chains by the strong shears in the vicinity of the grid. The lumley scale shifts towards lower wave-numbers with increasing viscoelasticity, hence it seems to decrease when the polymer is destroyed during the experiment. The temporal decrease of the Lumley scale can be predicted using a cascade model for the molecular weight of polymer chains, assuming that the breakage of each molecule statistically produces two half parts of similar masses. This still shows one of the limits of fixed grid devices for the study of turbulence in DPS: reaching high levels of turbulence requires high flow rate which causes important degradation of the polymer throughout the measurements. Another limitation is that turbulent velocity fluctuations are even smaller compared to mean flow velocities than for the water case.
Interesting developments would be to use fractal or active grids in DPS, but the complexity of turbulent production behind such grids would require a thorough design and characterization process. The choice has been made here to use an oscillating grid device, which may not be able to reach high turbulent Reynolds number either, but should at least reduce the polymer degradation by imposing lower fluid-grid relative velocities (see section 3.4.1.a).

3.1.3.b Oscillating grid turbulence

Citing Vonlanthen and Monkewitz (2013), "*The difference between the effect of polymers on turbulence without and with mean shear is that in the former case the polymers can only provoke additional local energy dissipation, while in the latter case they can in addition modify the mean shear and with it long-range energy exchange by instabilities*". The non-Newtonian properties of the fluid are in such a way supposed to affect the OGT turbulence decay law, since they act on local turbulence dissipation. The previous sentence also implies that the secondary flows inside the grid stirred tank are very likely to be different in dilute polymer solution than for the Newtonian case. An early use of OGT to stir dilute polymer solution can be found in Kostazos et al. (1994) where the mixing time between salted water and dilute polymer solution in an OGT tank is studied, but no mention of any viscoelastic or shear thinning behavior of the polymer solution are made, and the grid oscillation stroke covered the whole liquid height in the tank making any comparison to classical OGT results difficult.

The first study of OGT in viscoelastic dilute polymer solutions (PEO) was made by Liberzon et al. (2009), who observed the propagation velocity of the boundary between turbulent and non-turbulent regions in the tank, at the first instants after the onset of the grid's oscillations. They found that the turbulent/non turbulent interface moved globally faster in dilute polymer solution than in water. However, the characteristics of turbulence and mean flow in a steady state are not mentioned, and the author later admitted that results could have been contaminated by the presence of mean shear at the walls of the tank (*i.e.* by the unexpected mean flow) (Cocconi et al., 2017).

Wang et al. (2015) and Wang et al. (2016) later used a two oscillating grid device to study the viscoelastic effects of surfactants and dilute polymer on coherent structures. Using proper orthogonal decomposition (POD), they confirm that the addition of polymer tends to decrease the small scale effects of turbulence, and that this decrease can not only be attributed to the overall viscosity increase, since it is not associated with a decrease of the turbulent kinetic energy. Hence the non-Newtonian property of the flow seems to strongly modify the spectrum size of the turbulent structures. They also found that this turbulent suppression effect arises only when reaching a critical polymer concentration (unfortunately not quantified), which may not be the same in OGT than in channel flows or fixed grid experiments, and seems to be higher than the critical concentration for drag reduction effects.

To our best knowledge, no existent study mentions the possible mean flow that could have developed in the tank, and even less its probable polymer concentration dependency. The stationary turbulence vertical profiles such as turbulent kinetic energy and velocity fluctuations rms (analogs to Hopfinger and Toly's law) also remain unknown in single oscillating grid systems with dilute polymer solutions. The aim of this chapter in to describe the influence of viscoelasticity and shear dependency of the viscosity on both mean flows and turbulence production and decay in the oscillating grid stirred tank.

3.1.4 Summary

As shown in the previous paragraphs, agitation and turbulence of DPS have been studied from two perspectives: the fluid mechanics oriented view mostly dealing with viscoelastic effects on turbulence, inspired and motivated by the drag reduction phenomenon; and the bio-process engineering concerns around viscosity and shear thinning effects on stirred mixing efficiency and power consumption.

From this non exhaustive and brief review of the existing bibliography about turbulence dilute polymer solutions, the following conclusions can be drawn:

- Historically, the effects of polymer addition on liquid phase hydrodynamics were first observed through the drag reduction phenomenon. To better understand drag reduction, a comprehensive knowledge of both the polymer chain dynamics and their interactions with all scales of the flow is needed. Conceptual theories exist (Lumley, 1969; Tabor and de Gennes, 1986) and typical behaviors have been identified (Sreenivasan and White, 2000; Virk, 1975a,b), but numerical or experimental data at small scales are still needed.

- The addition of a minute concentration of polymer into a Newtonian solvent with almost no overall viscosity variation may confer to the fluid viscoelastic properties. The small scale quantities are significantly damped as the polymer absorbs energy at high wave numbers thus reducing viscous dissipation. The polymer effects propagate up to the larger scales of the flow. A cutoff wavelength is introduced in the turbulent cascade under which the viscoelastic dissipation takes place. Turbulent forcing under this scale will lead to strong differences between flows of Newtonian fluids or DPS (drag reduction effects). When forcing turbulence above this scale, higher polymer concentrations are needed for the flow to differ significantly from the Newtonian case (inertial forcing).

- In both numerical and experimental approaches, the major bottleneck is the resolution of small scales. In DNS, the convergence of computations requires the introduction of non physical artificial viscosity which could bias the results at small scale and has to be reduced as much as possible (Nguyen et al., 2016). On the experimental side, sub-Kolmogorov resolved / 3 dimensional experimental data would be needed to fully understand the effect of polymer chains on the flow (Liberzon, 2011).

- For cases where viscosity increases together with shear thinning effects, a rearrangement of mean and oscillatory flow structures and turbulence is observed.

- Even though viscoelasticity has been widely studied, the effects caused by viscosity variations of shear thinning or shear thickening fluids are still poorly known outside of stirred vessels, and have never been studied in grid turbulence experiments. This is surprising since pseudo-plasticity for example is an important property of numerous fluids in a wide range of applications (see section 1.3). This is precisely the scope of the current chapter.

Finally, PIV measurements of mean flows and turbulence production and dissipation in a grid stirred tank should of great use for the better understanding of turbulent mass transfer experiments presented in chapter 4. One indeed needs to know the characteristics of turbulence reaching the surface before studying the interfacial effects on it.

3.2 A model fluid: Xanthan gum solutions

This section introduces the polymer used for the making of dilute polymer solutions in the present work. For several reasons detailed hereinafter (pH and temperature stability, frequent use in the literature...), Xanthan gum (XG) proved to be the best candidate for the experimental investigations of both this chapter and the next one (chapter 4). A brief literature review about XG applications and properties is first proposed. Extensive characterization of the solutions produced with the available molecule is then presented.

3.2.1 About Xanthan gum (XG)

3.2.1.a Introduction

XG is a polysaccharide (B-1459, Wypych (2012)) discovered in the 1950s at the Northern Regional Research Laboratories (NRRL) of the United States Department of Agriculture. It is produced by the bacterium Xanthomonas campestris NRRL B-1459 (Garcia-Ochoa et al., 2000). A small quantity of XG dissolved in a solvent gives remarkable shear thinning and noticeable viscoelastic properties to the fluid. It is used in many industrial applications (see table 3.1):

- In the food industry (Katzbauer, 1998; Young and Torres, 1989), its pseudo plasticity and slight surface activity are useful to stabilize emulsions, dressing sauces, soups, bread doughs. It can also be used to maintain texture in sugar free or gluten free food and beverages, or protect preparations during freezing.
- In the Oil and Gas industry, its resistance to extreme pressure and temperature conditions makes it of great interest for enhanced oil drilling and recovery (Garcia-Ochoa et al., 2000; Katzbauer, 1998). Solutions of XG at concentrations above 20 ppm exhibit a type B drag reduction (Bewersdorff and Singh, 1988; Virk, 1975b) with a drag reduction percentage increasing with concentration (Sohn et al., 2001; Wyatt et al., 2011).
- The shear thinning property of XG is also used in the formulation of many cosmetic products such as toothpastes or hair and body gels. (Katzbauer, 1998)

Moreover, XG solutions are widely used in experimental fluid mechanics to investigate non-Newtonian behavior, since they remain optically clear for concentrations up to 10 000 ppm and are therefore compatible with optical measurements. It is used for example as a model fluid for the study of hydrodynamics in fermentation systems (Gabelle et al., 2011; Garcia-Ochoa and Gomez, 1998; Kawase and Hashiguchi, 1996; Pedersen et al., 1994), as a model fluid to mimic penicilin fermentation (Pedersen et al., 1993, 1994), and is an excellent blood analog when combined to glycerol (Najjari et al., 2016).

Domain	Use	Concentrations (ppm)	Reference
Food industry	Texture stabilisation	[500 – 5000]	Garcia-Ochoa et al. (2000); Katzbauer (1998); Young and Torres (1989)
Oil and gas	Fluid extraction	[500 – 2000]	Garcia-Ochoa et al. (2000); Katzbauer (1998)
Cosmetics	Creams and pastes	[2000 – 10000]	Garcia-Ochoa et al. (2000); Katzbauer (1998)
Process industry	Fermentation broth model	[100 – 2000]	Gabelle et al. (2011); Garcia-Ochoa and Gomez (1998)
Medicine	Blood analog	[200 – 400]	Najjari et al. (2016)
Fluid mechanics	Drag reduction	[20 – 2000]	Bewersdorff and Singh (1988); Escudier et al. (1999); Wyatt et al. (2011)

Table 3.1 – Some applications of XG and typical concentrations used

One of XG's most remarkable property is also its strong resistance to severe pH and temperature conditions. Once dissolved, its rheological properties have been showed to remain constant even close to the solution's boiling point (Shojaeian et al., 2016), and at pHs ranging from 3 to 13 (Whitcomb and Macosko, 1978). For pH below 4 or above 9, the chemical structure of XG is modified (change in acetylation's degree) but this has almost no impact on the solution's viscosity, which only begins to change with acidity above pH 13 or below pH 3 (Garcia-Ochoa et al., 2000). The pH of XG solution dissolved in pure water is slightly acidic (down to 5.3) for high XG concentrations (Young and Torres, 1989). The XG also resists well to the presence of biocides (pesticides, insecticides...) (Escudier et al., 2001). Temperature tends to decrease the overall viscosity of XG solutions, but this behavior is fully reversible between 10 °C and 80 °C. The pH stability is of particular interest for the study of carbon dioxide dissolution in dilute polymer solutions presented in chapter 4.

3.2.1.b Structure and conformation

The backbone carbonate chain of XG consists of 1,4-1inked -D-glucose residues, having a trisaccharide side chain attached to alternate D-glucosyl residues (Milas et al., 1996). Depending on production and gum dissolution conditions (temperature, pH, salinity ...) the polymer chains may arrange in different conformations leading to different macroscopic properties for the fluid (Garcia-Ochoa et al., 2000). The ordered conformations are generally assumed helical (single, double or even triple helix conformations have been proposed in the literature, see Garcia-Ochoa et al. (2000); Katzbauer (1998); Milas and Rinaudo (1986); Milas et al. (1996); Whitcomb and Macosko (1978); Wyatt and Liberatore (2009)). This ordered conformation may transition to a disordered one (called form III by Milas and Rinaudo (1986)) under given circumstances, or with time. The disordered conformation consist in random coil chains that are more flexible and thus lead to lower overall viscosity for the solutions (Milas and Rinaudo, 1986). The transition to form III leads to the formation of cloudy stripes suspended in the solution which is a good indicator of an aged solution.

The surface tension of aqueous XG solutions also depends on its conformation. Because of the tendency of the long carbon chain molecules to absord at interfaces, Xanthan tends to slightly decrease surface tension when its concentration is high enough (Lee et al., 2012; Young and Torres, 1989). The disordered form is found more surface active than the ordered one (Young and Torres, 1989).

3.2.1.c Rheological properties

The main effect of XG is to increase the viscosity, especially at low shear rates, giving shear thinning behavior to the solution. The enhanced overall viscosity can be mostly explained by the polymer-polymer interactions, and thus increases with increasing polymer concentration (Wyatt and Liberatore, 2009). When applying a shear stress to the solution, weak polymer-polymer interactions break, polymer chains begin to deform, and the viscosity drops.

Several concentration regimes can be distinguished in salt free solutions (Wyatt and Liberatore, 2009):

- The dilute regime, in which polymer chains are assumed to have no mechanical interactions and only weak attraction-repulsion effects on each other. According to Wyatt and Liberatore (2009) this regime exists up to 100 ppm concentrations.
- The un-entangled semi-dilute regime corresponds to the case where polymer chains are close enough to each other for the electrical interactions to be significantly in-

creased, but with still no mechanical entanglement. Further increase in concentration is logically followed by an entangled semi-dilute regime where mechanical entanglement of chain does begin to occur. The transition between the two semi-dilute regimes is around 400 ppm.

- The concentrated regime is the one where chain entanglement dominates and in which the polymer-polymer interactions are the strongest. It begins around 2000 ppm and reaches up to 10 000ppm, where the fluid like behavior of dissolved solution transitions to a gel like behavior (Talukdar et al., 1996).

Each of these regime exhibits a different scaling of zero shear rate viscosity and characteristic relaxation time scale with concentration (see later, figure 3.6). All regime's scaling can be predicted by existing models for polymers in solution (Wyatt and Liberatore, 2009). In this chapter, only the two first regimes are considered [1].

3.2.1.d Effect of salt on conformation and viscosity

The literature datas on XG rheological properties (viscosity, characteristic time scales, modulii...) show considerable discrepancy (figure 3.3).

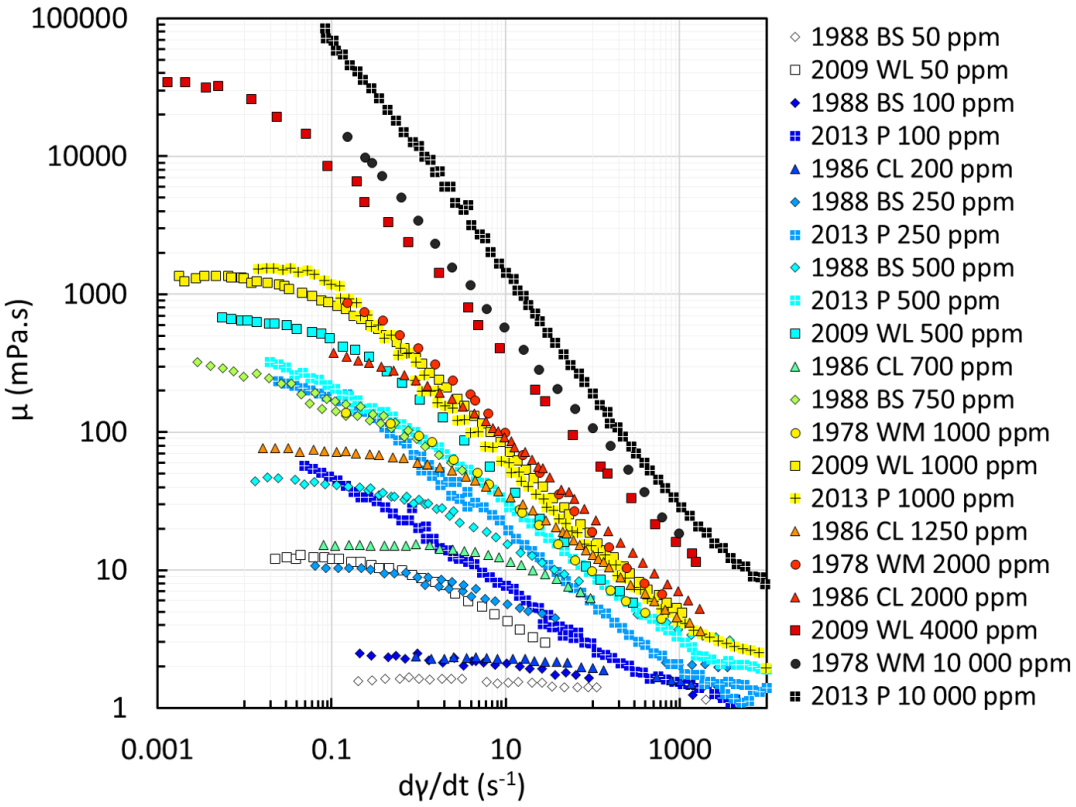

Figure 3.3 – Non-exhaustive list of XG viscosity curves found in the litterature. WM (circles) refers to Whitcomb and Macosko (1978), CL (triangles) to Cuvelier and Launay (1986), BS (diamonds) to Bewersdorff and Singh (1988), WL (squares) to Wyatt and Liberatore (2009) and P (crossed squares) to Pereira et al. (2013)

[1] In the concentrated regime, viscoelasticity appears. This is evidenced by the increasing dominance of the storage (elastic) modulus G′ over the loss (viscous) modulus G″ with increasing polymer concentrations

This can be explained by the strong dependency of the conformation on production and dissolution conditions. Indeed, it has been shown that dissolution temperatures above 40−60 °C could lead to the direct formation of disordered form III (Garcia-Ochoa et al., 2000), the exact critical temperature being fixed by the solvent salt concentration. Salt concentration is indeed another key feature to explain the observed divergences in XG visosity and viscoelasticity. The viscosity of XG solution with salt can be lower to that of salt free solutions by up to an order of magnitude for some polymer concentrations (Katzbauer, 1998; Wyatt and Liberatore, 2009). At low polymer concentration and high salt rate, XG solutions may even exhibit a Newtonian behavior (Wyatt and Liberatore, 2009).

For high concentrations however, an opposite effect has been observed by Talukdar et al. (1996): the presence of salt tends to increase both elastic and viscous modulii and the viscosity of XG gel-like solutions.

Quite surprisingly, Escudier et al. (2001) found xhantan gum rheological properties to be fairly reproducible and independent of many of the factors previously stated (water composition, dissolution temperature). However, they only worked at high polymer concentrations (0.25 percent in mass, *i.e.* 2500 ppm) well in the entangled regime, so their observation may only hold for that regime.

3.2.1.e Drag reduction properties

The molecular structure of XG makes it an efficient type B drag reducing polymer (Virk, 1975b). Drag reduction is evidenced for concentrations higher than 20 ppm and increases up to a critical concentration that varies between 200 and 2000 ppm depending on salt concentration and molecular weight of polymer chains (Bewersdorff and Singh, 1988; Sohn et al., 2001; Ungeheuer et al., 1989; Wyatt et al., 2011). The concentration required for maximum drag reduction is found to decrease with molecular weight (Sohn et al., 2001). The presence of salt may decrease drag reduction efficiency depending of the preparation conditions of sample solutions (Wyatt et al., 2011) and on their concentration (Bewersdorff and Singh, 1988).

3.2.1.f Mechanical degradation and aging

Like any long chain polymer, XG is subject to mechanical degradation when submitted to high shear stress. Several studies report a decrease in drag reduction efficiency when the polymer solution undergoes a sustained shearing (Sohn et al., 2001; Ungeheuer et al., 1989; Wyatt et al., 2011). XG however shows a much better resistance to mechanical stress than other long chain linear polymers. The effect of mechanical degradation is observed to be lower for high polymer concentrations (Ungeheuer et al., 1989). This is explained by the fact that highly concentrated solutions have an important "stock" of unbroken molecules that can store energy and keep the non-Newtonian effects significant. Molecules can also exert a mechanical shielding effect on each other, reducing the stress felt by each individual polymer chain and thus the probability of it to break. Out of mechanical degradation, XG tends to degrade to lower viscosity conformation with time. This aging effect depends on environmental conditions (humidity, temperature...). It is first evidenced by a decrease in apparent viscosity, typically occurring after one or two days. At advanced stage of degradation, cloudy stripes begin to appear and the solution becomes slightly milky. This last process takes a few days. In order to avoid aging effects, XG solutions should be prepared as close to the experiments as possible, and no solution should be kept longer than a few days.

3.2.2 Characterization of Xanthan gum solutions

3.2.2.a Fabrication of Xanthan gum solutions

The XG used in this work has been purchased from PKelco in powder form and used with no further purification. For each solution fabrication, the required mass of XG is weighted by a precision balance (0.01 g accuracy), and the volume of solvent measured using a calibrated flask. The solvent is pre-heated and pre-agitated and the powder is added progressively to the liquid in order to avoid the formation of lumps. Dissolution is carried out under moderate stirring and heating (the dissolution temperature is typically 30°C). Some polymer concentrations are not achievable with the available equipment (most of the time insufficient mass weighting precision) and can only be produced by dilution of higher concentration stock solution. When it is possible however, fabrication of XG solutions by direct dissolution of powder is preferred over stock solution dilution. Uncertainties on polymer concentration are discussed in appendix A. All solutions are in preference prepared the same days the measurement are carried out, and no solution is kept for longer than 6 days (Wyatt and Liberatore, 2009).

3.2.2.b Density of XG solutions

Since a solid mass is added to the fluid volume during dissolution, the density of final solutions should theoretically be superior to that of water alone for a given temperature. Yet, the mass of XG added is most of the time so small that it is safe to assume that the density of dilute polymer solutions (DPS) is equal to the density of water. For validation of this hypothesis, different volumes of XG solutions have been weighted by a precision balance, for XG concentrations equal to 100, 500 and 2000 ppm. No significant difference between apparent density of the three solutions is observed, and the estimated density is equivalent to that of water. It will be therefore assumed that $\rho_{XG} = \rho_{water} = \rho = 998$ g/L at 20°C in the rest of this thesis.

3.2.2.c pH of XG solutions

The pH of pure XG solutions is measured after dissolution or dilution of concentrated solutions into distilled water, using a Metler Toledo InPro 3100 UD or a Hanna pH Checker probe. Since XG is neither a salt nor a strong acid or base, and only added in minute concentration, such measurements are subject to large uncertainties. The results of two different measurement runs performed on two different sets of solutions are shown in figure 3.4. XG is slightly acidic and the pH of XG solutions is never below 6.0 for the range of concentration measured.

Experimentally, the effect of XG acidity on carbon dioxide dissolution into water is found to be negligible, in the range of concentration used (see 4.2.3).

3.2.2.d Shear thinning

Measurements of different XG solutions viscosities are performed using an Anton Paar MCR 302 rheometer operated in "flow curve" mode. A 50 mm cone-plate device with a 0.103 mm gap is used, and shear rates is increased from 0.1 to 5000 s^{-1} with a logarithmic increment. Temperature is controlled by the rheometer and kept constant at 20 °C throughout the measurements. Point for which the measured torque falls below the minimum precision torque of the rheometer are rejected.

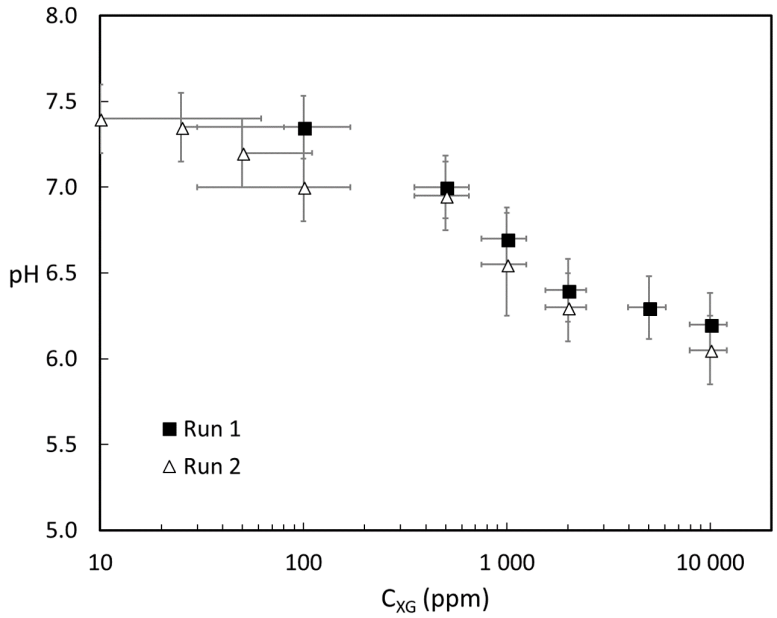

Figure 3.4 – Measured pH of XG into distilled water solutions as a function of polymer concentration. Error bars on pH are estimated from the standard deviation of n=10 measurements on the same sample. Error bars on concentration are estimated by uncertainty propagation of weighting uncertainty, as discussed in appendix A. Run 1 (full squares) and 2 (empty triangles) have been performed in the same experimental conditions, with the same polymer supply, but at different times and with different solutions.

Dynamic viscosity evolution with shear rate for salt-free XG solutions at different concentration is plotted on figure 3.5a and compared to relevant literature data in figure 3.5b. The viscosity at all shear rate logically increases with increasing XG concentration. Infinite shear rate and zero shear rate plateau are clearly visible for low XG concentrations and progressively reduce when entering the semi-dilute and concentrated regimes. All experimental curves on figure 3.5a are fitted by a Carreau-Yasuda (CY) model (see chapter 1, section 1.3.1).

As shown in figure 3.3 and 3.5b a considerable discrepancy exists in the literature data for XG viscosity. This comes from the fact that the conformation and molecular properties are strong dependent on production and dissolution conditions, which are not easily reproducible between studies, and also depends on the supplier, purification and many other parameters. However, similar trends for Newtonian maximum viscosities and relaxation times, respectivey noted μ_∞ and t_{CY}, can be extracted from litterature data (eg. Wyatt and Liberatore (2009)) and the fittings of present measurements, as shown in figure 3.6

Three of the four different concentration regimes are clearly observable in figure 3.6 a) even if the time scales are about an order of magnitude lower than those of Wyatt and Liberatore (2009). From our data, the increase in zero shear rate viscosity is globally the same but concentration regimes are less clearly evidenced due to a lack of data points (see figure 3.6). The differences observed are not surprising and should be put into the perspective of the strong impact of the polymer production and dissolution steps, conformation, and fitting uncertainties.

3.2.2.e Viscoelasticity

Oscillatory measurements of G' and G" are performed on XG samples at different concentrations using the same rheometer equipped with a plane plate mobile. A wide range of ampli-

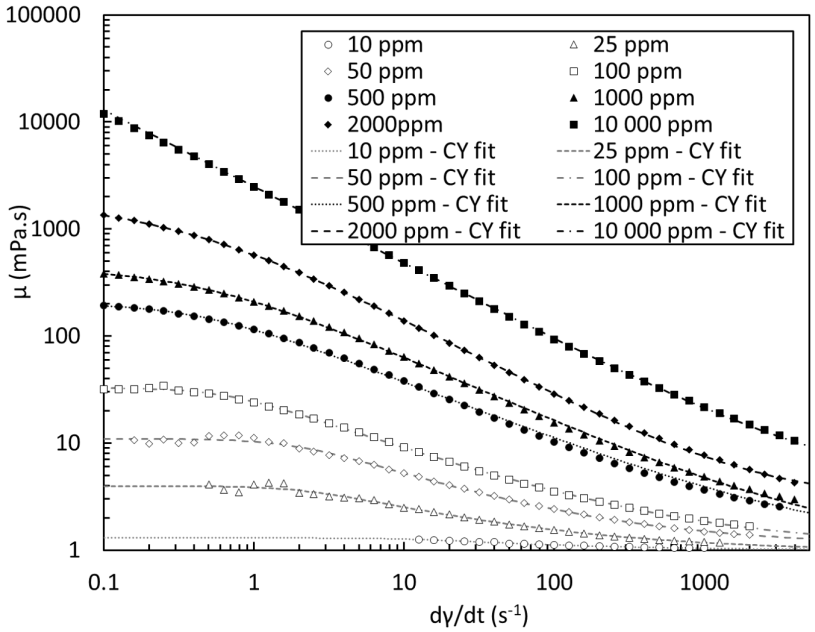

(a)

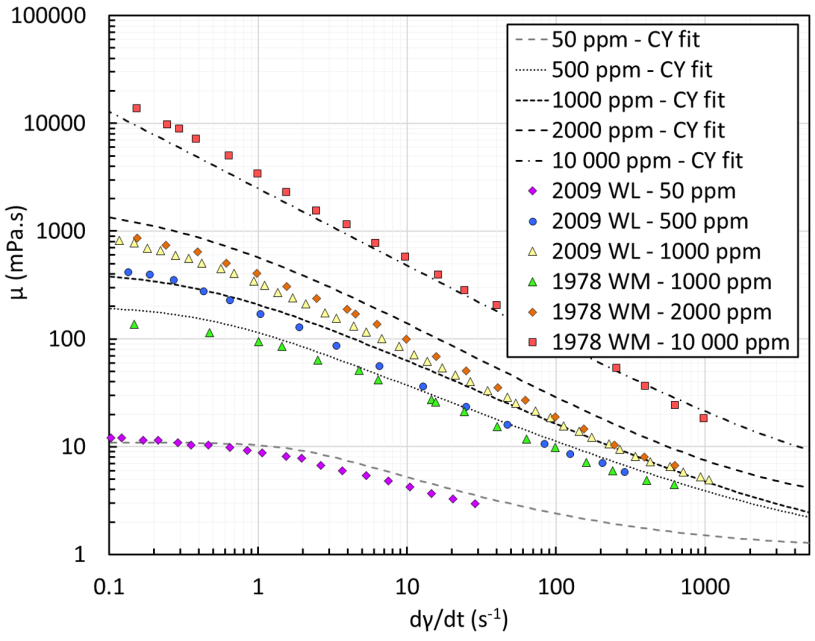

(b)

Figure 3.5 – Viscosity versus shear rate curves for XG solutions in distilled water at different concentrations. a) Present study measurements and Carreau-Yasuda fitting, b) Litterature data compared to present study fittings. WL refers to Wyatt and Liberatore (2009) and WM to Whitcomb and Macosko (1978)

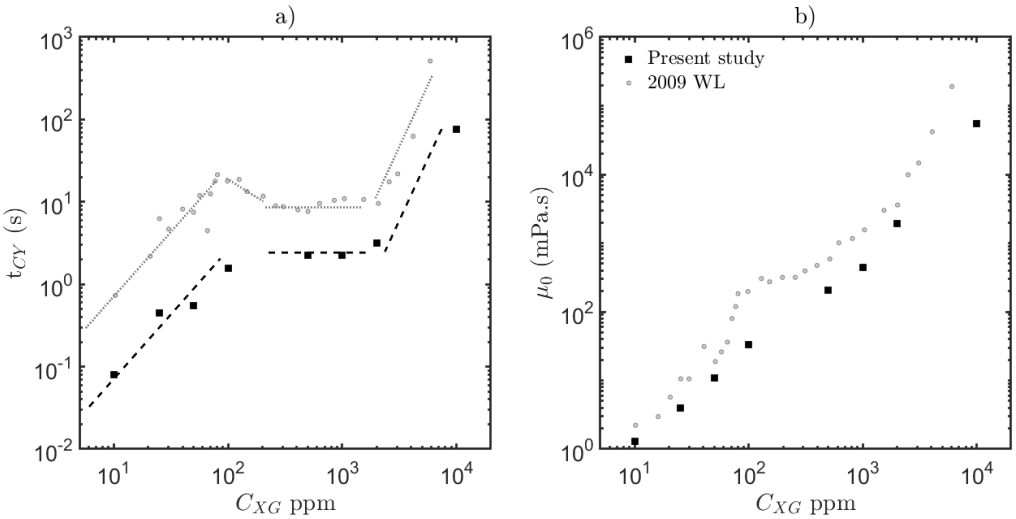

Figure 3.6 – Evolution of a) characteristic solution time scale t_{CY} and b) zero shear rate viscosity μ_0 with XG concentration in salt free solutions, compared to the trends of by Wyatt and Liberatore (2009)

tude of deformation is first covered at two different oscillations frequency to determine the linear domain of deformation. It is found that deformations of 10 % remain in the linear domain between 10^{-3} Hz and 10 Hz oscillation frequencies. Frequency sweeps are thus made at constant deformation of 10 % in the $[10^{-3} - 10^{1}]$ frequency range.

Storage modulus G′ and loss modulus G′ are plotted as a function of oscillation frequency for different XG concentrations in figure 3.7. The viscous like behavior found in the literature for low XG concentrations is confirmed here for $C_{XG} < 1000$ ppm where G′ stays under G" on the whole frequency range. 1000 ppm and 2500 ppm samples seem to present a crossover frequency around respectively 1.5 and 0.06 Hz, lower than the crossover frequencies found by Wyatt and Liberatore (2009) for similar concentrations. The 5000 ppm case exhibits the expected gel-like behavior also found by Talukdar et al. (1996). In the dilute an semi-dilute regimes considered in section 3.4, XG is mostly shear thinning and slightly viscoelastic.

3.2.2.f Surface tension

Since XG is used later in chapter 4 for mass transfer studies at gas-liquid interfaces in non-Newtonian liquids, the surface tension of XG solutions at different concentrations has also been measured with two different types of tensiometers. Surface tension σ is expected to stay close to that of water for low polymer concentration, and slightly decrease when reaching concentrated, entangled solutions (Lee et al., 2012; Young and Torres, 1989). Surface tension measurement of higly viscous, non-Newtonian polymer solutions is however delicate. The datas found in the litterature for surface tension of XG solutions show considerable discrepancy at high concentrations (see figure 3.8). An increase in surface tension can even be found with intrusive measurement techniques such as the commonly used Du Nouy ring method which is based on the measurement of the pull-out force of a ring dragged out of the fluid sample. This is surprising since polymer additives generally tend to decrease surface tension of water. Lee et al. (2012) explained it as an effect of additional resistive forces applying on the Du Nouy ring during its removal from the sample and caused by polymer aggregation around the ring. In this study, two types of metrology have been used: needle measurements (based on the measurement of the pull-out force of a needle, comparable to the DuNouy ring method) with a Kibron needle tensiometer, and a Laplace-Young profile

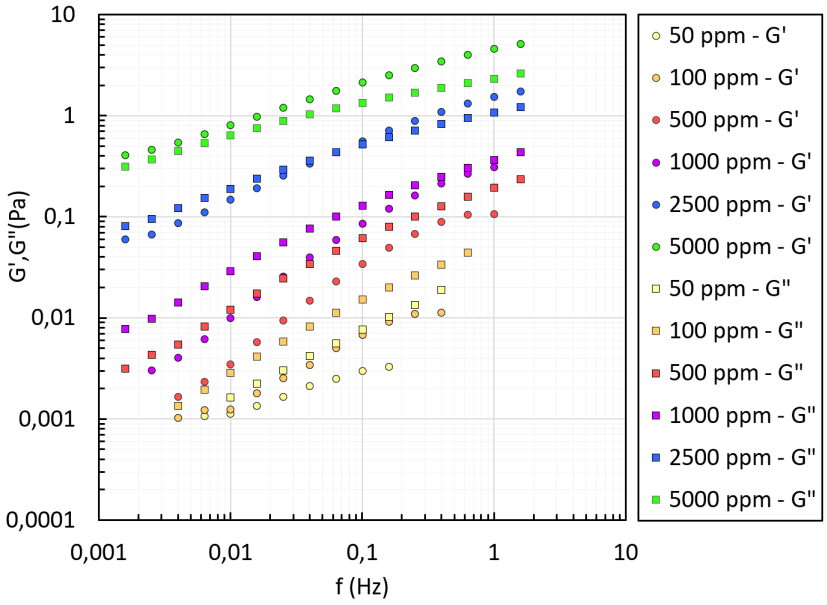

Figure 3.7 – Storage/elastic and loss/viscous moduli G′ and G" (resp. circles and squares) as a function of oscillations frequency and XG concentration

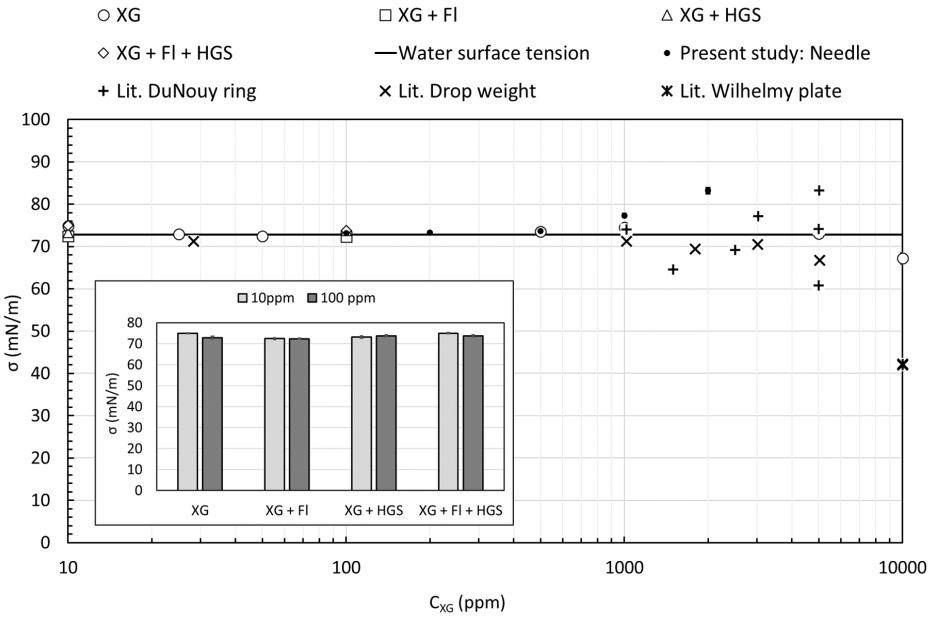

Figure 3.8 – Surface tension measurements and litterature data for XG solutions and XG solutions with additives (sub-figure). Litterature data has been collected from Lee et al. (2012) and Kawase and Hashiguchi (1996). Fl and HGS refer to fluorescein sodium (used here for PLIF) and hollow glass spheres (used here for PIV) additives at respectively 5.10^{-7} M and 0.06 g/L. Error bars of measurements are smaller than the marker size.

fitting of pendant drops shape images, with a Dataphysics OCA20 tensiometer.

The results are presented in figure 3.8 along with different measurements found in the literature. Surface tension of XG solutions at concentration lower than 1000 ppm is found to be equal to the surface tension of water. At concentrations higher than 5000 ppm, a surface active behavior is captured by the Laplace-Young measurements but not by the needle

method.

In any case, it can thus be assumed that the surface active effects of XG is negligible in the dilute and semi-dilute domains used here. Sample of XG solution with fluorescein sodium used in PLIF measurements and/or hollow glass sphere particles used in PIV measurements (see chapter 4) have also been tested, and surface tension is found to remain constant even in presence of those additives.

A relevant complementary information in terms of surface tension could be brought by the measurement of dynamic surface tension. Indeed, the surface tension measurements detailed above are static, and only give the equilibrium surface tension resulting from the final organization of polymer chains at the interface. However, the dynamics of this adsorption/organization should come with a typical timescale. This timescale could be an interesting information to compare with the shear thinning timescale t_{CY}, in order to quantify the dynamical effects of the polymer at the interface in terms of surface tension versus shear thinning properties.

Now that the main concepts of turbulence in DPS have been introduced an the properties of the XG presented, the next section will focus on the description of the oscillating grid experimental setup.

3.3 Oscillating grid apparatus

3.3.1 Tank and grid design

For this study, the grid is placed in a prismatic tank of inner dimension 277-277-550 mm. The walls and the lid of the tank are made of transparent plexiglass to allow flow visualization from various angles.

The grid has been made from a plexiglass plate shaped by water jet cutting (Oseguedа-Paredes, 2013). It has square section bars of side $d = 7$ mm and its mesh size is $M = 35$ mm so that its solidity is $\Xi = \frac{d}{M}\left((2 - \frac{d}{M}\right) = 0.36$. This is below the maximum value of $\Xi_{max} = 0.4$ recommended by Thompson and Turner (1975) for optimal homogeneity of such turbulence (see section 3.1.1.a). Two of its corners are fixed to piston rods driving its oscillations, and the other two corners are connected to vertical rail rods in order to stiffen the grid during its motion (figure 3.9 a,b).

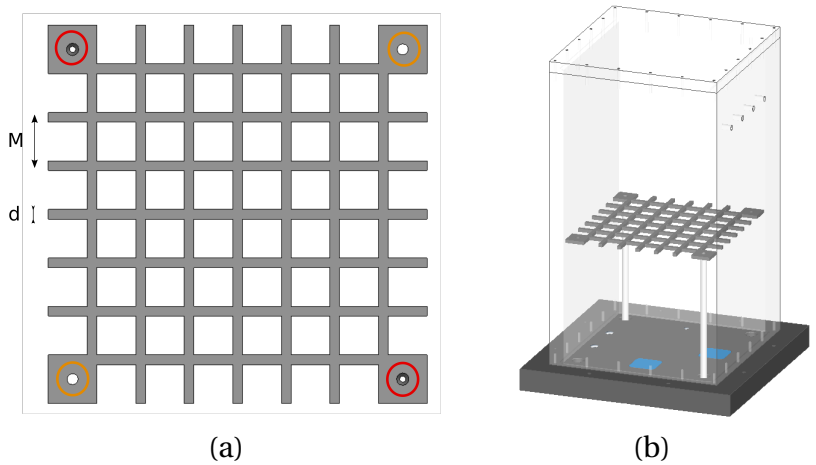

(a) (b)

Figure 3.9 – a) Grid design, in red the location of driving rods, in orange the position of stiffening rods b) Grid and tank

3.3.2 Oscillating system

In order to give a periodic translation motion to the grid, several techniques are available. Most of the time, rotary engines are used along with a crankshaft system (Asher and Pankow, 1986; Bouvard and Dumas, 1967; Chiapponi et al., 2012; Hopfinger and Toly, 1976; Mcdougall, 1979; Shy et al., 1997; Thompson and Turner, 1975; Turner, 1968; Xuequan and Hopfinger, 1986) or a cam-rod system (Dickinson and Long, 1978; Matsunaga et al., 1999). It is also possible to use a linear motor directly driving the grid (Liberzon et al., 2009). Rotary motors are often cheaper and allow for more robust setups and higher oscillation frequencies. The simplest design to turn rotation into translation is the crankshaft one, which is why it is the most commonly used in the literature. Because grid position, velocity and acceleration variations produced by such systems are not purely sinusoidal (see appendix B). The crankshaft system introduces an additional velocity frequency (figure B.3d) as compared to sinusoidal motion that can be achieved with cam-rod systems or linear motors. This may lead to an over-representation of some frequencies in the produced turbulence spectrum. Yet, no mention of such an effect has ever been made in the literature, and classical behaviors of OGT are found equally with crankshafts or cam-rod systems. For this study, a cam-rod system was initially designed, but had to be quickly replaced by a crankshaft system because it lead to systems jamming due to its high hyperstaticity. The two systems were confirmed to produce similar mean flows and turbulence properties in the tank. The description of the crankshaft system and its behavior is found in appendix B

This oscillating grid apparatus has been deigned, built and tested during the master thesis of Cosson (2014); Morge (2015); Osegueda-Paredes (2013) and improved as a part of the present work. It is used to study OGT in non-Newtonian DPS (in the following section), and mass transfer at the free surface (in chapter 4).

3.4 Experimental study of oscillating grid turbulence in Newtonian and non-Newtonian fluids

3.4.1 Experimental setup

3.4.1.a Experimental conditions

The OGT system presented in section 3.3 is used to study the characteristics of oscillating grid turbulence in Newtonian and non-Newtonian fluid. Oscillations parameters and grid Reynolds number Re_g are kept constant throughout all measurements. Unless stated otherwise, the distance between the grid average position and the bottom of the tank is $\mathrm{H_G} = 5.5\mathrm{M}$ (with M the mesh parameter), the grid oscillation frequency is $f = 1$ Hz and the stroke is $\mathrm{S} = 4.5$ cm. This gives $\mathrm{Re}_g = 2010$ for water at 20 °C. The tank is filled with fluid up to $\mathrm{H}_{tot} = \mathrm{H_G} + \mathrm{H_S} = 46$ cm which corresponds to a total volume of fluid of about 35.5 L and a grid-surface average distance of $\mathrm{H_S} \simeq 7\mathrm{M}$.

Polymer degradation: As mentioned in section 3.1.3, oscillating grid apparatus produce turbulence with a low grid-fluid relative velocity compared to fixed grid devices. With the oscillation parameters used here, the relative velocity is $\mathrm{U_{GF}} \simeq 4.5$ cm.s^{-1} and the Taylor scale Reynolds number $\mathrm{Re}_\lambda \simeq 30$. As a comparison, $\mathrm{U_{GF}} \simeq 120$ cm.s^{-1} for $\mathrm{Re}_\lambda \simeq 100$ in Vonlanthen and Monkewitz (2013). For our setup, the relative velocity would have been $\mathrm{U_{GD}} \simeq 45$ cm.s^{-1} for the oscillating grid device at $\mathrm{Re}_\lambda \simeq 100$, obtained by increasing oscillation frequency up to $f = 5.5$ Hz and stroke up to $\mathrm{S} = 7.5$ cm. The intensity of turbulence is lower in our case

because of the limitation in frequency and stroke, but the probability of polymer breakup is also reduced.

In order to check that the polymer chains are not destroyed during experiments, a test run is performed. The tank is filled with a 100 ppm XG solution, the viscosity curve of which is measured just before the beginning of grid oscillations. Grid oscillations are started with the same parameters as above. Samples of polymer solution are regularly removed from the tank. The sampling point is located about 2 cm under the free surface and in the middle of the tank (X = 0). Viscosity curve of each sample is measured directly after sampling. As shown in figure 3.10a, no significant differences are observed between initial viscosity curves and viscosity curves after 2 hours of grid oscillations. Viscosity does not seem to depend on time, no matter the shear rate at which it is measured (figure 3.10b). A modulus measurement is also performed on both the reference and the last sample taken, and the viscoelastic properties seem unaffected by grid oscillations (3.10c). It is thus confirmed that polymer chains are not degraded by our grid shearing.

Fluid velocity measurements: Several vertical planes for PIV measurements are defined in the tank according to figure 3.11 c. The letter B in a plane's name indicates that the plane is horizontally aligned with a grid bar. The letter C indicates that it falls between two grid bars and thus corresponds to velocity measurements over a series of "cavities" or grid "holes". The index indicates the position with respect to the central plane (grid bar 0), positive index being the closest to the PIV camera. The origin of the frame of reference is placed at the center of the grid when it lays at its average altitude. Z = 0 in the middle of the oscillations amplitude, Y = 0 in plane B0 and X = 0 on the central bar.

The experimental work is divided into two sub-studies sketched in figure 3.11 a and b :

- **Grid closeup** (CG) experiments are meant to visualize the mechanisms contributing to turbulence generation by the grid, especially the interaction of jets, wakes, and structures produced by its motion. They are performed in planes B0 and C1 only, for both water and polymer solution at C_{XG} = 100 ppm, and at the highest recording frequency available. Data is then treated performing a triple decomposition of the velocity fields (see section 3.4.1.band 3.4.2). The region of interest is the grid oscillations area plus about 4 cm above and under, and is called CG (Close Grid). It can be separated into two sub-regions: the grid Sweep Zone (SZ) for which $-S < Z < S$, and the Grid Neighborhood (GN=CG-SZ).

- **Full Tank** (FT) experiments aim at characterizing mean flow and turbulence distribution and dissipation in the region above the grid up to the gas-liquid interface. The full tank behavior is measured for water and XG solution at C_{XG} = 100 ppm in planes $B-2$ to B2. The influence of the XG concentration is studied in planes B0 and C1 for the concentration range $C_{XG} \in [10, 500]$ ppm.

Measurements used in the paragraphs 3.4.3, 3.4.4, and 3.4.5 are performed in the full tank (FT) region for mean flow and turbulence propagation studies, and in the close grid (CG) region for turbulence generation investigations. Results presented in this thesis are for the B0 plane only. Additional data is available for plane C1 at 100 ppm in the CG region, in plane C1 at all concentrations in the FT region, and in planes B1,B-1,C-1,C2,C-2,B2,B-2 at 100 ppm in the FT region. Unfortunately data treatment is a very long process which could not be achieved for all measurement cases in the available time of this PhD.

Before going any further, it is worth noting that in plane B0, as in other B-type planes, the grid's cross section is full, that is to say that when the grid moves in plane B0, the fluid has to

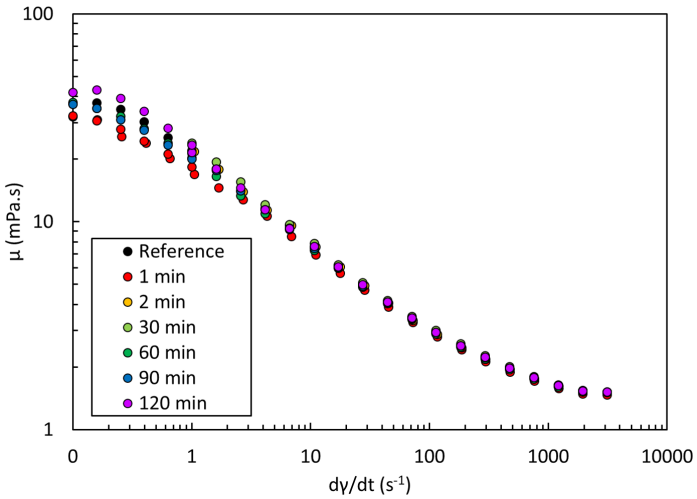

(a)

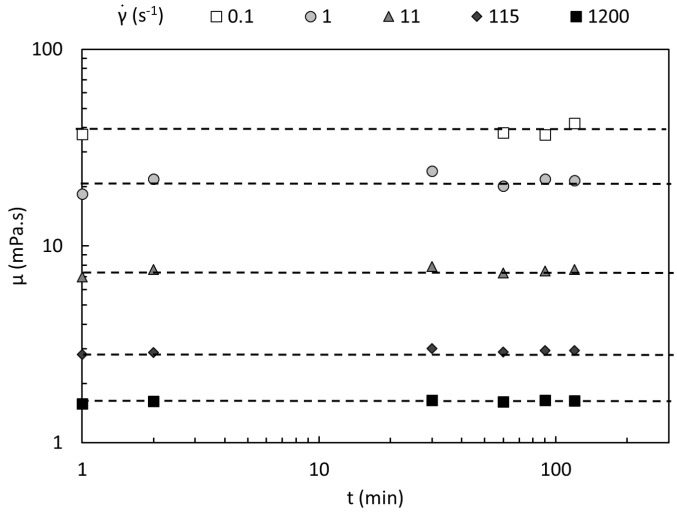

(b)

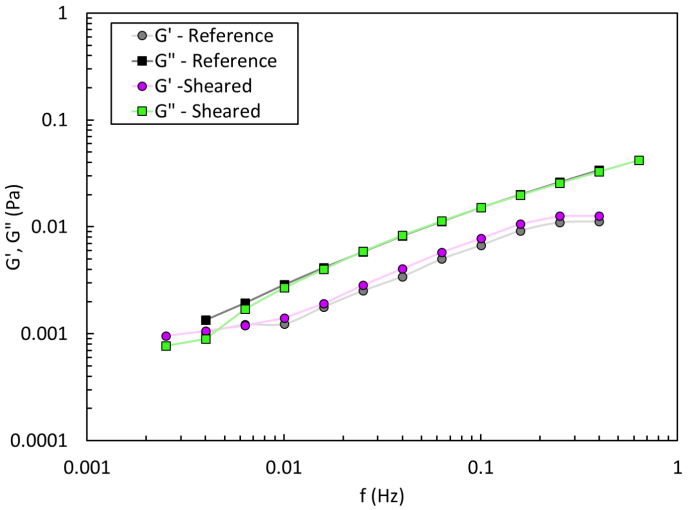

(c)

Figure 3.10 – Evidence of polymer stability to the grid's oscillations for 100 ppm XG concentration, f = 1 Hz and S = 0.0491 m. a) Flow curves of the polymer solution at different times after the beginning of grid oscillations. b) Non-evolution of viscosity at different shear rates with time. c) Storage and loss moduli before and after grid oscillations (here f in horizontal axis is the rheometer oscillation frequency)

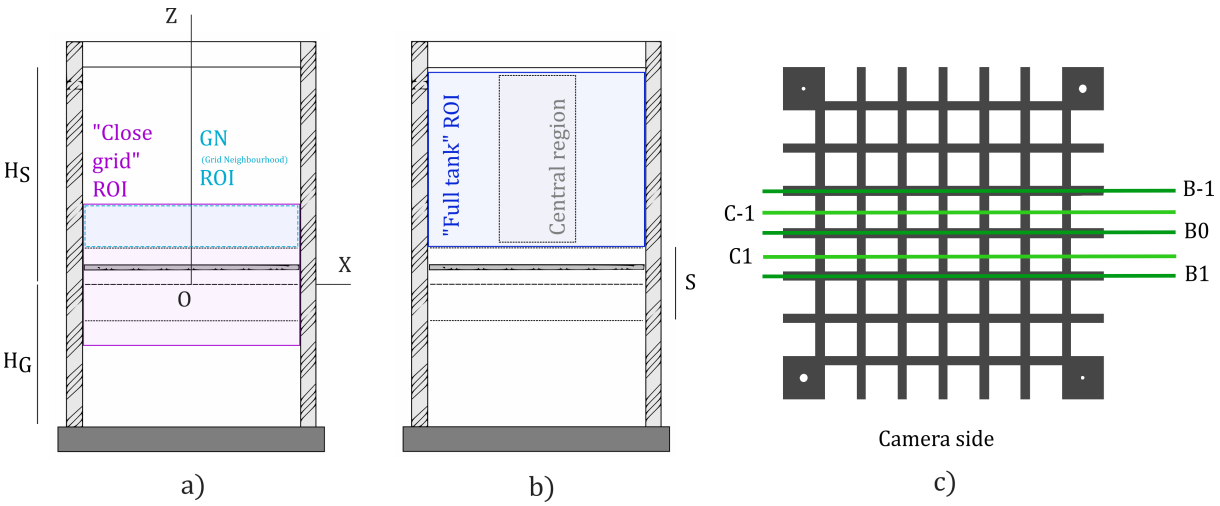

Figure 3.11 – Regions of interest (ROI) and of calculation for a) close grid and b) full tank experiments, and labeling of the planes of measurement c)

come outside of this plane to go around the grid. This is not the case in C-type planes (C1, C-1 ...) where the grid cross section is an array of bars that the fluid can avoid while staying in the plane of measurement. The physics of the flow is thus bounded to be different in these two sets of planes. Anyway in both cases, the knowledge of the third velocity component would be needed to efficiently describe the flow around the grid. The results shown hereinafter for this plane yet provide many clues about the differences between OGT in water and DPS.

3.4.1.b PIV measurements

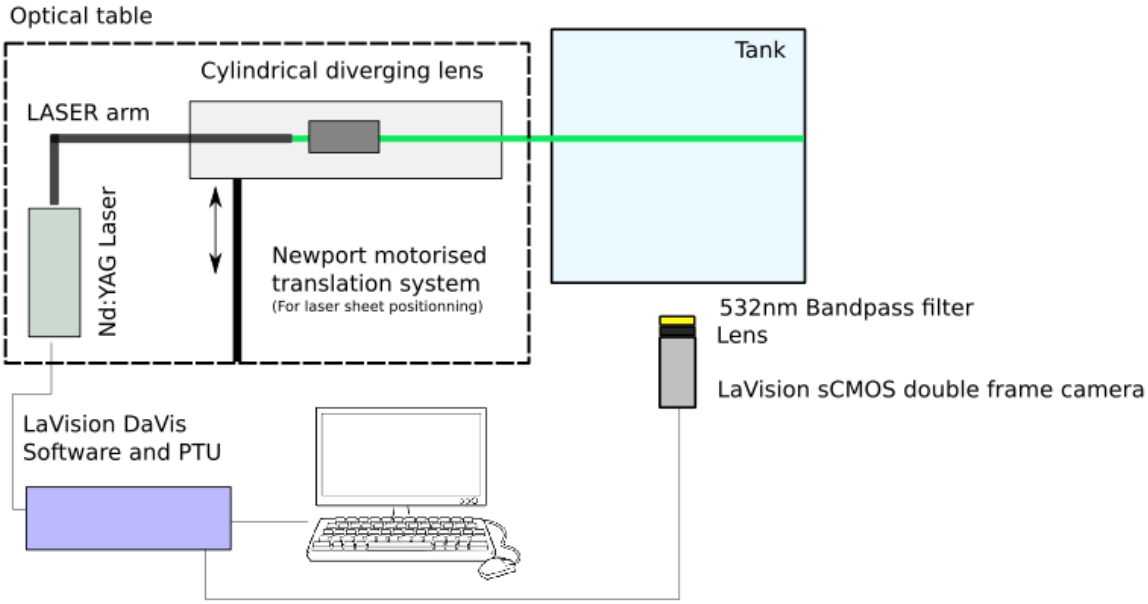

Figure 3.12 – Experimental setup for PIV study of oscillating grid turbulence

A classical PIV setup (2D2C) is used to measure velocity fields in the tank (figure 3.12). The flow is seeded with 50 µm diameter polyamide particles at a 0.03 g.L^{-1} concentration.

In order to check that these particles are appropriate for flow seeding, the Stokes number defined in chapter 2 equation (2.2) is computed for every used fluid using the product = fS as the velocity scale and the Stroke S as length scale of the flow. St never reaches order of magnitudes higher than 10^{-4} for water or DPS at any concentration (and so any viscosity), ensuring that PIV particles do follow the flow. A laser sheet at 532 nm wavelength is generated using a Quantel pulsed Nd:YAG laser. The sheet can be moved through the tank thanks to a Newport translation system in order to select the plane of measurement. Particle images are recorded on a Lavision SCmos camera in front of which is placed a 50 mm focal length lens. Acquisition and laser pulses are timed by a Lavision Programmable Timming Unit (PTU) associated with DaVis 8 software. Image scaling and distortion correction is achieved using an image of a test pattern positioned in the laser plane.

The grid is masked out from images before processing as explained in section 3.4.2. PIV acquisition and processing parameters for grid closeup and full tank studies are indicated in table 3.2.

Spurious vectors are removed from PIV fields by applying a threshold of 1.2 on the peak ratio, and replaced using median filtering. It is checked that the proportion of replaced vector is always less than 10% of the total vector number.

3.4.2 Data treatment

3.4.2.a Grid masking and tracking

For close grid experiments, the oscillating grid is visible on the recorded images, which is an asset for grid tracking but problematic for the velocity field calculation. The grid has therefore to be first removed from images for velocity calculation and then isolated for the grid tracking step. Grid masking is achieved using DaVis software from LaVision. At first, an horizontal median filter is applied on every recorded image. These images are then binarized using an arbitrary threshold based on the image gray values such that the pixel corresponding to the grid are set to zero and the rest of the image to one. Thus, each mask image is then applied to the corresponding image when calculating the velocity field (figure 3.13). One effect that can not be easily corrected with this procedure is the shaded area visible on the left part of figure 3.13 a) under the grid. Here the PIV laser sheet was directed so that it always met the grid from the top, and the shaded region was always under the grid. In doing so, the region above the grid is always well lighted, and measurements can always be considered re-

Study	Grid closeup	Full tank, $C_{XG} < 250$ ppm	Full tank, $C_{XG} \geq 250$ ppm
PIV type	Double frame	Double frame	Single frame
Δt (ms)	4	18	100
f_{acq} (Hz)	10	4	10
Interrogation window size (px-px)	48-48, 24-24	64-64, 32-32	64-64, 32-32
Camera-plane distance (cm)	30-40	80-100	80-100
f-number	16	16	16
Spatial resolution (mm)	3.4	2.3	2.3

Table 3.2 – Parameters for PIV study of oscillating grid turbulence. Spatial resolution denotes the distance between two PIV computed vectors (same along X and Z).

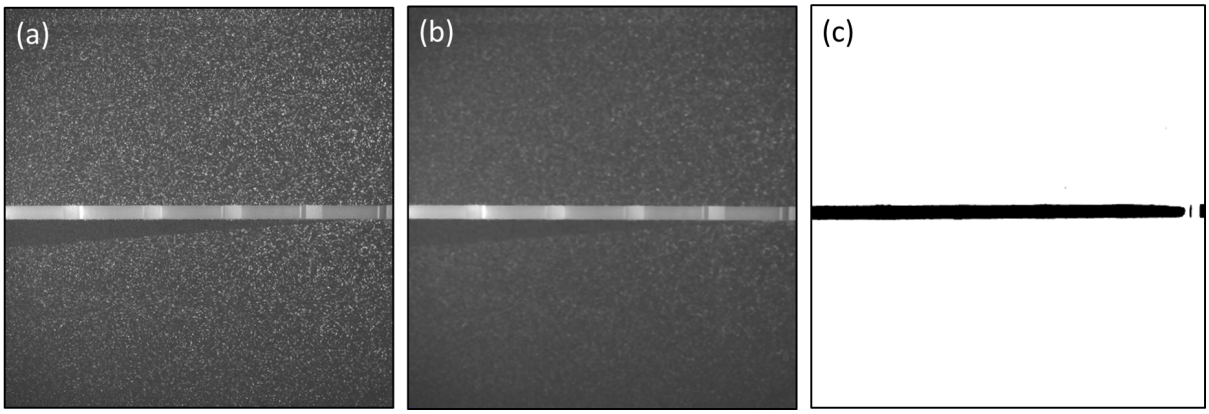

Figure 3.13 – Grid masking procedure. (a) Recorded image showing both the grid and PIV particles, (b) particles smoothed out by applying an horizontal median filter, (c) Mask obtained using an arbitrary intensity threshold

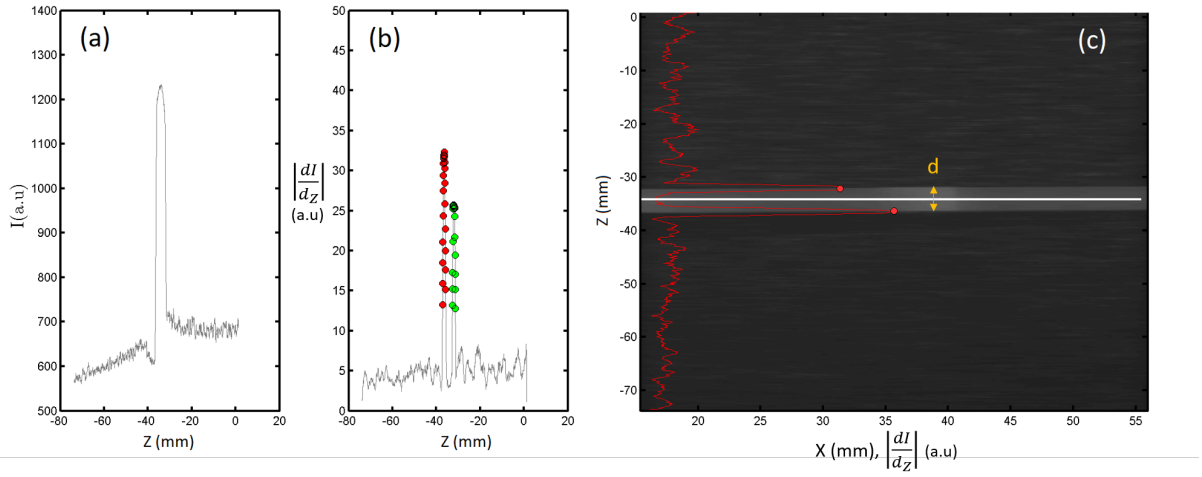

Figure 3.14 – Grid tracking procedure. (a) Horizontally averaged intensity profiles and (b) intensity gradient. Gradient values above a given threshold (green and red dots) are used to detect the grid's edges and position (c). The vertical axis is denoted Y on this figure only.

liable there. The shaded particles region is represented by a gray zone on each PIV-deduced fields to recall that this region is prone to errors.

Grid tracking is performed by a Matlab custom script. It also start by an horizontal median filtering step to smooth particles off the image. Gray level intensity is then horizontally averaged on the whole image width, and the peaks of width averaged intensity gradients are used to detect grid boundaries on the image (figure 3.14). Finally, the grid position is defined at equal distance from the two peaks. Once the grid tracking step is made, every couple of frames and its corresponding vector field can be associated to a grid position. The grid direction (going up or going down) for this instantaneous fields can be found using the grid position difference between frame 1 and 2.

3.4.2.b Conditional averaging and triple decomposition

As mentionned in chapter 1, a triple decomposition of the velocity field into mean, oscillatory, and turbulent components is a usefull tool to study the dynamics of flows which exhibit a periodic pulsation or sustained by a periodic forcing. Escudié and Liné (2003) detailed a method to extract mean, oscillatory and turbulent component of the flow from sta-

tistical analysis of non time resolved 2D-PIV measurements synchronized on blade motion. The main idea was to perform different sets of PIV measurements corresponding each to a different but known position of the blade (or here the grid), the synchronization between blade/grid position and measurement being enforced by an outside detection system. Here the method used to achieve phase resolved measurements is not based on an external trigger but rather on image processing of a collection of randomly sampled instantaneous fields. The main principle of statistical estimation of the triple decomposition component still stays the same, and is detailed in what follows.

Sampling of the grid stroke: A conditional averaging of velocity fields is performed based on the grid position previously detected. To that end, the total measured stroke is sampled into N_p parts of constant size ΔS such that $S = N_p \times \Delta S$. Based on its measured grid position, each instantaneous field is then associated to the slice it lies into, and is thus affected to a closest matching sample grid position. Phase averaging is performed by averaging all the velocity fields stored at a given sampling grid position (*i.e.* in a given slice). Ultimately, the typical period of oscillation is described using $2 \times N_p$ point in time (N_p for the grid going up, same for the grid going down). N_p is chosen as the best compromise between high period sampling and convergence of each position's mean velocity field. Indeed if N_p is too large, each slice may not include enough instantaneous field to achieve statistical convergence (see the next paragraph). On the other hand if N_p is too low, one may not be able to describe accurately oscillatory velocity fields around the grid. The results presented hereinafter are for $N_p = 12$. This allow every slice to always store at least 250 instantaneous data fields, which has proven to be sufficient for mean velocity fields calculation.

Flow statistics: Knowing the phase averaged velocity fields, it is then possible to perform a triple decomposition of the velocity field as proposed by Hussain and Reynolds (1970) and explained in section 1.2.1.h. It is worth noting that triple decomposition has never been applied to the study of oscillating grid turbulence despite its obvious oscillatory behavior.

Here for a velocity component i, the mean velocity field is taken as the ensemble average of all velocity fields:

$$\overline{U}_i = \frac{1}{N} \sum_{p=1}^{N} U_i^p \tag{3.6}$$

Where N is the total number of instantaneous fields. Phase averaged velocity for a given grid position k is defined as

$$\langle U_i \rangle_\phi^k = \frac{1}{N_k} \sum_{p=1}^{N_k} U_i^p \tag{3.7}$$

With N_k the number of instantaneous fields U^p at grid position k ($U^{p=k}$).

The oscillatory component at this same grid position is the phase averaged velocity from which the mean component is removed:

$$u_i^{*k} = \frac{1}{N_k} \sum_{p=1}^{N_k} U_i^p - \overline{U}_i \tag{3.8}$$

The turbulent fluctuation accounting for the grid position k is thus :

$$u_i^{'k} = U_i - \overline{U}_i - u_i^{*k} \tag{3.9}$$

The phase rms velocity can then be defined as the root mean square of turbulent fluctuations at position k:

$$\langle u_i' \rangle^k_{\phi,rms} = \sqrt{\frac{1}{N_k} \sum_{p=1}^{N_k} \left(u_i'^p \right)^2} \tag{3.10}$$

It can be used to estimate the intensity of turbulence at position k. Finally, the non phase-averaged rms of oscillatory and turbulent velocity fluctuations are defined respectively as

$$\langle u_i^* \rangle_{rms} = \sqrt{\frac{1}{N_p} \sum_{p=1}^{N_p} \left(u_i^{*p} \right)^2} \tag{3.11}$$

and

$$\langle u_i' \rangle_{rms} = \sqrt{\frac{1}{N} \sum_{p=1}^{N} \left(u_i'^p \right)^2} \tag{3.12}$$

Statistical convergence and data weight/size: For all quantities, it has to be checked that statistical convergence is reached. The number of independent instantaneous fields used for average or rms computation on the whole set of data (N) or at the k position (N_k) should be large enough for the computed quantity to be independent of it. This is verified by computing the sliding statistics using larger and larger N until the chosen indicator for statistical convergence reaches a constant value [2]. For non time resolved PIV measurements of turbulent flows, it is commonly said that a few hundreds of independent fields are sufficient to reach convergence of averaged quantities, and about 1000 is required for second order statistical quantities (rms for example). This criterion is yet arbitrary, so statistical convergence has been rigorously checked for our measurements. Our phase resolved measurement by design provide uncorrelated fields for phase rms computation, since two fields recorded at the same grid position are separated by a minimum amount of time of 1 s corresponding to at least one grid period. In order to perform phase averaged statistical analysis, a minimum of a few hundreds of images is needed for each grid sample position. The typical number of images recorded here to fulfill this requirement is thus around 10 000, with a number of images per grid position N_k laying between 300 and 500. Here N_k is a consequence of the true grid frequency, the acquisition frequency of the PIV system, the lag between these two frequencies and the accuracy of the grid detection procedure. The amount of data collected for a single measurement and the size of the set of files recorded is huge, around 250 Go per trial. It is the reason why phase averaged measurements have only been performed for a single XG concentration and water, in the CG region and for planes B0 and C1 only. Full tank measurements are not phase resolved and their files are smaller, around 20 Go per run.

Statistical convergence is checked for both FT and CG region, and at all grid sample positions in the CG region. To that end, the average and rms values are plotted as a function of the sample size N or N_k for all velocity components (along X and Z), at several random locations in the ROI or averaged over the whole ROI. An example of a convergence graph is shown in figure 3.15. Globally, all indicators are found to converge in all ROIs and planes. Only the statistical convergence of RMS values at extreme grid positions is sometimes not well established.

[2] A more rigorous approach could be lead via an ensemble probability estimation method (Simoëns, 1992), in which the amount of independent fild needed to achieve statistical convergence is pre-determined by the analysis of the expected shape of concentration fluctuations PDF.

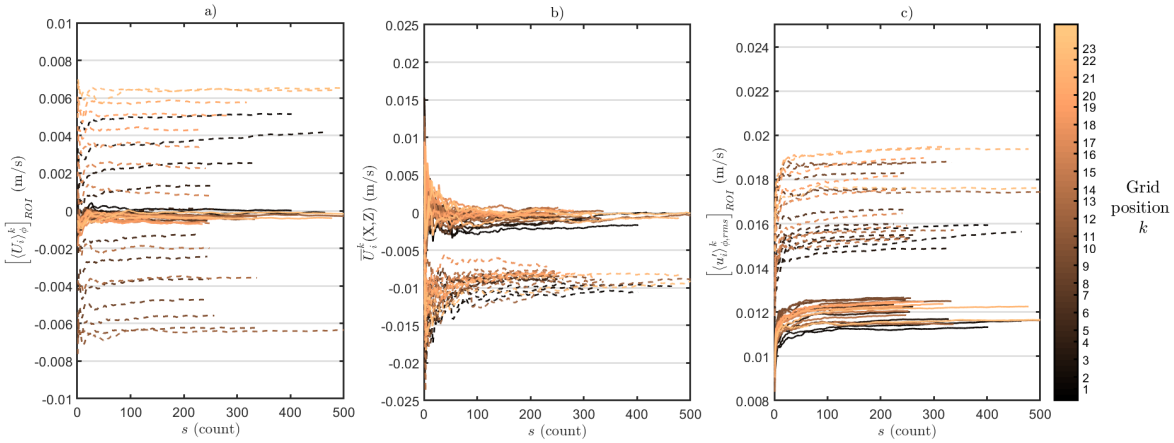

Figure 3.15 – Graph of convergence of statistical quantities. s is the size of sample used for statistical analysis. a) Convergence of the phase average velocity value averaged over the whole ROI. b) Statistical convergence of the same quantity at a given probing location (X,Z) of the ROI (here X=0, Z=50 mm). c) Convergence of the phase rms averaged over the ROI. Full lines are for horizontal velocity components and dashed lines for vertical velocity components.

The experimental procedure has now been detailed from the polymer and the oscillating grid device used to PIV measurements and data treatment. The next three paragraphs display results on mean flow, turbulence production and oscillatory motion close to the grid, and turbulence properties in the tank. A complementary POD analysis performed on some of the measurements is presented in appendix C.

3.4.3 Mean flows

The existence of mean flows and recirculations is a key aspect of oscillating grid turbulence. It is most of the time an unwanted feature of the flow since OGT was initially meant to study turbulence alone in absence of mean flow (Hopfinger and Toly, 1976), but can unfortunately not be avoided. They are supposedly due to the grid tendency to drift out of alignment, allowing mean flow patterns to persist once developed (Variano and Cowen, 2008; Variano et al., 2004). By analogy with non-Newtonian flows in impeller stirred tanks, we anticipate that dilute polymer may have a strong influence on the main structures of mean flows. It is thus necessary to start this study with an investigation of the effect of dilute polymer on persistent motion in the tank. The first observation is that in the central vetical cross section of the tank, the mean flow is structured in two main recirculation vortices close to the grid and near the walls. Figures 3.16 and 3.17 respectively show the average velocity field and associated streamlines. In figure 3.18 is represented the vorticity of the average velocity field $\overline{\Omega} = \nabla \wedge \overline{\mathbf{U}}$. The recirculation patterns observed in figure 3.17 are evidenced by two opposite sign high magnitude vorticity patches on both sides of the tank, just above the grid sweep zone. Isovalue lines of vorticity are drawn at the arbitrary threshold $\overline{\Omega} = \pm 0.02\overline{\Omega}_m$ whith $\overline{\Omega}_m$ the maximum vorticity value at a given concentration defined in the following parapgraph. They represent estimation of the boundaries of the mean flow vortices. These flow patterns have also been observed by McKenna and McGillis (2004a) for water.

By observation of figure 3.16, 3.17 and 3.18, the effect of polymer addition on the mean flow seems to be the following. When adding polymer to water, the flow structures itself into two main regions dominated by the two counter rotative side vortices illustrated by the streamlines or the vorticity isovalues. Increasing polymer concentration causes the mean flow vortices to grow in size until they reach the top of the fluid volume, at a concentration

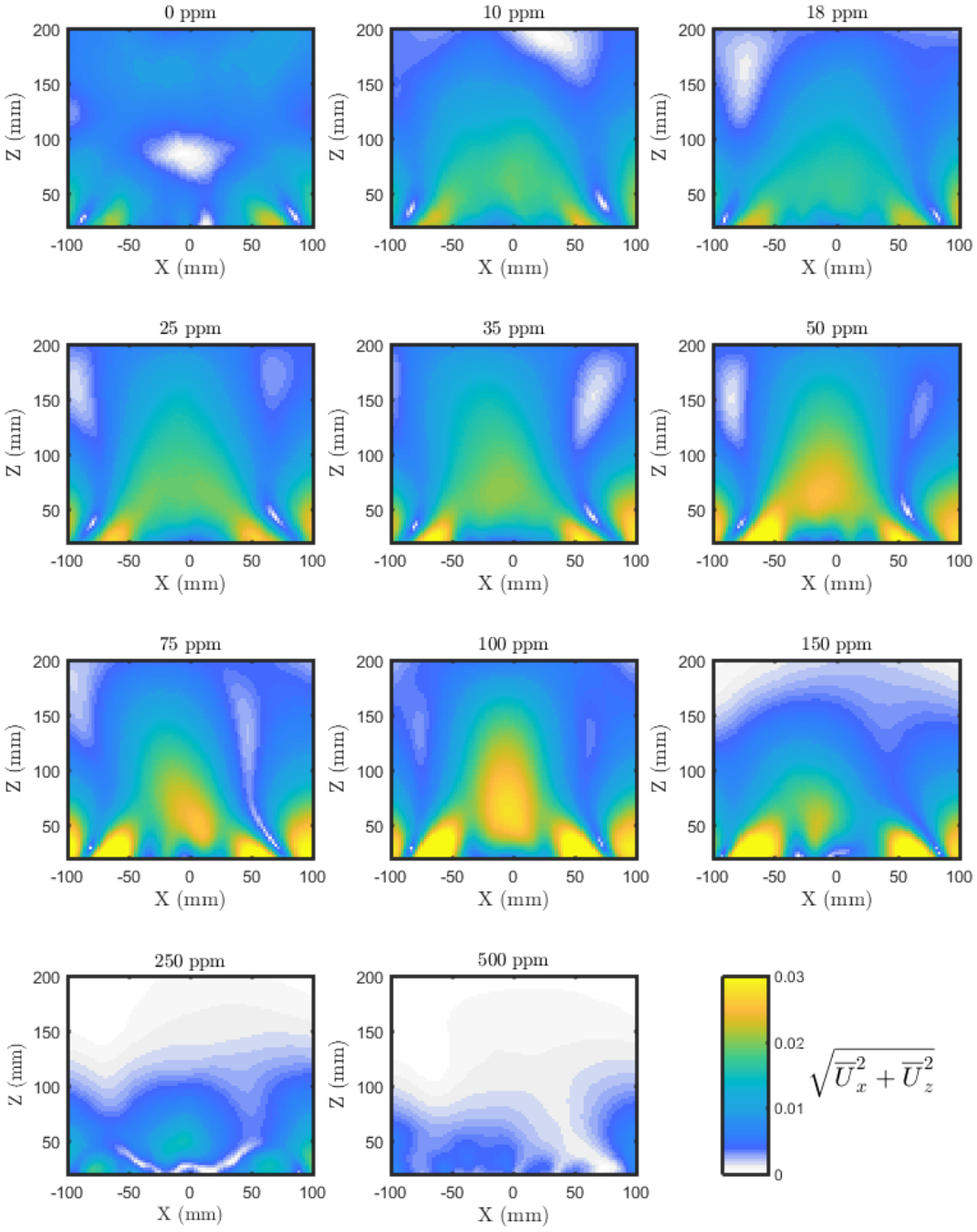

Figure 3.16 – Mean flow inside the grid stirred tank at different XG concentrations: 2D norm of the mean velocity field $\sqrt{\overline{U}_x^2 + \overline{U}_z^2}$ in m/s.

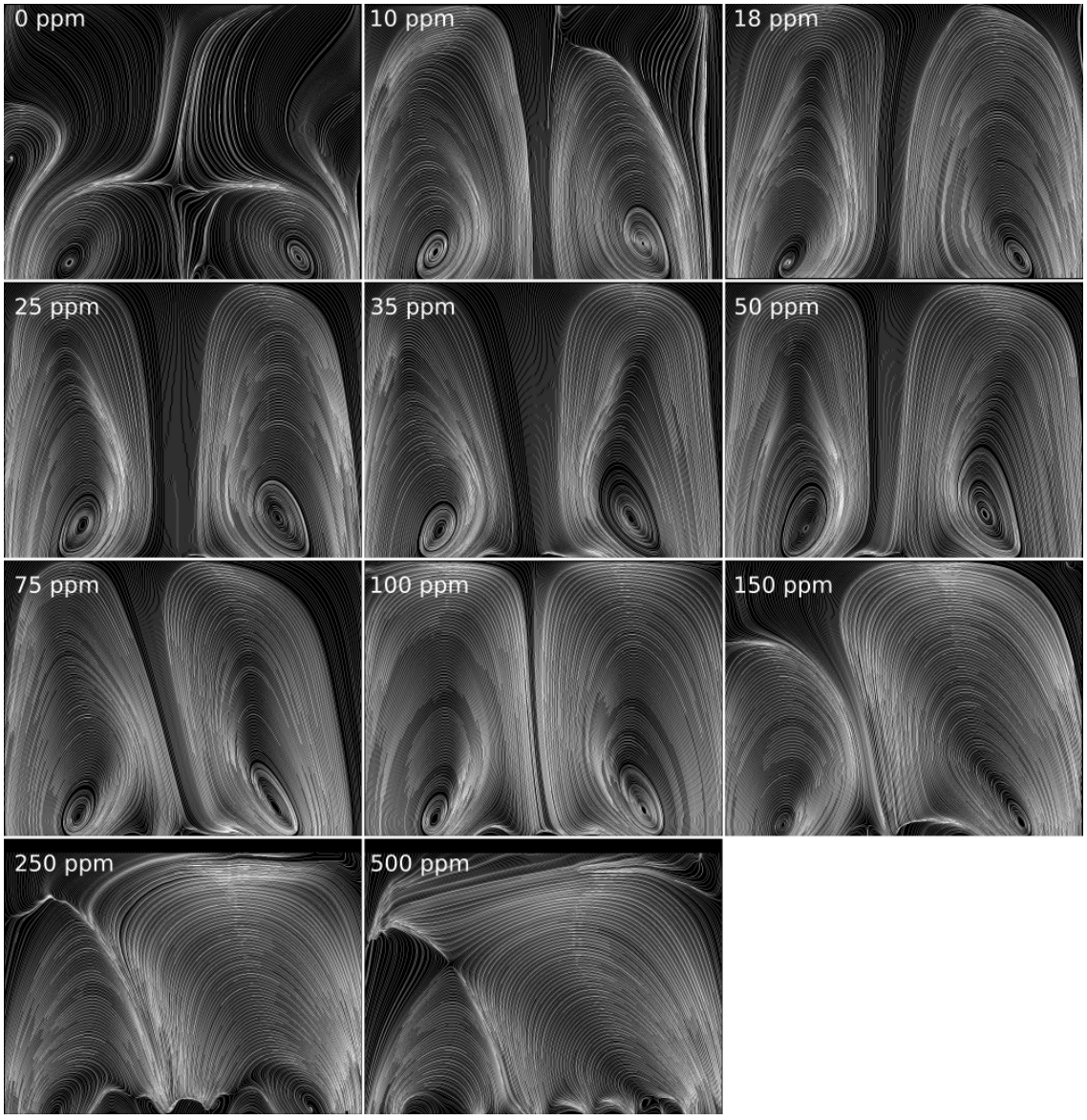

Figure 3.17 – Streamlines of the mean flow inside the grid stirred tank at different XG concentrations. The region of measurement and scales are the same than figure 3.16.

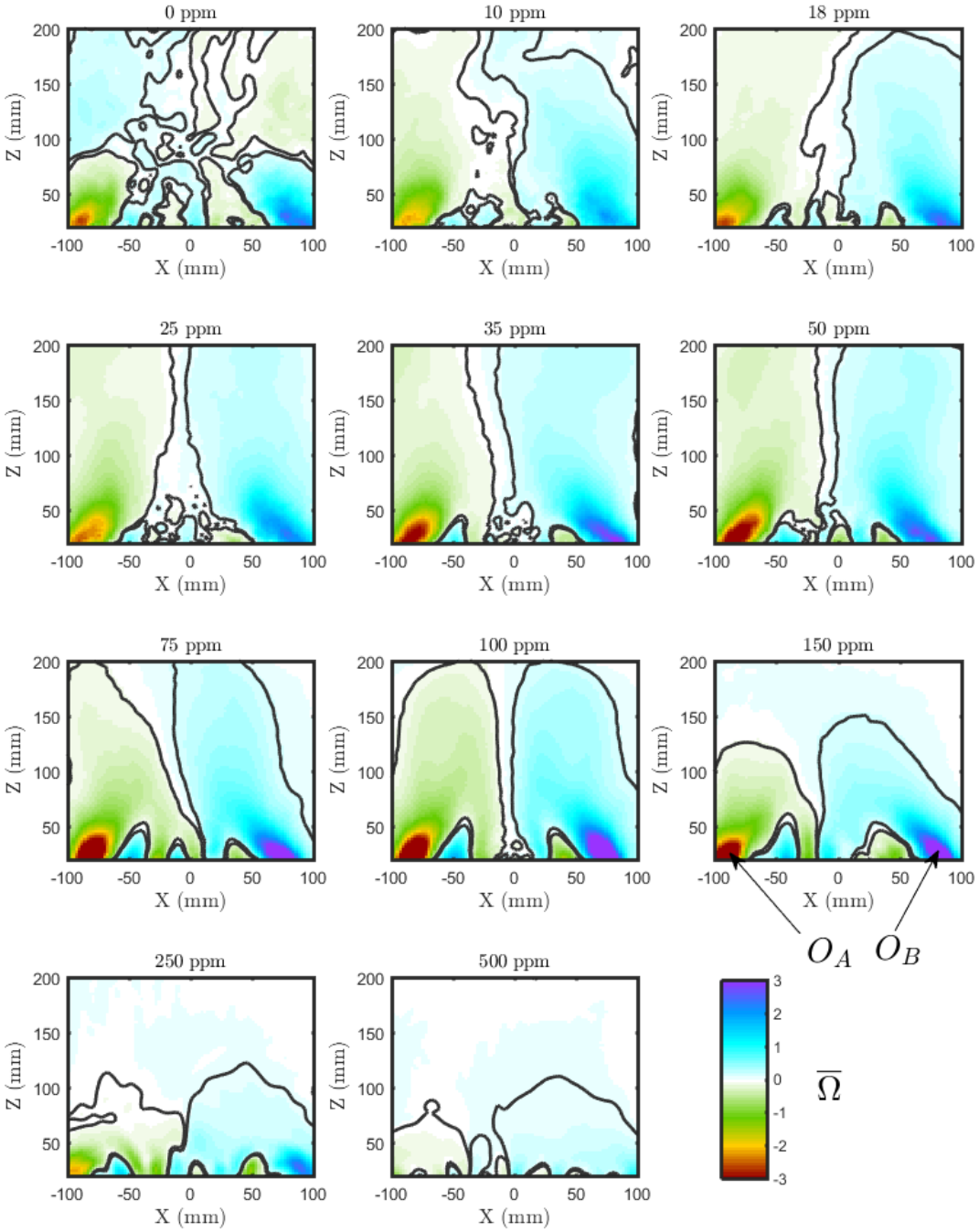

Figure 3.18 – Mean flow inside the grid stirred tank at different XG concentrations: vorticity of the mean velocity field $\overline{\Omega} = \nabla \wedge \overline{\mathbf{U}}$ in (1/s). The black lines are isovalues of vorticity at $\overline{\Omega} = \pm 0.02\overline{\Omega}_m$, with $\overline{\Omega}_m$ the maximum vorticity value at a given concentration defined in the following paragraph.

between 10 and 25 ppm. The flow is then divided into two main regions separated by a global up-going region at the center of the plane for concentrations between 25 and 100 ppm, as seen on figures 3.16 and 3.17. A further increase in concentration leads to the collapse of these recirculating regions: their size reduces (figure 3.18), and the central up-flowing region progressively disappears.

The addition of polymer to the water therefore has two successive effects: first an organization of the flow by the intensification and expansion of the two pre-existing side recirculations, and second a collapse of the mean flow region. In what follows, the mean flow enhancement that appears at small concentrations will be studied with more details, since this thesis is focuses of the dynamics and mass transfer inside of polymer solutions in the dilute regime. Hypothesis will also be made on the probable reasons for the higher concentration behavior.

Simple indicators can be defined in order to measure the intensity and region of influence of the mean flow, and quantify the mean flow enhancement.

- The first criterion is the value of the curl of the average velocity field at the center of the side vortices. This is a measurement of the maximum vorticity in the mean flow, and thus of the intensity of the side eddies. Here it is defined as $\overline{\Omega}_m = \max(\overline{\Omega}(O_A), \overline{\Omega}(O_B)$ where O_A is the central point of the left vortex and O_B the central point of the right vortex (see figure 3.18).

- The second indicator is the peak-to-peak amplitude of the vertical velocity profile along X $\overline{U}_z(X, Z = Z_p)$ at a given probing altitude Z_p. It is also a measurement of the intensity of the mean flow, but this time associated to the up-going motion. Here we take Z_p = 2M = 70mm, but a similar trend than the one presented hereinafter is observed for different Z_p.

- The last indicator defined here is the position along Z of the maximum vertical velocity on the X = 0 line (regardless of the value of this intensity). This is an estimation of the area of influence of the mean flow rather than of its intensity and comes as a complement of the two other indicators.

The evolution of the peak vorticity magnitude with concentration (indicator 1) is shown in figure 3.19 and table 3.3. It increases with polymer concentration in the [0-150] ppm range and brutally decreases for the last two points. The critical concentration above which vortex intensity stops increasing, here 150 ppm, can be related to the transition concentration between the dilute and semi-dilute regime evidenced by Wyatt and Liberatore (2009). In this study, it is also around 100 ppm as shown in figure 3.6 a). The evolution of mean vortex intensity thus seems to depend on the concentration regime of the polymer solution: in the dilute regime, increasing polymer concentration and consequently the solution typical response time leads to an increase in maximum vorticity. When reaching the semi-dilute regime, further increase in concentration on the contrary reduces vorticity associated to mean re circulations. These observation are consistent with the streamline patterns observed in figure

C_{XG} (ppm)	10	18	25	35	50	75	100
De≡t_{CY}	0.08	0.28	0.45	0.49	0.55	1.06	1.60
$\overline{\Omega}$ (1/s)	2.01	2.69	2.42	3.20	3.10	4.70	5.02

Table 3.3 – Evolution of maximum vorticity associated to mean flow structures as a function of polymer concentration in the dilute range

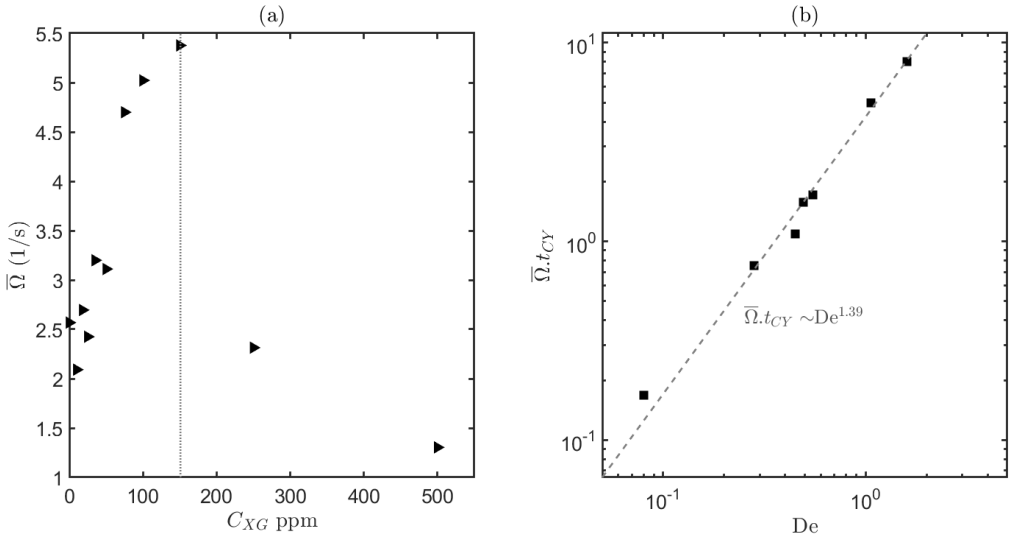

Figure 3.19 – Evolution of maximum vorticity associated to mean flow structures as a function of polymer concentration (a) and Deborah number (b). (a) is the maximum vorticity $\overline{\Omega}$ averaged between the two counter-rotatives vortex plotted for all concentrations, (b) is the no-dimensional quantity $\overline{\Omega}.t_{CY}$ in the dilute regime range ($C_{XG} < 100$ ppm).

3.17: well defined structures build up upon polymer addition and grow in the dilute regime, and begin to collapse above 100 or 150 ppm.

In the dilute regime, the characteristic time scale has been shown to depend on concentration with the scaling $t_{CY} \sim C_{XG}^{1.1}$ (see figure 3.6 a)). Since here $T = 1/f = 1$ s, scaling based on t_{CY} or De are equivalent. The dimensionless quantity $\overline{\Omega}.t_{CY}$ is represented as a function of De (figure 3.19). It follows a power law such that $\overline{\Omega}.t_{CY} \sim \mathrm{De}^{1.39}$. Since here $t_{CY} \equiv \mathrm{De}$, it implies that $\overline{\Omega} \sim \mathrm{De}^{0.39}$. The intensity of mean recirculations increases with the solution time scale, but this increasing rate is reduced as the Deborah number increases (index below 1). Mean flow enhancement by polymer addition thus seems to be a low-concentration effects that loses efficiency in semi-dilute regime. This may be explained by the fact that as the relaxation time increases with polymer concentration, viscosity also does. In the dilute regime, the zero shear rate viscosity scales as $C_{XG}^{1.4}$, hence it increases more rapidly than the relaxation time scale. In the semi-dilute regime, it keeps increasing with the same trend [3], but t_{CY} stays constant. In that sense, it may be assumed that viscosity and time scale increase have two different and maybe opposite effects on mean flows: the increase of the solution's time scale seems to enhance re-circulations, whereas increasing viscosity tends to dissipate the flow structures and ultimately make them collapse. In order to verify this hypothesis, additional experiments need to be performed on Newtonian fluids with high viscosity. If the previous hypothesis is valid, increasing the viscosity without non-Newtonian properties (*i.e.* keeping the fluid response time equal to zero) should not lead to mean flow enhancement.

A similar trend is observed when looking at the second criterion, that is to say the evolution of peak-to peak amplitude of the horizontal profile of $\overline{U}_z(0,2M)$ with polymer concentration. Figure 3.20 (a) shows that polymer addition tends to promote an up-going effect: the black dotted curve for water does not have its maximum value close to X = 0 mm, but it is the case for every DPS at any concentrations. This peak effect is increased with polymer concentration until it reaches its maximum for $C_{XG} = 100$ ppm. When plotting the evolution of the curves' peak-to-peak amplitude $A_{\overline{U}_z}$ as a function of the concentration, a trend sim-

[3] Note that Wyatt and Liberatore (2009) observed a change of slope for the semi-dilute regime that is not observed here, with a new slope slightly lower that the dilute regime one but still greater than 1.

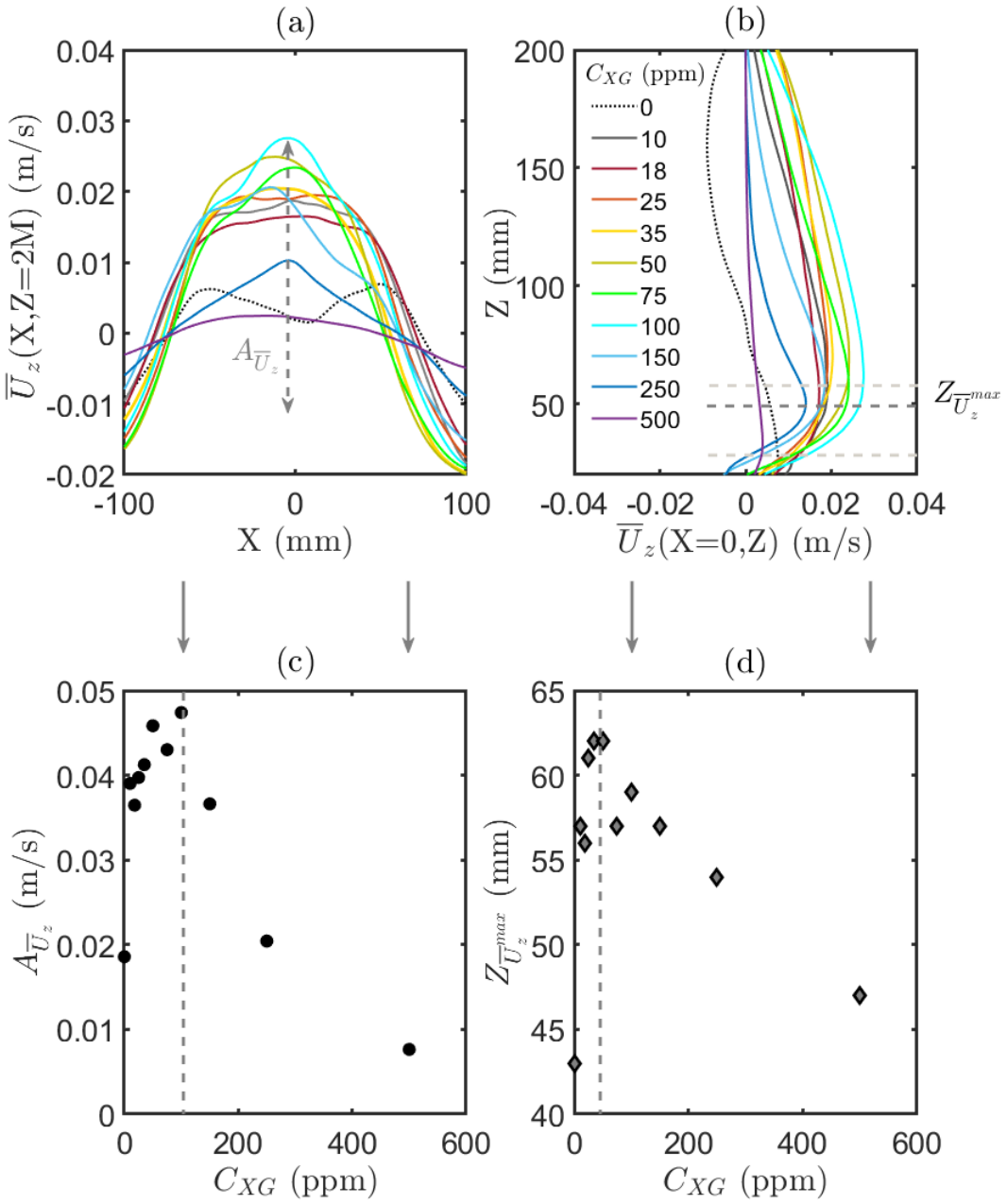

Figure 3.20 – Effect of polymer concentration on vertical velocity. (a) Horizontal profiles of the vertical velocity at Z = 2M = 70mm, (b) Vertical profiles of the vertical velocity at X = 0 mm, (c) Peak-to-peak amplitude of the profiles of (a), (d) location along Z of the maximas of profiles (b).

ilar to the one observed for vortex intensity is observed (see figure 3.20 c), that is to say an increase in the dilute regime and a collapse in the semi-dilute regime. This confirms that the intensity of the up-going central motion and that of the side vortices are strongly coupled, and that they are both related to the polymer concentration regime.

The third indicator is illustrated by figures 3.20 (b) and (d). The vertical profiles of vertical velocity at X = 0 mm plotted in figure 3.20 (a) all present a maximum value at small Z (close to the grid). However the Z location of this maximum varies with polymer concentration. This can also be observed on the average velocity fields in figure 3.16, and is a consequence of the flow organization into two side vortices. The impact region of both vortex meet in the plane of symetry (X = 0 mm). Since the vortex are ellipsoidal and that their main axis is neither vertical nor horizontal, the maximum vertical velocity is found at a given altitude which depends on the inclination of the vortices and their topology. This third criterion thus evaluates the vortex pair's spatial influence more than their intensity. The altitude at which maximal vertical velocity is found $Z_{\overline{U}_z^{max}}$ is plotted versus concentration in figure 3.20 (d). It shows an increasing trend in the early part of the dilute regime. However unlike the vortex or up-going intensities, it begins to decrease at a lower typical concentration, around 35 or 50 ppm.

The effects of polymer addition and polymer concentration on mean flows inside the tank can thus be summarized as follows:

- Polymer addition has an organizing effect on the mean flow. Existing vortices are enhanced by addition of even a small concentration of polymer, and the flow structures itself into two distinct vorticity regions ruled by the pair of counter rotative eddies. A global up-going motion appears at the center of the tank.
- Increasing polymer concentration while staying in the dilute regime tends to increase the vortex and up-going motion intensity. Both indicators for vortex and up-going motion intensity increase until concentration reaches the critical concentration for which solution switches from dilute to semi-dilute regimes. In the concentration range corresponding to the dilute regime, the maximum vorticity of the mean flow scales as a power law of the Deborah number.
- The region of influence of the mean flow is observed to increase at the onset of polymer addition, but the maximum effect of the up-going motion is attained at a concentration lower than the dilute to semi-dilute transition. This suggests that the dilute regime is itself composed of two sub-regimes: a very dilute one in which both vortex intensity and size increase, and a transition to semi-dilute one in which the vortex intensity keeps increasing but its region of influence reduces.
- In the semi-dilute domain, vortex intensity an size both decrease. The hypothesis is that in this regime, viscosity keeps increasing upon polymer addition while elasticity of the polymer chains is limited because of emerging polymer-polymer interactions. This however still needs to be confirmed.

It is now established that the mean flow in dilute polymer solutions stirred by an oscillating grid is different, more organized than the one in water. In the next section, the effects of polymer addition on turbulence generation by the grid is studied.

3.4.4 Turbulence generation

To that extent, close grid (CG) PIV measurements are used, and the data is analyzed using phase averaged quantities. Only the case of water and DPS at 100 ppm are considered. This

last concentration is chosen so that the solution is still in the dilute regime for entanglement, with the strongest possible concentration effects within that regime. An example of instantaneous velocity field for both fluids is pictured in figure 3.21 for a bottom grid position.

In both cases, the wake of the grid is evidenced by a series of counter rotating vortices behind each grid bars. DPS visually exhibits stronger but larger vortices than water. Using the grid detection procedure presented in section 3.4.2.a, each instantaneous field is associated to a specific grid position. The mean velocity field is computed by averaging all instantaneous velocity fields, and phase averaged velocity fields by averaging all instantaneous velocity fields at the same grid position, as explained in section 3.4.2.b. The oscillatory component is deduced by removing the mean velocity field from phase averaged velocity field at each grid position, and fluctuating velocity fields are derived by substraction of mean and oscillatory fields to each instantaneous field.

Figure 3.22 gathers, for the two studied fluids, their mean velocity field, a phase averaged and oscillatory velocity field at a given grid position (bottom position), and the fluctuating velocity field corresponding to instantaneous fields that are shown in figure 3.21. The background color represents the vorticity of each velocity field, respectively $\overline{\Omega}$, $\langle\Omega\rangle_\phi$, Ω^* and Ω' for the average, phase averaged, oscillatory and fluctuating vorticity.

The average velocity field is consistent with the one observed previously, and show two side vortex above the grid sweep zone. It is as expected stronger in DPS than in water, and the central up-going motion is found again. Phase average velocity field exhibit more clearly the grid bar wakes, together with the side vortices. The oscillatory component mostly displays the wakes, since it is the result of the substraction between phase averaged measurement and mean flow. A new interesting difference between water and DPS appears when comparing the oscillatory components at the low grid position: DPS fields exhibit two symmetric pairs of vorticity patches at the edges of the ROI above the grid sweep zone, which are not visible for water. Finally, the fluctuating velocity fields allow to see the turbulent structures produced behind the grid. Eddies are created close to the grid and interact so that turbulence diffuses towards the bulk.

These experiments are to the author's knowledge the first observations of turbulence generation focused at the grid, and of the so called "interactions between jets and wakes" that are said to create turbulence (Thompson and Turner, 1975). There are many reasons to believe that the presence of dilute polymer in the fluid will modify the characteristics of turbulence generation. Since the effect of polymer is known to be felt at small scales (Nguyen et al., 2016), but also obviously impacts the large scales of the mean flow in the tank, it is of interest to carry on a comparative study of the mechanisms of turbulence generation in the neighborhood of the grid for water and DPS. Measurements performed here are planar (2D PIV) and give access to only two components of the velocity field. It is thus not possible to compute all the terms of the governing equations introduced in chapter 1, but only a part of the terms involving the components and their gradients along X and Z. In the remainder of this section, analysis of the velocity fields is carried out as if the flow was two dimensional, assuming that velocities and gradients along the Y direction are nil. This is a strong and reductive hypothesis. In order to perform a complete analysis of the production, dissipation, and transfer terms of turbulence of the governing equations in the whole volume of interest, full three dimensional three component velocity data would be required.

3.4.4.a Periodic flow and turbulence production

Let us focus on the 2D analysis and start this investigation by looking at the periodic properties of the flow. For that we consider the phase averaged velocity field $\langle U\rangle_\phi$, oscillatory

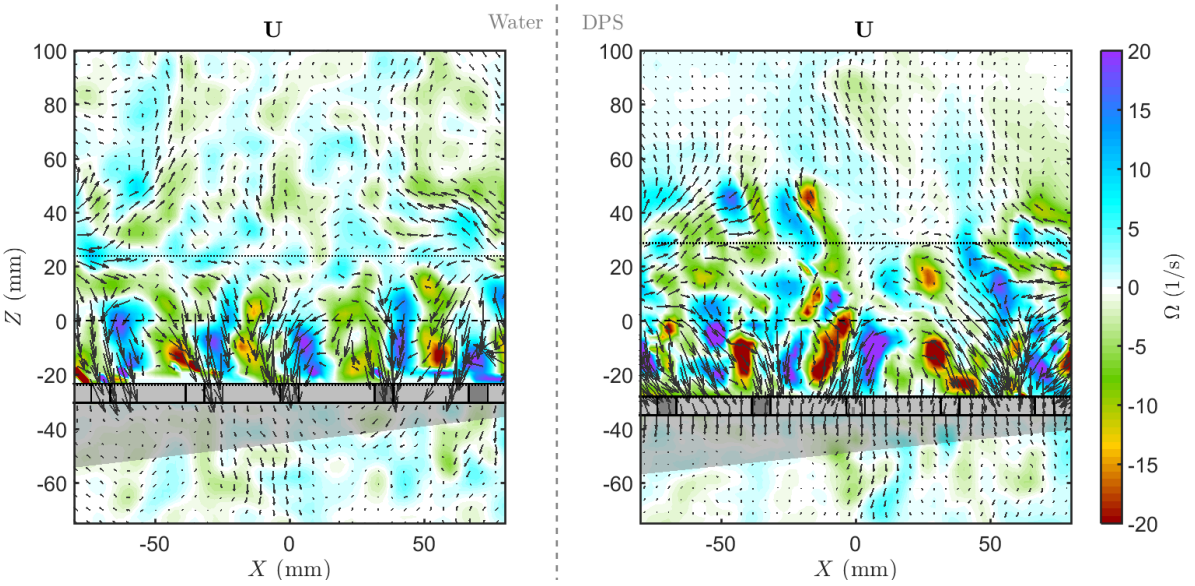

Figure 3.21 – Example of close grid instantaneous velocity and vorticity fields in water (left) and DPS (right). The colorbar represents the out-of-plane vorticity of U. The gray area under the grid represents the area of the ROI for which the laser sheet was shaded by the grid and were measurements could be inaccurate. For figure's clarity, only one every two vector in both dimensions is plotted.

components u_x^* and u_z^*, and phase rms of turbulent fluctuations $\langle u'_x \rangle_{\phi,rms}$ and $\langle u'_z \rangle_{\phi,rms}$. This last quantities represent the periodic intensity of turbulence around the grid. Figure 3.23, 3.24 and 3.25 display a typical period of oscillations for respectively water and DPS in terms of oscillatory component of the velocity field, phase rms of turbulent fluctuations for water, and phase rms of turbulent fluctuations for DPS. Figure 3.23 is the oscillatory component of the vorticity field for different grid positions during a typical period of oscillations. A snapshot has already been presented in figure 3.22 for the lower grid position. The trailing vortices behind grid bars are found again, and their growth and decay can be visualized as a function of the grid position. In DPS, a periodic vortex shedding is observed on both sides of the ROI, specifically in the region where the two mean vortices are formed. For both water and DPS, high intensity turbulent fluctuations are mostly found in the wake of the moving grid, as evidenced by figures 3.24 and 3.25. Turbulence is thus as expected generated in the wake of the grid. What seems to be added to this mechanics by the polymer is an enhancement of the role of oscillatory motion, which is especially evidenced by a periodic vortex shedding at the walls, but also by increased oscillatory velocities.

3.4.4.b Turbulence and oscillatory flow intensity and stresses

In order to quantify the relative intensity of oscillatory versus turbulent fluctuations in both fluids, the root mean square (RMS) over the whole set of instantaneous fields of oscillatory and turbulent fluctuations (regardless of the grid position) is represented on figure 3.26. The Reynolds and "oscillatory" stresses $\overline{u'_i u'_j}$ and $\overline{u^*_i u^*_j}$ are shown in figures 3.27 and 3.28. In these figures the grid is sketched at its mean position (Z = 0 mm). The stresses for which $i = j$ are refereed to as "normal" stresses, and the other ones as "tangential" stresses.

Both turbulent fluctuations are logically much higher in the sweep region of the grid around Z=0. They also exist at a lower level outside of the stroke region in both water and DPS (non zero RMS of turbulent fluctuations). The RMS of the oscillatory component is strong in the grid sweep region, as also suggested by the snapshots of typical oscillation pe-

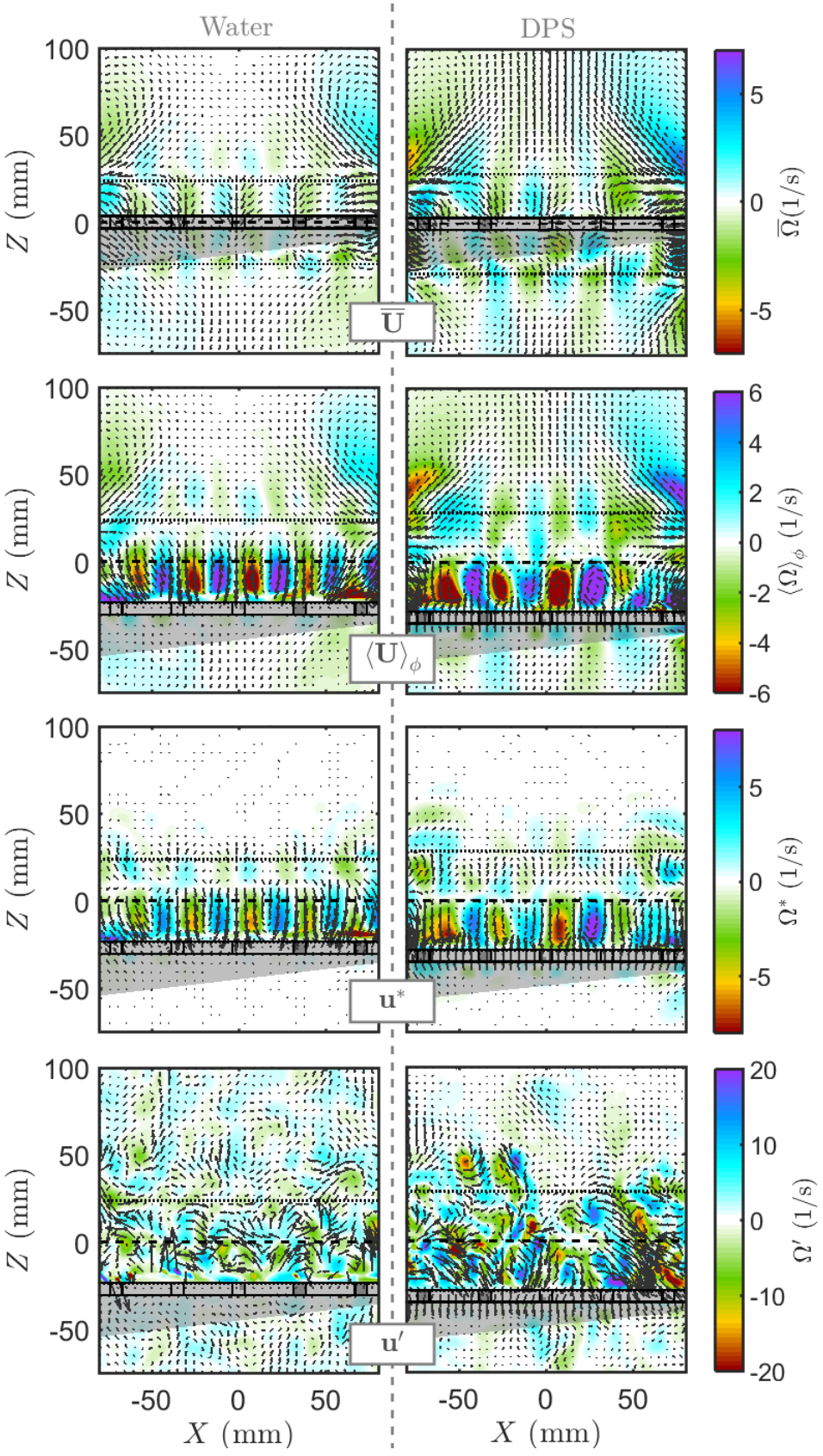

Figure 3.22 – Average, phase average, oscillating and fluctuating velocity and vorticity fields for water and 100 ppm DPS

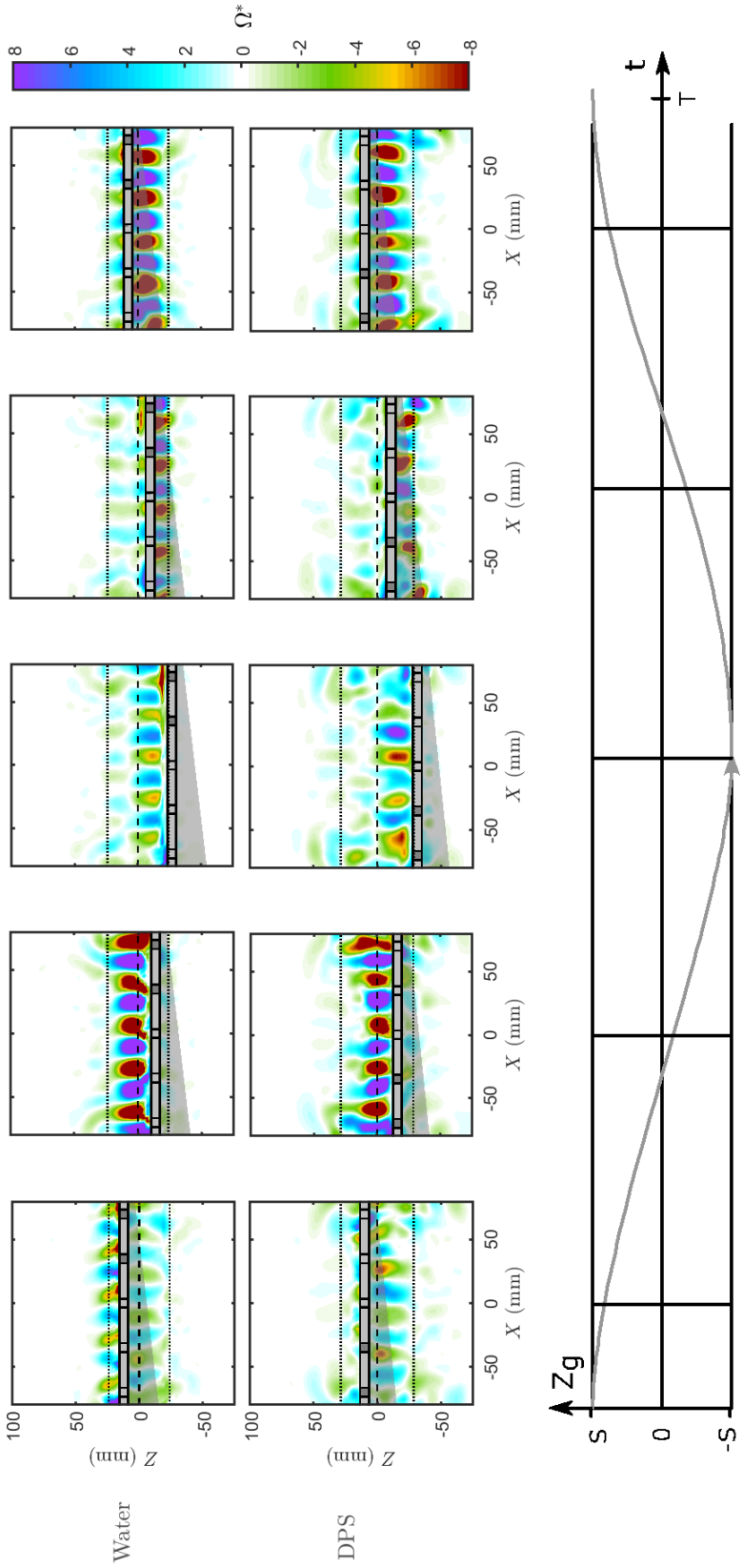

Figure 3.23 – Oscillating vorticity Ω^* field in (1/s) at different grid positions in the close grid region for water and DPS. The sampling of the grid period is sketched alongside the figure, on the Z_g versus time plot, where Z_g is the distance from the grid to its mean position.

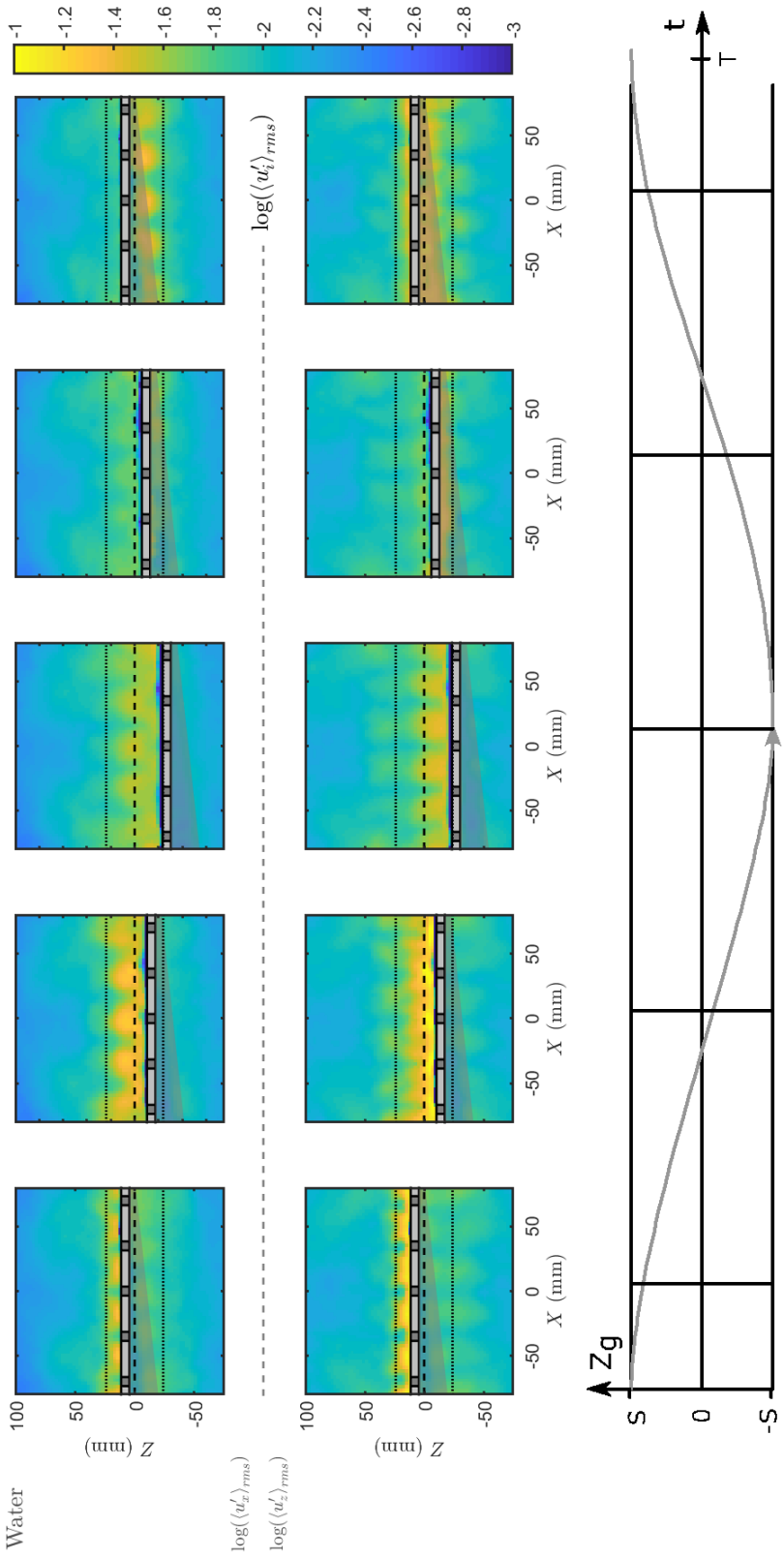

Figure 3.24 – RMS of turbulent fluctuations $\langle u_i' \rangle_{rms}$ (in m/s) with i=x,z at 5 different grid positions in the close grid region for water. The first and second lines are plots of the horizontal and vertical components. The sampling is the same as in figure 3.23.

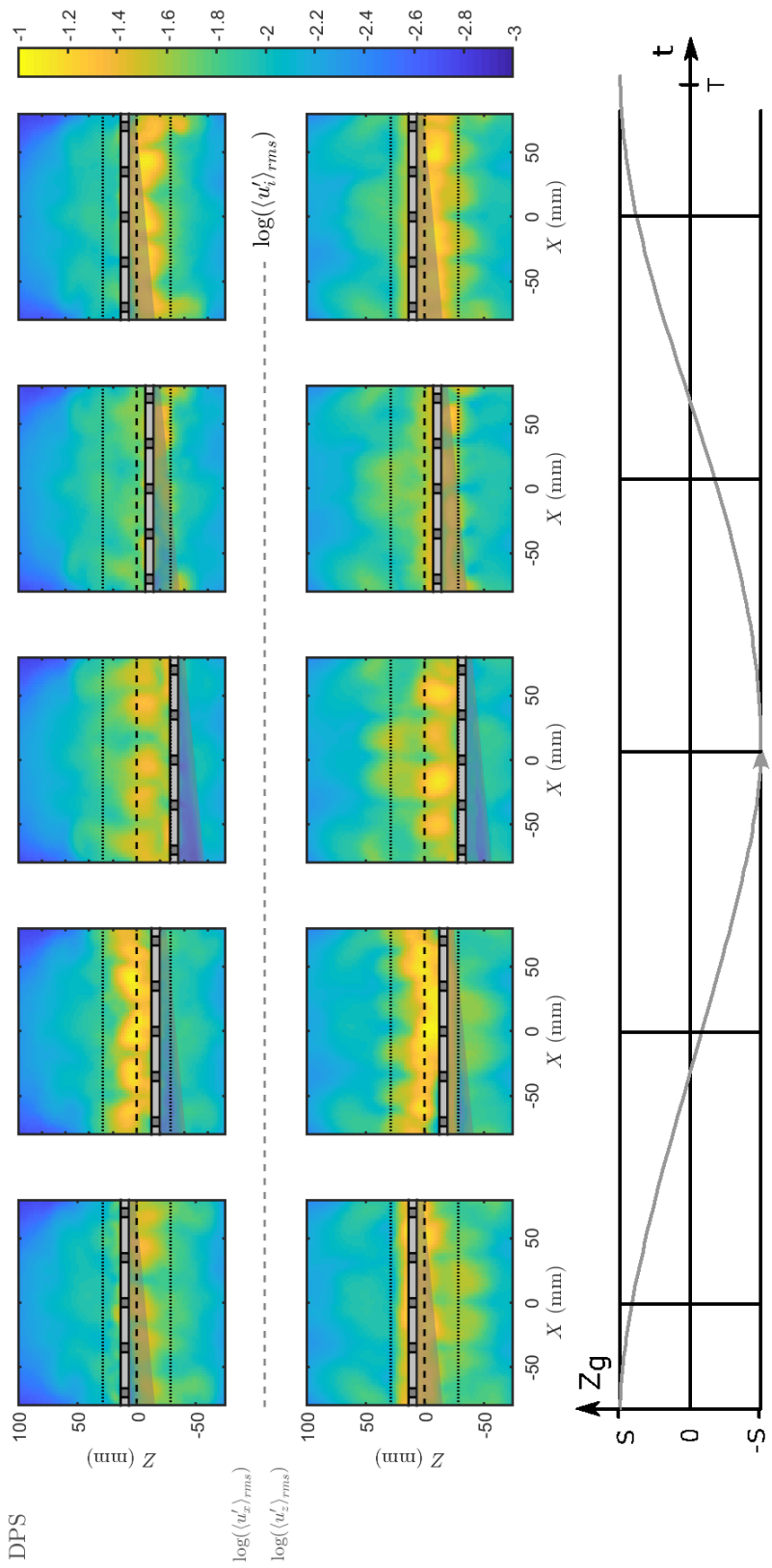

Figure 3.25 – RMS of turbulent fluctuations $\langle u_i' \rangle_{rms}$ (in m/s) with i=x,z at 5 different grid positions in the close grid region for 100 ppm XG solution. The first and second lines are plots of the horizontal and vertical components. The sampling is the same as in figure 3.23.

riod shown in figure 3.22 and 3.23, but quickly vanishes when moving away from the grid. In DPS, the RMS of oscillatory motion is slightly increased outside of the grid region compared to water. It is also more blurry along the X dimension. Figure 3.26 thus confirms that the oscillatory component of the flow is mostly relevant in the sweep region of the grid, and quickly becomes negligible compared to turbulence outside of this region. The effect of DPS seems to be an enhancement of the oscillatory fluctuations intensity and a modification of their spatial distribution.

Similar conclusions can be drawn from figures 3.27 and 3.28: Reynolds stresses and oscillatory stresses are high in the sweep region for both water and DPS. They decrease when moving away from this region, and oscillatory stresses rapidly become nil. The presence of polymer tends to increase the spatial decay of Reynolds stresses, but slightly decrease that of oscillatory stresses, especially for the normal horizontal ones. The organizing effect of polymer is here again observed: oscillatory motion is enhanced with respect to turbulence in the DPS case.

Stress fields yet allow to make a few more observations. First, both the Reynolds and oscillating stress seem to be increased at Z = 0 mm in DPS compared to water. Second, the intensity of normal Reynolds stress in DPS is enhanced at the center of the ROI whereas that of oscillatory stress is larger on the sides of the ROI. Finally, the two side vortices evidenced from the mean flow study are found to correspond to two patches of tangential Reynolds stress with a significant magnitude, and that for both water and DPS, as visualized on figure 3.27 second row.

In order to get the full picture of energy transfer between mean oscillatory and turbulent velocities, the other transfer terms need to be computed. This is the scope of the next paragraph.

3.4.4.c Energy transfers

The transfer terms have been defined in chapter 1, equations (1.40), (1.41) and (1.42). The computation of this transfer terms requires the knowledge of mean and oscillatory velocity gradients, and of Reynolds stresses $\overline{u_i' u_j'}$ and phase average correlation of the turbulent fluctuations $\langle u_i' u_j' \rangle_\phi$. The mean to turbulent transfer term is here written as

$$\mathcal{T}_{mt} = \mathcal{T}_{mt}^{xx} + \mathcal{T}_{mt}^{xy} + \mathcal{T}_{mt}^{yx} + \mathcal{T}_{mt}^{yy} = -\overline{u_x' u_x'}\frac{\partial \overline{\mathrm{U}}_x}{\partial x} - \overline{u_x' u_y'}\frac{\partial \overline{\mathrm{U}}_x}{\partial y} - \overline{u_y' u_x'}\frac{\partial \overline{\mathrm{U}}_y}{\partial x} - \overline{u_y' u_y'}\frac{\partial \overline{\mathrm{U}}_y}{\partial y} \quad (3.13)$$

The $\mathcal{T}_{mt}$ (mean to turbulence), $\mathcal{T}_{mo}$ (mean to oscillatory) and $\mathcal{T}_{ot}$ (oscillatory to turbulence) fields for water and DPS are shown in figure 3.29. Several observations can be made:

- The variations of transfer terms are larger in DPS than in water. Since transfer terms are a product of stress and spatial gradient, the origin of these variations may come from both of these parameters. Reynolds and oscillatory stresses spatial variations are more important in DPS than in water (see figure 3.27 and 3.28). Mean and oscillatory flows are enhanced by the presence of polymer (as shown in figure 3.22), and their gradients are sharper.

- All the transfers mostly occur within the grid sweep region. The only small but noticeable exception is observed for $\mathcal{T}_{mt}$ fields in DPS, just above the grid's top position, where two transfer regions are observed on both sides of the ROI. They correspond to the mean flow vortices observed previously.

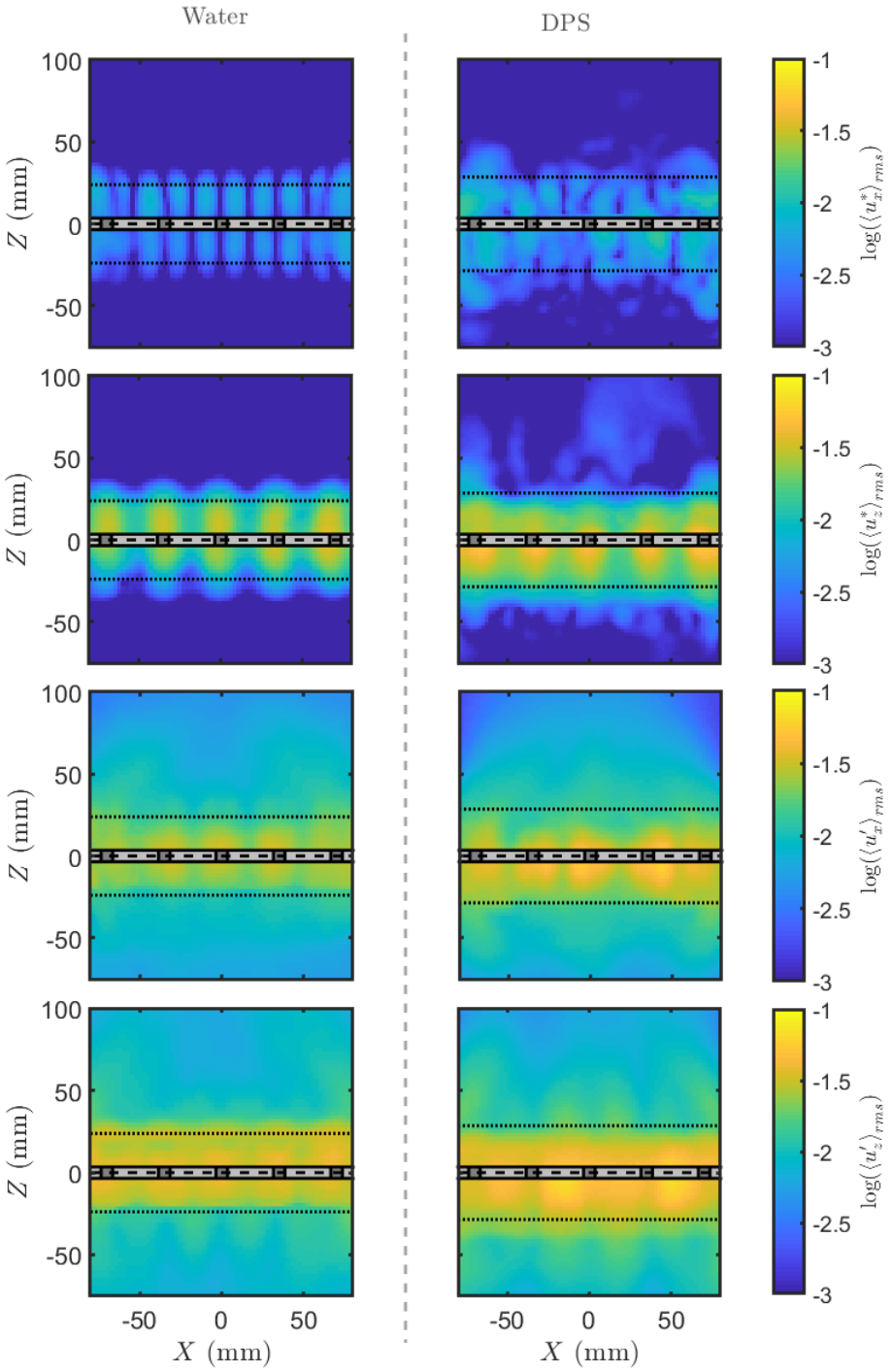

Figure 3.26 – RMS of oscillatory (lines 1 and 2) and turbulent (lines 3 and 4) velocity fluctuations along the horizontal (lines 1 and 3) and vertical (lines 2 and 4) directions, in water and DPS. Velocities are expressed in m/s

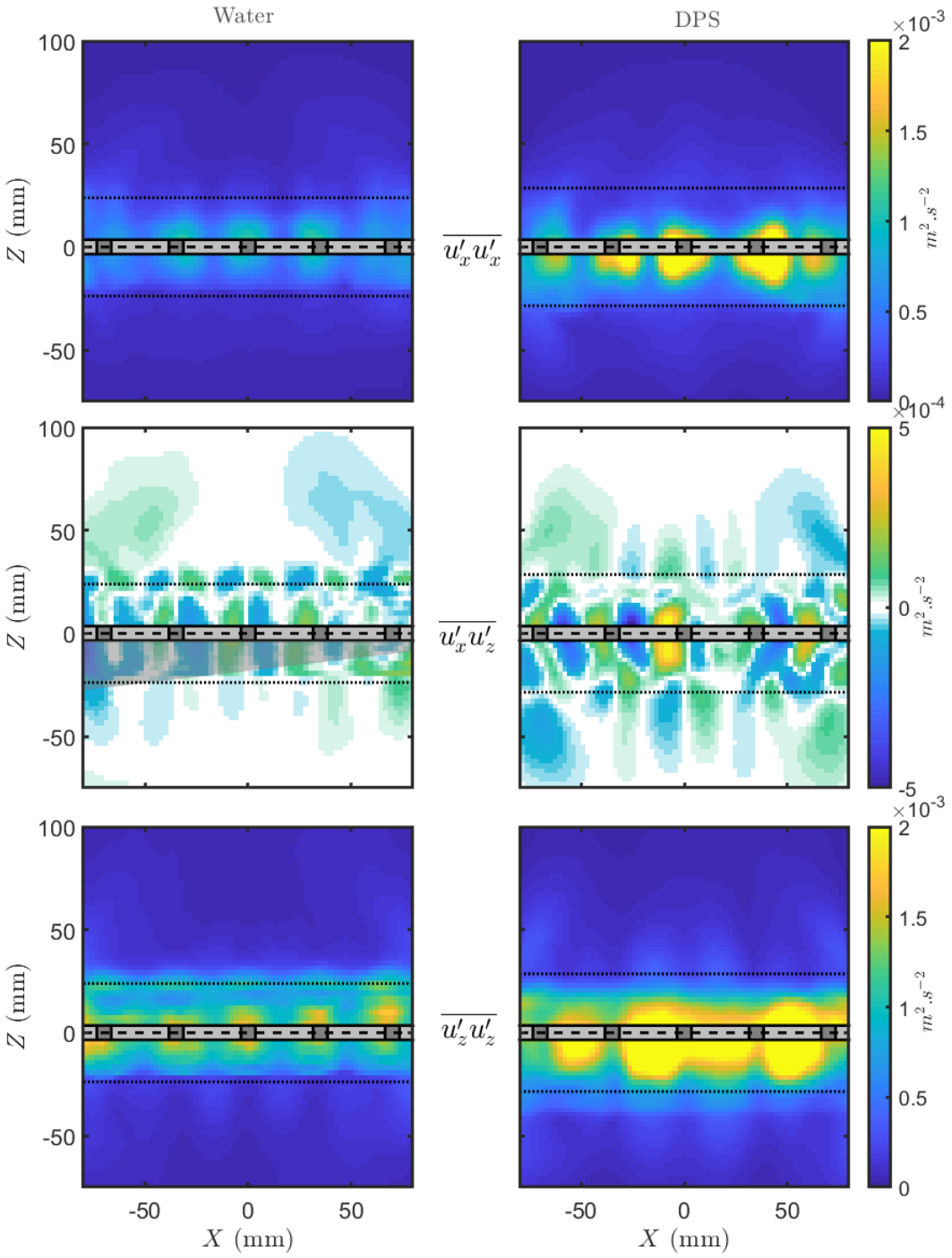

Figure 3.27 – Reynolds stresses in water and DPS.

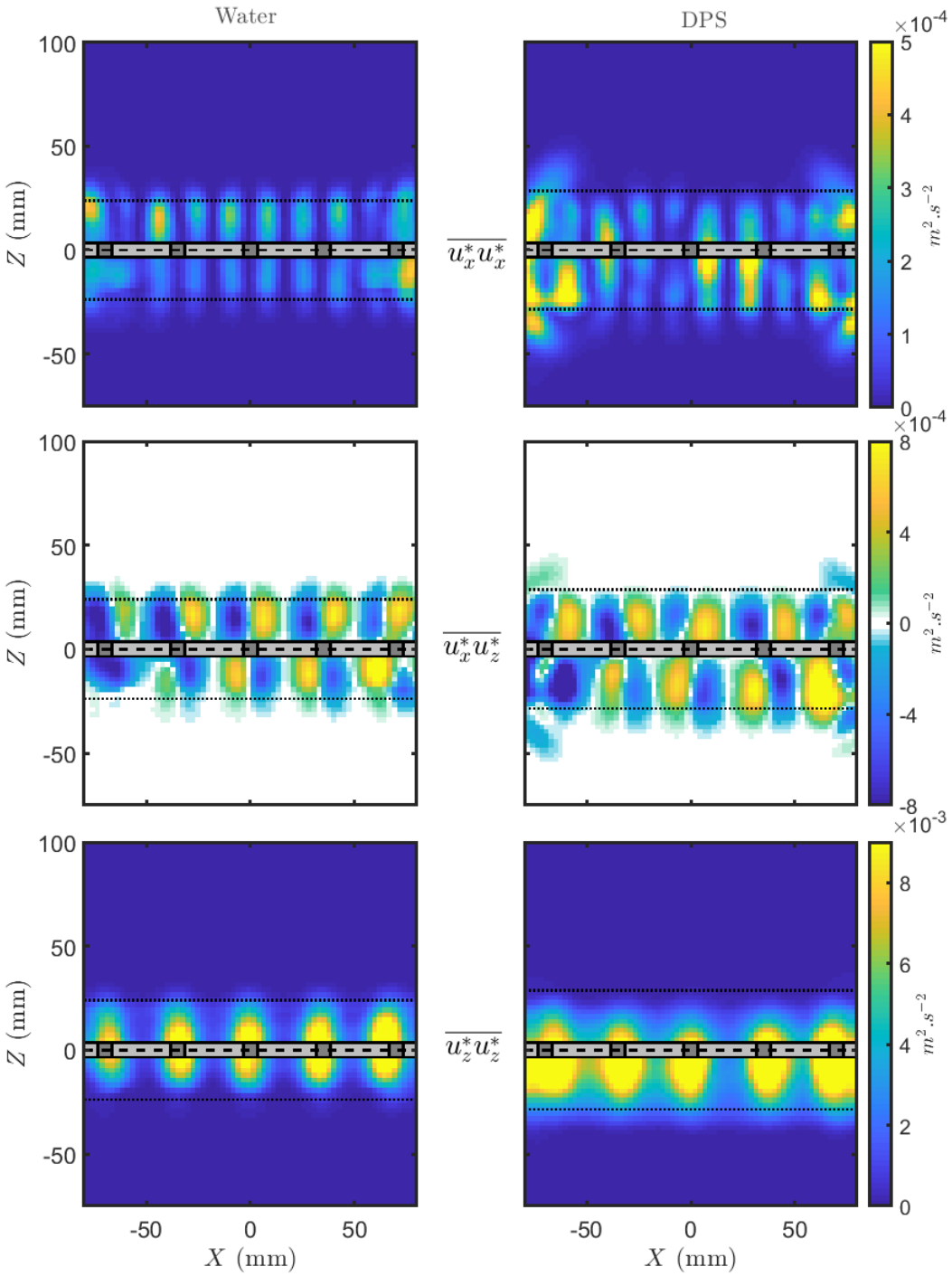

Figure 3.28 – Oscillatory stresses fields induced by the periodic velocity fluctuations in water and DPS.

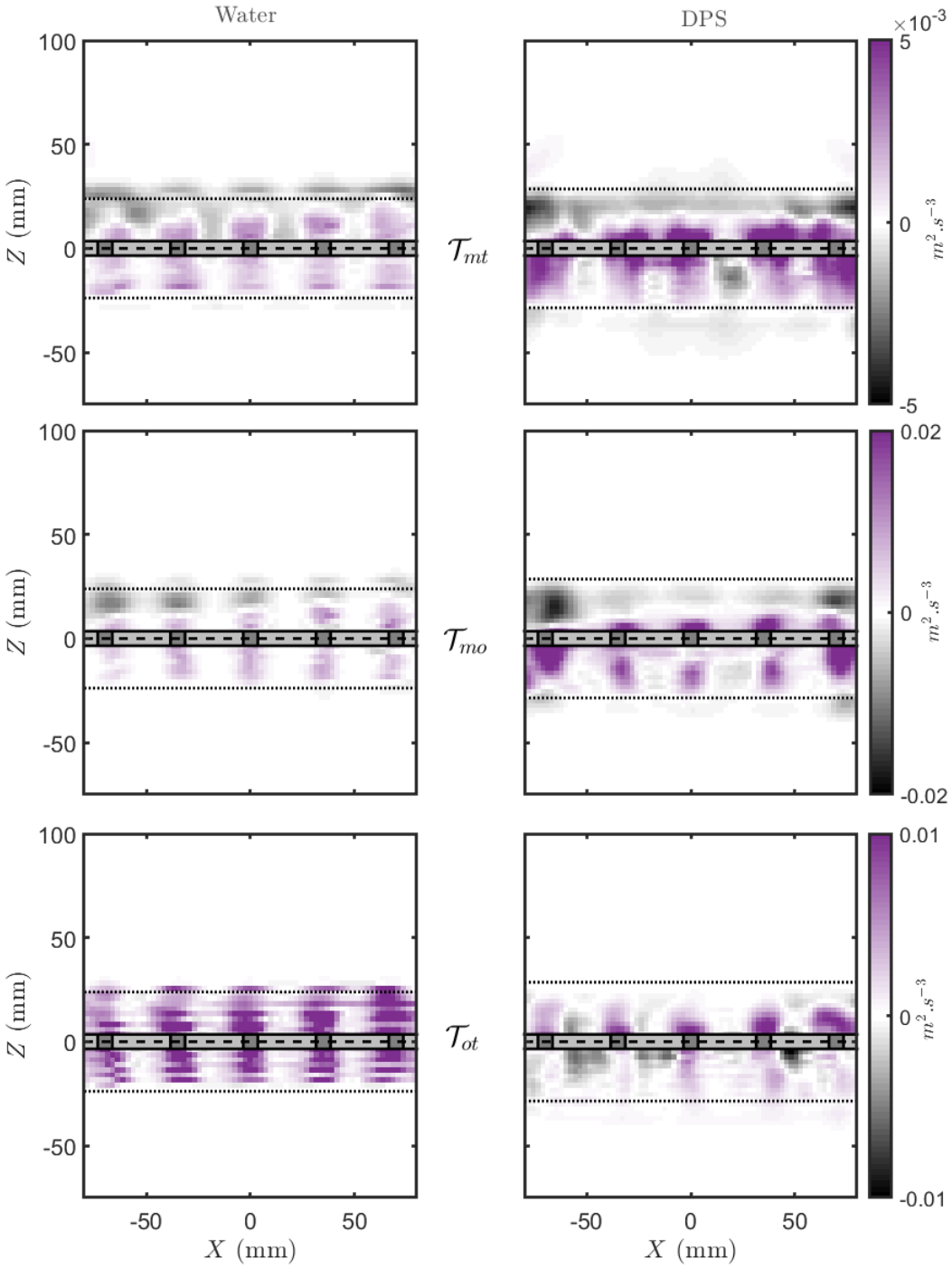

Figure 3.29 – Triple decomposition transfer terms $\mathcal{T}_{mt}$ (mean to turbulent), $\mathcal{T}_{mo}$ (mean to oscillatory or periodic) and $\mathcal{T}_{ot}$ (oscillatory to turbulent) in water and 100 ppm XG solution. Transfer terms are expressed in $m^2.s^{-3}$.

- $\mathcal{T}_{mo}$ seem stronger in the DPS than in the water case, as illustrated by the second row of the figure. This underlines the increased importance of the oscillatory field in DPS.
- In water, $\mathcal{T}_{ot}$ mostly occur in vertical regions aligned with the grid bars, and the transfer term is always positive, so that oscillatory motion seems to always transfer energy to turbulence and not the other way around. In DPS, the pattern of the $\mathcal{T}_{ot}$ field is more elaborate and both positive and negative regions exist, which means that energy transfer is a two way process.

It is worth noting that these energy transfer terms are not complete, since the third component of the velocity field and the gradient of all components along the third direction are lacking. The physical interpretation of the observations above is thus limited.

Figure 3.30 summarizes figures 3.27, 3.28 and 3.29 in terms of vertical profiles of Reynolds and oscillatory stresses and transfer terms. All curves have been obtained by width averaging the corresponding fields over the $-50 < X < 50$ mm range. Only the values for $Z > 0$ are shown.

These curves confirm and complete the earlier observations. Oscillatory and Reynolds stresses are maximum in the core of the grid sweep region, close to $Z = 0$. Oscillatory stress decays much faster than the Reynolds stresses with increasing Z, and are negligible compared to the Reynolds stresses outside of the sweep region, by at least a factor 10. For a given fluid and a given type of fluctuations, the vertical stress is always larger than the horizontal one. This is obviously because of the vertical grid displacement. This effect is all the more important for the oscillatory stresses which are directly due to this grid motion. The presence of polymer slightly increases the Reynolds stress value at the origin, but also the decay rate of the stresses with Z. In other words, DPS tends to concentrate the effects of turbulence in the sweep region. As for the effect of polymer on the oscillatory component, it was previously observed that DPS solutions showed enhanced oscillatory structures outside of the sweep region on the sides of the ROI. However this effect was found to be related to tangential stresses and not to normal ones, hence it is not visible on the $\overline{u_i^* u_i^*}$ fields and on their vertical profiles.

Finally, the figure also shows that the vertical variations of transfer terms is increased in DPS as compared to water in the sweep region. This is supposedly due to both the enhancement of oscillatory and Reynolds stresses and to the spatial gradients of mean and oscillatory velocities. Such results suggest that gradient-based models such as the ones presented in 1.2.1.c could be good candidates as closure relationships for the estimation of these transfer terms.

3.4.4.d Viscosity estimation and statistics

The last approach for studying polymer influence on the origins of OGT detailed in this thesis is by estimation of the local viscosity field and its statistics. The main idea is to derive local shear rate fields from instantaneous, phase averaged or time averaged velocity fields. Local shear rate values are then used to estimate an apparent viscosity through the consitutive equation of the polymer, here a Carreau Yasuda law for the rheological behavior derived in section 3.2.2. This method is limited because the velocity data is only 2D and lacks the third velocity component. Shear rate values can thus only roughly approach the real local shear rate, and no precise quantitative study can be performed. Moreover, it is not possible to compute the polymeric stress terms defined in section 1.3.2: viscosity is derived from the local shear rate, and the estimation of these polymeric stresses would require separate measurements of shear rate and viscosity. However this method allows to qualitatively estimate the viscosity variations in a plane of measurement. Of course, this is only relevant for DPS.

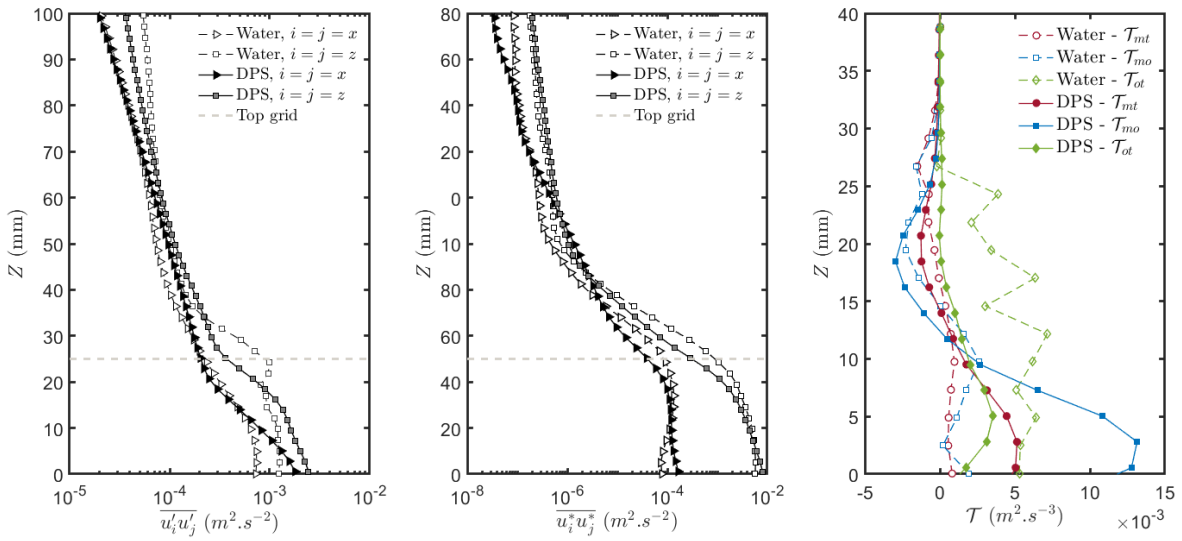

Figure 3.30 – Vertical profiles of oscillatory and Reynolds normal stress and transfer terms for water and DPS.

In practice, the apparent instantaneous shear rate is computed as

$$\dot{\Upsilon}_{app} = \sqrt{\left(\frac{\partial U_x}{\partial z}\right)^2 + \left(\frac{\partial U_z}{\partial x}\right)^2} \tag{3.14}$$

an the instantaneous apparent viscosity as

$$\mu_{app} = f_{CY}(\dot{\Upsilon}_{app}) \tag{3.15}$$

with f_{CY} the Carreau Yasuda function defined in equation (1.59), and using fitting parameters obtained in section 3.2.2 for 100 ppm XG solutions. Statistics for viscosity are then obtained by ensemble averaging over the whole set of field for $\overline{\mu}_{app}$, or grid position by grid position for μ^*_{app} exactly like what is done for the velocity field.

Figure 3.31 shows the fields of ensemble average viscosity $\overline{\mu}_{app}$, ensemble rms of turbulent viscosity fluctuations $\langle \mu'_{app} \rangle_{rms}$ and fields of maximum and minimum viscosity values over time $\mu_{app,max}$ and $\mu_{app,min}$. Oscillatory viscosity fields μ^* at different grid positions are also plotted in figure 3.32.

The first subfigure of figure 3.31 shows that viscosity is minimal close to Z = 0 inside the sweep grid region. It then increases when moving away from Z = 0 until it reaches its zero shear rate plateau value at Z > 100 mm. The maximum of RMS velocity fluctuations is found just above the grid's top and bottom positions, around X = 0. Here the viscosity varies from a value close to its zero shear rate plateau when the grid is on the other side of its stroke, to a much lower value when the grid departs from this position and releases high shearing eddies, as shown in figure 3.32. Vertical trails of high viscosity rms are also observed in regions associated to grid holes (even if grid holes are not in the B0 planes). Since this plot represents the rms of turbulent viscosity fluctuations, it means that these trails are not due to oscillatory motion, but rather to strong fluctuations of the shear rate fields because of turbulent structures in those regions. The minimum viscosity fields shows that viscosity is always higher than the infinite shear rate viscosity, which means that during the experiments, no shear rate (mean, oscillatory or turbulent) is high enough for the fluid to behave like a low viscosity Newtonian fluid, even locally. Finally, the maximum viscosity field shows that almost everywhere in the fluid, the maximum viscosity value may be reached at some time,

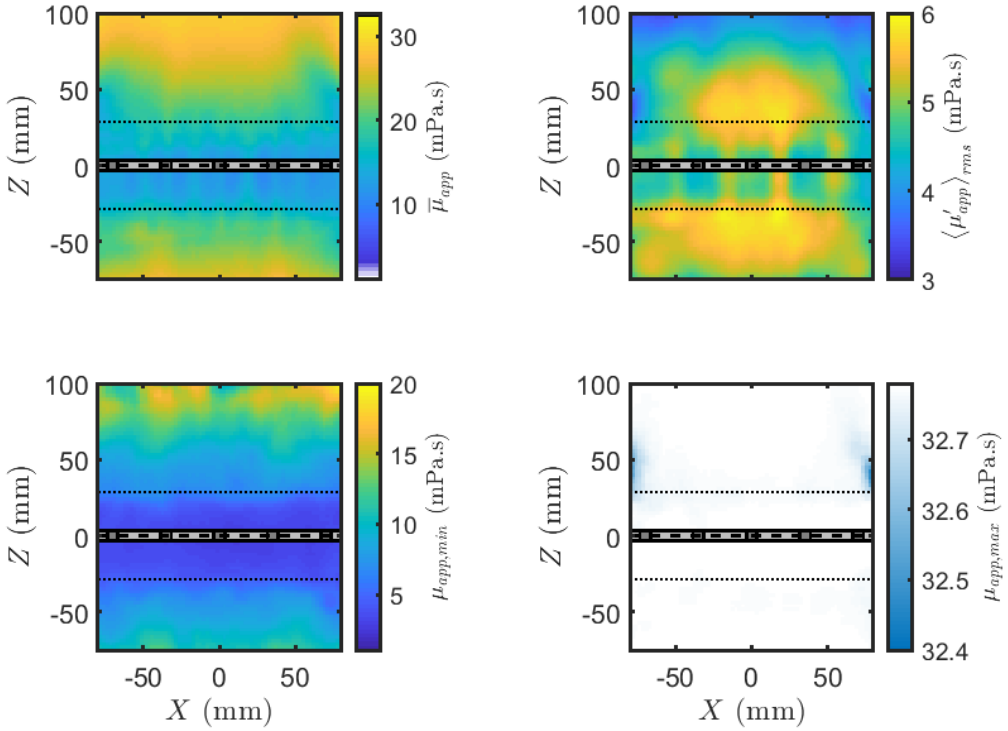

Figure 3.31 – Local statistics of apparent viscosity: average (a), rms of turbulent fluctuations (b), minimum (c) and maximum (d). The zero shear rate viscosity in 100 ppm XG solutions is 32.78 mPa.s and the infinite shear rate viscosity is 1.05 mPa.s.

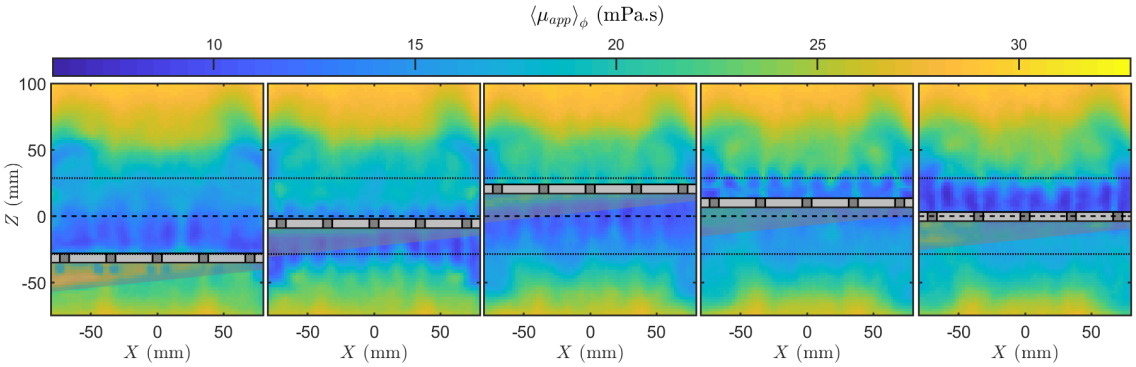

Figure 3.32 – Example of phase averaged viscosity fields $\langle \mu_{app} \rangle_{\phi}$ deduced from the local shear rate, at different grid positions

i.e that almost everywhere in the fluid, at some time, the shear rate is almost nil. The only locations where this is not the case are just above the grid sweep region. Here lower maximum viscosity patches are found which correspond to the shape and location of the mean flow vortices.

3.4.4.e Conclusion

The main conclusions on turbulence and oscillatory motion in the close-grid (CG) region are summarized here.
In water: The grid periodic motions create oscillatory vortices behind the grid bars. At the walls (on both sides of the ROI), these periodic vortices feed the large mean flow eddies. Oscillatory component is strong within the grid sweep region, but quickly vanishes when moving away from the grid's action. Turbulence is created by both oscillatory and mean flow in the sweep region, and to a lesser extent in the mean flow vortices. It is highly anisotropic in the sweep region, with a much higher intensity along the vertical direction, as imposed by the grid motion.
The effects of polymer addition: Polymer addition has several effects on the flow sructure and energy exchanges around the grid. The first one is an enhancement of the oscillatory flow, especially on the sides of the ROI near the walls. This leads to a periodic vortex shedding that feeds the mean recirculations and increase their intensity, thus possibly explaining the mean flow enhancement. The second effects is a modification of the spatial distribution of turbulence. Reynolds stress and turbulence intensity are increased in the core of the sweep region close to Z=0, and decrease quicker with increasing Z magnitude. Turbulence is enhanced at the center of the ROI (far from the walls), both in the sweep region and far from the grid. Finally, the transfer from oscillatory to turbulent fluctuations seems more complex in DPS than in water, and suggests that oscillatory motion may both give and take energy from turbulence, which was not the case for water.

Now that the origins of turbulence in the grid stirred tank have been observed, let us consider its propagation and decay in the upper part of the tank.

3.4.5 Turbulence propagation and dissipation

To that end, the full tank (FT) region is considered, for water an DPS at different concentrations, and in plane B0. Results from the previous section indicate that the oscillatory component can be neglected in the central part of the FT region, for water and DPS solutions. Historically, the existence of oscillatory fluctuation has never been considered in OGT turbulence models. For both reasons, the "classical" Reynolds decomposition will be used in this section, assuming that the turbuent fluctuations in Reynolds decomposition and triple decomposition are equivalent, *i.e.* that $\mathbf{u}^* \simeq 0$ and $\mathbf{u}^* + \mathbf{u}' \equiv \mathbf{u}'$.

The first quantities considered are the rms value of velocity fluctuations and turbulent kinetic energy. These are the ones commonly used to describe turbulence evolution with the altitude in OGT and at the root of the reference models of Hopfinger and Toly (1976) and Matsunaga et al. (1999).

3.4.5.a RMS velocity fluctuations and turbulent kinetic energy

Figure 3.33 shows example of Turbulent Kinetic Energy (TKE) fields k for water and 3 different polymer concentrations.

TKE decays with increasing distance from the grid. The TKE level is decreased with increasing polymer concentrations, and its decay rate is modified. Hopfinger and Toly (HT)

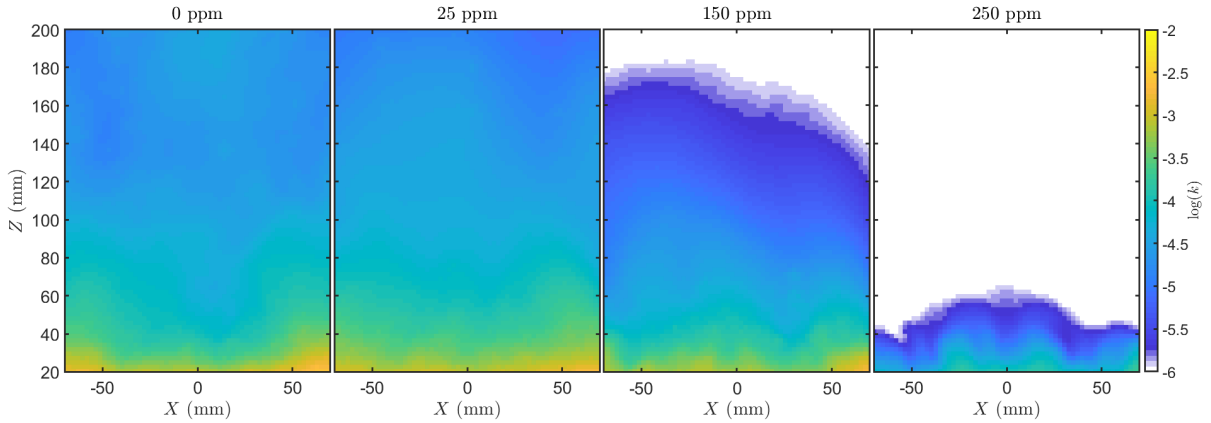

Figure 3.33 – Turbulent kinetic energy fields (in log scale, $m^2.s^{-2}$) for water and DPS at different concentrations

type profiles are used to quantify turbulence decay. To plot them, the fluctuating velocity rms fields are averaged over the image width (horizontal direction). The width average operator (along dimension X) is hereinafter denoted $[.]_X$. These profiles for water and DPS at different concentrations are compared in figure 3.34. First of all, the power law of HT model is evidenced for both velocity components in water, but also in DPS [4].

The power law slopes of water and DPS are almost equivalent for the horizontal and vertical velocities in both water and DPS. For OGT in water with low stroke over mesh parameter ratios, Wan Mohtar (2016) explained that the vertical fluctuation should decay faster than the horizontal one since "*vertical kinetic energy is also used for kinetic energy transport*". However we have here a stroke versus mesh size ration around 1.3, a case for which the two HT exponent should be very close, as evidenced by Wan Mohtar (2016).

Two interesting behaviors are observable in figure 3.34. First, high polymer concentrations break the power law behavior, and a variation in slope of the HT profile can be observed in the bulk for samples with $C_{XG} \geq 150$ ppm. It is worth noting that this slope variation is opposed to the one predicted by a Matsunga model. Second, polymer addition leads to a first decrease in n, which then re-increases with increasing polymer concentration in the dilute regime. Contrary to mean flow evolution, no critical concentration effect (other than the break in slope for $C_{XG} \geq 150$ ppm) is observed.

3.4.5.b Isotropy and homogeneity

In OGT, it is known that the vertical component of turbulence is stronger than the horizontal one, because this is the orientation of the grid forcing. Hence OGT is by nature not fully isotropic in a vertical plane. 3D homogeneity is also impossible to obtain because turbulent fluctuations are damped when moving awards from the grid. Homogeneity in a horizontal plane is yet possible in the central region of the tank, far from the side effects and strong mean flows.

An indicator of the 2D isotropy of turbulence in the ij plane can be defined as $I_s^{ij} = \langle u_j' \rangle_{rms} / \langle u_i' \rangle_{rms}$. Vertical profiles of I_s^{xz} averaged in width over the central region are shown in figure 3.35. This is equivalent to plotting the HT profiles of the vertical component di-

[4] The trend predicted by Matsunaga et al. (1999) is not visible. This may be explained by the rather weak oscillatory forcing (low frequency and stroke) and the small dimension of the tank used here, which are not sufficient for the dissipation scaling predicted by Matsunaga et al. (1999) to develop.

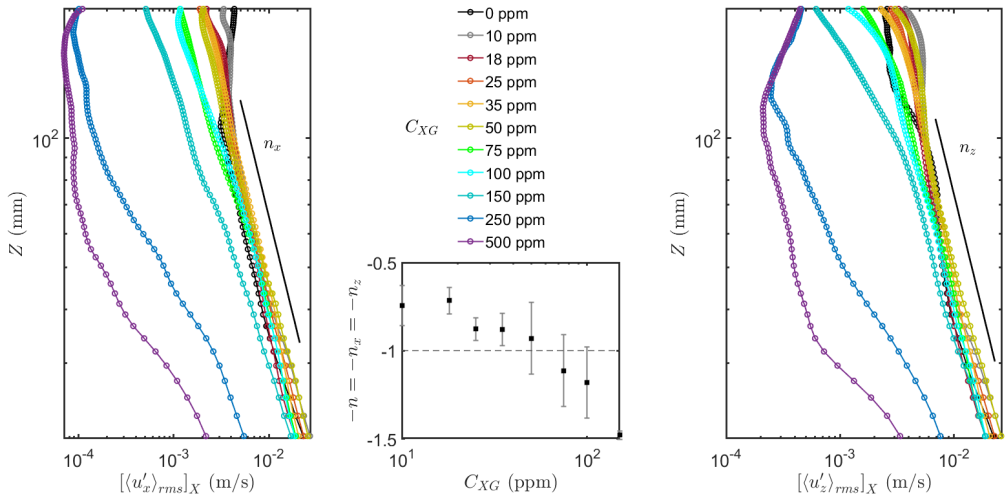

Figure 3.34 – Hopfinger and Toly's type profiles of the rms of horizontal (left) and vertical (right) turbulent velocity fluctuations. The central subfigure shows the evolution of the common power law decay exponent $n = n_x = n_z$ with polymer concentration in the dilute regime (250 and 500 ppm slopes not shown). Error bars show the difference of measured exponent between horizontal and vertical velocity components.

vided by the horizontal one. In order to measure horizontal homogeneity, we define the quantity $H^i_j(Z)$ as the standard deviation over an horizontal line at altitude Z of the field $\langle u'_j \rangle_{rms}$ from figure 3.33, normalized by the average rms value along this line. For example $H^x_x = \frac{[\langle u'_x \rangle_{rms}]_{STD,X}}{[\langle u'_x \rangle_{rms}]_X}$. The smaller the H^x_x or H^x_z the higher the homogeneity in dimension X at a given Z.

Regarding isotropy, the fist observation is that the I^{xz}_s indicator is generally above 1, thus confirming that the vertical velocity fluctuations rms is always larger than the horizontal one, for water and all DPS concentrations. For DPS, a slight increase of anisotropy is observed with increasing Z. This increase seems all the more important that polymer concentration is high. This is a consequence of the HT exponent for u'_x being slighty higher than the one for u'_z. When approaching the free surface (located here at Z close to 200 mm), the trend is reversed and the values of I^{xz}_s rapidly decrease and fall below 1. This suggests that the free surface damps the vertical fluctuations of turbulence more efficiently than the horizontal ones. This point is discussed extensively in chapter 4. Using the picture of Hopfinger and Toly (1976), and assuming that the rms of vertical velocity fluctuations is proportional to the rms of horizontal ones with a constant coefficient (which is strictly speaking not the case here for the higher polymer concentrations), the anisotropy coefficient corresponding to the second HT constant C_{2HT} is defined as the ratio between rms of vertical and horizontal velocity fluctuations, averaged over the full height of measurement. According to Hopfinger and Toly (1976), its value is between 1.1 and 1.4 for water

The curve for C_{2HT} as a function of XG concentrations are deduced by averaging the $[I^{xz}_s]_X$ profiles over Z, and also plotted in figure 3.35. C_{2HT} is found to increase with polymer concentration, first really slowly, and then faster above 100 ppm concentrations. The first conclusion is thus that the presence of polymer tends to promote turbulence anisotropy, and that this increased anisotropy is all the more important than polymer concentration is large. For concentrations lower than 100 ppm, the value of Hopfinger an Toly's second constant stay inside the range found in the literature for water, even if a slight increase is observed.

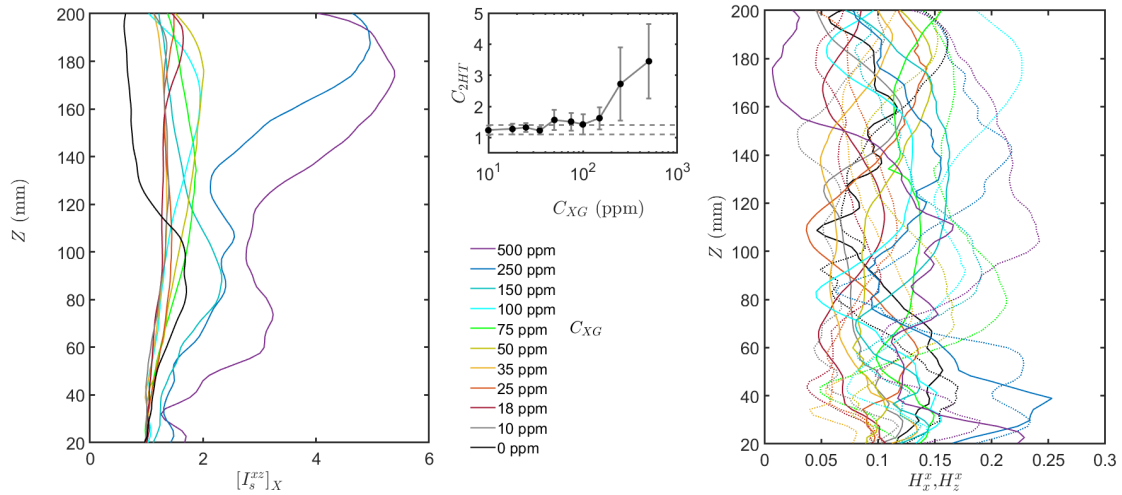

Figure 3.35 – Vertical profiles of isotropy and horizontal homogeneity for water and DPS solutions at different concentrations. Left plot: Isotropy profiles. Central subfigure: evolution of C_{2HT} with polymer concentration deduced from the isotropy profiles. Dashed lines are boundaries of the usual range of values found for water. Error bars are obtained by taking the standard deviation of C_{2HT} around its average value for each concentration. Right plot: horizontal homogeneity profiles, dotted lines for H_x^x and full lines for H_z^x.

When entering the semi-dilute regime, that is to say at concentrations above 100 ppm, the slope brutally changes and C_{2HT} increases much faster with concentration. This is another evidence of the importance of the polymer concentration regime in terms of flow properties. It has been shown before that the critical 100 ppm concentration was important for mean flow considerations, inasmuch as it marked the transition between mean flow enhancement by the polymer and mean flow decay. This same critical concentration is also relevant for turbulence properties: it points out the transition between a concentration regime where turbulence anisotropy is only weakly increased, and a regime in which it is strongly increased.

Homogeneity indicators H_x^x and H_z^x do not show any trend along Z. Their value is between 0.05 and 0.25. This value does not seem to depend on polymer concentration. This implies that polymer has a lesser effect on turbulence homogeneity than on its isotropy.

3.4.5.c Mean flow to turbulence ratio

A key quantity of oscillating grid turbulence is the local mean to turbulence ratio, denoted Γ with $\Gamma_{i,j} = \frac{|\overline{U}_i|}{\langle u_j' \rangle_{rms}}$ where i=x,y or z. Γ is a 9 component tensor since the ratio of three different mean flow components magnitude over three different component of fluctuations can be defined. For 2D PIV measurements, Γ is reduced to a 4 component tensor:

$$\Gamma = \begin{bmatrix} \frac{|\overline{U}_x|}{\langle u_x' \rangle_{rms}} & \frac{|\overline{U}_x|}{\langle u_z' \rangle_{rms}} \\ \frac{|\overline{U}_z|}{\langle u_x' \rangle_{rms}} & \frac{|\overline{U}_z|}{\langle u_z' \rangle_{rms}} \end{bmatrix} \tag{3.16}$$

Most of the times, the values used to estimate the efficiency of a device in terms of turbulence versus mean flow production are values of M_{ii}. For OGT in water, a review by Variano et al. (2004) reports typical values of $\Gamma_{ii} = 0.25$ with a best case value of 0.1 in a single coordinate direction.

Γ_{xx} and Γ_{zz} fields are pictured in figure 3.36 in color log scale. The overall mean flow

to turbulence ratio, defined as $\|\Gamma\| = \sqrt{\Gamma_{ii}^2 + \Gamma_{jj}^2}$ with i=x and j=z is also presented. Positive log values correspond to regions where the mean flow is stronger than turbulence ($|\overline{U}_i| > \langle u_i' \rangle_{rms}$) and negative log values to regions where turbulence is stronger than the mean flow. Here the reported maximum values for water are $\Gamma_{xx} \simeq 2.5$ and $\Gamma_{zz} \simeq 7$. However, these extreme values are mostly obtained on the sides of the ROI, where the influence of mean flow vortex is strong. In the central region of the plane, the average values of $\Gamma_{xx} \simeq 0.5$, $\Gamma_{zz} \simeq 3$ and $\|\Gamma\| \simeq 3$. Turbulence is thus here quite weak compared to mean flow in the present device. This is one of the main limitations of the present experimental setup.

In DPS, the $\|\Gamma\|$ levels are almost constant with increasing concentration in the very dilute range, with $C_{XG} < 35$ ppm. For concentrations above 50 ppm, all $\|\Gamma\|$ levels increase, and reach values up to 20 for high polymer concentrations. This is a sign that turbulence damping is much stronger than mean flow attenuation for high polymer concentrations.

3.4.5.d Integral length scales

The final characteristics of turbulence to be considered here are the integral length scales, which are an estimation of the size of the largest turbulent eddies in different dimensions. The region of interest is again the FT central region. Integral lenghtscales are computed as a function of the distance to the grid using as follows. Correlation coefficient along the horizontal dimension $R_{i,j}(r_x, t)$ are evaluated for all Z by sampling line by line the space of measurement, and averaging the values of R over the sample line and over time. Correlation coefficients along the vertical dimension are obtained in the same way, but this time the sample zone is of the width of the ROI, centered around the targeted altitude Z, and of height equal to 60 mm. Values of R are once again averaged over this sample zone and time. An example of correlation coefficient curves at different altitudes Z obtained for a given polymer concentration is shown in figure 3.37.

As can be seen on the figure, some correlation curves may not fall to zero in the sample zone used. In that case the definition of the integral length scale in equation 1.29 cannot be used since the integral does not converge. A threshold correlation value is then defined, and the integral length scales are computed as

$$L_{ij,\alpha}^k = \int_0^{r_\alpha} R_{ij}((r_k, 0, 0), t) dr_k \tag{3.17}$$

Here the threshold is taken such that $R_{ij}^k(r_\alpha) = 0.5$, and the corresponding integral length scales are denoted $L_{ij,50}^k$. This unconventional definition unfortunately limits us to qualitative and comparative analysis, since it underestimates the "true" integral length scale value. The evolution of the 50 percent integral length scales for water and DPS is shown in figure 3.38. The linear increase of integral length scales advanced by Thompson and Turner (1975), Hopfinger and Toly (1976) is found in water: all integral length scale increase proportionally to the grid distance until the influence of the surface is felt and integral length scales begin to decrease. This surface influence is discussed in the next chapter, but it can be already mentionned that the surface influenced depth increases with polymer conentration and can reach up to 80 mm for $L_{xx,50}^x$ at 50 or 100 ppm concentrations. In water, length scales involving the horizontal velocity components increase more than the ones involving the vertical velocity components, as evidenced by Brumley and Jirka (1987). More surprisingly, the evolution of integral lentghscales with Z in DPS also seem to follow a linear trend, but with a steeper slope. All integral length scales are generally higher for DPS than for water at the same altitude. This suggests that polymer promotes the growth of large structures of turbulence. Increased integral lenghscales in DPS were observed as well by De Angelis

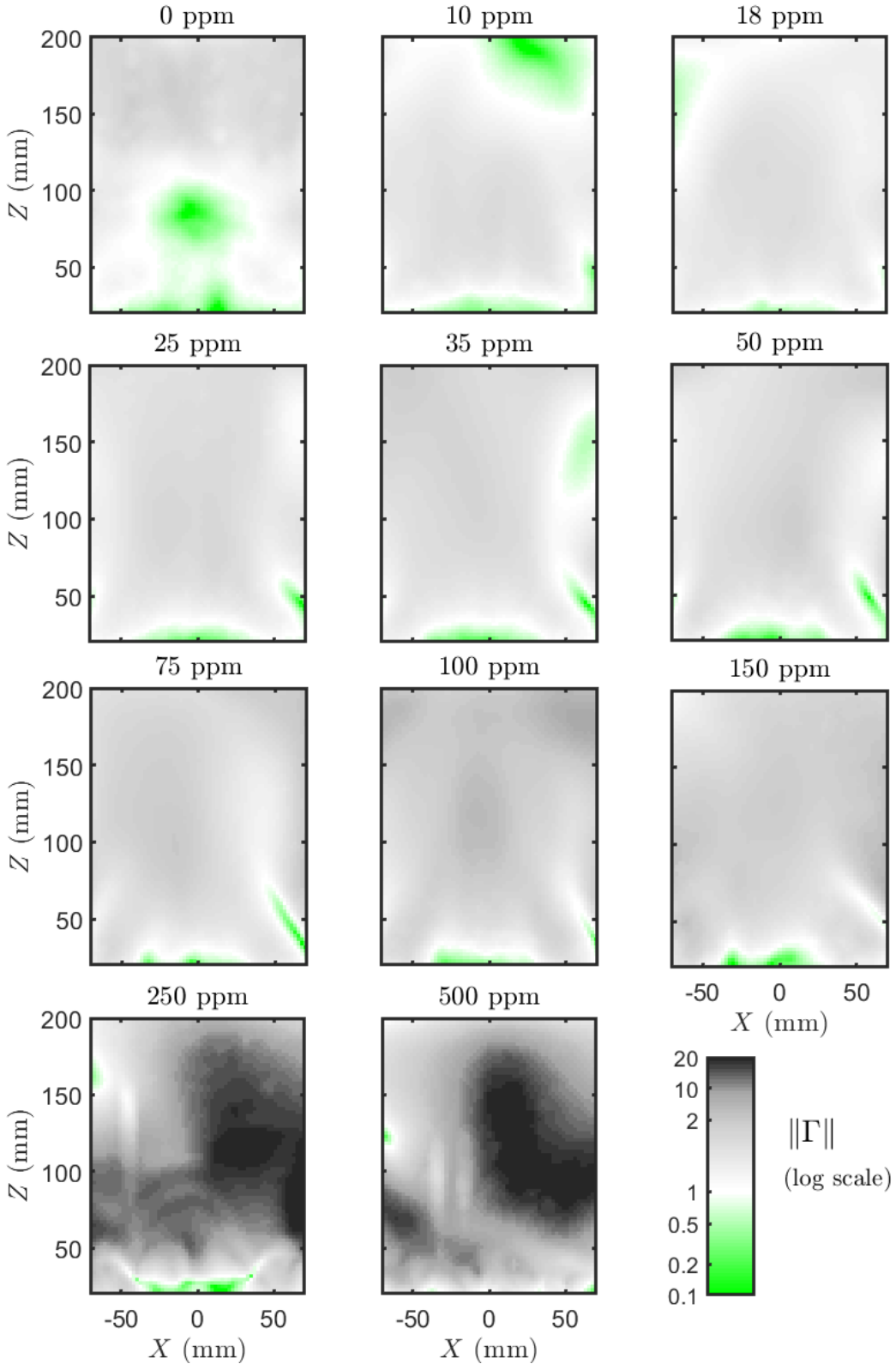

Figure 3.36 – Fields of mean flow over turbulence ratio $\|\Gamma\| = \sqrt{\Gamma_{xx}^2 + \Gamma_{zz}^2}$ for water and DPS at different concentrations. The colormap for $\|\Gamma\|$ values is in log scale.

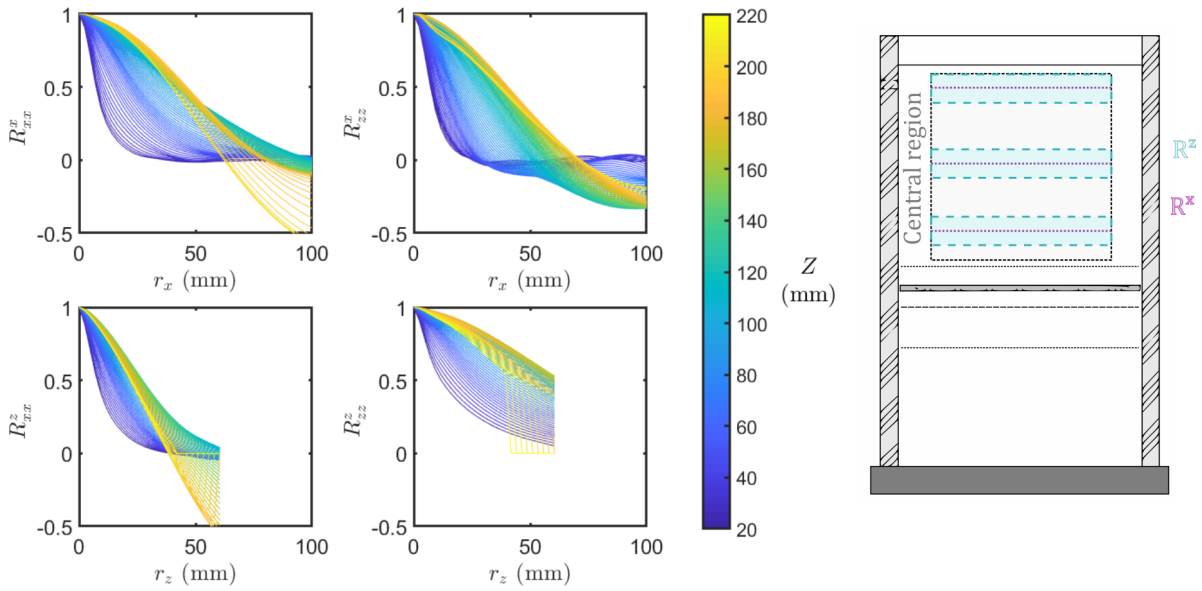

Figure 3.37 – Example of correlation coefficients as a function of Z for 50 ppm XG solution. The sample zones are sketched on the right hand side of the figure: purple lines are sample lines for horizontal correlation, blue rectangles are sample areas for vertical correlations. Both are scanned through the central region to get the curves of the left hand side of the figure.

et al. (2005); Liberzon (2011); Liberzon et al. (2006). The slope of $L^x_{xx,50}$ curves is about 0.06 for water, 0.10 for 10 ppm XG solutions, and up to 0.30 for 50 ppm solutions (dashed lines on the figure). Values are reported in table 3.4. Because the 50 percent length scale is used here, $L_\infty \equiv L^x_{xx}$ is slightly underestimated and the slope value for water is below the 0.1 reference found by Thompson and Turner (1975). For the horizontal length scale of horizontal fluctuations $L^x_{xx,50}$ the effect of polymer seems to reach its maximum efficiency at 50 ppm concentration, since the slope of the 100 ppm curve is not further increased. The same effect is observed on the other length scales $L^x_{zz,50}$, $L^z_{xx,50}$ and $L^z_{zz,50}$ where the slope of the 50 ppm curves (green curve) at Z<120 mm (far from the surface influence) is always the steepest. The vertical length scale of vertical velocity fluctuations seems to increase quicker with polymer concentration than the other ones. $L^x_{xx,50}$ at Z=120 mm increases from 19 mm at 10 ppm to 36 mm at 50 ppm while it increases from 23 mm at 10 ppm to 45 mm at 50 ppm for $L^z_{zz,50}$ at the same altitude. The large structure enhancement attributed to polymer thus seems to preferentially act on the vertical motion. We also notice that the evolution of this last length-scale with Z is no longer linear for the highest concentrations measured.

C_{XG} (ppm)	$\frac{dL^x_{xx,50}}{dZ}$	$\frac{dL^x_{zz,50}}{dZ}$	$\frac{dL^z_{xx,50}}{dZ}$	$\frac{dL^z_{zz,50}}{dZ}$
0	0.06	0.02	0.02	0.04
10	0.10	0.08	0.08	0.11
18	0.12	0.11	0.08	0.15
25	0.27	0.16	0.14	0.23
50	0.30*	0.18	0.18*	0.50*
100	0.27*	0.14	0.14*	0.34*

Table 3.4 – Slopes of the linear part of integral length scales profiles versus depth in water and DPS. Starred values are those for which the linear trend is only observable for Z<125 mm (arbitrary value).

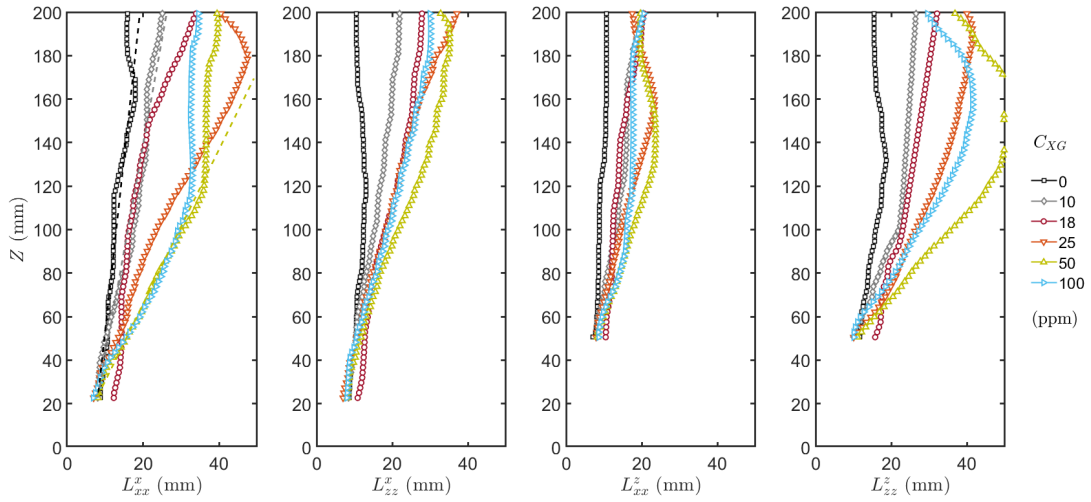

Figure 3.38 – Integral length scales of OGT defined at 50% correlation for water (squares) and DPS at 10 ppm (diamond), 18 ppm (circles), 25 ppm (downward triangles), 50 ppm (upward triangles) and 100 ppm (right pointing triangles). Dashed lines are the linear approximations of $L^x_{xx,50}$ in the bulk region for water, 10 ppm and 50 ppm DPS.

3.4.6 Summary and conclusions

In this section, an experimental study of oscillating grid turbulence in water and dilute polymer solution was detailed. The analysis was performed in a vertical plane of symmetry of the tank, in two regions. The full tank region is defined as the space between the top of the grid's oscillations and the free surface was used to study mean flow characteristics and turbulence properties in the tank. The close grid region (CG) focused around the grid sweep zone, in which phase resolved measurement could be performed, was used to investigate the oscillatory behaviors of the flow and the mechanisms of turbulence generation by the grid. POD analysis were also performed in both regions to complete the analysis. The main results of these observations are summarized hereinafter.

3.4.6.a Summary of the main results

OGT in water: Even though the original purpose of OGT was to study turbulence alone in absence of mean flow, the installation of persistent flow structures can not be avoided, and the mean velocities are not negligible. As a matter of fact, the mean-to-turbulence ratio can be quite poor in some regions of the tank. As for the structure, two main counter-rotative recirculating vortices are observed on the sided of the ROI. They are caused by the interractions between the flow induced by the grid and the walls of the tank. Speaking of the flow around the grid, the interactions between jets and wakes, defined as the origin of turbulence in the tank, has been observed experimentally for the first time. It was shown that the periodic component of the flow, corresponding actually to these jets and wakes, was only significant in the grid sweep region for water. There the oscillatory motion interacts with the mean flow, and generates turbulence. The oscillatory nature of the mean flow and its generation of large scale structures of turbulence is quite complex. When moving away from the grid sweep region, periodic motion quickly becomes negligible compared to turbulence. Turbulence also has its main intensity within the grid sweep region, and is advected away by both mean and oscillatory motion. Above the grid, its intensity decays according to the well known relationship of Hopfinger and Toly (1976). The integral length scale of turbulence

linearly increase with the altitude as predicted by Thompson and Turner (1975). Spatial homogeneity of turbulence is quite good in the central region of the tank. Turbulence is statistically not isotropic, its vertical fluctuations being stronger than the horizontal ones.

Effects of polymer addition in the dilute regime: Oscillating grid turbulence in water has been the subject of many studies in the last 40 years. On the other hand, OGT in dilute polymer solutions has been investigated in only a handful of studies, none of which considered the effects of polymer on mean flows or turbulence distribution and decay in the tank. In this work we showed that the first effect of polymer addition was an enhancement of the mean flow, evidenced by an increased intensity of the two side vortices, and the appearance of a global up-going effect in the center of the tank. This leads to mean to turbulence ratios even higher than in the water case. In the grid region, the oscillatory flow is also enhanced. Periodic fluctuations and periodic flow structures are observable outside of the grid sweep zone, and the horizontal distribution of oscillatory component inside the sweep region is modified. Turbulence intensity is concentrated inside the sweep region and far from the walls of the tank. Turbulence production is also evidenced in the region corresponding to the mean flow vortices. The energy exchanges between mean, organized, and turbulent components of the flow are enhanced, and turbulence seems able to give back energy to the oscillatory motion. In the rest of the tank, the evolution of turbulence with the distance to the grid is also altered. Turbulence is found to be less isotropic, with a vertical component further increased compared to the horizontal one. This is consistent with the observations of Cai et al. (2009); Doorn et al. (1999): turbulent fluctuations in the same direction than the mean flow (here the up-going motion) are enhanced with respect to the transverse ones. While n_x and n_z remain almost equal in dilute solutions, the decay rate of the two component in semi dilute solutions is no longer the same. The decay of horizontal components is faster than the vertical one and anisotropy increases with the altitude. Homogeneity however remains almost unchanged in the central region of the tank. Finally, the integral length scales of turbulence are also found to increase linearly with the distance from the grid, but their increasing rate is greater than that of water. The vertical length scales seem to increase faster than the horizontal ones, which reinforces with the picture of an increased anisotropy. In appendix C, this large scale enhancement is confirmed by POD analysis. Energy concentrates in lower order modes for DPS, evidencing a shift of energy towards larger scales of the flow. The damping of small scales mentionned by Wang et al. (2016) is observed here as well.

Polymer concentration regimes: Polymer science and rheology provide many information on the concentration dependency of polymer solutions properties. In particular, several entanglement states are possible based on the solution's concentration: dilute, semi-dilute or concentrated. Here the evolution of flow properties inside the dilute range and at the edge of the semi-dilute range were investigated. The results show that three main hydrodynamic regimes could be defined. Between 0 and around 50 ppm, polymer addition leads to an organization of the flow and a shift of energy towards large structures. This is characterized by a strong mean flow enhancement, a slight increase in integral length scales and anisotropy, with only a slight weakening of turbulence. Between 50 ppm and around 100 or 150 ppm, the structure of the flow reaches a stagnation state, while attenuation of turbulence keeps increasing. Above 150 ppm, the flow structures eventually collapse and both turbulence and mean flow are reduced. The third regime starts at a critical concentration really close from the 100 ppm critical concentration marking the onset of the semi-dilute entanglement regime, so that all the evolution of hydrodynamic properties within this regime may be at-

tributed to interactions between polymer chains [5]. The two first regimes are however both part of the dilute regime, so the explanation of the different trends has to be found somewhere else. One possible explanation may be a competition between variable viscosity effects and polymer chains elasticity. The existence of several hydrodynamic subregimes of the dilute domain were observed by Ouellette et al. (2009) for another polymer (Polyacrylamide).

3.4.6.b Outlook

The study detailed above is only a first step towards the understanding of oscillating grid turbulence mechanisms in DPS. Interpretation of available additional data, in other planes of measurement will come as a complement of the results presented here. Ultimately, the reconstruction of flow statistics in the three dimensions could be possible at specific locations of the volume of measurement. Three dimensional three component measurements would yet be needed to estimate all the terms of the kinetic energy equations and fully describe the generation and evolution of turbulence in the tank. POD has also proved to be an efficient and low, time and data, space consuming tool for the study of scale by scale behavior and of polymer influence on the flow (appendix C). Once a framework for the identification of oscillatory motion in the OGT is developped, it could even be used to study the interactions between mean, oscillatory and turbulent components of the flow.

[5] The interactions are first electrical in the un-entangled semi-dilute regime, and then mechanical with polymer chains entanglement (Wyatt and Liberatore, 2009)

Chapter 4

Hydrodynamics and gas-liquid mass transfer at a flat interface enhanced by bottom shear turbulence

> Dans un œuf, y'a du blanc et du jaune. Eh bien plus on mélange, plus il n'y a que du jaune !
>
> Coluche

Contents

Abstract (En)

The goal of this final chapter is to provide experimental data for a better understanding of near surface turbulence and mass transfer in dilute polymer solutions. It starts with a summary of the literature background regarding turbulence and mass transfer at flat interfaces in water, and an anticipation of the probable non-Newtonian effects. The experiments made during this thesis are introduced, along with specific data treatment procedures. In a first result section, the hydrodynamics under the free surface is described. The concepts of horizontal stretching of velocity structures and of energy transfer from vertical to horizontal motion, evidenced in water, remain valid and even enhanced in DPS. Nevertheless, the viscous sub-layer properties and the hydrodynamics within differ. In the following sections, gas concentration statistics and turbulent mass fluxes are studied for a single DPS concentration. In both water and DPS ass transfer enhancement by turbulence is the result of a complex combination of surface renewal and injection events. Yet differences already arise, such as vertically elongated scalar structures, and increased mass transfer events at higher depths in DPS compared to water.

Résumé (Fr)

L'objectif de ce dernier chapitre est d'apporter des données expérimentales pour une meilleure compréhension de la turbulence en proche surface et du transfert de masse qu'elle implique dans des solutions de polymère dilué. Il débute par un rapport bibliographique sur la turbulence et le transfert de masse aux interfaces planes, au cours duquel les possibles effets non-Newtoniens sont également discutés. Les expériences effectuées et les procédures de traitement des résultats sont ensuite détaillées. Une première partie de résultats détaille l'hydrodynamique proche de la surface libre. Les concepts principaux d'élongation horizontale des structures, et de transfert d'énergie de la composante verticale vers les composantes horizontales de vitesse, établies pour l'eau, sont également mises en évidence et même accentuées pour le polymère. Néanmoins des différences significatives des propriétés de la sous couche visqueuse et de l'hydrodynamique en son sein sont observées. Dans les deux parties suivantes, les statistiques de concentration de gaz dissout et les flux de masse turbulents sont étudiés pour une expérience en solution de polymère dilué et une en eau. Dans les deux cas, l'accélération du transfert de masse par turbulence est la conséquence d'une combinaison complexe d'évènement d'injection et de renouvellement de surface. Des différences apparaissent cependant, comme une élongation verticale des structures scalaires et l'existence d'évènements de transfert de masse significatifs à des profondeurs supérieures dans le fluide non-Newtonien par rapport à l'eau.

Publications

Lacassagne T., EL Hajem M., Morge F., Simoëns S., and Champagne J.-Y. Study of Gas Liquid Mass Transfer in a Grid Stirred Tank. *Oil & Gas Science and Technology – Revue d'IFP Energies nouvelles*, 72 (1), Jan. 2017. doi: 10.2516/ogst/2017001.

For many industrial and environmental applications involving two-phase flows, higher diffusivity of chemical species in the gas than in the liquid phase, and low solubility in the liquid allows the gas side concentration to homogenize efficiently while a concentration boundary layer develops on the liquid side. This concentration boundary layer interacts with near surface motion. In this thesis, the focus is made on this type of gas-liquid mass transfer processes, ruled by the liquid side phenomenon.

The aim of this chapter is to provide experimental data on turbulent dissolution and mass transfer mechanisms of low diffusivity gases in water, and on the influence of shear thinning and/or viscoelasticity on these mechanisms. By controlling the exchange area a, we could eventually relate mass transfer mechanisms to K_L alone, and thus have further insight on the fundamental process of mass transfer in non-Newtonian liquids. The study of near surface hydrodynamics and mass transfer mechanisms in such a simplified situation is a necessary first step for the understanding and modeling of turbulent mass transfer in more complex cases, such as bubbly flows.

4.1 Background

Turbulent mass transfer at gas-liquid interface has been a topic of interest of many fields for a very long time, almost 100 years since the work of Lewis and Whitman (1924), and remains open today. The reason is that the physical basis of the process are still unclear, especially when adding non-Newtonian effects to an already complex set of phenomena. How does turbulence behave when approaching a free surface? What are the interactions between turbulence and diffusion? How efficient is turbulence close to the interface in terms of advection and mixing? What are the relative impacts of the key parameters (surface pollution, surface area, turbulence, diffusivity, viscosity, fluid rheology...) on the efficiency of mass transfer?

As shown in this section, a huge amount of work made throughout the years has already brought together part of the answers. There are many ways to organize such a huge literature. One of them is to distinguish between what could be called "realistic" studies, and fundamental studies. The first type is directly linked to a well defined industrial or environmental application, and investigates mass transfer situations that are most of the time complex, involving many different phenomena. Experimental measurements can be made in on site / real life situations (field measurements in rivers, seas, lakes harbors (Gharahjeh et al., 2017; Jones and Smith, 1977)), in industrial or lab scale stirred tanks (de Lamotte et al., 2017; Gabelle et al., 2011) or in bubble columns (Barrut et al., 2013). The focus is made on global mass transfer properties, mostly through the quantification of mass transfer velocity (K_L or K_La). Numerical simulations can also be performed, on full scale or down scaled models. For these simulations to be accurate however, the modeling of physical phenomena occurring at scales smaller than the computed ones (turbulence, molecular interactions, chemical reactions...) is required. Such modeling is the result of more fundamental studies.

This second type of study is based on simplifications of the geometry, the fluid property or the boundary conditions. It facilitates local measurements, direct numerical simulations or theoretical approaches, and is used as a first step to understand the physical interactions between several parameters and to develop the models later used in global simulations or measurements. Controlled turbulence can be experimentally generated by fixed (McComb et al., 1977; Simoens and Ayrault, 1994; Vonlanthen and Monkewitz, 2013) or oscillating grids (Janzen et al., 2010; Liberzon et al., 2009), or more sophisticated experiments (Cocconi et al., 2017; Liberzon et al., 2005; Variano and Cowen, 2013) in both Newtonian and non-Newtonian media. The gas-liquid interface effects can be studied around single rising

bubbles (Calderbank et al., 1970; Valiorgue et al., 2013), bubbles swarms (Alméras et al., 2015; Bouche et al., 2013), Taylor bubbles in pipes or Hele Shaw cells (Butler et al., 2016; Kuhn and Jensen, 2012; Poryles and Vidal, 2017) or under free surfaces in stirred tanks and channel flows (Brumley and Jirka, 1987; Janzen et al., 2010; Turney and Banerjee, 2013; Variano and Cowen, 2013). Similar configurations can be studied numerically using Large Eddy Simulation (LES) or DNS (Bodart et al., 2010; Falcone et al., 2018; Hasegawa and Kasagi, 2009; Herlina and Wissink, 2016; Magnaudet and Calmet, 2006). Recent advances in computer performance make it nowadays possible to use DNS to study small scale phenomena such as polymer-turbulence interactions (De Angelis et al., 2005; Nguyen et al., 2016).

Since the goal of this chapter is to investigate the fundamental mechanisms of turbulent gas-liquid mass transfer at flat interfaces in presence of non-Newtonian fluids, most of the references presented here belong to this second type of studies. First the interaction between bulk liquid turbulence and free surfaces in water are presented. The actions of turbulence on gas-liquid mass transfer at this free surface are then briefly explained, and a list of the most used models for mass transfer is proposed [1]. Finally , the non-Newtonian effects on turbulence and mass transfer are discussed. An overview of the main references is available in table 4.1.

4.1.1 Turbulence approaching flat gas-liquid interfaces

In order to be able to understand its impact on gas-liquid mass transfer, one first needs to know the properties of turbulence close to the interface. This is all the more important than mass transfer events occur in very thin sub-layers, typically smaller than a few millimeters, under the surface (Jirka et al., 2010). The first step is thus to study how turbulence behaves within these thin sub-layers.

4.1.1.a Turbulence behavior close to the interface

Surface influenced layer: The first question to ask oneself is the depth at which the interface can actually be "seen" by the turbulence. This depth is usually defined as the surface influenced, blocking, or source layer, and its depths is conceptually assumed to be about one integral length scale of the bulk turbulence. In other words, the surface is supposedly only able to act on eddies once they touch it, and so the maximum depth of influence of this interface is about the size of the larger existing eddies. In the case of a flat horizontal interface, only vertical motion is constrained by the free surface, and so vertical velocity fluctuations in the source layer are supposed to be damped while horizontal fluctuation may either increase or decrease. Approaching the interface, energy should thus be transfered from vertical to horizontal motion. Eddies originally isotropic should deform and strecth along horizontal dimensions. This pictured view was stated by Hunt and Graham (1978), later completed by Hunt (1984), and is considered as the first theoretical framework of turbulent boundary layer at a flat free surface. This theory was first confirmed by Perot and Moin (1995) with DNS simulation and the pioneer measurements of Brumley and Jirka (1987) who evidenced that the depth of the source layer was about one "undisturbed" integral length scale. The "undisturbed" integral length scale is the one that would have been measured at the location of the interface if there were no interface. It thus depends on the bulk turbulence properties only. The dominance of horizontal scales in the blocking layer has been confirmed both numerically (Calmet and Magnaudet, 2003; Magnaudet and Calmet, 2006) and experimentally

[1] The models discussed here are only relative to mass transfer at plane free surfaces (deformed or not). A wide range of model exists for bubbly flows, but is not detailed here.

(Janzen et al., 2010; Variano and Cowen, 2013). More recently, Bodart et al. (2010) observed that velocity dynamics in the source layer are mostly independent of the surface boundary condition, which suggests that the results of Hunt and Graham's theory (hereinafter refereed to as HG) applies equally well to clean, contaminated and no-slip surfaces up to a certain proximity with the interface.

This higher level of proximity is defined by another smaller typical depth called the viscous sub-layer, which scales as (Brumley and Jirka, 1987; Magnaudet, 2003):

$$\delta_\nu = L_\infty Re_T^{-1/2} \tag{4.1}$$

This sub-layer is defined as the depth from which a typical eddy adjusts to the boundary condition set by the interface by viscous effects. In this region, vertical gradients of horizontal velocity fluctuations fall to zero (Magnaudet and Calmet, 2006). According to Hunt (1984), this should lead to a reduced increase rate of horizontal velocity fluctuations for clean free surfaces. For dirty surface, the horizontal surface velocity is also limited, and this additional boundary condition leads to a decrease in horizontal velocity fluctuations.

Several experimental studies (Brumley and Jirka, 1987; Herlina and Jirka, 2008; Janzen et al., 2010; Variano and Cowen, 2013) and DNS simulations Calmet and Magnaudet (2003); Magnaudet (2003); Magnaudet and Calmet (2006) showed that, even if HG theory holds very well in most of the blocking layer, it does not accurately predict the behavior of horizontal velocity fluctuations in the viscous sub-layer. Results of Brumley and Jirka (1987); Herlina and Jirka (2008); Janzen et al. (2010) found that a peak in horizontal velocity fluctuations exists slightly under the interface, and the shape of the rms profile is analog to what it would have been for a contaminated interface (figure 4.1, full green line). The reasons advanced by Herlina and Jirka (2008) for this deviations is that the HG theory does not take into account several second-order effects, e.g. it assumes a uniform (*i.e.* constant with depth) dissipation rate in the whole source layer. It thus does not predict the peak of horizontal fluctuations at depth equal to the viscous sub-layer first evidenced by Brumley and Jirka (1987). However, recent DNS in absence of mean shear by Herlina and Wissink (2014) do not show such a trend and present profiles shape that are qualitatively closer to the HG prediction for clean interfaces. The experiments by Variano and Cowen (2013) also show a peak of transverse velocity fluctuations, and they explain it by the fact that despite skimming and cleaning of the surface, residual surfactants may still be present at the interface thus leading to the polluted type behavior in the viscous sub-layer. The difference between literature and experimental data could then either be explained by residual surface pollution in experiments, unrealistic boundary conditions in simulations, or by a mean flow inducing its own turbulence through wall and surface interactions.

Zoomming close to the interface, it is possible to define a last typicall sub-layer, named the Kolmogorov sub-layer, in which the flow is assumed to be purely irrotational, viscosity dominant velocity, and all fluctuation to decay linearly along the vertical direction. According to Brumley and Jirka (1987) and Magnaudet (2003), it should scale as

$$\delta_\eta = 2L_\infty Re_T^{-3/4} \tag{4.2}$$

The irrotational flow assumption should yet only be seen from the statistical point of view: nothing prevents instantaneous structures from reaching the interface, but fluctuations are damped by viscosity. All the previous sub-layers are summarized in figure 4.1. In stirred tanks (Herlina and Jirka, 2008; Janzen et al., 2010) or RASJA tanks (Variano and Cowen, 2013), typical values of sub-layers are around 3 to 8 cm for the source layer, 1 to 4 mm for the viscous and below 1 mm (0.5 to 1) for the Kolmogorov one. These values decrease with increasing Reynolds number. Experimental observation of the hydrodynamics within

these sub-layers is thus very challenging, and numerical simulation of equivalent situations quite computationally expensive.

Spectral behavior: Despite the significant amount of work around HG theory and free surface turbulence, only a few studies present measured velocity spectra in the vicinity of the interface (Brumley and Jirka, 1987; Herlina and Jirka, 2008; Variano and Cowen, 2013). In these studies, reminiscence of the -5/3 slope, characteristic of isotropic turbulence, is found, but is most of the time too subtle for thorough analysis. In the work of Variano and Cowen (2013) the energy spectrum of the vertical velocity fluctuations close to the interface shows a lower intensity at all scales, and a larger relative importance of small scales for spectra at larger depths. This feature seems consistent with the HG theory of preferential damping of the vertical motion.

A recent DNS study by Flores et al. (2017) suggests that the -5/3 slope observed could be an intrinsic feature of near surface turbulent, independent on the homogeneity and isotropy (or anisotropy) of the forcing, under the strong vertical shearing of horizontal velocity fluctuations. The energy transfer from vertical to horizontal motion, under free surface influence, is assumed to lead to an HIT type range for horizontal velocity components. This has however only be shown in a high mean shear situation (channel flow), and remains unverified for turbulence without (or with negligible) mean shear.

4.1.1.b The influence of surface pollution

An important factor affecting the behavior of turbulence approaching a gas-liquid interface is the cleanliness of this interface. Clean surfaces allow horizontal velocity fluctuations at the very limit between the gas and the liquid. On the other hand, when a free surface is covered by organic or surface active material (surfactants), the rheological properties of these materials may be such that it creates a tangential stress and damps turbulent velocity fluctuations (Herlina, 2005; McKenna and McGillis, 2004a; Wissink et al., 2017). From a hydrodynamic point of view, turbulence close to highly polluted interfaces is thus still different from that of turbulence close to a rigid wall (Wissink et al., 2017).

The mechanisms responsible for this damping have been extensively studied by McKenna (2000); McKenna and McGillis (2004a) and can be explained as follows. Surfactant are most of the time organic molecules composed of an hydrophobic part (the tail) and an hydrophilic part (the head). In air water systems, they tend thus tend to align at the interface and create an organic surface film. When an upcoming eddy impacts the surface film, it moves surface active molecules along the interface, but the repulsion of the neighbor surfactant molecules creates an extra tangential stress. This tangential stress is balanced by an increased viscous stress in the fluid, which damps the turbulent eddy, and the apparent viscous sub-layer is increased. This last phenomenon is a manifestation of the Marangoni effect. In the viscous sub-layer, the shape of rms profiles sketched in figure 4.1 is modified: the decay rate of $\langle u_z' \rangle_{rms}$ curve is increased, and the $\langle u_x' \rangle_{rms}$ show a purely decreasing trend, without any specific rms peak at the viscous sub-layer depth Herlina and Wissink (2014). This could indicate that the aforementioned difference in trends for $\langle u_x' \rangle_{rms}$ profiles could be due to something else different than surface contamination of the experiments.

The presence of surfactant has a great impact on mass transfer , both at flat free surfaces (Hebrard et al., 2009; Herlina and Wissink, 2016; Jamnongwong et al., 2010) and around bubbles (Jimenez, 2013; Sardeing et al., 2006) since they affect both turbulence and molecular diffusion in thin boundary layers at the interface.

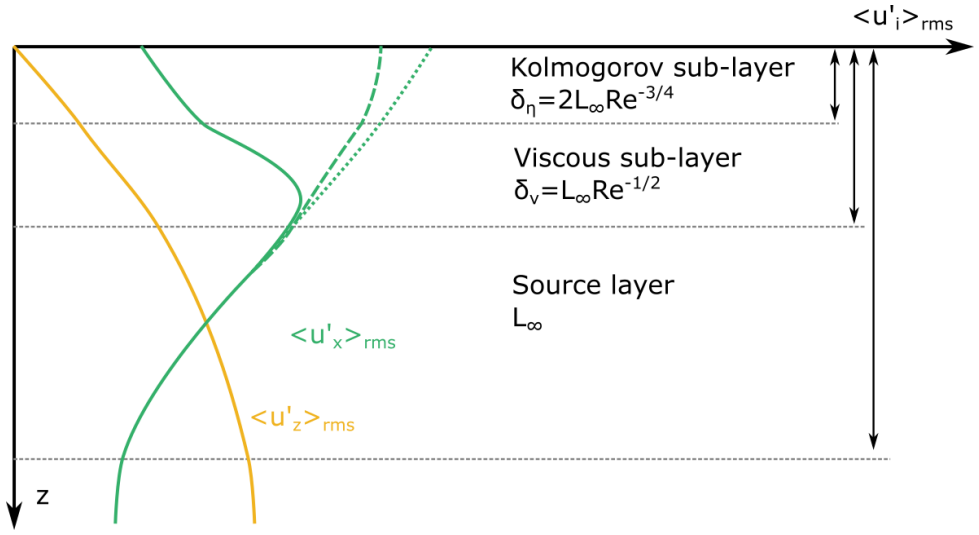

Figure 4.1 – Sketch of the characteristic hydrodynamic sub-layers of near surface turbulence adpated from Brumley and Jirka (1987). Orange curve is the rms of vertical velocity fluctuations generally agreed on in the litterature (Brumley and Jirka, 1987; Herlina and Wissink, 2014; Hunt, 1984; Jirka et al., 2010; Wissink et al., 2017). Green curves are rms of horizontal fluctuations predicted by HG (dotted line), obtained by DNS by Herlina and Wissink (2014) (dashed) and measured experimentally by Janzen et al. (2010); Variano and Cowen (2013) (full).

4.1.1.c Turbulence and surface shape: limitation of flat surface hypothesis

Depending on its intensity and length scales, bottom shear turbulence may also induce free surface deformation, oscillations, or even breakup and atomisation. The relationship between liquid phase bulk turbulence and free surface shape has been investigated by Brocchini and Peregrine in two extensive articles (Brocchini and Peregrine, 2001a,b). They found that the shape of a free surface depends on two main turbulence parameters: the turbulent velocity and integral length scale at the interface. Several behaviors, from flat to splashing trough for example wavy or bubbly can be defined, many free surface phenomena such as hydraulic jumps or ships wakes can be defined in terms of liquid turbulence paths in the velocity-lengtscale plane. The flat domain is found only for low intensity turbulent flows. Increasing the intensity, waves may appear more or less rapidly depending on the typical length scale of turbulence. For very high turbulence intensity, the free surface ultimately breaks into pieces the size and shape of which depends on the length scale of turbulence.

Chiapponi et al. (2012) performed an experimental investigation of oscillating grid turbulence and its place in this velocity-length scale diagram. By varying stroke, frequency, and grid-surface distance, they managed to reach several free surface domains (flat, wavy...) and to find links between small scales of turbulence and free surface elevation in the weak turbulence regime. For moderate grid Reynolds numbers, the free surface fluctuations when they arise depend on the grid frequency, whereas for high grid Reynolds number, the free surface disturbance is completely uncorrelated from the grid movement. For low Re_g, grid motion does not induce any surface oscillations. This study has been used in the present work to anticipate that grid stirring parameters would not lead to surface oscillation.

4.1.2 Mass transfer at flat gas-liquid interfaces

The second step can now be taken, that is to say estimating the effect of hydrodynamics on mass transfer at the interface. Historically, the question was addressed a long time before the

first models and observations on near surface hydrodynamics were made, and so the first models appeal to very conceptual views. The increasing understanding of turbulence and the access to new measurable parameters characterizing the hydrodynamics of turbulent liquid flow then made it possible to try and estimate mass transfer velocities as a function of bulk turbulence parameters. The most recent trend in mass transfer coefficient estimation is to use an hydrodynamic parameter accessed not through bulk turbulence measurement but through free surface hydrodynamics visualization. This parameter is the root mean square value of surface divergence, the divergence of horizontal velocities in the interface plane. It has proven to be quite efficient in estimating K_L values for a wide range of situations. In this section, the main principles of gas-liquid mass transfer at a flat surface as considered in this thesis are first recalled, and a non exhaustive list of conceptual, hydrodynamic, and surface divergence models is proposed. Key results from the latest studies are summarized. The boundaries of our hypothesis of a flat and clean surface are explored, and the effects of wind shear, surface deformation and surface pollution in terms of mass transfer are discussed in appendix E.

4.1.2.a Main principles

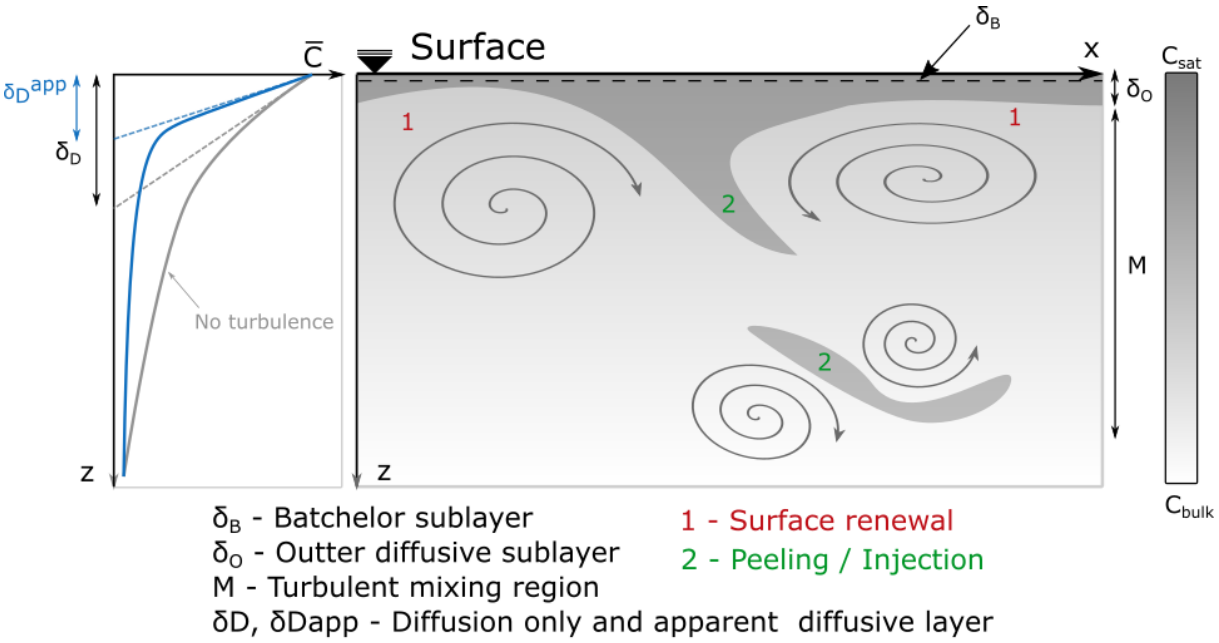

Figure 4.2 – Main principles of turbulent mass transfer at a flat interface. On the left hand side of the figure, the contraction effect of the apparent diffusive boundary layer in presence of turbulence. On the right hand side, an illustration of surface renewal and peeling/injection events and of the typical scalar sub-layers.

In chapter 1, section 1.1.2.b, the concept of interfacial liquid film is illustrated. If no liquid side motion occurs, this liquid film develops according to Fick's laws of diffusion, and the mass transfer velocity is ruled by diffusion only. When liquid phase motion arise, mass transfer velocity is modified by the interactions between velocity structures and the diffusive boundary layer. It is usually considered that the main effect of fluid motion is to remove saturated liquid from the vicinity of the interface, thus making the boundary layer thinner and enhancing mass transfer by diffusion. This is the principle of surface renewal or film

renewal (Danckwerts, 1951; Higbie, 1935). Another mechanism responsible for mass transfer has been recently evidenced (Herlina and Jirka, 2008; Variano and Cowen, 2013): peeling of the boundary layer by velocity structures resulting in the injection of saturated fluid inside the bulk where it is mixed by turbulence. In turbulent flows, the picture is made complex by the wide range of structure sizes and energy, and the various ways eddies can interact with the scalar boundary layer. This results in an intricate combination of surface renewal and injection event responsible of global turbulent mass transfer. The hypothesis and conditions used to assess the relative impact of these events are discussed hereinafter. A sketch of the renewal and injection events is shown in figure 4.2.

Before going any further, one may define *a priori* several sub-layers characteristic of the dissolved gas concentration in a turbulent liquid, in a way similar to what has been done for turbulent hydrodynamic sub-layers. The first one is called the outer diffusive layer and can be seen as the apparent boundary layer as caused by large turbulent eddies by the interface (Herlina, 2005). According to Brumley and Jirka (1987), it scales as

$$\delta_O = 2L_\infty Sc^{-1/2} Re_T^{-1/2} \tag{4.3}$$

On the other hand, the Batchelor sub-layer is defined as the boundary caused by the smallest concentration eddies, in reference to the Batchelor micro scale of turbulent scalar on which it is based. It is of order

$$\delta_B = \eta Sc^{-1/2} \tag{4.4}$$

Magnaudet and Calmet (2006) showed that in DNS of a turbulent channel flow, a peak of scale concentration variance is observed at a depth close to δ_O. For high Schmidt number gases, δ_B correspond to the smallest theoretical sub-layer that can be defined. Within the Batchelor sub-layer, the mean concentration profile evolves linearly with depth. This is illustrated in figure 4.3

A precise estimation of these sub-layer scales requires a good knowledge of the properties of turbulence approaching the interface, which are not always easily accessible even for quite fundamental situations. In complex situations or industrial applications, one generally needs to estimate a global mass transfer velocity K_L, if possible without having to perform extensive measurements of local turbulent properties or scalar concentrations. In order to predict mass transfer velocities/coefficients based on simple hydrodynamics of this liquid phase, several 1D models have been developed throughout history. What follows consist in a non-exhaustive brief review of the milestones models necessary to understand the concepts of mass transfer under the interface. Further details are provided by literature review in Herlina (2005).

4.1.2.b History of mass transfer models

Conceptual models: Historically, the first assumption made was that turbulent structures could not penetrate the diffusion layer (Lewis and Whitman, 1924) and that two distinct regions could be distinguished: a pure diffusion sub-layer of depth δ_D, and a turbulent mixing region beneath this sub-layer. The mass transfer coefficient K_L can thus be expressed by Lewis and Whitman's film model as

$$K_L = \frac{D}{\delta_D} \tag{4.5}$$

This rather basic conceptual model can also be seen as a first order approximation of mass transfer coefficient in more complex situation. Indeed, the effects of many mass transfer relevant phenomena such as chemical reaction or turbulence can be expressed by a sta-

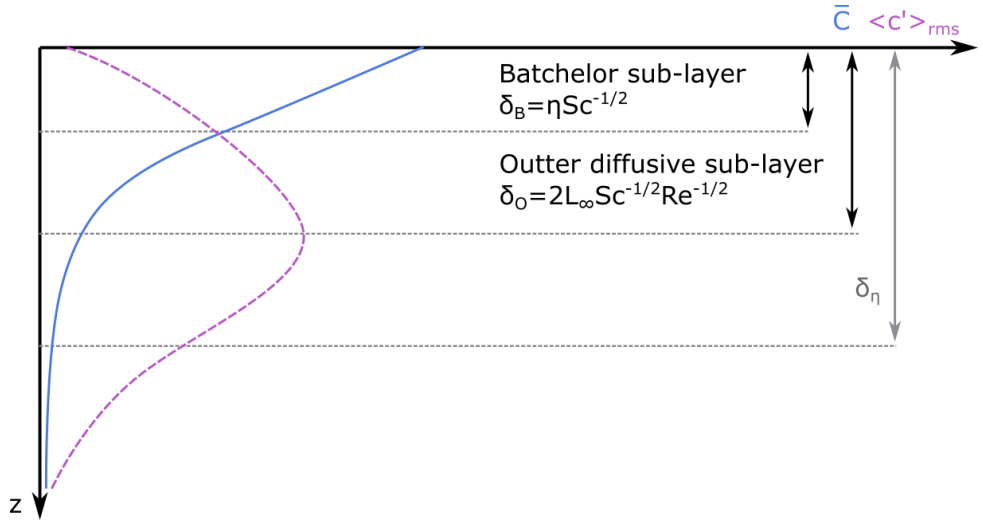

Figure 4.3 – Sketch of the characteristic scalar sub layers of near surface turbulence adpated from Brumley and Jirka (1987), and shape of the profiles of mean concentration (blue full line) and concentration variance (purple dashed line) obtained numerically by Magnaudet and Calmet (2006) and experimentally by Janzen et al. (2010) among others.

tistical modification of the size of the diffusion layer. All that is needed is then an estimation of the statistically averaged apparent diffusive layer δ_D^{app} accounting for those effects. Providing that one is able to measure passive scalar concentration profiles under the interface, δ_D^{app} can then be written as:

$$\delta_D^{app} = \frac{C_{sat} - C_b}{\partial \overline{C} / \partial z_{z=0}} \tag{4.6}$$

If turbulence is present in the liquid phase, then the apparent diffusive layer δ_D^{app} is thinner than the one that would establish under purely diffusive conditions (see figure 4.2), and so K_L is increased. It is, by that mean, possible to evaluate roughly the effects of turbulence on mass transfer velocity using this very old model designed on a pure diffusion hypothesis, fueled by information on sub-surface concentration profiles.

Back to the original time-line, further studies introduced the idea that turbulent eddies could break inside this diffusion layer and replace it with "fresh", accelerating mass transfer in doing so. This gave birth to Higbie's "film penetration" model (Higbie, 1935)

$$K_L \simeq 2\sqrt{\frac{D}{\pi T}} \tag{4.7}$$

where T corresponds to a characteristic "renewal time" that would correspond to a typical turbulent eddy turnover time scale. However, this still did not allow to account for the randomness of turbulent eddies.

This model was upgraded by Danckwerts (1951) by including a stochastic surface renewal rate r instead of the constant time scale T. This is called the surface renewal model:

$$K_L \simeq \sqrt{D.r} \tag{4.8}$$

To that point, the fact that turbulence interacts with the diffusion layer was well established. Another model combining the notion of surface film and surface renewal was also proposed by O'Connor and Dobbins (1956). Yet, the eddies were still assumed too large to

deform this layer, and only a full or partial renewal was assumed possible (Chan and Scriven, 1970).

In all those conceptual models, the estimation of the diffusive layer depth and/or of the surface renewal time/rate is necessary to predict the mass transfer velocity. One can either get those from measurements. As explained above, a Lewis and Whitman (1924) type model based on the measurement of concentration profiles can be used to estimate mass transfer velocity accounting for turbulence effect.

Surface renewal time or boundary layer depths are nevertheless conceptual parameters that are not easily accessible to measurement. The idea to improve the usefulness of the previous models was to derive estimations of a renewal time from more easily accessible flow properties, and more specifically turbulence parameters, such as the typical velocity and length scales of bulk turbulence or the Reynolds number. The addition of turbulence properties to estimate the missing quantities in conceptual models gave birth to hydrodynamic models.

Hydrodynamic models: Referring to bulk turbulence properties, one should acknowledge the multiscale aspect of turbulence and choose a parameter than allows to describe the relative influence of all scales. At the birth of hydrodynamic models, ideas still diverged on which of large eddies or small eddies contributed the most to mass transfer and should be used for surface renewal rate estimation. This was expressed by the competition between two models

1. Fortescue and Pearson's Large Eddy Model (LEM) (Fortescue and Pearson, 1967) uses the assumption that large eddies are the one responsible for mass transfer. They use the surface renewal model of Danckwerts (1951) (equation (4.8)) where the renewal rate r is expressed as $r = u'/L_\infty$ so that

$$K_L \sim \sqrt{\frac{D.u'}{L_\infty}} \tag{4.9}$$

   where u' and L_∞ are large scale characteristic velocity and size of turbulence. In terms of flow Reynolds number, this leads to a $Re^{-1/2}$ dependency for K_L.

2. Banerjee et al. (1968) and Lamont and Scott (1970) on the other hand assumed that it is the small eddies that are the most relevant for mass transfer. Their Small Eddy Model (SEM), uses a renewal rate r based on the small scale quantity ϵ and is written

$$K_L \sim \sqrt{D}\left[\frac{\epsilon}{\nu}\right]^{1/4} \tag{4.10}$$

   where ϵ is the turbulence dissipation rate. This gives a $Re^{-1/4}$ dependency for K_L.

Theofanous (1984) reconciled these theories by showing that LEM behaviour is dominant for low Reynolds number and SEM behaviour for high Reynolds number, and proposed:

$$\begin{aligned} K_L &= 0.73 u' Sc^{-0.5} Re^{-0.5}, \quad for \quad Re < 500 \\ K_L &= 0.25 u' Sc^{-0.5} Re^{-0.25}, \quad for \quad Re > 500 \end{aligned} \tag{4.11}$$

The idea that large eddies dominate mass transfer at low Reynolds numbers and that small eddies become relevant at high Reynolds numbers has been confirmed by several studies since then (Herlina and Wissink, 2014; Herlina and Jirka, 2008; Janzen et al., 2010). In all

cases, mass transfer velocity increases with increasing bulk Reynolds number. What is also well established in all models is the $-1/2$ exponent on the Schmidt number: an increase in diffusivity D leads to a decrease in Sc and hence to an increased mass transfer velocity. On the other hand an increase in viscosity leads to a decrease in turbulent intensity associated to an increased Schmidt number and a decreased mass transfer velocity.

Those models are interesting for global applications inasmuch as they allow an estimation of K_L based on the simple knowledge of the flow Reynolds number and the gas Schmidt number (in Newtonian liquids). However they still show some limits. First, they rely on empirical constants that may depend on the type of flow considered. In some situations such as real life environmental flows (oceanic currents, rivers), estimating a Reynolds number that can be used within the Theofanous (1984) correlation framework can also be arduous. Finally, hydrodynamic parameters relying on bulk turbulence can not account for surfacic events such as surface pollution or wind shears inducing turbulence.

Surface divergence models: A new range of models called Surface Divergence Models (SDM) based on the works of McCready et al. (1986), Jirka and his co-workers (Brumley and Jirka, 1987; Chu and Jirka, 1992), Hasegawa and Kasagi (2009) and Banerjee and his co-workers (Banerjee et al., 2004; Turney and Banerjee, 2013) show that the global and local mass transfer coefficients may be linked with the rms of instantaneous surface divergence $\langle\beta\rangle_{rms}$, that is to say the horizontal divergence of the velocity field at the air water interface (see also Law and Khoo (2002); Tamburrino and Gulliver (2002); Tsumori and Sugihara (2007) among others. The generic expression of these models is

$$K_L \sim \sqrt{\langle\beta\rangle_{rms}.D} \tag{4.12}$$

The power of such models is that they allow to account for surface deformations, surface pollution, wind shear, and that they only rely on measurement of the interfacial velocity, which only require an optical access to the interface (Asher et al., 2012; Turney and Banerjee, 2013).

They are based on the incompressibility equation of velocity fluctuations (1.22), stating that

$$\beta'(x,y,t) = \left(\frac{\partial u'_x}{\partial x} + \frac{\partial u'_y}{\partial y}\right)_{\text{interface}} = -\left(\frac{\partial u'_z}{\partial z}\right)_{\text{interface}} \tag{4.13}$$

Assuming that mass transfer is a statistically 1 dimensional mass transfer problem (Tamburrino and Gulliver, 2002), the instantaneous surface divergence can be used to estimate vertical turbulent mass fluxes, and the rms of β' thus allows to calculate a global value for K_L. This description finds an echo in the vertical view of mass transfer: it has been observed that small concentration fluctuation occurring within the diffusive sub-layer are well correlated to surface divergence fluctuations (Magnaudet and Calmet, 2006).

Surface divergence models have been extensively used in the last decades to study mass transfer at air-water interfaces in presence of bottom shear and or mean shear, and with or without mean flows (Asher et al., 2012; Banerjee, 2007; Banerjee et al., 2004; Hasegawa and Kasagi, 2009; Kermani et al., 2011; Mckenna and Mcgillis, 2002; McKenna and McGillis, 2004a; Tamburrino and Gulliver, 2002; Tamburrino et al., 2007; Tsumori and Sugihara, 2007; Turney and Banerjee, 2013). An extensive review can be found in Turney and Banerjee (2013).

It is worth noting that their expression is similar to the one proposed by Danckwerts (1951), where $\langle\beta'\rangle_{rms}$ is analog to the renewal rate r. A recent study by Turney and Banerjee (2013), proposed a further development of the SDM based on both surface divergence and

lifetime to account for the different lifetimes and intensity of turbulent structures contributing to surface divergence. This last model as proved its efficiency in bottom shear turbulence situations but also for wind shear turbulence at moderate surface deformation.

A recent study by Katul et al. (2018) suggests that LEM, SEM, and SDM models can be reconciled by defining K_L as a scale dependent turnover velocity and no longer as a piston velocity. The formulation of all three models can then be recovered from the shape of the vertical velocity structure function for for near surface turbulence, assumed homogeneous and isotropic.

4.1.2.c Recent observations

Back to vertical observations of flat surfaces mass transfer, it has been observed by Herlina and Jirka (2007, 2008); Janzen et al. (2010); Tsumori and Sugihara (2007), and confirmed by Variano and Cowen (2007, 2013) that surface renewal is not the only mechanism responsible for turbulent mass transfer.

Contrary to what was previously assumed by Danckwerts, turbulent structures can indeed deform the diffusion layer and tend to "peel" high concentration patches and bring them down to the bulk fluid where they can be quickly mixed. This smaller scale convection like phenomena, also called "injection" events, were found to be not only observable Herlina (2005); Janzen et al. (2010) but also quantitatively non negligible in the total mass flux exchanged (Asher et al., 2012; Variano and Cowen, 2013). Mass transfer is therefore enhanced by a combination of injection and renewal events at different scales.

Turbulence action on dissolved gas at the interface can thus be summarized as follows (see figure 4.2). A turbulent eddy coming from the bulk enters the surface influenced region and begins to be deformed by surface action (see section 4.1.1). If its typical size is very large compared to the apparent scalar sub-layer depth, it mainly contracts the scalar sub-layer thus sharpening the concentration gradient and increasing mass transfer. This is the picture of the film model by Lewis and Whitman (1924). Smaller eddies however have the ability to peel the diffusive film and send saturated fluid downards (Q3 or Q4 events defined by Variano and Cowen (2013)), while replacing it with fresh fluid brought from the bulk (Q2 event, same reference). Under-saturated fluid being brought at the interface, concentration gradients are increased and so is near surface diffusion. This is in some ways the idea behind surface renewal models of Higbie (1935) and Danckwerts (1951). This renewal is associated with injection events: the patches of fluid sent downwards are over concentrated with respect to the surrounding bulk fluid, also enhancing mass transfer by diffusion. Moreover, going downwards, concentrated patches enter higher turbulence intensity regions where they can be efficiently mixed by several other eddies.

In the light of this description, the efficiency of surface divergence models is easily explained: the root mean square of surface divergence is a quantity able to account for both up and down-going fluid patches carried by large to intermediate size vortices. It thus encompasses all type of events into a single quantity usable in preexisting models.

However, the exact link between surface renewal properties an the complex combination of injection and renewal events remain poorly understood, mostly because of the difficulty of measuring fluid velocity and dissolved gas concentration very close to interfaces. DNS studies have found that surface divergence is quite representative of concentration fluctuations induced by turbulence in the Batchelor layer, but experimental observation of turbulent mass transfer events within the viscous and Batchelor sub layers are still lacking to understand the scale by scale influence of turbulent structures on turbulent mass fluxes.

Moreover, injection or renewal events are often identified using 2 dimensional information in a vertical plane. However, even if mass transfer is ultimately a global 1D problem, local flow structures are obviously highly three dimensional and so are passive scalar patches. 2D visualisation of such 3D phenomena can thus be misleading (Tsumori and Sugihara, 2007).

This work will hopefully bring additional information to the problem by presenting 2 dimensional 3 components measurements of the velocity field coupled with 2D scalar field at a higher spatial resolution than previous works. In doing so, the viscous sub-layer could be described with more details, and the third velocity component will allow both the identification of three dimensional velocity structures and the computation of surface divergence properties under the interface from vertical measurements.

4.1.3 Non-Newtonian effects

To this already quite complex picture, we will, during this work, add the non-Newtonian aspects with dilute polymer solutions. Polymer addition may have many physical-chemistry effects on the solvent that are specific to each polymer molecules and to each solvent. The significant effects of XG addition into water have been discussed in chapter 3. In this section, we will focus on known polymer effects on the parameters relevant for our mass transfer situation: diffusivity, passive scalar mixing ability, and near surface turbulence.

4.1.3.a Non-Newtonian effects on diffusion

It was mentioned in chapter 1 that according to Stokes-Einstein relationship (1.4), an increase in liquid phase viscosity leads to a decrease of the diffusion coefficient with $D \sim \frac{1}{\mu}$ for large molecules, and so the Schmidt number should scale as $Sc \sim \mu^2$. For the other limiting hypothesis of small molecules diffusing in a Newtonian solvent of large molecules, Hiss and Cussler (1973) showed that $D \sim \frac{1}{\mu^{2/3}}$. Nevertheless, the behavior of dilute polymer solutions has already proved to be more complex than that of a viscous Newtonian solutions with large or small molecules, and the Stokes-Einstein or other relationships based on a Newtonian viscosity value may not hold in their case.

Experimentally, the diffusivity of small molecules in polymer solutions are found to depend only weakly on viscosity, or even to be completely independent of it (Lohse et al., 1981). In some cases, the diffusivity may even increase with increasing polymer concentration and/or viscosity (Lohse et al., 1981; Perez and Sandall, 1973, 1974; Tan and Thorpe, 1992; Wasan et al., 1972). For a given molecule diffusing into a polymer solution, the ratio between diffusion coefficients in polymer solution and in water may be written as (Lohse et al., 1981; Torrestiana et al., 1989):

$$\frac{D^{DPS}}{D^{water}} = \left(\frac{\mu^{DPS}}{\mu^{water}}\right)^{-A} \tag{4.14}$$

where A mostly depends on the polymer molecular weight, but possibly also on the concentration regime or on polymer-molecule interactions. It can be either positive (resp. negative) if diffusivity is decreased (resp. increased) with the DPS overall viscosity, or close to zero if the effects of viscosity are not significant on diffusion.

For CO_2 dissolving into polymer solutions, Lohse et al. (1981) found values of A of order of magnitude 0.1 to 0.01, corresponding to quite small diffusivity variations with viscosity. To explain that, they stated that the presence of polymers does increase the macroscopic viscosity through polymer-polymer interactions (electrical or mechanical) but does not ef-

fect as much diffusivity which is governed by short range interactions of the molecules and the solvent.

Estimating the diffusion of molecules into dilute polymer solutions is thus quite a complex task since it depends on many factors among which, the molecule size (or molar weight), the polymer size (or molar weight) and concentration, and all the solvent-polymer, polymer-molecule and molecule-solvent interactions. In what follow we will assume diffusivity to remain constant with viscosity in dilute polymer solutions.

4.1.3.b Non-Newtonian effects on passive scalar mixing

The effects of viscoelasticity and shear thinning properties on the bulk mixing of a passive scalar are mostly explained by the modification of turbulence by such properties, if one compares Newtonian and non-Newtonian cases with similar Schmidt numbers. For example, cavern effects in stirred tanks have direct consequences on mixing efficiency: since the flow inside the cavern is turbulent, passive scalar is homogeneously mixed, whereas outside of the cavern only diffusion occurs and macro mixing takes much more time (Arratia et al., 2006). The first to visualize the effects of non-Newtonian behaviors on passive scalar mixing in a liquid flow was Gadd (1965, 1966). They found that the small spatial scalar structures of a colored jet injected in a transparent fluid at rest were reduced compared to the Newtonian case. Barnard and Sellin (1969) and McComb et al. (1977) later found the same small tendency for small scale structure suppression by visualizing the mixing of a dye injected in a fixed grid turbulence.

Another phenomenon is the re-organisation of flows and the apparition of low or high mean flow versus low or high turbulence regions, leading to the formation of high scalar transport filaments sometimes called preferential paths. Mixing is enhanced in preferential paths as compared to the rest of the flow, and the presence of such filaments can enhance the overall scalar transfer if they are connected to a scalar source. Such features have been observed by Gupta et al. (2005) in DNS heat transfer study in a drag reduction situation, and experimentally by Nguyen (2013) for the mixing of a dye at a T junction.

Both features can intuitively be linked to turbulence properties in non-Newtonian fluids: the suppression of the small scales of velocity observed in viscoelastic bulk turbulence logically leads to the suppression of some small scales of scalar mixing. The regions of higher or lower shear rates leading to higher or lower viscosity tends to form preferential paths for turbulence intensity, hence preferential paths for mixing (see chapter 3).

Quite surprisingly, in laminar flow, non-Newtonian fluids can on the opposite tend to enhance mixing. This has been observed by Groisman and Steinberg (2001) and can be explained by the fact that dilute polymer or comparable molecules add elastic instabilities to the flow and favor the transition to chaotic flow state, known for higher mixing capability that stable laminar flows.

4.1.3.c Non-Newtonian effects on gas-liquid mass transfer

Due to its presence in the bioprocess industry (see chapters 1 and 3), gas-liquid mass transfer in visoelastic shear thinning fluids has been the subject of many studies since the end of the 1960's. The most frequent multiphase reactor studied are aerated stirred tanks (Arjunwadkar et al., 1998; Cabaret et al., 2008; Gabelle et al., 2011; Garcia-Ochoa and Gomez, 1998; Nishikawa et al., 1981; Puthli et al., 2005; Ranade and Ulbrecht, 1978; Yagi and Yoshida, 1975) and bubble columns (Godbole et al., 1984; Han et al., 2017; Kawase and Hashiguchi, 1996; Kawase and Moo-Young, 1987; Kawase et al., 1987, 1992; Nakanoh and Yoshida, 1980).

In both devices, the effects of shear thinning and viscoelasticity on mass transfer in such devices is double: first, hydrodynamics of the liquid phase act on the gas phase properties, that is to say the bubble size, size dispersion, rising velocity, or residence time (Han et al., 2017; Kawase et al., 1987; Ranade and Ulbrecht, 1978). It thus sets the surface of exchanges, the a in $K_L a$. Second, mixing in the liquid phase also differs from that in Newtonian media, as shown in the previous paragraph. The turbulent enhancement of mass transfer should therefore be fairly different. Understanding the effects of turbulence in non-Newtonian fluids on gas-liquid mass transfer is precisely the objective of this chapter.

In stirred tanks, the efficiency of gas-liquid mass transfer is completely modified by the non-Newtonian properties and designs, that proved efficient for viscous Newtonian liquids but may no longer be the most appropriates for gas-liquid mass transfer in shear thinning fluids (Cabaret et al., 2008). As for the hydrodynamics, many studies try and correlate the non-Newtonian effects to the apparent fluid viscosity defined by Metzner and Otto (1957) (Gabelle et al., 2011; Han et al., 2017; Nishikawa et al., 1981; Puthli et al., 2005). Increasing effective viscosity tends to decrease turbulence intensity (Gabelle et al., 2011) and to increase the average bubble size (Arjunwadkar et al., 1998; Kawase and Hashiguchi, 1996), both effects leading to a decrease in mass transfer coefficients (Garcia-Ochoa and Gomez, 1998; Godbole et al., 1984; Puthli et al., 2005). Above a given viscosity threshold, it is found that the mass transfer coefficient varies as $K_L \sim \mu_{eff}^{\lambda}$ with $-0.4 < \lambda < -1$ (Gabelle et al., 2011).

However, such an approach does not allow to easily distinguish between effects due to increased overall viscosity and effects due to shear thinning, and even less to consider the effects of viscoelasticity. The scaling in μ_{eff}^{λ} is quite sensitive to polymer nature, concentration, and rheological behavior (Gabelle et al., 2011; Garcia-Ochoa and Gomez, 1998). Ranade and Ulbrecht (1978) and Yagi and Yoshida (1975) have noticed quite early that the diminution in K_L in shear thinning liquids is much higher that the diminition that would be caused by an increase in Newtonian viscosity. This effect can be attributed to the structural changes in bubble size distribution and gas holdup (Han et al., 2017; Ranade and Ulbrecht, 1978), and to the modification of bubble dynamics by non-Newtonian properties (Yagi and Yoshida, 1975). On the other hand, viscoelasticity is found to increase mass transfer by changing the bubble shape (Calderbank et al., 1970; Zana and Leal, 1978). The modification of mass transfer efficiency around bubbles in non-Newtonian liquids thus seems to be the result of a competition between viscous and elastic effects. The role played by bubbles is even more important in bubble colums and airlifts for which liquid phase turbulence is also a consequence of the bubble population and motion dynamics (Kawase and Hashiguchi, 1996; Kawase and Moo-Young, 1987; Kawase et al., 1987, 1992).

Global models for $K_L a$ based solely on apparent viscosity are thus not expandable to any solutions, and fail to predict mass transfer coefficients in highly viscoelastic polymer solutions (Kawase and Hashiguchi, 1996; Kawase et al., 1987). In order to account for viscoelasticity in those models, Yagi and Yoshida (1975) introduced the Deborah number into the correlation. Correlations including the Deborah number yield much better results for viscoelastic fluids than the ones based on apparent viscosity only, and that for both stirred tanks and bubble columns (Nakanoh and Yoshida, 1980; Ranade and Ulbrecht, 1978).

In both stirred tanks and bubble columns, the non-Newtonian effects on mass transfer velocity are addressed through their effects on $K_L a$. It is indeed hard to estimate interfacial area in such devices, even in Newtonian medium, and thus separate K_L from a (Bouaifi et al., 2001). Fundamental studies of turbulent mass transfer at controlled interfacial areas a, similar to the ones made at air-water interfaces (see sections 4.1.2 and 4.5), still have to be performed in order to get further insight on the fundamentals of turbulent gas-liquid mass transfer in non-Newtonian liquids.

Reference	Type of study	Gas-liquid interface	Turbulence	Mass transfer		Non-Newtonian effects	Subject
				Global	Local		
Present data	EXP: OGT	■	■	■	■	■	
Herlina and Wissink (2014, 2016); Wissink and Herlina (2016)	NUM: DNS	■	■	■	■		BST, Bo, Surfactants
Variano and Cowen (2013)	EXP: SJ	■	■	■	■		BST
Turney and Banerjee (2013)	EXPE: FSC	■	■	■	■		BST, WT
Rashidi et al. (1991); Tamburrino and Gulliver (2002)	EXPE: FSC	■	■	■			BST
Asher and Pankow (1986); Chu and Jirka (1992); Herlina and Jirka (2004, 2008); Janzen et al. (2010); Tsumori and Sugihara (2007)	EXPE: OGT	■	■	■	■		BST
Brumley and Jirka (1987)	EXPE: OGT	■	■				BST
Hunt (1984); Hunt and Graham (1978); Hunt et al. (2011); Magnaudet (2003)	TH	■	■				BST, WT
Hasegawa and Kasagi (2009)	NUM:DNS/LES, FSC	■	■		■		BST, WT
Calmet and Magnaudet (2003)	NUM:LES,FSC	■	■				BST
Magnaudet and Calmet (2006)	NUM:LES,FSC	■	■	■	■		BST
Bodart et al. (2010); Perot and Moin (1995)	NUM:DNS	■	■				BST
Flores et al. (2017); Pan and Banerjee (1995)	NUM:DNS,FSC	■	■				BST
Theofanous (1984)	REV(EXP,TH)	■	■	■			BST, WT
Liberzon et al. (2009)	EXP:OGT		■			■	BST, TNTI
Vonlanthen and Monkewitz (2013)	EXP:FGT		■			■	ET
De Angelis et al. (2005); Nguyen et al. (2016)	NUM:DNS		■			■	ET
Gabelle et al. (2011); Ranade and Ulbrecht (1978)	EXP:ST	■	■	■		■	RT
Han et al. (2017); Kawase and Hashiguchi (1996); Yagi and Yoshida (1975)	EXP:BC	■	■	■		■	RT
Danckwerts (1951); Higbie (1935); Lewis and Whitman (1924)	EXP	■		■			

Table 4.1 – Literature overview on turbulent mass transfer, non-Newtonian effects and gas-liquid interfaces. NUM=Numerical study, EXP=Experimental study, TH=Theoretical study, REV=Review. DNS=Direct Numerical Simulation, LES=Large Eddy Simulation. SJ=Synthetic Jets, FSC=Free Surface Channel, OGT=Oscillating Grid Turbulence, FGT=Fiwed Grid Turbulence, ST=Stirred Tank, BC=Bubble Column. BST=Bottom Shear Turbulence, WT=Wind induced Turbulence, ET=Elastic Turbulence, TNTI=Turbulent/Non-Turbulent Interface, Bo=Bouoyancy effects, Sf=Surfactant effects, RT=Reactors.

4.1.3.d Non-Newtonian effects on near surface turbulence

Many questions remain open about both the behavior of turbulence close to an air-water interface and non-Newtonian turbulence. It is therefore not surprising that no experimental data, numerical simulation, or theoretical approach yet exist to investigate the fundamental effect of sheared free surfaces on turbulence of non-Newtonian media. Several studies previously mentioned address the effect of turbulence on bubble shape, growth, breakup and coalescence in shear thinning fluids. However the reciprocal effect of interfaces on turbulence is rarely considered.

From what we can infer, the increased apparent viscosity of shear thinning fluids, and the increase in integral lenth-scale found in chapter 3 should lead to an increase in the surface influenced layer, viscous sub-layer and Klomogorov sub-layer. However there is no indication that shear thinning fluids will behave like viscous Newtonian solutions close to the interface, and viscoelasticity should also play a role.

4.2 Experiments

After the introduction to the main concepts of turbulent mass transfer at gas-liquid interfaces, let us detail the experimental bench built for our study, and the way it has been used to measure coupled velocity-concentration fields. In the following section, the variability of physical and geometrical parameters during the experimental runs is discussed and the various experimental runs are characterized in terms of non dimensional numbers. The experimental setup and the conditions in which it is used during the experiments is also specified. Interactions between CO_2 and XG that could possibly interfere with mass transfer measurements are discussed, and the complex arrangement of optical techniques used to obtain simultaneous measurements of velocity and scalar fields is described. The section ends with a summary of all experimental runs performed for this chapter.

4.2.1 Variable parameters

The turbulent dissolution of CO_2 into DPS is a complex case involving multiple physical and chemical phenomena that can be either coupled or independent. This thesis consists in a first fundamental approach of the subject, and an angle of attack among others had to be selected. The choice was made to consider only the liquid phase as the domain of study, and to vary a single input parameter, polymer concentration, keeping all other geometrical and thermodynamic parameters constant. This was motivated by the fact that the arrangement of the experimental setup was quite complicated and time consuming. Performing measurements in similar conditions, simply changing the fluid between two runs, was in practice the most convenient way of doing.

However, choosing this option, one has to acknowledge the variations of several physical properties and characteristics caused by changes in polymer concentration. Those variations especially regard turbulence generated by the grid and polymer solution properties. They have been investigated in chapter 3. Hereinbelow is a recap of all the relevant dimensional parameters characterizing physical phenomena occurring in the experiments, with specification on whether they are kept constant throughout the study or not. All are defined for the liquid phase. The relevant non-dimensional parameters that can be built from those dimensional quantities are recalled, and their variations are finally discussed.

4.2.1.a Constant parameters

Geometric

- *Grid related*: Grid stroke (S), grid period (T) or frequency (f), mesh parameter (M), grid-bottom distance (H_G), grid-surface distance (H_S)
- *Tank related*: Tank width (W), liquid depth ($H_{tot} = H_G + H_S$)

Physical

- *Liquid phase related*: Liquid phase temperature, initial pH (pH_0), surface tension (σ), density[2] (ρ)
- *Polymer related*: Molar mass (M_{XG}), conformation, molar mass (M_{XG})
- *CO_2 related*: Concentration (C_{sat}), molar mass (M_{CO_2})
- *Others*: gravity (g)

4.2.1.b Variable parameters

Control parameter: XG concentration (C_{XG})
Physical parameters: Viscosities (μ_0,μ_∞), time scale (t_{CY}), velocity ($\mathbf{U}$,$\mathbf{u}'$), CO_2 diffusivity (D)

4.2.1.c Dimensionless numbers

Based on the previous list, the equation fully describing the system's behavior, of unknown exact expression, depends on a set of 16 independent parameters and is of the form

$$X = f\left(S, M, f, H_G, H_S, W, \sigma, \rho, D, C_{sat}, u', \mu_0, \mu_\infty, t_{CY}, C_{XG}, g\right) \tag{4.15}$$

All these quantities can be expressed using only 3 reference scales: distance [m], time [s], and mass [Kg]. According to the Vaschy-Buckingham theorem, 16-3=13 dimensionless numbers can thus be defined, and the previous equation can for example be re-written as

$$X = f\left(\frac{u'}{fS}, Re_g, Re_T, De, Sc, Ca, Fr, \frac{C_{XG}}{C_{sat}}, \frac{\mu_0}{\mu_\infty}, \frac{H_S}{M}, \frac{H_G}{M}, \frac{W}{M}, \frac{S}{M}\right) \tag{4.16}$$

In this expression, H_S/M,H_G/M,W/M, and S/M are tank or grid related geometrical parameters. u'/fS measures, with $u' \equiv \langle u'_x \rangle_{rms}$ at the interface for example, is a ratio between typical turbulent velocity and the grid velocity. $Re_g = \frac{\rho f S^2}{\mu_0}$ and $Re_T = \frac{\rho u' L_\infty}{\mu_0}$ are grid based and turbulence based Reynolds numbers defined in chapter 3, representative of turbulence in the tank. The free surface influence is represented by the capillary number $Ca = \frac{\mu_0 u'}{\rho\sigma}$ and the Froude number $Fr = \frac{u'}{\sqrt{g H_S}}$. Mass transfer and passive scalar transport is quantified by the Schmidt number $Sc = \frac{\mu_0}{\rho D}$. Polymer effects are described by the Deborah number $De = f\, t_{CY} = \frac{t_{CY}}{T}$, concentration number C_{XG}/C_{sat}, and the viscosity ratio μ_0/μ_∞.

All geometrical parameters being kept constant during this study; we are left with a set of 8 non dimensional numbers that can vary throughout the experiments. Their values depend on geometric and grid parameters (f, S, H_S), viscosity, polymer time scale, surface tension, diffusivity, and a velocity and a length scale.

[2] Upon XG or gas dissolution

As previously mentioned, geometric and grid parameters are kept constant, their values being f = 1 Hz, S = 0.049 m and H_S = 7M. The diffusivity of CO_2 is assumed constant with polymer concentration and equal to that in water (see discussion in section 4.1.3.a). The same assumption is made for surface tension, based on the measurements shown in section 3.2.2.f. Viscosity has been measured as a function of polymer concentration in the previous chapter. The velocity and length scales used to estimate these numbers are respectively the undisturbed integral length scale L_∞ and the undisturbed rms of horizontal velocity fluctuations $u' = \langle u'_x \rangle_{rms}$ (Z = Z_s), that is to say the value that these two quantities would take at the interface location if there were no interface. Velocity scales are extrapolated from the HT type profiles of figure 3.34. 50 % integral length scales profiles are shown in figure 3.38. These are slightly different than the integral length scale defined in the TT relationship, since the threshold used to compute them is not the same. In order to estimate the "true" integral lenghtscale from their 50 percent counterpart, we simply assume that the two are proportional and determine the proportionality factor by using the reference C_{TT} value for water such that $L_\infty = C_{TT}Z = aL^x_{xx,50}$. From the data presented in chapter 3 it falls that $a \simeq 2$ and so $L_\infty \simeq 2L^x_{xx,50}$. The undisturbed integral scale values are thus determined by doubling the undisturbed $L^x_{xx,50}$ values obtained by linear fitting of curves in figure 3.38. Values of u' and L_∞ as a function of concentration are given in table 4.2.

The values of corresponding non-dimensional parameters are estimated in table 4.3 as a function of the control parameter, polymer concentration.

With the decrease in turbulent fluctuation intensity observed in chapter 3, the u'/fS parameter logically decreases. The μ_0/μ_∞ ratio confirms that shear thinning effects increase with polymer concentration. The Froude number Fr is a ratio between kinetic and potential energy of the fluid. High Froude numbers correspond to situations for which turbulence is energetic enough to likely deform the interface. The Fr number slightly decreases with polymer concentration because turbulence decreases and gravity effects remain constant. In all cases, Fr$\ll 1$, with an order of magnitude between 10^{-3} and 10^{-4}. It can thus be assumed that the interface remains flat for all experimental runs (which is, as a first approach, visually confirmed). Moreover, using respectively L_∞ and u' as the reference length and velocity scales, all experimental runs fall well within the flat surface domain according to Brocchini and Peregrine (2001a).

The capillary number Ca on the other hand somewhat increases with polymer concentration because of the increase in viscous effects and a constant surface tension. For all concentration in the dilute regime, it still appears that Ca$\ll 1$, with order of magnitude around 10^{-4} to 10^{-5}, and so variations in surface tension effects can be neglected.

Reynolds numbers (grid or turbulence based) strongly decrease with increasing polymer concentration. The decrease trend is found to be similar for Re_g and Re_T, which indicates that the dominant mechanisms for the diminution in Reynolds number is the increase in viscosity, more than the damping of velocity fluctuations.

This viscosity increase also leads to a strong increase in the Schmidt number with polymer concentration. The Deborah number does not depend on viscosity but on the evolution of the typical polymer time scale with polymer concentration. Here the De number increases with XG concentration [3].

The key numbers considered here are the velocity and viscosity ratios, turbulent Reynolds number, Schmidt number and Deborah number. The characteristic equation of

[3] All the previous conclusions are valid only in the dilute regime, which is the scope of the present study

Concentration	u' (mm/s)	L_∞ (mm)
0 ppm (water)	4.5	24.5
10 ppm	3.0	45.6
25 ppm	2.0	127.8
50 ppm	1.5	149.1
100 ppm	1.0	138.4

Table 4.2 – Table of characteristic undisturbed velocity and length scale variations with polymer concentration through the experimental runs of the dissolution study

Concentration	u'/fS	μ_0/μ_∞	Re_g	Re_T	Sc	De	Fr	Ca
0 ppm (water)	0.092	1	2401	110	527	0	2.90×10^{-3}	6.25×10^{-5}
10 ppm	0.061	1.3	1849	106	683	0.08	1.94×10^{-3}	5.41×10^{-5}
25 ppm	0.041	4.2	605	64	2090	0.46	1.29×10^{-3}	1.10×10^{-4}
50 ppm	0.031	10.0	220	20	5757	0.55	9.68×10^{-4}	2.28×10^{-4}
100 ppm	0.020	31.3	73	4	17253	1.58	6.45×10^{-4}	4.55×10^{-4}

Table 4.3 – Table of dimensionless parameters variations with polymer concentration through the experimental runs of the dissolution study

the system can thus be simplified as

$$X = f\left(\frac{u'}{fS}, Re_T, De, Sc, \frac{\mu_0}{\mu_\infty}\right) \tag{4.17}$$

Where u'/fS is representative of the grid action on turbulence, Re_T of the intensity of turbulence reaching the interface, De and μ_0/μ_∞ of the polymer properties, and Sc of molecular diffusion. All of these parameters are set through experimental runs by tuning the polymer concentration. Measurements are performed at least twice for each fluid insofar as possible. Different runs at the same concentration are labeled A, B (e.g; XG10A) and so on.

4.2.2 Experimental setup

4.2.2.a Experimental bench

The experimental setup used for the measurement of coupled sub-surface velocity and dissolved gas concentration fields is presented in this section. Both single color and ratiometric versions of inhibited PLIF have been used leading to two slightly different setups for the experiments. The two experimental setups are sketched in figure 4.4.

4.2.2.b Oscillating grid turbulence parameters

Oscillations parameters used for the present mass transfer study are the same as the one used in chapter 3. The free surface is located at $\frac{H}{M} \simeq 7$ from the grid average position. The incident turbulent scales under the interface are predictable thanks to HT and TT relationships for water, and thanks to the results obtained in chapter 3 for DPS. It can thus be checked using Chiapponi et al. (2012) experiments of surface fluctuations in grid stirred tanks, and Brocchini and Peregrine (2001a) diagram of free surface deformation by liquid-side turbulence

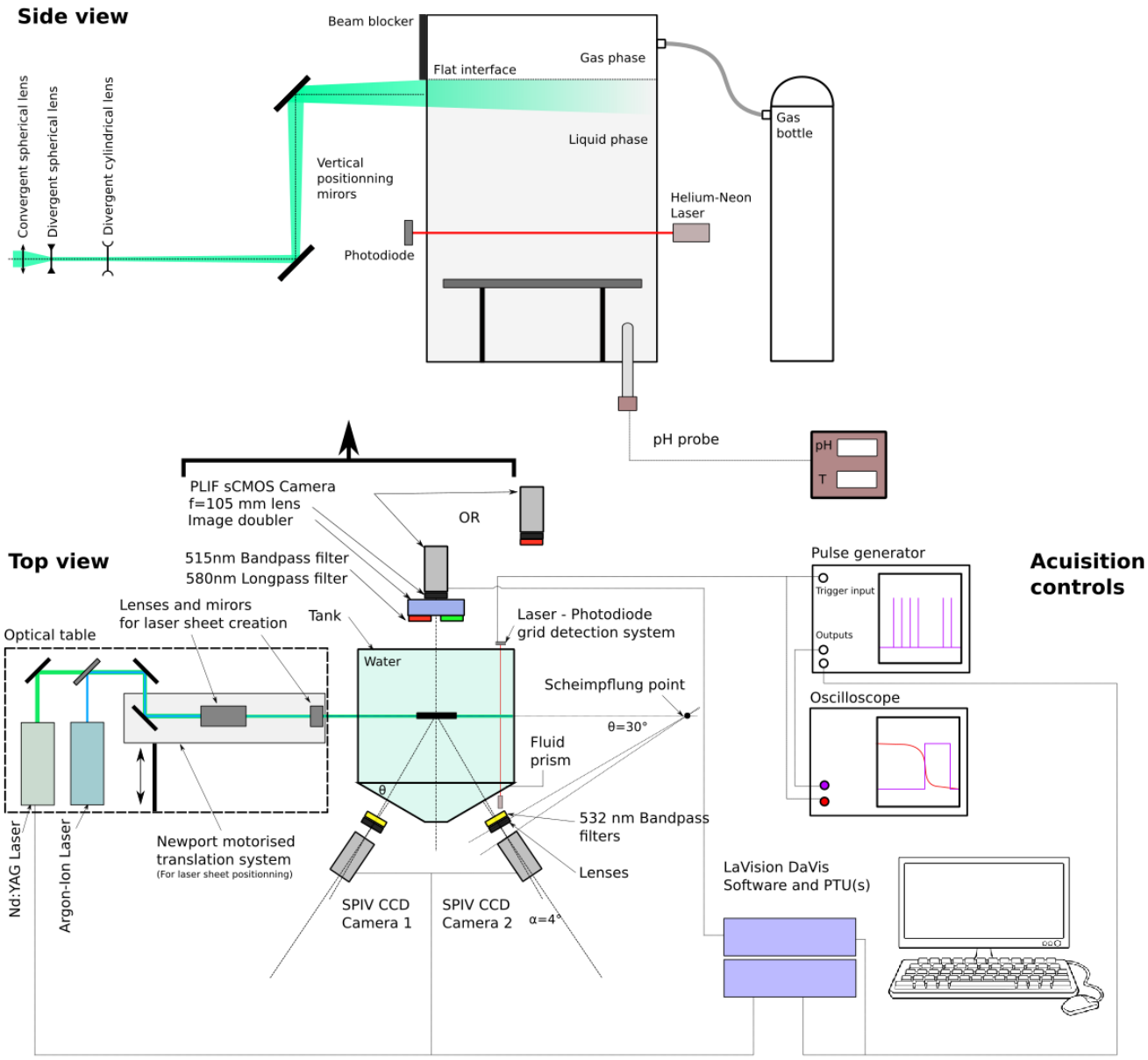

Figure 4.4 – Full experimental setup for SPIV and PLIF coupled measurements

that the shape of the interface remains in the "flat" domain.[4]

Oscillations of the grid are started at least 30 minutes before each experimental runs so that measurements are performed on a steady state, established oscillating grid turbulence. It has been checked in chapter 3 that the polymer was not destroyed by grid oscillations in two hours, which is more than the total time between the onset of grid oscilations and the end of the measurement runs for DPS.

4.2.2.c Free surface

After filling the tank with the working fluid and PIV seeding particles, the surface is cleaned in order to get rid of the floating particles and possible surfactant effects. In the 2016 runs, the only cleaning step is a removal of floating particles by skimming the free surface with an adequate tool. In the 2017 runs, floating particles are first removed by skimming, and then vacuum cleaning of the free surface is executed, using a pipette connected to a suction pump. In total, the top 1 cm layer of fluid in the tank is removed by the vacuum cleaning step, so that the free surface can be assumed surfactant free, at least at the beginning of the experiments.

4.2.2.d Gas injection

After cleaning of the free surface, the tanks is hermetically sealed by closing the top lid. The air volume above the liquid is quickly removed and replaced by 99.99% pure CO_2 (supplied by AirLiquide). Injection is controlled by a manometer and a flow meter, and it is checked that the whole volume of gas is replaced in less than 10 s of injection. The gas inlet and outlet are then closed by valves so that the gas volume is isolated. The partial pressure of CO_2 in the gas phase is thus close to 1 atm.

4.2.3 Gas-polymer interactions

4.2.3.a Hypothesis on the diffusion coefficient

According to section 4.1.3.a, we assume that due to the very dilute characteristic of DPS solutions used in this work, the value of the diffusion coefficient of CO_2 into DPS is close to its value in water, and that one may write $D_{CO_2}^{DPS} \simeq D_{CO_2}^{water} = D_{CO_2}$. As a comparison, Park et al. (2007) estimated the diffusion coefficient of CO_2 into XG solutions according to the method of Lohse et al. (1981) and found a decrease of 3% for 1500 ppm solutions compared to water.

4.2.3.b Xanthan gum (XG) effect on pH-CO_2 equilibria

The pH of solutions of XG dissolved into distilled water was previously found to be slightly acidic at large XG concentrations (see chapter 3, section 3.2.2). Here only dilute solutions are considered, so according to figure 3.4, XG should not have any effect on the initial pH of the fluid. It still needs to be checked that the variations of pH with dissolved CO_2 concentration are not modified by the presence of polymer. To do so, the experimental setup of appendix D is used again, and CO_2 is bubbled through XG solutions (with 5.10^{-7}M of fluorescein sodium) at different concentrations. In-situ calibrations are also performed in the grid stirred tank

[4] It should be noted that this diagram has been build only from water measurements and should therefore be restricted to that case. However, since surface tension in DPS solutions is very close to that of water as shown below, the diagram may also be used for a first estimation of the flat or non flat state of a free surface of DPS liquid.

using the same pH and dissolved gas probes. Results of these experiments are summarized in figure 4.5.

In the precision limit of the dissolved gas probe, that is to say at high dissolved gas concentrations, all curves follow the numerically predicted trend quite well. However for lower CO_2 concentrations, they drift away from the predicted trend and tend to higher pH than what is expected. This can be attributed to a lack of precision of the probe, which overestimates the value of dissolved gas concentration at higher pH since it is not able to measure the very low expected concentration values at those pH. Typically, it appears that pH=7 is reached at [CO_2]=1 mg/L but this 1 mg/L measured value could in reality correspond to a zero concentration, not measurable by the probe. Another, less probable but still possible explanation is that the water used is not perfectly distilled, and that it contains residual ions leading to a higher initial pH than the theoretical $pH_0 = 7$ value. A last hypothesis would be that the bottom of the grid stirred tank is polluted by pH active species, justifying that *in situ* calibrations are mostly the ones which do not follow the numerical trend. In any cases, the addition of XG up to 100 ppm concentration does not seem to modify this behavior. It is thus possible to use the same pH-CO_2 calibration curve for DPS and water in this study, be it numerical or experimental, and the effects of XG on pH-CO_2 equilibrium can be neglected.

4.2.3.c pH and CO_2 effect on Xanthan gum rheology

In order to make sure that XG viscous properties are not evolving during the measurements, the effects of pH and CO_2 concentration on XG rheology are tested by measuring flow curves of XG solutions at different pH set either by pH buffering or by CO_2 bubbling. The details of theses tests are shown in appendix D.5. It appears that pH variations induced by CO_2 dissolution have almost no influence on viscosity of polymer solutions. The use of pH buffers however leads to a decrease of the low shear-rate viscosity by up to an order of magnitude. This is explained by the fact that buffered solutions are highly salt concentrated: chemical species used for pH buffers are salts and increase the ionic strength of solutions. This is observed to change the conformation of XG chains and decrease its low shear rate viscosity (see litterature review in chapter 4). However, when pH is set by CO_2 concentration, only the carbonated species of CO_2 tend to increase the ionic strength of the solution. They are however present in very low concentrations compared to the concentration of salt used for pH buffers, and do not induce changes in viscosity.

It it thus checked that CO_2 dissolution does not change XG rheology during the experiments.

4.2.4 Optical measurements

4.2.4.a SPIV

Velocity fields are measured using a Stereoscopic Particle Image Velocimetry (SPIV) arrangement (see chapter 2.1). The configuration chosen here is that of angular SPIV, in which the optical axis of each camera is shifted from the normal to the laser plane by an angle of $\theta = 20°$ This value was found to be the best compromise between the maximum precision angle of 45° (as stated by Prasad (2000)), and the camera adjustments. A transparent Plexiglas®prism is placed between the cameras and the tank and filled with the same fluid as the one in the tank. The optimal Scheimpflung angle was found to be $\alpha_S = 4°$. The cameras used are double frame PCO CCD sensors of 1280 by 1024 pixels. Both are equipped with a 60 mm focal Macro lens. The $\#f$ numbers of camera 1 and 2 are set respectively at 16 and 11. Theses two numbers are different to account for the fact that camera 2 collects more light than camera 1 since

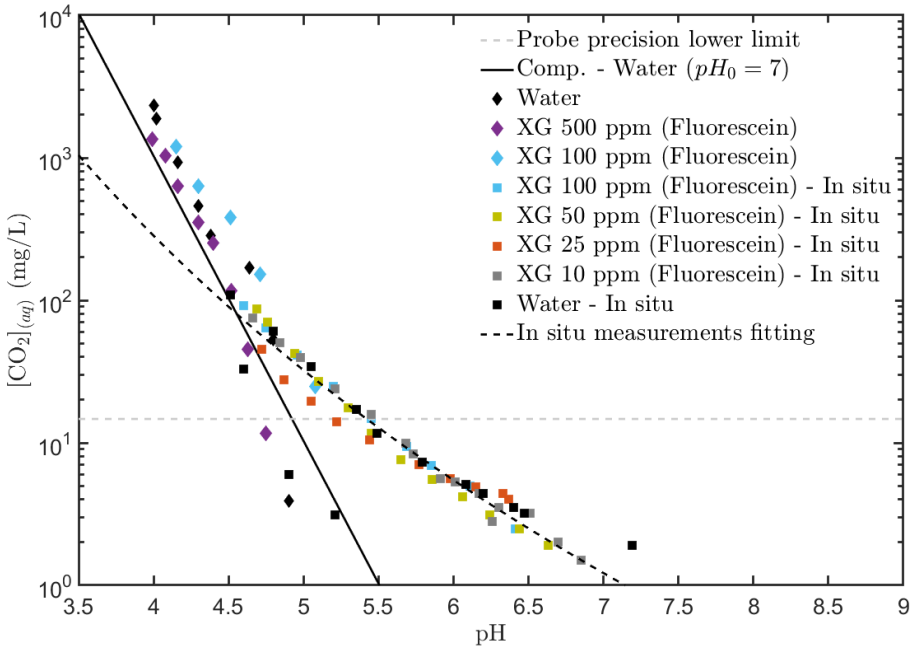

Figure 4.5 – Experimental pH-CO_2 curves in XG solutions. Black markers are reference points for distilled water. Squares denote in-situ calibrations (in the grid stirred tank), diamonds are for measurements made in the small tank of appendix D.

it faces the optical setup. A pulsed Quantel Nd:YAG laser emitting at $\lambda_{Nd:YAG} = 532$ nm is used to illuminate Hollow Glass Spheres (HGS) particles of nominal diameter $d_{particles} = 10$ µm. Once again the Stokes number is calculated (equation (2.2)) to check that particles follow the flow. For this, the expected size of the viscous sub-layer and the undisturbed velocity scale predicted by the HT type profiles are used. It always yields $St \ll 10^{-3}$. Hence the particles are suitable as flow tracers. Band pass filters with a central wavelength of 532 nm and a band width of 10 nm are used to reduce background noise and record only the light reflected by the particles.

The interval between two successive laser pulses is set at $dt_{SPIV} = 12$ ms. Vector fields are computed with DaVis software using a multipass processing: a first pass using 64 by 64 pixels and 2 following passes with 32 by 32 pixels round Gaussian weighted interrogation windows with a maximum 50% overlap. A post-processing similar to the one described in section 3.4.1.b is applied.

Uncertainties on SPIV velocity measurements are estimated by the DaVis software according to the method of Wieneke (2015) (see section 2.1.3.b). They have been evaluated in detail for the WB run. Error estimation is performed separately for each vector of each instantaneous field and for the three velocity components. Local rms of uncertainties over time is computed using the full data set. The error levels for each velocity component is finally estimated by averaging the rms uncertainty field over the ROI for each flow component. This yields the following typical errors: $\Delta U_x = 0.2$ mm/s, $\Delta U_y = 0.4$ mm/s, $\Delta U_z = 0.1$ mm/s. The uncertainty on the out-of-plane velocity component U_y is higher than on the in-plane components because of stereoscopic reconstruction step. The stereo reconstruction error evaluated in the same way is typically of 0.15 px.

4.2.4.b $I_{pH}-$PLIF **and** $I^r_{pH}-$PLIF

Dissolved CO_2 concentration fields are measured using fluorescein based inhibited fluorescence techniques. Because $I^r_{pH}-$PLIF was still under development during the measurements presented in this chapter, it could only be used for a few runs only. The single color version used otherwise is the one presented by Valiorgue et al. (2013).

In each cases, fluorescein sodium concentration in the working fluid is 5.10^{-7} M. Fluorescence is triggered by a Stabilite 2017 Argon-Ion Continuous Wave Laser (CWL). The effective maximum output power is 0.6 W and the laser sheet thickness is $e_{Ar} = 250$ µm. Fluorescence fields are recorded by a Lavision sCMOS camera equipped with a 105 mm focal length Macro lens. The sensor is a 2560 by 2160 pixel grid.

For $I_{pH}-$PLIF measurements, the lens is only associated to a a long-pass filter to suppress the PIV and fluorescence excitation wavelengths from measured intensities. For $I^r_{pH}-$PLIF measurements, an image doubler is added in front of the lens, and the setup becomes similar to the one used in section 2.2.6.a, with similar filters but a different lens.

The camera is used in its single frame configuration with an opening time of $dt_f = 10$ ms. For water measurements, in order to use the full dynamics of the pH-intensity curve, the pH of the water can be initially fixed at $pH_0 = 10$ by addition of sodium hydroxide NaOH. With this initial condition, the fluorescence intensity of regions with zero dissolved CO_2 concentration fluoresce at the higher intensity as possible, which increases the signal over noise ratio up to about 8 dB. In a will of keeping polymer rheology under control, no sodium hydroxide addition has been made to polymer solutions.

Some difficulties were encountered with the CWL: its power was found to slowly decrease over time, leading to an artificial reduction of the overall intensity of fluorescence which was not due to pH variations. As previously explained, $I^r_{pH}-$PLIF allows to account for such power drift inasmuch as the intensity on both spectral bands remains sufficient for high signal over noise ratios. For single color I-PLIF however, power drift may be misinterpreted as a global pH increase and alter the measurements. Fortunately, the Stabilite Laser control panel provides a measurement of the real time power output. The power value is given in a custom unit, but additional measurements performed with a power meter located directly after the laser output made it possible to establish the conversion rate from custom units to watts (W). Since our measurements remain within the linear fluorescence domain (see section 2.2.6.b), all fluoresced intensities are simply proportional to the laser power output. Knowing its evolution with time make it thus possible to correct fluoresced intensities and account for the power drift effect on 1 color PLIF measurements.

pH calibration: For the ratiometric measurements, calibration of the ratio versus pH is performed as explained in chapter 2. An example of data points measured in water and DPS at several concentrations is available in figure 2.28. Figure 4.6 shows an example of R=f(pH) curve obtained for the 10 and 25 ppm XG solutions. The associated fit constants are shown in the table of figure 4.6. In cases where the single color method is applied, the I=f(pH) curve is also fitted by an hyperbolic tangent function.

[CO_2] calibration: [CO_2] versus pH curves in water and DPS have already been discussed in sections 2.2.1 and 4.2.3. Here because of low concentration bias introduced by the dissolved gas probe, the numerically computed curves are chosen over the experimental ones. This yields for all runs (water and DPS at any concentration]

$$[CO_2] = Ae^{-BpH} \tag{4.18}$$

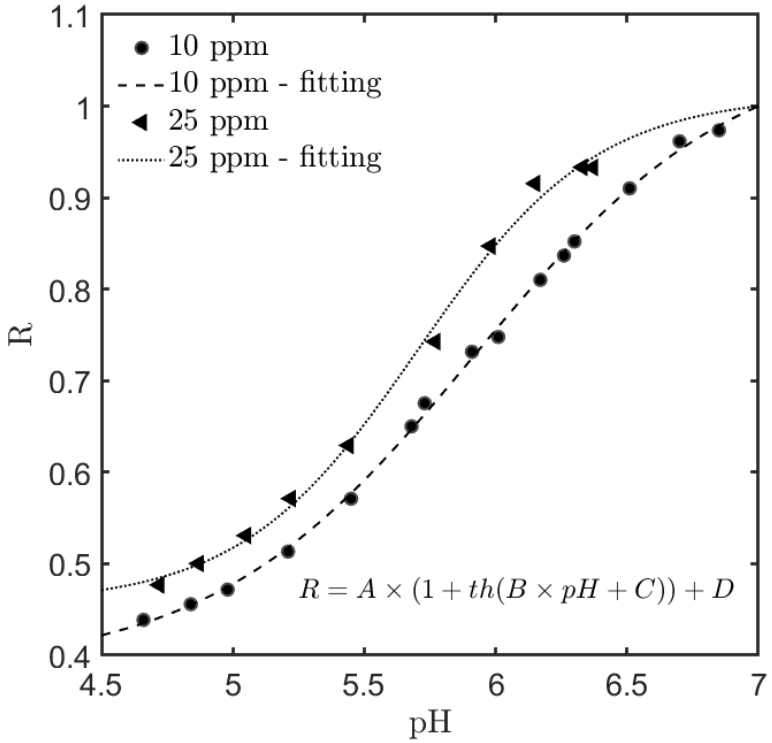

Run	A	B	C	D
XG10A, XG10B	0.34	1.05	-5.94	0.38
XG25A, XG25B	0.28	1.48	-8.45	0.0.46

Figure 4.6 – Example of I^r_{pH} – PLIF calibration curves and fitting constants

with A=1.55×10^{11} mg/L and B = 4.63.

Uncertainties: Using the tools developed in section 2.2.9, one may estimate the maximum relative uncertainties on ratio, pH, and concentration, for the present experimental setup. With maximum intensities of around 8000 gray-level (gl) for band 1 and 4000 gl for band 2, and a pixel noise of about 10 gl (gray levels), the signal over noise ratio is around 200 at all pH and falls close to 10 for pH=4.5. The relative uncertainty on the ratio is below 1.2%. The maximum relative uncertainty on pH is close to 1% (at pH=7, ΔR/R=0.5%). Relative uncertainties on concentration are below 10% for pH<5 and pH>6.5.

As for the 1 color PLIF technique, relative uncertainties still fall below 5% in the same range because the measurement of intensities gray level has a lower uncertainty than that of a ratio of intensities. However additional errors due to reflection and darker stripes are introduced. If one used the fluctuation intensity associated to these darker stripes instead of the random pixel noise for the estimation of δI/I, the subsequent relative concentration uncertainty can be multiplied by a factor 10. Moreover, we are here in a situation where the laser beam crosses fluid regions that are not included in the ROI but subjects to pH variations: this introduces variations of excitation intensity that single color LIF is unable to account for.

Example of calibration procedure for a single image: The calibration extensively detailed in section 2.2.6.b is applied here with the R-pH and pH-CO_2 relationship established above. In figure 4.7, a sample pair of fluoresced light images taken from the XG10A run is turned into a ratio field, then into a pH field and ultimately into a [CO_2] field (shown here in linear scale and log scale).

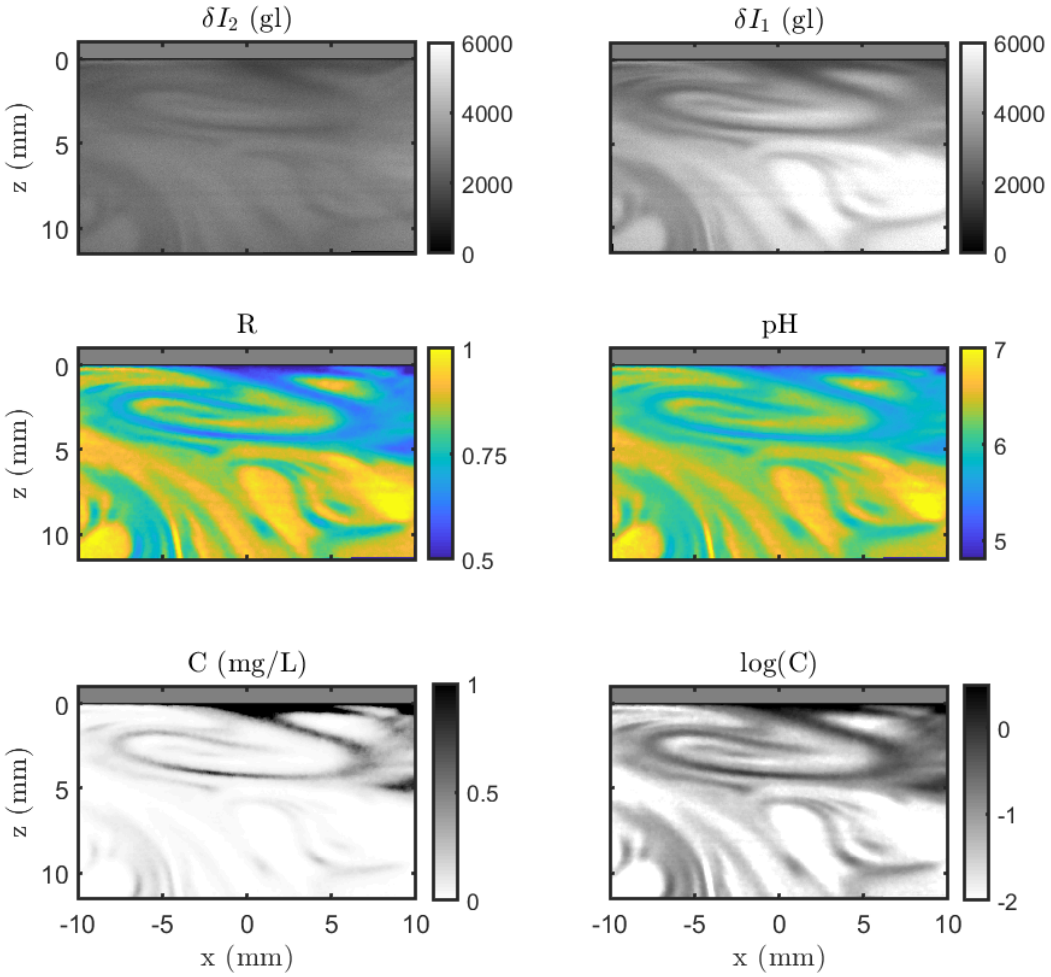

Figure 4.7 – Example of I^r_{pH} – PLIF calibration procedure for a instantaneous fluorescence measurement in a 10 ppm DPS. δI_2 and δI_1 are fluoresced light intensities from band 2 and 1 in gray level (gl). R and pH are ratio and pH fields. The last two pictures are concentration field in linear or log color scale

4.2.4.c Coupling and synchronisation

Spatial coupling: Spatial calibration of both sets of cameras is performed by taking an image of a LaVision standard reference pattern. In order to be able to superimpose velocity and dissolved gas concentration field, one also needs to set a common reference frame to both measurement devices. This is achieved using a transparent test pattern placed inside the fluid and imaged simultaneously by all cameras prior to the experiments.

The surface location of camera's sensors may vary of several pixels between runs. The z=0 pixel is consequently fixed for each run on each camera by detecting the free surface on images cleaned off of spatial distortion. This detection is made possible on SPIV images by the smallest particles floating on the free surface and reflecting laser light, resulting in a high intensity line on camera images. On PLIF images, it is also evidenced by a high intensity line due to direct laser reflection, and above which no fluorescence signal is visible.

Once all images are placed onto the same reference frame, SPIV fields remain under-resolved as compared to PLIF fields. Indeed, PLIF is resolved up to the pixel size whereas

SPIV is only resolved up to the smallest interrogation window used. To go beyond a simple visual interpretation of the results and compute for example turbulent mass fluxes or velocity-concentration correlations (Simoens and Ayrault, 1994; Variano and Cowen, 2013), one needs to get both fields at the same spatial resolution. This is achieved either by artificially increasing the spatial resolution of velocity fields (Nguyen, 2013), or by reducing that of concentration fields (Variano and Cowen, 2013).

In the first case, velocity field is spatially interpolated so that each pixel of the PLIF camera is associated to a velocity value as well. The coupled measurement resolution is thus artificially set to that of the PLIF measurements. In the second, a single concentration value is associated to each PIV vector, *i.e.* to each PIV interrogation window. This last case is called "Binning" and reduces the overall resolution to that of PIV measurements. It has been applied here since it require far less time for data treatment than pixel interpolation.

When using a binning procedure, the concentration value for a given vector can be chosen as the one at the center of the SPIV interrogation window projected on the scalar field, as in Variano and Cowen (2013). This may be called *binning at center*. It can also be taken as the fully spatially averaged scalar value on each SPIV window projected on the scalar field. This would be called *full binning*. Binning at center is a faster processing technique but it needs the velocity field's resolution to be high enough not to artificially sharpen scalar structures as in figure 4.8. Full binning is slower but is physically closer to the principle of PIV algorithms where the velocity information is averaged over the interrogation window. It also tends to smooth local noise of scalar images. This is the option that has been selected here.

For the used set-up, it is found that 32 by 32 pixels interrogation windows on SPIV cameras' sensors correspond to 43 by 43 pixels squares on the BPLIF camera's sensor. In all cases (interpolation, binning at center or full binning), it is not possible to visualize the effect on transport phenomena of structures smaller than the maximum PIV resolution. PIV sets the resolution limit to all further mass transfer studies, where local mass fluxes are required.

Temporal synchronization: The timing of two ore more cameras is achieved using software triggering of laser and camera shutters. The triggers are TTL signals generated by a Lavision Programmable Timming Unit. They can be internally generated (by DaVis) at a given frequency, manually sent by the user, or synchronized with an external source signal. Each laser-camera system (eg. SPIV setup, PLIF camera ...) is associated with its own PTU. When using two techniques simultaneously, a pulse generator is used as an external source to pilot both PTU. The signal emitted by the pulse generator can be shaped by the user (frequency, number of pulses ...) or by the measurement of a physical parameter, for example the grid's position (see figure 4.9 next section).

When coupling PIV and PLIF, there may be overlaps between the time of exposition and laser emission of each systems (see figure 4.9). In particular, the exposure time required for fluorescence measurement can be longer than the interval between two laser pulses, which leads to the recording of PIV laser light on the PLIF camera. When using Continuous Wave Lasers (CWL) for PLIF measurements along with PIV, the PIV sensors also record continuous laser light and fluorescence intensity during their opening time, which may lead to strong noise on particle images and a loss of accuracy on PIV computations. To overcome those issues, appropriate optical filters have to be used to prevent fluorescence or PLIF excitation light from reaching PIV camera's sensors, and to prevent pulses from the PIV laser from reaching the PLIF camera's sensor during its exposure time. For PIV, narrow bandpass filters centered around 532 nm are used. The filters used for PLIF camera(s) depend on the type of PLIF being applied and have been presented in section 2.2.6.a.

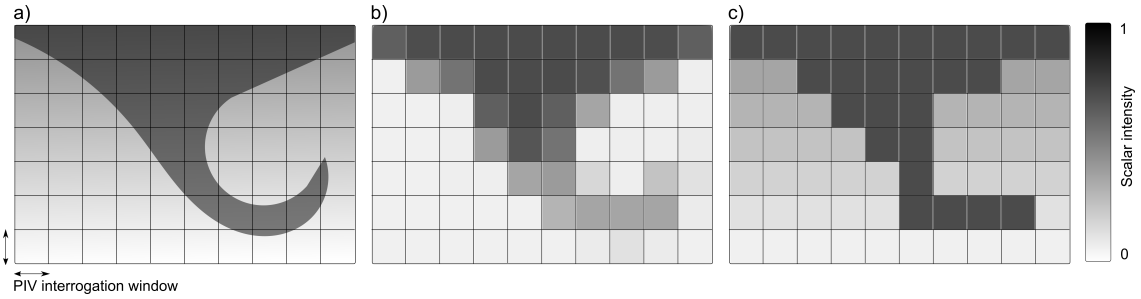

Figure 4.8 – Binning options: a) no binning, b) full binning, c) binning at center

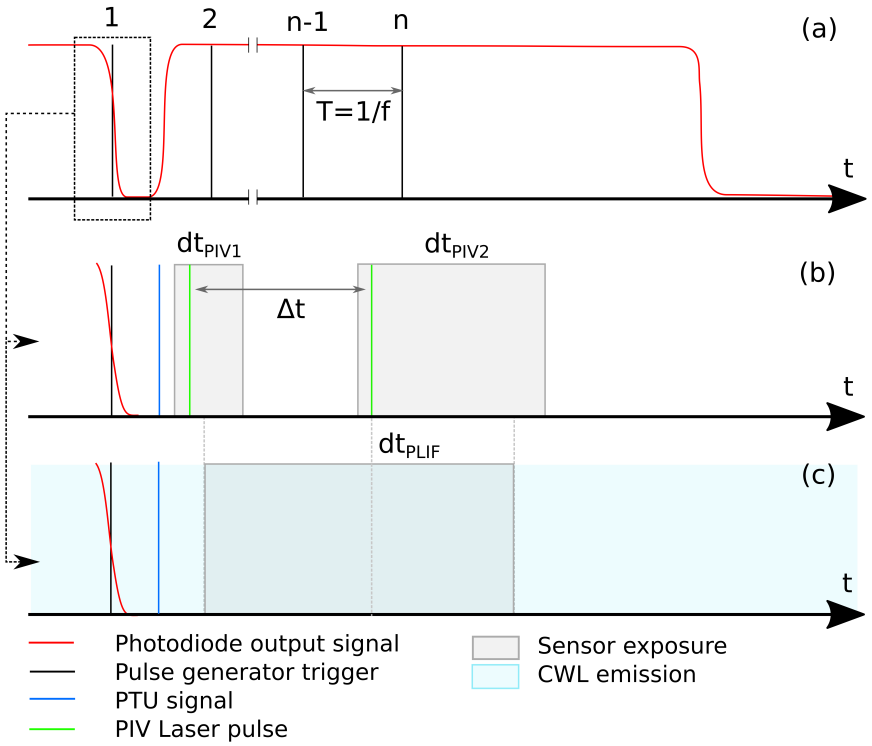

Figure 4.9 – Schematic representation of the timming of PLIF and PIV synchronisation. (a) Triggering by the grid's oscillations, (b) time-line of PIV measurement, (c) time-line of PLIF measurement

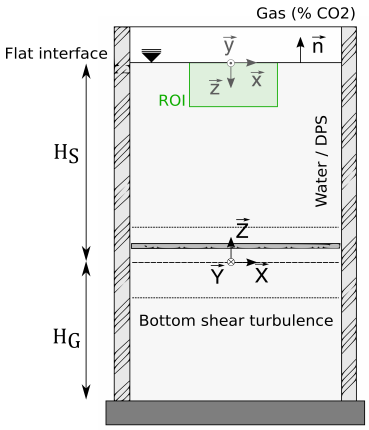

Figure 4.10 – Depths and ROI for coupled measurements

A last problem that could arise when coupling PIV and PLIF is the effect of particles on the fluorescence signal. Indeed, even when using appropriate filters, particles tend to

block fluorescence light, and once filtered out, leave darker spots on fluorescence intensity fields. Lenoir (2011) showed that this effect could lead to significant error on the shape of the PDF curve of concentration fluctuations, but not on first order concentration statistics. It is nonetheless limited as long as the concentration of particles is not too high and that they are not too large on images. Here no darker spots are observed, so we can assume that LIF measurements are not altered by PIV particles.

4.2.4.d Grid detection and trigger

The beginning of acquisition is timed on the grid's position. To do so, a red Helium Neon laser is used to generate an horizontal beam crossing the tank and exciting a photo detector. When the grid crosses the red beam, the phototiode signal falls to zero. The pulse edge of the photodiode signal therefore indicates the exact moment at which the grid is at the laser's vertical position. The output signal from the photodiode is then reshaped by the pulse generator into a TTL signal understandable by DaVis PTUs, of given frequency and number of repetition, piloting the rest of the measurement sequence.

Alternatively, it can translate a single grid pulse edge into a series of pulse at higher frequency, so that the measurements are dispatched within a grid oscillation period. This allows for the determination of velocity fields at different known grid positions without requiring the grid to be in the field of view. Such method has been used to perform a triple decomposition analysis in the sub-surface region for the water case. Results of this analysis confirm what can be inferred from chapter 3: the free surface is too far from the grid's position for oscillatory motions induced by the grid to reach it.

4.2.4.e Region of interest and spatial resolution

The region of interest consists in a circa 30 mm wide and circa 20 mm rectangle located in the center of the tank underneath the interface, as sketched on figure 4.10 The depth of the ROI (height of the rectangle, z dimension) is chosen so that the measurements are focused inside the surface influenced layer, in order to get the highest spatial resolution and the best description of the viscous sub-layer possible (see following section 4.4.2). The depth of the surface influenced layer can be estimated *a priori* from Brumley and Jirka (1987) for water. Here it is estimated to be around 25 mm for water, and up to 135 mm for 100 ppm DPS.

With the optical setup described above, the spatial resolution of velocity field is between 0.21×0.21 mm^2 and 0.34×0.34 mm^2. For the XG10A run only, 64×64 pixels PIV windows were used instead of 32×32 pixels windows and the spatial resolution is thus reduced by a factor 2 in both directions. In both PLIF cases, the spatial resolution for concentration fields is about 0.006×0.006 mm ^{2}.

4.2.5 Recap of experimental runs

A recap of all experimental runs that have been performed is available in table 4.4. Several factors made impossible an extensive repeatability testing. First the important weight of data for each run: around 200 Go for a single run of 10 000 instantaneous coupled measurement. The time needed for LIF calibration and data treatment was also an obstacle: each calibration procedure took more than half a day, and PLIF treatment last between 1 and 2 days for a complete run on a regular desktop computer. Finally, the SPIV setup was only available for a limited time during the thesis: only two period of time (series 2016 and 2017) for a total of around 8 months. Each fluid (water or specific XG concentration) was yet submitted to at least two measurements. Sub-surface grid-synchronized measurements were

Series	Run	Fluid	C_{XG} (ppm)	SPIV	PLIF	PLIF type	Grid sync.	Sample size
2016	WS	Water	0	X			X	30000
2016	WA	Water	0		X	1C		1000
2016	WB	Water	0	X				2000
2016	WC	Water	0	X	X	1C		3000
2017	WD	Water	0	X	X	1C		6000
2017	XG10A	DPS	10	X	X	2C		10000
2017	XG10B	DPS	10	X	X	2C		10000
2017	XG25A	DPS	25	X	X	2C		10000
2017	XG25B	DPS	25	X	X	2C		10000
2017	XG50A	DPS	50	X	X	2C		10000
2017	XG50B	DPS	50	X	X	2C		10000
2017	XG100A	DPS	100	X	X	1C		10000

Table 4.4 – Recap of the experimental runs for near surface turbulence and dissolution study. 1C denotes usual (one color) I_{pH}−PLIF and 2C the two-color I^r_{pH}−PLIF. The sample size is the number of instantaneous fields recorded. Data weights in Go include images and processed fields of all methods used.

only performed for water prior to the extensive OGT study shown in chapter 3. It was in the meantime established that oscillatory motion did not reach the interface either in water or in DPS, so grid-synchronized measurements were not performed for XG solutions. As previously mentioned the ratiometric I^r_{pH} – PLIF technique was developed in parrallel, and was thus not available for all coupled measurements. Fluorescence measurements anterior to the ratiometric method development used the more classical single color version as in Asher and Pankow (1986); Valiorgue et al. (2013) or Variano and Cowen (2013) without specifically accounting for fluorescence extinction variations or time of treatment reasons. The fluorescence method used for each run is specified in table 4.4 as well.

If not specified otherwise, all geometrical and grid stirring parameters are kept constant, with the values detailed in the previous sections. Scales and dimensionless numbers depend on polymer concentration as detailed in section 4.2.1.

4.3 Data treatment

Before presenting experimental results, let us briefly detail some specific data treatment procedure that require explanations. In particular, the definition of concentration statistics and their convergence are not trivial since all experimental runs are by nature transient in terms of concentration. We should also define the mass transfer event sorting chart in order to apply quadrant or hexadecan decomposition.

4.3.1 Definition of concentration statistics

Each run consists in the measurement of a stationary phenomenon, namely turbulence under the interface, acting on a transient one, namely mass transfer. While the definition of mean and fluctuating velocities from measurements is quite trivial, it is not the case for concentration. Indeed at a given point in the flow, concentration varies with time due to both diffusion acting on $\overline{C}$ and turbulence causing c'. The estimation of mean and fluctuating concentrations can be done in two ways: either by repeating the same experiments multiple

times, or by using a time fitting to estimate time varying local values of $\overline{C}$. The first option leads to many technical difficulties, especially related to calibration and treatment time and hard drive memory required to store the data, as discussed above. The second option is more convenient, and has been chosen by Variano and Cowen (2013). It is also used in this study. First, all instantaneous concentration fields are averaged over the horizontal dimension into the quantity $[C(z,t)]_x$. For all depths z, time series of $[C(z,t)]_x$ are plotted. This curves should exhibit two main features: a global increase of concentration at any depth until saturation concentration is reached in the whole ROI, and strong fluctuations of the concentration around this globally increasing trend due to turbulent mass transfer events.

For water, both features are observed in the example time series shown later in figure 4.25. At a given depth, the expected concentration value $C_E(z,t)$ is set by the global concentration increase, that is to say the time series trend smoothed from its turbulent fluctuations. $C_E(z,t)$ is best described by exponential fitting of time series. Variano and Cowen (2013) used polynomial fitting, which was found to induce too much sensitivity of the expected concentration result on the fitting with the present data. The fitting expression is of the type

$$C_E(z,t) = k_c(z)(1 - e^{-k_t(z)t}) \tag{4.19}$$

The fitting parameter k_c is homogeneous to a concentration and represents the concentration value reached at depth z at the end of the measurements. Parameter k_1 represents the speed of mass transfer at depth z and should be related to K_L.

For DPS, this expression can be modified to account for a low increase of mean concentration at short times (see figure 4.25):

$$C_E(z,t) = k_c(z)(1 - e^{-k_{t1}(z)t - k_{t2}(z)t^2}) \tag{4.20}$$

It is worth noting that $C_E(z,t)$ is not strictly equivalent to a statistical average concentration since it is not evaluated from a repetition of statistically independent experiments. It is however a very relevant quantity in our case, since it estimates the concentration that would be expected at a given depths without the presence of turbulent scalar structures. We thus assume in the following that $C_E(z,t) \equiv \overline{C}(z,t)$ and concentration fluctuations are defined as $c'(x,z,t) = C(x,z,t) - \overline{C}(z,t)$.

4.3.2 Statistical stability and convergence

4.3.2.a First order statistics

All measurements are performed once the oscillating grid turbulence is established and stationary. Velocity measurements can thus be considered statistically stationary, and first order statistics computed using the full data range. Convergence tests were performed on each run to validate statistical convergence of the mean velocity fields. With the previous definition of the mean concentration, there is no need to demonstrate its statistical convergence.

4.3.2.b Second order statistics

The second order statistics of concentration and/or mass fluxes can then be estimated in time intervals over which they are statistically stationary. As mentionned above, velocity fluctuations are intrically statisticaly stationary in the experiments. Concentration fluctuations are however not stationary by design, since mass transfer is a transient phenomena. The computation of second order statistical properties such as rms of concentration fluctuations or turbulent mass fluxes can only be made in time intervals on which all fluctuations are statistically stationary, or by using sliding averages.

It is possible to verify the stationary hypothesis in a time interval by plotting the time series of concentration fluctuations, and check that it is distributed around a zero mean value with no apparent variations of the amplitude of fluctuations with time. Variano and Cowen (2013) use the stationary assumption in their water experiments on a time interval of 400 s. Here we find that statistical convergence of concentration fluctuations is achieved between 200 and 1250 s for water and between 700 and 1750 s for 10 ppm DPS, leaving a 1000 s time interval open for statistical analysis (see section 4.5.3.b). For statistical convergence of second order statistics to be reached, the stationary interval must include a sufficient amount of independent large scale events, typically a few hundreds. The typical lifetime of a scalar event can be estimated from the integral time scale, that is to say the integral of time correlation coefficient (see the following section 4.5.4.b). Here the order of magnitude of integral time scale of concentration fluctuations is 10 s and so the stationary time interval is 100 times greater than the typical scalar eddy turnover. Convergence tests of statistical values have also been performed to check that the amount of data is adequate. Cases where data convergence is questionable are clearly pointed out in the analysis hereinafter.

4.3.3 Event classification for conditional analysis

Quadrant analysis is a simple but efficient data processing technique, widely used in the investigation of turbulent flows. It consists in sorting local flow events according to the sign of their fluctuation, and performing a conditional analysis of turbulent mass or momentum fluxes based on this sorting. This can be used in particular to analyse Reynolds stress data or turbulent mass fluxes and determine which type of fluctuating velocity events are the most relevant for mass and momentum transfer in complex situations. The first use of quadrant analysis was proposed by Wallace et al. (1972) in a study of Reynolds stresses in the wall boundary layer of a turbulent channel flow. Since then, many studies have used quadrant analysis and its derivatives for the study of various phenomena such as mixing at turbulent boundary layers (Vinçont et al., 2000), ejection events in rough bed channel flows (Mignot et al., 2009), sediment motion (Carvalho and Aleixo, 2014), and even mass transfer at gas-liquid interfaces (Variano and Cowen, 2013). An extensive review of the method and its application has been published by Wallace (2016). The basic principles of the method and its application to the present data are briefly explained hereinafter.

Turbulent event, joint probability density function, and covariance integrand: A turbulent event is defined as an instantaneous fluctuation of one or several flow characteristic (velocity component, concentration, temperature...). The joint probability density function (PDF or co-variance) $\mathrm{P}(a',b')$ of any pair of properties' fluctuations a' and b' represents the occurring probability of a turbulent event with fluctuation values equal simultaneously to a' and b' at a given location of the flow or in a ROI. The joint PDF can be decomposed into four quadrants based on the sign of each fluctuation. For example, Q1 if $a'>0$ and $b'>0$, Q2 if $a'<0$ and $b'>0$, Q3 if $a'<0$ and $b'<0$ and Q4 if $a'>0$ and $b'<0$. Here for example, the integral of $\mathrm{P}(a',b')$ over Q1 is the total probability of appearance of events with both positive fluctuations in the ROI. The relative strength of each quadrant can be quantified by the co-variance integrand $a'b'\mathrm{P}(a',b')$. The higher this product the most probable and intense are the event of the associated quadrant. This decomposition can for example be used on PIV data where couple of instantaneous fluctuations u'_x and u'_y are easily accessible in the plane of measurement. Quadrant decomposition then allows to identify which of the turbulent velocity events are dominant in the flow dynamics(Wallace, 2016).

Conditional flux: Another analysis that can be done based on quadrant sorting is a conditional average of the turbulent fluxes or Reynolds stresses. For example the Reynolds stress $\overline{u'_x u'_y}$ can be decomposed into $\overline{u'_x u'_y} = \left(\overline{u'_x u'_y}\right)_{Q1} + \left(\overline{u'_x u'_y}\right)_{Q2} + \left(\overline{u'_x u'_y}\right)_{Q3} + \left(\overline{u'_x u'_y}\right)_{Q4}$ where $\overline{u'_x u'_{y_{Qi}}}$ is the contribution of quadrant i to the total Reynolds stress. This can be applied equivalently to mass fluxes $\overline{u'_j c'}$ in order to evidence the velocity events that are the major contributors to mass transfer, providing that concentration and velocity fluctuations are measured simultaneously (Vinçont et al., 2000).

Extension of the quadrant analysis: If the data allows to do so, the quadrant sorting can be extended to sets of more than two simultaneous fluctuations. Vinçont et al. (2000) used simultaneous PIV and PLIF measurement to study passive scalar dispersion in a turbulent boundary layer. They applied conditional averaging in 8 octants based on the signs of three fluctuations u'_x,u'_y and c'. In the present work, three velocity fluctuations are measured together with concentration fluctuations. Sorting could thus be extended to $2^6 = 16$ categories or "hexadecans". Since mass transfer events are mostly vertical, the quadrant terminology is also used as in the work by Variano and Cowen (2013). The sorting in quadrants, octants and hexadecans based on the signs of fluctuations is defined in table 4.5.

Quadrant	Octant	Hexadecant	u'_x	u'_y	u'_z	c'
Q1	O1	HX1	+	+	-	+
		HX2	-	+	-	+
	O2	HX3	+	-	-	+
		HX4	-	-	-	+
Q2	O3	HX5	+	+	-	-
		HX6	-	+	-	-
	O4	HX7	+	-	-	-
		HX8	-	-	-	-
Q3	O5	HX9	+	+	+	-
		HX10	-	+	+	-
	O6	HX11	+	-	+	-
		HX12	-	-	+	-
Q4	O7	HX13	+	+	+	+
		HX14	-	+	+	+
	O8	HX15	+	-	+	+
		HX16	-	-	+	+

Table 4.5 – Definition of quadrants and hexadecants for conditional analysis of Reynolds stresses and turbulent mass fluxes. The quadrants are defined according to Variano and Cowen (2013). The signs of u'_z in this work are opposed to those of VC since their vertical axis is oriented upwards whereas it is here oriented downwards.

The type of event described by each quadrant is the following:

- **Q1**: Up-going patch of fluid carrying higher concentration fluid. The concentration fluctuation is positive, meaning that the local concentration at the point of interest is higher than the mean concentration at this depth. This higher concentration patch is moved upwards where it merges into an area of higher (equivalent) concentration. Q1 events are thus supposed to reduce diffusion efficiency.

- **Q2**: Up-going patch of fluid carrying lower concentration fluid. If this low concentration patch enters high concentration boundary layer close to the interface, the event can be qualified as a surface renewal event (Variano and Cowen, 2013).

- **Q3**: Down-going patch of fluid carrying lower concentration fluid. The concentration fluctuation is negative, meaning that the local concentration is lower than mean concentration at this depth. Moving downwards, the fluid patch meets an area of lower concentration. As Q1 events, Q3 events are supposed to reduce diffusion efficiency.

- **Q4**: Down-going patch of fluid carrying higher concentration fluid. The patch of positive concentration fluctuation is moved downwards, towards an area of event lower mean concentration. Diffusion is thus greatly increased. Q4 events correspond to peeling/injection events.

Octants and hexadecans allow to describe the same type of up and down-going motion than the quadrants, but they bring the additional information of horizontal fluid motion, which can be used to characterize the efficiency of turbulent mixing at a given depth.

Now that the literature background has been introduced, and the experimental conditions and data treatment procedure defined, results of experimental runs will be detailed. First hydrodynamics under the interface is studied in water and DPS using SPIV results. Concentration statistics in both fluids are then detailed using PLIF measurements only. Both sets of fields are finally coupled, and turbulent mass fluxes are studied using conditional analysis.

4.4 Hydrodynamics under the interface

4.4.1 Mean flow and turbulence

As detailed extensively in chapter 3, the appearance of a mean flow inside a grid stirred tank is inevitable, especially in presence of dilute polymer. Mean flows have two unwanted effects on our study of interfacial mass transfer. First, a large mean circulation in the tank may lead to a contraction of the scalar boundary layer that is not due to turbulence, hence to biased estimation of turbulent mass transfer coefficient K_L. Second, if the region of Eulerian observations is smaller than the width of the tank, velocity and scalar structures may move in and out of view under the action of mean circulation. This makes the statistical analysis of mass transfer events more difficult. Unfortunately, a large field of view comes to the cost of spatial resolution. Since the objective here is to achieve high spatial resolution of the source layer and if possible the viscous layer, the ROI cannot include the full tank's width. The choice was made to locate it at the center of the tank, horizontally aligned with the grid's central bar, as sketched in figure 4.10.

4.4.1.a Mean flow fields

We previously noticed that the mean flow over turbulence ratio in the present apparatus could be poor in the tank used for this study (section 3.4.5.c). It is thus important to have an estimation of the mean flow in the chosen ROI.

Mean flows obtained in the ROI for the experimental runs of table 4.4 are shown in figure 4.11. Vectors are projections of the 3 components SPIV measured vectors in the laser plane. Background color represents the magnitude of the out-of-plane velocity component.

First, the repeatability of mean flow under the interface is limited, especially for water where very different mean flow structures can be observed among the runs. Mean flow in

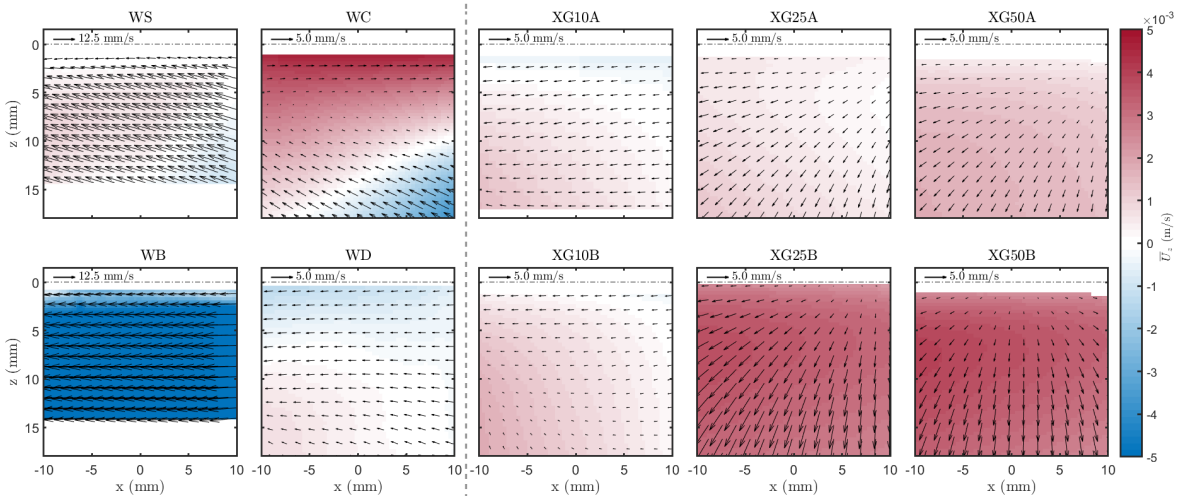

Figure 4.11 – Mean flow under the gas-liquid interface for water (runs WS,WB,WC and WD) and DPS at different concentrations (XG10A, WG10B, XG25A, XG25B, XG50A and XG50B). Vectors show the two in-plane components of the velocity field, and colorbar the out-of-plane velocity component. For clarity, only one every four vector is represented and XG100A run not shown.

the tank is forced at the grid's altitude. Mean re-circulation develop in the tank, but in the water case they are not observed to reach the interface (cf chapter 3). Various secondary recirculations may then be established between the two side vortices above the grid and the interface. These secondary flows have already been observed to be poorly repeatable (McKenna and McGillis, 2004b). In particular, strong lateral motion is observed in run WS but the out-of-plane motion is quite low, whereas both out-of-plane and lateral motions are strong in the WB run. The WC experiment exhibits a more elaborated three dimensional mean structure. As for the WD run, it only has a low lateral motion and almost no out-of-plane motion.

For DPS, the topologies of sub-surface mean flows are more similar between two runs. Runs XG10A and XG10B show similar in-plane lateral motion. Runs XG25A and XG25B exhibit a weak leftward down-welling structure, with a significantly higher out-of-plane lateral motion in the XG25B case. It is the same for XG50A and XG50B, but this time the down-welling of XG50B is centered in the ROI. A single run is available for 100 ppm solutions, which does not allow for repeatability verification, so it is not presented here. In chapter 3, it was observed that in DPS, the mean flow structures around side vortices are produced by the grid, and that these mean recirculating structures reach up to the interface, with a gobal up-going motion at the center of the tank. The down-welling observed in sub-surface ROI could thus be consequences of the up-going motion in the depth of the tank.

4.4.1.b Mean-to-turbulence ratio

As far as turbulence is concerned, its intensity should not vary along the horizontal direction x but only with depth (vertical direction) z, unless some strong mean flows are involved. Moreover, the action of the free surface is not equivalent on all velocity fluctuations, as mentioned in the background (section 4.1.1). This point is addressed in the following sections. Here we only need to estimate local levels of turbulence intensity to check that it is sufficiently high compared to the mean flow. The local intensity of turbulence is thus calculated as the norm of the fluctuating velocity rms field: $\sqrt{\langle u_x' \rangle_{rms}^2 + \langle u_x' \rangle_{rms}^2 + \langle u_z' \rangle_{rms}^2}$. Dividing locally averaged velocity by this scale velocity, representative of turbulence intensity, one gets

the mean-to-turbulence ratio field, called Γ (short for $\|\Gamma\|$) as in chapter 3. The Γ fields are averaged over their width, and the profiles of $[\Gamma]_x$ under the interface are plotted in figure 4.12.

Γ values are very dependent on the structures of mean flow in the ROI. However figure 4.12 shows that for any XG concentration and any mean flow, the value of mean-to-turbulence ratio is most of the time below 2 in the ROI, and is globally of the order of unity, which means that turbulence is at least as intense as the mean flow. This is better that what the results of chapter 3 led to expect. It can be explained by the fact that the interface damps both mean flow and turbulence velocities.

4.4.2 Instantaneous velocity fields and three dimensional effects

Example of instantaneous velocity fields for water and DPS are displayed in figure 4.13. Only one every four vector is represented in both the x and z dimension for the sake of readability. On the left part, velocities are projected in the x-z plane, leading to velocity patterns similar to what could have been obtained by classical PIV measurements (Herlina, 2005; Janzen et al., 2010). Several type of flow structures can be observed and combined: lateral sweeping (XG25B frame 3382), up or-down going large scale motions (XG50B frame 1854, XG100A frame 637), or swirling structures (WC frame 2917, WD frame 217 and 494, XG25B frame 3382, XG50B frame 1854). SPIV allows to make out the three dimensional structure of instantaneous eddies reaching the interface, which is not accessible through classical PIV. Lateral sweeping motion is for example evidenced for both the in-plane and out-of-plane horizontal velocity component (XG50B frame 1854, XG100A frame 637). Horizontal swirling structure can also be noticed (example in WD frame 494, XG100A frame 637). The flow in the ROI is most of the time a complex combination of all types of structures (WD frame 494).

The existence of out-of-plane swirling motion has an impact on both mass transfer and our measurement of it: it can be responsible of non-vertical turbulent mass fluxes contributing to turbulent mixing, and it can move scalar patches in and out of the plane of measurement, making observable scalar structures even more complex than what would have been under 2D turbulence. An example of fluorescence imaging of scalar structures in horizontal planes under the interface (see appendix F) illustrates the existence of horizontal scalar transport by 3D motion.

Another qualitative but yet meaningful observation is the fact that flow structures seem smaller in water than in DPS (see for example the larger eddies in fields XG25B frame 3382 and XG50B frame 1854). This point is still to be verified by quantitative estimation of the size of the structures by two point statistics for example, but it is likely to have a great importance for mass transfer, since the balance between injection and surface renewal events is conditioned by the size of the structures able or not able to deform and/or peel the scalar boundary layer. Larger flow structures in DPS solutions could for example lead to a dominance of surface renewal or contraction of the scalar diffusion layer whereas smaller flow structures observed in water could increase the probability of injection events.

Based on the estimation of the undisturbed integral length scale values L_∞ shown in table 4.2, and under the hypothesis of Brumley and Jirka (1987) stating that the surface influenced layer has a depth of approximately L_∞, one can say that the present ROI is included within the surface influenced layer. With the defined ROI and spatial resolution, we are not able to visualize the onset of energy redistribution between components when entering the surface influenced layer and to check for its size. However we will hopefully be able to detail more accurately the smaller characteristic depths of the flow.

What can still be done regarding the surface influenced layer is to observe of the shape

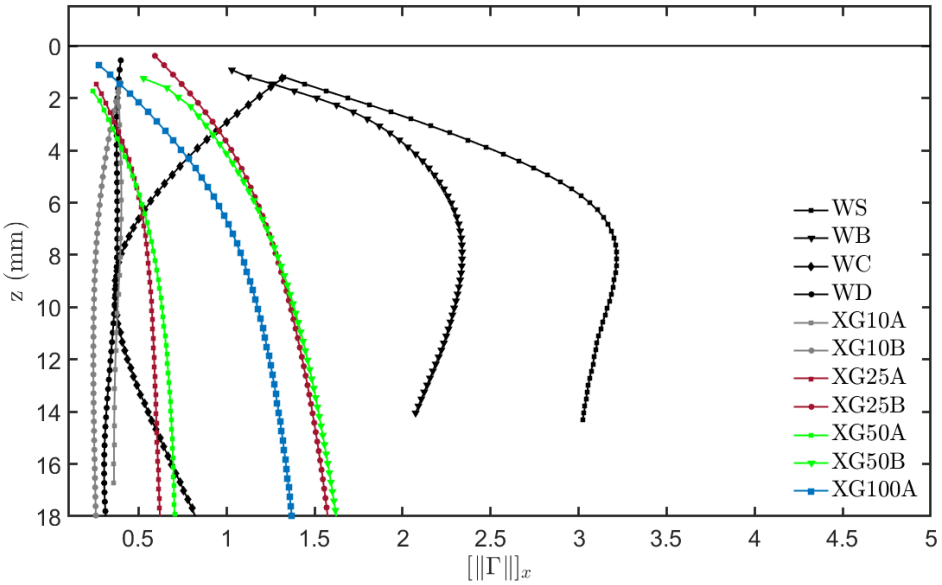

Figure 4.12 – Mean to turbulence ratio Γ under the gas-liquid interface for water and DPS at different concentrations.

of velocity fluctuations rms profiles, evidence the strong damping of vertical fluctuations, and see if its dynamics is modified by the presence of polymer. To do so, the width averaged profiles of rms of vertical and horizontal velocity fluctuations are plotted in figure 4.14 a and b. Sub-figure a is simply the with averaged profiles of vertical fluctuations $[\langle u_z' \rangle_{rms}]_x$, sub-figure b is the width averaged profile of the norm of horizontal fluctuations $[\sqrt{\langle u_x' \rangle_{rms}^2 + \langle u_y' \rangle_{rms}^2}]_x$.

From these graphs, several observations can be made:

- The repeatability of measurements seems to be harder to achieve in water than in DPS: all pair of curves for similar concentration DPS runs are relatively close to each other whereas significant differences are observed in water. This can be due to several factors, among which the various mean flow encountered in water, or surface pollution. The issue of surface pollution is addressed when analyzing the viscous sub-layer hydrodynamics in a following paragraph.

- The WB run is obviously biased. The trends compare well to the other runs, but turbulence levels are unexpectedly high. This runs is also associated to very high levels of mean flow (see figure 4.11). It will be put aside for the following analysis.

- As expected in the surface influenced layer, the horizontal velocity fluctuations are stronger than the vertical ones. Curves for vertical fluctuations are always below 5 mm/s, and curves for horizontal fluctuations always above this value. This is verified for all water and DPS runs no matter the concentration. Moreover, the vertical fluctuations strongly decrease when approaching the interface, whereas horizontal fluctuations only weakly decrease, stay approximately constant or even increase. The concept of energy transfer from vertical to horizontal motion is verified. Turbulence coming from the oscillating grid is more energetic in the vertical direction due to the grid motion, and decays when moving away from the grid. If there were no interface, both vertical and horizontal fluctuations would decay, with vertical fluctuations staying always stronger than the horizontal ones. Here inside the blocking layer, the vertical

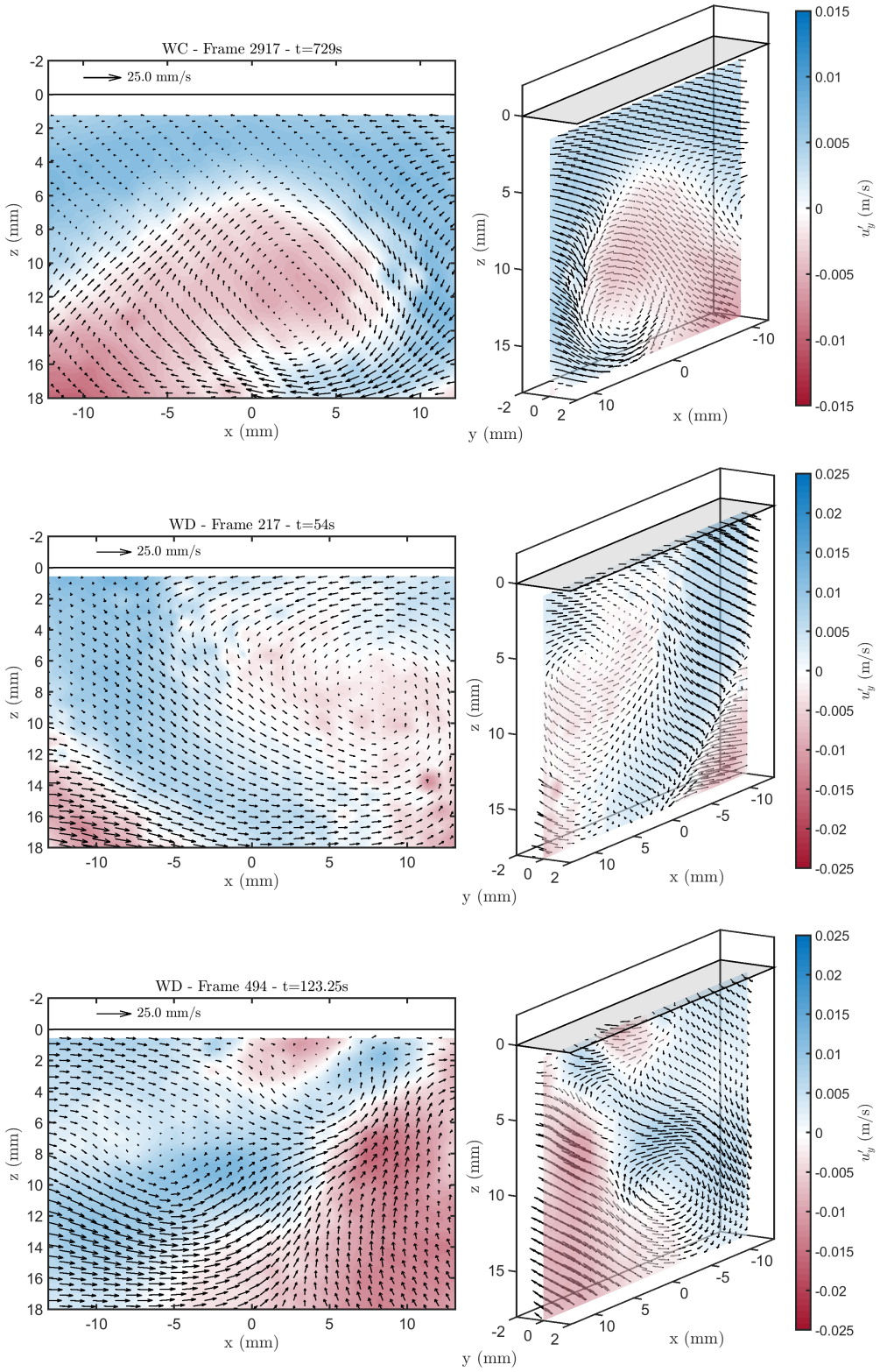
WC - Frame 2917 - t=729s
25.0 mm/s
z (mm)
x (mm)
y (mm)
u'_y (m/s)
WD - Frame 217 - t=54s
25.0 mm/s
z (mm)
x (mm)
y (mm)
u'_y (m/s)
WD - Frame 494 - t=123.25s
25.0 mm/s
z (mm)
x (mm)
y (mm)
u'_y (m/s)

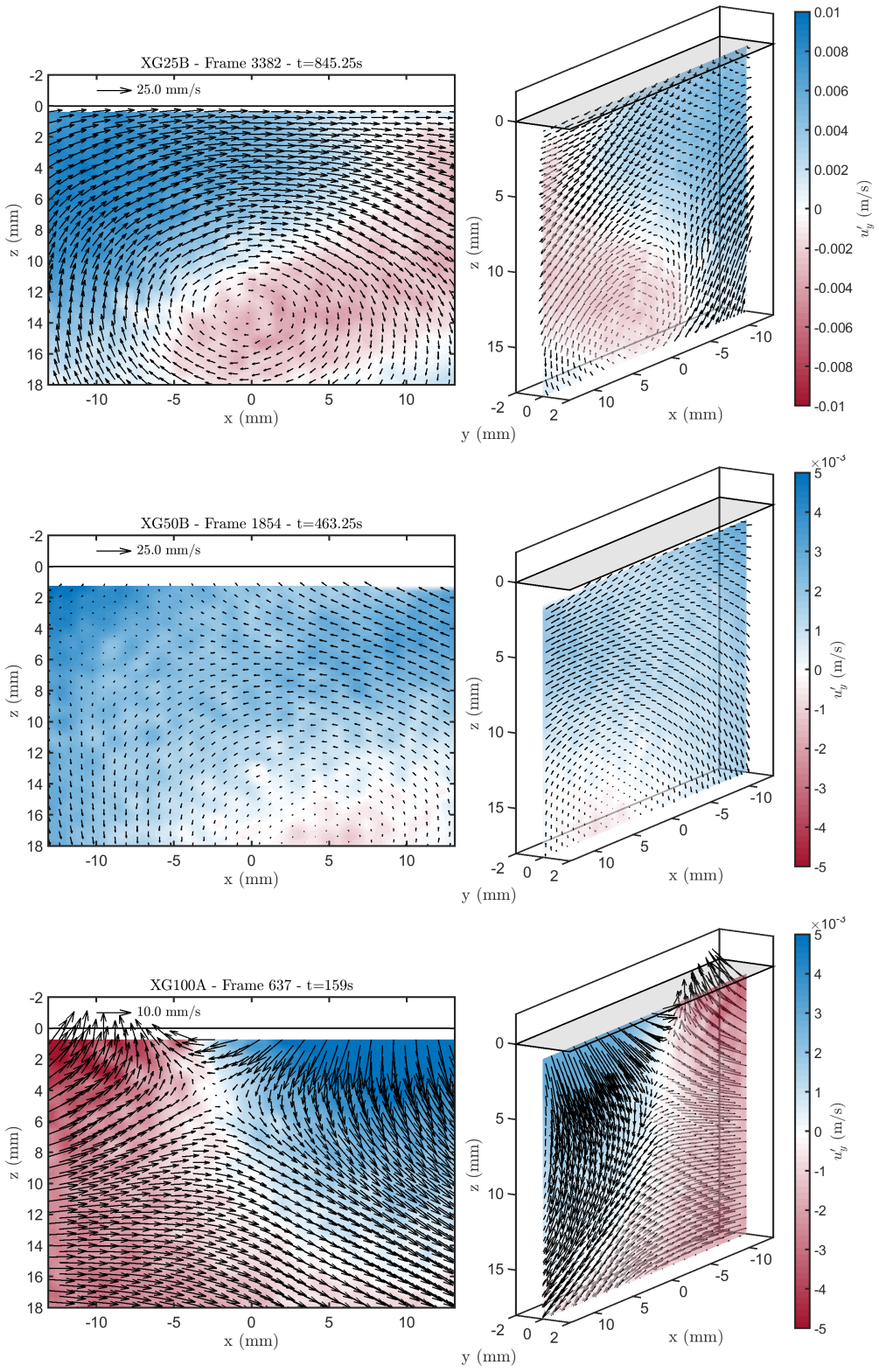

Figure 4.13 – Example of instantaneous $\mathbf{u}'$ fields in water (first page) and DPS (second page). Only one every four vector in both x and z dimension is plotted. A scale velocity vector is shown in the top left corner of each sub-figure.

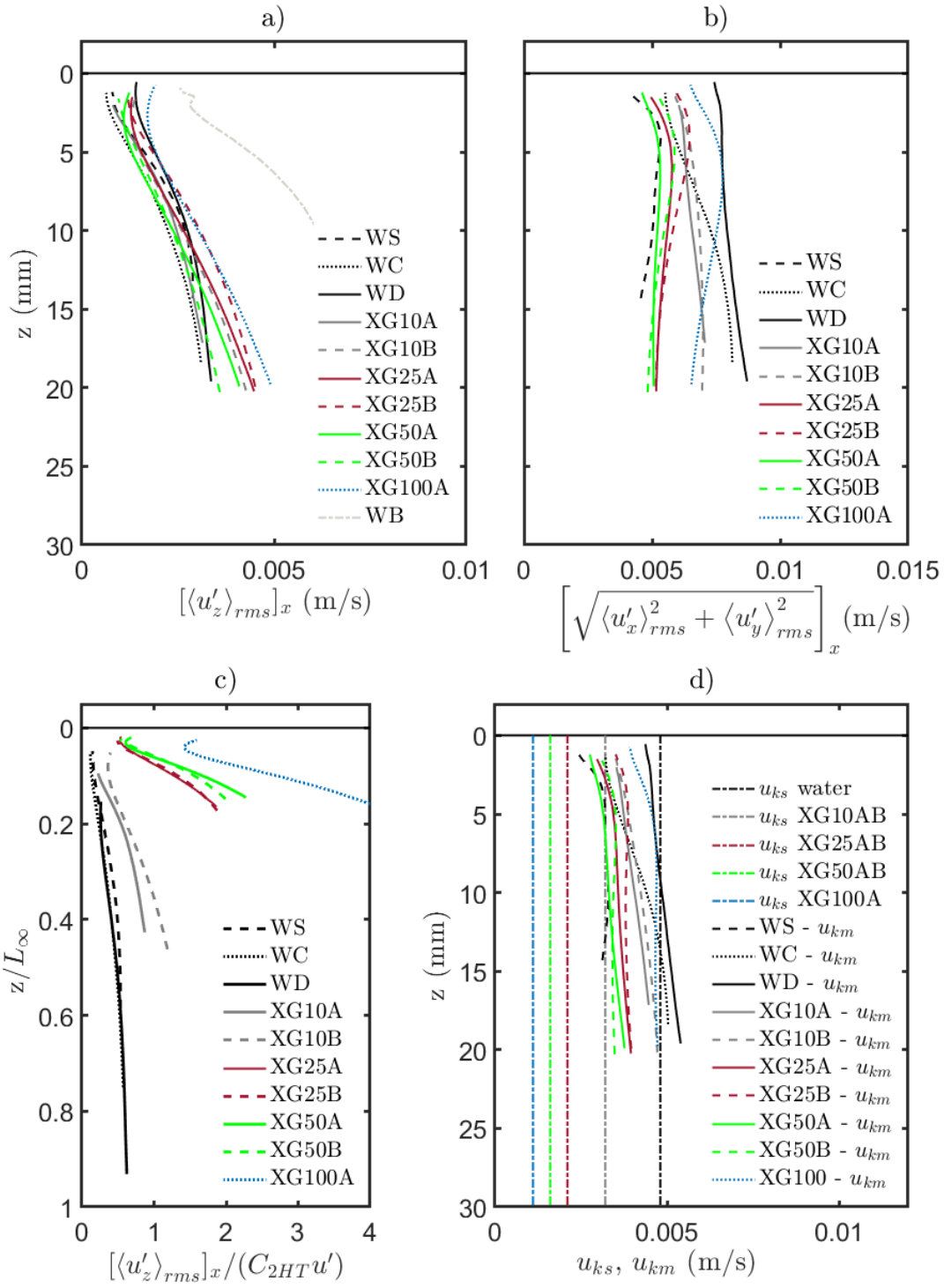

Figure 4.14 – Sub-surface profiles of rms velocities and turbulent intensity. a) rms of vertical velocity fluctuations b) norm of the rms of horizontal velocity fluctuations. c) rms of vertical velocity fluctuations scaled by the expected undisturbed vertical velocity scale C_{2HT}, along depth normalized y the theoretical surface influenced layer depth. d) undisturbed kinetic energy velocity scale u_{ks} and measured kinetic energy velocity scale profiles u_{km}. All curves are shown for the available runs except for the spurious run WB.

ones decay much faster than the horizontal ones and are lower: their energy has been transferred to the horizontal ones that are stronger and see their decay balanced which may event lead them to increase.

- The intensity of vertical velocity fluctuations does not seem to depend on polymer concentration. For horizontal fluctuations however, the rms is globally decreased with increasing polymer concentration, except for the WS water run (that as we will see later is likely subject to surface pollution) and for the 100 ppm single run. For horizontal fluctuations, the trend observed on the HT profiles and predicted by the evolution of the undisturbed scale u' is retrieved under the interface. Increasing polymer concentration leads to decreasing horizontal turbulence. However, the turbulent intensity measured is stronger that what could be expected from u' estimation, indicating that the relationship between OGT and subsurface turbulence is less trivial in DPS than in water. The case of the 100 ppm run seems to indicate a critical concentration effect after which near surface horizontal turbulence intensity could further increase. However only a single measurement has been treated for this concentration and results should be considered carefully. For vertical velocities in DPS, lower values were expected from the HT type profiles derived in chapter 3. Indeed those profiles show that the decay rate of turbulent intensity is increased with increasing polymer concentration. The undisturbed velocity scale at the interface u', and its vertical counterpart (approximately $C_{2HT}u'$) should be decreased, which is not obvious on the figure. However we are here focused inside the source layer, and so the fluctuating velocity magnitudes strongly depend on the energy transfer between velocity directions as well, which has no reason to be equivalent for water and DPS.

In order to investigate this last point further, the rms profiles of figure 4.14 b are plotted along the z coordinate scaled by the undisturbed integral length scale, which is used to estimate the depth of the surface influenced layer (figure 4.14 c). Rms values are scaled by the product of the undisturbed velocity scale u' and the second HT constantC_{2HT}, which is an estimation of the undisturbed vertical velocity scale (u' being defined on horizontal velocities). The surface influenced layer is defined as the depth at which the largest flow structures begin to see the interface. The turbulent structures produced by the grid tend to be larger along the grid oscillating direction, here the z axis. Hence, the value of L_∞ should be a good parameter to scale rms profiles of data. At $z/L_\infty = 1$, $\left[\langle u_z' \rangle_{rms}\right]_x / C_{2HT}u'$ should be less than unity. Indeed the value of u' is only asymptotically reached at the interface location in absence of interface, and so the value of bulk turbulence rms fluctuation at the surface influenced layer is theoretically below u'. It is verified for all water runs, for which the value of $\left[\langle u_z' \rangle_{rms}\right]_x / C_{2HT}u'$ is between 0.5 and 1 at $z/L_\infty = 1$. For DPS however, two main features can be observed. Firstly, polymer solution display rms velocity values higher than the undisturbed velocity scale, resulting in $\left[\langle u_z' \rangle_{rms}\right]_x / C_{2HT}u'$ values greater than one. This is surprising since u' is supposed to be an upper bound of all velocity fluctuations, Secondly, the decay of vertical fluctuations, which appeared to follow a similar slope in water an DPS on figure 4.14, displays a much steeper trend when scaled by the estimated undisturbed integral length scale.

Putting aside for the moment the questionability of estimation of the undisturbed length scale estimation, then the previous observations remark can be interpreted in two ways:

- The same type of energy transfer may occur in water and DPS, but the difference observed in trends after scaling could lay within the purely kinematic definition of the surface influenced layer. In the BJ (Brumley and Jirka, 1987) definition, the interface is

said to be seen by turbulence at depths corresponding to the size of the largest eddies, which is a kinematic criterion. It may be so that the effects of the interface are felt at depths smaller than L_∞ in DPS, and that the undisturbed integral length scale is not the appropriate quantity to define the interface depth of influence.

- The energy transfers within the surface influenced layer may be fundamentally different in presence of polymer and the decay of vertical fluctuations concentrated in a region smaller than the surface influenced layer, and thinner with increasing polymer concentration. The unexpectedly high turbulent velocities could then be the result of completely different interactions occurring in the higher depths of the surface influenced layer.

When further looking at the horizontal rms profiles of figure 4.14 for DPS, one notices that they are all well above the undisturbed velocity scale u'. This is however not as surprising as it is for the vertical fluctuations, since energy is supposed to be transferred between velocity components and sub-surface fluctuations are bound to be higher than the undisturbed horizontal velocity. However one may check the consistency between the undisturbed turbulent kinetic energy and the measured one by constructing a kinetic energy based velocity.

The undisturbed TKE velocity scale is computed from the data available in chapter 3 as $u_{ks} = \sqrt{((C_{2HT}u')^2 + 2u'^2)/3}$ (Variano and Cowen, 2013). The profile of measured kinetic energy velocity scale is computed at all depths as $u_{km} = \left[\sqrt{(\langle u'_x\rangle^2_{rms} + \langle u'_y\rangle_{rms} + \langle u'_z\rangle_{rms})/3}\right]_x$. Figure 4.14 d shows that the measured velocity scale is always much higher than the undisturbed scale for DPS. For water, the maximum value of turbulent kinetic energy based velocity scale is at worst slightly underestimated by the undisturbed scales prediction (black curve for run WD). Values for u_{km} higher than u_{ks} indicate that for some reason, the turbulent kinetic energy is higher thant the maximum expected input coming from the bulk. Variano and Cowen (2013) found that the profile of u_{km} was almost flat in the surface influenced layer for water, and decreased in the viscous sub-layer. However they did not compare its value with its expected undisturbed level at equivalent depth or to the bulk input. Here u_{km} curves are either constant or purely decreasing, indicating that turbulence decays in all the ROI.

The reasons for the observed difference between u_{km} and u_{ks} can be explained in different ways. From an experimental point of view, it can be that the full tank measurement tend to underestimate the undisturbed scales at the interface. This is underlined by the fact that even for water, undisturbed prediction slightly underestimates the measured intensity. It would then mean that the HT description of OGT is not sufficient to accurately predict upcoming turbulent properties here. A second explanation could be that the solutions used in the dissolution experiments are degraded compared to those used in chapter 3, their viscosity decreased and turbulence level increased. Yet similar fabrication procedures have been used for experiments of chapter 3 and of the present chapter, and it has been checked that the rheology of solutions used for this chapter fitted well to the reference fittings, so this second explanation is less probable. The last explanation would be that the increase in measured turbulent kinetic energy is due to an additional mechanism of production in the surface influenced layer of polymer solutions, that the spatial resolution of chapter 3 measurements did not allow to foresee. This intrinsic polymer feature could then explain the fact that the difference between expected and measured kinetic energy increases with polymer concentration.

As a conclusion, the general concept of energy transfer from horizontal to vertical velocity components remains valid in DPS. However surprisingly high turbulent intensities in the

ROI and inefficiency of the scaling by the estimated surface influenced depth lead to interrogations about the exact mechanisms of energy transfer between velocity components in DPS. The present analysis is meant to understand the action of polymer on turbulent mass transfer, and so the choice was made to focus on the thin interfacial region. We can thus keep on with the study of thinner characteristic sub layers, simply acknowledging that our estimated undisturbed interfacial scales may underestimate the upcoming levels of turbulence. The understanding of what exactly goes on for turbulence approaching the interface would require to focus on the onset of surface influence, that is to say to estimate from direct measurements at in a larger ROI of the depth of the source layer.

4.4.3 Depth of the viscous sub-layer

Inside the surface influenced layer, the viscous sub-layer should be evidenced by a local maximum of horizontal velocity fluctuation gradients, whether the interface is polluted or not (see the background section 4.1.1). Based on DNS observations and the unpolluted surface HG theory, the $\langle u'_x \rangle_{rms}$ and $\langle u'_y \rangle_{rms}$ should keep increasing at inside the viscous sub-layer but with a lower gradient. Experimental results have yet shown that those profiles may also reach a maximum inside the viscous layer before decreasing when further approaching the interface. For low up-coming turbulence Reynolds numbers, horizontal rms may as well decrease in the surface influenced layer, but at a smaller rate than the vertical ones. The viscous sub-layer is then evidenced by an increase in the decay rate (Janzen et al., 2010).

In all cases, the viscous sub-layer is thus evidenced by a peak or at least a change of slope in the gradient profile of horizontal rms. Horizontal and vertical velocity fluctuations rms profiles, are plotted on figure 4.14 a and b. The gradient of the horizontal rms profiles along the depth z are shown in figure 4.15 a (for velocities along x) and b (for velocities along y).

In figure 4.15 a, an abrupt decrease in vertical gradient of horizontal fluctuations is clearly evidenced for all DPS and water runs between z=2.5 mm and z=12 mm, except for the WC and XG10B runs. This decrease is associated with a near-surface local maximum for all runs, except for the 10 ppm runs where the maxima are less visible. Gradient profiles for the two horizontal components match quite well for all runs, indicating a good isotropy of turbulence in horizontal planes parallel to the interface. The viscous sub-layer size δ_ν is defined as the depth of the local maximum of the gradient curves, or if not visible the depth at which gradient begin to strongly decrease. The evolution of δ_ν with C_{XG} is plotted in figure 4.15 c. Error bars are computed as the standard deviation of measured δ_ν over all velocity components and all samples at the same polymer concentration.

The depth of the viscous sub-layer δ_ν increases with increasing polymer concentration. In order to check wether this effect can simply be attributed to the increase in viscosity or if it is more complex, the estimated Newtonian-equivalent viscous sub-layer depth is computed. It is based on the expression of Brumley and Jirka (1987), equation (4.1), where L_∞ is taken as the undisturbed integral length scale (values in table 4.2, and the turbulent Reynolds number is $Re_T = \rho u' L_\infty / \mu_0$. Equivalently, other Newtonian-equivalent viscous sub-layer can be defined using other typical viscosities and the same velocity and length scales. $\delta_\nu^{\mu_m}$ is defined on the average viscosity $\mu_m = (\mu_0 + \mu_\infty)/2$. $\delta_\nu^{\mu_\infty}$ is defined on the infinite shear rate viscosity μ_∞. The value of $\delta_\nu = \delta_\nu^{\mu_0}$, $\delta_\nu^{\mu_m}$ and $\delta_\nu^{\mu_\infty}$ thus estimated corresponds to the theoretical depth of viscous sub-layer for a Newtonian fluid of viscosities μ_0, μ_m and μ_∞ and with incident properties of turbulence similar to the present case. The evolution of those predicted Newtonian-equivalent sub-layers is plotted in figure 4.15 c, and the measured viscous sub-layer scaled by estimated values δ_ν^* is shown in figure 4.15 d.

For water, the measured viscous sub-layer depth is approximately twice the value pre-

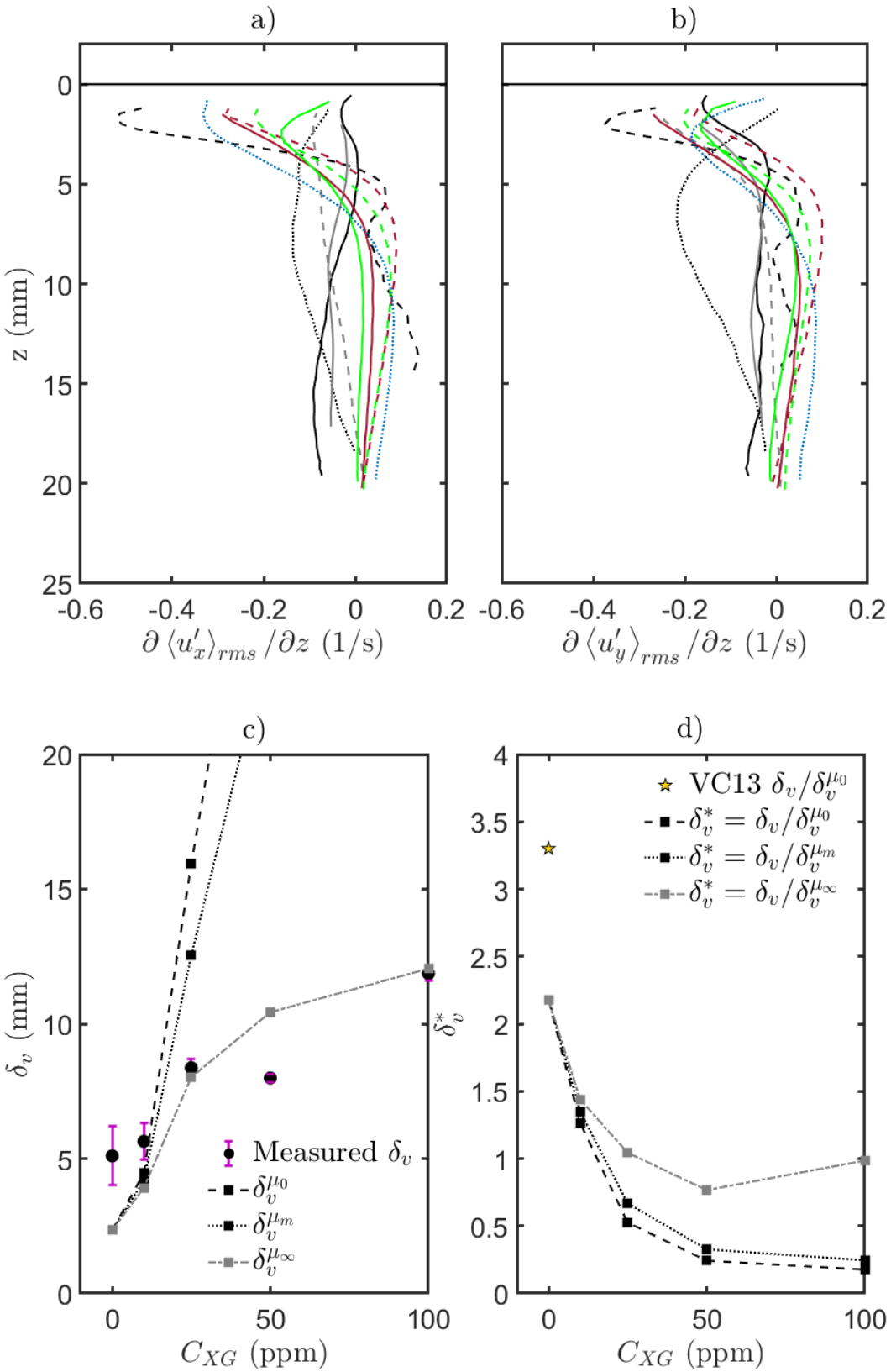

Figure 4.15 – Sub-surface rms profiles of horizontal velocity fluctuations (a along x, b along y, same color code as in figure 4.14) and evolution of the viscous sub-layer depth with polymer concentration. c) is the measured depth compared to prediction for Newtonian fluids at equivalent viscosities using equation (4.1). d) is the ratio of measured over predicted depths. VC13 is the viscous sub-layer depth extracted from Variano and Cowen (2013) experiments in water compared to their prediction using equation (4.1).

dicted by Brumley and Jirka (1987)'s relationship. Variano and Cowen (2013) also evidenced a viscous sub-layer larger than expected: their rms peak, attributed by the authors to surface pollution, was found at around twice the depth predicted by Brumley and Jirka (1987). By estimating the vertical gradient of their data, we find their viscous sub-layer to be about 3.3 times deeper than the prediction ($z \simeq 6.3$mm for a prediction of $\delta_\nu^{\mu_0=\mu_m=\mu_\infty} = 1.9$ mm). The corresponding data point is shown in figure 4.15 d. It is worth noting that in the present measurements, no significant difference is observed for the depth of the viscous sub-layer in water among runs identified as polluted and non-polluted, and ratios to prediction are close to the one found by Variano and Cowen (2013). It is therefore an indication that surface pollution only acts on the dynamics within the viscous sub-layer, but not on its depth.

The increase in viscous sub-layer depth with polymer concentration is much smaller than what it would have been for Newtonian viscous fluids of viscosity μ_0 or μ_m or even μ_∞. For concentrations higher than 25 ppm, zero and mean shear rate viscous fluid analogies largely overestimate the depth of the viscous sub-layer. Predictions based on the infinite shear rate viscosity yield better results, and the increase rate of measured δ_ν and $\delta_\nu^{\mu_\infty}$ are comparable in the [10-100] ppm range with a noticeable exception at 50 ppm. These results confirm for the near surface region what was well understood in bulk turbulence and close to rigid walls: dilute polymer solutions behave in no manner like viscous Newtonian fluids in terms of viscous boundary layers and typical scales. The results from figure 4.15 are yet surprising: the evolution of viscous sub-layer at larger scales is close to the prediction based on infinite shear rate viscosity. Yet, shear rate values under the interface are typically too low to reach the lower viscosity plateau of the polymer solution. An hypothesis to explain this behavior would be that polymer molecules tend to move away from the interface and leave a low concentration fluid layer under the surface where the fluid behavior is close to that of the solvent. This hypothesis is unfortunately difficult to check without any method to measure the local polymer concentration. We will also see that it does not agree well with the results presented in the next section about the evolution of velocity fluctuations inside the viscous sub-layer.

Viscosity thus does not seem to be the relevant parameter to describe the increase of the viscous sub-layer. Figure 4.15 d suggest that a scaling of δ_ν^* based on a dimensionless number for polymer concentration could be useful. In figure 4.16, $\delta_\nu^* = \delta_\nu/\delta_\nu^{\mu_0}$ is plotted versus (1+De), which is quantity equal to unity in polymer free solutions, so that water points can be included to the correlation.Using a first approach power law approximation in the moderate range of De studied, one could then write

$$\frac{\delta_\nu}{L_\infty} \sim \mathrm{Re}_\tau^{-1/2} \mathrm{De}^\alpha \tag{4.21}$$

Here $\alpha \simeq -2.3$ (determination coefficient R^2=0.84 for the power law fitting). This approximation is yet to be considered with caution due to the limited De range and amount of data points.

4.4.4 Velocity fluctuations inside the viscous sub-layer

In paragraph 4.4.2 the evolution of turbulence inside the surface influenced layer was briefly discussed. In a similar way, this paragraph focus on the behavior of turbulent velocity fluctuations inside the smaller viscous sub-layer. It can be emphasized that the present measurement have been performed at a higher spatial resolution than the existing literature experiments: at least 6 points of measurement are obtained inside the viscous sub-layer for the run with the smallest δ_ν (run WS). This allow us to explore the evolution of turbulent veloc-

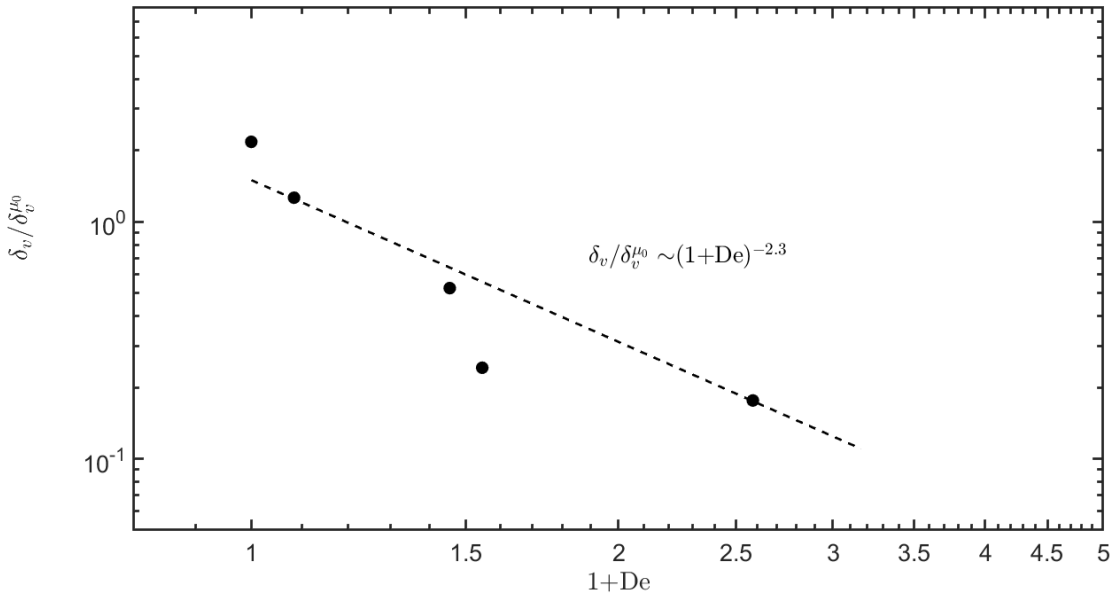

Figure 4.16 – Evolution of $\delta_v/\delta_v^{\mu_0}$ with the Deborah number in the very dilute range. The dotted line is the power law fitting, R^2=0.84.

ities inside this thinner interfacial region. They are also the only local measurement of flow properties in shear free viscous boundary layers of dilute polymer solutions.

The rms profiles of horizontal and vertical velocity fluctuations are plotted in figure 4.17 a and b along depth scaled by the measure viscous sub-layer value. Velocities profiles are scaled by their values at $z = \delta_v$.

Close to z=δ_v, vertical fluctuation profiles collapse on a linear trend of equation $\frac{u'_N}{u'_N(z=\delta_v)} = \frac{z}{\delta_v}$. They depart from this trend around $z \leq 0.6\delta_v$ (except for the WD and XG10B run) where they seemingly tend to a constant u'_N value. This non-zero vertical velocities at z=0 is explained in the next paragraph. Horizontal fluctuations profiles have two possible shapes: with or without rms peak. In HG theories, rms peaks are caused by interface pollution. Here we notice that rms peaks are sometimes observed for water (runs WS and WB) but not on all runs. This was also the case in the experiments of Janzen et al. (2010). For DPS, rms peak is repeatable for 25 and 50 ppm, and present on the only 100 ppm run but not on the two 10 ppm runs. The question is then the following: are these peaks due to surface pollution or polymer action?

4.4.4.a Surface pollution or polymer solution ?

In the 2016 series of experiment including the WS and WB experiments, the surface was only quickly skimmed prior to the experiments. After visualization of the rms profiles, a thorough cleaning procedure was established for the 2017 series of experiments in order to get rid of this probable surface pollution, and the WD run appeared peak-free. It is thus highly probable that the rms peaks evidenced in WS and WB are due to a higher surface pollution than expected. On the other hand, the 2017 water and lowest concentration DPS run do not show any rms peak, and higher concentration polymer display repeatable ones. Since the cleaning procedure remained the same during all the 2017 series, we can infer that the presence of rms peak in the associated experimental runs is not due to surface pollution but can be attributed to the presence of polymer. However the fact that surface pollution can

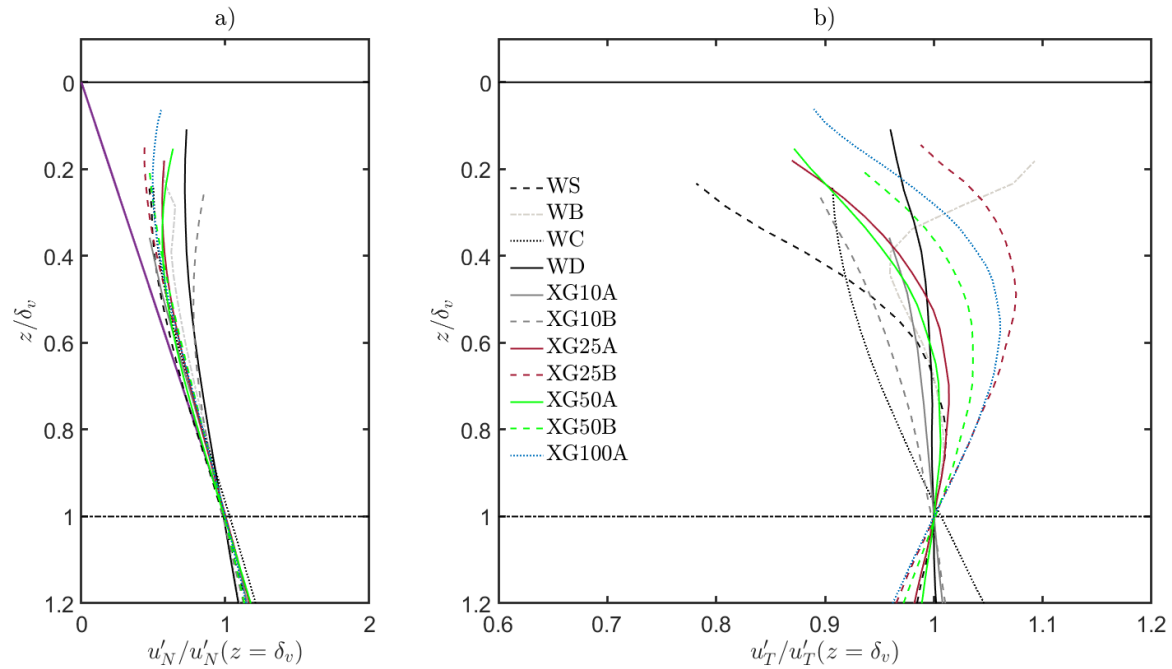

Figure 4.17 – Sub-surface profiles of rms of velocity fluctuations scaled by their value at the viscous sub-layer depth. a) are vertical fluctuations, normal to the interface, denoted u'_{N}. b) are horizontal fluctuations tangential to the interface, denoted u'_{T} such that $u'_{\mathrm{T}} = \sqrt{\langle u'_x \rangle^2_{rms} + \langle u'_y \rangle^2_{rms}}$. The purple plot on sub-figure a) is the $\frac{u'_{\mathrm{N}}}{u'_{\mathrm{N}}(z=\delta_v)} = \frac{z}{\delta_v}$ linear trend.

not be completely avoided has to be kept in mind for the rest of the analysis. It should also be recalled that the WB run is likely spurious. Scaled profiles are yet added to the graph for comparison.

Water runs without rms peaks display decreasing rms profiles of horizontal velocities, as could be found in the recent experiments of Janzen et al. (2010) for low grid Reynolds number. This indicates that the decay of horizontal fluctuations ruled by bulk turbulence properties is larger than the increase rate imposed by inter-components exchanges in the source layer. On the other hand, water run profiles with rms peaks have increasing horizontal rms profiles under these peaks. Since bulk turbulence properties are supposedly the same for all water runs, this implies that the inter-components exchanges in the source layer is highly dependent on the surface boundary condition. With surface pollution, energy exchanges between horizontal and vertical fluctuations seems stronger than with clean interfaces. The increase of horizontal rms caused by the interface is stronger than the decay rate imposed by bulk turbulence in polluted situations, whereas it is not in clean situations.

For DPS, but also for water run evidencing signs of surface pollution (WB and WS), the horizontal fluctuation peak's depth varies between $z = 0.5\delta_v$ and $z = 0.8\delta_v$. In the water case, we have already explained how surface active molecules are responsible for the further decrease of horizontal fluctuations.

By analogy with this surface-active mechanism, we can attempt to conceptually understand the similar behavior observed in surfactant free DPS: when a turbulent eddy enters the surface influenced layer, its energy is transferred from vertical to horizontal motion. Reaching the interface, it induces an horizontal motion and local shear stress due to its interactions, not with the surface active molecules but with deeper, less deformed eddies in which the local shear rate and thus local viscosity is different. Local additional horizontal shear

stresses are thus created by local viscosity variations, leading to a damping of fluctuation as induced by surface tension effects caused by surfactants.

To that extent, one may assume that the behavior of turbulence at interfaces between gas and DPS resembles that of turbulence at surfactant polluted air-water interfaces, but with different physical mechanisms at the origin of this behavior. In other words, the interfacial boundary condition regarding turbulence could be equivalent, but in the surfactant case it is fixed by interactions between surface active molecules at the interface only, whereas in the DPS case it derives from non-Newtonian hydrodynamics in the viscous sub-layer, without any surface active effect. In order to check that hypothetical and pictured view, one would need to access polymeric stress tensor components defined in equation (1.67). This unfortunately requires the measurement of instantaneous viscosity values, which is for now not achievable. We are thus limited to the clues brought by the examination of Reynolds stresses $\overline{u_i' u_j'}$, performed in section 4.4.5.

A last remark: the onset concentration of these effects seems to be between 10 and 25 ppm. As a comparison, the onset concentration for drag reduction of XG was found to be at best 20 ppm by Wyatt et al. (2011), and a critical concentration for DR was found at 70 ppm by the same authors. Our range of concentration thus compare quite well to the relevant concentrations for drag reduction, and we confirm that polymer may indeed have an action on boundary layer turbulence even in the very dilute regime.

4.4.4.b Evidence of interface mili-oscillations

The vertical gradients of vertical velocity fluctuations are shown in figure 4.18 a, plotted versus the z/δ_ν coordinate. They are found to reach a negative minimum value (maximum norm) at a depth δ_ν^z slightly smaller than δ_ν and start to increase when further approaching the interface. This is observed for all runs, in water or DPS. The value of δ_ν^z/δ_ν is almost constant with polymer concentration, around 0.8 (see sub-figure inserted), with a slight decrease upon increasing polymer concentration. This means that under the free surface, the mechanisms of energy transfer from vertical to horizontal fluctuations is modified, and energy seems to be transferred back to the vertical motion. Figure 4.17 and 4.18 show that for all runs, vertical velocity fluctuations rms does not exactly tend to zero at the interface location, and that their vertical gradient is close to or even slightly above zero. This means that a thin layer of almost constant $\langle u_z' \rangle_{rms}$ exists under the interface. This layer's depth is about $z/\delta_\nu = 0.3$ and the vertical fluctuations about 50% to 90% of their value at δ_ν.

These observations are not consistent with the HG theory, which states that vertical velocity fluctuations should keep decreasing to zero when approaching the interface, even within the viscous sub-layer, and even decrease linearly with a constant negative gradient inside the Kolmogorov sub-layer. At the interface we should thus have $\langle u_z' \rangle_{rms} = 0$ and $\partial \langle u_z' \rangle_{rms} / \partial z = cst < 0$. On the other hand, $\langle u_z' \rangle_{rms} > 0$ and $\partial \langle u_z' \rangle_{rms} / \partial z \simeq 0$ as observed here could be features characteristic of millimetric or sub-milimetric oscillations of the free surface: small gradients and non zero vertical fluctuations denote a persistent solid like vertical motion as would be caused by surface slow and large scale oscillations.

When taking a closer look at the source PIV images of all runs, we can indeed observe a small amplitude oscillating motion. Its amplitude is measured by processing the SPIV and PLIF recorded images. To evidence this point, some images are averaged over 25 grid oscillations, corresponding to a sample of 100 images. On PIV images, the interface can be evidenced by a higher gray level intensity caused by residual floating particles on the interface and laser reflections. On PLIF images , the interface is visible thanks to the high intensity gradient between fluorescent liquid an non-fluorescent files, and also to laser reflection (at

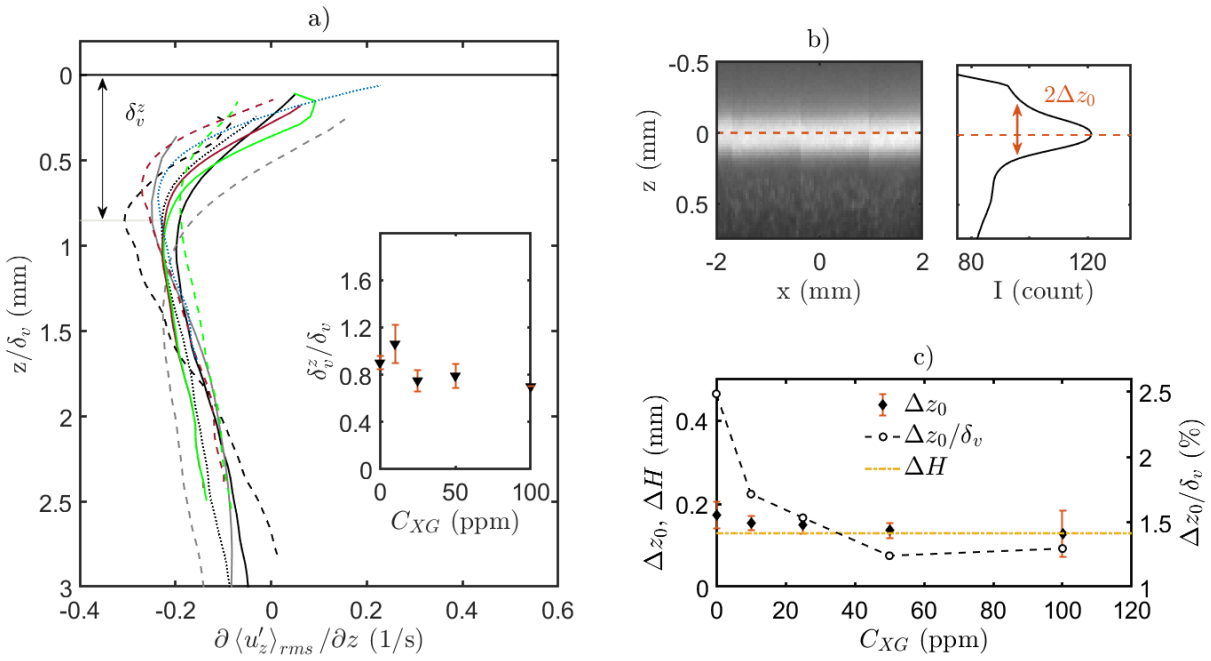

Figure 4.18 – Vertical gradient of vertical velocity fluctuations (a) and quantification of the surface oscillations (b and c). The "vertical" viscous sub-layer δ_v^z extracted from the profiles of vertical gradient of $\langle u_z' \rangle_{rms}$ is approximately constant with polymer concentration (insert in sub-figure a). Surface oscillations measured as shown in b) are small compared to the viscous sub-layer depth and welle predicted by the liquid depth variation ΔH induced by the motion of driving rods (c).

the meniscus). The average processing results for both type of images in a higher gray level band in the area covered by oscillations of the interface.

From these averaged images, vertical gl profiles are deduced. The semi-width of the averaged Gaussian shaped gray level intensity profile across this band gives the altitude variations of the interface around the z=0 position Δz_0 such that the total amplitude of oscillations is $2\Delta z_0$. An example of SPIV averaged image and the estimated oscillation amplitude is shown in figure 4.18 b. The amplitude of surface oscillations is measured by this method for each run and plotted in figure 4.18 c.

It is found that the oscillations of the free surface have an amplitude between 0.25 and 0.35 mm, decreasing with polymer concentration. These oscillations are worth 1.3 to 2.5% of the typical viscous sub-layer, and so 1.6 to 3.1 % of the "vertical" viscous sub-layer δ_v^z.

We can finally estimate a surface fluctuating velocity magnitude $u'_{z,surf}$ using the altitude variations Δz_0 and the time interval between frames dt such that $u'_{z,surf} = \Delta z_0/\mathrm{dt}$. Its value is around $u'_{z,surf}$ = 0.6 mm/s and is slightly decreasing with concentration: 0.69±0.25 mm/s for water, 0.61±0.14 mm/s for 10 ppm DPS, 0.60±0.16 mm/s for 25 ppm DPS, 0.55±0.14 mm/s for 50 ppm and 0.52±0.32 mm/s for 100 ppm. Its order of magnitude compares quite well to the asymptotic value of $\langle u_z' \rangle_{rms}$ that can be extracted from figure 4.14: 0.60 mm/s for WS or WD, 1.30 mm/s for XG25B or XG50B. However these asymptotic values do not show any decreasing trend with increasing polymer concentration.

Our observations of surface oscillations are here purely qualitative, and the accuracy of detection is not sufficient to study the origin of those waves. It is by the way worth noting that they are here observable only because our experimental setup allows for sub-millimetric spatial measurement. It is not unlikely that such oscillations occur in all OGT or RASJA setup but could not be evidenced in previous studies with lower spatial resolution. Their most probable origin would be vibrations of the tank induced by the motor or the crankshaft sys-

tem, or the minor liquid phase volume variations in the tank caused by the in and out motion of rods supporting the grid. For this last probable cause, we can easily estimate the liquid depth variations induced by the displacement of the supporting rods. It is evaluated as $dH = 2 \times S \times \pi r_{rod}^2 / W^2$, where r_{rod} is the radius of a supporting rod, and is constant for a constant stroke. Its value is here 0.13 mm. From figure 4.18 c it seems that surface oscillations can be well predicted by this volume variation. The correspondence between Δz_0 and ΔH increases with polymer concentration. It shows that if any other surface oscillation mechanisms exist in water, such as vibrations or turbulence-induced motion of the free surface, they are reduced upon polymer addition.

The amplitude of the oscillations are always under 5 % of the viscous sub-layer, and so they are quite limited in depth. If the surface oscillations were the dominant mechanism in the present experiments, then the viscous sub-layer scaling of figure 4.17 would not hold, and the evolution of its depth with polymer concentration would not be visible. Yet they correspond to vertical velocities of the interface high enough to explain the asymptotic trend of vertical velocity fluctuations profiles at the interface.

Zooming closer to the interface, one should encounter the Kolmogorov sub-layer where viscosity statistically damps all turbulent fluctuations. Kolmogorov sub-layer depth predicted by equation (4.2) is about 1 mm for water, which is closer to the amplitude of surface oscillations. The properties of turbulence in the Kolmogorov sub-layer for water are very likely modified by surface oscillations. For DPS, predicted Kolmogorov depths based on equation (4.2) and scale viscosities μ_0,μ_m andμ_∞ may be much larger than 1 mm. Yet viscous scaling has proven inadequate to estimate the evolution of viscous sub-layer evolution, so the applicability of equation (4.2) is also questionable. In both water and DPS cases, the linear decrease of vertical fluctuations expected to occur in the Kolmogorov sub-layer is never observed. The question of interactions between surface oscillations and Kolmogorov sub-layer dynamics is still open. Experimental investigation of hydrodynamics within the Kolmogorov sub-layer would require surfaces completely free of any oscillations even at the micrometer scale, which is probably impossible to achieve with oscillating grid setups.

Finally, surface oscillations is a point worth keeping in mind for the following mass transfer analyses. Indeed, typical concentration sub-layers (e.g. δ_B) are smaller than the viscous one, and their size may be comparable to the amplitude of surface oscillations, thus making their identification more complex.

In the following paragraph, we will complete the study of near surface hydrodynamics with a conditional analysis of velocity fluctuations. This analysis is operated within the quadrant framework detailed in section4.3.3.

4.4.5 Velocity PDFs and turbulent momentum fluxes

No mass transfer is considered yet, and events are classified with respect to the sign of the velocity fluctuations of all three components. Eight type of events are thus possible, and since no concentration fluctuation is defined, several quadrants, octants or hexadecans are equivalent:

- $Q_1 \equiv Q_2$, $Q_3 \equiv Q_4$
- Inside $Q_{1,2}$ or $Q_{3,4}$ it comes that $O_i \equiv O_{i+2}$ (e.g. $O_1 \equiv O_3$).
- Inside the octant decomposition, one also has $HX_i \equiv HX_{i+4}$ (e.g. $HX_1 \equiv HX_5$)/

For simplification, we will thus only use two quadrant, Q_1 and Q_3 allowing to distinguish between up-going (Q_1) and down-going motion (Q_3), and the four associated octants and

heigth hexadecans allowing to discriminate the vertical motions. Results are shown for two water runs, with and without rms peak (WS and WD), and for a single run for all DPS concentrations (XG10B, XG25B, XG50B and XG100A).

4.4.5.a PDFs of velocity fluctuations

In this section the PDF of velocity fluctuations are shown at three relative depths for water and DPS: $z/\delta_\nu = 0.5$, $z/\delta_\nu = 1$ and $z/\delta_\nu = 2$. The first depth is inside the viscous sub-layer, and should evidence hydrodynamic effects characteristic of it. The last one is inside the source (surface influenced) layer and should evidence the transfer between component characteristic of this source layer. The intermediate point is at the viscous sub-layer depth and should mark the transition between the two regions.

PDF of velocity fluctuations are shown in figure 4.19 for the considered runs and depths. Markers are PDF measurements, and full, dashed and dotted lines are fittings by a Gaussian function. The first point to be observed is the shape of the horizontal fluctuations PDF: at all depth, curves for fluctuations along x and y present a similar Gaussian shape characteristic of homogeneous isotropic turbulence in horizontal panes. The plots are almost superimposed, indicating a good degree of horizontal isotropy of turbulence. This is true inside and outside of the viscous sub-layer, for water and all DPS concentration, no matter if an rms peak is present or not.

For the unpolluted water run, the PDF of vertical velocity fluctuations also exhibits a quasi Gaussian shape, but with a thinner distribution width than the horizontal components. This is a consequence of the preferential damping of vertical motion in all the surface influenced layer.

In the viscous sub-layer of DPS, the distribution of horizontal fluctuations is also wider than that of vertical ones, and the shape of u'_z's PDF is non Gaussian. Moving out of the viscous sub-layer, all pdf collapse on the same curve indicating a good isotropy level. This is also the case for the polluted water run, but not for the unpolluted one. Turbulence is already quite istoropic in the region between the surface influenced and the viscous sub-layer depth. This could be confirmed by a spatial spectra analysis as done by Lenoir (2011).

4.4.5.b Turbulent momentum flux profiles

The quadrant analysis of covariance integrand of velocity fluctuations only allow to identify the most probable and intense momentum events. In order to state which one is effectively dominant, one can compute the quadrant averaged momentum fluxes (or Reynolds stress) as defined in section 4.3.3, at each point of the ROI. It is then possible to plot width averaged profiles of these sorted Reynolds stresses and evidence which quadrant is dominant at which depth. Width averaged profiles of $\overline{u'_x u'_y}$, $\overline{u'_y u'_z}$, and $\overline{u'_x u'_z}$ conditioned in quadrants Q1 ($u'_z < 0$, up-going fluctuation) and Q3 ($u'_z > 0$, down-going fluctuation) are plotted in figure 4.20.

Several observations can be made on figure 4.20. First the norm of Reynolds stresses globally decreasing with increasing polymer concentration between 0 and 50 ppm, logically following the increase in overall viscosity and the decrease of incident Reynolds number. The 100 ppm run displays surprisingly high Reynolds stress values. Horizontal Reynolds stresses are repeatably higher than Reynolds stresses involving vertical fluctuations, indicating that turbulence is stronger in horizontal planes, and that for water and DPS and all concentrations. However the features of this turbulence are quite different in water and DPS horizontal stresses are essentially negative in the near surface region for water and positive for DPS. When approaching the interface, the dominance of Q3 Reynolds stresses over Q1 ones is re-

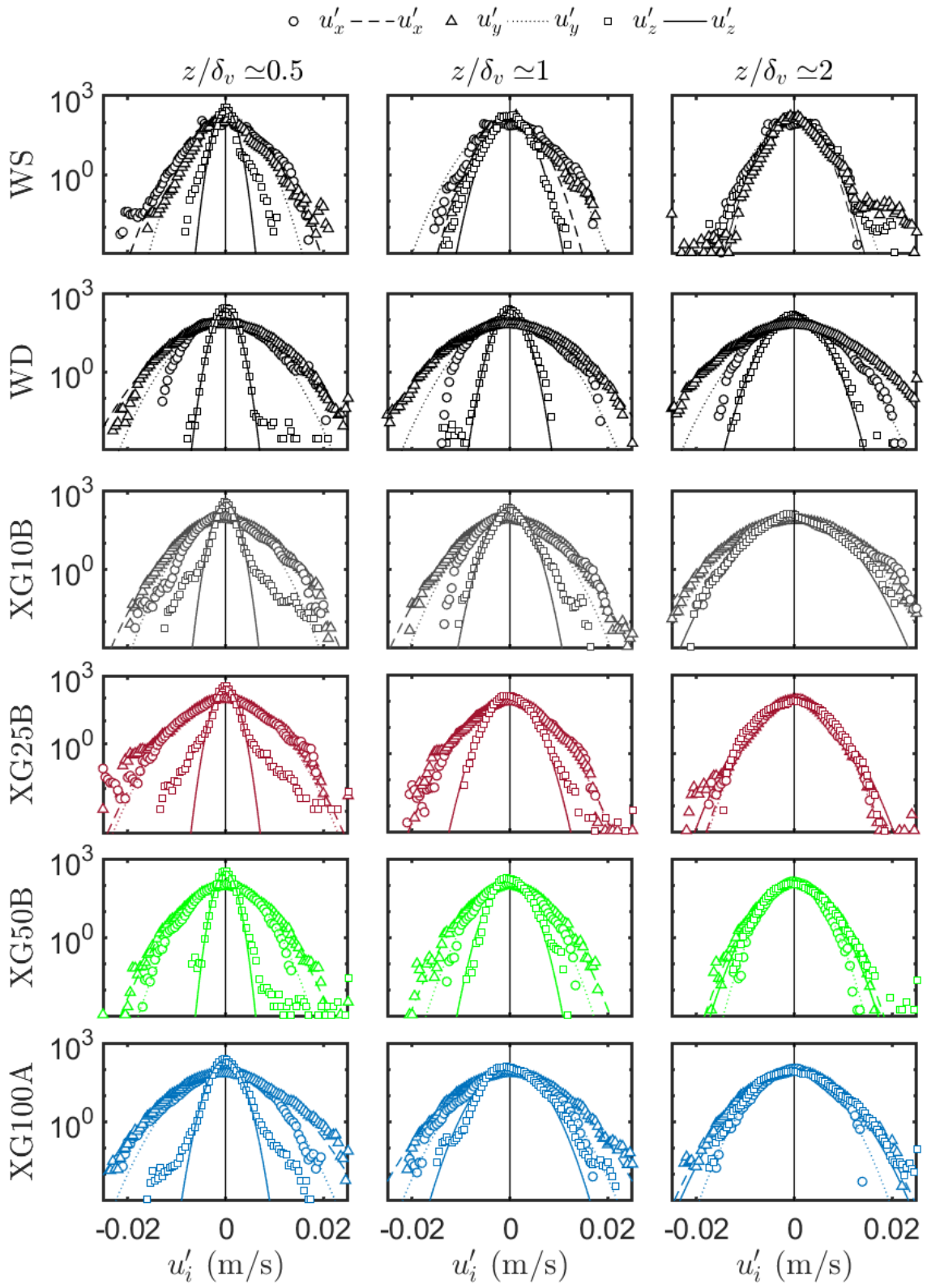

Figure 4.19 – PDF of velocity fluctuations for water and DPS at three relative depths. Results are presented for the runs WD, WS, XG10B, XG25B XG50B and XG100A, at depths $z/\delta_v \simeq [0.5, 1, 2]$. PDF values are shown in log scale. Lines are Gaussian fittings or the data points (markers).

duced and stresses value in the Q1 quadrant become of the same order of magnitude than that in Q3, or event higher.

In figure 4.21, the width averaged profiles of ensemble rms of instantaneous $u'_i u'_j$ correlations are shown. This ensemble rms operator,defined in section 1.2.1.e, somehow quantifies the intensity of instantaneous correlations.

Horizontal correlations rms (circles) are higher than the ones involving vertical fluctuations at depths typically smaller than 14 mm. These last curves are strictly decreasing with decreasing depth for water and DPS in both quadrants. Their decay rate is reduced at small depths. On some runs they appear to reach a constant value that would be explained by the sub-millimetric surface oscillations as discussed previously. All these observations are valid for both quadrants. Correlations rms involving vertical fluctuations are always higher in the Q3 quadrant for water. In all DPS however, they are higher in the Q1 quadrant at small z. The depths at which Q1 and Q3 curves cross is between 6 and 10 mm for 10 ppm, 4 mm and 8 mm for 25 and 50 ppm and above 14 mm for 100 ppm. This is approximately 1.5 to 2 times the order of magnitude of δ_ν.

Horizontal cross correlation rms profiles for water are weakly decreasing with decreasing depth. Increasing polymer concentration, this trend gradually changes, rms of the cross correlation begins to increase with decreasing depths at large z until a peak is reached, and they further decrease when approaching the interface. The dominance of Q3 quadrant is once again reduced at small depths, and even reversed for the 100 ppm run in which Q1 quadrant dominates the horizontal correlation rms for z under 6 mm, approximately $\delta_\nu/2$. The depth at which Q1 and Q3 curves meet is of the order of $\delta_\nu/2$.

The peak observed on the profiles of rms for horizontal velocity fluctuations for DPS (figure 4.14) translates into a peak of rms of horizontal cross correlation profile in the viscous sub-layer for the 25 ppm, 50 ppm and 100 ppm runs. The 10 ppm and "clean" water runs did not show any rms velocity peak, and neither do they display any strong horizontal cross correlation rms peak. A small peak is yet visible for the WD run. However a decrease in horizontal cross correlation rms is still observed close to the interface. The point where it starts

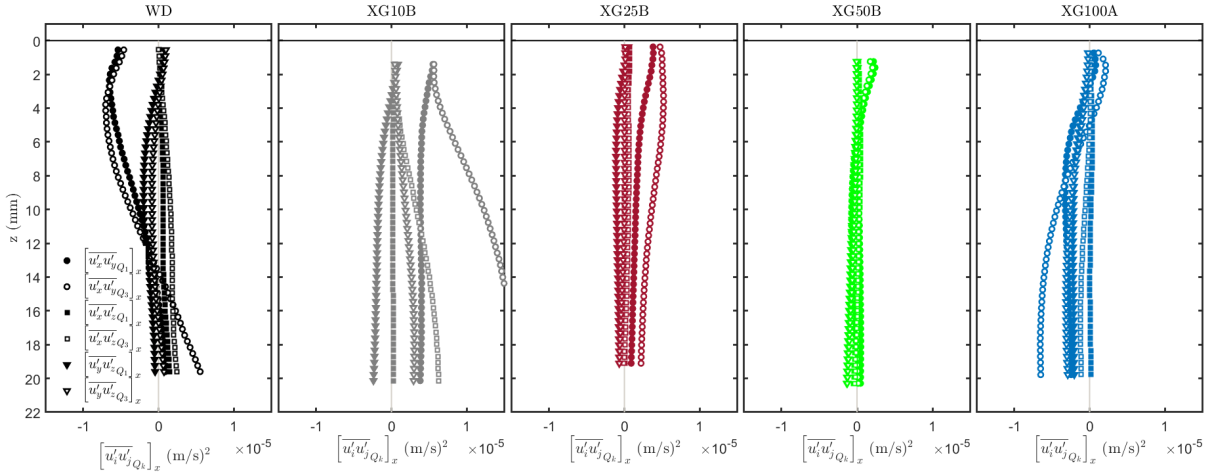

Figure 4.20 – Conditional analysis of the Reynolds stresses in water and DPS. Conditional Reynolds stresses are computed for quadrant Q1 corresponding to up-going vertical fluctuation $u'_z < 0$ (full markers) and Q3 to down-going vertical fluctuation $u'_z > 0$ (empty markers). Results are shown for runs WD, XG10B, XG25B, XG50B and XG100A. Squares and triangles are Reynolds stresses involving vertical fluctuations, respectively $\overline{u'_y u'_z}_{Qi}$ and $\overline{u'_x u'_z}_{Qi}$. Circles are horizontal Reynolds stresses $\overline{u'_x u'_y}_{Qi}$.

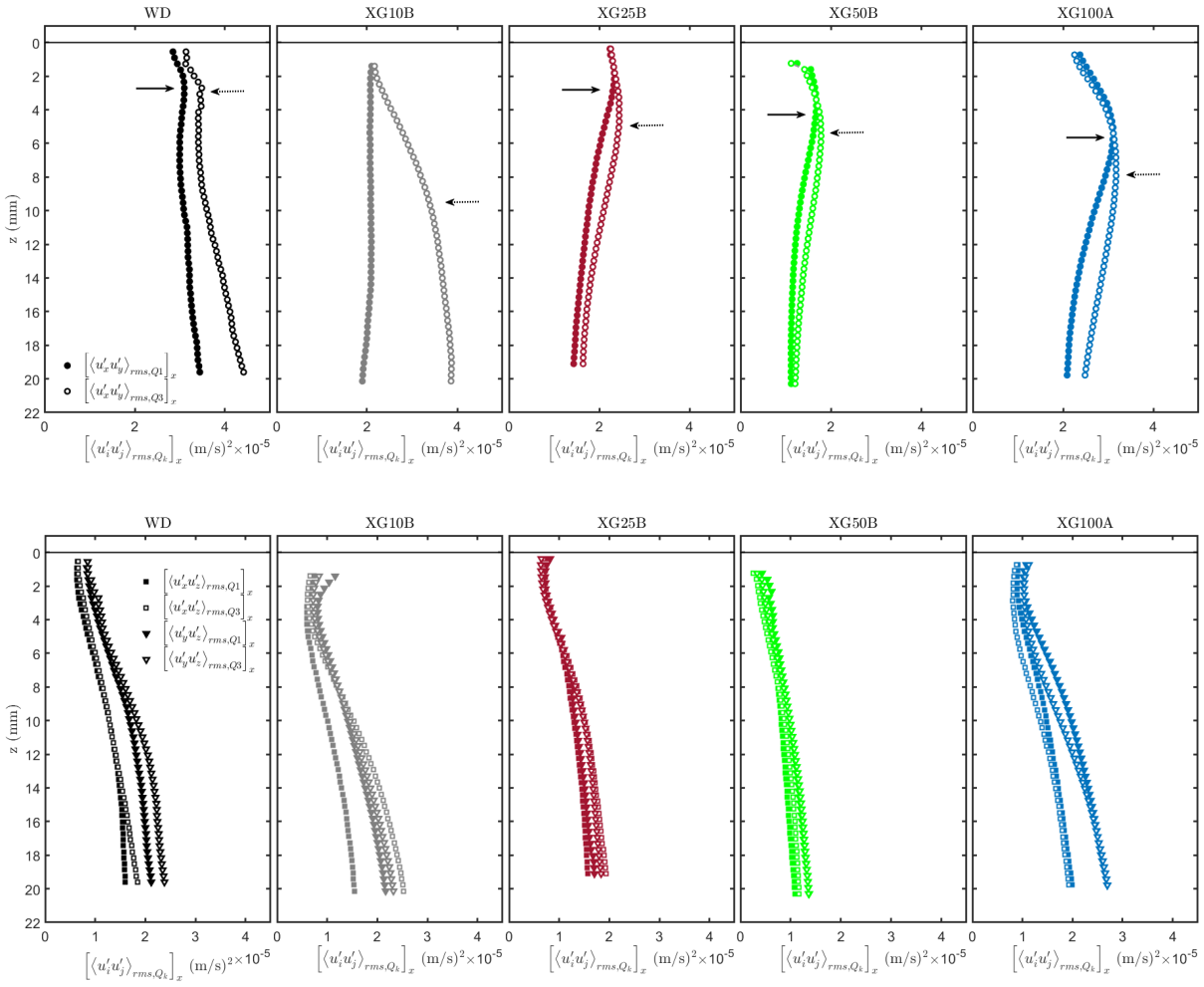

Figure 4.21 – Conditional analysis of the rms of $u'_i u'_j$ cross correlations in water and DPS. Conditional cross correlation rms are computed for quadrant Q1 corresponding to up-going vertical fluctuation $u'_z < 0$ (full markers) and Q3 to down-going vertical fluctuation $u'_z > 0$ (empty markers). Results are shown for runs WD, XG10B, XG25B, XG50B and XG100A. Squares and triangles are cross correlation rms involving vertical fluctuations, respectively $\langle u'_y u'_z\rangle_{rms,Qi}$ and $\langle u'_x u'_z\rangle_{rms,Qi}$. Circles are horizontal Reynolds stresses $\langle u'_x u'_y\rangle_{rms,Qi}$. Full and dotted arrows point show the depth of the inflexion of horizontal cross correlation rms profiles for respectively Q1 and Q3.

to significantly decrease inside the viscous sub-layer is at higher depths for Q3 events that for Q1.

The previous observations on conditional Reynolds stresses and cross correlation rms allow to extract the following information on near surface hydrodynamics:

- The vertical turbulence damping is confirmed for both quadrants in water and DPS at all concentrations. Horizontal turbulence damping that was evidenced by horizontal velocity rms peaks for DPS at concentration higher than 10 ppm is also visualized on the cross correlation rms profiles for both quadrants. For the "clean" water run WD and the 10 ppm run, no rms peak where observed, and yet a small correlation rms peak is observed for water. An increase in Reynolds stresses decay rate is still visible for 10 ppm quadrant Q3. For water this could indicate residual surface pollution that was not visible on rms profiles. For 10 ppm DPS, this is either also residual surface pollution, or the onset of polymer effect on near-surface turbulence, here limited by

the very small polymer concentration.

- Horizontal turbulence associated to down-going structures is stronger than the one associated to up-going ones especially at large depths, for water and low polymer concentrations. This is quite surprising: turbulence coming here from the bulk and being damped by the presence of the interface, one would expect the intensity of the up-going turbulence to be stronger than that of the down-going one. It can be explained by the fact that down-going motion brings turbulence from a region where it is weak towards a region of higher fluctuation. Down-going turbulence is thus fed by deeper structures while up-going turbulence is strongly damped by the interface. On the other hand, up-going motion is damped by the approaching interface.

- The typical depth at which the horizontal cross correlation rms begins to decrease in DPS but also in the WD run is different for the two quadrants. It is smaller for an up-going turbulent motion than for a down-going one. It can be conceptually explained in the following way. In Q1 events, turbulence is brought upwards by an up-going vertical fluctuation (Q1 quadrant). This vertical fluctuation is blocked by the interface and its energy is transferred to horizontal components, thus increasing the horizontal Reynolds stresses. This increase is stopped when viscous damping of the horizontal turbulence is high enough to compensate its increase by energy transfer, that is to say when coming extremely close to the interface. On the other hand, Q3 events are associated to down-going turbulence motion, which, depending on the size of the structure, also "see" the interface in terms of horizontal viscous damping, but for which no energy transfer from vertical to horizontal motion is imposed since they move away from the interface. Viscous damping thus acts at larger depths since it may not be balanced by inter-component transfer. This mechanism is already present for water, but increased by the presence of polymer and with polymer concentration. It can thus be viewed as an intrisic feature of the viscous sub-layer, which also increases with polymer concentration.

- While the two previous observations are valid at all depths in water, the case is somehow different for DPS. Q1 (up-going) events prevail inside the viscous sub-layer while Q3 (down-going) events dominate at larger depths. This is evidences by the cross-over between vertical correlation rms curves at depths smaller than $\delta_\nu/2$, and the convergence of horizontal correlation rms curves at depths lower than $2\delta_\nu$. Polymer however seems to promote Q1 events over Q3 events close to the interface.

Using conditional average on Q1 and Q3 only, we were here able to evidence interesting mechanisms of near-surface turbulence associated to the presence of polymer or not. First it seems that horizontal turbulence intensity associated to down-going motion is globally higher than that associated to up-going motion in water. This may be seen as turbulence "bouncing on the interface". Second, it is confirmed that the effect of polymer in the surface influenced layer, far from the viscous sub-layer depth, is quite complex. Here it appears that the relative weight of quadrant in the overall Reynolds stresses is modified by the presence of polymer in a different way depending on polymer concentration. Third, horizontal turbulence is not damped in the same way depending on wether it moves towards the interface or towards the bulk. This feature, present in water, is enhanced in DPS.

Finally, the key effect of polymer on sub-surface hydrodynamics seems to happen inside the viscous sub-layer: while Q3 events prevail in the rest of the surface influenced layer, Q1 events become dominant there. This dominance is all the more visible as the viscous sub-layer is deep, hence as the polymer concentration is high. This feature is interesting

inasmuch as it could ultimately influence mass transfer. Scalar events are conditioned by the hydrodynamic events evidenced here, and the present results indicate that surface renewal could be more significant than injection in the DPS case. This remark echoes the one previously made when commenting on instantaneous velocity fields (section 4.4.2): velocity structures appeared larger in DPS than in water, thus less likely to peel small scale scalar patches from the boundary layer and more likely to promote surface renewal.

Quadrant analysis come to complete the observations already made from the observation of the rms peaks. Several mechanisms may act on horizontal fluctuations (inter-component transfer, viscous damping...), and the balance between their production and dissipation sets the depth of their maximum intensity. This balance is seemingly different for up or down-going turbulent structures, which makes the full mechanism even more complex. Further analysis could evidence a link between the cross-over depth at which the quadrant behavior of up-going motion shifts from stronger up-going to stronger down-going, and the characteristic depths at which horizontal turbulence decays in each quadrant.

The next step would be to compute the full energy budget of Reynolds stresses inside the viscous sub-layer. With the present data, one can directly access all vector components and all gradients in two of the three dimensions (x and z). Out-of plane (along y) gradient of the out-of plane velocity component can be derived from the x and z gradients of the in-plane velocity components using the mass conservation equation (1.22). Yet the out-of-plane gradients of in-plane velocity components are still missing. This information gap can be filled using the hypothesis that turbulence is statistically isotropic in vertical planes parallel to the interface. In doing so, the ensemble average of all horizontal gradients in both the x and y direction should tend to zero. In that case, out-of plane gradients of in-plane velocity components could be neglected since the out-of-plane direction is horizontal. This hypothesis can be easily checked by verifying that the gradients along x, accessible through measurements, are close to zero. Because of time limitations, the energy budget analysis could not be carried out during this thesis, but it is achievable with the available data and using the hypothesis previously stated, at least in the water case. In the DPS case, energy transfer terms between the flow and polymer chains would be missing.

Another possible analysis of the results would be to use the full decomposition over all types of octants or hexadecans to relate those Reynolds stress fluxes to mean flow gradients under the interface, as done in Vinçont et al. (2000). Data for the triple correlation of all velocity fluctuations are also available and could be interpreted. A spectral analysis of velocity fluctuations could finally be performed in order to determine the size of the structures responsible for up and down-going motion and explain the quadrant trends.

4.4.6 Integral length scales

The integral length scales of turbulence are defined as the integral of correlation coefficients computed over sampling regions at different depths (as in chapter 3 section 3.4.5.d). As in chapter 3, the correlation coefficient curve may not fall to zero in the sampling region. Here the choice is made to fit this curve with a Gaussian function and compute the integral length scale by integrating this Gaussian function from zero to infinity.

6 different auto-correlation coefficients R_{ii}^{j} and their associated integral length scales L_{i}^{j} can be computed, corresponding to the auto-correlation of velocity component i along dimension j, with $i = x, y, z$ and $j = x, z$. Length scales along x are computed on sampling regions wide as the ROI and including 3 vectors in the z direction. Length scales along z are computed on sampling regions of width equal to the ROI's and 10 mm large along z. An example of all 6 integral length scales extracted from the WD run is shown in figure 4.22 a.

The vertical and horizontal integral length scales are defined acording to Janzen et al. (2010) respectively as [5]:

$$L^x = \sqrt{(L^x_{xx})^2 + (L^x_{yy})^2 + (L^x_{zz})^2} \tag{4.22}$$

$$L^x = \sqrt{(L^x_{xx})^2 + (L^x_{yy})^2 + (L^x_{zz})^2} \tag{4.23}$$

Horizontal and vertical lenth-scales of all runs are shown in figure 4.22 b). Comparison with integral length-scales values measured by Janzen et al. (2010) could be misleading since the grid Reynolds number and grid-surface distance are not comparable, so it is not done here. From figure 4.22, it appears that horizontal length scales are larger than vertical one. This has already been evidenced for water by Janzen et al. (2010) and explained as the consequence of inter-component exchanges for turbulence approaching the interface: eddies become "flat" and tend to stretch along horizontal dimensions. Such a behavior is also observed for DPS at all sketched concentrations. At depths higher than 5 mm, horizontal length scales are between 1.95 and 2.15 times larger than the vertical ones. This ratio increases up to between 2.4 and 3.4 for 50 ppm DPS. The horizontal stretching of turbulent structures thus seems to be amplified by the presence of polymer.

Regarding the evolution of integral length scales along depths, results for water are consistent with the trends found by Janzen et al. (2010): The vertical length scale is globally constant at the depths considered. The horizontal length scale is also nearly constant except at small depths (a few millimeters) under the interface where it increases. A similar evolution is observed for the 10 ppm DPS. The trend is however quite different for 25 and 50 ppm concentrations: the vertical scale slightly decrease when approaching the interface, and the increase of horizontal scales at z<5 mm disappears to be replaced by a slow decrease with decreasing z.

Two main conclusions can thus be made from the previous observations:

- The presence of polymer enhances the stretching of turbulent structures in the surface influenced layer. This enhancement seems to depend on polymer concentration.
- This horizontal stretching is all the more important at small depths, typically lower than 5 mm, for water and low concentration DPS. When increasing polymer concentration, the trend is reversed and stretching is reduced at small depths.

4.4.7 Measured Reynolds number

With the latest information about integral length scale of sub-surface turbulence, and the measurements of rms velocities shown in section 4.4.2, we can re-estimate the turbulent Reynolds number value based on equation (3.4), as done in section 4.2.1.c with undisturbed scales. This time however, we use measured parameters for both velocity and length scales. Since both parameters vary with depth, Re has to be evaluated at a specific depth for the sake of comparison. Here we arbitrarily take its value at $z=\delta_v$, either directly measured or interpolated, so that $L_\infty = L^x_{xx}(\delta_v)$ and $u' = \left[\langle u'_x \rangle_{rms}\right]_x(\delta_v)$. As in 4.2.1.c, zero shear rate viscosities are used. Table 4.6 shows the measured parameters and estimated Reynolds numbers for polymer concentrations up to 50 ppm (100 ppm integral length scales have not been computed). Reynolds number based on undisturbed parameters are recalled as well. It should

[5] In Janzen et al. (2010), the velocity component is not available in the measurements. $(L^x_{xx})^2 + (L^x_{yy})^2$ is replaced by $2(L^x_{xx})^2$ in equation (4.22) ,$(L^z_{xx})^2 + (L^z_{yy})^2$ in by $2(L^z_{xx})^2$ (4.23)

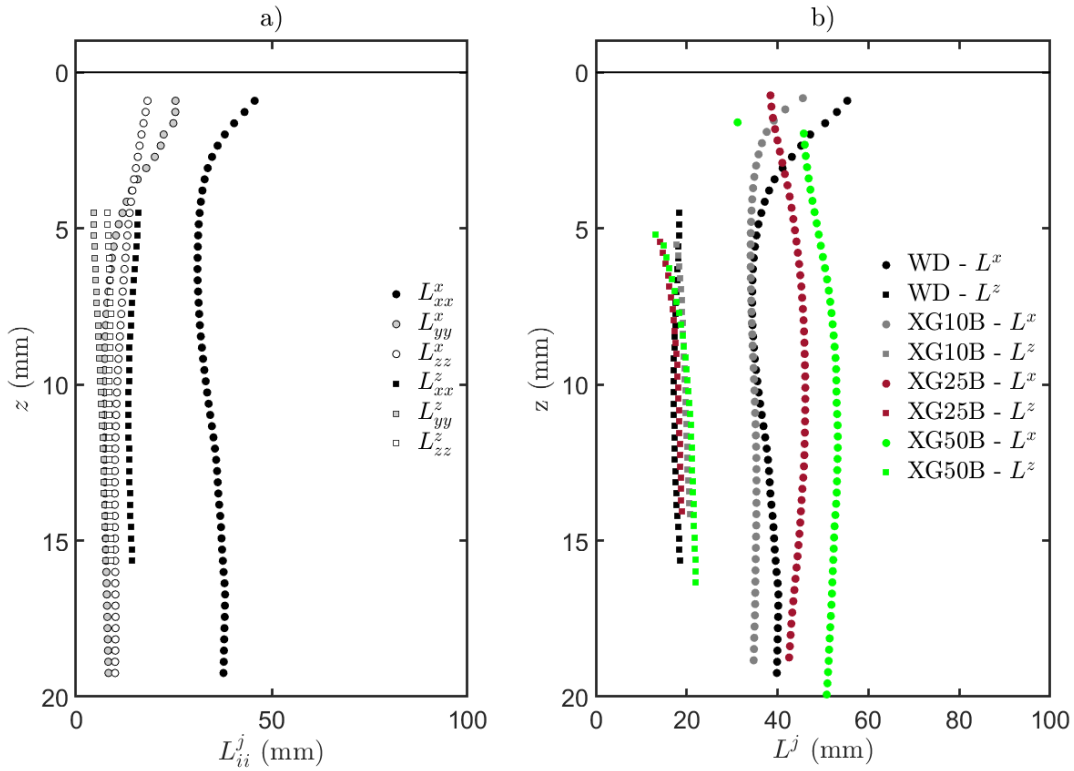

Figure 4.22 – Sub-surface integral length scales in water and DPS. a) All 6 integral length scales for the WD run. b) Horizontal and integral equivalent velocity length scales for water and DPS up to 50 ppm concentration.

be emphasized that by using z=δ_ν, Reynolds numbers are estimated at different depths depending on polymer concentrations. We see here that turbulence acting on the interface is stronger than expected in water and low concentration DPS, as previously observed. However measured Reynolds number at 25 or 50 ppm are close to those predicted by the undisturbed scales, even if their rms velocities are higher. This is a consequence of a significantly higher undisturbed integral length scale for higher polymer concentration. In further experiments, special care should thus be taken to understand the evolution of integral length scales and horizontal velocities inside the surface influenced layer of DPS. These considerations about integral length scales and Reynolds numbers come as a complement of the previous results on sub-surface hydrodynamics. The results gathered about sub-surface hydrodynamics of water and DPS are summarized and put into perspective in the following section.

4.4.8 Conclusions on sub-surface hydrodynamics

4.4.8.a About mean flows

Mean flow are an un-avoidable feature of OGT. We here find mean flow to turbulence ratios close to unity, better than what could have been expected from the OGT study of chapter 3, and acceptable for mass transfer observations. One may argue that better results could have been obtained in a RASJA setup (Variano and Cowen, 2013). However, RASJA's efficiency in DPS has never been demonstrated. The repeatability of mean flow is harder to achieve in water than in DPS. This supposedly comes from the fact that mean flow structures generated around the grid do not reach the interface in the water case, while they do for DPS. The

Concentration	u' (mm/s)	L_∞ (mm)	Re_T (measured)	Re_T (undisturbed)
0 ppm (water)	7.7	34.1	262	110
10 ppm	6.5	34.0	170	106
25 ppm	6.0	45.8	69	64
50 ppm	5.5	52.2	26	20

Table 4.6 – Table of characteristic velocity and length scales at z=δ_v

topology of mean flows in sub-surface DPS runs relates well to the mean recirculations in the full tank.

4.4.8.b Near surface turbulence for water

The multiple experiments made with water allow to compare surface polluted and unpolluted runs. In the present experiments, the small Reynolds number of the up-coming turbulence is such that both horizontal and vertical turbulence intensities decay when approaching the interface for runs identified as unpolluted, as in Janzen et al. (2010), so the asymptotic increase of horizontal velocity fluctuations predicted by HG is never observed. Turbulence in the ROI is only slightly under-predicted by estimated undisturbed scales extracted from the OGT study. For runs identified as surface polluted, horizontal fluctuation intensity increases in the surface influenced layer, and the expected rms peak is observed. Turbulence properties are more repeatable than mean flows, providing that one can control the degree of surface pollution of the interface. However, the viscous sub-layer can be identified in clean or polluted runs from the gradient profiles. It is about twice the value predicted by BJ. When approaching the interface, energy is transferred from vertical to horizontal motion, resulting in a much faster decay of vertical turbulence rms and, slower decay or even increase of horizontal turbulence, and in larger horizontal velocity length scales. In horizontal planes both inside and outside the viscous sub-layer, horizontal isotropy of turbulence is quite good. A quadrant analysis of Reynolds stresses and rms of correlations allows to evidence a different behavior for up or down-going turbulent events. Outside of the viscous sub-layer, down-going turbulent event are stronger than up-going ones. Inside the viscous sub-layer, the distribution is more balanced and Q1 and Q3 events have equivalent shares. In the surface influenced layer, up-going turbulence is weaker with decreasing z because of the increasing distance from its source of production (the grid), and because it approaches the interface. Down-going turbulence decays with decreasing z because of the increasing distance to the source. It is yet not damped by the approaching interface, but rather fed by the up-coming turbulence it meets. In the viscous sub-layer, viscous damping equally damps both up and down-going motion, thus leading to equilibrium.

4.4.8.c Effect of polymer on energy redistribution on the surface influenced layer

In DPS, undisturbed length scales from the OGT study fail to predict turbulence properties in the sub-surface ROI. Unfortunately our experimental setup does not allow to investigate turbulence behavior in the whole surface influenced layer. Whether this is only due to experimental reasons or a feature of DPS turbulence in the source layer is thus still an open question. Repeatability of turbulence properties in DPS is yet better than for water and available measurements sufficient to show that the energy redistribution from vertical to horizontal motion also occurs in DPS. From integral velocity length scale measurements, it seems that the horizontal stretching of structures is event stronger in DPS than in water. DPS at concentrations higher than or equal to 25 ppm finally always exhibit an horizontal RMS peak at the

viscous sub-layer depth location, similar to the one observed for polluted water runs. This peak can not be attributed to surface pollution, or surface activity since XG was not found to have any surface active properties in the range of concentration used. The value of 25 ppm compares quite well to the onset concentration for drag reduction in XG.

4.4.8.d About the size of the viscous sub-layer in DPS

The depths of the viscous sub-layer can be measured for all DPS, whether the rms peak is present (C_{XG} > 10 ppm) or not (C_{XG} = 10 ppm). It is found to increase with polymer concentration. No theoretical prediction exists for the depth of the viscous sub-layer in shear thinning viscoelastic fluids, so the measured depths were compared to BJ predictions for Newtonian fluids with viscosities representative of the DPS (plateau viscosities). It appears that the evolution of δ_ν can not be predicted by the BJ prediction based on zero shear rate or average viscosity, but rather on the infinite shear rate viscosity. This is surprising since the shear rates reached under the interface are always much lower than the ones required to lower viscosity down to μ_∞.

4.4.8.e Hydrodynamics inside the viscous sub-layer for DPS

As previously mentioned, an rms peak appears when increasing polymer concentration, that can not be attributed to surface pollution. By analogy with surfactant mechanisms, we infer that this rms peak is due to horizontal resistive shear stresses. Those tangential stresses are not induced by surface active molecule interactions, but supposedly by local variations of viscosity caused by the shear-thinning property, or by elastic response of the polymer chains.

Quadrant analysis shows that as for water, down-going events prevail in the surface influenced layer, outside of the viscous sub-layer. The explanation is the same as for water: motion towards the interface in one case, and towards bulk turbulence in the other. Inside the viscous sub-layer, Q1 events are not only of equivalent strength (in terms of rms of correlation) than Q3 events, but may event dominate. This behavior is all the more visible that the viscous sub-layer depth is increased (hence with increasing polymer concentration). Yet it seems to be an intrinsic feature of polymer: no crossover occurs at all inside the viscous sub-layer for water, but it does for DPS. As for the decay of horizontal turbulence inside the viscous sub-layer, both quadrant Q1 and Q3 show an rms peak at a depth close to δ_ν, but the peak associated to down-going Q3 event is found a larger depth than the one associated to up-going Q1 events. Viscous damping mechanisms inside the viscous sub-layer are apparently quite different in water and in DPS. Computation of the full energy budget and of the polymeric stress tensor would be required to model this dissipation. It is yet already possible to infer that the dominance of Q1 hydrodynamic events in DPS could lead to an increased share of surface renewal events in terms of mass transfer.

4.4.8.f Prospects

Towards the resolution of the Kolmogorov sub-layer ?: As mentioned beforehand, submillimetric surface oscillations were evidenced in all water and DPS runs. Even if their amplitude is small compared to the viscous sub-layer depth, the order of magnitude of the subsequent surface velocity compares quite well to the non zero asymptotic vertical rms velocity. Further experimentation should be undertaken, taking special care of vibrations in the grid setup, and adapting the grid device in order to be able to discriminate between oscillations introduced by the grid setup, those possibly caused by turbulence, and ultimately reduce as much as possible. This is a first step necessary to achieve better

spatial resolution under the interface, and ultimately the resolution of the Kolmogorov sub-layer, here estimated to be of the same order of magnitude than the amplitude of surface oscillations.

The link between surface divergence and viscous sub-layer dynamics: With SPIV, horizontal divergence of the velocity field is accessible while measuring velocities in vertical slices of the flow. Surface divergence is thus measured along the x dimension at the top of the ROI. Since turbulence can be assumed homogeneous and isotropic in horizontal plane, surface divergence measured along this line should be representative of surface divergence statistics at the whole interface (minus the side effects). Using the present data, it would thus be possible to compare surface divergence statistics with the viscous sub-layer dynamics and reconcile surface divergence models with conceptual surface renewal models.

4.5 Carbon dioxide dissolution and mixing

Now that sub-surface hydrodynamics in water and DPS have been described, let us focus on dissolved gas concentration fields and concentration statistics. During this thesis, scalar fields for DPS at 10, 25, 50 and 100 ppm polymer concentration were recorded, but only one polymer concentration could be extensively treated in the available time. The 10 ppm concentration was chosen because it showed the most promising results in terms of number and shape of scalar structures recorded. Comparing water and 10 ppm runs allows to distinguish the onset of polymer action on mass transfer. The treatment of higher concentration runs would then make it possible to investigate concentration effects.

From now on let us focus only on the comparison between passive scalar dissolution into clean water (WD run) and 10 ppm DPS (XG10A run). In this section and in the remainder of the manuscript, C refers to aqueous CO_2 concentration $[CO_2]_{aq}$. Fluorescent dye concentration is named C_{F0} when needed.

A first very important remark is that we are here trying to compare runs in two different fluids for which concentration has been measured by two different methods. Water measurement are only available in single-color PLIF version while ratiometric PLIF could be used for the XG10A experiment. We should thus be aware of the differences that may be introduced by the concentration measurement technique, so as not to mistake them for polymer effects. To that end, similar images from the XG10A run have been treated using the single color and ratiometric method in order to extract dissolved gas concentration fields. It appears that $I_{pH}-$PLIF yields lower concentration values than $I^r_{pH}-$PLIF when applied to the same instantaneous fluoresced light fields. We are here in a situation where ratiometric should be used instead of single-color method, since pH dependent laser absorption occurs outside of the ROI (see figure 2.7). It thus seems that $I_{pH}-$PLIF underestimates local concentration values. This effect is discussed in details in appendix G. In order to check whether it has an impact on concentration statistics, structure shapes, and mass flux profiles along depths, all the statistical analysis presented hereinafter for the ratiometric XG10A measurement have also been performed using single-color computed concentration fields. As discussed in the end of appendix G, it appears that even if concentration value and so mass flux magnitudes are indeed underestimated compared to ratiometric measurements, the same concentration structures are evidenced by both methods. The shape of average concentration, rms concentration, quadrant-sorted turbulent mass fluxes or all other statistical quantities remains the same.

The important foreword to the next two sections is that the WD and XG10A results should not be quantitatively compared in terms of concentration or flux values, because of the use

of single-color PLIF in the WD case. Observation of concentration and mass transfer events and comparison of integral time and length scales, event probability, or evolution of the mass transfer characteristics with depth remain however completely valid.

4.5.1 Scalar structures

PLIF methods allow to visualize instantaneous dissolved gas spatial structures in the ROI. Example of instantaneous concentration fields in water are shown in figure 4.23 (WC run, measurements performed in 2016). The colors show values of $(C - C_b)/(C_s - C_b)$ with C_b and C_s values respectively of order 10^{-2} mg/L and 10^0 mg/L. Figure 4.24 shows four other examples of instantaneous concentration fields, two for water (WD run, 2017) and two for 10 ppm DPS. The colorbar corresponds this time to instantaneous concentration C in mg/L, in log scale.

In both figures 4.23 and 4.24, concentration is higher close to the z=0(location of the gas liquid interface) and decreases with increasing z. Between the interface and the bulk, a complex combination of filament and spiral like structures of high concentration exist. These are characteristic of injection events either occuring in the ROI, or that have occurred outside of the ROI and been transported in it. The time interval between all samples of the WC run in figure 4.23 is too small for global increase of the concentration to be observed. However in figure 4.24, one clearly see that the bulk concentration increases between the first instants (first row) and the following ones (second row). Apart from the clearly visible high concentration scalar structures, one notices that the concentration at z=0 can locally and instantaneously be close to zero, when highly concentrated fluid at the interface is replaced by fresh one coming from the bulk.

We notice on the WD run around z=3.2 mm an horizontal lighter line on concentration fields. It is attributed to the presence of a bubble or dirt particle on the wall of the tank outside of the ROI that appeared after the calibration procedure. Since concentration fields of the WD run were obtained by single color PLIF, this source or error could not be easily corrected. It will thus impact concentration and mass flux statistics hereinafter.

It is worth noting that the theoretical saturation concentration predicted by Henry's law is here never measured in the ROI. Typical concentrations at the lowest measurable depths, where we supposedly find the highest local concentration, only reach up to 100 mg/L, that is to say about 10 times lower than the 1394 mg/L value given by Henry's law. Henry's law saturated CO_2 concentration value is also never attained in sub-surface measurements of Variano and Cowen (2013) and bubble-wake measurements of Valiorgue et al. (2013), both using classical $I_{pH}-$PLIF. In the works of Herlina and Jirka (2008); Janzen et al. (2010) on sub-surface oxygen dissolution, the concentration measured at the depth closer to the interface by their $I_{O_2}-$PLIF method is not clearly compared to the Henry's saturation value. The difference between the maximum measured concentration and the theoretical C_{sat} may thus have several origins. First, the partial pressure of CO_2 in the gas phase may be lower than 1 atm if the initial replacement of air by pure CO_2 is not total . This would lead to lower saturation concentration. Yet explaining the observed difference by this hypothesis only would mean that the effective partial pressure is about 0.07 atm, hence that only 7 % of the gas volume has been replaced during CO_2 filling prior to the experiment, which is very unlikely. Second, the sensitivity of pH sensitive PLIF techniques is only guaranteed in the 4.5 to 7. Yet the saturation concentration corresponding to P_{CO_2} = 1 atm leads to an equilibrium pH of 4 in distilled water, outside of the measurement range. Concentrations lower than about 100 mg/L corresponding to pH 4.5 can not be measured efficiently. Third, the spatial resolution of concentration measurements is not sufficient to clearly visualize the Batchelor

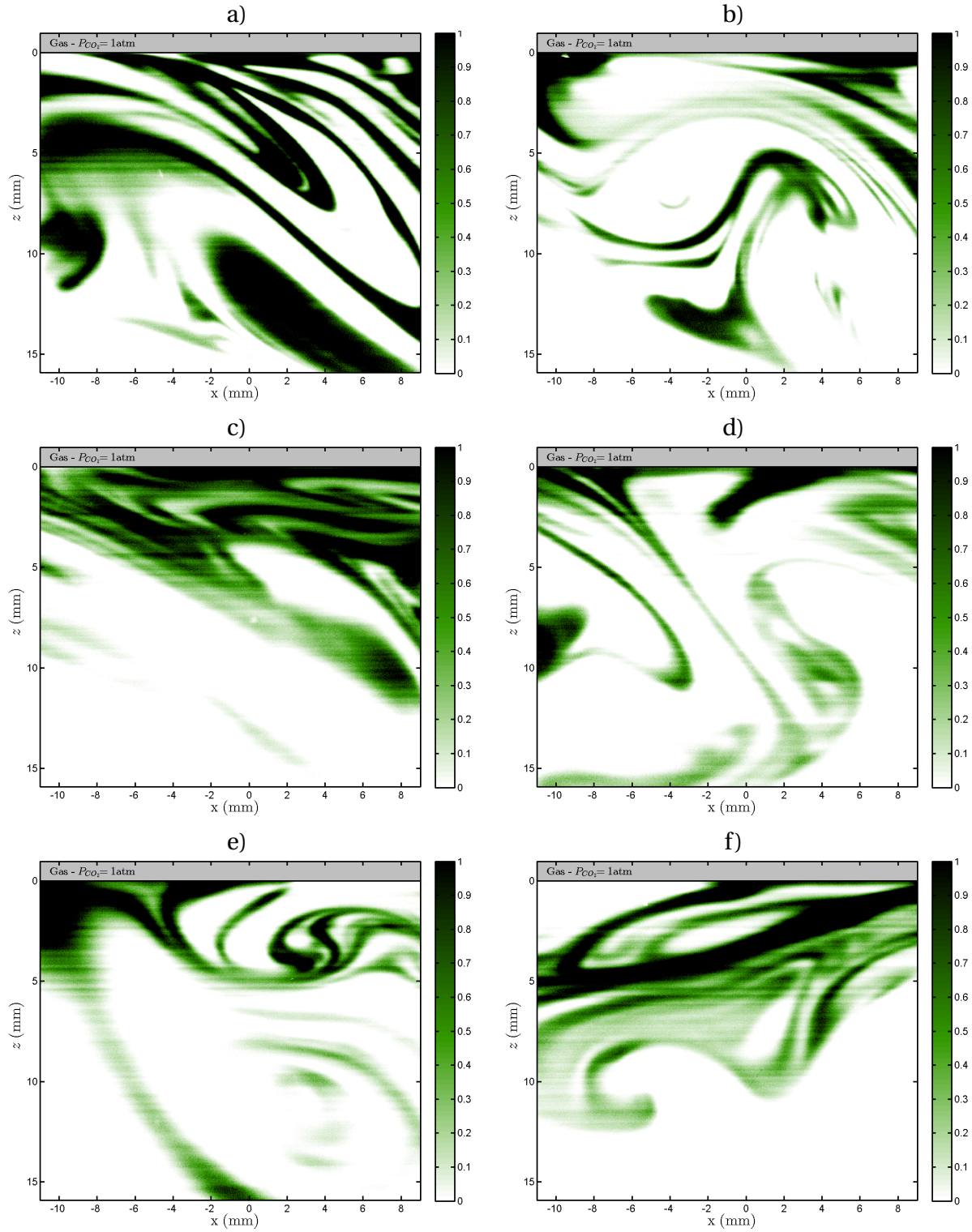

Figure 4.23 – Instantaneous dissolved CO_2 concentration fields in water, WC run. The colorbar ranges from $(C - C_b)/(C_s - C_b)$=0 to 1.

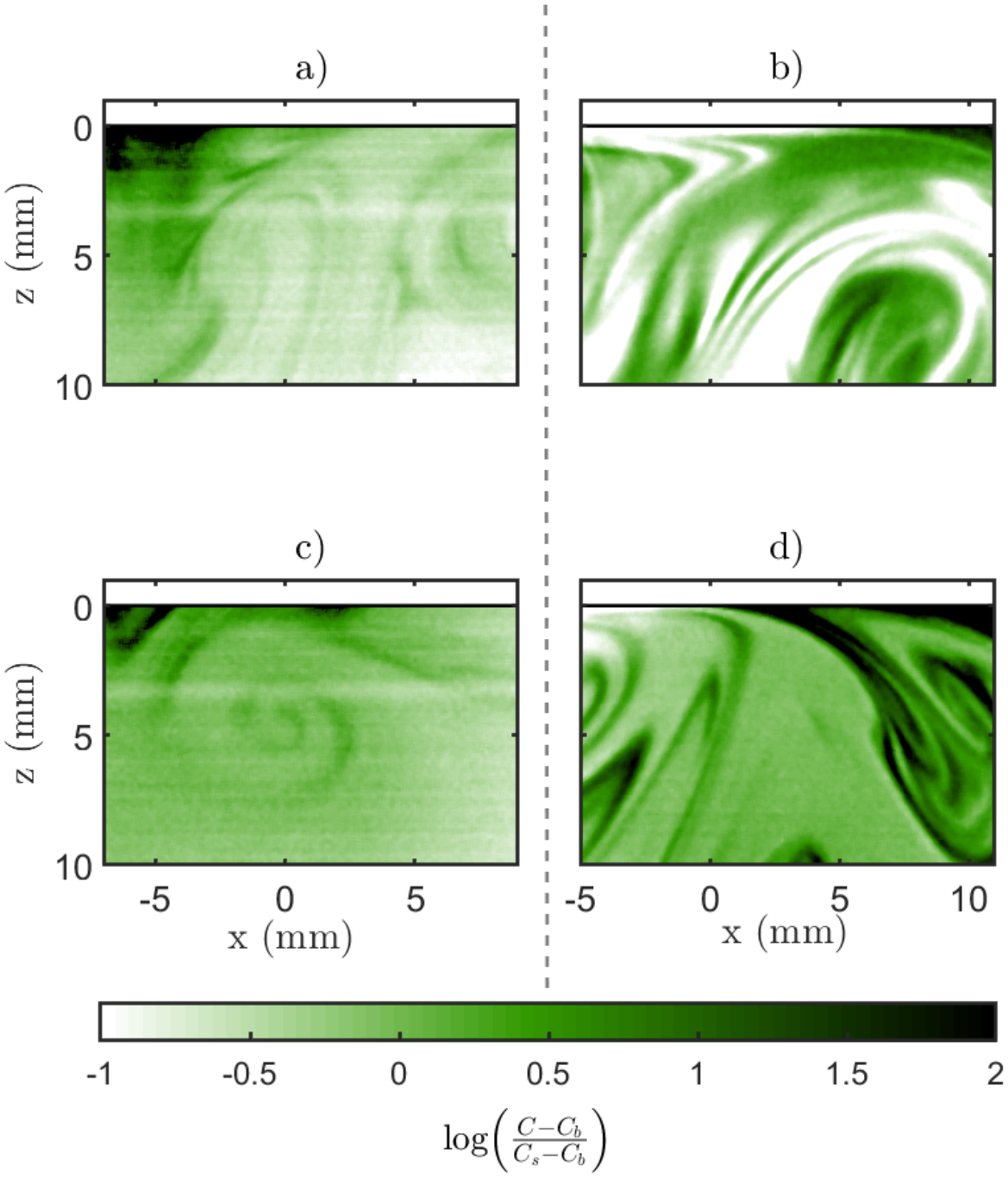

Figure 4.24 – Instantaneous dissolved CO_2 concentration fields in water (left) and DPS (right). The colormap represents instantaneous concentration values in mg/L in log scale. Sub-plots a and c come from run WD, frames number 500 and 2823. Sb-plots b and d belong to run XG10A, frame number 500 and 4302.

sub-layer in which concentration is the closest to its saturation value. The Batchelor typical depth is close to 50 µm in the present experiments, as predicted by equation (4.4). Even though the pixel spatial resolution is closer to that value (between 8 and 20 µm/px depending on the runs), sub-millimetric surface oscillations evidenced in section 4.4 are of the same order of magnitude and do not allow to see the Batchelor sub-layer. Finally, it can be so that surface renewal and injection events tend to sweep concentration patches away from the interface before they have time to reach saturation concentration.

4.5.2 Average concentration

Average concentration fields should theoretical be computed by repeating dissolution experiments many times (more than 100), and average concentration fields at the same instant t. Doing so would however require tremendous hard drive space for data storage and the repetition of very long calibration procedures. In order to estimate average concentration values using only a single run for each fluid, the method proposed by Variano and Cowen (2013) was adopted, as explained in section 4.3.1. Strictly speaking, this method does not compute the average concentration but rather the expected concentration value at given depths. Here we assume that the expected concentration value at a given depth is equal to the average concentration value at this depth, *i.e.* that $\overline{\mathrm{C}}(x,z,t) = \overline{\mathrm{C}}(z,t) = \mathrm{C_E}(z,t)$.

Time series of $[\mathrm{C}]_x$ are shown for two absolute depths in water and 10 ppm DPS: 0.6 mm and 5.5 mm similar to the ones chosen by Variano and Cowen (2013). It is worth noting that the viscous sub-layer depth of 10 ppm XG runs is higher than that of water, 5.64 mm versus 5.10 mm. In terms of relative depths, times series are thus shown for z/δ_ν=[0.11 1.08] for water, z/δ_ν=[0.10 0.98] for 10 ppm DPS. Exponential fittings of the time series are also shown in white thick lines.

For both water and DPS, concentration increases quite logically faster at small depths. Concentration fluctuations also reach higher values for z=0.6 mm than for z=5.5 mm in both water and DPS. The global trend is yet quite different: in the water case, concentration quickly increases at all depth immediatly after gas injection, and an apparent concentration plateau is reached after about 1000 s. It is worth noting that the plateau concentration seemingly is much smaller than the theoretical saturation concentration value, below 10 mg/L while $\mathrm{C}_{sat} \sim 10^3$ mg/L, and that even for the smallest depth. In the XG10A run, concentration increase is smaller at short times, and much steeper at intermediate times. It does not show any plateau behavior, even after 1000 s. Moreover, the time series presents peaks at higher concentration values, up to 100 mg/L for z=0.6 mm.

4.5.2.a Expected or average concentration profiles

Average concentration profiles at different times are obtained by fitting of concentration time series at each depth. Water curves show a brutal variation around z=3.2 mm that is attributed to the presence of a bubble or dirt particles on the wall of the tank, as discussed previously. Concentration at depth z is estimated for each time t using the time series exponential fitting (dashed lines). Thus constructed average concentration profile are fitted by an exponential function of expression $\overline{\mathrm{C}}(z,t) = \mathrm{C}_b(t) + (\mathrm{C}_s(t) - \mathrm{C}_b(t))e^{-kz}$. In this expression, C_b is the bulk concentration which only depends on time. It is a measurement of the global mass transfer. $\mathrm{C}_s(t)$ is the apparent interfacial concentration. Due to several reasons discussed in the introduction of section 4.5, C_s is always lower than the saturation concentration predicted by the Henry's law. Finally, k is a fitting parameter inversely homogeneous to a distance, and may also be expressed as $k = 1/\delta_\mathrm{D}$ where δ_D is the apparent scalar boundary layer thickness.

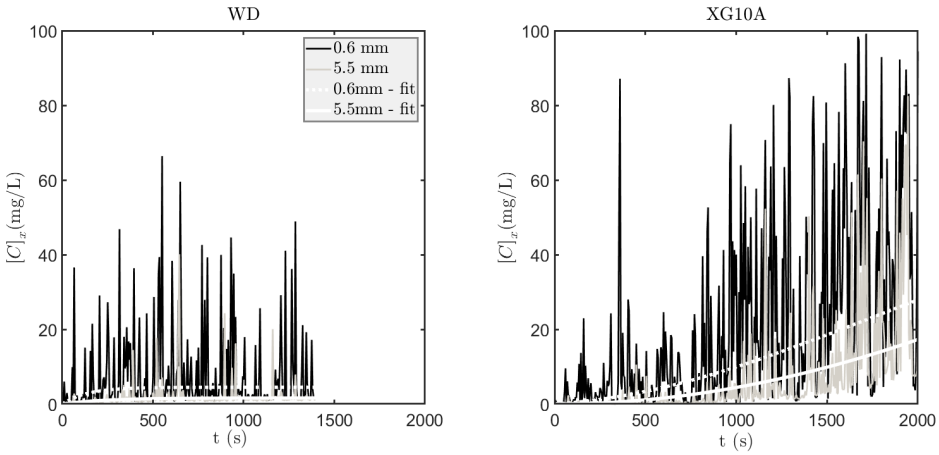

Figure 4.25 – Time series of x averaged instantaneous concentration for water and 10 ppm DPS at two different depths (dark lines for z=0.6 mm, gray lines for z=5.5 mm). Full and dotted white lines are exponential fittings of the time series at respectively z=0.6 mm and z=5.5 mm.

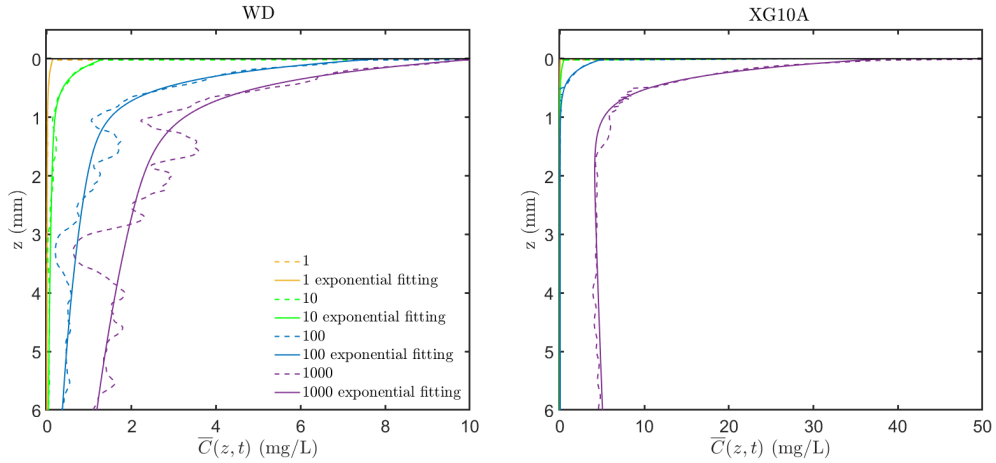

Figure 4.26 – Average concentration profiles at different times obtained by fitting of concentration time series at each depth. Concentration at depth z is estimated for each time t using the time series exponential fitting (dashed lines). Thus constructed average concentration profile are fitted by an exponential function of expression $\overline{C}(z,t) = C_b(t) + (C_s(t) - C_b(t))e^{-kz}$.

From figure 4.28 at t>100 s, it appears that the apparent scalar boundary layer thickness δ_D is thinner in the DPS case than in water: close to 0.5 mm for the WD run, 0.2 mm for XG10A. According to the film and surface renewal model, this should lead to faster global mass transfer for 10 ppm than for water, which is the case here.

4.5.2.b Evolution of bulk and surfacic concentration

This global mass transfer can also be evidenced by the evolution of surfacic and bulk liquid side concentration C_s and C_b. Values of C_s and C_b are obtained at each time t from the fitted concentration profiles shown previously. Their evolution with time is plotted in figure 4.27. The global mass transfer is confirmed to be faster in the XG10A case than in the WD case at t>10^2 s. Comparable evolution of C_s at short time for water and DPS would likely represent an initial diffusive regime of dissolution that establishes before the first peeling structures arising at the interface. Non zero C_b at t<10^1 for water can either indicate initial presence of CO_2 in the water, or be consequences of the experimental noise of single color PLIF. Values

of C_b and C_s for water are likely to be underestimated because of the use of single color PLIF.

4.5.3 Concentration fluctuations

4.5.3.a Concentration fluctuation fields

Once the average concentration is known at each depth, it is possible to compute local concentration fluctuation values such that $c'(x,z,t) = C(x,z,t) - \overline{C}(z,t)$.

4.5.3.b Time series and RMS of concentration fluctuations

Time series of $[c']_x$ are shown for our two probing depths for water and DPS at 10 ppm concentration. Vertical dashed lines show the time interval over which concentration statistics are computed.

4.5.3.c PDF of concentration fluctuations

Probability density functions of concentration statistics are plotted during the concentration statistics time interval of each run. Figure 4.29 displays the PDF of c' in both fluids at z=0.6 mm, z=2 mm and z=5.5 mm, restricted to small amplitude concentration fluctuations (-10<c'<10 mg/L).

All pdfs are clearly non-symmetric and not centered around $c' = 0$, shifted towards negative fluctuation. For water the peak is clearly evidenced at all three depths, and moves from $c' = -2.32$ mg/L at z=0.6 mm to $c' = -0.28$ mg/L at z=5.5 mm. At z=0.6 mm, the tail on the negative side of the peak is wider than that on the positive side. For the two other depths, the opposite trend is observed and the PDF displays a larger tail on the positive side. Nevertheless, the right side of the curve extends wider. All these observations indicate that for water, renewal scalar event are more probable at very small depths. Moderate amplitude renewal events are the most likely, but the probability of higher amplitude renewal events is also significant. With increasing depth, moderate amplitude renewal events are still the most probable, but the probability of higher amplitude ones decreases and the probability of injection events (positive c') increases. At z=5.5 mm, the probability peak is close to c'=0 and the tail of the PDF is larger on the positive fluctuations side, indicating a higher probability of injection events. This confirms the qualitative observations made on instantaneous scalar fields: fluid renewal is essentially observed very close to the interface (surface renewal), injection events are significant at moderate depths, and scalar statistics tend to that of turbulent mixing of a passive scalar in THI at large depths (Lenoir, 2011).

The shape of behavior of PDF curves is significantly modified for DPS: at z=0.6 mm, the probability of the most negative fluctuations is still higher than that of positive or less negative fluctuations but no clear peak is observed and the PDF curve is essentially flat below $c' = -3.53$ mg/L. With increasing depth, negative fluctuation peak does appear, while the PDF curve at the largest amplitude negative fluctuations remains flat. The tail on the right side of the peak becomes slightly larger. PDF curves at z=2 mm and z=5.5 mm are very similar. In DPS, concentration renewal events are thus also dominant in at very small depth, but the spectrum of amplitude of probable renewal events is larger. The dominance of fluid renewal seems to persist at larger depths than for water.

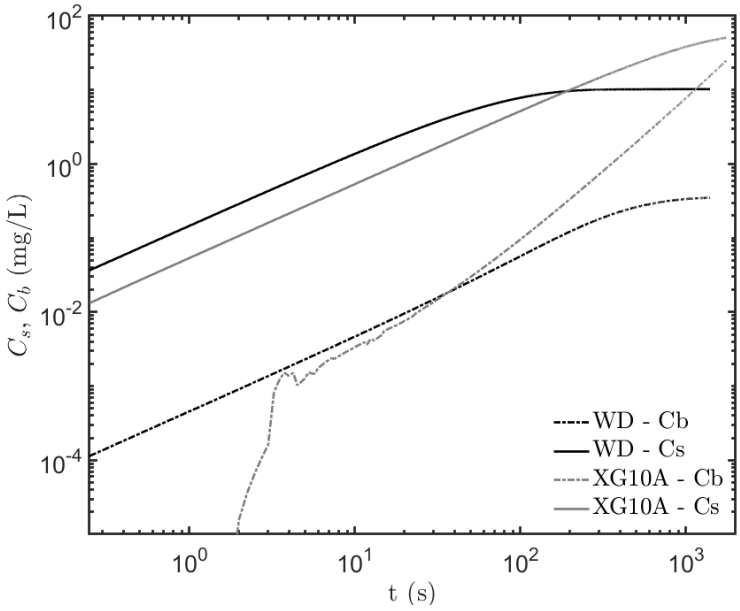

Figure 4.27 – Time series of bulk and apparent surface concentration estimated by exponential fitting of average concentration profiles. Results are shown in log-log scale.

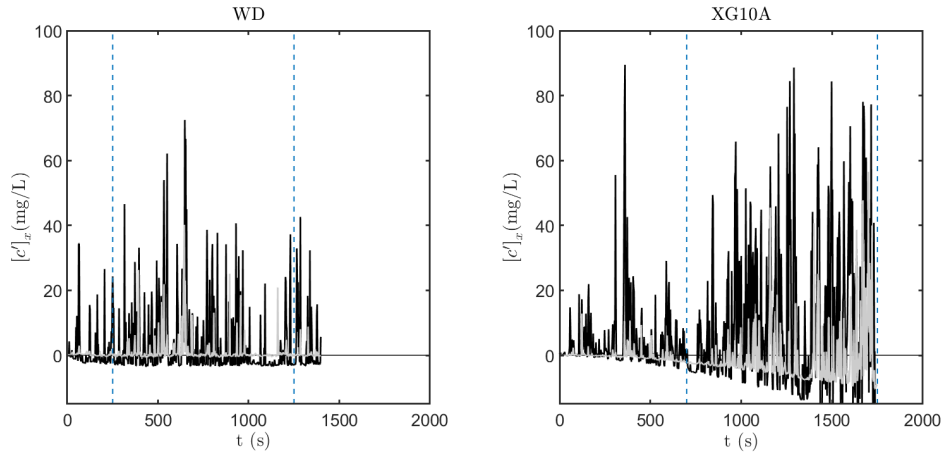

Figure 4.28 – Time series of x averaged concentration fluctuations for water and 10 ppm DPS at two different depths (dark lines for z=0.6 mm, gray lines for z=5.5 mm). Vertical dashed lines denote the time interval over which concentration statistics (rms, PDFs, correlations) are evaluated.

4.5.4 Two points and two times statistics

4.5.4.a Concentration length scales

The same way two point velocity correlations are defined, it is possible to compute the correlation coefficient of concentration fluctuations between two points separated by a distance r_i along dimension i. The correlation coefficient at a given depth is z is then:

$$\mathrm{R}_c^i(z, r_i) = \left[\frac{\overline{c'(r_i^0, z, t)c'(r_i^0 + r_i, z, t)}}{\overline{c'^2}} \right]_x \tag{4.24}$$

An example of correlation coefficients R_c^z plotted versus the separation length r_z along dimension z, for the XG10A run, at different depths is shown in the insert of figure 4.30 (the blue curve being the closest to the interface and the yellow curve the furthest). Correlation

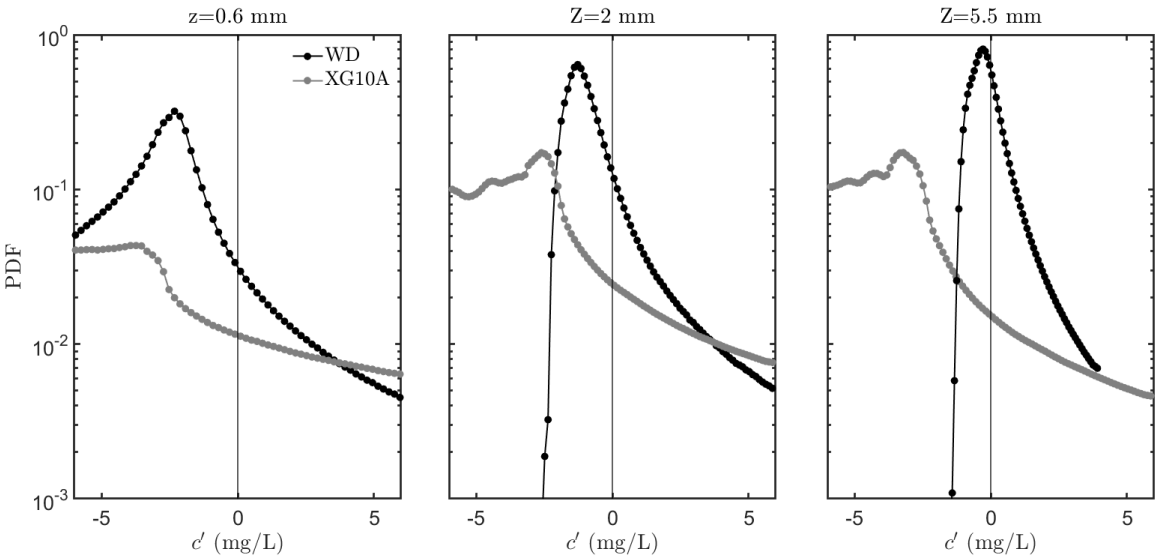

Figure 4.29 – PDF of small amplitude concentration fluctuations for WD and XG10A runs at three different depths. PDF values are shown in log scale.

curves can be fitted by a sum of exponential functions. Integrating the fitted curve from r_z=0 mm to infinity gives the spatial integral length scale for concentration along dimension y. A similar process is applied to correlation coefficient along the horizontal direction x, and for water. Integral concentration length scale are plotted versus depth in figure 4.30. Like for the integral velocity length scales, vertical length scales are not computed at the smallest depth due to the size of the sampling region.

The first observation than can be made from figure 4.30 is that horizontal length scales for water are likely to be not completely converged, and show some spreading: the black curve with full markers oscillates around a constant value at depth larger than 1 mm, which is not the case for the grey curve. Nevertheless, comparison can still be made between trends for the horizontal and vertical length scales in water, and it appears that the horizontal one is always greater than the vertical one. This last one stays approximately constant between z=8.5 mm and z= 4mm around L_c^z =2 mm. In the same depth range, but also up to z=1 mm the horizontal scale is $L_c^x \simeq$2.6 mm. For z<1 mm, L_c^x increases up to its maximum value of 4.24 mm at z=0 mm. These trends imply that patches of turbulent concentration fluctuations are always larger in the horizontal dimension than in the vertical one. The typical size of these patches along z remains constant at moderate depths. The increase of L_c^x for z<1 mm is an evidence of the development of the scalar boundary layer, of depth δ_D under the interface. In this sub-layer, concentration patches are large horizontal stripes of high concentration, partially and randomly broken by renewal events (see for example figure 4.23 b,d or e). At larger depths, concentration structures are stretched and deformed in both dimensions by turbulent structures and the length scales in both dimensions tend to similar values with increasing depths, still with a preferential horizontal dimension inherited from the peeling process.

Similarities with water can be found for the integral length scales of the XG10A run: almost constant horizontal scale inmost of the ROI, with an abrupt increase at small z, here for z<2 mm. We thereby evidence the development of a scalar boundary layer in DPS as well, which was also observed in the instantaneous concentration fields (see figure 4.24). The depth at which L_c^x begins to increase is yet surprising since it is larger than the depth δ_D estimated from the mean concentration profiles. Several other difference between water and

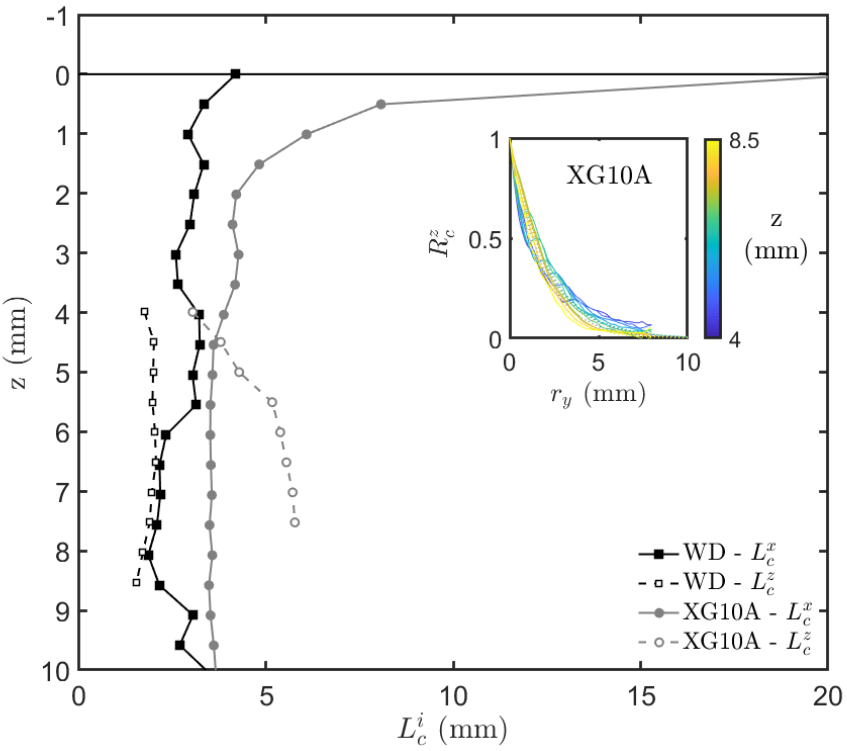

Figure 4.30 – Two point concentration correlation coefficient (insert) and concentration fluctuations integral length scale for WD and XG10A runs. Full markers are scales along the horizontal dimention, empty markers are scales along the vertical dimension. Full lines in the sub-figure are computed correlation coefficients, dashed lines are exponential fittings.

DPS are observed. First, both vertical and horizontal length scales are always higher in DPS than in water: an increase of 1 mm for L_c^x in the constant region and of 1.4 mm to 3.9 mm for L_c^z. The asymptotic value of L_c^x at z=0 mm is 21.2 mm, that is to say 5 times bigger than the one for water. Second, the vertical length scale is higher than he horizontal at depths higher than z=4.5 mm. While it stayed quite constant with depth in water, it is here clearly decreasing with decreasing z.

The first observations indicate that in DPS generally tends to increase the size of concentration patches in all dimensions: this is not surprising since DPS has an increased viscosity compared to water, hence increased Kolmogorov and Batchelor scales, if turbulence still exist. It yet implies that horizontal scalar patched that can be found in the boundary layer are statistically longer in DPS than in water: they are less likely to be broken by renewal events.

This is an important difference in the mass transfer mechanisms between water and DPS. From concentration fluctuations PDF, we previously noticed that surface renewal was more probable in DPS than in water. Here we see that even if it is more probable, it is less likely to break the scalar boundary layer. Hence surface renewal in the DPS case seemingly takes the form of a contraction of the scalar boundary layer with partial replacement of the saturated fluid from the bottom of the boundary layer. Strong sweeping events locally replacing saturated fluid up to z=0, and leading to a split of the boundary layer are less frequent in DPS than in water.

The second observations point out that DPS tends to promote vertical elongation of concentration structures outside of the scalar boundary layer. The vertical scale increases with increasing depth, which is not the case for water, and even become larger than the horizontal

one.

4.5.4.b Concentration time scales

Due to the slow motion of concentration structures compared to velocity structures, it is possible to follow some of them in time, between frames. A point in the ROI thus stays at a given concentration value for a time depending on the speed and shape of concentration patches moving through the ROI. The temporal concentration correlation coefficient is defined for a given location (x, z) as the correlation between concentration fluctuations at instants t and $t+\tau$. The correlation coefficient at a given depth z is then:

$$R_c^t(z,\tau) = \left[\frac{\overline{c'(x,z,t)c'(x,z,t+\tau)}}{\overline{c'^2}} \right]_x \tag{4.25}$$

As defined by Janzen et al. (2010). An example of correlation coefficients R_c^t plotted versus the separation time τ, for the XG10A run, at different depths is shown in he insert of figure 4.31 (the blue curve being the closest to the interface and the yellow curve the furthest). Time correlation curves are also non Gaussian, and can be fitted by a sum of exponential functions. The integral concentration time scale T_c is obtained by integrating R_c^t fittings from zero to infinity. This can be done inasmuch as R_c^t curves fall to zero within the time of measurement, which is verified here.

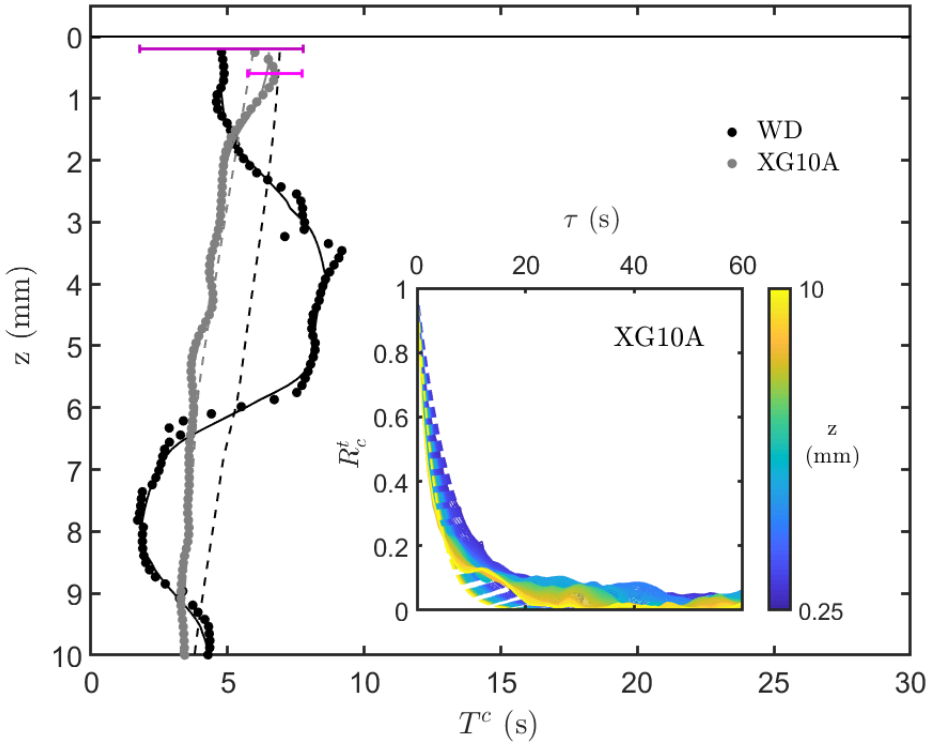

Figure 4.31 – Two times concentration correlation coefficient (sub-figure) and concentration fluctuations integral time scale for WD and XG10A runs. Markers are computed scales, dashed lines are smoothing of the computed scales. Full lines in the sub-figure are computed correlation coefficients, dashed lines are exponential fittings. Error bars on L^t profiles are estimated as the maximum, among all curves, of the difference between numerical integration of R_c^t at a given depth and analytic integration of its exponential fitting. Uncertainties are typically of ±3 s for water and ±1 s for XG10A (purple and pink errorbars). They are shown at a single depth for each curve for clarity reasons.

This integral time scale is a statistical quantification of how long a given point stays at the same concentration value. The higher the integral time scale the longer the time available for diffusion. Here we notice that integral time scales increase with decreasing z, which is consistent with the establishment of a scalar boundary layer close to the interface where turbulent stretching of scalar patches is less intense and diffusion has time to occur. The concentration time scales are quite close for water and DPS: respectively about 3.5 s and 4.1 s at z=9 mm and 5.7 s and 6.8 s at z=1 mm.

However, the statistics for temporal length scale seems badly converged, especially for water. The temporal resolution of scalar fields is still quite poor: typical persistence times for concentration are of the order of a few seconds. The exponential fitting of correlation curves is done with a limited number of points. In order to estimate the uncertainty of our integral time scale measurement, we compute for a given fluid and a given depth the time scale as the numerical integral of the measured R_c^t curve, using a trapezoidal method. This value is compared to the one obtained by integration of the exponential fitting. The maximum differences found are of about 1 s for the XG10A measurements, and 3 s for WD. We are thus not able to go beyond a simple estimation of a typical time scale for concentration.

4.5.5 Conclusions on passive scalar properties

4.5.5.a Scalar structures and concentration events

In both water and low concentration DPS, scalar fields in the sub-surface ROI consist in a complex combination of scalar structures of various sizes and shapes. In the first 1 or 2 mm underneath the interface, a statistical concentration boundary layer establishes and takes the form of a long horizontal saturated patch, randomly broken or made thinner by turbulent flow structures. Below this scalar boundary layer, injection-type structures prevail. They correspond to coiled and.or stretched scalar patches plunging towards the bulk. At the highest depths of the ROI, these patches are eventually broken and mixed by stronger turbulent events.

4.5.5.b Concentration statistics in water and 10 ppm DPS

The PDF of concentration fluctuations of both water and 10 ppm DPS indicate that concentration renewal is the most probable concentration fluctuation event. The population of renewal events is yet quite different in water and in DPS: in water, renewal occurs essentially close to the interface, while it is distributed over depths in DPS. Concentration length and time scale though not well converged, show that scalar patches are larger and more vertically elongated in DPS than in water, and that their residence time close to the interface is higher for DPS.

4.5.5.c Evolution of concentration with time

Average concentration in the tank and in the ROI is by design transient. Using time series of measured concentration along the z direction, expected concentration profiles at all times are constructed, and used to estimate the mean concentration value at all depths $\overline{C}(z,t)$. It appears that after an initial period during which it remains almost constant in DPS, the average concentration increases faster in the XG10A run than in the WD run. The exponentially shaped diffusive like profile establishes quicker in water than in DPS.

This can be explained by concentration statistics discussed above: in water, renewal events close to the interface are stronger, they are thus ore likely to fully refresh the con-

centration boundary layer, thus preventing C_s from approaching the C_{sat} value, and keeping moderate concentration gradients inside the scalar boundary layer. On the other hand, renewal events in DPS are less likely to fully refresh the scalar boundary layer (larger patches and higher residence time at small z). C_s thus has enough time to increase and establish stronger concentration gradients inside the boundary layer.

This completes the surface renewal conceptual picture of mass transfer. Mass transfer velocity is conditioned by the speed at which turbulent eddies come and reduce the thickness of the scalar boundary layer, but also by the ability of these eddies to totally sweep the saturated fluid from the interface and reduce the instantaneous C_s value. Historically, the assumption was made that no turbulent structure is able to refresh the interfacial concentration and that concentrations close to C_{sat} always establish within the first few micro-meters under the interface, thus keeping a high interfacial gradient. However if one assumes that some turbulent structures can remove saturated fluid up to the interface, event within the smallest sub-layers, then interfacial concentration may be reduced, and so the interfacial gradient and interfacial mass flux. Under this last hypothesis, surface renewal has a two side effect: enhancing mass transfer by making the scalar boundary layer thinner in depth, but simultaneously reducing the interfacial gradient by not letting enough time for C_s to reach S_{sat}. Surface renewal would thus be an efficient mass transfer enhancing mechanisms in situations when interfacial properties prevent turbulent structures from sweeping the interface, such as surfactant polluted interfaces or in DPS. In clean water however both boundary layer thinning are sweeping effects can be found and the enhancement is not as efficient.

The spatial resolution of our experimental methods is not good enough to be able to visualize concentration in the first few micro-meters under the interface, and check this last hypothesis. Moreover, ratiometric measurements in water are required in order to be able to compare rigourously saturated concentration values and determine the truly established concentration gradients for water.

We have so far described the features of flow hydrodynamics under the interface, and the scalar properties resulting from these hydrodynamic features. The next step of our analysis is to use coupled measurements to evidence the link between velocity and scalar fields, and determine which velocity and concentration structures give birth to efficient mass transfer events.

4.6 Conditional analysis of coupled measurements

4.6.1 Instantaneous coupled fields and mass transfer events

The first step in this coupled fields analysis is to qualitatively visualize the correspondence between velocity and scalar fields. Fields are superimposed using the image of a transparent test pattern placed in the ROI and recorded by both camera sets. Yet, even when the accurate superimposition of fields is achieved, finding good symbolic examples of coupled scalar and velocity fields is not an easy task, mostly because of the non negligible mean flow that tends to move concentration structures in and out of the ROI.

Figure 4.34 shows three example of coupled instantaneous fields for the WD run, at t=123.5 s, 124.5 s and 706.75 s. Three examples for the XG10A run, at times t=31 s, 124.75 s and 1075.25 s are shown in figure 4.35. Fluctuating concentration fields at the same instants for the two runs are displayed in figures 4.34 and 4.35.

We here again see the horizontal shading of the bubble or dirt particle at z around 3.2 mm for the WD run. Concentration fields are most of the time well explained by velocity fluctuation fields in the 2D view. However, frame 500 of the XG10A run for example shows that

near surface concentration structures such as apparent surface renewal can be independent of any up-going or down-going motion, but rather due to horizontal swirling structures. It should be noted that concentration structures that could be at first sight interpreted as injection events, such as the one at the top right of WD frame 495, correspond in fact to negative concentration fluctuations and thus to concentration renewal. Instantaneous fields should thus be interpreted carefully, and statistical analysis is needed to distinguish effectively between injection events and surface renewal ones

4.6.2 Velocity-concentration correlations

With instantaneous information about velocity and concentration fluctuations, it is possible to compute the ensemble average of velocity-concentration correlations $\overline{u_i'c'}$ and the ensemble rms $\langle u_i'c'\rangle_{rms}$, and plot their width averaged profiles along depth $\left[\overline{u_i'c'}\right]_x$ and $\left[\langle u_i'c'\rangle_{rms}\right]_x$ (see figure 4.36). Triple correlations $\overline{u_i'u_j'c'}$ and corresponding ensemble rms $\langle u_i'u_j'c'\rangle_{rms}$, and the quadruple correlation $\overline{u_x'u_y'u_z'c'}$ and rms $\langle u_x'u_y'u_z'c'\rangle_{rms}$ have also been computed and found to be negligible compared to double correlations, so they are not plotted here.

Vertical mass fluxes $\overline{u_z'c'}$ are found to be always positive, verifying the fact that turbulence tends to enhance mass transfer. Horizontal turbulent mass fluxes are also significant. They contribute to horizontal turbulent mixing of the dissolved gas. Horizontal mass fluxes do not appear isotropic in the x and y direction from figure 4.36 a), especially for the XG10A run. However, 4.36 b) shows that in terms of rms, horizontal mass fluxes along x and y are equivalent. Conditional analysis will allow us to compute conditioned averaged of turbulent mass fluxes by sorting instantaneous events according to the signs of fluctuations.

4.6.3 Joint PDF and co-variance integrands

As done for turbulent momentum fluxes in section 4.4.5, it is possible to plot the two joint PDF of u_z' and c' fluctuations and their covariance integrand (PDF weighted by the product of the two fluctuations).

Low amplitude concentration fluctuations: Figure 4.37 shows joint PDFs of P(u_z', c') for water and DPS in the ranges [-8 8] mm/s for u_z' and [-25 25] mg/L for c'. The [u_z',c'] space is decomposed in 101 bins along both directions. 6 contour plots of the joint PDF are shown, at values regularly distributed along a log scale indicated by the colorbar. The same representation is adopted for the covariance integrand in figure 4.38). Note that the sample depths are close but not equal to the ones previously used for concentration statistics analysis, since coupled measurement statistics are only available at SPIV vector locations. Those two figures can still be compared to c' PDF, and the same shift towards themost negative c' is found for both water and DPS.

The balancing towards $c' = 0$ with increasing depth is here again evidenced for water but not for DPS. Water PDF figures compare qualitatively well to the results of Variano and Cowen (2013): a high probability peak at moderate negative c' and a long tail of low probability events at low u_z' and positive c', reducing with depth. As for co-variance integrand, they are also quite similar, keeping in mind that $u_z' > 0$ here corresponds to $u_z' < 0$ in VC. The major difference with VC experiments that can be observed in both PDF and covariance integrand plots is that we do not reach here sufficient depths for an evened balance between quadrants to be observed.

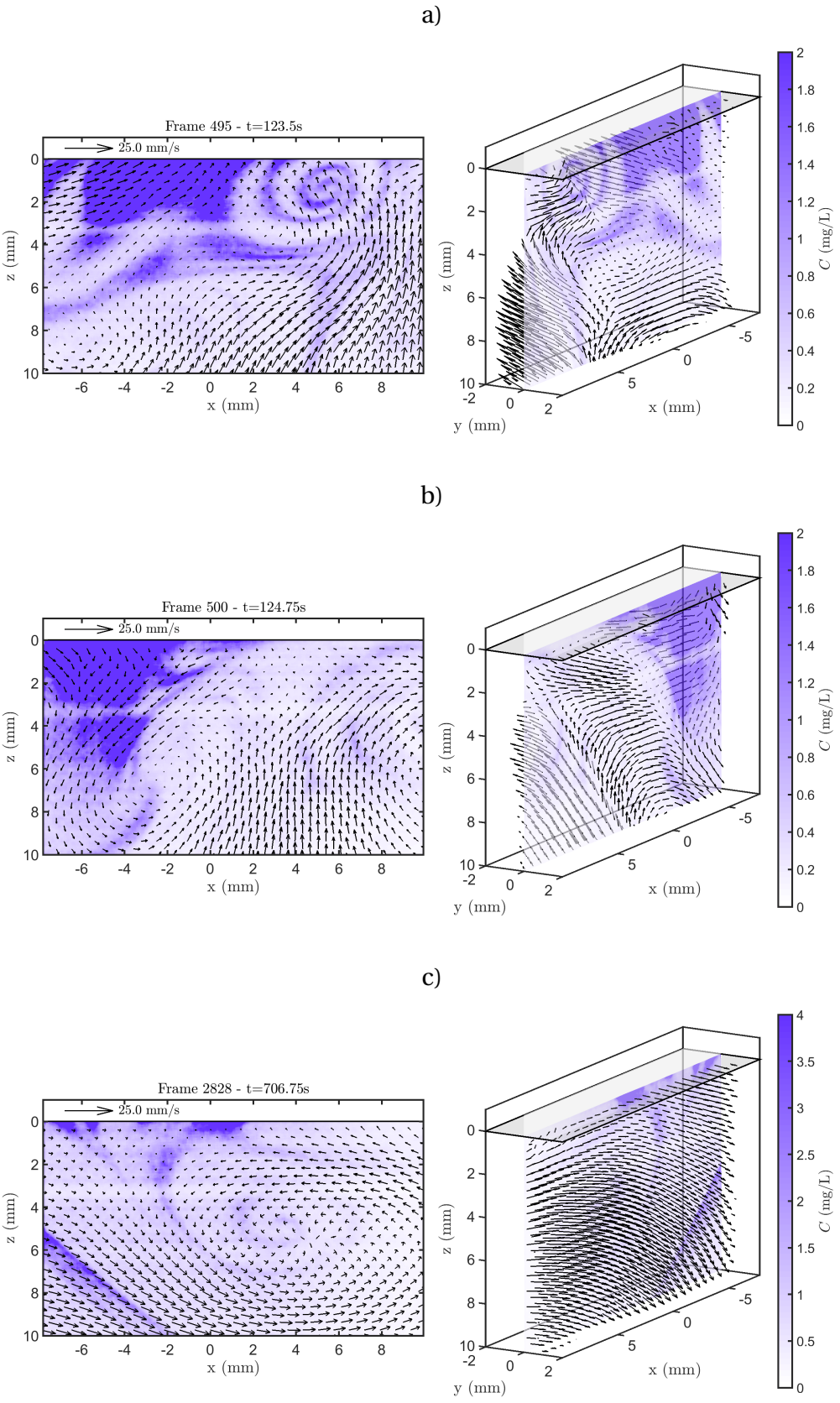

Figure 4.32 – Coupled instantaneous velocity and dissolved gas concentration fields in water, WD run, at three different times.

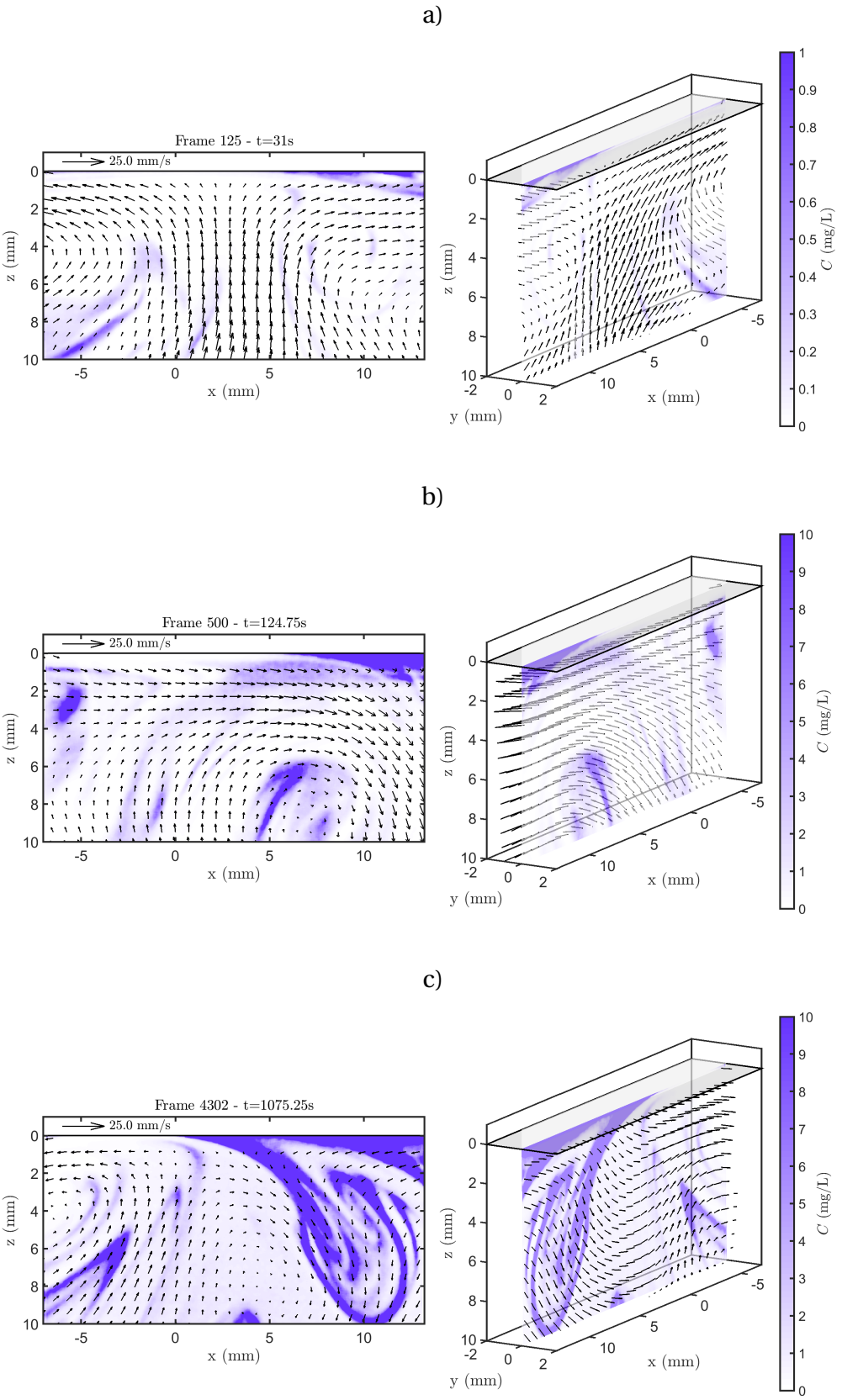

Figure 4.33 – Coupled instantaneous velocity and dissolved gas concentration fields in 10 ppm DPS, XG10A run, at three different times.

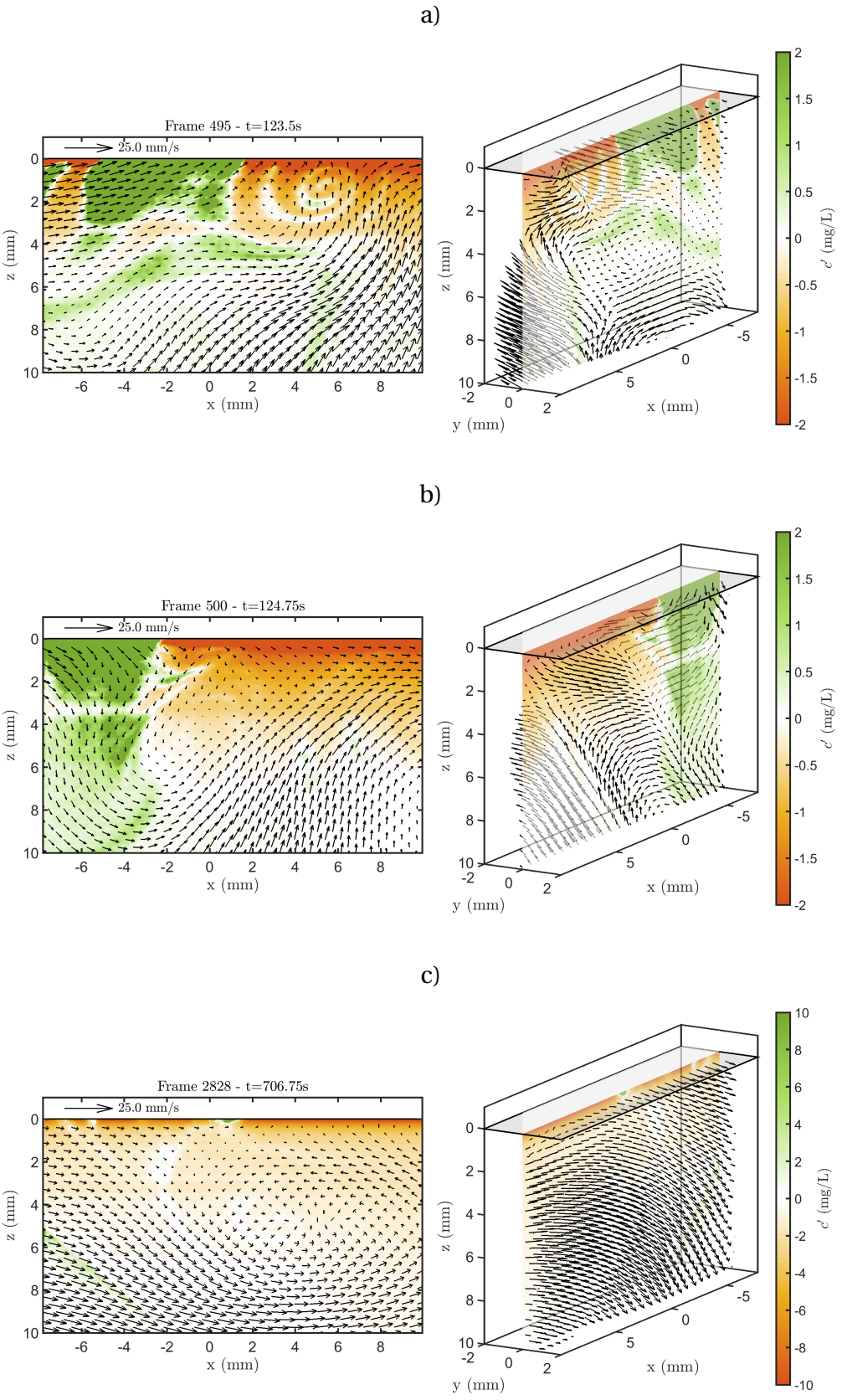

Figure 4.34 – Coupled fluctuating velocity and dissolved gas concentration fields in water, WD run, at three different times.

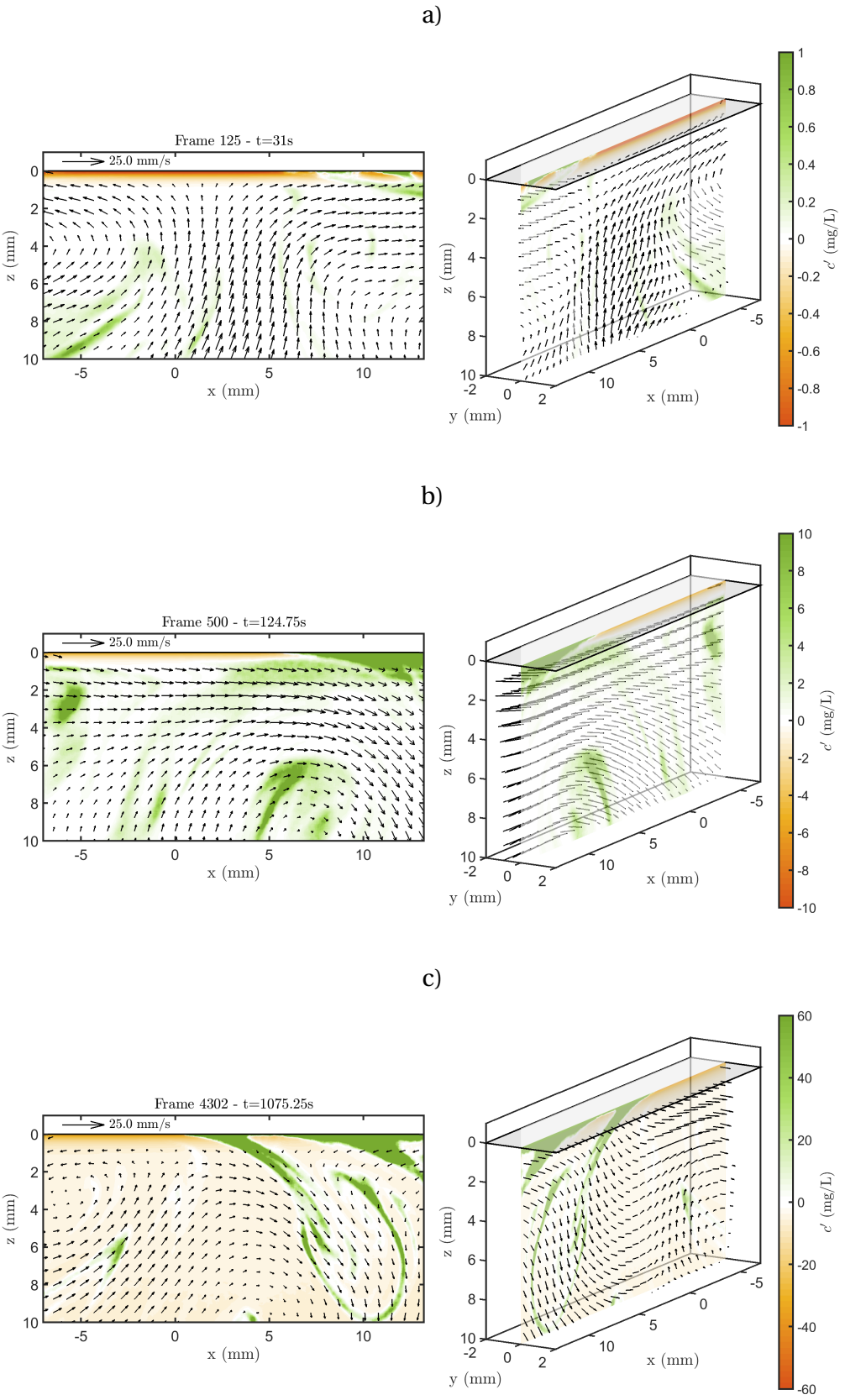

Figure 4.35 – Coupled fluctuating velocity and dissolved gas concentration fields in 10 ppm DPS, XG10A run, at three different times.

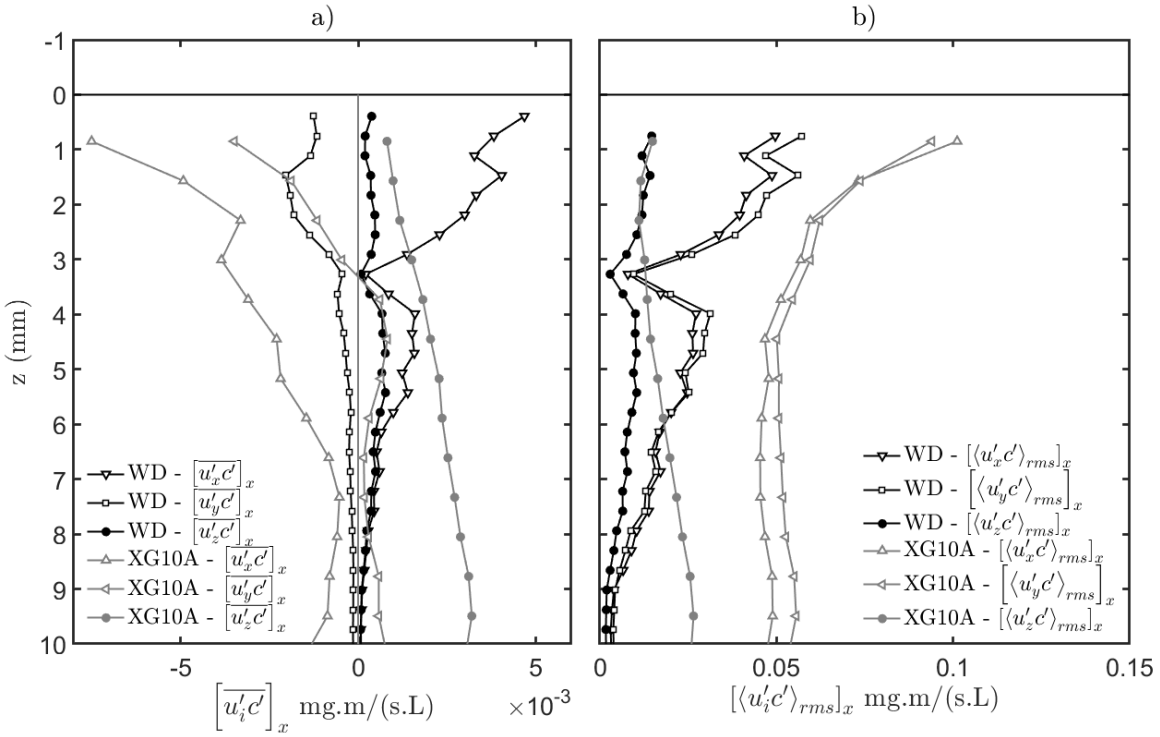

Figure 4.36 – Width averaged profiles of $u'_i c'$ correlations (a) and their rms (b) for water and DPS.

In DPS, the persistence of large amplitude negative c' events with increasing depth, first observed on c' PDFs in figure 4.29, is also visualized here. Yet we see from the covariance integrand plot of figure 4.38 that injection events are significant as well. As in water, the tail of low u'_z and positive c' events reduces with increasing depth.

Co-variance integrand plots show that even if the quadrants are quite balanced at larger depths, Q4 events are more probable than Q1 and Q2 than Q3. Q4 corresponds to concentrated fluid moving downwards, and Q2 to low concentration fluid going up. We thus here evidence the existence of surface renewal and injection mechanisms in DPS.

All concentration fluctuations: In order to get access to the high c' injection events, covariance interand plots are plotted this time restricting to $c' \in$ [-25 125] mg/L, still using 101 bins and 6 contour plots regularly spaced in a log color scale. This new figure confirms what was visible of injection events in figure 4.39: the tail at large positive c' values progressively disappears with increasing z for both water and DPS. Yet we here evidence the existence of two covariance integrand peaks at high positive c', characteristic of strong injection events in the Q4 case. It is worth noting that we here see a peak because of the limitations of the PLIF measurements: concentration values higher than about 100 mg/L correspond to pHs lower than 4 which are beyond measurement accuracy. Image processing and PLIF procedure are such that concentration fields are "saturated" at this value close to 100 mg/L, thus explaining the peak behavior. With a sufficient measurement accuracy at lower pHs, the peak would probably spread over a wider range of high c' values.

On this new representation of the covariance integrand, Q2 and Q3 events completely disappear from the water balance at high depths, for which a combination of high and low c' Q1 and Q4 events dominate. In DPS, Q2 and Q3 events still persist at high depths. The balance between Q1 and Q4 events, which was at equilibrium at small z, is shifted towards Q4 for increasing concentration.

To conclude, joint PDF and covariance integrand plots bring several information on ver-

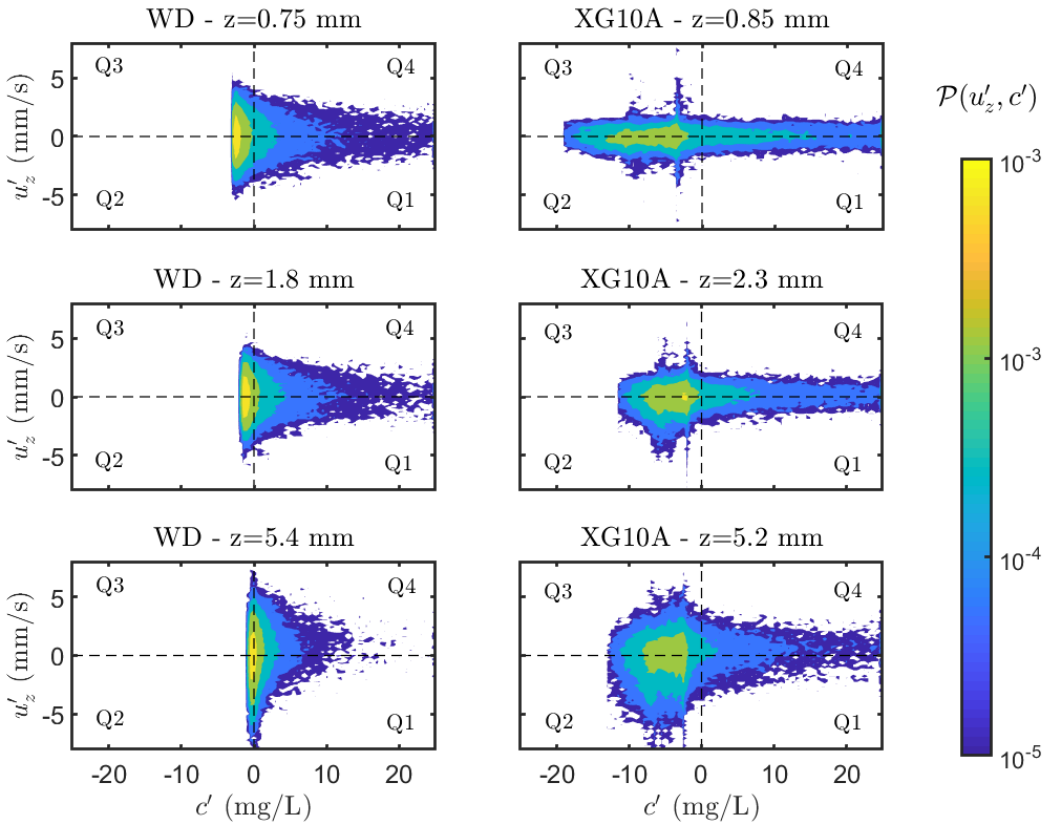

Figure 4.37 – Joint PDF of u'_z and c' for $c' \in$[-25 25] mg/L, for water and DPS. Results are shown at three sample depths. The variable space is divided in 101 bins in both dimensions. Contour plots are shown at values regularly distributed along a log scale indicated by the colorbar.

tical turbulent concentration events:

- The most probable events are those at moderate negative c', for water and DPS. Positive c' events are displayed over a wider range of c' values.
- At small depths for water and DPS, joint PDF and covariance plots are symmetric with respect to the $u'_z = 0$ axis. With increasing depths, the dominannce of Q2 over Q3 and Q4 over Q1 begins to emerge, especially in DPS. Injection (Q4) and renewal (Q2) events are thus confirmed to contribute to mass transfer in both water and DPS.
- From co-variance integrand plots, one clearly sees that even if they are less probable than renewal events, injection events are associated to stronger fluctuations.

We have here detailed the joint probability of vertical velocity fluctuations associated to concentration fluctuations at three sample depths through joint PDF and co-variance integrated analysis. This already gives a good idea about which type of events are the most likely to contribute to mass transfer. The next step in our study is to generalize the study of events probability to the whole ROIs' depth, and perform a conditional analysis of turbulent mass fluxes along z.

4.6.4 Probability profiles of quadrants and hexadecans

First, the probability of each type of events is plotted as a function of depth. To do so, the probability of each hexadecan type $\mathscr{P}_{\mathrm{HX}i}$ is evaluated at each point of the ROI by counting

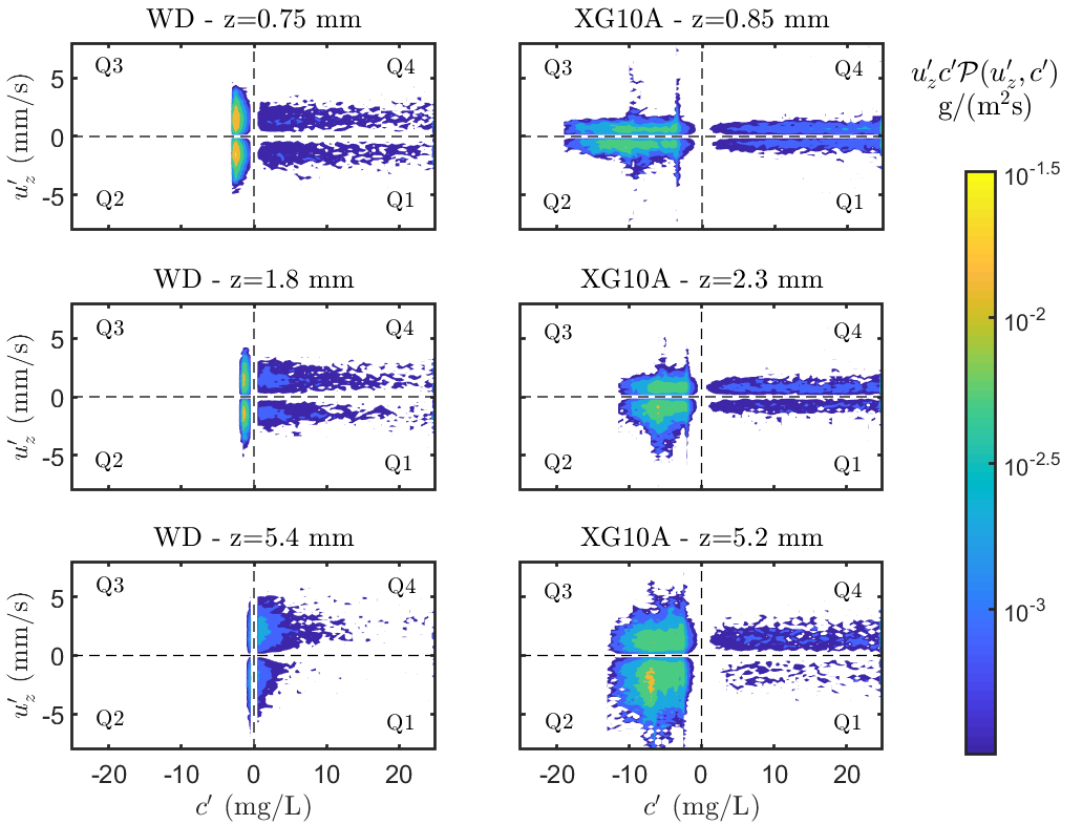

Figure 4.38 – Covariance of u'_z and c' for $c' \in$[-25 25] mg/L, for water and DPS. Results are shown at three sample depths. The variable space is divided in 101 bins in both dimensions. Contour plots of are shown at values regularly distributed along a log scale indicated by the colorbar.

the number of occurrence N_{HXi} of each type of event at this location and dividing by the total number of instantaneous fields N_{tot} such that $\mathscr{P}_{HXi} = N_{HXi}/N_{tot}$. $[\mathscr{P}_{HXi}]_x$ Profiles are then obtained by width averaging the probability fields of each type.

Figure 4.40 shows the probability profile of each hexadecan and figure 4.41 the probability of each quadrant (computed in a similar fashion as $\mathscr{P}_{Qi} = N_{Qi}/N_{tot}$) in water and DPS. $\mathscr{P}_{Qi}$ may be seen as the integral of the joint PDF $\mathscr{P}(u'_z, c')$ over the range defined by quadrant Qi.

From figure 4.40, one sees that the probability of all hexadecans included in the same quadrant are close to each other and have similar evolution along depth. Blue and yellow curves (Q1 and Q4) and red and green curves (Q2 and Q3) are comparable, indicating that quadrant Q1 and Q4, and Q2 an dQ3 have equivalent probabilities. This is verified in figure 4.41 in water and DPS. Q1 and Q4 correspond to positive concentration fluctuations, and Q2 and Q3 to negative ones. In a first approach, one can thus focus only on the analysis of the quadrant decomposition. We by the way notice that the measurement noise introduced by the bubble or dirt at z=3.2 mm in the water run leads to out-of trend points around z=3.2 mm for all turbulent mass fluxes statistics.

Q2 and Q3 probabilities are higher that Q1 and Q4 ones close to the z=0 interface in both water and DPS. This corresponds to the shift of c' PDF's towards negative fluctuations observed in section 4.5.3. In DPS, quadrants with $c' < 0$ are more probable than those associated to $c' > 0$ at all depths, which is another evidence of the preserved dominance of concentration renewal with increasing depth that was observed in section 4.5.3 as well. For water Q1 and Q4 quadrants show higher probability at depths z>7 mm. The main differ-

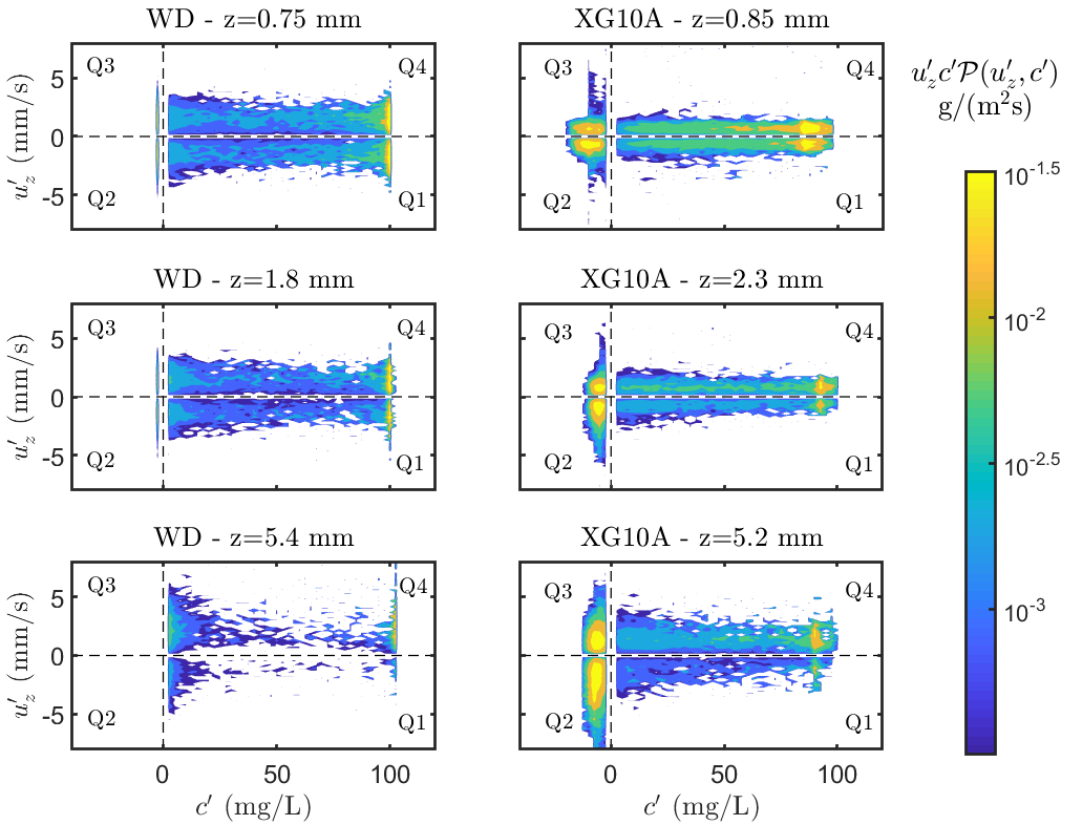

Figure 4.39 – Covariance of u'_z and c' for $c' \in$[-25 125] mg/L, for water and DPS. Results are shown at three sample depths. The variable space is divided in 101 bins in both dimensions. Contour plots of are shown at values regularly distributed along a log scale indicated by the colorbar.

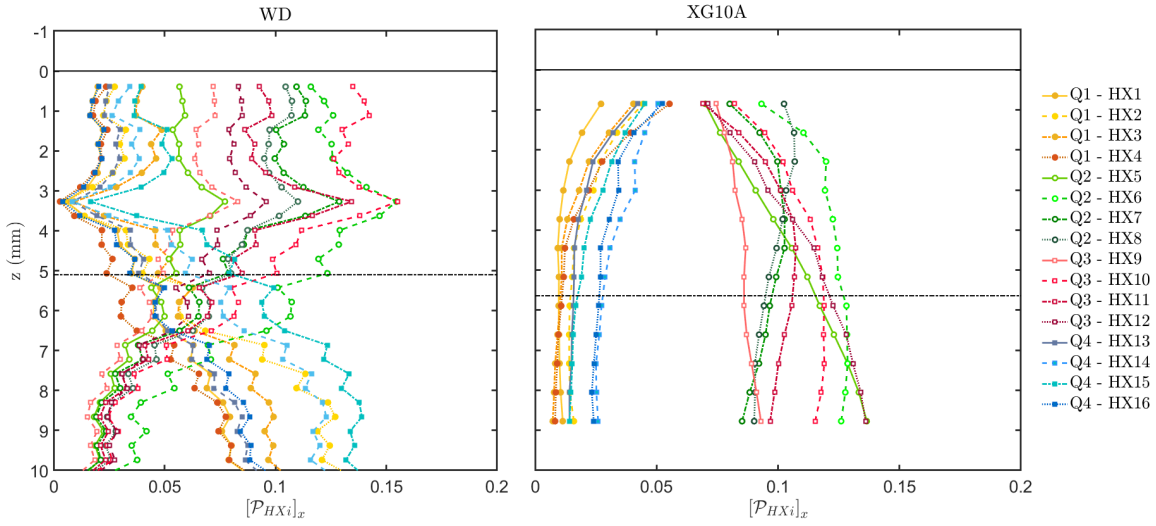

Figure 4.40 – Width averaged probability profile of each hexadecan in water and DPS. The horizontal dashed line marks the viscous sub-layer depth z=δ_ν.

ence between water and DPS is found in the evolution of probabilities with depth. In the WD run, the probability of Q2 and Q3 events increases with decreasing z, and the probability of Q1 and Q4 events decreases. The quadrants that are supposedly efficient in mass transfer enhancement are those for which $u'_z c' > 0$, *i.e* Q2 and Q4. Q2 corresponds to up-going

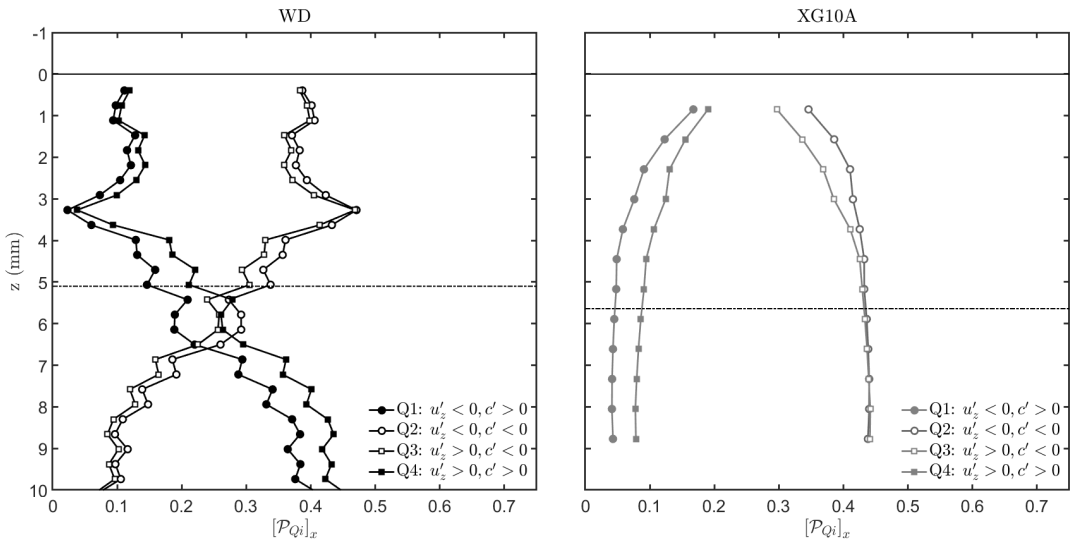

Figure 4.41 – Width averaged probability profile of each quadrant in water and DPS. The horizontal dashed line marks the viscous sub-layer depth z=δ_ν.

under-saturated fluid: renewal events. Q4 defines down-going over concentrated patches of fluid, thus corresponding to injection events. For water, the probability of injection and renewal events are equivalent at moderate depths, leading to symmetrical c' PDFs. When approaching the interface however, the probability of injection events Q4 decreases versus that of renewal events Q2, leading to a shift in concentration PDFs towards negative values. In DPS, renewal events Q2 are always more probable that injection ones. Yet, the probability of these renewal events decreases when approaching the interface, while that of injection events increases.

We are still though only discussing probability of events, which indicates the chance each type of events has to occur, but not the strength of the occurring events. To tell which events are the most relevant in terms of turbulent mass fluxes, and not only the most probable, one needs to compute sorted conditional averages.

4.6.5 Vertical turbulent mass fluxes

The main interest in turbulent mass transfer studies is to be able to predict the turbulent mass flux normal to the interface. Let us therefore focus on the conditional analysis of vertical mass fluxes $\overline{u'_z c'}$. Quadrant averaged vertical mass fluxes $\overline{u'_z c'}_{Qi}$ are computed for each point of the ROI. It is checked that all mass fluxes are well homogeneous along the x direction, and mostly depend on depth z. The absolute value of their width averaged profile are plotted as a function of depth on figure 4.42 for the WD and XG10A runs. Mass fluxes associated to Q1 and Q3 are supposed to be negative since they are time averages of products of negative fluctuations.

The influence of measurement noise at z close to 3.2 mm is here again evidenced by three data points out of trend. For water, Q1 and Q4 quadrant corresponding to positive concentration fluctuations yield higher turbulent mass fluxes than quadrants Q2 and Q3, especially at z<δ_ν. Turbulent mass fluxes of all quadrants increase whith decreasing z, but Q1 and Q4 increase faster than Q2 and Q3, thus increasing their share in the total turbulent mass flux when approaching the interface. Values of Q1 and Q4 and Q2 and Q3 are respectively close, but at all depths though, $\overline{u'_z c'}_{Q4} > \overline{u'_z c'}_{Q1}$ and $\overline{u'_z c'}_{Q2} > \overline{u'_z c'}_{Q3}$, thus confirming that both renewal and injection events tends to create positive turbulent mass fluxes

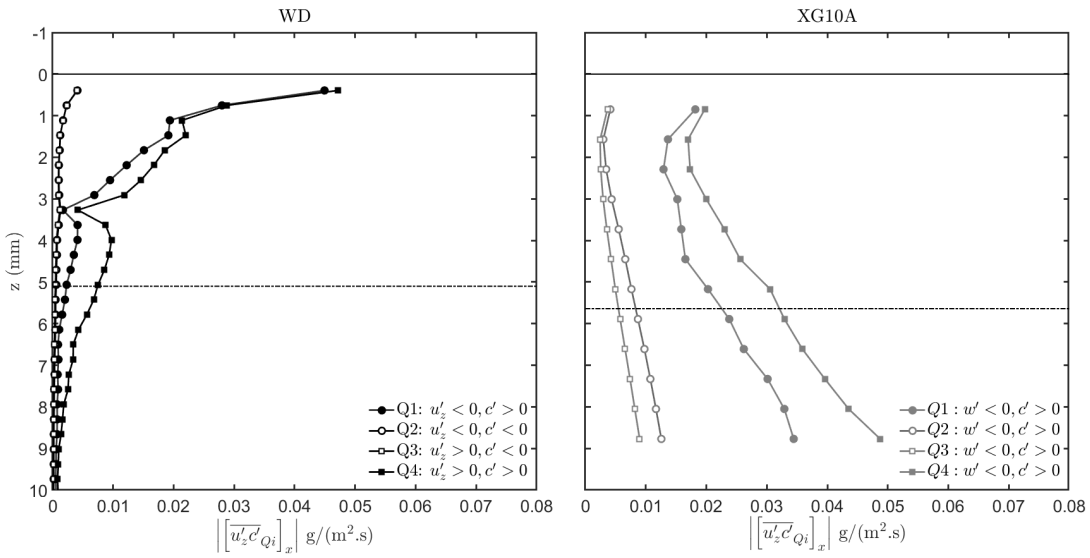

Figure 4.42 – Quadrant sorted vertical turbulent mass fluxes $\overline{u'_z c'}$ as a function of depth, in water and DPS. The horizontal dashed line marks the viscous sub-layer depth z=δ_ν.

and enhance mass transfer. Yet, it seems that injection events corresponding to Q4 quadrant are the major contributor to the turbulent mass transfer. The same order of importance $\overline{u'_z c'}_{Q4} > \overline{u'_z c'}_{Q1} > \overline{u'_z c'}_{Q2} > \overline{u'_z c'}_{Q3}$ can be observed at all depth for the 10 ppm DPS run. Several differences with water are yet to be mentioned. First is the fact that all quadrant sorted turbulent mass fluxes decrease with decreasing z, both inside and outside of δ_ν except at very small depths (top two depths of measurement). The difference between renewal and injection events does not seem to depend on depth z.

For both water and DPS, turbulent events opposed to the mass transfer direction are not negligible, but the overall turbulence tends to promote mass transfer through both renewal and injection events. It seems that injection events are the main contributor to mass transfer in the two fluids. The mechanisms of turbulent mass transfer are yet quite different: in water, turbulence mostly acts close to the interface and less outside of the viscous sub-layer, while in DPS, the renewal and injection actions is spread over the full depth of the ROI. This confirms what was expected from the analysis of concentration PDFs regarding renewal, and show that it is also the case for injection. Turbulent mass fluxes are quite intense in the bulk, reach a minimum at z$\simeq$ 1.5 mm before further increasing. We are here at the onset of polymer action, at low concentration for which hydrodynamic effects of polymer is still moderate. For example, no peak of the profiles of orizontal rms velocities are observed at 10 ppm, they only appear at 25 ppm. Yet the statistics of mass transfer are quite different from the water case and reflect the complex hydrodynamics occurring inside the viscous sub-layer.

4.6.6 Conclusions

4.6.6.a Mass transfer in water

In water, we confirmed that turbulent mass transfer is a combination of injection and renewal events. All four types of events relevant to vertical turbulent mass transfer as defined by the quadrant decomposition have non negligible probability of occurrence at all depths. At small depths, negative concentration fluctuation events have moderate c' amplitude but high probability, while positive concentration fluctuation occur at a larger range of c' but with lower probability. With increasing depths, the probability of Q2 and Q3 decreases and

that of Q1 and Q4 increases. In terms of conditionnal mass fluxes, Q4 is always stronger than Q1 and Q2 stronger than Q3 at all depths, confirming that both surface renewal and injection events contribute to mass transfer. Even though they are not the most probable, injection events Q4 are found to be the main contributors to the overall down-going turbulent mass flux.

4.6.6.b Mass transfer in DPS

The mechanisms of turbulent mass transfer in DPS presents some similarity with the water case:

- Turbulent events opposed to vertical mass transfer (Q1 and Q3) have non negligible probability of occurrence and mass fluxes, but events in favor of downward mass fluxes (Q2 and Q4) are always respectively stronger, and mass transfer is effectively enhanced.
- Vertical turbulent mass transfer is thus a combination of surface renewal and injection events.
- The probability of renewal events is higher, but injection events are associated to stronger concentration fluctuations, at all depths.
- Injection events are also the main contributors to turbulent mass transfer.

However, several differences can be observed:

- The relative share of renewal mass flux versus injection mass flux is increased in DPS compared to water.
- While the probability of renewal events decreases with depth in water, it increases in DPS. On the other hand, the probability of injection events decreases with depth in DPS while it increases in water.
- The strength of renewal and injection mass fluxes reaches a minimum at a depth between 1 mm and 2 mm under the surface while it constantly increases with decreasing depth in water. High turbulent mass fluxes are observed at depths $z>\delta_\nu$ in DPS whereas they are concentrated inside the $z<\delta_\nu$ region in water.

To summarize, the physical mechanisms behind turbulent mass transfer are similar in water and DPS: mass transfer is enhanced by a combination of surface renewal and injection events. The first ones are the most probable but only weakly contributing to mass transfer, while the second ones are less probable but associated to higher concentration fluctuations and thus the major contributors to vertical turbulent mass transfer. The major difference between water and DPS, besides the increased importance of renewal, lays in the distribution of mass transfer events along depth. In water, most of the mass transfer events are concentrated inside the hydrodynamic viscous sub-layer, whereas in DPS, strong turbulent mass fluxes are observed at depth higher than δ_ν, and a minimum value is found inside the viscous sub-layer. It is worth reminding that this phenomenon is observed at a very low polymer concentration, with a viscous sub-layer depth is close to that of water, and for which no fundamental change in the viscous sub-layer is observed (no rms peak yet). The next interesting step would be to perform a similar analysis for a 25 ppm DPS run and see if the same mechanisms are observed, or if they are increased or altered by the presence of the horizontal velocity rms peak.

4.7 Global mass transfer

4.7.1 Temporal evolution of bottom tank concentration

Global mass transfer in the tank is measured by monitoring the pH at its bottom pH_{bt} with a pH probe. Using the same $[CO_2] = f(pH)$ calibration curve than for PLIF measurements, pH_{bt} can be turned into the bottom gas concentration C_{bt}. Both quantities are plotted for the WD and XG10A runs in figure 4.43 a) and b). The evolution of C_s and C_b in the ROI is also shown for the XG10A run, but not for water since the estimated values are debatable [6].
Figure 4.43 c) shows the temporal evolution of concentration in a semi log plot for the two considered runs. The slope of the XG10A curve is steeper than that of the WD run, indicating a faster mass transfer in the 10 ppm solution. This result is consistent with the previous observations on time series, concentration profiles, and scalar boundary layer depth.

4.7.2 Mass transfer velocity

The expression relating the evolution of C_{bt} to mass transfer velocity is

$$\frac{C_{bt} - C_{bt,0}}{C_{sat} - C_{bt,0}} = (1 - e^{-\frac{K_L}{H}t}) \tag{4.26}$$

with $C_{bt,0}$ the initial bulk concentration equal to 0, C_{sat} the saturation concentration fixed by Henry's law and H=46 cm the distance between the interface and the probe. This equation can also be written

$$\ln\left(1 - \frac{C_{bt}}{C_{sat}}\right) = -\frac{K_L}{H}t \tag{4.27}$$

so K_L is equal to -H times the slope of the curve $\ln\left(1 - \frac{C_{bt}}{C_{sat}}\right)$=f(t).

Global mass transfer velocity has been measured for all runs of the 2017 series listed in table 4.4. Two additional runs are also included, WE (water) and XG100B (100 ppm DPS), performed in the same conditions that runs WD and XG100A respectively, but for which velocity and scalar fields are not available. All measured K_L are shown in figure 4.44. The data shows considerable uncertainty between K_L values at 10 and 50 ppm. The uncertainty is smaller for other concentrations but still non negligible bearing in mind that the K_L axis is displayed here in log scale. Measured K_L increase upon polymer addition at low concentration, and decrease when concentration further increases above 25 ppm.

This would indicate that the modification of mass transfer mechanisms upon polymer addition tend to enhance mass transfer efficiency, when considering only turbulence action and not the interface shape.

Nevertheless, before any links can be made between mass transfer velocities and turbulence in DPS, several points have to be carefully considered. The accuracy of bulk pH measurement is questionable. It is worth noting that even minor uncertainties on the pH may lead to important error on concentration values. Any source of chemical pollution near the bottom of the tank (dirt, residual particles) is a source of error on concentration measurement. The quite large discrepancy of measured K_L still needs to be explained. The other factors playing a part in mass transfer at the interface should be studied carefully. For example, important side effects have been observed during the dissolution experiments into

[6] It is by the way worth noting that the concentration measured at the bottom of the tank reach values up to 2.5 mg/L, higher than the final value of C_b obtained by fitting, which is 0.35 mg/L. Since the ROI is closer to the interface than the bottom probe, one should always have $C_b \geq C_{bt}$. C_b is thus most likely underestimated

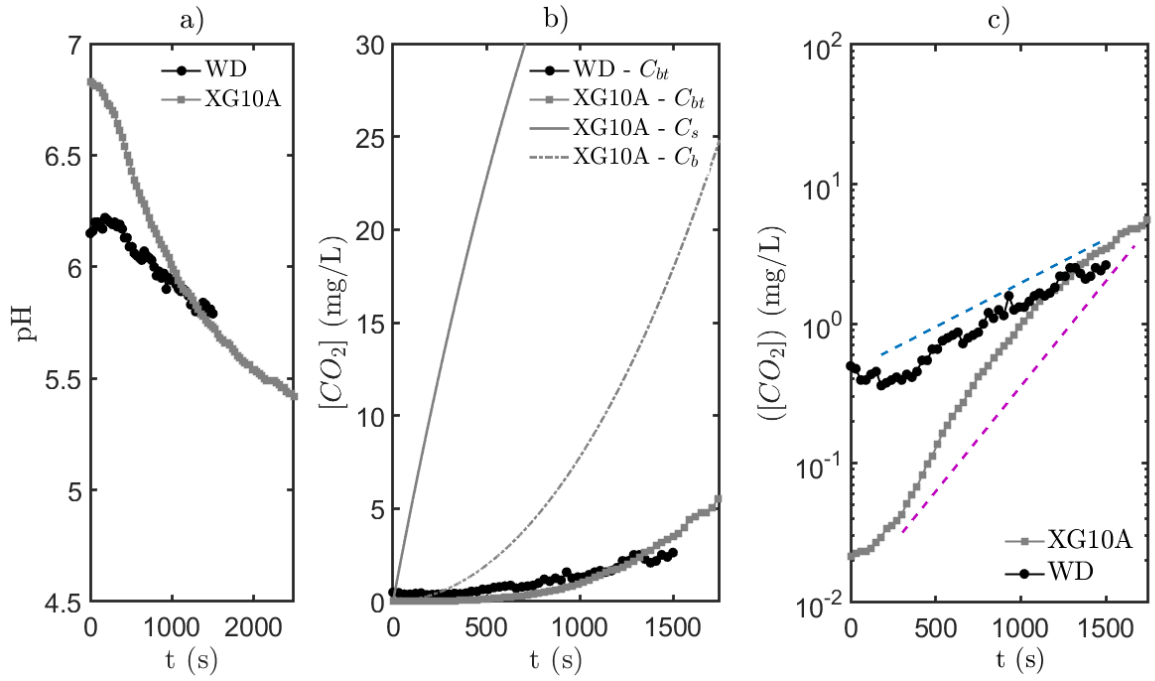

Figure 4.43 – Global mass transfer for the WD and XG10A runs. a) pH temporal evolution. b) Evolution of C_{bt} compared to C_s and C_b. c) Semi log plot of C_{bt} with time. The blue and purple dashed curves are the slopes for the WD and XG10A respectively.

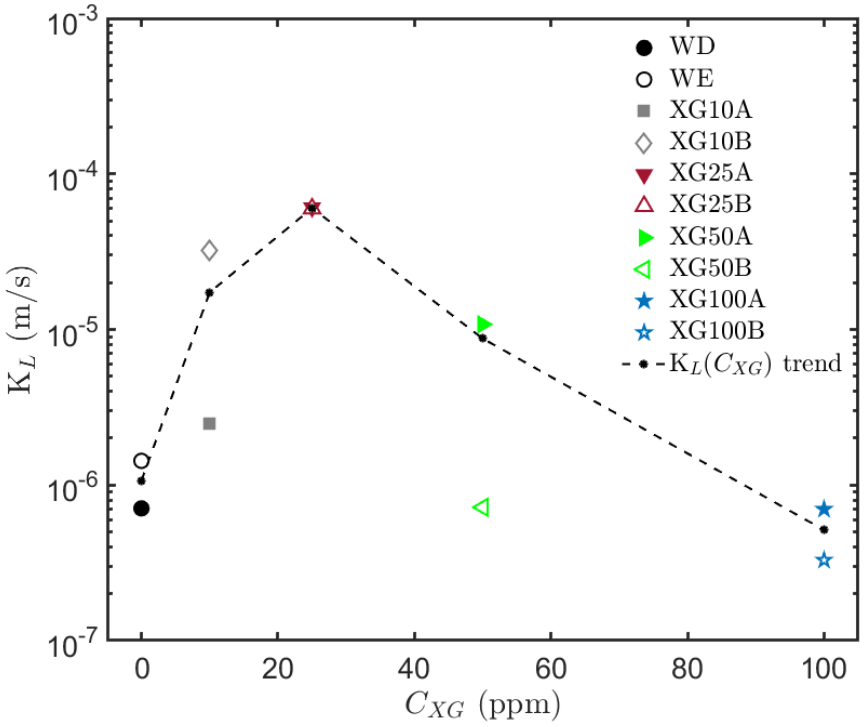

Figure 4.44 – Global mass transfer velocities K_L estimated from bottom tank pH measurements

DPS, with for example persistent plunging concentration filaments near the walls of the tank. These very likely impact the K_L value without being turbulence.

The present estimation of K_L values are thus greatly limited by the mixing state at the bottom of the tank where the probe is located. The mixing there is probably far from being fully

achieved, due to the strong mean velocity structures and these side effects. A more rigorous method would have been to use several probes located at different position of the bottom panel in order to estimate accurately C_{bt} and the mixing state at the bottom. Hence, the results shown in figure 4.44 should only be considered as first order qualitative observations.

Once these issues have been carried out, analysis of coupled velocity and concentration data available for all the runs should allow to establish correlations between mass transfer velocities and relevant mass flux statistics, themselves related to fluid properties, and ultimately construct mass transfer models valid for shear-thinning viscoelastic solutions.

4.8 Concluding remarks

In this concluding section,we will summarize the results presented through the present chapter, and use them to address several key questions regarding turbulent mass transfer at flat free surfaces and the effect that polymer addition may have on it. These are still open questions, and the present concluding remarks should only be seen for what they are: clues left by new but partial investigations.

4.8.1 Conclusion and discussion

In section 4.4, the properties of near-surface turbulence in water and DPS at various concentrations were addressed. Mean flows were found to be non negligible for water and all DPS concentrations. While mean flow for water are hardly repeatable, DPS runs show better rerpoducibility, probably because of the strong recirculating structures produced by the grid's oscillations. The properties of turbulence in water were detailed. The presence of the interface causes turbulent velocity structures to deform, to stretch along horizontal dimensions, and to transfer their energy from the vertical to horizontal velocity components. This mechanism is dominant in the surface influenced layer. At smaller depths, distinction could be made between runs evidencing signs of interfacial pollution and runs for which the interface may be considered clean. No rms peak of horizontal velocity fluctuations is observed in the last case while it is in the first. In both cases, the vertical gradient of horizontal rms profiles allows to define a viscous sub-layer inside of which the evolution of flow properties are different than inside the surface influenced layer. Several interesting behavior were evidenced, such as the existence of a vertical viscous sub-layer, surface oscillations, and different properties of near surface turbulent structures depending on whether they are moving upwards or downwards.

First observations of the effect of polymer on near surface hydrodynamics could be made. Energy redistribution is still evidenced, even if the effect of polymer addition on turbulence in the source layer remain unclear. It yet seems that the horizontal stretching of turbulent structures is enhanced in DPS. At concentrations higher or equal to 25 ppm, rms peaks are systematically observed in DPS runs. It is safe to assume that these peaks are not due to surface pollution, but caused by the polymer itself. In that we infer that even if XG is not in itself surface active, its action on viscous sub-layer hydrodynamics seems in some way similar to the effect of surfactant, in that shear dependent viscosity allows tangential shear stresses to establish at the interface. The depth of the viscous sub-layer was also found to increase with increasing polymer concentration, but much slowly than what can be expected from viscosity estimations. Damping mechanisms in the viscous sub-layer are apparently quite different in water and in DPS, thus stressing the fact that DPS are much more complex than viscous fluids.

In the next section, focus was made on the comparison of dissolved gas concentration structures in clean water situation and 10 ppm DPS. Scalar patches are found at higher concentration in DPS than in water but this is most certainly an effect of the use of single color PLIF for the water run. Yet concentration increase in the first case is quicker than in the second, after a first stagnation step. In both cases, scalar fields in the sub-surface ROI consist in a complex combination of scalar structures of various sizes and shapes. Concentration length and time scale show that scalar patches are larger and more vertically elongated in DPS than in water, and that their residence time close to the interface is higher for DPS. Renewal events are in both fluids the most probable. With water, this probability decreased with increasing depth while in DPS, persistence of concentration renewal along depth was observed. These observations were the first evidence of fundamental differences in mass transfer mechanisms for water and DPS.

A conditional analysis detailed in section 4.6 allowed to extract several probabilities and strength of turbulent mass transfer events, and discuss the relative impact of renewal and injection on vertical but also horizontal mass fluxes. In both fluids, injections events are less probable but stronger than renewal events, and the main contributors to mass transfer. The fundamental difference found between water and DPS lays in the evolution of event statistics and turbulent mass fluxes with depth. In water, the probability of renewal events increases when approaching the interface and the probability of injection events-increase with increasing depth, while it is the opposite in DPS. Renewal and injection mass fluxes are concentrated in the first millimeters under the interface for water, but distributed over depth in DPS.

Finally, the estimation of mass transfer velocities at all polymer concentrations confirmed that for the two compared runs, mass transfer was faster in 10 ppm DPS than in water. Mass transfer velocity even seems to increase with polymer concentration up to 25 ppm, and to decrease for increasing polymer concentrations between 25 and 100 ppm.

One point that sticks out of hydrodynamic studies is the similarities of behaviors between dilute polymer solutions and what are believed to be surface polluted interfaces for water. In particular, rms peaks of horizontal velocity fluctuations are observed in water polluted cases and for DPS at concentrations higher or equal to 25 ppm. The polymer used here is however not a surfactant, and so fundamental differences exist between water polluted runs and DPS. In particular, surfactant are generally found to reduce mass transfer velocity (McKenna and McGillis, 2004a), while polymer is here found to increase mass transfer at least at low concentrations. For example, the 25 ppm run does exhibit an rms peak with a higher K_L value than water.

As regards to the effects of polymer concentration, we are here only able to discuss them in terms of hydrodynamics and global mass transfer in the [0 100] ppm range. The hydrodynamic evolution is monotonous in this range, while ite seems to exist a critical 25 ppm concentration for mass transfer. This critical concentration is lower than 50 ppm, the lower hydrodynamic critical concentrations found in chapter 3, and close to the onset of Drag reduction observed by Wyatt et al. (2011).

4.8.2 Perspectives

The next analyses to perform are concentration and turbulent mass flux analysis of 25 to 100 ppm runs. It is worth mentioning than since mass transfer velocities are much higher for 25 ppm and 50 ppm runs than for water, concentration rapidly increased in the tank during the corresponding experiments, and PLIF measurements may be limited in terms of number of instantaneous fields with sufficient dynamics. With the 10 ppm runs and the results of

these other treatments, it would become possible to explore the causes of the increased mass transfer and compare turbulent mass fluxes to near surface hydrodynamics.

Further work can also be done with two point statistics in both water and DPS. We have here only briefly estimated integral length scales of velocity and scalar structures, and integral scalar time scales. Integral length scales of turbulent mass fluxes evaluated as in Variano and Cowen (2013) would bring additional information about the size of structures of each mass transfer events. Fourier transform of velocity, scalar, and turbulent mass fluxes mappings and representation of turbulent kinetic energy, scalar co-variance, and mass fluxes spectra could then be used to establish a scale-by-scale mass transfer budget and determine at which scales each type of event is the most efficient.

Finally, another analysis that would be of great interest in terms of mass transfer modeling is the estimation of surface divergence statistics in water and DPS. As previously mentioned, our measurement techniques offer the possibility of estimating coupled statistics for surface divergence and vertical mass fluxes. We could then evidence the correlation between vertical turbulent mass fluxes and surface divergence, and confirm or improve surface divergence models.

General conclusions

> Science never solves a problem without creating ten more.
>
> George Bernard Shaw

Summary

Development of the PLIF technique

In the experimental section of this thesis, an improvement of inhibited PLIF techniques, was introduced. It allows to efficiently account for many noise and uncertainty sources inherent to classical single color PLIF methods, while using a single fluorescent dye, thus simplifying the experimental design, and reducing its cost and chemical intrusiveness. Here, fluorescein sodium is chosen as the fluorescent dye, because of its high sensitivity to pH variations between pH 5 and pH 7. This pH range corresponds well to the acidity variations induced by CO_2 dissolution into aqueous media, which makes the developed technique suitable for the measurement of dissolved CO_2 concentration in water. Measurement in dilute XG solutions is also possible providing that the amount of XG added to the solution has no impact on chemical equilibria and fluorescence. The theoretical bases of the method are detailed and supported by an extensive spectrofluorimetric analysis of the dye. The method has then been tested on monophasic test case: a turbulent jet of acidic solution mixing into water. This test case confirms the efficiency of the novel I^r_{pH} – PLIF method. Apart from its quickness in data treatment compared to advanced single color PLIF method, two main advantages can be emphasized: its ability to account for time varying excitation intensities, and the fact that it can be used on any ROI of the fluid without the need of knowing the full laser path across the working fluid. Some limitations are still to be mentioned. Spectral conflicts of type III can not be avoided, which limits the applicability of the technique to optically thin systems, *i.e.* low dye concentration and/or short optical paths. Longer camera exposure time than those required for single color PLIF methods are also needed, in order to record both fluorescence colors with a sufficient signal over noise ratio and achieve low uncertainty levels.

Oscillating grid turbulence in shear thinning polymer solutions

The third chapter aimed at describing and characterizing turbulence in the OGT setup, in particular for DPS for which it had never been studied in the literature.

Even though OGT was initially designed to study turbulence alone in absence of mean flow, the installation of persistent flow structures can not be avoided, and the mean velocities are not negligible. This is especially the case in DPS for which the development of mean flow structures is enhanced: two main counter-rotative recirculating vortices are observed on the side of the ROI, above the grid, associated to a global up-going motion at the center of the tank. This is supposedly caused by the interactions between the flow induced by the grid and the walls of the tank. The interactions between jets and wakes, defined as the origin of turbulence in the tank, has been observed experimentally for the first time. It was shown that the periodic component of the flow, corresponding actually to these jets and wakes, was only significant in the grid sweep region. The oscillatory nature of the mean flow and its generation of large scale structures of turbulence is quite complex. In DPS, the energy exchanges between mean, organized, and turbulent components of the flow are enhanced, and turbulence seems able to give back energy to the oscillatory motion. Turbulence also has its main intensity within the grid sweep region, and is advected away by both mean and oscillatory motion.

Above the grid, its intensity decays according to the well known relationship of Hopfinger and Toly (1976) for both water and DPS. However, the decay rate is modified by polymer addition, and turbulence is found to be less isotropic in DPS, with a vertical component further increased compared to the horizontal one. The integral length scale of turbulence linearly increase with the altitude as predicted by Thompson and Turner (1975),and the increasing rate is greater in DPS than in water.

In terms of critical concentration the results show that three main hydrodynamic regimes for OGT in DPS could be defined. Between 0 and around 50 ppm, polymer addition leads to an organization of the flow and a shift of energy towards large structures. This is characterized by a strong mean flow enhancement, a slight increase in integral length scales and anisotropy, with only a slight weakening of turbulence. Between 50 ppm and around 100 or 150 ppm, the structure of the flow reaches a stagnation state, while attenuation of turbulence keeps increasing. Above 150 ppm, the flow structures eventually collapse and both turbulence and mean flow are reduced. These concentrations can be compared to the 100 ppm critical concentration marking the onset of the semi-dilute entanglement regime.

Turbulent mass transfer at a gas-liquid interface

In the fourth chapter, turbulence near the gas-liquid interface and the role it plays in mass transfer was finally described. First, the effects ot the free surface on the upcoming turbulence have been detailed. The horizontal stretching and energy transfer from vertical to horizontal motion in the surface influenced layer is evidenced for both water and DPS at different concentrations. Horizontal stretching of turbulent structures even seems enhanced in DPS. At concentrations equal to 25 ppm or higher, a peak of horizontal velocity fluctuations rms is always observed, indicating that polymer may have an effect on near surface turbulence similar to that of a surfactant, without being surface active itself. The depth of the viscous sub-layer increases with increasing polymer concentration, but not at the rate that would be expected from viscosity considerations. The increase rather seems to be correlated with the Deborah number representative of the shear-thinning property. The conditional analysis of up and down going turbulent structures evidences the fact that turbulence "bounces" on the interface in a different manner in DPS than in water.

As for dissolved gas concentration and mass transfer events, the analysis could only be carried out for a single 10 ppm DPS concentration experiment in the available time for this thesis. Scalar patches are found at higher concentration in DPS than in water, and the con-

centration increase rate is faster in DPS than in water, corresponding to a higher mass transfer velocity. In both fluids, scalar fields in the sub-surface ROI are a complex combination of injection and renewal events. The measurement of concentration length and time scales show that scalar patches are larger and more vertically elongated in DPS. Renewal events are the most probable in both fluids, but injection events are stronger in terms of vertical mass fluxes. In water, most mass transfer events are located within the first few millimeters under the interface while significant turbulent mass transfer occurs at higher depths for DPS.

Future work and prospects

Improvements of PLIF metrology

The novel I^r_H – PLIF method offers many perspectives of applications. It is currently used for the measurement of CO_2 dissolution around dissolving CO_2 bubbles in water and DPS. In these experiments, our new method allow to efficiently account for laser reflections on gas bubble, which are time dependent because of the bubble's reducing volume. The technique could also be applied to freely rising bubbles or bubble swarms as in Kong et al. (2018); Kováts et al. (2017).

The need of longer camera exposure times can be limited by using more powerful laser sources, taking care of staying in the linear excitation regime for fluorescence. For fluorescein sodium, it appears that a second excitation wavelength could be used to improve fluoresced light intensity at low pHs. Increasing fluorescent dye concentration in order to increase fluorescence signal is not such a good way of improving the quality of measurements. Indeed, the main lock inhibited PLIF techniques are still confronted to its fluoresced light re-absorption and the optically thin systems limitation it implies, and re-absorption increases with dye's concentration. Methods for the correction of fluoresced light re-absorption have been proposed in the past for temperature measurements (Lavieille et al., 2004), and could be an interesting base to work on.

Innovative and efficient PLIF and inhibited PLIF methods for mass transfer measurements in challenging multiphase situations are currently being developed and improved (Kong et al., 2018; Kováts et al., 2017; Rüttinger et al., 2018). The one proposed here, among others, is an interesting tool to develop and use for a better understanding of local multiphase mass transfer phenomenon. The methodology applied for the development of our method can be generalized to any couple of dye and inhibitor.

Oscillating grid turbulence in polymer solutions

The results of chapter 3 show that shear thinning has a strong impact on OGT hydrodynamics both close and far away from the grid and at various scales of the flow. The analysis of available PIV measurement in other vertical planes of the tank will ultimately lead to a better understanding of the mean flow structure and turbulence distribution in three dimensions in the tank. 3D3C data are necessary to estimate the full energy budget of turbulence in the kinetic energy equation and describe accurately the generation and evolution of turbulence in the tank. Such data could be obtained either by making symmetry hypothesis in order to use available 2D2C data, or by performing innovative volumetric measurements, as suggested in the last section of this conclusion. As discussed in appendix C, POD could be an interesting tool for the study of scale by scale behavior and of polymer influence on the flow.

Near surface turbulence and mass transfer in polymer solutions

The next analysis to be performed is the interpretation of concentration and turbulent mass fluxes measurements for 25 ppm, 50 ppm and 100 ppm concentrations. All the comparisons between water and DPS presented before are only based on two runs and a low concentration DPS case. Additional concentrations, and repetition of measurements are still necessary in order to fully describe the effect of DPS on turbulence and mass transfer at the interface. Two limitations yet arise from our measurements. First is the fact that with increasing polymer concentration, one increases the mean flow over turbulence ratio and thus reduces the relevance of our measurements. Second, the apparent increase in mass transfer velocity for 25 ppm and 50 ppm makes it more difficult to collect a sufficient amount of exploitable and statistically stationary concentration data. This last increase in mass transfer velocity at very low XG concentrations is quite surprising and yet potentially interesting. If such a behavior is confirmed, it would mean that polymer addition initially tends to enhance turbulent mass transfer. This enhancement is counter-balanced by a reduction of mass transfer caused by the decrease of turbulent intensity. Yet as it appears, there could exist a very dilute concentration range for which shear thinning enhancement is stronger than viscous reduction.

Thus staying at low polymer concentrations, an interesting next step would be to investigate the available measurement by two point statistics. This would allow to explore the turbulent velocity, concentration, and mass fluxes spectra. In doing so, one could establish a scale by scale budget for mass transfer and determine which velocity scales mostly act on which type of mass transfer events. To that end, POD could also be a useful tool for the analysis of concentration structures.

Towards volumetric measurements

The next step to improve the understanding of interfacial mass transfer phenomena is to get access to time resolved three dimensional data for velocity and concentration under the interface with even better resolutions than here. Until the last few years, numerical simulations have been limited by the high Schmidt numbers characteristic of atmospheric gases dissolved in liquids. Indeed, the accurate simulation of passive scalar transport require the spatial resolution of the small scalar scales of the flow, which are as small as the Schmidt number is high. In 3D solvers, the computational cost increases as Sc^3 making numerical simulation even more expensive in terms of computational power. Only recent works done by Herlina and Wissink (2014, 2016); Wissink and Herlina (2016) use realistic Sc numbers for CO_2, with Sc$\simeq$500.

This latest simulations are encouraging for the study of interfacial mass transfer phenomena, but experimental validations are still missing. Performing accurate time resolved volumetric measurements through optical techniques is a key challenge in nowadays research.

PLIF measurements are intrinsically planar. Volumetric measurements or passive scalar concentration are made possible by scanning PLIF techniques, which consist in scanning the laser plane through the volume of measurement (Partridge et al., 2018; Prasad and Sreenivasan, 1990). However this method requires the scanning rate to be faster than the fastest scalar structures of the flow, which makes its application to turbulent mixing situations technically challenging.

3D3C velocity measurements are on the other hand now made possible by methods such as 3D PIV techniques also called Tomo-PIV, or by 3D PTV. The first one is an extension of SPIV where more than two cameras are used, and where the volume of fluid is illuminated by a laser beam, that is no longer shaped into a plane. The volume of measurement is recon-

structed from 2D particle images by tomographic reconstruction algorithms, and velocity vectors are computed by cross correlation of all particle images in a Cartesian grid of voxels. This method is actually the 3D3C counterpart to classical PIV. It is however quite time consuming, both in the camera calibration step and in the data treatment process (Schanz et al., 2016).

The second method aforementioned, namely 3D Particle Tracking Velocimetry, is fundamentally different from Tomo-PIV in the way that it tracks individual particles in their trajectory through the volume of fluid instead of using image correlation in voxels. 3D PTV is thus intrinsically time resolved: time resolution is needed in order to be able to track down particles. The data extracted from particle tracking is Lagrangian: velocity can only be measured where the particles are found. Interpolation of Lagrangian PTV measurement on an Eulerian grid require the recording of a very large number of particle trajectories. Spatial resolution of PTV is thus defined in a very different way than for PIV where it is fixed by the size of the interrogation window. Here it is fixed by the total amount of particles tracked at any instant in the volume of measurement. 3D PTV algorithms have historically been limited in terms of spatial resolution by their ability to efficiently track many particles simultaneously (Schanz et al., 2016; Wieneke, 2013).

A recent algorithm developed by Schanz et al. (2016), called the "Shake The Box" algorithm, allows to track particles at quite high particle density. This algorithm was tested in the oscillating grid setup used for this thesis, in water and DPS, with a volume of interest including both the bulk region of the tank (above the grid, FT region defined in chapter 3) and the free surface. The shake the box algorithm was operated by the DaVis 10 software, using images recorded with LaVision MiniShaker L set of cameras. As this thesis is being written, data are still being processed, but a first glimpse of the measurement (figure 4.45) is quite encouraging.

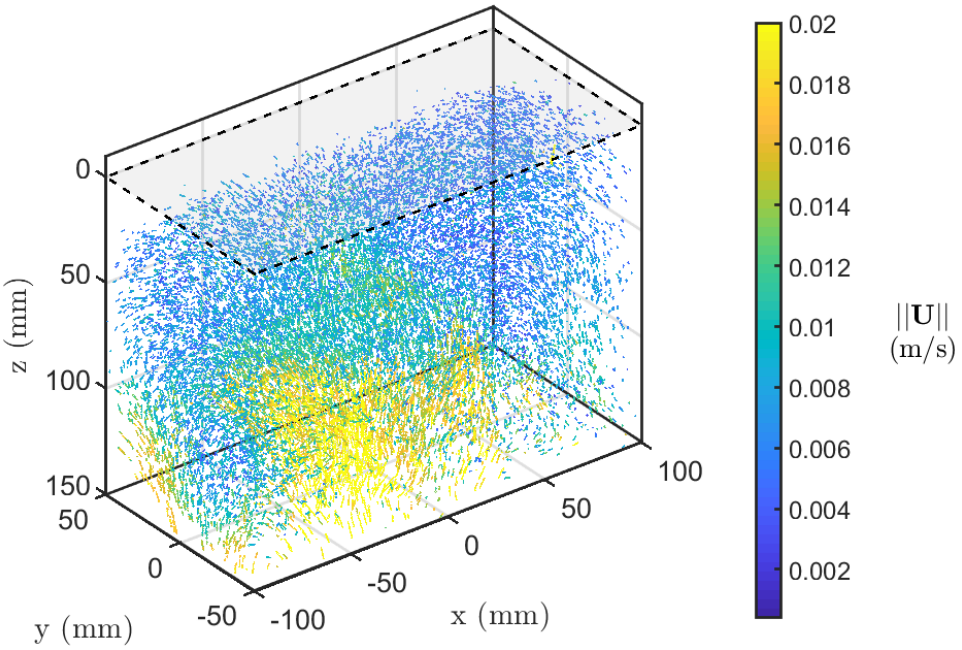

Figure 4.45 – An insight on 3D3C measurements in 25 ppm DPS using LaVision MiniShaker cameras and the "Shake The Box" algorithm. About 5000 particles are tracked at all time in the volume of measurement. Here are shown the trajectories of particles over 11 consecutive snapshots (0.25 s) colored by the norm of their instantaneous velocity, in the surface reference frame. The interface location is indicated by the gray horizontal plane with dashed contour.

Bibliography

Abdullah B. and Adesina A. A. Evaluation of gas–liquid mass transfer in gas-induced stirred tank reactor using electrical resistance tomography. *Journal of Chemical Technology & Biotechnology*, 92(8):2123–2133, Aug. 2017. 12

Adams L. W. and Barigou M. CFD Analysis of Caverns and Pseudo-Caverns Developed During Mixing of Non-Newtonian Fluids. *Chemical Engineering Research and Design*, 85(5): 598–604, 2007. 92

Adrian R. J. Twenty years of particle image velocimetry. *Experiments in Fluids*, 39(2):159–169, Aug. 2005. 36

Al Mansoori S. K., Itsekiri E., Iglauer S., Pentland C. H., Bijeljic B. and Blunt M. J. Measurements of non-wetting phase trapping applied to carbon dioxide storage. *International Journal of Greenhouse Gas Control*, 4(2):283–288, Mar. 2010. 45

Alméras E., Risso F., Roig V., Cazin S., Plais C. and Augier F. Mixing by bubble-induced turbulence. *Journal of Fluid Mechanics*, 776:458–474, Aug. 2015. 12, 150

Alméras E., Plais C., Euzenat F., Risso F., Roig V. and Augier F. Scalar mixing in bubbly flows: Experimental investigation and diffusivity modelling. *Chemical Engineering Science*, 140: 114–122, Feb. 2016. 12

Ansari M., Turney D. E., Yakobov R., Kalaga D. V., Kleinbart S., Banerjee S. and Joshi J. B. Chemical hydrodynamics of a downward microbubble flow for intensification of gas-fed bioreactors. *AIChE Journal*, 64(4):1399–1411, Apr. 2018. 12

Arjunwadkar S. J., Sarvanan K., Kulkarni P. R. and Pandit A. B. Gas-liquid mass transfer in dual impeller bioreactor. *Biochemical Engineering Journal*, 1(2):99–106, Mar. 1998. 161, 162

Arratia P. E., Kukura J., Lacombe J. and Muzzio F. J. Mixing of shear-thinning fluids with yield stress in stirred tanks. *AIChE Journal*, 52(7):2310–2322, July 2006. 92, 161

Asher W. E. and Litchendorf T. M. Visualizing near-surface concentration fluctuations using laser-induced fluorescence. *Experiments in Fluids*, 46(2):243–253, Aug. 2008. 51, 52, 53

Asher W. E. and Pankow J. F. The interaction of mechanically generated turbulence and interfacial films with a liquid phase controlled gas/liquid transport process. *Tellus B*, 38B(5): 305–318, Nov. 1986. 85, 106, 163, 178

Asher W. E., Liang H., Zappa C. J., Loewen M. R., Mukto M. A., Litchendorf T. M. and Jessup A. T. Statistics of surface divergence and their relation to air-water gas transfer velocity. *Journal of Geophysical Research: Oceans*, 117(C5):C05035, May 2012. 158, 159, 290, 291

Banerjee S. The Air-Water Interface: Turbulence and Scalar Exchange. In Garbe P.-D. D. C. S., Handler D. R. A. and Jähne P. D. B., editors, *Transport at the Air-Sea Interface*, Environmental Science and Engineering, pages 87–101. Springer Berlin Heidelberg, 2007. 12, 158

Banerjee S., Scott D. S. and Rhodes E. Mass Transfer to Falling Wavy Liquid Films in Turbulent Flow. *Industrial & Engineering Chemistry Fundamentals*, 7(1):22–27, Feb. 1968. 157

Banerjee S., Lakehal D. and Fulgosi M. Surface divergence models for scalar exchange between turbulent streams. *International Journal of Multiphase Flow*, 30(7–8):963–977, July 2004. 158

Barnard B. and Sellin R. Grid turbulence in dilute polymer solutions. *Nature*, (222):1160–1162, 1969. 88, 93, 161

Barnes H. A. The yield stress—a review or 'παντα ρει'—everything flows? *Journal of Non-Newtonian Fluid Mechanics*, 81(1–2):133–178, Feb. 1999. 28

Barrut B., Blancheton J.-P., Champagne J.-Y. and Grasmick A. Mass transfer efficiency of a vacuum airlift—Application to water recycling in aquaculture systems. *Aquacultural Engineering*, 46:18–26, Jan. 2012. 11, 12

Barrut B., Blancheton J.-P., Muller-Feuga A., René F., Narváez C., Champagne J.-Y. and Grasmick A. Separation efficiency of a vacuum gas lift for microalgae harvesting. *Bioresource Technology*, 128:235–240, Jan. 2013. 12, 149

Baskurt O. K. and Meiselman H. J. Blood Rhéology and Hemodynamics. *Seminars in thrombosis and hemostasis*, 29(5), Nov. 2003. 26

Bassnett S., Reinisch L. and Beebe D. C. Intracellular pH measurement using single excitation-dual emission fluorescence ratios. *American Journal of Physiology - Cell Physiology*, 258(1):C171–C178, Jan. 1990. 56

Bewersdorff H.-W. and Singh R. P. Rheological and drag reduction characteristics of xanthan gum solutions. *Rheologica Acta*, 27(6):617–627, Nov. 1988. 96, 98, 99

Bodart J., Cazalbou J.-B. and Joly L. Direct numerical simulation of unsheared turbulence diffusing towards a free-slip or no-slip surface. *Journal of Turbulence*, 11:N48, Jan. 2010. 150, 151, 163

Bouaifi M., Hebrard G., Bastoul D. and Roustan M. A comparative study of gas hold-up, bubble size, interfacial area and mass transfer coefficients in stirred gas–liquid reactors and bubble columns. *Chemical Engineering and Processing: Process Intensification*, 40(2):97–111, Feb. 2001. 162

Bouche E., Cazin S., Roig V. and Risso F. Mixing in a swarm of bubbles rising in a confined cell measured by mean of PLIF with two different dyes. *Experiments in Fluids*, 54(6):1552, June 2013. 12, 56, 150

Bouvard M. and Dumas H. Application de la méthode de fil chaud à la mesure de la turbulence dans l'eau. *La Houille Blanche*, (3):257–270, Apr. 1967. 84, 106

Brocchini M. and Peregrine D. H. The dynamics of strong turbulence at free surfaces. Part 1. Description. *Journal of Fluid Mechanics*, 449:225–254, Dec. 2001a. 153, 166, 167

Brocchini M. and Peregrine D. H. The dynamics of strong turbulence at free surfaces. Part 2. Free-surface boundary conditions. *Journal of Fluid Mechanics*, 449:255–290, Dec. 2001b. 153

Bruchhausen M., Guillard F. and Lemoine F. Instantaneous measurement of two-dimensional temperature distributions by means of two-color planar laser induced fluorescence (PLIF). *Experiments in Fluids*, 38(1):123–131, Jan. 2005. 54, 55, 65, 79

Brumley B. H. and Jirka G. H. Near-surface turbulence in a grid-stirred tank. *Journal of Fluid Mechanics*, 183:235–263, Oct. 1987. xv, 2, 85, 86, 140, 150, 151, 152, 153, 155, 156, 158, 163, 177, 184, 189, 191, 193

Brust M., Schaefer C., Doerr R., Pan L., Garcia M., Arratia P. E. and Wagner C. Rheology of Human Blood Plasma: Viscoelastic Versus Newtonian Behavior. *Physical Review Letters*, 110(7):078305, Feb. 2013. 26

Buckler K. J. and Vaughan-Jones R. D. Application of a new pH-sensitive fluoroprobe (carboxy-SNARF-1) for intracellular pH measurement in small, isolated cells. *Pflügers Archiv*, 417(2):234–239, Oct. 1990. 56

Burghelea T., Segre E., Bar-Joseph I., Groisman A. and Steinberg V. Chaotic flow and efficient mixing in a microchannel with a polymer solution. *Physical Review E*, 69(6):066305, June 2004. 21

Butler C., Cid E. and Billet A.-M. Modelling of mass transfer in Taylor flow: Investigation with the PLIF-I technique. *Chemical Engineering Research and Design*, 0(0), Sept. 2016. 12, 150

Cabaret F., Fradette L. and Tanguy P. A. Gas–liquid mass transfer in unbaffled dual-impeller mixers. *Chemical Engineering Science*, 63(6):1636–1647, Mar. 2008. 27, 91, 92, 161, 162

Cai W.-H., Li F.-C., Zhang H.-N., Li X.-B., Yu B., Wei J.-J., Kawaguchi Y. and Hishida K. Study on the characteristics of turbulent drag-reducing channel flow by particle image velocimetry combining with proper orthogonal decomposition analysis. *Physics of Fluids*, 21(11): 115103, Nov. 2009. 90, 91, 144

Calderbank P. H., Johnson D. S. L. and Loudon J. Mechanics and mass transfer of single bubbles in free rise through some Newtonian and non-Newtonian liquids. *Chemical Engineering Science*, 25(2):235–256, Feb. 1970. 150, 162

Calmet I. and Magnaudet J. Statistical structure of high-Reynolds-number turbulence close to the free surface of an open-channel flow. *Journal of Fluid Mechanics*, 474:355–378, Jan. 2003. 150, 151, 163

Carvalho B. and Aleixo R. Quadrant method application to the study of the beginning of sediment motion of sedimentary particles. Porto, Portugal, Nov. 2014. 180

Chan W. C. and Scriven L. E. Absorption into Irrotational Stagnation Flow. A Case Study in Convective Diffusion Theory. *Industrial & Engineering Chemistry Fundamentals*, 9(1): 114–120, Feb. 1970. 157

Charonko J. J. and Vlachos P. P. Estimation of uncertainty bounds for individual particle image velocimetry measurements from cross-correlation peak ratio. *Measurement Science and Technology*, 24(6):065301, 2013. 44

Chaumat H., Billet-Duquenne A. M., Augier F., Mathieu C. and Delmas H. Mass transfer in bubble column for industrial conditions—effects of organic medium, gas and liquid flow rates and column design. *Chemical Engineering Science*, 60(22):5930–5936, Nov. 2005. 12

Chaze W., Caballina O., Castanet G. and Lemoine F. The saturation of the fluorescence and its consequences for laser-induced fluorescence thermometry in liquid flows. *Experiments in Fluids*, 57(4):58, Apr. 2016. 52, 54, 55, 65, 72, 79

Chaze W., Caballina O., Castanet G. and Lemoine F. Spatially and temporally resolved measurements of the temperature inside droplets impinging on a hot solid surface. *Experiments in Fluids*, 58(8):96, Aug. 2017. 52, 54, 55, 80

Chhabra R. P. Non-Newtonian Fluids: An Introduction. In *Rheology of Complex Fluids*, pages 3–34. Springer, New York, NY, 2010. 29, 87

Chhabra R. P. and Richardson J. F. *Non-Newtonian Flow in the Process Industries: Fundamentals and Engineering Applications*. Butterworth-Heinemann, 1999. 87

Chiapponi L., Longo S. and Tonelli M. Experimental study on oscillating grid turbulence and free surface fluctuation. *Experiments in Fluids*, 53(5):1515–1531, Sept. 2012. 2, 85, 106, 153, 167

Chu C. R. and Jirka G. H. Turbulent gas flux measurements below the air-water interface of a grid-stirred tank. *International Journal of Heat and Mass Transfer*, 35(8):1957–1968, Aug. 1992. 86, 158, 163

Chu F., Li S., Chen H., Yang L., Ola O., Maroto-Valer M., Du X. and Yang Y. Modeling photocatalytic conversion of carbon dioxide in bubbling twin reactor. *Energy Conversion and Management*, 149:514–525, Oct. 2017. 12, 45

Cocconi G., De Angelis E., Frohnapfel B., Baevsky M. and Liberzon A. Small scale dynamics

of a shearless turbulent/non-turbulent interface in dilute polymer solutions. *Physics of Fluids*, 29(7):075102, July 2017. 89, 90, 94, 149

Cohen Y. Mass transfer across a sheared, wavy air-water interface. *International Journal of Heat and Mass Transfer*, 26(9):1289–1297, Sept. 1983. ISSN 0017-9310. 291

Comte-Bellot G. and Corrsin S. The use of a contraction to improve the isotropy of grid-generated turbulence. *Journal of Fluid Mechanics*, 25(4):657–682, Aug. 1966. 83

Coolen M. C. J., Kieft R. N., Rindt C. C. M. and Steenhoven A. A. v. Application of 2-D LIF temperature measurements in water using a Nd : YAG laser. *Experiments in Fluids*, 27(5): 420–426, Oct. 1999. 52, 54, 55

Coppeta J. and Rogers C. Dual emission laser induced fluorescence for direct planar scalar behavior measurements. *Experiments in Fluids*, 25(1):1–15, 1998. 54, 55

Cosson T. Etude du transfert de masse gaz-liquide dans un écoulement stratifié. Rapport de stage - Master 2 MEGA spécialité mécanique des fluides, INSA de Lyon, 2014. 106, 266

Crawford A. M., Mordant N., Xu H. and Bodenschatz E. Fluid acceleration in the bulk of turbulent dilute polymer solutions. *New Journal of Physics*, 10(12):123015, 2008. 89, 90, 91

Crimaldi J. P. Planar laser induced fluorescence in aqueous flows. *Experiments in Fluids*, 44 (6):851–863, Apr. 2008. 52

Cuthbertson A. J. S., Samsami F. and Dong P. Model studies for flocculation of sand-clay mixtures. *Coastal Engineering*, 132:13–32, Feb. 2018. 2, 85

Cuvelier G. and Launay B. Concentration regimes in xanthan gum solutions deduced from flow and viscoelastic properties. *Carbohydrate Polymers*, 6(5):321–333, Jan. 1986. 98

Dahm W. J. A. and Dimotakis P. E. Measurements of entrainment and mixing in turbulent jets. *AIAA Journal*, 25(9):1216–1223, 1987. 72, 73

Dahm W. J. A., Southerland K. B. and Buch K. A. Four-Dimensional Laser Induced Fluorescence Measurements of Conserved Scalar Mixing in Turbulent Flows. In *Applications of Laser Techniques to Fluid Mechanics*, pages 3–18. Springer, Berlin, Heidelberg, 1991. 52

Danckwerts P. V. Significance of Liquid-Film Coefficients in Gas Absorption. *Industrial & Engineering Chemistry*, 43(6):1460–1467, June 1951. 155, 156, 157, 158, 159, 163

De Angelis E., Casciola C. M., L'vov V. S., Piva R. and Procaccia I. Drag reduction by polymers in turbulent channel flows: Energy redistribution between invariant empirical modes. *Physical Review E*, 67(5):056312, May 2003. 270, 272, 280

De Angelis E., Casciola C. M., Benzi R. and Piva R. Homogeneous isotropic turbulence in dilute polymers. *Journal of Fluid Mechanics*, 531:1–10, May 2005. 89, 90, 91, 142, 150, 163

de Lamotte A., Delafosse A., Calvo S., Delvigne F. and Toye D. Investigating the effects of hydrodynamics and mixing on mass transfer through the free-surface in stirred tank bioreactors. *Chemical Engineering Science*, 172:125–142, Nov. 2017. 12, 36, 149

de Lamotte A., Delafosse A., Calvo S. and Toye D. Analysis of PIV measurements using modal decomposition techniques, POD and DMD, to study flow structures and their dynamics within a stirred-tank reactor. *Chemical Engineering Science*, 178:348–366, Mar. 2018. 269, 270

Dickinson S., C and Long R. R. Laboratory study of the growth of a turbulent layer of fluid. *The Physics of Fluids*, 21(10):1698–1701, Oct. 1978. 106

Dietrich N. and Hebrard G. Visualisation of gas-liquid mass transfer around a rising bubble in a quiescent liquid using an oxygen sensitive dye. *Heat and Mass Transfer*, pages 1–9, Feb. 2018. 11

Doorn E. v., White C. M. and Sreenivasan K. R. The decay of grid turbulence in polymer and surfactant solutions. *Physics of Fluids (1994-present)*, 11(8):2387–2393, Aug. 1999. 87, 93, 144

Doughty M. J. Fluorescence characteristics of sodium fluorescein–rose bengal ophthalmic solution mixtures. *Contact Lens and Anterior Eye*, 37(5):358–362, Oct. 2014. 56

Duplat J., Grandemange M. and Poulain C. Convective mass transfer around a dissolving bubble. *Physical Review Fluids*, 2(11):114001, Nov. 2017. 74

Durbin P. A. Some Recent Developments in Turbulence Closure Modeling. *Annual Review of Fluid Mechanics*, 50(1):77–103, 2018. 16

Escudié R. and Liné A. Experimental analysis of hydrodynamics in a radially agitated tank. *AIChE Journal*, 49(3):585–603, Mar. 2003. 12, 19, 20, 111

Escudier M. P., Presti F. and Smith S. Drag reduction in the turbulent pipe flow of polymers. *Journal of Non-Newtonian Fluid Mechanics*, 81(3):197–213, Mar. 1999. 96

Escudier M. P., Gouldson I. W., Pereira A. S., Pinho F. T. and Poole R. J. On the reproducibility of the rheology of shear-thinning liquids. *Journal of Non-Newtonian Fluid Mechanics*, 97 (2):99–124, Feb. 2001. 97, 99

Fabula A. *An experimental study of grid turbulence in dilute high-polymer solutions*. PhD thesis, The Pennsylvania State University, University Park, PA, 1966. 88, 93

Falcone M., Bothe D. and Marschall H. 3d direct numerical simulations of reactive mass transfer from deformable single bubbles: An analysis of mass transfer coefficients and reaction selectivities. *Chemical Engineering Science*, 177:523–536, Feb. 2018. 150

Fenner A. and Stephan P. Two dye combinations suitable for two-color/two-dye laser-induced fluorescence thermography for ethanol. *Experiments in Fluids*, 58(6):65, June 2017. 54, 55, 80

Fenner A. J. C. *Two-Color/Two-Dye Planar Laser-Induced Fluorescence Thermography for Temperature Measurements at an Evaporating Meniscus*. Ph.D. Thesis, Technische Universität, Darmstadt, 2017. 55

Fick A. Ueber Diffusion. *Annalen der Physik*, 170(1):59–86, Jan. 1855. 7

Fleischer C., Becker S. and Eigenberger G. Detailed modeling of the chemisorption of CO2 into NaOH in a bubble column. *Chemical Engineering Science*, 51(10):1715–1724, May 1996. 12

Flores O., Riley J. J. and Horner-Devine A. R. On the dynamics of turbulence near a free surface. *Journal of Fluid Mechanics*, 821:248–265, June 2017. 152, 163

Fortescue G. E. and Pearson J. R. A. On gas absorption into a turbulent liquid. *Chemical Engineering Science*, 22(9):1163–1176, Sept. 1967. 157

Fox C. J. J. On the coefficients of absorption of nitrogen and oxygen in distilled water and sea-water, and of atmospheric carbonic acid in sea-water. *Transactions of the Faraday Society*, 5(September):68–86, Jan. 1909. 48

Friehe C. A. and Schwarz W. H. Grid-generated turbulence in dilute polymer solutions. *Journal of Fluid Mechanics*, Oct. 1970. 93

Gabelle J.-c. *Analyse locale et globale de l'hydrodynamique et du transfert de matière dans des fluides à rhéologie complexe caractéristiques des milieux de fermentation*. PhD thesis, Toulouse, INSA, Sept. 2012. 36

Gabelle J.-C., Augier F., Carvalho A., Rousset R. and Morchain J. Effect of tank size on kLa and mixing time in aerated stirred reactors with non-newtonian fluids. *The Canadian Journal of Chemical Engineering*, 89(5):1139–1153, Oct. 2011. 1, 2, 12, 27, 29, 91, 92, 96, 149, 161, 162, 163

Gabelle J.-C., Morchain J., Anne-Archard D., Augier F. and Liné A. Experimental determination of the shear rate in a stirred tank with a non-newtonian fluid: Carbopol. *AIChE Journal*, 59(6):2251–2266, June 2013. 93, 269, 270

Gabelle J.-C., Morchain J. and Liné A. Kinetic Energy Transfer between First Proper Orthogonal Decomposition Modes in a Mixing Tank. *Chemical Engineering & Technology*, 40(5): 927–937, May 2017. 93, 269, 270

Gadd G. E. Turbulence Damping and Drag Reduction Produced by Certain Additives in Water. *Nature*, 206(4983):463–467, May 1965. 88, 161

Gadd G. E. Reduction of Turbulent Friction in Liquids by Dissolved Additives. *Nature*, 212 (5065):874–877, Nov. 1966. 88, 161

Garcia-Ochoa F. and Gomez E. Mass transfer coefficient in stirred tank reactors for xanthan gum solutions. *Biochemical Engineering Journal*, 1(1):1–10, Jan. 1998. 91, 96, 161, 162

Garcia-Ochoa F., Santos V. E., Casas J. A. and Gomez E. Xanthan gum: production, recovery, and properties. *Biotechnology Advances*, 18(7):549–579, Nov. 2000. 96, 97, 99

Gavrilov A. A. and Rudyak V. Y. Reynolds-averaged modeling of turbulent flows of power-law fluids. *Journal of Non-Newtonian Fluid Mechanics*, 227:45–55, Jan. 2016. 30, 31

Gharahjeh S., Situ R., He Y., Wenxian L. and Brown R. A review on ocean acidification as a result of shipping emissions in harbors. *Australasian Coasts & Ports 2017: Working with Nature*, page 483, 2017. 12, 149

Godbole S. P., Schumpe A., Shah Y. T. and Carr N. L. Hydrodynamics and mass transfer in non-Newtonian solutions in a bubble column. *AIChE Journal*, 30(2):213–220, Mar. 1984. 161, 162

Gori F. and Boghi A. Two new differential equations of turbulent dissipation rate and apparent viscosity for non-newtonian fluids. *International Communications in Heat and Mass Transfer*, 38(6):696–703, July 2011. 30

Graftieaux L., Michard M. and Grosjean N. Combining PIV, POD and vortex identification algorithms for the study of unsteady turbulent swirling flows. *Measurement Science and Technology*, 12(9):1422, 2001. 269

Greated C. A. Effect of Polymer Additive on Grid Turbulence. *Nature*, 224(5225):1196–1197, Dec. 1969. 88, 93

Groisman A. and Steinberg V. Efficient mixing at low Reynolds numbers using polymer additives. *Nature*, 410(6831):905–908, Apr. 2001. 161

Guilbault G. G. *Practical Fluorescence, Second Edition*. CRC Press, Oct. 1990. 57

Guillard F., Trägårdh C. and Fuchs L. A study of turbulent mixing in a turbine-agitated tank using a fluorescence technique. *Experiments in Fluids*, 28(3):225–235, Mar. 2000. 12

Gupta V. K., Sureshkumar R. and Khomami B. Passive scalar transport in polymer drag-reduced turbulent channel flow. *AIChE Journal*, 51(7):1938–1950, July 2005. 90, 161

Hamdi J., Assoum H., Abed-Meraïm K. and Sakout A. Volume reconstruction of an impinging jet obtained from stereoscopic-PIV data using POD. *European Journal of Mechanics - B/Fluids*, 67:433–445, Jan. 2018. 269

Han M., González G., Vauhkonen M., Laari A. and Koiranen T. Local gas distribution and mass transfer characteristics in an annulus-rising airlift reactor with non-Newtonian fluid. *Chemical Engineering Journal*, 308:929–939, Jan. 2017. 12, 161, 162, 163

Hasegawa Y. and Kasagi N. Hybrid DNS/LES of high Schmidt number mass transfer across turbulent air–water interface. *International Journal of Heat and Mass Transfer*, 52(3–4): 1012–1022, Jan. 2009. 150, 158, 163, 291

Hearst R. J. *Fractal, classical, and active grid turbulence: From production to decay*. PhD thesis, University of Toronto (Canada), 2015. 83

Hebrard G., Zeng J. and Loubiere K. Effect of surfactants on liquid side mass transfer coefficients: A new insight. *Chemical Engineering Journal*, 148(1):132–138, May 2009. 152

Henry W. Experiments on the Quantity of Gases Absorbed by Water, at Different Temperatures, and under Different Pressures. *Philosophical Transactions of the Royal Society of London*, 93:29–276, 1803. 9

Herlina and Jirka G. H. Application of LIF to investigate gas transfer near the air-water interface in a grid-stirred tank. *Experiments in Fluids*, 37(3):341–349, May 2004. 163

Herlina H. *Gas transfer at the air-water interface in a turbulent flow environment*. PhD thesis, Universitätsverlag Karlsruhe, Karlsruhe, June 2005. 51, 84, 85, 86, 152, 155, 159, 184, 290

Herlina H. and Jirka G. H. Turbulent Gas Flux Measurements near the Air-Water Interface in a Grid-Stirred Tank. In Garbe P.-D. D. C. S., Handler D. R. A. and Jähne P. D. B., editors, *Transport at the Air-Sea Interface*, Environmental Science and Engineering, pages 25–41. Springer Berlin Heidelberg, 2007. 159

Herlina H. and Wissink J. G. Direct numerical simulation of turbulent scalar transport across a flat surface. *Journal of Fluid Mechanics*, 744:217–249, Apr. 2014. 1, 2, 151, 152, 153, 157, 163, 242

Herlina H. and Wissink J. G. Isotropic-turbulence-induced mass transfer across a severely contaminated water surface. *Journal of Fluid Mechanics*, 797:665–682, June 2016. 150, 152, 163, 242, 291

Herlina n. and Jirka G. H. Experiments on gas transfer at the air–water interface induced by oscillating grid turbulence. *Journal of Fluid Mechanics*, 594:183–208, Jan. 2008. 36, 151, 152, 155, 157, 159, 163, 210

Hideharu M. Realization of a large-scale turbulence field in a small wind tunnel. *Fluid Dynamics Research*, 8(1):53–64, Oct. 1991. 83

Higbie R. *The rate of absorption of a pure gas into still liquid during short periods of exposure,*. New York, 1935. 155, 156, 159, 163

Hiss T. G. and Cussler E. L. Diffusion in high viscosity liquids. *AIChE Journal*, 19(4):698–703, 1973. 160

Holdsworth D. W., Norley C. J. D., Frayne R., Steinman D. A. and Rutt B. K. Characterization of common carotid artery blood-flow waveforms in normal human subjects. *Physiological Measurement*, 20(3):219, 1999. 19

Hopfinger E. J. and Toly J.-A. Spatially decaying turbulence and its relation to mixing across density interfaces. *Journal of Fluid Mechanics*, 78(01):155–175, Nov. 1976. xv, 2, 84, 85, 86, 106, 114, 136, 138, 140, 143, 240

Hori T. and Sakakibara J. High-speed scanning stereoscopic PIV for 3d vorticity measurement in liquids. *Measurement Science and Technology*, 15(6):1067, 2004. 40, 42

Hu H. Stereo Particle Imaging Velocimetry Techniques: Technical Basis, System Setup, and Application. In *Handbook of 3D Machine Vision: Optical Metrology and Imaging*, pages 71–99. CRC Press, Mar. 2013. 40, 42

Hu Y., Liu Z., Yang J., Jin Y. and Cheng Y. Study on the reactive mixing process in an unbaffled stirred tank using planar laser-induced fluorescence (PLIF) technique. *Chemical Engineering Science*, 65(15):4511–4518, Aug. 2010. 12

Hunt J. C. R. Turbulence Structure and Turbulent Diffusion Near Gas-Liquid Interfaces. In Brutsaert W. and Jirka G. H., editors, *Gas Transfer at Water Surfaces*, number 2 in Water Science and Technology Library, pages 67–82. Springer Netherlands, 1984. 150, 151, 153, 163

Hunt J. C. R. and Graham J. M. R. Free-stream turbulence near plane boundaries. *Journal of Fluid Mechanics*, 84(02):209–235, Jan. 1978. 150, 163

Hunt J. C. R., Stretch D. D. and Belcher S. E. Viscous coupling of shear-free turbulence across nearly flat fluid interfaces. *Journal of Fluid Mechanics*, 671:96–120, Mar. 2011. 163

Huppert H. E. and Neufeld J. A. The Fluid Mechanics of Carbon Dioxide Sequestration. *Annual Review of Fluid Mechanics*, 46(1):255–272, 2014. 46

Hussain A. K. M. F. and Reynolds W. C. The mechanics of an organized wave in turbulent shear flow. *Journal of Fluid Mechanics*, 41(2):241–258, Apr. 1970. 19, 112

Isaza J. C., Warhaft Z. and Collins L. R. Experimental investigation of the large-scale velocity statistics in homogeneous turbulent shear flow. *Physics of Fluids*, 21(6):065105, June 2009. 83, 84

Jacquot P. and Rastogi P. K. Influence of out-of-plane deformation and its elimination in white light speckle photography. *Optics and Lasers in Engineering*, 2(1):33–55, Jan. 1981. 40

Jahne B., Münnich K. O. and Siegenthaler U. Measurements of gas exchange and momentum transfer in a circular wind-water tunnel. *Tellus*, 31(4):321–329, Jan. 1979. 290

Jamnongwong M., Loubiere K., Dietrich N. and Hébrard G. Experimental study of oxygen diffusion coefficients in clean water containing salt, glucose or surfactant: Consequences on the liquid-side mass transfer coefficients. *Chemical Engineering Journal*, 165(3):758–768, Dec. 2010. 152

Janzen J. G., Herlina H., Jirka G. H., Schulz H. E. and Gulliver J. S. Estimation of mass transfer velocity based on measured turbulence parameters. *AIChE Journal*, 56(8):2005–2017, Aug. 2010. 85, 149, 150, 151, 153, 156, 157, 159, 163, 184, 191, 194, 195, 205, 207, 210, 219

Jähne B. and Haußecker H. Air-Water Gas Exchange. *Annual Review of Fluid Mechanics*, 30 (1):443–468, 1998. 290

Jimenez M. *Etude du transfert de matière gaz/liquide en milieux complexes : quantification du transfert d'oxygène par techniques optiques*. PhD thesis, Toulouse, INSA, Oct. 2013. 52, 152

Jirka G. H., Herlina H. and Niepelt A. Gas transfer at the air–water interface: experiments with different turbulence forcing mechanisms. *Experiments in Fluids*, 49(1):319–327, Apr. 2010. 150, 153

Jones E. P. and Smith S. D. A first measurement of sea-air CO2 flux by eddy correlation. *Journal of Geophysical Research*, 82(37):5990–5992, Dec. 1977. 149

Katul G., Mammarella I., Grönholm T. and Vesala T. A Structure Function Model Recovers the Many Formulations for Air-Water Gas Transfer Velocity. *Water Resources Research*, 0 (0), 2018. 159

Katzbauer B. Properties and applications of xanthan gum. *Polymer Degradation and Stability*, 59(1):81–84, Jan. 1998. 27, 96, 97, 99

Kawase Y. and Hashiguchi N. Gas—liquid mass transfer in external-loop airlift columns with newtonian and non-newtonian fluids. *The Chemical Engineering Journal and the Biochemical Engineering Journal*, 62(1):35–42, Apr. 1996. 96, 104, 161, 162, 163

Kawase Y. and Moo-Young M. Influence of antifoam agents on gas hold-up and mass transfer in bubble columns with non-newtonian fluids. *Applied Microbiology and Biotechnology*, 27(2):159–167, 1987. 161, 162

Kawase Y., Halard B. and Moo-Young M. Theoretical prediction of volumetric mass transfer coefficients in bubble columns for Newtonian and non-Newtonian fluids. *Chemical Engineering Science*, 42(7):1609–1617, Jan. 1987. 11, 12, 27, 161, 162

Kawase Y., Halard B. and Moo-Young M. Liquid-Phase mass transfer coefficients in bioreactors. *Biotechnology and Bioengineering*, 39(11):1133–1140, May 1992. 27, 161, 162

Keane R. D. and Adrian R. J. Optimization of particle image velocimeters. I. Double pulsed systems. *Measurement Science and Technology*, 1(11):1202, 1990. 36, 39

Kermani A., Khakpour H. R., Shen L. and Igusa T. Statistics of surface renewal of passive scalars in free-surface turbulence. *Journal of Fluid Mechanics*, 678:379–416, July 2011. 158

Klonis N. and Sawyer W. H. Spectral properties of the prototropic forms of fluorescein in aqueous solution. *Journal of Fluorescence*, 6(3):147–157, 1996. xiv, 58, 61, 63, 296

Kolmogorov A. N. On the degeneration of isotropic turbulence in an incompressible viscous fluid. *Dokl. Akad. Nauk SSSR*, (31):319–323, 1941a. 18

Kolmogorov A. N. Dissipation of energy in isotropic turbulence. *Dokl. Akad. Nauk SSSR*, (32):325–327, 1941b. 18

Kolmogorov A. N. Equations of turbulent motion in an incompressible fluid. *Dokl. Akad. Nauk SSSR*, (30):299–303, 1941c. 18

Kolmogorov A. N. A refinement of previous hypotheses concerning the local structure of turbulence in a viscous incompressible fluid at high Reynolds number. *Journal of Fluid Mechanics*, 13(1):82–85, May 1962. 18

Komori S., Nagata K., Kanzaki T. and Murakami Y. Measurements of mass flux in a turbulent liquid flow with a chemical reaction. *AIChE Journal*, 39(10):1611–1620, Oct. 1993. 52

Kong G., Buist K. A., Peters E. A. J. F. and Kuipers J. A. M. Dual emission LIF technique for pH and concentration field measurement around a rising bubble. *Experimental Thermal and Fluid Science*, 93:186–194, May 2018. 56, 64, 80, 241

Koochesfahani M. M. and Dimotakis P. E. Mixing and chemical reactions in a turbulent liquid mixing layer. *Journal of Fluid Mechanics*, 170:83–112, Sept. 1986. 52

Kostazos A. E., Apikides P. S., Kastrinakis E. G. and Nychas S. G. Oscillating grid turbulence and bulk mixing at high schmidt numbers. *The Canadian Journal of Chemical Engineering*, 72(3):431–439, June 1994. 94

Kováts P., Thévenin D. and Zähringer K. Characterizing fluid dynamics in a bubble column aimed for the determination of reactive mass transfer. *Heat and Mass Transfer*, pages 1–9, Sept. 2017. 12, 36, 55, 56, 80, 241

Kräuter C., Trofimova D., Kiefhaber D., Krah N. and Jähne B. High resolution 2-D fluorescence imaging of the mass boundary layer thickness at free water surfaces. *Journal of the European Optical Society - Rapid publications*, 9(0), Mar. 2014. 56

Kuhn S. and Jensen K. F. A pH-Sensitive Laser-Induced Fluorescence Technique To Monitor Mass Transfer in Multiphase Flows in Microfluidic Devices. *Industrial & Engineering Chemistry Research*, 51(26):8999–9006, July 2012. 12, 49, 52, 53, 150

Kukura J., Arratia P. C., Szalai E. S., Bittorf K. J. and Muzzio F. J. Understanding pharmaceutical flows. *Pharmaceutical technology*, 26(10):48–73, 2002. 87

Lamont J. C. and Scott D. S. An eddy cell model of mass transfer into the surface of a turbulent liquid. *AIChE Journal*, 16(4):513–519, July 1970. 157

Launay G. *Etude expérimentale du tourbillon en fer à cheval au pied d'un obstacle émergent dans un roulement laminaire à surface libre*. PhD thesis, Lyon, Nov. 2016. 36

Lauwaert J., Raghuveer C. S. and Thybaut J. W. A three-phase Robinson-Mahoney reactor as a tool for intrinsic kinetic measurements: Determination of gas-liquid hold up and volumetric mass transfer coefficient. *Chemical Engineering Science*, 170:694–704, Oct. 2017. 12

Lavieille P., Delconte A., Blondel D., Lebouché M. and Lemoine F. Non-intrusive temperature measurements using three-color laser-induced fluorescence. *Experiments in Fluids*, 36(5): 706–716, May 2004. 54, 55, 241

LaVision . *DaVIs 8 Manual*. LaVision GmbH, 2011a. 41

LaVision . *DaVIs Flowmaster Manual*. LaVision GmbH, 2011b. 44, 270

Law C. N. S. and Khoo B. C. Transport across a turbulent air-water interface. *AIChE Journal*, 48(9):1856–1868, Sept. 2002. 158, 290, 291

Ledwell J. J. The Variation of the Gas Transfer Coefficient with Molecular Diffusity. In Brutsaert W. and Jirka G. H., editors, *Gas Transfer at Water Surfaces*, number 2 in Water Science and Technology Library, pages 293–302. Springer Netherlands, 1984. 291

Lee B.-B., Chan E.-S., Ravindra P. and Khan T. A. Surface tension of viscous biopolymer solutions measured using the du Nouy ring method and the drop weight methods. *Polymer Bulletin*, 69(4):471–489, Aug. 2012. 97, 103, 104

Lee C. H., Moturi V. and Lee Y. Thixotropic property in pharmaceutical formulations. *Journal of Controlled Release*, 136(2):88–98, June 2009. 29

Lehwald A., Thévenin D. and Zähringer K. Quantifying macro-mixing and micro-mixing in a static mixer using two-tracer laser-induced fluorescence. *Experiments in Fluids*, 48(5): 823–836, May 2010. 55

Lenoir J.-M. *Temps de cohérence temporelle de structures turbulentes porteuses de scalaires passifs au sein d'une turbulence homogène quasi-isotrope*. PhD thesis, Lyon 1, July 2011. 177, 199, 215

Lewis W. K. and Whitman W. G. Principles of Gas Absorption. *Industrial & Engineering Chemistry*, 16(12):1215–1220, Dec. 1924. 1, 9, 50, 149, 155, 157, 159, 163, 290

Liberzon A. On the effects of dilute polymers on driven cavity turbulent flows. *International Journal of Heat and Fluid Flow*, 32(6):1129–1137, Dec. 2011. 36, 89, 90, 95, 142, 272

Liberzon A., Guala M., Lüthi B., Kinzelbach W. and Tsinober A. Turbulence in dilute polymer solutions. *Physics of Fluids*, 17(3):031707, Mar. 2005. 89, 90, 149

Liberzon A., Guala M., Kinzelbach W. and Tsinober A. On turbulent kinetic energy production and dissipation in dilute polymer solutions. *Physics of Fluids*, 18(12):125101, Dec. 2006. 89, 90, 91, 142, 272

Liberzon A., Holzner M., Lüthi B., Guala M. and Kinzelbach W. On turbulent entrainment and dissipation in dilute polymer solutions. *Physics of Fluids (1994-present)*, 21(3):035107, Mar. 2009. 2, 87, 90, 91, 94, 106, 149, 163

Liné A., Gabelle J. C., Morchain J., Anne-Archard D. and Augier F. On POD analysis of PIV measurements applied to mixing in a stirred vessel with a shear thinning fluid. *Chemical Engineering Research and Design*, 91(11):2073–2083, Nov. 2013. 269, 270, 272

Lindqvist L. *A flash photolysis study of fluorescein*. Almqvist & Wiksell, 1960. 52, 58, 283

Lohse M., Alper E., Quicker G. and Deckwer W.-D. Diffusivity and solubility of carbondioxide in diluted polymer solutions. *AIChE Journal*, 27(4):626–631, July 1981. 160, 169

Lumley J. L. Drag Reduction by Additives. *Annual Review of Fluid Mechanics*, 1(1):367–384, 1969. 87, 88, 95

Lumley J. L. Drag reduction in turbulent flow by polymer additives. *Journal of Polymer Science, Part D: Macromol Rev*, 7, 1973. 88

Magnaudet J. High-Reynolds-number turbulence in a shear-free boundary layer: revisiting the Hunt-Graham theory. *Journal of Fluid Mechanics*, 484:167–196, June 2003. 151, 163

Magnaudet J. and Calmet I. Turbulent mass transfer through a flat shear-free surface. *Journal of Fluid Mechanics*, 553:155–185, Apr. 2006. 12, 150, 151, 155, 156, 158, 163

Mahamod M. T., Mohtar W. H. M. W. and Yusoff S. F. M. Spatial and temporal behavior of pb, cd and zn release during short term low intensity resuspension events. *Jurnal Teknologi*, 80(1), Dec. 2017. 2, 85

Manjrekar O. N., Sun Y., He L., Tang Y. J. and Dudukovic M. P. Hydrodynamics and Mass Transfer Coefficients in a Bubble Column Photo-bioreactor. *Chemical Engineering Science*, 2017. 12

Martin M. M. and Lindqvist L. The pH dependence of fluorescein fluorescence. *Journal of Luminescence*, 10(6):381–390, July 1975. 52, 57, 61, 63

Massey W. T., Harris M. C. and Deglon D. A. The effect of energy input on the flotation of quartz in an oscillating grid flotation cell. *Minerals Engineering*, 36-38:145–151, Oct. 2012. 85

Matsunaga N., Sugihara Y., Komatsu T. and Masuda A. Quantitative properties of oscillating-grid turbulence in a homogeneous fluid. *Fluid Dynamics Research*, 25(3):147–165, Sept. 1999. 85, 86, 106, 136, 137

McComb W. D., Allan J. and Greated C. A. Effect of polymer additives on the small-scale structure of grid-generated turbulence. *The Physics of Fluids*, 20(6):873–879, June 1977. 93, 149, 161

McCorquodale M. W. and Munro R. J. Experimental study of oscillating-grid turbulence interacting with a solid boundary. *Journal of Fluid Mechanics*, 813:768–798, Feb. 2017. 85

McCorquodale M. W. and Munro R. J. Analysis of intercomponent energy transfer in the interaction of oscillating-grid turbulence with an impermeable boundary. *Physics of Fluids*, 30(1):015105, Jan. 2018. 2, 85, 86

McCready M. J., Vassiliadou E. and Hanratty T. J. Computer simulation of turbulent mass transfer at a mobile interface. *AIChE Journal*, 32(7):1108–1115, July 1986. 158

Mcdougall T. J. Measurements of turbulence in a zero-mean-shear mixed layer. *Journal of Fluid Mechanics*, 94(03):409–431, Oct. 1979. 85, 86, 106

McKenna S. P. *Free-Surface Turbulence and Air-Water Gas Exchange*. PhD thesis, Sept. 2000. 85, 152, 291

Mckenna S. P. and Mcgillis W. R. Surface Divergence and Air-Water Gas Transfer. In Donelan M. A., M.ennan W., Saltzman E. S. and Wanninkhof R., editors, *Gas Transfer at Water Surfaces*, pages 129–134. American Geophysical Union, 2002. 158

McKenna S. P. and McGillis W. R. The role of free-surface turbulence and surfactants in air–water gas transfer. *International Journal of Heat and Mass Transfer*, 47(3):539–553, Jan. 2004a. 85, 86, 114, 152, 158, 237, 291, 292

McKenna S. P. and McGillis W. R. Observations of flow repeatability and secondary circulation in an oscillating grid-stirred tank. *Physics of Fluids (1994-present)*, 16(9):3499–3502, Sept. 2004b. 183

Melrose J. R., van Vliet J. H. and Ball R. C. Continuous Shear Thickening and Colloid Surfaces. *Physical Review Letters*, 77(22):4660–4663, Nov. 1996. 26

Metzner A. B. and Otto R. E. Agitation of non-Newtonian fluids. *AIChE Journal*, 3(1):3–10, Mar. 1957. 29, 91, 92, 162

Mignot E., Hurther D. and Barthelemy E. On the structure of shear stress and turbulent kinetic energy flux across the roughness layer of a gravel-bed channel flow. *Journal of Fluid Mechanics*, 638:423–452, Nov. 2009. 180

Mignot E., Cai W., Launay G., Riviere N. and Escauriaza C. Coherent turbulent structures at the mixing-interface of a square open-channel lateral cavity. *Physics of Fluids*, 28(4): 045104, Apr. 2016. 19

Milas M. and Rinaudo M. Properties of xanthan gum in aqueous solutions: Role of the conformational transition. *Carbohydrate Research*, 158:191–204, Dec. 1986. 97

Milas M., Reed W. F. and Printz S. Conformations and flexibility of native and re-natured xanthan in aqueous solutions. *International Journal of Biological Macromolecules*, 18(3): 211–221, Apr. 1996. 97

Moreau J. and Liné A. Proper orthogonal decomposition for the study of hydrodynamics in a mixing tank. *AIChE Journal*, 52(7):2651–2655, July 2006. 270

Morge F. Etude du transfert de masse gaz-liquide dans un écoulement stratifié. Rapport de stage - Master 2 MEGA spécialité mécanique des fluides, INSA de Lyon, 2015. 106, 293

Morris S. Real-time multi-wavelength fluorescence imaging of living cells. *BioTechniques*, 8 (3):296–308, Mar. 1990. 56

Mydlarski L. and Warhaft Z. On the onset of high-Reynolds-number grid-generated wind tunnel turbulence. *Journal of Fluid Mechanics*, 320:331–368, Aug. 1996. 83

Nadolink R. H. and Haigh W. W. Bibliography on Skin Friction Reduction With Polymers and Other Boundary-Layer Additives. *Applied Mechanics Reviews*, 48(7):351–460, July 1995. 87

Nagami Y. and Saito T. An Experimental Study of the Modulation of the Bubble Motion by Gas–Liquid-Phase Interaction in Oscillating-Grid Decaying Turbulence. *Flow, Turbulence and Combustion*, 92(1-2):147–174, Sept. 2013. 2, 85

Najjari M. R., Hinke J. A., Bulusu K. V. and Plesniak M. W. On the rheology of refractive-index-matched, non-Newtonian blood-analog fluids for PIV experiments. *Experiments in Fluids*, 57(6):96, June 2016. 87, 96

Nakanoh M. and Yoshida F. Gas Absorption by Newtonian and Non-Newtonian Liquids in a Bubble Column. *Industrial & Engineering Chemistry Process Design and Development*, 19 (1):190–195, Jan. 1980. 11, 161, 162

Natrajan V. K. and Christensen K. T. Two-color laser-induced fluorescent thermometry for microfluidic systems. *Measurement Science and Technology*, 20(1):015401, 2009. 54, 55

Nguyen M. Q., Delache A., Simoëns S., Bos W. J. T. and EL Hajem M. Small scale dynamics of isotropic viscoelastic turbulence. *Physical Review Fluids*, 1(8):083301, Dec. 2016. 28, 32, 88, 89, 90, 95, 122, 150, 163

Nguyen T. D. *Influences des propriétés non-Newtoniennes sur un mélange de scalaire passif*. PhD thesis, Lyon, INSA, Sept. 2013. 24, 28, 29, 161, 175

Nishikawa M., Nakamura M. and Hashimoto K. Gas absorption in aerated mixing vessels with non-newtonian liquid. *Journal Of Chemical Engineering of Japan*, 14(3):227–232, June 1981. 91, 161, 162

Nogueira S., Sousa R. G., Pinto A. M. F. R., Riethmuller M. L. and Campos J. B. L. M. Simultaneous PIV and pulsed shadow technique in slug flow: a solution for optical problems. *Experiments in Fluids*, 35(6):598–609, Oct. 2003. 12

Nokes R. I. On the entrainment rate across a density interface. *Journal of Fluid Mechanics*, 188:185–204, Mar. 1988. 85, 86

O'Connor D. J. and Dobbins W. E. The Mechanics of Reaeration in Natural Streams. *Journal of the Sanitary Engineering Division*, 82(6):1–30, Dec. 1956. 156

Osegueda-Paredes L. Étude expérimentale du transfert de masse à l'interface gaz-liquide à partir d'une turbulence de grille oscillante. Rapport de stage - Master 2 MEGA spécialité mécanique des fluides, INSA de Lyon, 2013. 105, 106

Ouellette N. T., Xu H. and Bodenschatz E. Bulk turbulence in dilute polymer solutions. *Journal of Fluid Mechanics*, 629:375–385, June 2009. 89, 90, 91, 145

Pan Y. and Banerjee S. A numerical study of free-surface turbulence in channel flow. *Physics of Fluids (1994-present)*, 7(7):1649–1664, July 1995. 163

Papanicolaou P. N. and List E. J. Investigations of round vertical turbulent buoyant jets. *Journal of Fluid Mechanics*, 195:341–391, Oct. 1988. 52, 65, 72

Papantoniou D. and List E. J. Large-scale structure in the far field of byoyant jets. *Journal of Fluid Mechanics*, 209:151–190, Dec. 1989. 65, 72

Park S.-W., Choi B.-S., Song K.-W., Oh K.-J. and Lee J.-W. Absorption of Carbon Dioxide into Aqueous Xanthan Gum Solution Containing Monoethanolamine. *Separation Science and Technology*, 42(16):3537–3554, Dec. 2007. 169

Partridge J. L., Lefauve A. and Dalziel S. B. A versatile scanning method for volumetric measurements of velocity and density fields. *arXiv:1805.01181 [physics]*, May 2018. arXiv: 1805.01181. 242

Pashaei H., Ghaemi A. and Nasiri M. Experimental investigation of CO2 removal using Piperazine solution in a stirrer bubble column. *International Journal of Greenhouse Gas Control*, 63:226–240, Aug. 2017. 12

Passaggia P.-Y., Hurley M. W., White B. and Scotti A. Turbulent horizontal convection at high Schmidt numbers. *Physical Review Fluids*, 2(9):090506, Sept. 2017. 55

Patel D., Ein-Mozaffari F. and Mehrvar M. Tomography images to analyze the deformation of the cavern in the continuous-flow mixing of non-Newtonian fluids. *AIChE Journal*, 60(1): 315–331, Jan. 2014. 92

Pedersen A. G., Bundgaard-Nielsen M., Nielsen J., Villadsen J. and Hassager O. Rheological characterization of media containing Penicillium chrysogenum. *Biotechnology and Bioengineering*, 41(1):162–164, Jan. 1993. 96

Pedersen A. G., Bundgaard-Nielsen M., Nielsen J. and Villadsen J. Characterization of mixing in stirred tank bioreactors equipped with rushton turbines. *Biotechnology and Bioengineering*, 44(8):1013–1017, Oct. 1994. 27, 96

Pereira A. S., Andrade R. M. and Soares E. J. Drag reduction induced by flexible and rigid molecules in a turbulent flow into a rotating cylindrical double gap device: Comparison between Poly (ethylene oxide), Polyacrylamide, and Xanthan Gum. *Journal of Non-Newtonian Fluid Mechanics*, 202:72–87, Dec. 2013. 98

Perez J. F. and Sandall O. C. Diffusivity measurements for gases in power law non-Newtonian. *AIChE Journal*, 19(5):1073–1075, Sept. 1973. 160

Perez J. F. and Sandall O. C. Gas absorption by non-Newtonian fluids in agitated vessels. *AIChE Journal*, 20(4):770–775, July 1974. 160

Perot B. and Moin P. Shear-free turbulent boundary layers. Part 1. Physical insights into near-wall turbulence. *Journal of Fluid Mechanics*, 295:199–227, July 1995. 150, 163

Petříček R., Moucha T., Rejl F. J., Valenz L. and Haidl J. Volumetric mass transfer coefficient in the fermenter agitated by Rushton turbines of various diameters in viscous batch. *International Journal of Heat and Mass Transfer*, 115:856–866, Dec. 2017. 12

Pinho F. T. A GNF framework for turbulent flow models of drag reducing fluids and proposal for a k–ϵ type closure. *Journal of Non-Newtonian Fluid Mechanics*, 114(2):149–184, Sept. 2003. 30, 32

Poole R. J. The Deborah and Weissenberg numbers. *Rheology Bulletin*, 53(2):32–39, 2012. 30

Portier S. and Rochelle C. Modelling CO2 solubility in pure water and NaCl-type waters from 0 to 300 °C and from 1 to 300 bar: Application to the Utsira Formation at Sleipner. *Chemical Geology*, 217(3–4):187–199, Apr. 2005. 48

Poryles R. and Vidal V. Rising bubble instabilities and fragmentation in a confined polymer solution. *Journal of Non-Newtonian Fluid Mechanics*, 241:26–33, Mar. 2017. 27, 150

Prasad A. K. Stereoscopic particle image velocimetry. *Experiments in Fluids*, 29(2):103–116, Aug. 2000. 40, 41, 170

Prasad A. K. and Jensen K. Scheimpflug stereocamera for particle image velocimetry in liquid flows. *Applied Optics*, 34(30):7092, Oct. 1995. 40, 42

Prasad R. R. and Sreenivasan K. R. Quantitative three-dimensional imaging and the structure of passive scalar fields in fully turbulent flows. *Journal of Fluid Mechanics*, 216:1–34, July 1990. 52, 242

Prata A. A., Santos J. M., Timchenko V. and Stuetz R. M. A critical review on liquid-gas mass transfer models for estimating gaseous emissions from passive liquid surfaces in wastewater treatment plants. *Water Research*, 130:388–406, Mar. 2018. 12, 290, 291

Puthli M. S., Rathod V. K. and Pandit A. B. Gas–liquid mass transfer studies with triple impeller system on a laboratory scale bioreactor. *Biochemical Engineering Journal*, 23(1): 25–30, Mar. 2005. 161, 162

Raffel M., Willert C. E., Wereley S. T. and Kompenhans J. *Particle Image Velocimetry: A Practical Guide*. Springer, Dec. 2013. 36, 39

Ranade V. R. and Ulbrecht J. J. Influence of polymer additives on the gas-liquid mass transfer in stirred tanks. *AIChE Journal*, 24(5):796–803, Sept. 1978. 161, 162, 163

Rashidi M., Hetsroni G. and Banerjee S. Mechanisms of heat and mass transport at gas-liquid interfaces. *International Journal of Heat and Mass Transfer*, 34(7):1799–1810, July 1991. 163

Rastello M., Michallet H. and Marié J.-L. Sediment erosion in zero-mean-shear turbulence. *Coastal Dynamics*, (094):597–607, 2017. 2, 85

Reiner M. The deborah number. *Physics today*, 17(1):62, 1964. 28

Rochlitz H. and Scholz P. Application of laser-induced fluorescence technique in a duct flow with one heated wall | SpringerLink. *Experiments in Fluids*, pages 59–54, Mar. 2018. 55

Rodi W. *Turbulence Models and Their Application in Hydraulics*. Routledge, Nov. 2017. 16

Roudet M., Billet A.-M., Cazin S., Risso F. and Roig V. Experimental investigation of interfacial mass transfer mechanisms for a confined high-reynolds-number bubble rising in a thin gap. *AIChE Journal*, 63(6):2394–2408, June 2017. 52

Rouse H. J. and Dodu J. Turbulent diffusion across a density discontinuity. *La Houille Blanche*, (4):522–532, 1955. 84

Rüttinger S., Spille C., Hoffmann M. and Schlüter M. Laser-Induced Fluorescence in Multiphase Systems. *ChemBioEng Reviews*, 5(4):253–269, Aug. 2018. 241

Safari M., Harris M. and Deglon D. The effect of energy input on the flotation of a platinum ore in a pilot-scale oscillating grid flotation cell. *Minerals Engineering*, 110:69–74, Aug. 2017. 85

Sakakibara J. and Adrian R. J. Whole field measurement of temperature in water using two-color laser induced fluorescence. *Experiments in Fluids*, 26(1-2):7–15, Jan. 1999. 54, 55

Sakakibara J., Hishida K. and Maeda M. Vortex structure and heat transfer in the stagnation region of an impinging plane jet (simultaneous measurements of velocity and temperature fields by digital particle image velocimetry and laser-induced fluorescence). *International Journal of Heat and Mass Transfer*, 40(13):3163–3176, Sept. 1997. 52

Sakakibara J., Nakagawa M. and Yoshida M. Stereo-PIV study of flow around a maneuvering fish. *Experiments in Fluids*, 36(2):282–293, Feb. 2004. 40, 42

San L., Long T. and Liu C. C. K. Algal Bioproductivity in Turbulent Water: An Experimental Study. *Water*, 9(5):304, Apr. 2017. 1, 2, 12, 45, 85

Sanjou M., Nezu I. and Okamoto T. Surface velocity divergence model of air/water interfacial gas transfer in open-channel flows. *Physics of Fluids*, 29(4):045107, Apr. 2017. 12

Sardeing R., Painmanakul P. and Hébrard G. Effect of surfactants on liquid-side mass transfer coefficients in gas–liquid systems: A first step to modeling. *Chemical Engineering Science*, 61(19):6249–6260, Oct. 2006. 152

Schanz D., Gesemann S. and Schröder A. Shake-The-Box: Lagrangian particle tracking at high particle image densities. *Experiments in Fluids*, 57(5):70, May 2016. 243

Schulz H. E., Janzen J. G. and Souza K. C. d. O. Experiments and theory for two grids turbulence. *Journal of the Brazilian Society of Mechanical Sciences and Engineering*, 28(2): 216–223, June 2006. 85

Sciacchitano A., Neal D. R., Smith B. L., Warner S. O., Vlachos P. P., Bernhard Wieneke and Scarano F. Collaborative framework for PIV uncertainty quantification: comparative assessment of methods. *Measurement Science and Technology*, 26(7):074004, 2015. 44

Sellin D., Hiessl R., Bothe M., Timmermann J., Becker M., Schlüter M. and Liese A. Simultaneous local determination of mass transfer and residence time distributions in organic multiphase systems. *Chemical Engineering Journal*, 321:635–641, Aug. 2017. 12

Seoud R. E. and Vassilicos J. C. Dissipation and decay of fractal-generated turbulence. *Physics of Fluids (1994-present)*, 19(10):105108, Oct. 2007. 83

Sharp N. S., Neuscamman S. and Warhaft Z. Effects of large-scale free stream turbulence on a turbulent boundary layer. *Physics of Fluids*, 21(9):095105, Sept. 2009. 84

Shojaeian M., Sezen M. and Koşar A. Pool boiling heat transfer characteristics of non-Newtonian Xanthan gum solutions. *Experimental Thermal and Fluid Science*, 70:77–84, Jan. 2016. 97

Shy S. S., Tang C. Y. and Fann S. Y. A nearly isotropic turbulence generated by a pair of vibrating grids. *Experimental Thermal and Fluid Science*, 14(3):251–262, Apr. 1997. 85, 86, 106

Silva I. P. D. D. and Fernando H. J. S. Some aspects of mixing in a stratified turbulent patch. *Journal of Fluid Mechanics*, 240:601–625, July 1992. 86

Simoens S. and Ayrault M. Concentration flux measurements of a scalar quantity in turbulent flows. *Experiments in Fluids*, 16(3-4):273–281, Feb. 1994. 22, 84, 149, 175

Simoëns S. *Applications de l'analyse d'imagec à des phénomènes de mélange et de dispersion turbulents*. PhD thesis, Ecole Centrale de Lyon, 1992. 39, 113

Sirovich L. Turbulence and the dynamics of coherent structures. I. Coherent structures. *Quarterly of applied mathematics*, 45(3):561–571, 1987. 269

Sohn J. I., Kim C. A., Choi H. J. and Jhon M. S. Drag-reduction effectiveness of xanthan gum in a rotating disk apparatus. *Carbohydrate Polymers*, 45(1):61–68, May 2001. 96, 99

Soli A. L. and Byrne R. H. CO2 system hydration and dehydration kinetics and the equilibrium CO2/H2co3 ratio in aqueous NaCl solution. *Marine Chemistry*, 78(2–3):65–73, May 2002. 49

Soloff S. M., Adrian R. J. and Liu Z.-C. Distortion compensation for generalized stereoscopic particle image velocimetry. *Measurement Science and Technology*, 8(12):1441, 1997. 41

Solomenko Z. *Two-phase flows over complex surfaces : towards bridging the gap between computations and experiments with application to structured packings*. PhD thesis, Lyon, Dec. 2016. 12

Someya S., Bando S., Song Y., Chen B. and Nishio M. DeLIF measurement of pH distribution around dissolving CO2 droplet in high pressure vessel. *International Journal of Heat and Mass Transfer*, 48(12):2508–2515, June 2005. 46, 55

Sossa-Echeverria J. and Taghipour F. Mixing of Newtonian and Non-Newtonian Fluids in a Cylindrical Mixer Equipped with a Side-Entry Impeller. *Industrial & Engineering Chemistry Research*, 51(46):15258–15267, Nov. 2012. 93

Souzy N. *Experimental study and improvement of mass transfer in vertical bubble columns*. phdthesis, Université Claude Bernard - Lyon I, Oct. 2014. 53, 54, 69, 294, 295

Sreenivasan K. R. and White C. M. The onset of drag reduction by dilute polymer additives, and the maximum drag reduction asymptote. *Journal of Fluid Mechanics*, 409:149–164, Apr. 2000. 87, 95

Stumm W. and Morgan J. J. *Aquatic chemistry: chemical equilibria and rates in natural waters*. Wiley, 1996. 46, 47, 49, 50, 51, 53

Sturm P. Pinhole Camera Model. In *Computer Vision*, pages 610–613. Springer, Boston, MA, 2014. 41

Suzuki H., Nagata K., Sakai Y. and Ukai R. High-Schmidt-number scalar transfer in regular and fractal grid turbulence. *Physica Scripta*, 2010(T142):014069, 2010. 84

Tabor M. and de Gennes P. G. A Cascade Theory of Drag Reduction. *EPL (Europhysics Letters)*, 2(7):519, 1986. 88, 89, 95

Talukdar M. M., Vinckier I., Moldenaers P. and Kinget R. Rheological characterization of xanthan gum and hydroxypropylmethyl cellulose with respect to controlled-release drug delivery. *Journal of Pharmaceutical Sciences*, 85(5):537–540, May 1996. 98, 99, 103

Tamburrino A. and Gulliver J. S. Free-surface turbulence and mass transfer in a channel flow. *AIChE Journal*, 48(12):2732–2743, Dec. 2002. 158, 163

Tamburrino A. and Martínez N. Wave and wind effects on the oxygen transfer across an air-water interface: An experimental study. *The Canadian Journal of Chemical Engineering*, 95(8):1594–1604, Aug. 2017. 291

Tamburrino A., Aravena C. and Gulliver J. S. Visualization of 2-D Divergence on the Free Surface and its Relation to Gas Transfer. In Garbe P.-D. D. C. S., Handler D. R. A. and Jähne P. D. B., editors, *Transport at the Air-Sea Interface*, Environmental Science and Engineering, pages 73–86. Springer Berlin Heidelberg, 2007. 158

Tan K. K. and Thorpe R. B. Gas diffusion into viscous and non-Newtonian liquids. *Chemical Engineering Science*, 47(13):3565–3572, Sept. 1992. 160

Theofanous T. G. Conceptual Models of Gas Exchange. In Brutsaert W. and Jirka G. H., editors, *Gas Transfer at Water Surfaces*, number 2 in Water Science and Technology Library, pages 271–281. Springer Netherlands, 1984. 11, 157, 158, 163

Thompson S. M. and Turner J. S. Mixing across an interface due to turbulence generated by an oscillating grid. *Journal of Fluid Mechanics*, 67(02):349–368, Jan. 1975. xv, 2, 84, 85, 86, 105, 106, 122, 140, 142, 144, 240

Thormann A. and Meneveau C. Decay of homogeneous, nearly isotropic turbulence behind active fractal grids. *Physics of Fluids (1994-present)*, 26(2):025112, Feb. 2014. 84

Thurston G. B. and Henderson N. M. Effects of flow geometry on blood viscoelasticity. *Biorheology*, 43(6):729–746, Jan. 2006. 28

Tiffany J. M. Viscoelastic Properties of Human Tears and Polymer Solutions. In *Lacrimal Gland, Tear Film, and Dry Eye Syndromes*, Advances in Experimental Medicine and Biology, pages 267–270. Springer, Boston, MA, 1994. 26

Timmins B. H., Wilson B. W., Smith B. L. and Vlachos P. P. A method for automatic estimation of instantaneous local uncertainty in particle image velocimetry measurements. *Experiments in Fluids*, 53(4):1133–1147, Oct. 2012. 44

Toms B. A. Some observation on the flow of linear polymer solutions through straight tubes at large Reynolds numbers. volume 2, pages 135–141, Scheveningen, 1948. J.G. Oldroyd. 87

Torrestiana B., Galindo E. and Brito E. Diffusion of sucrose in xanthan gum solutions. *Bioprocess Engineering*, 4(6):265–273, Nov. 1989. 160

Tsumori H. and Sugihara Y. Lengthscales of motions that control air–water gas transfer in grid-stirred turbulence. *Journal of Marine Systems*, 66(1–4):6–18, June 2007. 158, 159, 160, 163

Turner J. S. The influence of molecular diffusivity on turbulent entrainment across a density interface. *Journal of Fluid Mechanics*, 33(04):639–656, Sept. 1968. 106

Turney D. E. and Banerjee S. Air–water gas transfer and near-surface motions. *Journal of Fluid Mechanics*, 733:588–624, Oct. 2013. 1, 11, 12, 36, 150, 158, 163, 290, 291

Ungeheuer S., Bewersdorff H.-W. and Singh R. P. Turbulent drag effectiveness and shear stability of xanthan-gum-based graft copolymers. *Journal of Applied Polymer Science*, 37 (10):2933–2948, May 1989. 99

Valiorgue P. *Mass transfer in intermittent horizontal gas-liquid flow and application to photobioreactors*. PhD thesis, Lyon 1, Dec. 2012. 12

Valiorgue P., Souzy N., Hajem M. E., Hadid H. B. and Simoëns S. Concentration measurement in the wake of a free rising bubble using planar laser-induced fluorescence (PLIF) with a

calibration taking into account fluorescence extinction variations. *Experiments in Fluids*, 54(4):1–10, Apr. 2013. 10, 11, 51, 52, 53, 150, 172, 178, 210, 294, 295, 296

Valiorgue P., Ben Hadid H., El Hajem M., Rimbaud L., Muller-Feuga A. and Champagne J. Y. CO2 mass transfer and conversion to biomass in a horizontal gas–liquid photobioreactor. *Chemical Engineering Research and Design*, 92(10):1891–1897, Oct. 2014. 1, 12, 45

Variano E. A. and Cowen E. A. Quantitative Imaging of CO2 Transfer at an Unsheared Free Surface. In Garbe P.-D. D. C. S., Handler D. R. A. and Jähne P. D. B., editors, *Transport at the Air-Sea Interface*, Environmental Science and Engineering, pages 43–57. Springer Berlin Heidelberg, 2007. 159

Variano E. A. and Cowen E. A. A random-jet-stirred turbulence tank. *Journal of Fluid Mechanics*, 604:1–32, June 2008. 114

Variano E. A. and Cowen E. A. Turbulent transport of a high-Schmidt-number scalar near an air–water interface. *Journal of Fluid Mechanics*, 731:259–287, Sept. 2013. xv, 1, 11, 45, 52, 149, 150, 151, 152, 153, 155, 159, 163, 175, 178, 179, 180, 181, 182, 190, 192, 193, 206, 210, 213, 222, 238

Variano E. A., Bodenschatz E. and Cowen E. A. A random synthetic jet array driven turbulence tank. *Experiments in Fluids*, 37(4):613–615, July 2004. 86, 114, 139

Vasumathi K. K., Nithiya E. M., Pandey R. and Premalatha M. Studies on the effect of wind speed on loss of carbon dioxide during bio sequestration. *International Journal of Hydrogen Energy*, 2017. 45

Vega-Martínez P., Enríquez O. R. and Rodríguez-Rodríguez J. Some Topics on the Physics of Bubble Dynamics in Beer. *Beverages*, 3(3):38, July 2017. 10

Venneker B. C. H., Derksen J. J. and Van den Akker H. E. A. Turbulent flow of shear-thinning liquids in stirred tanks—The effects of Reynolds number and flow index. *Chemical Engineering Research and Design*, 88(7):827–843, July 2010. 93

Vernet R. *Etude expérimentale d'un jet pulsé dans un écoulement transverse à faible nombre de Reynolds Influence de l'excitation sur le mélange et sur la dynamique tourbillonnaire*. PhD thesis, Université de Poitiers, Poitiers, 2010. 40, 42

Verso L., van Reeuwijk M. and Liberzon A. Steady state model and experiment for an oscillating grid turbulent two-layer stratified flow. *Physical Review Fluids*, 2(10):104605, Oct. 2017. 2, 85, 86

Vinçont J.-Y., Simoëns S., Ayrault M. and Wallace J. M. Passive scalar dispersion in a turbulent boundary layer from a line source at the wall and downstream of an obstacle. *Journal of Fluid Mechanics*, 424:127–167, Dec. 2000. 180, 181, 204

Virk P. S. Drag reduction fundamentals. *AIChE Journal*, 21(4):625–656, July 1975a. 87, 95

Virk P. S. Drag reduction by collapsed and extended polyelectrolytes. *Nature*, 253(5487): 253109a0, Jan. 1975b. 88, 95, 96, 99

Virk P. S. and Wagger D. L. Aspects of Mechanisms in Type B Drag Reduction. In *Structure of Turbulence and Drag Reduction*, International Union of Theoretical and Applied Mechanics, pages 201–213. Springer, Berlin, Heidelberg, 1990. 88

Vonlanthen R. *The Effects of Fluid Elasticity on Grid Turbulence*. PhD thesis, Ecole Polytechnique Fédérale de Lausanne, Lausanne, Suisse, 2010. 89

Vonlanthen R. and Monkewitz P. A. Grid turbulence in dilute polymer solutions: PEO in water. *Journal of Fluid Mechanics*, 730:76–98, Sept. 2013. 91, 93, 94, 106, 149, 163

Voropayev S. I. and Fernando H. J. S. Propagation of grid turbulence in homogeneous fluids. *Physics of Fluids*, 8(9):2435–2440, Sept. 1996. 84

Vreme A., Nadal F., Pouligny B., Jeandet P., Liger-Belair G. and Meunier P. Gravitational instability due to the dissolution of carbon dioxide in a Hele-Shaw cell. *Physical Review Fluids*, 1(6):064301, Oct. 2016. 11

Wagner N. and Wetzel E. D. Advanced body armor utilizing shear thickening fluids, Mar. 2009. 26

Walker D. A. A fluorescence technique for measurement of concentration in mixing liquids. *Journal of Physics E: Scientific Instruments*, 20(2):217, 1987. 52, 57, 61, 65

Wallace J. M. Quadrant Analysis in Turbulence Research: History and Evolution. *Annual Review of Fluid Mechanics*, 48(1):131–158, 2016. 180

Wallace J. M., Eckelmann H. and Brodkey R. S. The wall region in turbulent shear flow. *Journal of Fluid Mechanics*, 54(1):39–48, July 1972. 180

Wan Mohtar W. H. M. Oscillating-grid turbulence at large strokes: Revisiting the equation of Hopfinger and Toly. *Journal of Hydrodynamics, Ser. B*, 28(3):473–481, June 2016. 86, 137

Wang X., Feng X., Yang C. and Mao Z.-S. Energy Dissipation Rates of Newtonian and Non-Newtonian Fluids in a Stirred Vessel. *Chemical Engineering & Technology*, 37(9):1575–1582, Sept. 2014. 93

Wang Y., Cai W.-H., Wei T.-Z., Wang L. and Li F.-C. Experimental Study on Two-Oscillating Grid Turbulence With Polymer Additives. page V001T15A008, Seoul, South Korea, July 2015. ASME. 94

Wang Y., Cai W.-H., Wei T.-Z., Zhang H.-N., Wang L. and Li F.-C. Proper orthogonal decomposition analysis for two-oscillating grid turbulence with viscoelastic fluids. *Advances in Mechanical Engineering*, 8(11):1687814016679773, Nov. 2016. 2, 94, 144, 269, 272, 280, 281

Warholic M. D., Massah H. and Hanratty T. J. Influence of drag-reducing polymers on turbulence: effects of Reynolds number, concentration and mixing. *Experiments in Fluids*, 27(5):461–472, Oct. 1999. 88

Warholic M. D., Heist D. K., Katcher M. and Hanratty T. J. A study with particle-image velocimetry of the influence of drag-reducing polymers on the structure of turbulence. *Experiments in Fluids*, 31(5):474–483, Nov. 2001. 88, 90

Wasan D. T., Lynch M. A., Chad K. J. and Srinivasan N. Mass transfer into dilute polymeric solutions. *AIChE Journal*, 18(5):928–934, Sept. 1972. 160

Weiss R. F. Carbon dioxide in water and seawater: the solubility of a non-ideal gas. *Marine Chemistry*, 2(3):203–215, Nov. 1974. 48

Whitcomb P. J. and Macosko C. W. Rheology of Xanthan Gum. *Journal of Rheology (1978-present)*, 22(5):493–505, Oct. 1978. 97, 98, 102

Wieneke B. Application of self-calibration stereo PIV in enclosed measurement volumes. Lisbon, Portugal, 2004. 41, 43

Wieneke B. Stereo-PIV using self-calibration on particle images. *Experiments in Fluids*, 39(2):267–280, May 2005. 41

Wieneke B. Iterative reconstruction of volumetric particle distribution. *Measurement Science and Technology*, 24(2):024008, 2013. 243

Wieneke B. PIV uncertainty quantification from correlation statistics. *Measurement Science and Technology*, 26(7):074002, 2015. 44, 171

Willert C. E. Assessment of camera models for use in planar velocimetry calibration. *Experiments in Fluids*, 41(1):135–143, July 2006. 41

Wissink J. G. and Herlina H. Direct numerical simulation of gas transfer across the air–water interface driven by buoyant convection. *Journal of Fluid Mechanics*, 787:508–540, Jan. 2016. 163, 242

Wissink J. G., Herlina H., Akar Y. and Uhlmann M. Effect of surface contamination on interfacial mass transfer rate. *Journal of Fluid Mechanics*, 830:5–34, Nov. 2017. 1, 2, 152, 153, 291, 292

Woodrow P. T. and Duke S. R. Laser-Induced Fluorescence Studies of Oxygen Transfer Across Unsheared Flat and Wavy Air-Water Interfaces. *Industrial & Engineering Chemistry Research*, 40(8):1985–1995, Apr. 2001. 290

Woodrow P. T. and Duke S. R. LIF Measurements of Oxygen Concentration Gradients Along Flat and Wavy Air-Water Interfaces. In Donelan M. A., M.ennan W., Saltzman E. S. and Wanninkhof R., editors, *Gas Transfer at Water Surfaces*, pages 83–88. American Geophysical Union, 2002. 290

Wyatt N. B. and Liberatore M. W. Rheology and viscosity scaling of the polyelectrolyte xanthan gum. *Journal of Applied Polymer Science*, 114(6):4076–4084, Dec. 2009. 91, 97, 98, 99, 100, 101, 102, 103, 118, 119, 145

Wyatt N. B., Gunther C. M. and Liberatore M. W. Drag reduction effectiveness of dilute and entangled xanthan in turbulent pipe flow. *Journal of Non-Newtonian Fluid Mechanics*, 166 (1):25–31, Jan. 2011. 96, 99, 196, 237

Wypych G. XG xanthan gum, polysaccharide B-1459. In *Handbook of Polymers*, pages 683–684. Elsevier, Oxford, 2012. 96

Xi H.-D., Bodenschatz E. and Xu H. Elastic Energy Flux by Flexible Polymers in Fluid Turbulence. *Physical Review Letters*, 111(2), July 2013. 88, 89

Xiao Q., Yang N., Zhu J. and Guo L. Modeling of cavern formation in yield stress fluids in stirred tanks. *AIChE Journal*, 60(8):3057–3070, Aug. 2014. x, 2, 92

Xie X., Dietrich N., Fillaudeau L., Le Men C., Schmitz P. and Liné A. Local Hydrodynamics Investigation within a Dynamic Filtration Unit under Laminar Flow. *Chemical Engineering Research and Design*, Feb. 2018. 270

Xu F., Jimenez M., Dietrich N. and Hébrard G. Fast determination of gas-liquid diffusion coefficient by an innovative double approach. *Chemical Engineering Science*, 170:68–76, Oct. 2017. 52

Xuequan E. and Hopfinger E. J. On mixing across an interface in stably stratified fluid. *Journal of Fluid Mechanics*, 166:227–244, May 1986. 84, 85, 86, 106

Yagi H. and Yoshida F. Gas Absorption by Newtonian and Non-Newtonian Fluids in Sparged Agitated Vessels. *Industrial & Engineering Chemistry Process Design and Development*, 14 (4):488–493, Oct. 1975. 11, 92, 161, 162, 163

Yang L., Loubière K., Dietrich N., Le Men C., Gourdon C. and Hébrard G. Local investigations on the gas-liquid mass transfer around Taylor bubbles flowing in a meandering millimetric square channel. *Chemical Engineering Science*, 165:192–203, June 2017. 11, 12

Young S.-L. and Torres J. A. Xanthan: effect of molecular conformation on surface tension properties. *Food Hydrocolloids*, 3(5):365–377, Nov. 1989. 96, 97, 103

Zana E. and Leal L. G. The dynamics and dissolution of gas bubbles in a viscoelastic fluid. *International Journal of Multiphase Flow*, 4(3):237–262, Aug. 1978. 162

Zappa C. J., Asher W. E., Jessup A. T., Klinke J. and Long S. R. Microbreaking and the enhancement of air-water transfer velocity. *Journal of Geophysical Research: Oceans*, 109 (C8):C08S16, Aug. 2004. 291

Zappa C. J., McGillis W. R., Raymond P. A., Edson J. B., Hintsa E. J., Zemmelink H. J., Dacey J. W. H. and Ho D. T. Environmental turbulent mixing controls on air-water gas exchange in marine and aquatic systems. *Geophysical Research Letters*, 34(10):L10601, May 2007. 10, 12

Zarruk G. A. and Cowen E. A. Simultaneous velocity and passive scalar concentration measurements in low Reynolds number neutrally buoyant turbulent round jets. *Experiments in Fluids*, 44(6):865–872, June 2008. 72, 73

Zhang J.-f., Zhang Q.-h., Maa J. P. Y. and Qiao G.-q. Lattice Boltzmann simulations of oscillating-grid turbulence. *Journal of Hydrodynamics, Ser. B*, 29(1):68–74, Feb. 2017. 85

Appendices

Contents

A Fabrication of XG solutions and uncertainty on polymer concentration

The preparation conditions of XG solution are described in section 3.2.2.a. In this appendix, further precision on the equipment and conditions and uncertainties is brought. We can distinguish between two types of preparations: those made for the characterization of polymer properties or interactions with other species (rheology, chemical interactions, spectrofluorimetry ...), and those made for OGT or gas dissolution measurements in the tank.

In both cases, weighting of the necessary XG mass is made by a Δm=0.01 g accuracy precision scale.

A.1 Solutions prepared for tank measurements

XG solutions used in the tank are either prepared by direct dissolution of the appropriate XG mass previously weighted, or by dilution of a previously used solution already present in the tank. In the first case (F1), XG powder is first dissolved in a random small volume of distilled water under moderate stirring, and the concentrated beaker is then emptied into the tank which is then filled up to the fluid depth needed to obtain the targeted concentration. The relative uncertainty on concentration is then

$$\frac{\Delta \mathrm{C}}{\mathrm{C}} = \frac{\Delta \mathrm{V}}{\mathrm{V}} + \frac{\Delta m}{m} \tag{A.1}$$

With ΔV/V the relative uncertainty on fluid volume measurement, built from the uncertainties on depth measurement. Uncertainties range from 10 % at 10 ppm to 7 % at 500 ppm. In the second case (F2), the tank is partially emptied and refilled with clean distilled water. The uncertainty on concentration is then

$$\frac{\Delta \mathrm{C}}{\mathrm{C}} = \frac{\Delta \mathrm{C_0}}{\mathrm{C_0}} + \frac{\Delta \mathrm{DF}}{\mathrm{DF}} \tag{A.2}$$

With $\frac{\Delta \mathrm{C_0}}{\mathrm{C_0}}$ and $\frac{\Delta \mathrm{DF}}{\mathrm{DF}}$ the relative uncertainties on respectively concentration of the solution initially in the tank and on the dilution factor. This last quantity is related to the precision on depth measurement. Solutions prepared by this method have a maximum uncertainty on concentration of about 12 %.

A.2 Solutions prepared for characterization steps

XG solutions used in characterization experiments have been prepared either by direct dissolution of weighted XG mass, or by dilution of highly concentrated stock solutions. In the first case (F3), equation (A.1) is also used, but since smaller volumes of solution are prepared (of the order of 0.1 L), weighted masses m are much smaller than those needed for the full tank experiments. This method is thus limited to XG concentrations over 100 ppm, and relative uncertainties are important: from 20 % at 10000 ppm to 70 % at 100 ppm (uncertainty decreases with the weighted mass).

In the second case (F4), 1 L of stock solution at 10000 ppm is prepared, at a relative concentration uncertainty of $\Delta \mathrm{C_0}/\mathrm{C_0}$=0.15 %. This stock uncertainty is essentially due to the weighting precision (0.1 %), with a minute uncertainty brought by volumetric flask used for volume measurement (0.05 %). The final uncertainty on concentration is then estimated using equation (A.2), with $\frac{\Delta \mathrm{DF}}{\mathrm{DF}}$ depending on the equipment used for dilution. Micro-pipettes

with a precision up to the µL and volumetric flasks are used, and so the final uncertainty is always below 1 %.

Table A.1 summarizes the preparation method and order of magnitude of concentration uncertainty for each type of measurements presented in this thesis.

Method	Maximum relative uncertainty	Experiments	Chapters, section, figures
F1,F2	12 %	OGT PIV, SPIV for dissolution	Chap. 4, Chap. 3 sec. 3.4
F3	70 %	XG characterization (pH)	Chap. 3 sec.3.2.2, fig. 3.4
F4	1 %	XG characterization (rheology, surface tension, chemistry), PLIF developments	Chap. 3 sec.3.2.2, Chap. 2, Apdx. D.5

Table A.1 – Sumary of $\Delta C/C$ uncertainty levels

B Tank and grid design

B.1 General design

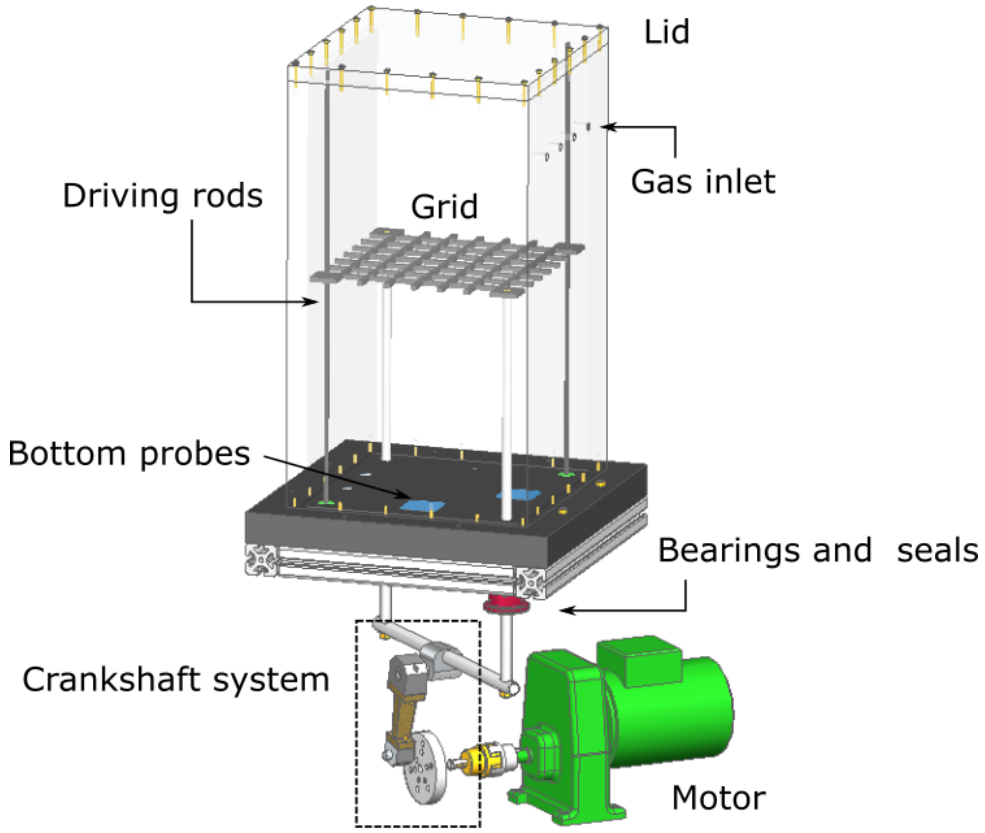

Figure B.1 – Computer aided design of the oscillating grid setup

B.2 Crankshaft oscillating system

B.2.a Design

Our driving system includes a Leroy-Sommer Motor associated with a variable speed unit to set it's rotation speed. A crank disk is fixed on the drive shaft. It is pierced at different distances from its axis, allowing for the variation of the eccentric r for the crankshaft system. This allows to select the stroke among thirteen values between S = 2.5cm and S = 7.3 cm (Cosson, 2014). A rod of length l is connected to the selected disk's hole at one end, and to the grid's driving rods to the other. The length of this crankshaft rod was chosen so that the crankshaft parameter $\xi = l/r$ lays between 3.0 and 9.0. The kinematic diagram of the whole system is presented on figure B.2. An example of theoretical temporal profiles for $\xi = 4.6$ and $f = 1$ Hz is presented on figure B.3.

B.2.b Grid motion equations

As mentioned in the manuscript, velocity and acceleration variations produced by crankshaft systems are not purely sinusoidal. Additional velocity frequency (figure B.3d) are

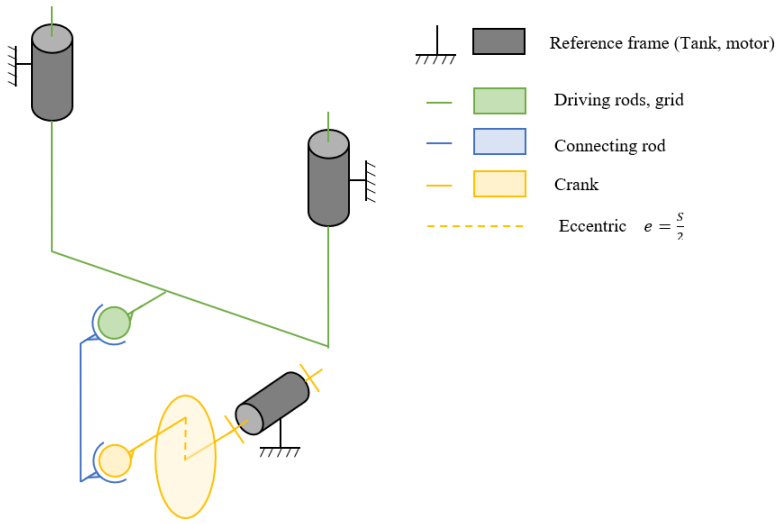

Figure B.2 – Kinematic diagram of the oscillation system

introduced as compared to sinusoidal motion that can be achieved with cam-rod systems or linear motors. The expression for the grid position s_g, velocity v_g and acceleration a_g are :

$$\begin{aligned} s_g &= r\left(sin(\theta) + \sqrt{\xi^2 + cos(\theta)^2}\right) \\ v_g &= \omega_g.r.cos(\theta)\frac{1-sin(\theta)}{\sqrt{\xi^2+cos(\theta)^2}} \\ a_g &= \omega_g.r^2.\left(-sin(\theta) - \frac{cos(\theta)^2-sin(\theta)^2}{\sqrt{\xi^2-cos(\theta)^2}} - \frac{sin(\theta)^2.cos(\theta)^2}{\sqrt{\xi^2-cos(\theta)^2}^3}\right) \end{aligned} \tag{B.1}$$

With θ and $\omega_g = \theta/t$ the rotation angle and velocity of the motor, r the eccentric radius, l the rod's length and ξ the crankshaft parameter. The temporal variations of s_g, v_g and a_g are plotted in figure B.3 along with their frequency spectrum. The additional frequency is thus twice the main oscillation frequency and is all the more visible that the ξ value is small. The grid's velocity has been measured by the means of an high speed camera for the same theoretical grid frequency and ξ value. The main frequency actually measured is $f = 1.03$ Hz which is very close to the wanted one. The measured additional frequency inherent to the crankshaft design is exactly twice the main frequency, namely 2.06 Hz, as shown of figure B.3d. The slight difference between the measured frequency and the targeted one comes from the coarse tuning of the motor's encoder.

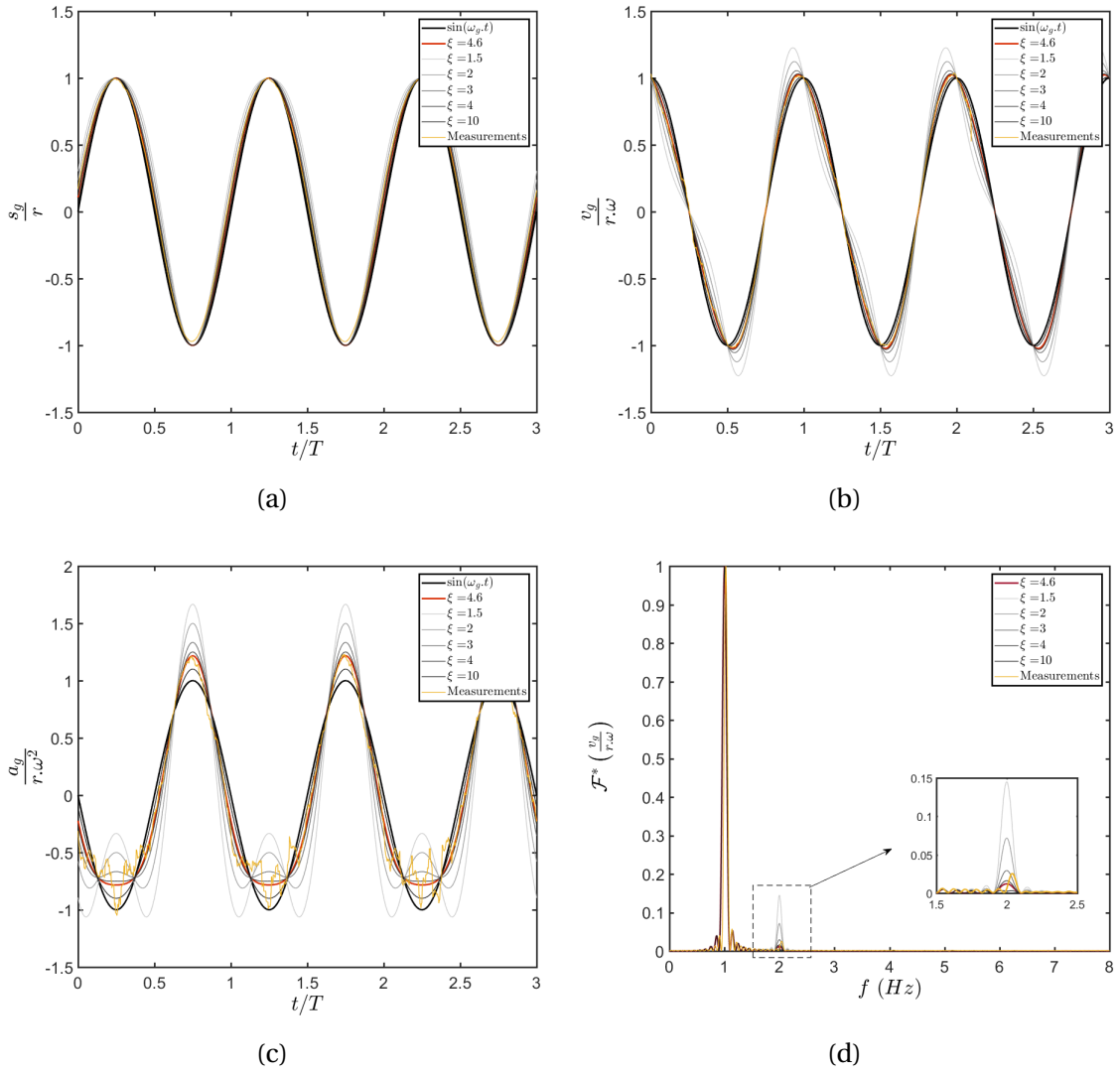

Figure B.3 – Normalized position (a), velocity (b) and acceleration (c) of the grid, along with its velocity spectrum normalized by its maximum value (d). Dark curve is the reference sinusoidal velocity, profiles computed according to equations (B.1) for different ξ are shown in gray and red (for ξ = 4.6). Orange curve are measured values for a ξ = 4.6 design.

C POD analysis of OGT

C.1 Introduction to Proper Orthogonal Decomposition (POD)

The goal is here to apply POD analysis in different regions of the flow in the grid stirred tank in both water and DPS, to see if the results are consistent with the ones obtained using phase averaged measurements, and to identify the additional information that can be deduced from such an analysis. Proper Orthogonal Decomposition (or POD) is a linear procedure that decomposes data, here a set of vector fields, into a modal base. It is now established as a quick and efficient tool for the study of turbulent flows (Gabelle et al., 2017; Graftieaux et al., 2001; Hamdi et al., 2018). In particular, it has been recently used in stirred tanks to identify periodic flows induced by blade motions and study their interactions with mean flows and turbulence (de Lamotte et al., 2018; Liné et al., 2013). However, it has been used only once to study oscillating grid turbulence (Wang et al., 2016) in a different setup than the present study (two grids). No conclusion on oscillatory flows in OGT has been drawn from this previous study.

The method applied here for decomposition is the one mostly used in fluid mechanics study, called the snapshot method. It has been developped by Sirovich (1987) and is explained in detail in several articles (de Lamotte et al., 2018; Gabelle et al., 2013, 2017). Its principle is briefly recalled here.

The processed data, here the velocity field, is decomposed into a sum of temporal amplitudes and spatial modes:

$$\mathbf{U}(x,t) = \sum_{i=1}^{\mathrm{N}} \theta^i(t)\boldsymbol{\phi}^i(x) \tag{C.1}$$

Where N is the number of modes needed to properly reconstruct instantaneous velocity fields, typically of the order of $400-1000$ (Gabelle et al., 2013) Instantaneous velocity fields obtained by PIV then have to be reorganized in the form of a sequence of snapshots. To do so, the $2\mathrm{RC}\times\mathrm{N}$ snapshot matrix $\mathrm{S_M}$ is written as a column-wise assembly of instantaneous velocity components, where R and C are the number of rows and columns of the vector field.

The POD algorithm then searches for the set of modes that gives the optimal approximation of each instantaneous velocity field in a least square sense, while satisfying the condition that each mode has to be orthogonal to each other:

$$\min_{\phi}(\mathbf{U_f} - \sum_{i=1}^{\mathrm{N}} \theta^{f,i}\boldsymbol{\phi}^{f,i}) \tag{C.2}$$

and

$$(\boldsymbol{\phi}_i)^{\mathrm{T}}\boldsymbol{\phi}^j = \boldsymbol{\delta}_{ij} \tag{C.3}$$

where f is the index of the instantaneous field, $(\boldsymbol{\phi}^i)^{\mathrm{T}}$ the transpose of mode i and $\boldsymbol{\delta}_{ij}$ the Kronecker delta.

According to Sirovich (1987), this is equivalent to an eigenvalue problem and can be written as

$$\mathbf{R}\boldsymbol{\phi} = \lambda\boldsymbol{\phi} \tag{C.4}$$

Where $\mathbf{R} = \frac{1}{\mathrm{N}}\mathbf{S_M}(\mathbf{S_M})^{\mathrm{T}}$ is the two point cross correlation matrix between velocity components, and λ is the eigenvalue associated to mode ϕ, expressed in m^2/s^2. λ quantifies the energy content of its associated mode. It is used to sort out the modes from the most to the least energetic.

Once decomposition is performed, instantaneous velocity fields can be estimated by reconstruction up to a given number of modes using equation (C.1) with an order of summation lower than N. This allows to suppress small scale turbulence (high order modes), measurement noise (higher order modes), or even oscillatory motions (coupled and/or oscillatory modes, see the next paragraph). For POD decomposition of time resolved PIV measurements, it is possible to use the temporal amplitude of modes θ to interpolate instantaneous velocity fields between measured ones. Since POD is a linear procedure, virtually any combination of mode can be used to isolate a relevant set of velocity scales, assuming that one can give a physical meaning to this collection of modes.

POD has been widely used since the end of the 2000's as an alternative to phase resolved measurements for the identification of trailing vortices and oscillatory flows in stirred tanks (de Lamotte et al., 2018; Gabelle et al., 2013, 2017; Liné et al., 2013; Moreau and Liné, 2006). Its main advantage is that it requires only a small number of velocity field (N in equation (C.1)) and no knowlege of the blade position for each recorded image, while phase resolved measurement require complex timing setups and the accumulation of much more instantaneous fields in order to achieve statistical convergence for each blade position. The number of image needed is typically N_k greater than for POD, with N_k the number blade position of measurement per phase. Gabelle et al. (2013); Liné et al. (2013) used the modes energy spectrum, i.e the evolution of eigenvalues as a function of the mode number, to identify modes that could correspond to the oscillatory component measured using the triple decomposition technique in a stirred tank. They showed that oscillatory motion is associated to a pair of successive modes of equivalent energy, in their case (for stirred tank with water and dilute polymer solution) mode 2 and 3. A weaker oscillatory behavior associated to modes 4 and 5 is also found (Gabelle et al., 2017; Xie et al., 2018). In a slightly different configuration (two impellers stirred tank), de Lamotte et al. (2018) also identify trailing vortices using paired modes 2 and 3, and also identify another oscillatory motion associated with higher order modes. It is therefore well established that organized motion in stirred tanks corresponds to modes 2 to 5. POD modes corresponding to organized motion can also be identified using their temporal coefficient $\theta(t)$. If the mode is oscillatory, then its temporal coefficient plotted against time should exhibit a sinusoidal trend. The probability density function of $\theta(t)$ should resemble that of a sinus or a cosinus, whereas the PDF of a "turbulent" mode approaches a Gaussian shape. The scatter plot of the θ coefficients of two coupled oscillatory modes are shown to organize in a zero circle in the θ_i,θ_{i+1} space (Gabelle et al., 2017).

It is worth noticing that the for studies cited above, the ensemble velocity average is not subtracted from the velocity fields, hence the first mode corresponds to the average velocity. In this work however, mean velocity is removed from instantaneous fields prior to POD decomposition, hence the average flow correspond to mode 0.

Once mean flow and oscillator motions are identified, higher order modes remaining can only correspond to turbulence (and noise). According to De Angelis et al. (2003); Liné et al. (2013), the eigenvalue value spectrum of a POD decomposition of a turbulent flow presents a $-11/9$ slope at high modes when plotted on a log-log scale. This slope can in some ways be linked to the famous homogeneous isotropic turbulence spectral slope of $-5/3$ (De Angelis et al., 2003).

C.2 Methodology

The POD method used here is the snapshot method implemented in DaVis 8 software (LaVision, 2011b). The average over 1000 fields is computed and subtracted to instantaneous fields. The POD decomposition is performed over 1000 modes using the double precision

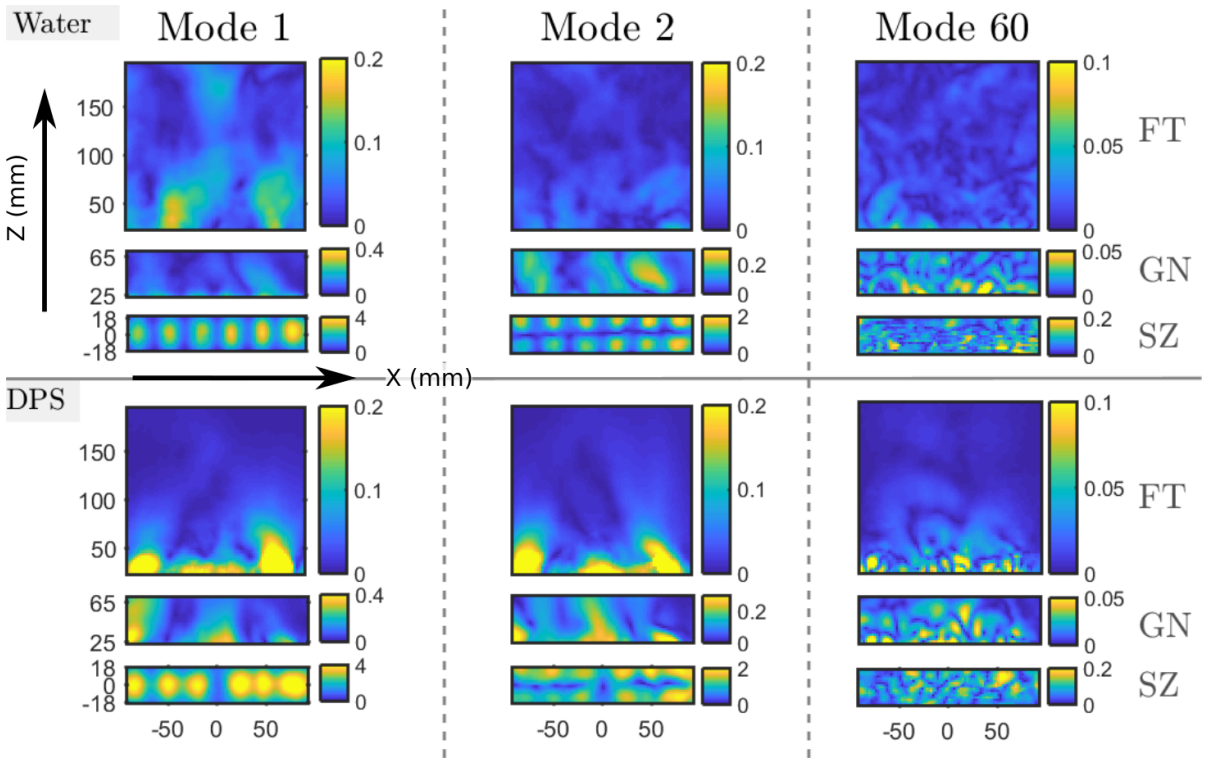

Figure C.1 – Example of POD modes: modes 1,2 and 60 for regions "Sweep Zone" (SZ), "Grid Neighbourhood" (GN) and "Full Tank" (FT), in water (top half) and DPS at 100 ppm concentration (bottom half). The colormap represents the local mode magnitude $\sqrt{(\phi_x^i)^2 + (\phi_z^i)^2}$ in m/s. Note that these are not reconstructed velocity magnitudes

option. Reconstruction can then be performed with a number of modes between 1 and 1000. Reconstruction using a specific set of modes excluding the first ones is deduced from linear combination of two other reconstructions. For example the reconstruction using modes 2 and 3 only is computed as the reconstruction up to mode 3 minus the reconstruction based on mode 1 alone.

POD is applied as described above to three regions of the flow in plane B0:

- the sweep zone (SZ) which is defined as the area covered by the grid's motion
- the grid neighborhood (GN) defined as the upper part of CG region minus the sweep zone (GN=CG-SZ)
- the full tank (FT) ROIs defined in figure 3.11

C.3 POD Modes

The first modes (1 and 2) and a higher number mode (chosen arbitrarily as 60) are represented in figure C.1 for SZ, GN and FT regions, for water and dilute polymer solution. In both liquids, modes 1 and 2 in the SZ region are structures according to the grid design: 6 regions of high magnitude corresponding to the 6 mesh "holes" in plane B0 are visible. Even though the mean velocity field has been subtracted from instantaneous fields prior to POD decomposition, modes 1 and 2 in the FT region show a magnitude field somehow similar to the mean flow intensity, in both water and DPS. Mode 60 is supposed to be associated with turbulence, since it is a high order mode. Indeed, the structures observed are much smaller

than for modes 1 and 2, and their magnitude decays when moving away from the grid. Moreover, in all three regions, the typical size of a high magnitude patch seems smaller in water than in DPS (see for example mode 60, region SZ in water and DPS).

This seems consistent with the general observation that polymer tends to promote larger organized structures and damp the small scales of turbulence (see section 3.1.2, Wang et al. (2016)). Turbulence in dilute polymer solutions sees its energy distribution between scales modified. This should be evidenced in the POD decomposition not only by a modification of the high mode structures, but also by an adaptation of the mode by mode energy distribution.

C.4 Energy distribution

Figure C.2 shows the eigenvalue spectrum of POD modes, that is to say the magnitude E_{λ_i} of each modes divided by the sum of all eigenvalues $\sum_i E_{\lambda_i}$. This ratio quantifies the portion of total kinetic energy included in each mode. The first modes are representative of large coherent structures (organized motions) and so contain most of the energy. This is especially the case close to the grid where the grid's motion forces the large structures: the first modes have a higher energy share in the SZ region than in the CG region, and in the CG region than in the FT region. The higher order modes are then said to represent turbulence. The -11/9 slope predicted by De Angelis et al. (2003); Liné et al. (2013) representative of homogeneous isotropic turbulence is also plotted on the the figure for illustration.

In dilute polymer solutions, this energetic dominance of the first modes seems to be enhanced: the first eigenvalues share is always higher in the non-Newtonian case than in water, and the eigenvalue spectrum curves for DPS and water cross at a given mode. Lower order modes than this crossover values see their energetic share amplified in DPS whereas higher order modes have their impact decreased. This trend can also be visualized by plotting the cumulative energy as a function of the number of modes, as in figure C.3. It shows that cumulative energy converges towards its total value quicker in DPS than in water, and that for every region of the flow. Fewer modes are necessary to capture most of the kinetic energy in DPS than in water for a given region of the flow. Energy concentrates in the first few modes. This has also been evidenced by De Angelis et al. (2003) while studying the drag reduction of polymers in turbulent channel flows, and by Wang et al. (2016) in two oscillating grids turbulence of viscoelastic fluids.

A final conclusion can be drawn using the eigenvalue spectrum. By plotting for each region of the flow the eigenvalue spectrum of DPS $E_{\lambda_i}^{DPS}$ normalized by the corresponding eigenvalue spectrum for water $E_{\lambda_i}^{w}$ (figure C.4), one shows that for the first modes, the energetic enhancement is all the more significant for the FT region, which does not include the sweeping zone of the grid. Indeed, the negative slope of $E_{\lambda_i}^{DPS}/E_{\lambda_i}^{w}$ is increased for FT as compared to the slopes of CG and SZ. This observation leads to the conclusion that the enhancement of energetic share of the first mode can not only be attributed to organized motions generated by the grid (which are dominant in SZ and CG regions), but is also a feature of turbulence in DPS. Small scales of turbulence are damped by the polymer, as previously observed in fundamental turbulence studies (Liberzon, 2011; Liberzon et al., 2006) and also using POD analysis (De Angelis et al., 2003; Wang et al., 2016). This translates into a decrease of the high POD modes energy, that are indicators of these small scales. For regions where the grid forcing is not directly felt, the eigenvalue spectrum is intrinsically flatter (see figure C.2) since mean and organized motion caused by the grid are weaker. In other words, even in Newtonian flows, the energy share is quite balanced between modes in the FT region whereas in the SZ region, energy is more contained in low order modes because of the grid.

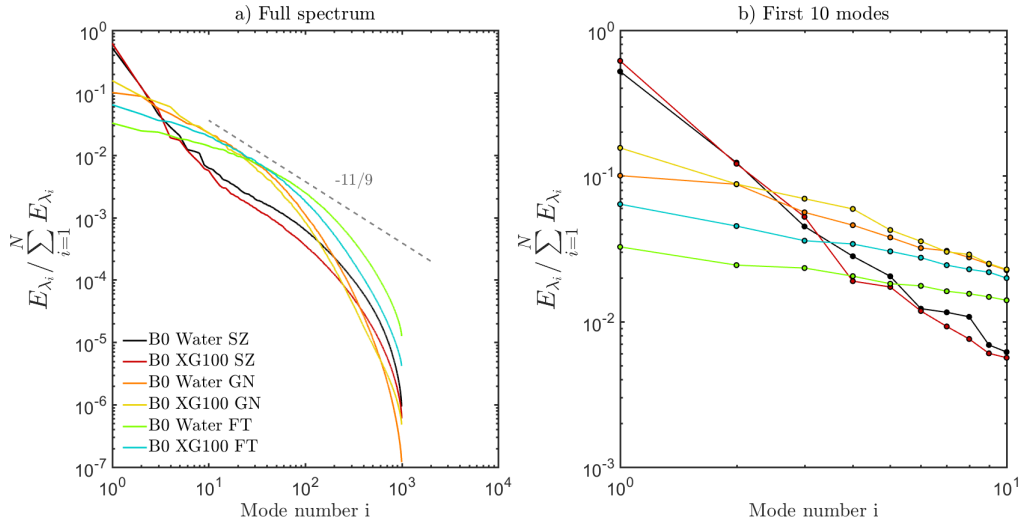

Figure C.2 – POD eigenvalue spectrum. a) Full spectrum, b) zoom over the 10 first modes

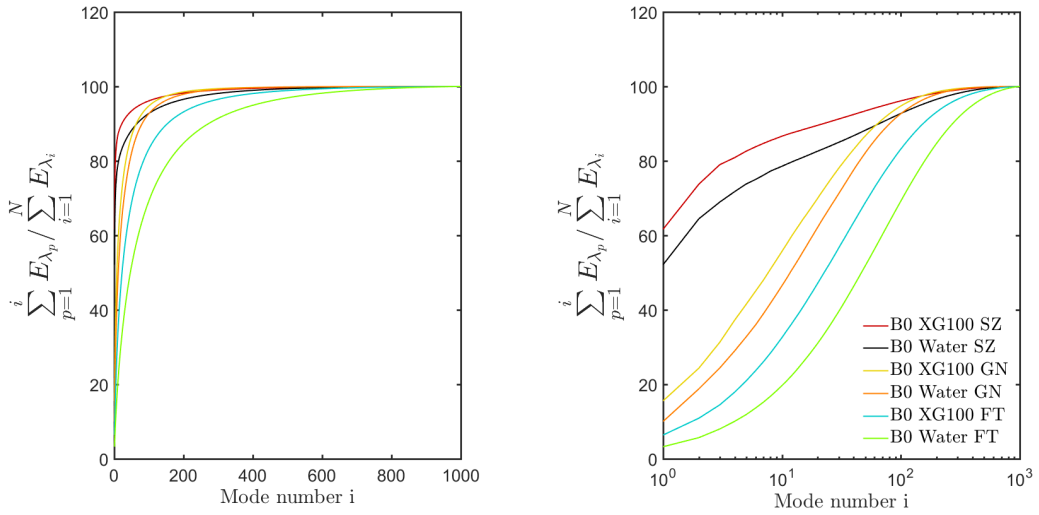

Figure C.3 – Cumulative energy contained in the POD modes, i axis in linear scale (left) and log scale (right)

A damping of small structures is thus more visible in the FT region for which these structures are significant in the flow's energy, than in the SZ region where they are less influential.

C.5 Identification of organized motion

Let us recall the criterion for the identification of oscillatory flows of the flow in stirred tanks. Oscillatory components are the results of coupled modes for which:

- two successive eigenvalue value are close to each other in the eigenvalue spectrum (the coupled modes have the same energetic impact).
- the temporal coefficient of each mode i, $\theta_i(t)$, shows a sinusoidal trend when plotted versus time, and its PDF is shaped like that of a sinus or a cosinus.
- the scatter plot of two coupled modes arranges in a circle in the θ_i-θ_{i+1} space.

From the eigenvalue spectrum figure C.2, no couple of successive eigenvalue of equivalent magnitude can easily be extracted, and that even in the SZ region where oscillatory motion is known to be dominant. The second identification criterion yields better results. Indeed, the plot of temporal coefficient intensity as a function of the field index (replacing here time since the measurements are not time resolved) allows to identify a clear sinusoidal behaviors for the first mode in the SZ region for both water and DPS. Modes 2 and 3 also seem to have a periodic behavior even if no obvious sinusoidal trend can be extracted. In the GN region for water, the sinusoidal behavior of mode 1 disappears and no periodic behavior is observed for the following modes. In the GN region for DPS however, an oscillatory behavior can be observed for mode 1 and 3.

The probability density function (PDF) of the values of θ^i coefficients over 1000 instantaneous fields for the same set of modes, represented by the histogram plots of figure C.6 completes the information on periodic mode behavior. The PDF of mode 10 always approaches a Gaussian shape, characteristic of random distribution. Coefficients θ^1 for water and DPS in the SZ region have a flat shaped distribution corresponding to their (poorly sampled since not time resolved) sinusoidal like behavior. The PDF of coefficient θ^2 and θ^3 also suggest a non-random time distribution of the mode in the SZ region, and so a possible periodicity. All PDFs in the GN region for water are bell-shaped, which is expected from figure C.5. Finally, PDFs of temporal coefficients for modes 1 and 3 in DPS for the GN region also exhibit a quasi-Gaussian shape even if their "time" series plot looks periodic.

To a first approach, all these observations are consistent with the previous remarks based on phase averaged measurements: oscillatory motion can logically be found in the sweep zone region, but is strongly damped when moving away from the grid, and as a consequence almost invisible in the GN region (for water at least). Polymer has an organizing effect on the flow which tends to promote this oscillatory motion and keep it significant in the vicinity of the grid. However, the distinction between periodic and non periodic modes is sometimes arduous due to the poor temporal resolution of our measurements, and also to the periodic behavior of modes that can be less pronounced than in stirred tanks. A conclusion is that

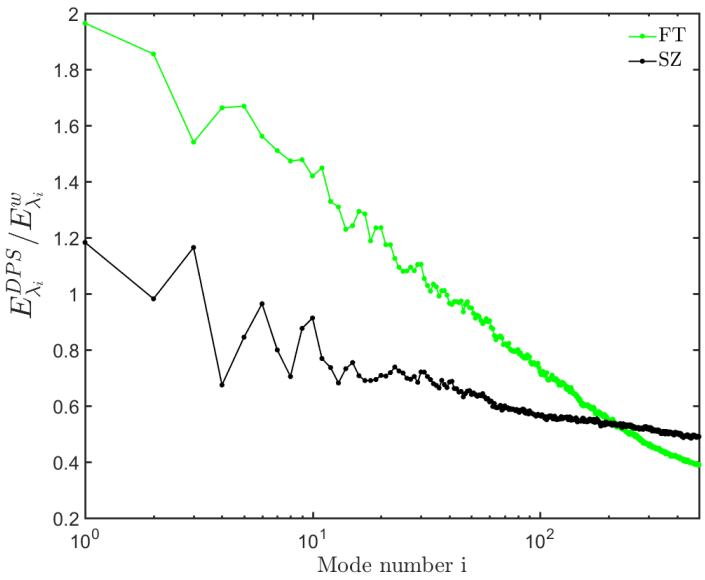

Figure C.4 – POD eigenvalue spectrum of dilute polymer solution normalized by the water spectrum for the three regions of the flow

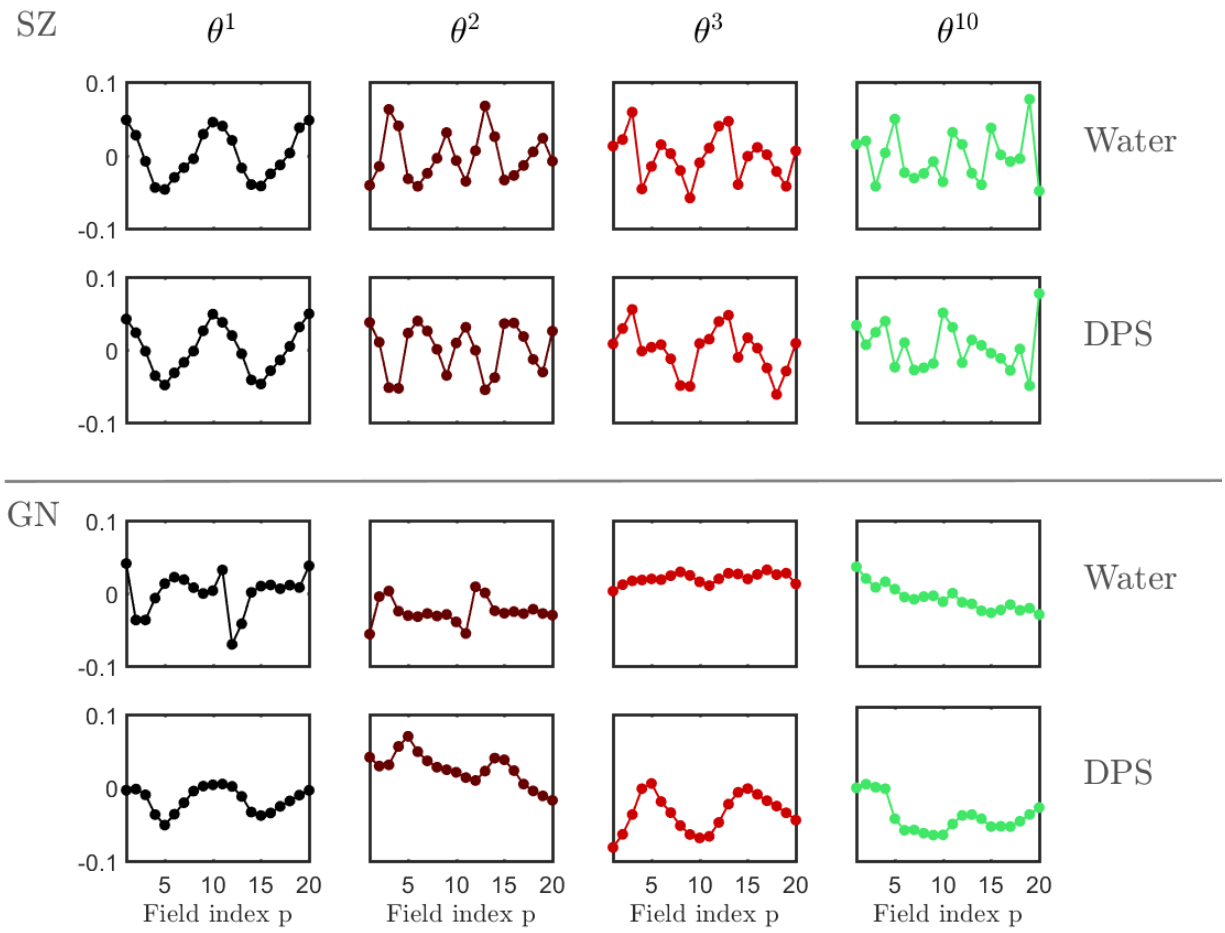

Figure C.5 – θ^i coefficients as a function of the instantaneous field index. Modes 1,2 and 3 are represented as modes for which a periodic behavior can be expected. Mode 10 (chosen arbitrarily among highest mode numbers) is used as a reference for non periodic modes.

evolution and PDF of θ coefficient alone may not be sufficient to identify clearly periodic modes. A complementary step is thus to check whether some modes are coupled with others or not.

No circular arrangement similar to the one found for oscillatory motion in stirred tank can be observed, for any region, fluid, or pair of successive coefficients (θ^i,θ^{i+1}). This is to some extent not surprising since in the stirred tank case, circular organization of the temporal coefficients is evidenced for a pair of successive modes that exhibit an equivalent magnitude in the eigenvalue spectrum, and no such pair of modes is observed here (figure C.2). In the SZ region for both water and DPS however, the scatter plots of θ^1 versus θ^2 and θ^2 versus θ^3 values are not randomly distributed as one would expect for uncoupled modes, but arrange in a more complex characteristic pattern, which can also be seen in three dimension by plotting the 3D scatter plot of θ^1 versus θ^2 versus θ^3 values (see figure C.7). The dispersion around those defined patterns is quite small. (θ^1,θ^2) pattern has a similar infinity symbol shape for water and DPS, with a variation of the two lobes' sizes and of the crossing point location. (θ^2, θ^3) patterns also include two lobes, but are yet quite different in the two fluids. In the GN region, this settlement disappears. The specific shape of these structures is yet to be explained. The observation of figure C.7 still allows to formulate two hypothesis:

- These shapes are a consequence of the strong oscillatory motion observed in the SZ region but not in the GN region, and this motion can not be described by a simple

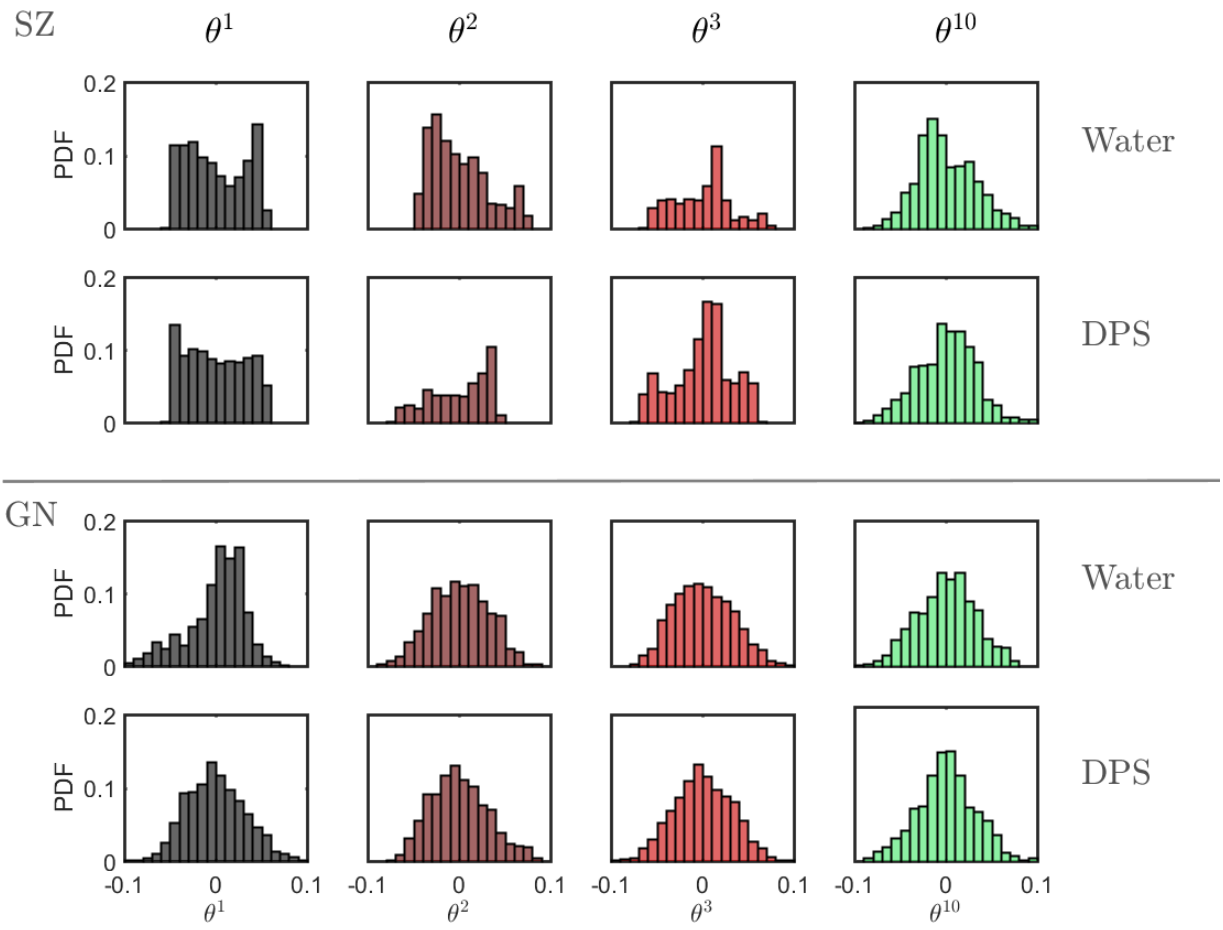

Figure C.6 – Histogram plot of θ^i coefficient values for 1000 instantaneous velocity fields. The same modes as figure C.5 are represented.

two-mode coupling.

- The presence of polymer modifies the features of oscillatory motion in the SZ region. This is expressed in POD decomposition by a variation in the coupling between low order modes

As one can see, organized motion is difficult to identify using the common criterion for stirred tanks. One of the interest of POD is that it makes it possible to reconstruct velocity field using a specific set of modes. It is thus easy to remove the oscillatory component from non phase resolved measurements, provided that the modes responsible for oscillatory motion can be identified. The main issue here is that this identification is still needed. It is now admitted that oscillatory motion is described by low order modes. What can be done is an approximate identification of the sum of modes needed to reconstruct the oscillatory motion, by comparing reconstructed velocity fields using N modes with the oscillatory motion visualized through phase averaged measurements.

C.6 POD Reconstruction of oscillatory motion

POD analysis is performed on the CG region (SZ+GN regions) using the same procedure as for the other regions. Reduced order POD reconstruction of FT measurements are performed

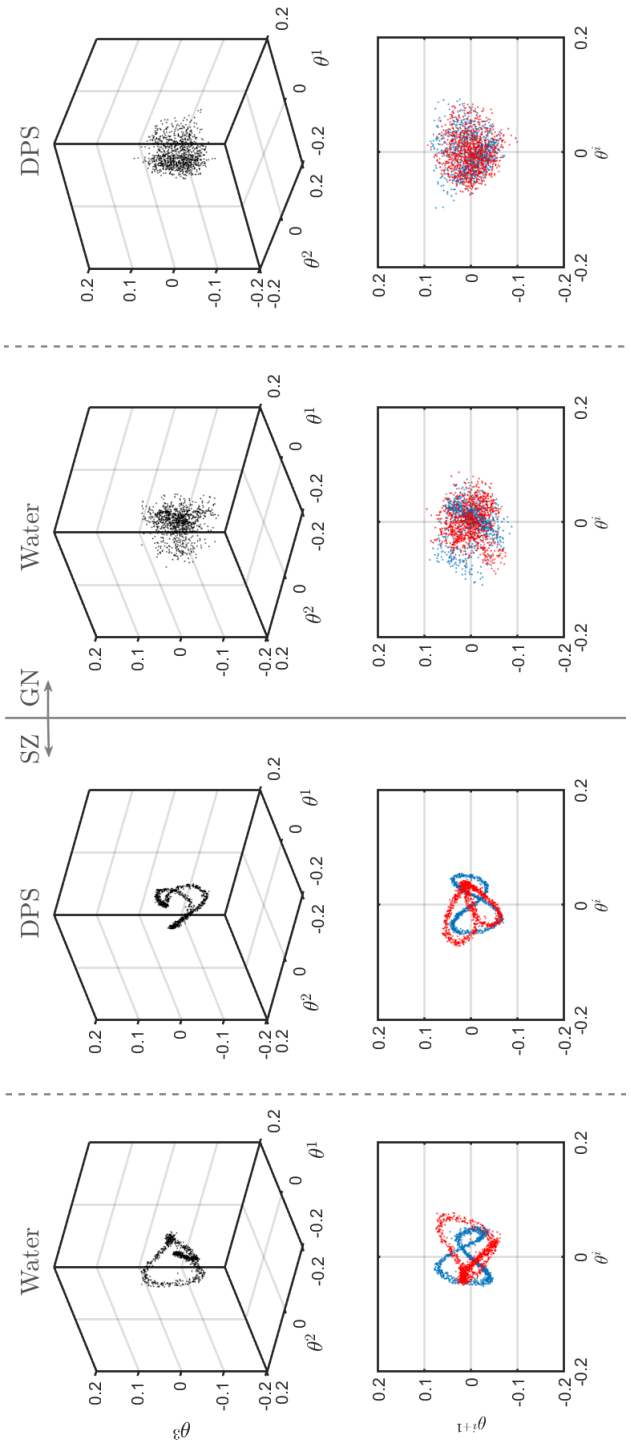

Figure C.7 – 2D and 3D scatter plots of (θ_1,θ_2) (blue), (θ_2,θ_3) (red) and (θ_1,θ_2,θ_3) (black) for water and DPS in the SZ and GN regions

using M_R modes, with $1 < M_R < 10$. The average velocity field is subtracted from the reconstructed instantaneous velocity fields. Instantaneous fields reconstructed are then compared to phase oscillatory velocity fields deduced from phase averaged CG measurements. The quantity used here for qualitative comparison of modes is the normalized vorticity of the vector field $\Omega_n^* = \Omega^* / \max(\Omega^*)$ with $\Omega^* = \nabla \wedge \mathbf{u}_\mathbf{R}^*$, where the vector field can be the measured

oscillatory motion $\mathbf{u}^*$ or the reconstructed one $\mathbf{u}^*_\mathbf{R}$.

The first mode alone is clearly not sufficient to reconstruct oscillatory motion. However for the water case, the fields are visually equivalent for $M_R = 3$. With a higher number of modes, large voticity structures begin to appear far from the grid on the reconstructed fields whereas they are not present on the oscillatory velocity fields. These are supposedly the large structures of turbulence captured by the first non oscillatory POD modes. In DPS, it seems to take a higher number of modes to converge towards the measured oscillatory velocity field. Qualitatively, one may say that 3 modes are not enough to capture the main vortices induced by the grid motion and the periodic vortex at on both sides (around Y = 30 mm and X = ±60 mm), but 4 or 5 seem necessary. Reconstruction for a higher M_R do not seem so different from the one at $M_R = 5$. It thus seems possible to reconstruct the periodic fluctuations of the flow using the first modes of POD. By setting a qualitative limit number of modes M_R required to capture it, one associates the first M_R modes to oscillatory motion and the following ones to turbulence. The limits of this qualitative approach should clearly be stated. First is the fact that the comparison between reconstructed and reference fields is here purely visual, it could be improved by using a matching criterion on relevant quantities (vorticiy as used here, velocity norm, or more elaborate indicators). The second and more important remark is that until appropriate criterion have been established, it is not possible to state with confidence if a mode is periodic or not, coupled with others or not. They can only be sorted by their energetic impact and thus according to the coherence of structures that they represent. The border between large scale coherent structures of turbulence and large scale organized periodic motion is thus not clear.

Taking a closer look at figure C.8 interesting information about the difference between water and DPS regarding periodic motion may be extracted. A higher number of mode seems needed to capture oscillatory velocity in DPS than in water. Hence, not only is energy concentrated in low order modes for DPS, as evidenced by the eigenvalue spectrum, but the complexity of organized motion in DPS is also higher than in water since more coupled modes are needed to describe it. This is consistent with the observation of the phase averaged measurements: vorticity structures such as the ones at Y = 30 mm and X = ±60 mm are present in DPS and not in water. Even the vorticity repartition in the wake of the grid bars is slightly different, with an increase in central and side wakes intensities(this feature is also observable in the visualisation of POD mode 1 in the SZ region, figure C.1).

C.7 POD reconstruction of turbulence properties

The task in this section is to use POD as an alternative option to phase averaged measurements in the identification of oscillatory motion. It seems that oscillatory motion is described by the more or less complex combination of low order modes. Here however, unlike the stirred tank case, the exact modes to combine and the nature of their coupling remains unknown. The previous paragraph shows that oscillatory motion can be roughly estimated by POD reconstruction of the velocity field using the first few modes together, without further precision on coupling. By setting a limit number of mode considered to be part of the oscillatory motion, say 3 or 6 modes for example, one implicitly sets a limit under which modes are considered periodic and non-turbulent, and above which they are considered as turbulent and non periodic. It is thus possible to use high order modes only for the reconstruction and estimation of turbulence properties, but there is a risk that large scales of turbulence have been artificially removed by suppressing the low order modes. What is proposed here is to check the influence of low order mode removal on the statistical properties of reconstructed velocity fields. Partially-reconstructed velocity fields are then calculated by

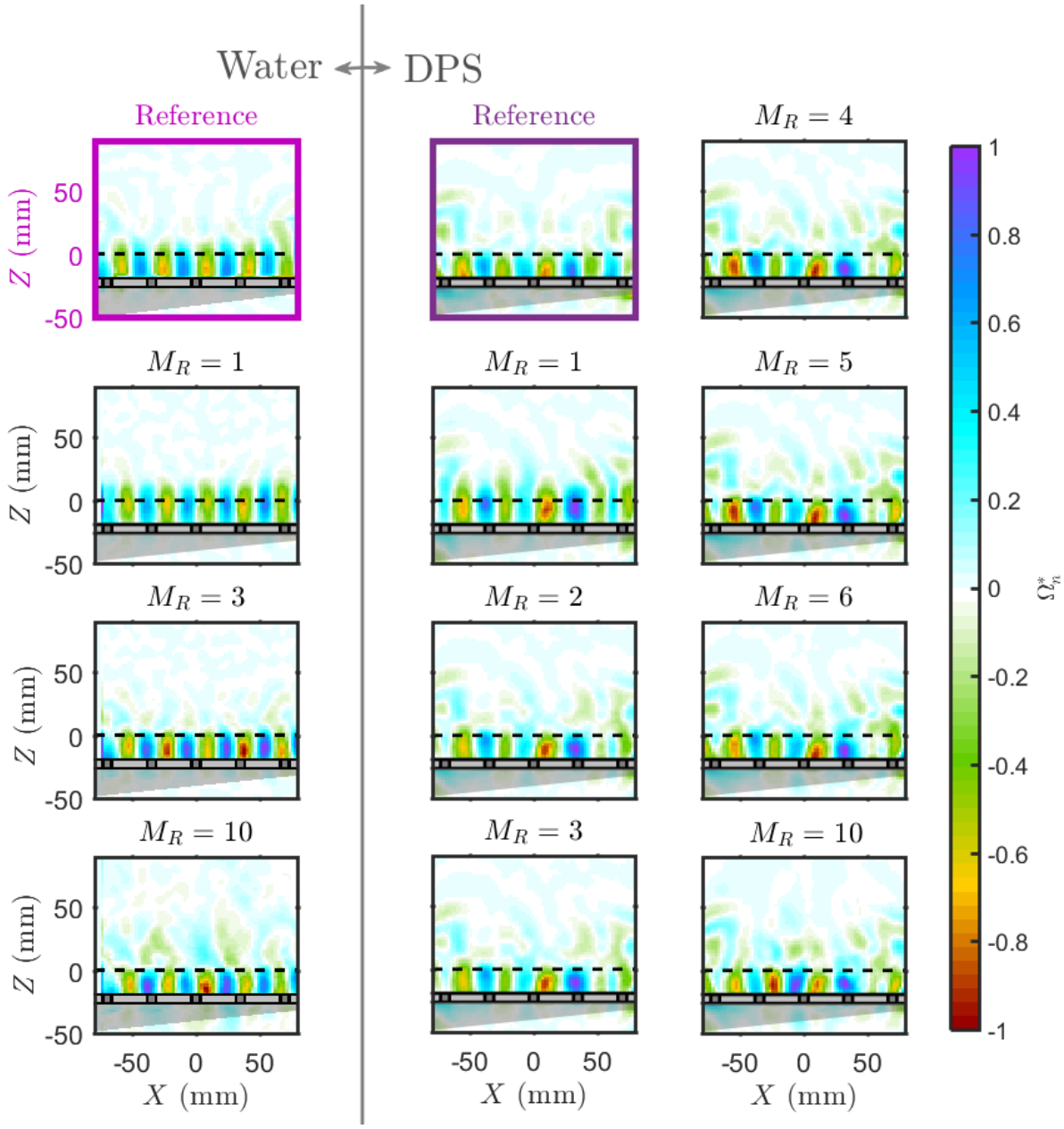

Figure C.8 – Comparison between oscillatory velocity fields obtained using phase averaged measurements (oink and purple framed "Reference") and and POD reconstruction with M_R modes between 1 and 10. All fields are represented for a grid position at the bottom of its stroke (Z = −S/2)

subtracting the reduced order models to the full reconstruction. By this method one gets velocity fields estimated using modes $M_R + 1$ to 1000. These are denoted as $M_R + 1 - end$ POD reconstructions. The RMS velocity profiles along the horizontal and vertical direction are then estimated by horizontal averaging over the central part of the FT region of the rms velocity fields.

Vertical profiles of $\left\langle u'_{x,M_R+1-end} \right\rangle_{rms}$, $\left\langle u'_{z,M_R+1-end} \right\rangle_{rms}$ for water and DPS in the FT region are plotted in figure C.9. The main effect of low order mode removal on reconstructed fields is visible in this figure. It is a decrease of the rms velocities and TKE. Removing the most energetic modes from reconstruction leads to a decrease in the rms of fluctuating velocity. This is not surprising since the first POD modes are the ones carrying most of the fluctuating kinetic energy. The effect is all the more significant in the DPS case where low order

modes have an increased energetic impact. In order to get beyond simple energy removal effects, one may consider the profiles of rms velocity $\left\langle u'_{x,\mathrm{M_R}-end} \right\rangle_{rms}$ and $\left\langle u'_{z,\mathrm{M_R}-end} \right\rangle_{rms}$ corrected by the energy loss due to mode removal (figure C.9). Here the chosen scaling is a division by a factor $\sqrt{1-e}$ where $e = \frac{1}{100} \frac{\sum_{p=1}^{\mathrm{M_R}} \mathrm{E}_{\lambda_p}}{\sum_{i=1}^{\mathrm{N}} \mathrm{E}_{\lambda_i}}$ is the portion of kinetic energy carried by the removed modes derived from figure C.3. The scaling factor $\sqrt{1-e}$ thus corresponds to a reference velocity built on the total energy carried by the remaining modes. Scaled rms velocity profiles are plotted in figure C.9, and are found to collapse in a single profile with a well defined power law region characteristic of oscillating grid turbulence (see previous section). Removing the first modes before velocity reconstruction does not affect the shape of the rms velocity profiles. It means that the contribution of the first modes to the rms has the same dependency on the grid distance than that of the following modes, that it to say the one depicted by the normalized profile. It either means that the decay law for oscillating velocity fluctuations is the same than the one for turbulent velocity fluctuations, or that the first modes are already representatives of turbulence. Here the most likely conclusion is that in the FT central region, oscillatory motion is nonexistent, or too weak for it to be captured efficiently by POD.

It is worth noting that for this FT region, no phase-resolved measurement is available, so there is no way to check that this oscillatory motion is indeed not present. However phase averaged measurements in the CG region have shown that periodic fluctuations are strongly damped when moving away from the grid, and are very low outside of the SZ region in the central part of the tank. It is thus not surprising that no oscillatory behavior is captured by POD in the FT central region. Applying a similar reconstruction procedure to the SZ, or GN region would probably lead to normalized rms profiles highly dependent on the presence or removal of the first POD modes.

C.8 Conclusion on POD analysis and future investigations

The following conclusion can be drawn from this POD analysis of OGT in water and DPS.

- Most of the kinetic energy of the flow is contained in the first POD modes. This is all the more true for regions of the flow close to or containing the grid's sweep zone since in this region, the flow is governed by large coherent structures create by the grid's motion which are described by the first modes of the decomposition. This is evidenced by the increasing eigenvalue magnitudes and faster cumulative energetic convergence for regions closer to the grid.

- The energetic dominance of the first modes is enhanced by the presence of polymer: fewer modes are necessary to capture most of the kinetic energy in DPS than in water for a given region of the flow. Energy concentrates in the first few modes (De Angelis et al., 2003; Wang et al., 2016). Such an observation confirms the "organizing" effect of dilute polymer that is also evidenced from the study of mean flows.

- The mode-by-mode ratio between eigenvalues for Newtonian and non-Newtonian solutions, in similar regions of the flow, shows decreases all the more rapidly for regions that do not include the forcing zone. The enhanced dominance of the first modes in DPS is thus a feature that can not be only attributed to the forcing of the flow, but that is also significant in purely turbulent regions. It endorses the idea that the small structures of turbulence (here represented by the high mode numbers) are significantly

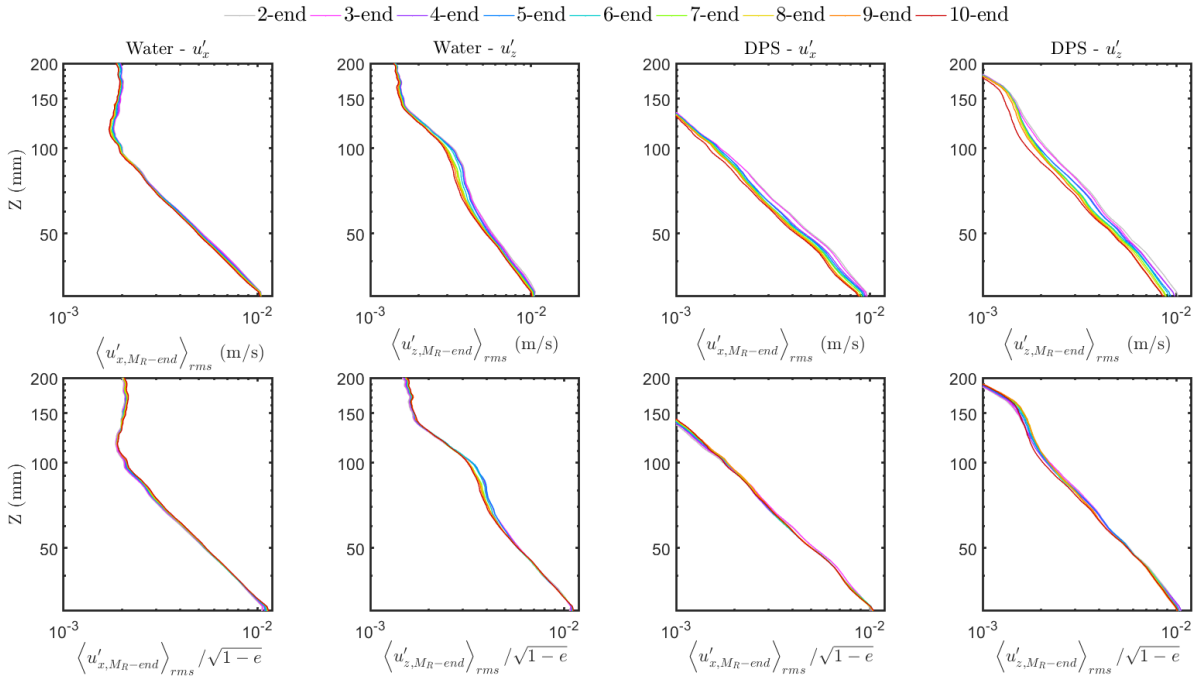

Figure C.9 – Reconstructed rms profiles $\left\langle u'_{x,\mathrm{M_R}+1-end}\right\rangle_{rms}$ and $\left\langle u'_{z,\mathrm{M_R}+1-end}\right\rangle_{rms}$ for water and DPS after removal of the first $\mathrm{M_R}$ modes, $\mathrm{M_R}=1$ to $\mathrm{M_R}=9$.

damped in dilute polymer solutions as observed in many studies Wang et al. (2016). Whether this effect is here due to viscosity or to non-Newtonian properties is still open for discussion.

- In regions close to the grid, the general structure of the first mode are similar in water an DPS, but the local repartition of magnitude is slightly modified. Far from the grid, even the structures of the modes varies. The effect of polymer seems to be felt differently depending on the region: close to the grid it acts on the shape of organized motion, far from the grid on the structure of turbulence.

- Without identifying precisely the modes associated to oscillatory motion, it is possible to estimate the periodic behavior of the flow by POD reconstruction using only the first low order modes in the CG region. The typical number of modes required to visually match phase averaged measurements is different in water and DPS. Until the oscillatory modes are clearly identified, this approximation can be used. However an arbitrary mode cutoff is not satisfactory. Removing the first POD modes leads to artificially remove kinetic energy from the reconstructed flow. Even if it does not change the decay power law in the far grid region, this is mostly because in this region the oscillatory motion can be assumed negligible. In close grid regions where oscillatory motion becomes significant, a misplaced mode number cutoff could alter the estimation of turbulence properties.

- Criterion for the identification of organized motion in stirred tanks based on eigenvalue spectrum and temporal coefficient mostly fail to reveal oscillatory motion in OGT. This is not surprising in the FT region, since it has be shown previously that the intensity of oscillatory motion quickly decreases when moving away from the grid. However, POD should be able to detect organized components of the flow in the SZ regions and in the GN region for DPS, where periodic behavior has been evidenced by

phase averaged measurements. Even if two-mode coupling is not as clear as in stirred tanks, a different type of coupling involving at least three modes seems to appear. The exact reasons to why the link between mode coupling and oscillatory motion seems more complex in the OGT situations than in stirred tank are yet to be understood. A first guess can be advanced: in POD studies applied to stirred tanks, the motion of the blade is always in the same direction. The oscillatory motion, that is to say vortex shedding by the blade, is thus always the same (same vortex propagation direction and rotation), and appears periodically. In the OGT case however, oscillatory eddies rotation is reversed whether the grid goes up or down, and this could make the model description more complex. The region of interest also does not include the sweeping region of the impeller's blade, whereas here oscillatory motion almost only occurs within the sweeping region.

Further investigations on the POD study of OGT should focus on this issue of oscillatory motion identification using modes. The structures observed on 3 modes temporal coefficient scatter plots suggest that a more complex mode coupling may exist, and so that criterion could be developed to identify periodic flows from POD decomposition in grid stirred tanks. This development of more universal criterions is of great interest for in the investigations of non-Newtonian effects on flow organization and oscillatory motion in grid stirred tanks, but also in more complex situations involving periodic forcing. Polymer concentration effect could then be investigated quite easily, even if a first simple approach using the tools of eigenvalue spectrum and Newtonian-normalized eigenvalue spectrum can also be considered (figures C.2 and C.4).

D Chemical interactions between fluorescein sodium, XG and dissolved CO_2

In this section, the methodology for the investigation on the interactions between fluorescein sodium, XG addition, and pH-CO_2 equilibria is detailed. The main results are commented in section 2.2.3.c of the thesis.

D.1 Method for chemical interactions testing

D.1.a Theoretical approach

In order to check for the chemical intrusiveness of fluorescein sodium beforehand, the equlibria of its dissolution into water have to be solved together with the ones of CO_2. The following equations thus come to complete the system presented in section 2.2.1.b.

$$K_n = \frac{[H_3O^+][Fl^n]}{[Fl^+]} = 10^{-2.2} \tag{D.1}$$

$$K_{f2} = \frac{[H_3O^+][Fl^-]}{[Fl^n]} = 10^{-4.2} \tag{D.2}$$

$$K_{f3} = \frac{[H_3O^+][Fl^{2-}]}{[Fl^-]} = 10^{-6.2} \tag{D.3}$$

Values for K_n, K_{f2} and K_{f3} are found in the work of Lindqvist (1960). With the assumption that there is no direct chemical reaction between carbonate species and all fluorescein forms, the interaction between the two chemical systems only comes from the electroneutrality equation which has to be modified as follows:

$$[Fl^-] + 2[Fl^{2-}] + [HCO_3^-] + 2[CO_3^{2-}] + [HO^-] - [H_3O^+] - [Na^+] - [Fl^+] = 0 \tag{D.4}$$

Four unknowns have been added to the system ($[Fl^-]$,$[Fl^{2-}]$,$[Fl^+]$ and$[Fl^n]$) but so far only three equations (D.1,D.2,D.3). The last equation to be added is the conservation equation for the total amount of fluorescein:

$$[Fl^-] + [Fl^{2-}] + [Fl^+] + [Fl^n] = C_{F0} \tag{D.5}$$

With C_{F0} the initial concentration of fluorescein added to the fluid before starting the experiment, that is to say the dye concentration.

Including these equation to the previous system of section 2.2.1.b, it becomes:

$$\begin{bmatrix} K_h & -1 & 0 & 0 & 0 & 0 & 0 & 0 \\ 0 & K_a & -10^{-pH} & 0 & 0 & 0 & 0 & 0 \\ 0 & 0 & K_b & -10^{-pH} & 0 & 0 & 0 & 0 \\ 0 & 0 & -1 & -2 & +1 & 0 & -1 & -2 \\ 0 & 0 & 0 & 0 & K_n & -10^{-pH} & 0 & 0 \\ 0 & 0 & 0 & 0 & 0 & K_{f2} & -10^{-pH} & 0 \\ 0 & 0 & 0 & 0 & 0 & 0 & K_{f3} & -10^{-pH} \\ 0 & 0 & 0 & 0 & 1 & 1 & 1 & 1 \end{bmatrix} \times \begin{bmatrix} [CO_2]_{aq} \\ [H_2CO_3] \\ [HCO_3^-] \\ [CO_3^{2-}] \\ [Fl^+] \\ [Fl^n] \\ [Fl^-] \\ [Fl^{2-}] \end{bmatrix} = \begin{bmatrix} 0 \\ 0 \\ 0 \\ C_s \\ 0 \\ 0 \\ 0 \\ C_{F0} \end{bmatrix} \tag{D.6}$$

With the term $C_s = -[Na^+] - 10^{-pH} + 10^{pH-pK_w}$.

It is then possible to test fluorescein's intrusiveness for different initial water composition, ie for different values of initial pH, by simply solving the system for different values of C_{F0} and $[Na^+]$.

Examples of pH – [CO_2] numerical curves at different $p\mathrm{H}_0$ values are given in figure 2.12 of the main text.It shows that for pure water ($p\mathrm{H}_0$ = 7), initial fluorescein concentrations down to 10^{-9} M have an influence on the system's behavior, especially at low CO_2 concentration. Indeed, fluorescein sodium being acidic, it shifts the theoretical initial pH of pure water to acidity when present at relatively high concentrations. The higher the fluorescein concentration, the lower the maximum pH and the stronger the shift from pure water curves. For higher initial pHs, this effect tends to reduce. Sodium hydroxide added to initially increase the pH balances the acidity of fluorescein. Therefore, as long as the fluorescein concentration remains low with respect to sodium hydroxide concentration, the equilibria stay unchanged. The apparent criteria illustrated by the last two graphs is that sodium hydroxide balances fluorescein's effects if $[HO^-]_0 = [N\mathit{a}OH] = 10^{p\mathrm{H}_0-14} > C_{F0}$.

The complexity of XG's chemistry makes its inclusion into the Matlab system beyond our skills. However, the interactions between XG and CO_2 dissolution can be investigated experimentally using the setup described below.

D.1.b Experimental approach

Equilibrium curves between pH and dissolved CO_2 concentration are measured using the experimental device sketched in figure D.1. Aqueous solutions containing different additives used (XG, sodium hydroxide, fluorescein sodium...) are poured in a 5 L glass tank through an inlet funnel. CO_2 may be either injected into or removed from the fluid by bubbling pure gaseous CO_2 or nitrogen N_2 in the tank (99.9 %, supplied by Air Liquide). Continuous agitation is ensured by a magnetic stirrer and its stirring bar. Dissolved gas concentration and pH are measured using respectively InPro 5000 and InPro 310 UD Metler Toledo probes. Both probes are also able to measure temperature in the fluid. Data points are recorded after pH stabilization under continuous stirring. After each measurement run, the tank is emptied by a pump connected to its outlet pipe and cautiously rinsed with distilled water. The CO_2 probe's precision is guaranteed for concentrations higher than 14.7 mg.L^{-1}, and security cautions regarding the releasing of pure CO_2 limit the reachable concentrations to 2000 mg.L^{-1}.

D.2 XG and pH-CO_2 equlibria

No numerical results are available for the action of XG on pH-CO_2 equlibria. Experimental results can be found in section 4.2.3.b for in-situ calibrations, and in figure D.2 for measure-

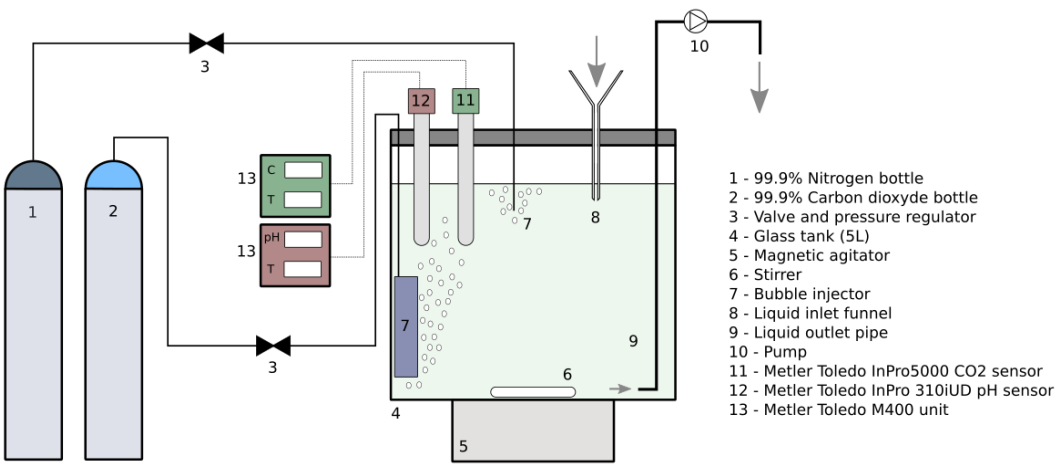

Figure D.1 – Experimental setup for pH-CO_2 curves measurement in presence of different additives

ments made with the experimental setup of figure D.1. As discussed in the main text, the precision of the dissolved gas probe again shows its limitations in terms of low gas concentration accuracy and response time. However within the precision range of the probe, pH-CO_2 equilibria with XG are close to the distilled water ones. XG and XG+fluorescein curves are similar either inside or outside of the probe precision range.

D.3 Fluorescein and pH-CO_2 equlibria

Numerical results for fluorescein in distilled water and sodium hydroxide solutions are represented in the main text, section 2.2.3.c, figure 2.12. Some experimental results corresponding to those curves are shown in figure D.2 below. Unfortunately the precision range of the dissolved CO_2 probe is not sufficient to measure low concentrations and only the main exponential trend can be captured. Within the available measurement region, experimental data points collapse well on the predicted curve. The numerical model allows to predict quite well the exponential part of pH-CO_2 equilibrium in different media, and fluorescein seems to have no effect on these equilibria inasmusch as the fluorescein concentration remains low or initial pH is high. In other words, the lower the C_{F0}/[NaOH] ratio, the lower the chemical intrusiveness of fluorescein and the better experimental results fit to numerical predictions. Measurements performed at high C_{F0} and low [NaOH] (stars) showed a curious foaming behavior, discussed below.

D.4 Chemical reaction between fluorescein sodium and carbonate species

From the previous experimental observations, the hypothesis used for the computations, which is that there is no chemical reaction between sodium and carbonate species, may be considered valid. Nevertheless, for experiments conducted at high fluorescein concentrations, an unexpected phenomena was observed: highly concentrated fluorescein sodium solutions tend to foam when bubbled with CO_2. At the beginning of the injection, bubbles are large and rapidly explode, but as bubbling goes on, they get smaller and the foam shows

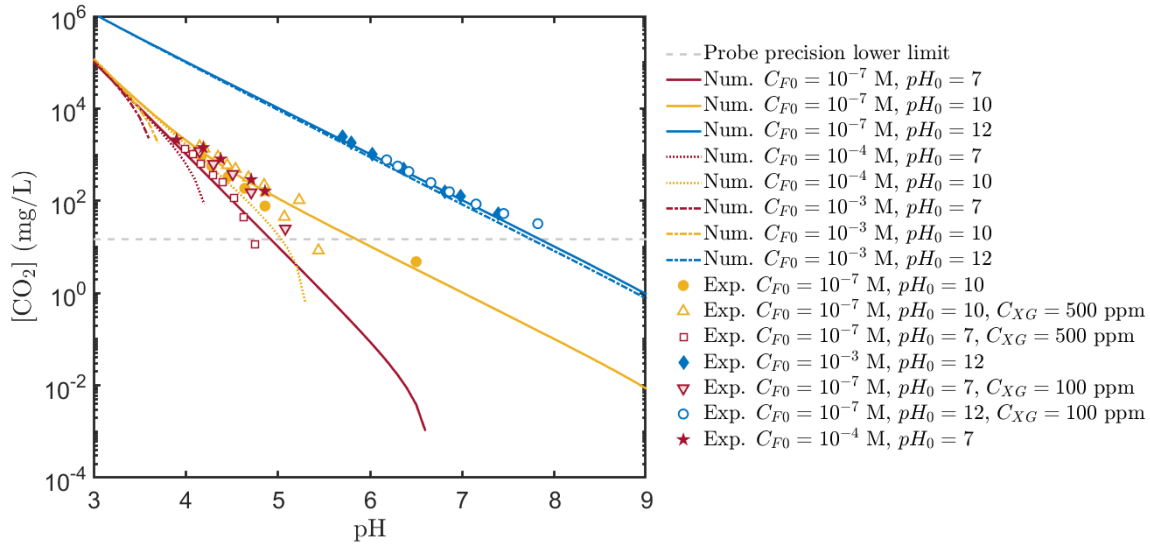

Figure D.2 – Experimental results of fluorescein's effect on pH-CO_2 equilibria. Lines are numerical predictions. Markers are measured pH-CO_2 points at various pH_0, C_{F0} and C_{XG} (if not indicated otherwise C_{XG} = 0 ppm)

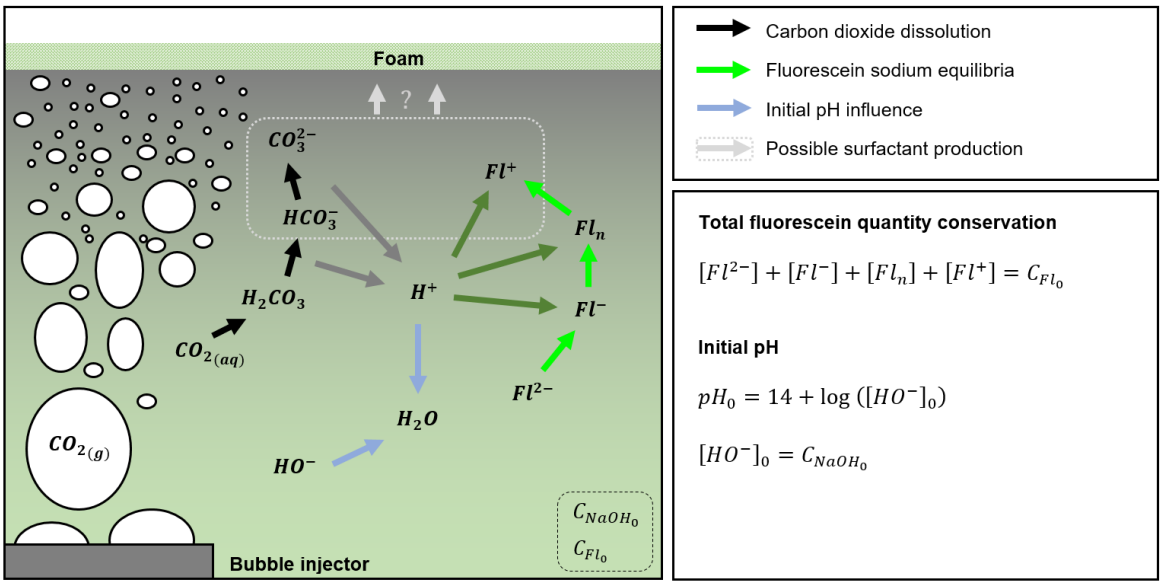

Figure D.3 – Chemical species production during CO_2 bubbling of fluorescein sodium solutions and possible surfactant production mechanism

a longer persistence time once injection is stopped. For long time bubbling, a floculation like behavior can even be observed.

The most concentrated the fluorescein solution, the higher the pH corresponding to the foaming onset. In other words, the higher the fluorescein concentration, the "quicker" it foams when bubbled with CO_2. Below 10^{-4} M of total fluorescein sodium concentration, no foaming is observed in the 4-12 pH range. The initial presence of sodium hydroxide does not seem to impact the onset of foaming but seem to reduce foam persistence time. After CO_2 bubbling and foam collapsing, foaming is also observed when further bubbling of the same solution with air or pure nitrogen whereas it was not prior to the CO_2 bubbling. Based on these observations, one may infer that a surfactant is produced when highly concentrated fluorescein is confronted to dissolved carbon dioxide. The following mechanism for surfactant production could be proposed (see figure D.3): Aqueous CO_2 transferred into water by the bubbles forms carbonic acid which then dissociates into bicarbonate and carbonate ions, hence releasing H^+ ions. By acid base reactions, those ions change the distribution of fluorescein forms in the solution, increasing the proportion of Fl^+. When the quantities of carbonate or bicarbonate ions and of Fl^+ ions are high enough, that is to say when going below a certain critical pH point, a chemical reaction between those carbonate species and the fluorescein cation supposedly occurs, producing a surfactant species leading to the observed foaming.

For initially high pH medium, the presence of an excess of HO^- ions in the fluid consumes part ot the H^+ ions produces by CO_2 injection, thus limiting acidification, fluorescein transformation, and thus limiting the probable surfactant production.

Such an explanation is for the moment purely hypothetical. This foaming phenomenon should be further investigated in order to confirm that surfactant is indeed created and to detail the associated chemical reaction and its kinetics. As for the scope of this thesis however, since no foaming is observed in the pH range of interest even for fluorescein concentrations 20 times greater than the one used in PLIF applications, the hypothetical surfactant production is assumed negligible.

D.5 Effect of pH and CO_2 on XG rheology

XG has been chosen partly because of its ability to withstand large pH variations without major modifications of its rheological properties. We have attempted to verify this pH stability versus acidification induced either by pH buffering or by CO_2 dissolution.

D.5.a pH buffered solutions

Flow curves of various solutions of XG diluted in buffered solutions have been measured. Desired pHs are obtained by mixture of a weak acid and a weak base: citric acid (CA) with sodium hydrogen phosphate (SHP) for pHs below 7.6, or sodium carbonate with hydrogen carbonate for pH higher than 7.6. Example of measured flow curves for buffered pHs 4,7 and 10 for 100 ppm,500 ppm an d 2000 ppm solutions are shown in figure D.4. Flow curves at similar concentrations but different pH are close to each other thus confirming that XG rheology is independent to pH variations. However viscosity values are surprisingly much lower than the reference unbuffered solutions, especially at low XG concentration. Dispersion between pH curves at different pHs but similar concentration also increases as C_{XG} decreases. These effects can be attributed to the fact that buffer species setting the solution's pH are salts. Salts have been found to modify the conformation of polymer chains and decrease the viscosity of XG solutions (see section 3.2.1.d).

D.5.b The effect of salt and ionic strength

In order to confirm this hypothesis, the total concentration of salt in each buffered solution has been computed by addition of the concentration of the weak base and of the weak acid. From this salt concentration C_{salt} we estimate an order of magnitude of the the molar ionic strength of the solution Is as

$$\mathrm{Is} = \frac{1}{2} \sum_{i=1}^{N_{species}} [X_i^n] n^2 \tag{D.7}$$

where Is is expressed in mol/L (M), and with $N_{species}$ the number of different ionic species, $[X_i^n]$ the molar concentration of the ionic salt X_i^n and n its charge, either positive or negative. Solutions of XG dissolved into water in presence of a strong base (sodium hydrodide NaOH), a weak acid (citric acid) and a weak base (sodium hydrogen phosphate) have also been tested. For these additional solutions, the salt concentration is simply the concentration of acid or base. In figure D.5 the relative viscosity decrease of zero shear rate viscosity, using distilled water as a reference, is plotted versus Is/C_{XG}. Is/C_{XG} is a non dimensional number that quantifies the relative action of ionic strength compared to that of XG. The higher this ratio, the more higher the amount of salt for each polymer chain, and so the stronger the effect of salt on rheology.

From the shape of the cloud of data, we see that ionic strength is indeed a key parameter of the viscosity drop observed in pH buffered solutions. Our tests solutions with strong or weak acid or bases confirm that the trend is, to a first approach, quite independent from the nature of the salt or the pH it sets, but mostly depends on the ionic strength. With pH buffers, the ionic strength is maximum and viscosity drops considerably.

D.5.c CO_2 dissolution

During our experiments of chapter 4, pH variations are induced by dissolution of CO_2 into the aqueous medium. This acidification comes with the productions of carbonate ionic

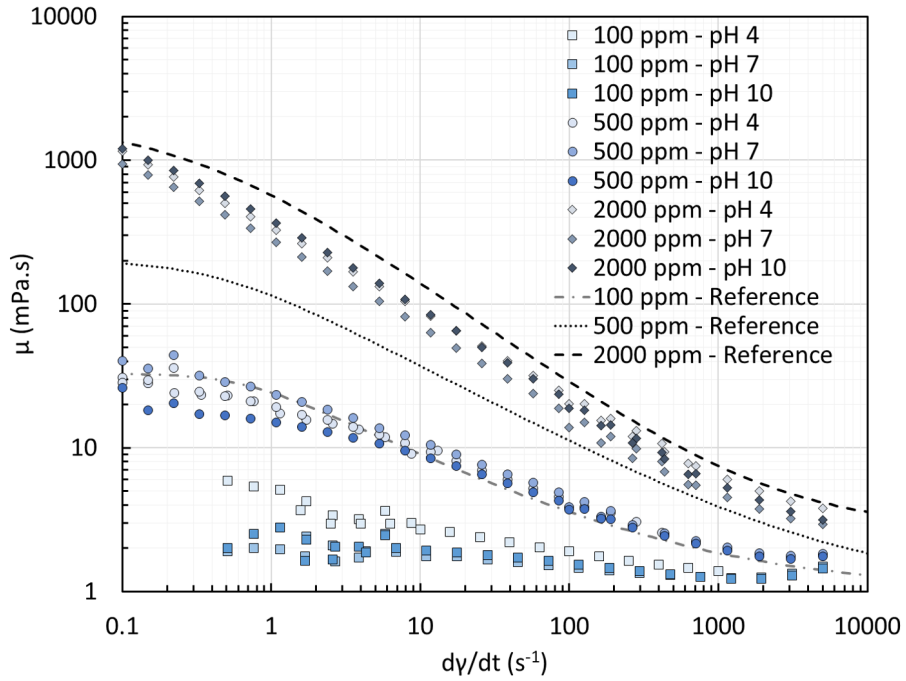

Figure D.4 – Effect of buffered pH on XG flow curves. Dashed lines are reference curves obtained for XG dissolved in distilled water.

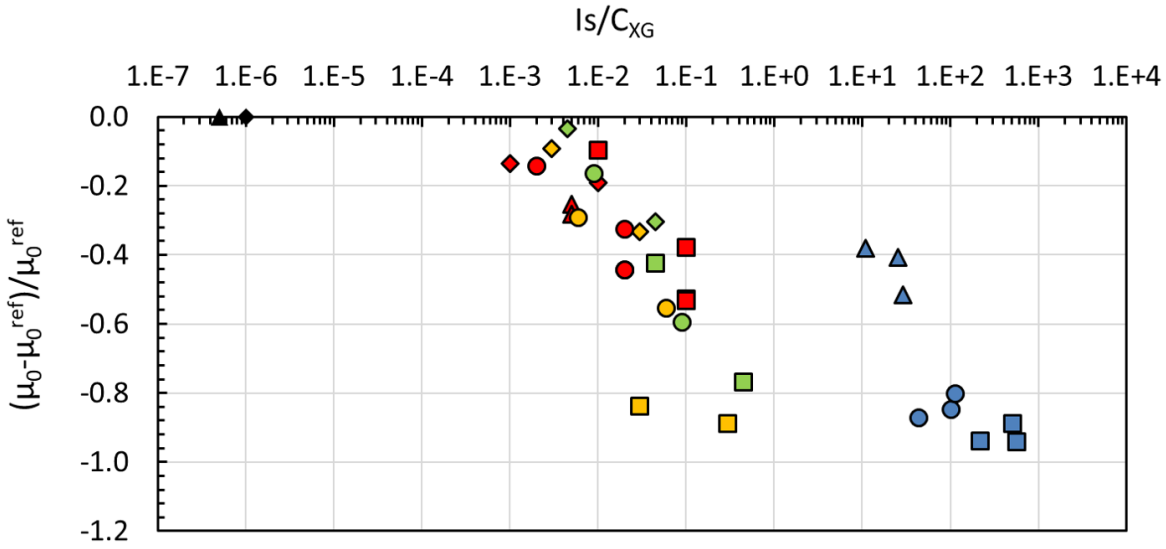

Figure D.5 – Relative variations of zero shear rate viscosity μ_0 in presence of acidic and basic salts with respect to its value for XG solutions in distilled water μ_0^{ref}. Squares, circles, diamonds and triangles denote respectively XG concentrations of 100,500,1000 and 2000 ppm. Black markers are for $C_s = 0$ M samples, blue for buffered solutions. Yellow, green and red are respectively for solutions with sodium hydrogen phosphate, citric acid, and sodium hydroxide.

derivatives. Dissolved CO_2 concentration and ionic compound concentrations are respectively of the order of $C_{sat} \sim 10^{-3}$ M and $[H_2CO_3]_{max} \sim [HCO_3^-]_{max} \sim [CO_3^{2-}]_{max} \sim K_h C_{sat} \sim 10^{-5}$ at their maximum. In the worst case scenario, that is to say for 10 ppm XG solutions at the most acidic pH, this leads to a Is/C_{XG} ratio of order 10^{-1}. From the previous experiments, we see that this may lead to variations of the zero shear rate viscosity. Flow curve measurements of XG solutions at different dissolved gas concentration have been measured

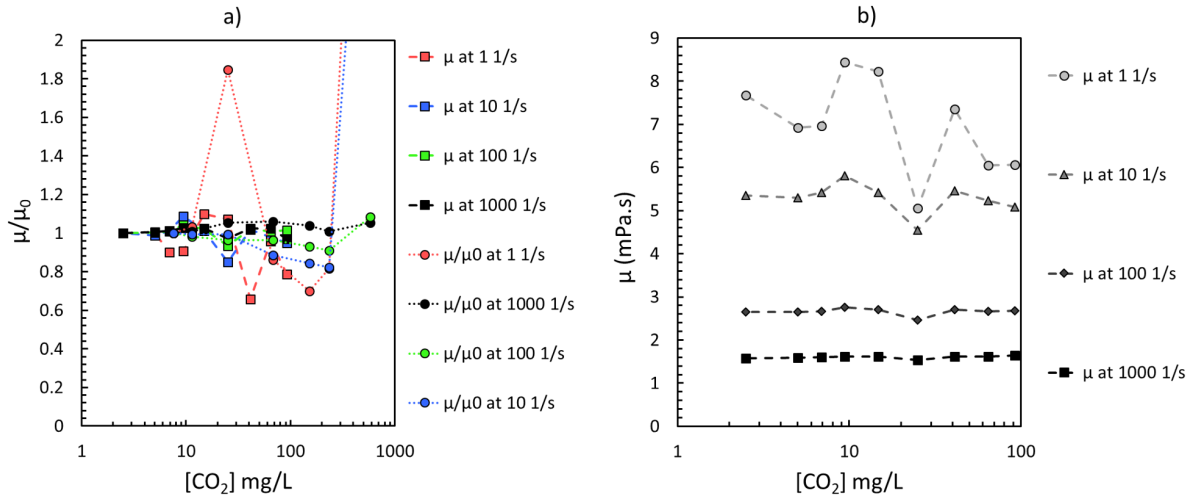

Figure D.6 – Effects of CO_2 dissolution on the rheology of XG. a) Ratio to the reference viscosity measured for XG in CO_2 free distilled water at different shear rates. b) Evolution of the viscosity at different shear rates with dissolved gas concentration.

and compared. If first appears that viscosities are of the same order of magnitude than the reference solutions. As expected from Is/C_{XG} estimation, ionic derivatives of CO_2 do not have the same ionic strength effect on XG than buffered solutions. Variations of zero shear rate viscosity with respect to the reference value in CO_2 free distilled water are also well below the 50 % variations that are expected fro figure D.5 at $Is/C_{XG} \sim 10^{-1}$. CO_2 dissolution as thus a different impact on XG rheology than simple acid or base addition as well. Finally, figure D.6 shows that viscosity at all shear rates remains constant with increasing dissolved gas concentration. Zero (or rather here 1 s^{-1}) shear rates viscosity are yet less stable than high shear-rate ones, proving that ionic strength variations do affect XG rheology in a limited fashion. For the experiments of chapter 4, flow curves of the working fluid have been measured before and after the experiments. By that mean we have checked that CO_2 dissoluton during the experimenal run did not affect the polymer rheology in experimental conditions.

E Wind, surface deformation, surface pollution and mass transfer

The whole present study is placed under the assumption that mass transfer occurs at a clean flat interface with no action of the gas phase hydrodynamics. The limitations of the flat surface hypothesis and the influence of surface pollution of near surface hydrodynamics have been previously mentioned. In this appendix we briefly discuss the implications of going beyond these hypothesis in terms of mass transfer.

E.1 Wind speed and gas phase turbulence

Considering the effect of gas motion is only relevant in the following cases.

- If one may assume that a large concentration boundary layer would develop in the gas phase above the interface in absence of gas phase velocity. If this is so, then the gas side mass transfer coefficient without gas motion becomes small enough in equation (1.8), and the overall $1/K_L$ resistance is a combination of the liquid and gas phase mass transfer resistance.

- If no bulk motion forcing exists in the liquid phase, and all liquid side motion is caused by momentum transfer or surface deformation from the gas phase motion. This case is called wind shear turbulence.

- If both bulk liquid and gas phase forcing exist, and the gas phase motion is at least as energetic as the liquid phase one. The near surface liquid phase motion derives from the interactions between liquid side and gas side forcing. It is generally admitted that wind shear should not be neglected for wind speed of the order of 1 $m.s^{-1}$ or faster (Herlina, 2005).

As for the first case and using the film model of Lewis and Whitman (1924) to explicit the k_g as $k_g = D^g \delta^g$, a low gas phase mass transfer coefficient k_g typically occurs for species with a low diffusion coefficient in the gas phase D^g and for which the film thickness remains large enough. For most of the common gases like CO_2 or oxygen, diffusivity is much greater in the liquid than in the gas phase and the gas-liquid film can be neglected when considering an over-saturated gas phase and under saturated liquid phase. However when reversing the problem and looking at mass transfer from a saturated liquid phase to an undersaturated gas phase, k_g becomes a relevant parameter since it is representative of the liquid film in the receptive (gas) phase. This can occur for example in waste water treatment plants where emissions from stagnant water volumes occur under the effect of air side motion, as reviewed by Prata et al. (2018). In general, the presence of wind above the interface always increases the overall mass transfer velocity. In the second of the two cases listed above, wind shear even becomes the dominant parameter since it is the only mechanism to induce motion in the fluid and reduction of the liquid side boundary layer. Many researchers studied the effects of wind friction at the interface on liquid side mass transfer coefficient, and the considerable discrepancy of data found in the literature reveals that the phenomenon is still far from being understood (Asher et al., 2012; Jahne et al., 1979; Jähne and Haußecker, 1998; Law and Khoo, 2002; Prata et al., 2018; Turney and Banerjee, 2013; Woodrow and Duke, 2001, 2002). For low wind speed, wind shear turbulence effects is well captured by the surface divergence model since surface divergence is a consequence of

liquid side motion produced. As long as the interface is not deformed, the SDM thus seems valid in both the second and the third situations (significant wind speed with or without bulk liquid side forcing) since it is based on the effective liquid side motion caused by both forcing mechanisms (Asher et al., 2012; Law and Khoo, 2002; McKenna and McGillis, 2004a; Turney and Banerjee, 2013). With increasing wind speed however, the interface begins to deform and this deformation introduces new mechanisms possibly playing a role in mass transfer.

E.2 Surface deformation and micro-breaking

At moderate wind speed, capillary waves begin to deform the free surface. Wind generated capillary waves are usually found to increase mass transfer (Cohen, 1983; Tamburrino and Martínez, 2017). However Turney and Banerjee (2013) suggest that depending on their size, these capillary waves have a too short time scale to contribute efficiently to mass transfer, while they may alter the efficienty of SDM since they still increase the apparent surface divergence. Classical SDM could thus overestimate mass transfer in presence of capillary waves. For high wind speeds typically above 10 $m.s^{-1}$, capillary waves are replaced by turbulent microscale breaking of the interface leading to the formation of multiple small size bubbles and droplets, and to a dramatical increase in mass transfer coefficient (Cohen, 1983; Turney and Banerjee, 2013). Zappa et al. (2004) showed that without imposed liquid side turbulence, this so called *microbreaking* of the free surface is the dominant mechanisms for gas to liquid mass transfer and may be responsible of up to 75% of the total mass flux (in absence of liquid side forcing). The outstanding efficient of this phenomenon is explained by the fact that it greatly increases the interfacial area at very small scales for which diffusion becomes efficient. When surface deformation is not caused by the wind but either by intense liquid side turbulence or by mechanical forcing, an increase in surface deformation always leads to an increase in mass transfer velocity, but the exacts mechanisms are still poorly understood (Prata et al., 2018; Tamburrino and Martínez, 2017).

E.3 Surface pollution

As for the surface pollution, it was previously mentioned that the presence of surfactant tends to dampen near surface turbulence and increase the depth of the viscous sub-layer. This translates into a decrease in the mass transfer coefficient K_L (McKenna, 2000; McKenna and McGillis, 2004a). Hydrodynamic models fail to predict mass transfer in presence of surfactant (McKenna and McGillis, 2004a). However, the effect of surface pollution on K_L can be accounted for by varying the exponent on the Schmidt number in usual correlations. For clean interfaces, it has been found that $K_L \sim Sc^{-0.5}$. With increasing surface pollution, the -0.5 exponent decreases and ultimately reaches $-2/3$ for very dirty interfaces which is similar to the exponent observed for rigid walls. Therefore, even if turbulence hydrodynamics in the vicinity of solid boundaries is not the same as that close to organic films, highly polluted interfaces are in some aspects equivalent to rigid walls in terms of mass transfer (Hasegawa and Kasagi, 2009; Herlina and Wissink, 2016; Ledwell, 1984; Wissink et al., 2017). An interesting information is that surface divergence models remain valid for polluted interfaces up to a certain level of surface pollution. Indeed, the presence of surfactant modifies the structure of turbulence close to the interface and tends to damp the upcoming turbulent eddies, thus reducing surface divergence. The surface divergence rms value measured thus

intrinsically accounts for surfactant effects, and so does the estimation of K_L (McKenna and McGillis, 2004a). Yet for high surface contamination, surface divergence and concentration scalar field become uncorrelated, and SDM are no longer able to predict K_L (Wissink et al., 2017).

F Horizontal fluorescence imaging under the interface

In this appendix, additional measurements of fluoresced light intensity fields in horizontal planes parallel to the interface at different depths are shown. These measurements have been performed by Fabien Morge during his master thesis (Morge, 2015). No PLIF calibration procedure was performed along with these measurements, so we are here only able to provide raw fluoresced light intensity fields, and a qualitative observation of dissolved gas structures.

Figure F.1 show that horizontal scalar structures, as vertical ones, consist in a complex combination of filaments and swirling patterns. Well defined horizontal swirling motions exist at all depths.

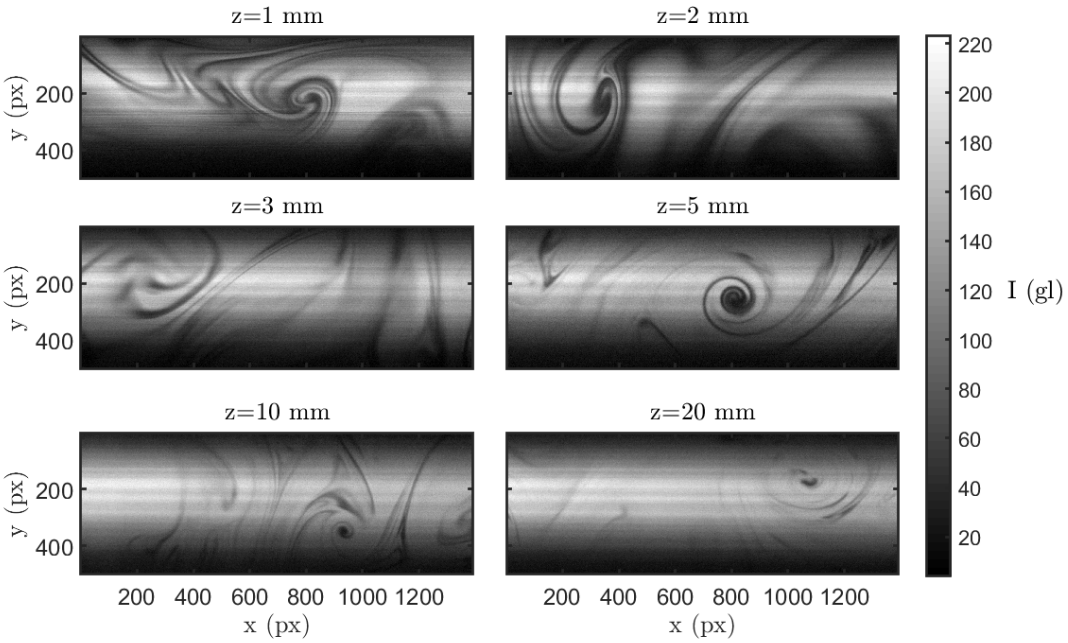

Figure F.1 – Horizontal scalar structures observed by qualitative fluoresced light intensity recording in horizontal planes parallel to the interface for z=1 mm to z=20 mm. Intensities are shown in gray level (gl). The spatial resolution of all fields is 0.054 mm/px.

G $I^r_{pH} - PLIF$ vs $I_{pH} - PLIF$ under the interface

Due to the central location and small size of the ROI with respect to the tank, PLIF measurements are here performed in the situation described in figure 2.7 c. The system can not be considered optically thin, and laser excitation intensity received by a given point of the ROI is conditioned by Beer-Lambert absorption. This absorption depends on dissolved gas structures encountered by the laser on its path, inside and outside of the ROI, because the absorption coefficient on fluorescein sodium depends itself on the gas concentration to be measured. Since scalar structures in the Outer Region (OR=ROV-ROI) are not visualized during the measurement, even advanced pixel by pixel calibration methods (Souzy, 2014; Valiorgue et al., 2013) are not able to account for extinction coefficient variations outside of the ROI. Measuring dissolved gas concentration without having to know local absorption values along the full laser path in the fluid was one of the motivation behind the development of the ratiometric technique $I^r_{pH} - PLIF$ (see chapter 2).

Unfortunately, as mentioned earlier, ratiometric measurements are only available for a few runs, and could for example not be performed in water. The aim of this appendix is hence to understand and estimate the errors one makes when using single color PLIF in such a situation where the ratiometric method is *a priori* required. For that we use an experimental run for which both single-color and ratiometric measurements are available (XG10A). We will use concentrations measured by the two-color method and their statistics as reference values, keeping in mind that $I^r_{pH} - PLIF$ is also subject to measurement errors as discussed in chapter 2. We also suggest a correction of single color measurements based on the knowlege of the mean concentration profile from ratiometric measurements.

G.1 Theory of single color measurements

G.1.a Calibration and measured intensity equations

Equation (2.30) provides the expression of recorded intensities for the full spectrum of fluorescence wavelengths as a function of laser input intensity, geometrical parameters, and dye properties. In single color methods a reference intensity field $I_{r,ref}$ measured at an homogeneous and known pH pH_{ref} is used to normalize recorded intensity fields. The non dimensional intensity at point M is then written

$$I^*(M) = \frac{I_r(M)}{I_{r,ref}(M)} = \frac{\phi(M).\epsilon(\lambda_e, M)}{\phi_{ref}.\epsilon_{ref}}.e^{-C_{F0}\int_0^{L_s(M)}(\epsilon(\lambda_e, pH(r)) - \epsilon_{ref})dr} \tag{G.1}$$

With $\phi_{ref} = \phi(pH_{ref})$ and $\epsilon_{ref} = \epsilon(\lambda_e, pH_{ref})$. In order to avoid later confusion with dissolved gas concentration C, the fluorescent dye concentration is hereinafter denoted C_{F0}. We notice that laser input intensity I_0 and the geometrical constant A have disappeared. However, the Beer-Lambert absorption term can not be canceled out because $\epsilon(\lambda_e, pH)$ is generally different from ϵ_{ref}. The expression of the received intensity thus still depends on laser absorption conditions, unlike that of the ratio of two intensities with similar ϵ variations. For the sake of simplicity, we will hereinafter drop the λ_e dependency in the equations. We here proceed with the equations for the full fluoresced light spectrum, but similar equations can easily be derived for specific fluorescence wavelengths or spectral band. One simply needs to replace ϕ by $S_\phi(\lambda_f)$ and if needed integrate the expressions over the chosen spectral band.

During the calibration process of both single color and ratiometric methods, fluoresced light intensities are recorded in homogeneous pH conditions. $\epsilon(r)$ is thus constant along L_s,

M and pH can be seen as independent variables and the expression becomes

$$I^*_{cal}(pH, M) = \frac{\phi(pH).\epsilon(pH)}{\phi_{ref}.\epsilon_{ref}}.e^{-C_{F0}L_s(M)(\epsilon(pH)-\epsilon_{ref})} \tag{G.2}$$

In the present situation, L_s can be divided into two parts: L_{ROI} which corresponds to the laser path inside the ROI, accessible to measurement, and L_{OR} which is the path in the outer region. Assuming that laser beams are horizontal and the location of the ROI kept constant, the path crossed in the OR does not depend on M. The exponential terms in equations (G.1) and (G.2) can thus be separated and the equations respectively become:

$$I^*(M) = \frac{\phi(M).\epsilon(M)}{\phi_{ref}.\epsilon_{ref}}.e^{-C_{F0}\int_0^{L_{OR}}(\epsilon(pH(r))-\epsilon_{ref})dr}.e^{-C_{F0}\int_{L_{OR}}^{L_{ROI}(M)}(\epsilon(pH(r))-\epsilon_{ref})dr} \tag{G.3}$$

and

$$I^*_{cal}(M, pH) = \frac{\phi(pH).\epsilon(pH)}{\phi_{ref}.\epsilon_{ref}}.e^{-C_{F0}L_{OR}(\epsilon(pH)-\epsilon_{ref})}.e^{-C_{F0}L_{ROI}(M)(\epsilon(pH)-\epsilon_{ref})} \tag{G.4}$$

It is worth noting that because of Beer-Lambert's absorption, every point M has by default a different calibration curve $I^*_{cal} = f(pH)$.

G.1.b Calibration strategies

In conventional single color methods, both exponential terms of the two equations are neglected as a first approach. For non-optically thin systems, it comes to assuming that the extinction coefficient stays close to its reference value during both calibration and the measurement steps. However in our case, the variations of ϵ in the studied pH range are important, and so this simplification leads, as we will see below, to substantial errors. These terms thus need to be accounted for.

In situations were $L_{OR} = 0$ or $L_{OR} << L_{ROI}$ the first exponential term of both equations (G.3) and (G.4) can be neglected. This is the case where one can apply a pixel-by-pixel calibration method as proposed by Valiorgue et al. (2013) and Souzy (2014). The principle is to no longer use the measured intensity but the normalized $(\phi\epsilon)^* = \frac{\phi\epsilon}{\phi_{ref}\epsilon_{ref}}$ as an indicator of pH. Contrary to I^*, which depends on Beer-Lambert extinction of the laser intensity, normalized ($\phi\epsilon$) only varies according to the local pH. Calibration and measurement fields are obtained by correcting recorded intensity fields by the exponential correction pre-factor:

$$(\phi\epsilon)^*_{cal}(M, pH) = I^*_{cal}(pH)\, e^{C_{F0}L_{ROI}(M)(\epsilon(pH)-\epsilon_{ref})} \tag{G.5}$$

and

$$(\phi\epsilon)^*(M) = I^*(M)\, e^{C_{F0}\int_{L_{OR}}^{L_{ROI}(M)}(\epsilon(pH(r))-\epsilon_{ref})dr} \tag{G.6}$$

Knowing the calibration relationship of equation (G.5) for each point M of the ROI, local pH values can be obtained by scanning equation (G.6) through the ROI.

G.1.c Absorption outside of the ROI

On the other hand, there are situations where $L_{OR} >> L_{ROI}$. In the experiments of chapter 4 for example, one typically has $L_{OR} = 12$ cm versus $L_{ROI} = 2$ cm. In such conditions one may assume that the absorption inside the ROI is negligible versus that in the OR. The first exponential term of equations (G.3) and (G.4) are no longer close to unity, but the second

exponential terms are. We can once again use the $(\phi\epsilon)^*$ ratio as an unambiguous indicator of the pH:

$$\left(\phi\epsilon\right)^*_{cal}(p\mathrm{H}) = \mathrm{I}^*_{cal}.e^{\mathrm{C_{F0}L_{OR}}(\epsilon(p\mathrm{H})-\epsilon_{ref})} \tag{G.7}$$

and

$$\left(\phi\epsilon\right)^*(\mathrm{M}) = \mathrm{I}^*(\mathrm{M}).e^{\mathrm{C_{F0}}\int_0^{\mathrm{L_{OR}})}(\epsilon(p\mathrm{H}(r))-\epsilon_{ref})dr} \tag{G.8}$$

As for the calibration step, the exponential correction factor $e^{\mathrm{C_{F0}L_{ROI}(M)}(\epsilon(p\mathrm{H})-\epsilon_{ref})}$ can be estimated, providing that one knows the $\epsilon = f(p\mathrm{H})$ relationship. This relationship can be obtained from the literature (Klonis and Sawyer, 1996; Valiorgue et al., 2013).

Nevertheless, for the measurement images where ϵ is not homogeneous, it becomes this time impossible to compute the exponential term $e^{\mathrm{C_{F0}}\int_0^{\mathrm{L_{OR}}}(\epsilon(r)-\epsilon_{ref})dr}$ since the local variations of ϵ are not measured in the outer region.

G.1.d Correction of single color measurements using first order statistics on concentration

In order to account for OR variations of extinction coefficient, one needs an information on the local value of pH, which is precisely the quantity that is measured. A way of getting around this problem is to rewrite the exponential term of equation (G.8) as

$$e^{\mathrm{C_{F0}}\int_0^{\mathrm{L_{OR}}}(\epsilon(r)-\epsilon_{ref})dr} = e^{\mathrm{C_{F0}L_{OR}}(\overline{\epsilon}-\epsilon_{ref})} \tag{G.9}$$

where $\overline{\epsilon}$ is the average extinction coefficient along $\mathrm{L_{OR}}$. Its value depends on the concentration statistics. As a first order approximation, on may write than

$$\overline{\epsilon}(z,t) = f\left(\overline{\mathrm{C}}(z,t)\right) \tag{G.10}$$

All that is needed is then an information on the mean concentration profile. In what follows, we will use concentration profiles obtained from ratiometric measurements of run XG10A to try and correct single color measurements of the same run. We will thus estimate the error made when applying single color processing without applying any correction.

G.2 PLIF method comparison

In this section, the results given by single color and ratiometric PLIF treatment of the same recorded fluoresced light fields are compared. The data come from the XG10A run. Single-color PLIF is applied using the fluorescence signal of spectral band 2, which is the one with the best signal over noise dynamics. Similar but more noisy results have been obtained using spectral band 1.

G.2.a Tested procedures

With the present data, pixel by pixel calibration and treatment are not possible since, calibration images have not be recorded with sufficient control on the interface location. However since here $\mathrm{L_{OR}} >> \mathrm{L_{ROI}}$, such processing would only lead to a minor improve of the results. Hereinafter, two procedures are applied our data for single color based estimation of pH fields:

- Standard procedure **S** for which we assume that $e^{C_{F0}L_s(\epsilon(pH)-\epsilon_{ref})}$=1 during both the calibration and measurement steps. This method was applied to the WD run images. It is the fastest method in terms of process time (among the single color ones) since in only requires the normalization of calibration and measurement images by an image recorded at an homogeneous and known pH. It should however lead to significant errors because the variations of extinction coefficient are neglected.

- Standard procedure accounting for absorption in the outer region **Sa**. This method consists in applying equations (G.7) and (G.8) respectively for the calibration and treatment steps, neglecting absorption inside the ROI, and using the mean concentration profile obtained from ratiometric measurement as an input data.

These two procedures are tested on one single instantaneous field, and compared to the ratiometric measurement **R**. We arbitrarily chose here the instantaneous field at t=200 s. A similar analysis has been performed for the S and Sa procedures on other instantaneous fields (e.g. at t=1000 s) and lead to the same conclusions.

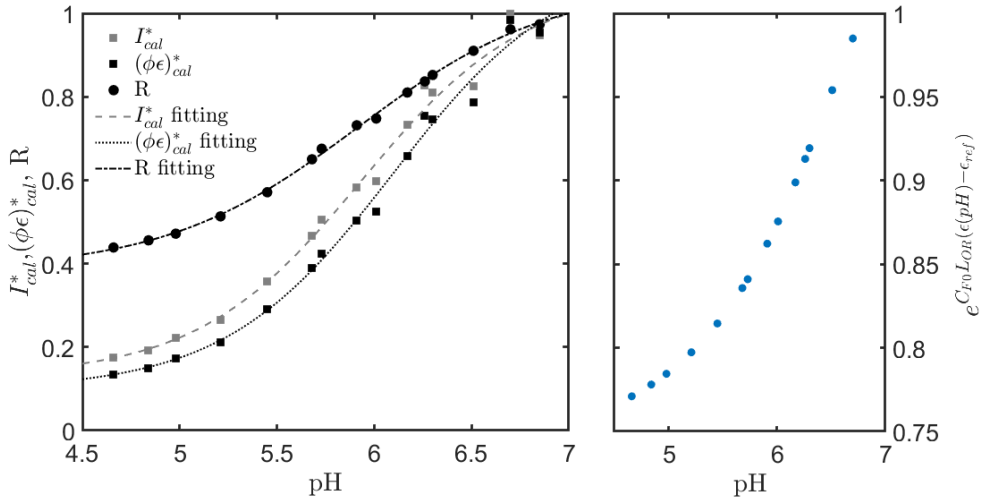

Figure G.1 – Calibration curves for single color methods S and Sa, and for the ratiometric method R. Markers are points measured from calibration images for respectively I^*_{cal}, $(\phi\epsilon)^*_{cal}$ and R. Dashed and dotted lines are hyperbolic tangent fittings later used to turn measured fields into pH fields. The exponential corrective factor $e^{C_{F0}L_{OR}(\epsilon(pH)-\epsilon_{ref}}$ is plotted versus pH in subfigure b.

G.2.b Calibration curves

Figure G.1 shows calibration curves for the S, Sa and R methods. Markers are measured points and lines are hyperbolic tan fittings. The ratio calibration is the one shown in chapter 4 figure 4.6. We see that the $(\phi\epsilon)^*_{cal}$ relative values are lower than I^*_{cal} values, especially at low pH. Indeed if we take $\epsilon_{ref} = \epsilon(7)$, the difference $\epsilon(pH) - \epsilon_{ref}$ is negative since the absorption coefficient decreases with the pH (see figure 2.10). The exponential correction term of equation (G.7) here ranges from about 0.75 to unity at pH=7 (figure G.1 b).

Absorption in the outer region is predicted from ratiometric concentration measurements. The $\overline{C}(z,t)$ profile at t=200 s corresponding to the treated image is estimated using the fitting method described in chapter 4. $\overline{C}(z,t)$ is turned into $\overline{pH}(z,t)$ using the previously established pH-$[CO_2]$ calibration. $\overline{pH}(z,t)$ is translated into $\overline{\epsilon}(z,t)$ thanks to hyperbolic

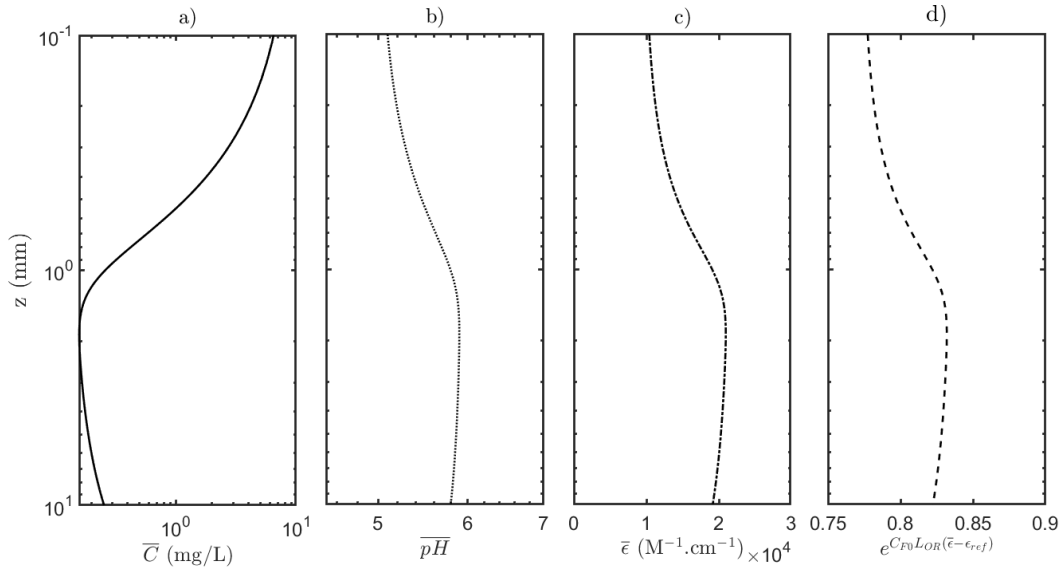

Figure G.2 – Correction of the outer region absorption based on ratiometric measurement of $\overline{C}(z,t)$, with t=200 s. a) is $\overline{C}$ profile in log-log scale. b)c)d) are profiles for $\overline{pH}$, $\bar{\epsilon}$ and $e^{C_{F0}L_{OR}(\bar{\epsilon}-\epsilon_{ref})}$ respectively, z in log scale.

tangent fitting of the literature data for epsilon (see figure 2.10), and the exponential factor $e^{C_{F0}L_{OR}(\bar{\epsilon}(z,t)-\epsilon_{ref})}$ can be computed as a function of z.

All these profiles are shown respectively in figure G.2 a), b), c) and d), in log scale z axis and log scale concentration values for sub-figure a). We see that even at the relatively short time of dissolution used here, t=200 s, dissolved gas concentration in the OR lead to correction factors between 0.75 and 0.85, even at the highest depths where concentration is minimum. This correction factor has to be considered together with the one on calibration curves in order to understand its impact on pH measurement. This is done in the next paragraph.

G.2.c Example of pH and concentration fields

From the observation of concentration fields in figure G.3, it appears that the S method underestimates concentration levels, especially at high concentrations. Correction of outer region absorption makes Sa fields more similar to R fields even if some scalar structure still seem less concentrated in the Sa picture than in the R one. pH fields from single color methods never display values higher than 6.5 while the reference pH=7 is reached at some regions of the fields obtained from ratiometric measurement. This however does not impact much concentration levels since pH between 6.5 and 7 correspond to concentration values lower than 10^{-1} mg/L. pH fields S and Sa are visually difficult to compare: variations are of about 0.1 to 0.2 pH units. Yet because of the exponential link between pH and concentration this leads to important differences in terms of local concentration values.

G.2.d Concentration profiles

The final comparison is made by extracting concentration profiles along depth at a given x value, here x=6.3 mm (figure G.4 a)), and by computing the width averaged concentration profile over the ROI (figure G.4 b)). Local profiles at x=6.3 mm confirm that single color measurements yield lower concentration values than the ratiometric one. Correction of the OR absorption allows to increase the measured concentration values but not exactly up to those measured by the R method. However when averaging over the ROI's width, it appears

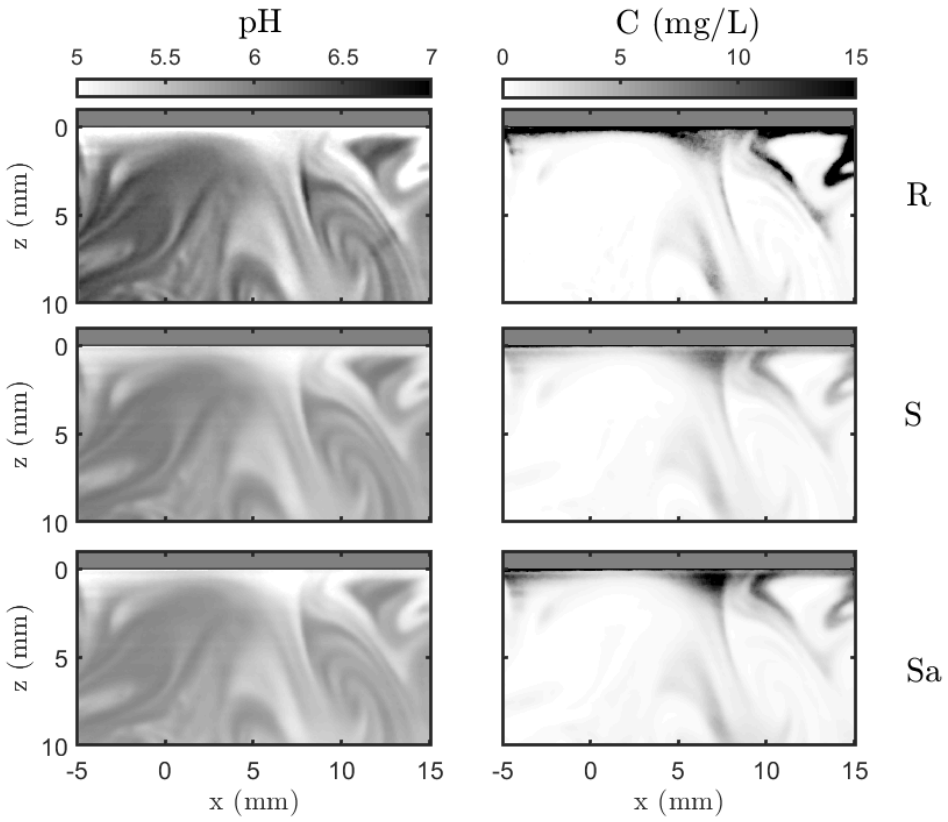

Figure G.3 – Comparison of pH and C fields obtained by R, S and Sa methods.

than the $[C]_x$ values obtained by the Sa method are similar to those obtained y the R method. Last but not least, the shape of the concentration profiles are unaffected by the method used to estimate them. Concentration values vary, but not their evolution with depth. It is of great interest since it implies that single color measurements can still be used for qualitative comparison of concentration structures and profiles with ratiometric measurements. This assumption has been confirmed by computing average and fluctuating concentration values as well as turbulent mass fluxes of the full XG10A run with fluorescence images treated by the uncorrected single color method (S). It is found that the choice of the PLIF method does not affect the evolution of mean concentration, concentration rms, or turbulent ass fluxes with depth, even if single color PLIF underestimates their value.

G.3 Conclusion

As shown above, the use of single color PLIF without any specific correction in a condition where absorption occurs outside of the ROI globally leads to slightly over estimate pH values and ultimately to a significant under estimation of concentration values.

This can be explained in the following way. During calibration, images are recorded in conditions that are somehow different from the measurement conditions: with a pH homogeneous over the full laser path in the fluid. During the experiment, the laser beam at a given depth z sees an average absorption value $\bar{\epsilon}$ defined by the mean concentration profile, hence by the measure phenomena. Because of high concentration scalar injection events, this average absorption is always smaller than the reference one, and excitation intensity reaches the ROI at a higher level than expected by the intensity calibration images I^*_{cal}. Neglecting extinction coefficient variations in the OR thus comes to explain higher recorded intensity

levels by higher local pHs and lower concentrations, whereas they are in fact due to an increased local excitation intensity. A very interesting result is yet that this under-estimation does not affect the spatial distribution of concentration structures or profiles along depth. It only changes the magnitude of the concentration. To that extend, WD (single color) and XG10A results (ratiometric) should not be used to compare local concentration levels in water and DPS, but can still usefull for the comparison of the shape of scalar structures, and of the evolution of scalar and mass flux statistics with depth.

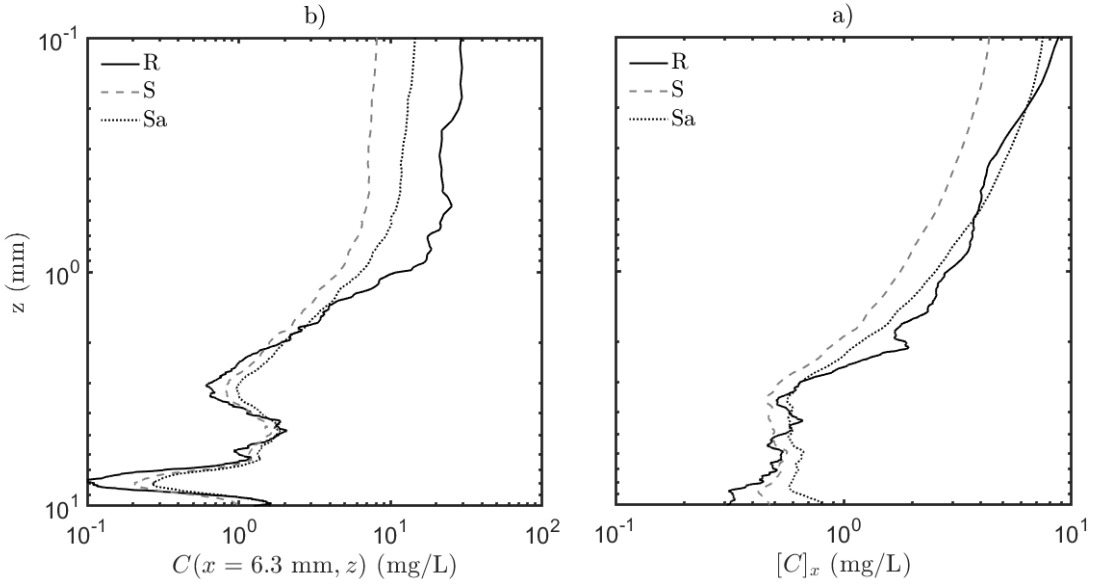

Figure G.4 – a)Local (x=6.3 mm) and b) width averaged concentration profiles along depth, obtained by R, S or Sa method, in log-log scale.

Département FEDORA – INSA Lyon - Ecoles Doctorales – Quinquennal 2016-2020

SIGLE	ECOLE DOCTORALE	NOM ET COORDONNEES DU RESPONSABLE
CHIMIE	**CHIMIE DE LYON** **http://www.edchimie-lyon.fr** Sec. : Renée EL MELHEM Bât. Blaise PASCAL, 3e étage **secretariat@edchimie-lyon.fr** INSA : R. GOURDON	M. Stéphane DANIELE Institut de recherches sur la catalyse et l'environnement de Lyon IRCELYON-UMR 5256 Équipe CDFA 2 Avenue Albert EINSTEIN 69 626 Villeurbanne CEDEX **directeur@edchimie-lyon.fr**
E.E.A.	**ÉLECTRONIQUE, ÉLECTROTECHNIQUE, AUTOMATIQUE** **http://edeea.ec-lyon.fr** Sec. : M.C. HAVGOUDOUKIAN **ecole-doctorale.eea@ec-lyon.fr**	M. Gérard SCORLETTI École Centrale de Lyon 36 Avenue Guy DE COLLONGUE 69 134 Écully Tél : 04.72.18.60.97 Fax 04.78.43.37.17 **gerard.scorletti@ec-lyon.fr**
E2M2	**ÉVOLUTION, ÉCOSYSTÈME, MICROBIOLOGIE, MODÉLISATION** **http://e2m2.universite-lyon.fr** Sec. : Sylvie ROBERJOT Bât. Atrium, UCB Lyon 1 Tél : 04.72.44.83.62 INSA : H. CHARLES **secretariat.e2m2@univ-lyon1.fr**	M. Philippe NORMAND UMR 5557 Lab. d'Ecologie Microbienne Université Claude Bernard Lyon 1 Bâtiment Mendel 43, boulevard du 11 Novembre 1918 69 622 Villeurbanne CEDEX **philippe.normand@univ-lyon1.fr**
EDISS	**INTERDISCIPLINAIRE SCIENCES-SANTÉ** **http://www.ediss-lyon.fr** Sec. : Sylvie ROBERJOT Bât. Atrium, UCB Lyon 1 Tél : 04.72.44.83.62 INSA : M. LAGARDE **secretariat.ediss@univ-lyon1.fr**	Mme Emmanuelle CANET-SOULAS INSERM U1060, CarMeN lab, Univ. Lyon 1 Bâtiment IMBL 11 Avenue Jean CAPELLE INSA de Lyon 69 621 Villeurbanne Tél : 04.72.68.49.09 Fax : 04.72.68.49.16 **emmanuelle.canet@univ-lyon1.fr**
INFOMATHS	**INFORMATIQUE ET MATHÉMATIQUES** **http://edinfomaths.universite-lyon.fr** Sec. : Renée EL MELHEM Bât. Blaise PASCAL, 3e étage Tél : 04.72.43.80.46 Fax : 04.72.43.16.87 **infomaths@univ-lyon1.fr**	M. Luca ZAMBONI Bât. Braconnier 43 Boulevard du 11 novembre 1918 69 622 Villeurbanne CEDEX Tél : 04.26.23.45.52 **zamboni@maths.univ-lyon1.fr**
Matériaux	**MATÉRIAUX DE LYON** **http://ed34.universite-lyon.fr** Sec. : Marion COMBE Tél : 04.72.43.71.70 Fax : 04.72.43.87.12 Bât. Direction **ed.materiaux@insa-lyon.fr**	M. Jean-Yves BUFFIÈRE INSA de Lyon MATEIS - Bât. Saint-Exupéry 7 Avenue Jean CAPELLE 69 621 Villeurbanne CEDEX Tél : 04.72.43.71.70 Fax : 04.72.43.85.28 **jean-yves.buffiere@insa-lyon.fr**
MEGA	**MÉCANIQUE, ÉNERGÉTIQUE, GÉNIE CIVIL, ACOUSTIQUE** **http://edmega.universite-lyon.fr** Sec. : Marion COMBE Tél : 04.72.43.71.70 Fax : 04.72.43.87.12 Bât. Direction **mega@insa-lyon.fr**	M. Jocelyn BONJOUR INSA de Lyon Laboratoire CETHIL Bâtiment Sadi-Carnot 9, rue de la Physique 69 621 Villeurbanne CEDEX **jocelyn.bonjour@insa-lyon.fr**
ScSo	**ScSo*** **http://ed483.univ-lyon2.fr** Sec. : Viviane POLSINELLI Brigitte DUBOIS INSA : J.Y. TOUSSAINT Tél : 04.78.69.72.76 **viviane.polsinelli@univ-lyon2.fr**	M. Christian MONTES Université Lyon 2 86 Rue Pasteur 69 365 Lyon CEDEX 07 **christian.montes@univ-lyon2.fr**

*ScSo : Histoire, Géographie, Aménagement, Urbanisme, Archéologie, Science politique, Sociologie, Anthropologie

FOLIO ADMINISTRATIF

THESE DE L'UNIVERSITE DE LYON OPEREE AU SEIN DE L'INSA LYON

NOM : LACASSAGNE DATE de SOUTENANCE : 30/11/2018

Prénoms : Tom

TITRE :

Oscillating grid turbulence and its influence on gas liquid mass transfer and mixing in non-Newtonian media
La turbulence de grille oscillante et son influence sur le transfert de masse gaz-liquide et le mélange en milieu non newtonien

NATURE : Doctorat Numéro d'ordre : 2018LYSEI103

Ecole doctorale : MEGA – Mécanique Energétique Génie Civil et Acoustique – ED 162

Spécialité : Mécanique des fluides

RESUME : L'étude du transfert de masse turbulent aux interfaces gaz-liquide est d'un grand intérêt dans de nombreuses applications environnementales et industrielles. Bien que ce problème soit étudié depuis de nombreuses années, sa compréhension n'est pas encore suffisante pour la création de modèles de transfert de masse réalistes (de type RANS ou LES sous maille), en particulier en présence d'une phase liquide à rhéologie complexe. Ce travail expérimental a pour but l'étude des aspects fondamentaux du transfert de masse turbulent à une interface plane horizontale entre du dioxyde de carbone gazeux et une phase liquide newtonienne ou non, agitée par une turbulence homogène quasi isotrope. Les milieux liquides non newtoniens étudiés sont des solutions aqueuses d'un polymère dilué à des concentrations variables et aux propriétés viscoélastiques et rhéofluidifiantes. Deux méthodes de mesure optiques permettant l'obtention du champ de vitesse de la phase liquide (SPIV) et de concentration du gaz dissout (I-PLIF) sont couplées tout en maintenant une haute résolution spatiale, afin de déduire les statistiques de vitesse et de concentration couplées dans les premiers millimètres sous la surface. Une nouvelle version de I-PLIF est développée pour les mesures en proche surface. Elle peut également s'appliquer dans différentes études de transfert de masse. La turbulence de fond est générée par un dispositif de grille oscillante. Les mécanismes de production et les caractéristiques de la turbulence sont étudiés. L'importance de la composante oscillante de la turbulence est discutée, et un phénomène d'amplification de l'écoulement moyen est mis en évidence. Les mécanismes du transfert de masse turbulent à l'interface sont finalement observés pour l'eau et une solution de polymère dilué à faible concentration. L'analyse conditionnelle des flux de masse turbulent permet de mettre en évidence les évènements contribuant au transfert de masse et de discuter de leur impact relatif sur le transfert total.

MOTS-CLÉS : Milieux non newtoniens, Turbulence de grille oscillante, Transfer de masse gaz-liquide, Mélange, PIV, PLIF

Laboratoire (s) de recherche : LMFA – Laboratoire de Mécanique des Fluides et d'Acoustique, UMR CNRS 5509

Directeur de thèse: Mahmoud EL HAJEM

Président de jury : Jean-Yves CHAMPAGNE

Composition du jury :

CHAMPAGNE, Jean-Yves	Professeur, INSA Lyon	Président du jury
HEBRARD, Gilles	Professeur, INSA Toulouse	Rapporteur
POLIDORI, Guillaume	Professeur, URCA, Reims	Rapporteur
HERLINA, Herlina	Dr. Ing., KIT, Karlsruhe	Examinatrice
EL HAJEM, Mahmoud	Maitre de Conférences, INSA Lyon	Directeur de thèse
SIMOENS, Serge	Directeur de Recherche, CNRS	Co-directeur de thèse